Durham University

Durham E-Theses

Characterising LINC complex roles in 3D epithelial migration and breast cancer metastasis

JAMES ROBERT CARTHEW

How to cite:

CARTHEW, JAMES ROBERT (2016) Characterising LINC complex roles in 3D epithelial migration and breast cancer metastasis. Doctoral thesis, Durham University.

Use policy

The full-text may be used and/or reproduced, and given to third parties in any format or medium, without prior permission or charge, for personal research or study, educational, or not-for-profit purposes provided that:

- a full bibliographic reference is made to the original source
- a https://etheses.durham.ac.uk/id/eprint/11453/ is made to the metadata record in Durham E-Theses
- the full-text is not changed in any way

The full-text must not be sold in any format or medium without the formal permission of the copyright holders.

Please consult the full Durham E-Theses policy for further details.

Academic Support Office, The Palatine Centre, Durham University, Stockton Road, Durham, DH1 3LE
e-mail: e-theses.admin@durham.ac.uk Tel: +44 0191 334 6107
https://etheses.durham.ac.uk

Durham University

School of Biological and Biomedical Sciences

Characterising *LINC* complex roles in 3D epithelial migration and breast cancer metastasis

James Robert Carthew

September 2015

A thesis submitted for the degree of Doctor of Philosophy

Declaration

The work described herein was carried out in the School of Biological and Biomedical Sciences, University of Durham between October 2011 and September 2015. All of the work is my own, except where specifically stated otherwise. No part has previously been submitted for a degree at this or any other university.

Statement of Copyright

The copyright of this thesis rests with the author. No quotations from it should be published without the prior written consent and information derived from it should be acknowledged.

Abstract

Cell migration is essential for the development of multicellular organisms; with disruptions in this process contributing to diseases such as cancer, neurological disorders and musculoskeletal diseases. The *LINC* (Linker of Nucleoskeleton and Cytoskeleton) complex is an evolutionary conserved proteinaceous structure, critical for maintaining proper cellular migration. This multifunctional complex provides a physical connection between the nuclear interior and the cytoskeleton, with disruptions stimulating loss of directed cell migration, compromised nuclear structure and abnormal cellular signalling. As it is also noted that the nucleus in many cells is the stiffest cellular component, it is suggested that *LINC* complex disruptions may be key in increasing the migration potential of cells through both *in vivo* and *in vitro* 3D environments.

This project aimed to investigate the roles of *LINC* complex disruptions on keratinocyte morphological and migratory behaviours in 2D, and both non-restrictive and space-restrictive 3D culture environments, through the application of dominant negative SUN1 mutants. Through extensive analysis, it was identified that these mutants exhibited altered cell-cell and cell-substratum attachment phenotypes, alongside increased nuclear heights. It was also demonstrated that the *LINC* disrupted mutants displayed a migration advantage in space-restricted 3D environments, which was attributed to a decrease in nuclear stiffness. Through fibroblast incorporation to the 3D scaffolds used, it was further shown that *LINC* disrupted keratinocytes displayed increased levels of differentiation markers, alongside increased cellular stacking phenotypes across scaffolds surface regions, potentially attributed to alterations in Hippo pathway signalling.

The migratory phenotypes observed in DN mutants closely resemble that of high-grade cancer cells, able to migrate through space-restrictive environments during metastasis. Comprehensive protein expression and localisation analysis across a range of breast cancer cell lines and tissues suggested that several *LINC* complex components display altered expression levels closely linked to cancer progression, most significantly a down-regulation of lower nesprin-1/-2 isoforms was identified. As following investigations later suggested Nup88 as an upstream regulator of nesprin-2, able to bind C-terminal regions, it's suggested that these phenotypes link closely to that observed in high-grade cancers.

Together, the data presented suggests that *LINC* complex disruptions increase migration potential of cells through restrictive 3D environments due to a decrease in nuclear stiffness, comparable to that observed across high-grade breast cancer cell lines.

Acknowledgments

I would like to start by acknowledging the BBSRC and Breast Cancer Now for funding this project, alongside Reinnervate Limited for providing the 3D scaffolds used throughout the project.

I would like to thank both of my supervisors Dr. Akis Karakesisoglou and Dr. Martin Goldberg for their tireless support and encouragement over the past four years. I would also like to thank Katherine O'Mahony for her endless enthusiasm in the lab keeping the atmosphere alive.

Outside of the lab group I'd like to thank all of lab 4, especially Elanor, Rosie, Dan, Kirsty and Becca for making the experience an enjoyable one. I would also like to thank all members of the ICBL lab, especially Miguel, Mattie, Rebecca, Simeon, and Pam for the endless fun in the lab over the past few years.

I would also like to thank Christine Richardson and Helen Grindley for all the help with both TEM and SEM over the past four years.

Outside of the university, I would like to thank all of Butlers MCR both past and present for keeping the year lively and giving me an excuse to forget about the thesis for a few hours every week.

I would also like to thank Rob and Carolyn Carthew for all of the help and support throughout the past four years. Finally I would like to thank Caitlin Langford for her endless patience in putting up with me for past few years, and endless words of encouragement throughout.

Publications arising from this work:

Papers

W. Lu, M. Schneider, S. Neuman, V. M. Jaeger, S. Taranum, M. Munck, S. Cartwright, C. Richardson, J. Carthew, K. Noh, M. Goldberg, A. A. Noegel, I. Karakesisoglou . "Nesprin interchain associations control nuclear size.," Cell Mol Life Sci, vol. 69 (20). pp. 3493-509, Oct 2012

J. R. Carthew, M. W. Goldberg, I. Karakesisoglou. (2015, in preparation) "The LINC complex; a regulator of nuclear shape and migration through both 2D and synthetic 3D environments"

J. R. Carthew, M. W. Goldberg, I. Karakesisoglou. (2015, in preparation) "The Loss of nesprin-2 C-terminal isoforms; a contributing factor to cancer metastasis"

J. R. Carthew, K. O'mahony, M. W. Goldberg, I. Karakesisoglou. (2015, in preparation) "Loss of the '*LINC*' between nucleoplasm and cytoplasm stimulates increased keratinocyte differentiation."

Book chapters

J. R. Carthew and I. Karakesisoglou. "Detection of diverse and high molecular weight nesprin-1 and nesprin-2 isoforms using western blotting" Springer Methods in Molecular Biology; The Nuclear Envelope (Accepted 2015, awaiting publication).

Oral presentations

J. R. Carthew, M. W. Goldberg, I. Karakesisoglou. (2015) "Deciphering *LINC* complex roles in nuclear stiffness and 3D cell migration." 7th Nuclear Envelope Disease and Chromatin Organisation Meeting (NEDCO).

Poster presentations

J. R. Carthew, M. W. Goldberg, I. Karakesisoglou. (2012) "Nup88, a novel nesprin-2 binding partner." 2012 British Biophysical Society Annual Conference, Durham, UK

J. R. Carthew, M. W. Goldberg, I. Karakesisoglou. (2013) "*LINC* complex roles on tissue formation *in vitro*" 23rd Wilhelm Bernhard Workshop on the cell nucleus Debrecen, Hungary

J. R. Carthew, M. W. Goldberg, I. Karakesisoglou. (2014) "Deciphering *LINC* complex roles in nuclear stiffness and 3D cell migration" 2nd Year Postgraduate Poster Presentation, Durham, UK

Table of Contents

Abstract i

Acknowledgments ii

Publications arising from this work: iii

Table of Contents iv

Table of Figures xiii

Table of Tables xxiv

Abbreviations xxv

1. Introduction 1

1.1 The LINC complex. 1

1.1.1 Components of the LINC complex. 2

1.2 Roles of the LINC complex in normal cell function. 17

1.2.1 LINC complex roles in maintaining nuclear architecture and correct nuclear movement. 17

1.2.2 LINC roles in force transmission and mechanotransduction across the NE. 22

1.2.3 The LINC complex displays functions in regulating signalling and chromatin anchorage across the NE. 25

1.3 Roles of the LINC complex in disease development. 28

1.3.1 LINC complex roles in neurodegenerative and musculoskeletal disease development. 29

1.3.2 Roles of the LINC complex in premature aging. 32

1.3.3 Roles of nesprin-3/-4 in disease development. 32

1.3.4 Roles of the LINC complex in cancer development. 35

1.4 Current 3D culture models are becoming increasingly more relevant to the in vivo situation. 36

1.4.1 Standard 2D cell culture imparts changes in gene expression, different to that found in vivo. 36

1.4.2 Current 3D culture models are becoming increasingly more biologically relevant. 37

1.5 Hypothesised Outcomes. 39

1.6 Thesis Overview. 39

2. Materials and Methods 42

2.1 Routine 2D cell culture. 42

2.1.1 Cell Lines: COS-7, WT HaCaT, HDF, SW480, SW620 and HeLa. 42

2.1.2 Cell Line: DN SUN1 expressing clonal HaCaT. 42

2.1.3 Cell Lines: MCF 10A and MCF 12A. 42

2.1.4 Cell Lines: MCF7, MDA-MB-231, T-47D and HCC-38. 43

2.1.5 Routine passaging and propagation of cells. 43

2.1.6 Passaging of MCF 10A and MCF 12A cell lines. 43

2.1.7 Cryopreservation of cells. 44

2.2 Scratch wound assay. 44

2.2.1 Growth in 2D culture. 44

2.2.2 Scratch wound assay. 44

2.2.3 Scratch wound assay analysis. 44

2.3 3D cell culture. 45

2.3.1 Scaffolds utilised. 45

2.3.2 Scaffold pre-treatment. 45

2.3.3 Preparation of cell suspensions for seeding scaffolds. 45

2.3.4 Seeding cells to the scaffolds. 45

2.3.5 Media changes. 46

2.3.6 Co-culture of fibroblasts and keratinocytes. 46

2.4 2D culture scaffolds. 47

2.4.1 Rhombic micro-pillar materials. 47
2.4.2 Polycarbonate inserts. 47
2.5 Cell counting. 47
2.5.1 Neubauer Improved Haemocytometer. 47
2.6 Plasmid preparation. 48
2.6.1 Bacterial transformation. 48
2.6.2 Plasmid purification. 48
2.7 Plasmid transfections. 48
2.7.1 Cellular transfection. 48
2.8 Sample Fixation. 50
2.8.1 2D monolayer cultures. 50
2.8.2 3D cultures. 50
2.9 Histological processing. 50
2.9.1 Dehydration and Embedding. 50
2.9.2 Sectioning. 51
2.10 Pathological samples. 51
2.11 Staining. 52
2.11.1 Haematoxylin and Eosin (H&E) staining. 52
2.11.2 Immunofluorescence staining of 2D monolayers. 52
2.11.3 Immunofluorescence staining of 3D paraffin embedded scaffolds. 54
2.11.4 Immunofluorescence of pathological sectioned breast tissue samples. 56
2.11.5 Super resolution microscopy staining. 57
2.12 Western Blotting. 57
2.12.1 Sample preparation: from cell culture to cell lysates. 57
2.12.1.1 2D Lysate production. 57
2.12.1.2 3D lysate production. 58
2.12.2 Sodium Dodecyl Sulphate Polyacrylamide Gel Electrophoresis (SDS-PAGE). 58

2.12.3 Tank (wet) western blot electro-transfer. 59

2.12.4 Membrane blocking and immuno-blotting. 59

2.13 Electron microscopy imaging. 62

2.13.1 Transmission electron microscopy (TEM) of 2D cultured samples. 62

2.13.2 Transmission electron microscopy (TEM) of 3D cultured samples. 63

2.13.3 Scanning electron microscopy (SEM) imaging. 64

2.14 Atomic force microscopy (AFM) imaging. 64

2.14.1 AFM under non-biological conditions. 64

2.14.2 AFM under biological conditions. 64

2.15 GST Pull-down. 65

2.15.1 GST-SR purification. 65

2.15.2 SR attachment to GST beads. 65

2.15.3 Cell lysate production and GST-Pulldown. 66

2.16 Förster resonance energy transfer (FRET) / fluorescence lifetime imaging microscopy (FLIM). 66

2.17 Statistical analysis. 67

3. The characterisation of *LINC* complex roles within 2D and 3D growth and migration. 68

3.1 Introduction. 68

3.1.1 LINC components function in maintaining directed cell migration, proliferation and cell signalling. 69

3.1.2 The growing field of 3D cell culture. 72

3.1.3 LINC complex roles in nuclear stiffness and cell migration. 74

3.2 Chapter Aims. 76

3.2.1 Objectives. 76

3.3 Results. 77

3.3.1 Disrupting the LINC complex stimulates altered 2D growth phenotypes in culture. 77

3.3.2 LINC complex disruption affects 2D directed cell migration. 91

3.3.3 DN HaCaT cells exhibit altered growth phenotypes within 3D culture to that of 2D culture. 93

3.3.4 Both Alvetex® scaffold and Alvetex® Strata environments produce cellular stresses not experienced in 2D culture systems. 120

3.3.5 SUN-KASH bridge disruption in keratinocytes increases 3D migration potential by decreasing nuclear stiffness. 123

3.3.6 SUN-KASH disruptions have variable effects on LINC associated protein organisation and expression patterns. 143

3.3.7 DN and WT HaCaTs display variable phenotypes when applied to alternate biomaterial models. 159

3.4 Summary of Experimental Findings. 164

3.4.1 DN SUN1 overexpression results in phenotypic abnormalities, including increased nuclear height, decreased cell-substratum attachment and reduced 2D migration in scratch-wound assays. 164

3.4.2 LINC complex disruption in HaCaT cells increases penetration into space-restrictive 3D culture environments. 166

3.4.3 LINC complex disruption in HaCaT keratinocytes significantly decreases nuclear stiffness. 169

3.4.4 DN SUN1 induced LINC complex disruption induces altered expression patterns for multiple LINC proteins, notably nesprin-1/-2 across both 2D and restrictive 3D culture conditions. 170

4. Assessing the roles of LINC complex disrupted keratinocytes using 3D fibroblast co-culture models 173

4.1 Introduction. 173

4.1.1 Keratinocytes and fibroblasts mediate numerous tissue functions in human skin through complex cross talk between dermal and epidermal regions. 174

4.1.2 Current In vitro models are able to accurately replicate the in vivo tissue conditions, allowing the assessment of cell migration and metastasis. 181

4.2 Chapter Aims. 183

4.2.1 Objectives. 183

4.3 Results. 184

4.3.1 Fibroblast introduction into space-restrictive and non-restrictive scaffolds reduces penetration potential of WT but not DN HaCaT cells. 184

4.3.2 DN HaCaT cells display increased cellular stacking across the surface of co-culture Strata Scaffold systems. 194

4.3.3 WT and DN HaCaT cells display varied expression patterns of differentiation markers across single and co-culture systems. 198

4.4 Summary of Experimental Findings. 207

4.4.1 Fibroblast inclusion into both Alvetex® Scaffold and Alvetex® Strata environments reduces migration potential of WT, but not DN HaCaT cells. 207

4.4.2 Inclusion of fibroblast cells into both scaffold systems stimulates increased cell stacking across surface regions for WT and DN HaCaT cells under air-liquid interface conditions. 209

4.4.3 DN HaCaT cells display increased expression of keratin 10, often associated with keratinocyte differentiation upon introduction to fibroblast co-culture systems. ..210

5. Assessing *LINC* protein roles in cancer progression and metastatic potential ...213

5.1 Introduction. 213

5.1.1 LINC roles in cancer development. 213

5.1.2 Current understanding of breast cancer development and metastatic mechanisms. 216

5.1.3 Current understanding of breast cancer migration and applications of 3D scaffold environments. 219

5.2 Chapter Aims. 222

5.2.1 Objectives. 222

5.3 Results. 223

5.3.1 LINC complex components vary drastically across low-, medium- and high-grade breast cancer cell lines. 223

5.3.2 Control, low- and high-grade breast cancer cell lines express differential migration potential through restrictive 3D environments. 261

5.3.3 Manipulating LINC complex connections stimulates altered cellular phenotypes in breast cancer cell lines. 269

5.3.4 Nesprin-2 C-terminal polyclonal antibody staining displays differential expression patterns between primary control, ER+ and triple negative breast cancers. 277

5.4 Summary of Experimental Findings. 286

5.4.1 LINC complex proteins display variable expression patterns across breast, cervical and colorectal cancer cell lines. 286

5.4.2 Variation in LINC protein expression is observed across breast cancer cell lines, alongside localisation defects in both cell lines and primary breast tissue samples; most significantly in low molecular weight nesprin-1/-2 isoforms. 287

5.4.3 LINC associated proteins including lap2α, E-cadherin and Nup88, alongside the protein chaperones HSP27, GFAP and CRYAB display variability in protein expression profiles across breast cancer cell lines. 289

5.4.4 High-grade MDA-MB-231 cells display significantly increased migration potential through space-restrictive 3D environments which is not reversible through nesprin-2 mini insertion. 290

6. Investigating binding potential between C-terminal regions of nesprin-2 and Nup88 294

6.1 Introduction. 294

6.1.2 Nup88, a potential nesprin-2 binding partner. 296

6.2 Chapter Aims. 299

6.2.1 Objectives. 299

6.3 Results. 300

6.3.1 Nesprin 2 CT domain displays strong co-localisation with the nuclear pore protein Nup88. 300

6.3.2 Nup88 and the C-terminal region of nesprin-2 display co-localisation within HaCaT cells across the NE. 301

6.3.3 The N2-SR fragment displays binding to Nup88 in GST-pulldown assays. ..309

6.3.4 A potential functional relationship exists between Nup88 and nesprin-2 in vitro. 311

6.3.5 Nup88 displays unique characteristics for nuclear pore proteins. 316

6.4 Summary of Experimental Findings. 319

6.4.1 C-terminal regions of nesprin-2 display close association to Nup88 in HaCaT cells through indirect immunofluorescence. 319

6.4.2 Interacting potential is displayed between Nup88 and the last 4 SRs preceding nesprin-2s C-terminal KASH domain. 321

6.4.3 Overexpression of pEGFP-Nup88 stimulates a reduction in nesprin-2 expression. 321

7. Summary and General Discussion 324

7.1 Thesis Background. 324

7.2 Summary of Experimental Findings. 326

7.2.1 LINC complex disruptions elicit phenotypic changes in cell/nuclear shape alongside 2D and 3D migration potential. 326

7.2.2 The incorporation of LINC disruptions into human keratinocyte cell lines increased penetration and differentiation potential when co-cultured in fibroblast-seeded scaffolds. 330

7.2.3 The loss of lower C-terminal retaining nesprin-1 and -2 isoforms is shown to correlate with breast cancer development. 334

7.2.4 Nup88 is an upstream regulator and binding partner of nesprin-2. 338

7.3 Theorised model - loss of correct nesprin localisation across the ONM leads to decreased nuclear stiffness and subsequent increased metastatic potential during cancer development. 340

7.4 Conclusions. 343

7.5 Future Work. 343

7.5.1 Further experiments arising from Chapter 3. 343

7.5.2 Further experiments arising from Chapter 4. 345

7.5.3 Further experiments arising from Chapter 5. 346

7.5.4 Further experiments arising from Chapter 6. 348

8. References.....349

Table of Figures

Figure 1.1: The *LINC* complex bridge across the NE…….3

Figure 1.2: SUN2-KASH binding overview……...9

Figure 1.3: Schematic of the major KASH proteins across mammals and C. elegans…...11

Figure 1.4: Schematic of the major cytoskeletal filament networks in mammalian systems……14

Figure 1.5: p.S143F progeria fibroblasts display normal nuclear morphology when expressing nesprin-2G……..19

Figure 1.6: *LINC* mediated mechanotransduction from the ECM to the nucleus…….23

Figure 1.7: Model of nesprin-2 and α-catenin roles in Wnt signalling……26

Figure 1.8: SUN2 proteome from control and EDMD/CMT patients……..31

Figure 1.9: Whole mount cochlea P14 displaying nuclear localisation in WT and nesprin-4 knockout OHCs……..34

Figure 2.1: Example images of Alvetex® scaffolds housed in their inserts…….46

Figure 3.1: Insertion of DN SUN1 results in the loss of KASH-SUN domain interactions……..68

Figure 3.2: Nuclear positioning in dividing cells and developing epithelium across multiple systems……....71

Figure 3.3: *TRITC-conjugated* Phalloidin and DAPI stained WT and DN HaCaT cells within a 70% confluence 2D culture……77

Figure 3.4: Phase contrast images of WT and DN HaCaT's at 60% confluence under standard growth conditions……...78

Figure 3.5: Differences in cell numbers observed between the DN and WT HaCaT cells in a defined 2D area of 100 μm^2……..79

Figure 3.6: Calculated cell area observed between the DN and WT HaCaT cells in 2D monolayer cultures…….80

Figure 3.7: Fluorescence images of WT and DN HaCaT Z-stacks……81

Figure 3.8: Example output from the Volocity® image analysis software from which nuclear height was calculated……..……..82

Figure 3.9: Average nuclear heights of WT and DN HaCaT cells measured at low, 20x objective, and high, 40x objective magnifications……83

Figure 3.10: Average nuclear volumes of WT and DN HaCaT cells measured at low, 20x objective, and high, 40x objective magnifications……83

Figure 3.11: Time course images of WT and DN HaCaT cells post trypsinisation, taken over an 18 h period……85

Figure 3.12: Vinculin stained images of WT and DN HaCaT cells post trypsinisation……87

Figure 3.13: Actin and vinculin stained WT and DN HaCaT cells 24 h post trypsinisation……...88

Figure 3.14: Actin stained WT and DN HaCaT cells post trypsinisation……...89

Figure 3.15: Numbers of nuclear cap positive (+ve) and negative (-ve) cells during cell-substratum attachment between WT and DN HaCaT cells……90

Figure 3.16: WT and DN HaCaT at 0 h, 24 h and 48 h time points post wounding……91

Figure 3.17: Wound closure of WT and DN HaCaT cells over 0 h, 24 h and 48 h time points……92

Figure 3.18: Differences between Alvetex® Scaffold and Alvetex® Strata materials……...94

Figure 3.19: H & E stained Alvetex® Scaffold 14 days after cell seeding……..95

Figure 3.20: Analysis method of cell penetration into Alvetex® Scaffold……...96

Figure 3.21: H & E staining of both WT and DN HaCaT cells in Alvetex® scaffolds at 2, 4, 6, 8, 10 and 14 day time points post seeding……97

Figure 3.22: Differences in Alvetex® scaffold penetration between WT and DN HaCaT cells over a 14 day period post-seeding……98

Figure 3.23: H&E stained Alvetex® Strata scaffolds 14 days after cell seeding……100

Figure 3.24: H&E staining of both WT and DN HaCaT cells in Alvetex® Strata scaffolds at 2, 4, 6, 8, 10 and 14 day time points post seeding……100

Figure 2.25: Differences in Alvetex® Strata scaffold penetration between WT and DN HaCaTs over a 14 days period post-seeding……..101

Figure 3.26: Migratory behaviour across the leading edge between WT and DN HaCaT cells in Strata® Scaffolds……103

Figure 3.27: Differences observed between the WT and DN HaCaT leading edge migration uniformity within the restrictive Strata scaffolds 6 days post seeding……103

Figure 3.28: H&E staining of WT HaCaT, and DN HaCaT cells grown at the air-liquid interface for 8 days in the Strata scaffold……105

Figure 3.29: H&E stained DN HaCaT cells grown at the air interface in restrictive Strata Scaffolds compared with human epidermis…….....106

Figure 3.30: Images of DN HaCaT cells across surface regions of Strata scaffolds……107

Figure 3.31: Fluorescence images displaying both WT and DN HaCaTs in the Alvetex® scaffold after 8 days at the air interface……109

Figure 3.32: Fluorescence images displaying both WT and DN HaCaTs in the Alvetex® Strata after 8 days at the air interface……..111

Figure 3.33: SEM images displaying WT and DN HaCaT cells within Alvetex® Strata after 14 days of growth……113

Figure 3.34: TEM images of WT and DN HaCaT cells in various regions of the Strata® Scaffolds……115

Figure 3.35: TEM images depicting assessment criteria for cytoplasmic distribution analysis……..116

Figure 3.36: Percentage cytoplasmic distribution across WT and DN HaCaT cells during migration through restrictive interconnecting windows……..117

Figure 3.37: TEM images depicting the criteria for Hourglass or Constricted phenotypes……118

Figure 3.38: Nuclear phenotypes observed in WT and DN HaCaT cells during migration through restrictive interconnecting windows……119

Figure 3.39: TEM images displaying cell indentations and keratin accumulation…….121

Figure 3.40: TEM images showing cytoskeletal accumulation across the NE upon restrictive interconnect migration……...122

Figure 3.41: Images displaying 14 day grown WT and DN HaCaT cells in Alvetex® Scaffold and Alvetex® Strata……..124

Figure 3.42: Image series displaying assessment criteria for calculating nuclear circularity in various scaffold regions……..125

Figure 3.43: : Differences observed between nuclear circularity index of WT and DN HaCaT cells across surface and central Alvetex® Strata regions…….127

Figure 3.44: Differences observed between nuclear circularity index of WT and DN HaCaT cells across surface and central Alvetex® Scaffold regions……..127

Figure 3.45: Differences observed between nuclear circularity index of WT HaCaT cells across surface and central Alvetex® Strata and Alvetex® Scaffold regions……...128

Figure 3.46: Differences observed between nuclear circularity index of DN HaCaT cells across surface and central Alvetex® Strata and Alvetex® Scaffold regions……...128

Figure 3.47: Image series displaying WT and DN HaCaTs incubated in both normal growth media and growth media + 640 mM Sucrose…….132

Figure 3.48: Nuclear circularity across WT and DN HaCaT cells following osmotic stress……..133

Figure 3.49: Normalised nuclear circularity across each sucrose concentration plotted using ‘R’ ……..……134

Figure 3.50: AFM height maps for WT and DN HaCaT cells under non-biological conditions……..136

Figure 3.51: Phase contrast, height map and Young’s Modulus analysis for both WT and DN HaCaT’s under biological conditions……..137

Figure 3.52: Calculated young’s moduli across three selected cellular regions of WT and DN HaCaT cells……138

Figure 3.53: Observed compression output data following biological AFM analysis……140

Figure 3.54: TEM images displaying measurement techniques used to assess nuclear envelope to plasma membrane distances……141

Figure 3.55: Calculated distance between nuclear envelope and plasma membrane in WT and DN HaCaT cells……142

Figure 3.56: Super resolution images of *TRITC-conjugated* Phalloidin staining in WT and DN HaCaT cells……144

Figure 3.57: Super resolution images of lamin A/C staining within WT and DN HaCaT cells……146

Figure 3.58: Super resolution images of lamin B staining within WT and DN HaCaT cells……147

Figure 3.59: Western blot analysis showing equal loading marker expression across our samples……149

Figure 3.60: Western blot data for each INM protein analysed across our samples.....151

Figure 3.61: Western blot data for nesprin-1/-2 ABD analysed across our samples……153

Figure 3.62: Western blot data for each *LINC* associated proteins analysed across our samples……154

Figure 3.63: Western blot data for tubulin expression analysed across our samples…..155

Figure 3.64: Western blot data for stress signalling markers analysed across our samples……157

Figure 3.65: H&E images of polycarbonate scaffolds 3 days post-seeding with WT and DN HaCaT cells……..159

Figure 3.66: High magnification images of 3 day H&E stained polycarbonate scaffolds seeded with WT and DN HaCaT cells……..160

Figure 3.67: Collated data displaying height differences between WT and DN HaCaT cells across the surface of polycarbonate scaffolds alongside observed cellular protrusions per 100 µm across the length of scaffold……161

Figure 3.68: Immunofluorescence images of both WT and DN HaCaT cells adhered to micro-pillared materials……...162

Figure 3.69: Collated data displaying calculated nuclear circularity index values in conventional 2D culture and micro pillared materials for WT and DN HaCaT cells……..163

Figure 4.1: Schematic of the stages of epidermal differentiation in human skin……174

Figure 4.2: Experimental design for the fibroblast + HaCaT co-culture penetration assessment in both restrictive and non-restrictive scaffolds……185

Figure 4.3: Non-restrictive Alvetex® scaffold, and restrictive Alvetex® Strata environments seeded with 250,000 HDF cells and grown for 14 days under submerged culture conditions……..186

Figure 4.4: H&E staining of both WT and DN HaCaT cells in Alvetex® co-cultures at 2, 4, 6, 8, 10 and 14 day time points post HaCaT seeding……187

Figure 4.5: H&E staining of both WT and DN HaCaT cells within Strata® co-cultures at 2, 4, 6, 8, 10 and 14 day time points post HaCaT seeding……188

Figure 4.6: Immunofluorescence staining of DAPI and vimentin in Alvetex® and Strata® scaffolds for both WT and DN HaCaT cells at the 14 d time point……..190

Figure 4.7: Alvetex® Scaffold co-culture penetration between WT and DN HaCaT's over a 14 days period post-seeding……..191

Figure 4.8: Alvetex Strata® co-culture penetration between WT and DN HaCaT's over a 14 days period post-seeding. ……...192

Figure 4.9: Differences between WT and DN HaCaT penetration through Alvetex® Scaffold and Alvetex® Strata scaffolds, under single and co-culture conditions over a 14 days period post-seeding……193

Figure 4.10: H&E stained Alvetex® and Strata® co-culture scaffolds after 8 days at the air-liquid interface……..196

Figure 4.11: Measurement technique used for the assessment of cellular stacking above the scaffolds seeding surface……197

Figure 4.12: Immunofluorescence staining of WT HaCaT cells for K14 and DAPI across single and co-culture, Alvetex® Scaffold and Alvetex® Strata systems……...199

Figure 4.13: Immunofluorescence staining of DN HaCaT cells for K14 and DAPI across single and co-culture, Alvetex® Scaffold and Alvetex® Strata systems……...200

Figure 4.14: Immunofluorescence staining of WT HaCaT cells for K10 and DAPI across single and co-culture, Alvetex® Scaffold and Alvetex® Strata systems……...201

Figure 4.15: Immunofluorescence staining of DN HaCaT cells for K10 and DAPI across single and co-culture, Alvetex® Scaffold and Alvetex® Strata systems……...202

Figure 4.16: Immunofluorescence staining of both WT and DN HaCaT cells for E-cadherin, YAP and DAPI across co-culture Alvetex® Scaffold systems……..204

Figure 4.17: Immunofluorescence staining of WT and DN HaCaT cells for E-cadherin, YAP and DAPI across co-culture Strata® scaffold systems……..205

Figure 5.1: Pathological examples of normal breast tissue and high grade triple negative breast tissue……..217

Figure 5.2: Pathological examples of each stage in breast cancer development, alongside associated severity of each stage……218

Figure 5.3: Western blot data for *LINC* complex proteins across a range of both cancerous and non-cancerous cell lines……..224

Figure 5.4: Coomassie Blue staining of breast cancer cell lines following SDS-PAGE…225

Figure 5.5: Western blot data for equal loading markers across breast cancer cell lines……226

Figure 5.6: *TRITC-conjugated* phalloidin stained MCF 10A, MCF7 and MDA-MB-231 cells displaying F-actin organisation……..228

Figure 5.7: *TRITC-conjugated* phalloidin stained MCF 10A, MCF7 and MDA-MB-231 cells displaying F-actin organisation at high magnifications……..229

Figure 5.8: β-tubulin stained MCF 10A, MCF7 and MDA-MB-231 cells displaying microtubule organisation……230

Figure 5.9: Cytokeratin stained MCF 10A, MCF7 and MDA-MB-231 cells displaying cytokeratin organisation……..231

Figure 5.10: Western blot staining for cytoskeletal proteins across breast cancer cells..232

Figure 5.11: SUN1 stained MCF 10A, MCF7 and MDA-MB-231 cell lines displaying inner nuclear envelope organisation……...235

Figure 5.12: SUN2 stained MCF 10A, MCF7 and MDA-MB-231 cell lines displaying inner nuclear envelope organisation……...236

Figure 5.13: Lamin A/C stained MCF 10A, MCF7 and MDA-MB-231 cell lines displaying inner nuclear envelope organisation……237

Figure 5.14: Lamin B stained MCF 10A, MCF7 and MDA-MB-231 cell lines displaying inner nuclear envelope organisation……238

Figure 5.15: Emerin stained MCF 10A, MCF7 and MDA-MB-231 cell lines displaying inner nuclear envelope emerin organisational differences……..239

Figure 5.16: Western blot analysis of INM proteins across breast cancer cell lines…… 240

Figure 4.17: Nesprin-1 (ABD) stained MCF 10A, MCF7 and MDA-MB-231 cell lines……242

Figure 5.18: Western blot data for Nesprin-1 C-terminal KASH and N-terminal ABD domains across breast cancer cell lines……..244

Figure 5.19: Nesprin-2 C-terminal stained MCF 10A, MCF7 and MDA-MB-231 cell lines displaying isoforms containing the C-terminal KASH domain……..245

Figure 5.20: Nesprin-2 N-terminal stained MCF 10A, MCF7 and MDA-MB-231 cell lines……246

Figure 5.21: Nesprin 2 C-terminal stained MCF 10A, MCF7 and MDA-MB-231 cell lines……247

Figure 5.22: Pixel intensity map of Nesprin-2 C-terminal stained MCF 10A, MCF7 and MDA-MB-231 cell lines……248

Figure 5.23: Western blot data for Nesprin-2 C-terminal KASH and N-terminal ABD domains across breast cancer cell lines……..249

Figure 5.24: Nesprin-3 stained MCF 10A, MCF7 and MDA-MB-231 cell lines……..251

Figure 5.25: Western blot data for nesprin-3 and nesprin-4 expressions across breast cancer cell lines……252

Figure 5.26: Western blot data for *LINC* associated proteins and known cancer marker expression across breast cancer cell lines……..254

Figure 5.27: Mab414 stained MCF 10A, MCF7 and MDA-MB-231 cell lines……256

Figure 5.28: Nup88 stained MCF 10A, MCF7 and MDA-MB-231 cell lines……257

Figure 5.29: Western blot data for NPC protein expressions across breast cancer cell lines……258

Figure 5.30: Western blot data for heat shock protein expressions across breast cancer cell lines……260

Figure 5.31: Western blot data for heat shock protein expressions across breast cancer cell lines……260

Figure 5.32: Cell penetration of MCF 10A (Control), MCF7 (Low-grade) and MDA-MB-231 (High-grade) cancer cell lines through restrictive Strata scaffold environments……263

Figure 5.33: Scanning electron microscopy images of MDA-MB-231 and MCF7 breast cancer cell lines……265

Figure 5.34: TEM images of MDA-MB-231 and MCF7 breast cancer cell lines displaying mitochondrial positioning during restrictive interconnect migration……266

Figure 5.35: TEM images of MDA-MB-231 and MCF7 breast cancer cell lines displaying nuclear deformities during restrictive interconnect migration……267

Figure 5.36: Quantification of MDA-MB-231 and MCF7 NE dilations pre and post restrictive interconnect migration……...268

Figure 5.37: TEM images of MDA-MB-231 and MCF7 breast cancer cell lines displaying cellular indentations during restrictive interconnect migration……..269

Figure 5.38: Fluorescence images displaying transfection efficiency across MCF7 and MDA-MB-231 cell lines……272

Figure 5.39: Images displaying hanging drop experimental analysis following *LINC* complex manipulation……..273

Figure 5.40: Quantification of restrictive scaffold penetration between MCF7, MCF7 + pEGFP, MCF7 + DN KASH, MCF7 + DN SUN1, MDA-MB-231, Mda-MB-231 + pEGFP and MDA-MB-231 + nesprin-2 mini, 3 days post seeding……274

Figure 5.41: LIVE/DEAD® Red Dead staining within MCF7 cells under varying cell G418 concentrations, to assess drug concentration required to kill 100% of cell in 7 days……276

Figure 5.42: Nuclear analysis across MCF7 cells transfected with GFP signal peptide, DN SUN1 and nesprin-2 mini……..……..277

Figure 5.43: Control pre-menopausal breast tissue stained for nesprin-2 C-terminal and actin……279

Figure 5.44: Control pre-menopausal breast tissue stained for nesprin-2 C-terminal and p63……..281

Figure 5.45: ER+ pre-menopausal breast tissue stained for nesprin-2 C-terminal and actin……283

Figure 5.46: Triple negative pre-menopausal breast tissue stained for nesprin-2 C-terminal and actin……284

Figure 5.47: Pixel topology analysis of nesprin-2 C-terminal domain staining and actin staining within non-cancerous breast tissue and ER+ cancerous breast tissue……285

Figure 6.1: Domain architecture of the largest nesprin family members in humans…….302

Figure 6.2: Nesprin-2G and N2-SR structural features, alongside NT and CT antibody binding regions……..304

Figure 6.3: Immunofluorescence staining against nesprin-2 C-terminal domain, Nup88 and DAPI. ……..308

Figure 6.4: Immunofluorescence staining against nesprin 2 C-terminal domain and Nup88 within HaCaT cells across the NE surface……...309

Figure 6.5: Immunofluorescence and peak intensity analysis between nesprin-2 regions and Nup88/Nup214/Mab414……..310

Figure 6.6: Percentage co-localisation data for each co-stain conducted……..311

Figure 6.7: FRET FLIM screenshot displaying analysis output of HaCaT nuclei stained for Nup88 and nesprin 2 C-terminal regions……313

Figure 6.8: Immunofluorescence staining against Nup88, myc-SR and merge…….314

Figure 6.9: Immunofluorescence staining of Nesprin-2 C-terminus and Nesprin-2 N-terminus in HaCaT cells……..315

Figure 6.10: Western blot staining against Nup88, GFP and GST for the GST Pulldown……317

Figure 6.11: Immunofluorescence staining displaying for control spGFP, pEGFP Nup88, myc-SR, nesprin 2 RNAi and Nup88 siRNA……319

Figure 6.12: Displays collated data of phenotypes observed in HaCaT cells 3 days post transfection with pEGFP Nup88……320

Figure 6.13: Western blot analysis of HaCaT transfections. Displays western blot staining observed……322

Figure 6.14: Immunofluorescence staining of Nup88, β-tubulin, β-actin, ER and KLC1 in HaCaT cells……..324

Figure 7.1: Theorised model for the roles of lower KASH containing nesprin-1/-2 isoforms situated across the ONM in the maintenance of nuclear architecture…….341

Table of Tables

Table 2.1: Plasmids used, alongside vectors and encoded antibiotic resistance……49

Table 2.2: Primary antibodies used for 2D immunofluorescence staining, with suppliers and working concentrations……..….53

Table2.3: Secondary antibodies used for 2D immunofluorescence staining, with suppliers and working concentrations…….…….54

Table 2.4: Primary antibodies utilised for 3D immunofluorescence staining, with suppliers and working concentrations……..55

Table 2.5: Secondary antibodies utilised for 3D immunofluorescence staining, with suppliers and working concentrations…….……55

Table 2.6: Primary antibodies utilised for 3D immunofluorescence staining of pathological samples, with suppliers and working concentrations……..……56

Table 2.7: Primary antibodies utilised for western blot detection, with suppliers and working concentrations…….…….60

Table 2.8: Secondary antibodies utilised western blot detection, with suppliers and working concentrations……..62

Table 3.1: Summarised data of western blot analysis across WT and DN HaCaTs in both 2D and 3D culture environments……...……158

Table 5.1: breast cancer staging categories through tumour development……...181

Abbreviations

% … percentage
°C … degrees Celsius
µ … micro
2D … 2-dimensional
3D … 3-dimensional
ADLD … autosomal dominant leukodystrophy
AFM … atomic force microscopy
AMC … arthrogryposis multiplex congenita
APS … ammonium persulfate
ARCA1 … autosomal recessive cerebellar ataxia
ASD … autosomal spectrum disorder
BDMA … benzyle dimethylamine
BMP … bone morphogenetic protein
BSA … bovine albumen
CH … calponin homology
CMD … congenital muscular dystrophy
CNS … central nervous system
CRM1 … chromosome region maintenance 1
CTGF … connective tissue growth factor
d … days
DAPI … 4',6-diamidino-2-phenylindole
DDSA … dodecenyl succinic anhydride
DMEM … Dulbecco's Modified Eagles Medium
DMSO … Dimethyl Sulfoxide
DN … dominant negative
DNA … deoxyribonucleic acid
DRF … diaphanous related formin
DRF … diaphanous related formin
dsDNA … double stranded DNA
EBS … epidermolysis bullosa simplex
ECL … enhanced chemiluminescence
ECM … extra cellular matrix
EDMD … Emery Dreifuss muscular dystrophy
EDTA … ethylenediaminetetraacetic acid
EGF … epidermal growth factor

EGTA … ethylene glycol tetraacetic acid
EMT … epithelial-mesenchymal transition
ER … endoplasmic reticulum
ER- … estrogen-receptor negative
ERK … extracellular signal-regulated kinase
F-actin … filamentous actin
FAK … focal adhesion kinase
FBS … Foetal Bovine Serum
FCS … foetal calf serum
FHOD … formin homology domain
FLIM … fluorescence lifetime imaging microscopy
FRET … Förster resonance energy transfer
GFP … green fluorescent protein
GST … glutathione S transferase
h … hours
H&E … hematoxylin and eosin
HEPES … (4-(2-hydroxyethyl)-1-piperazineethanesulfonic acid)
HGPS … Hutchinson-Guilford progeria syndrome
HRP … horseradish peroxidase
IF … intermediate filaments
IHC … Inner hair cell
IL … interleukin
INM … inner nuclear membrane
IPTG … Isopropyl β-D-1-thiogalactopyranoside
KASH … Klarsicht ANC-1 and *SYNE*-Nesprin-1/-2 homology
KGF … keratinocyte growth factor
KLC1 … kinesin light chain 1
kPa … kilopascals
LINC … linker of nucleoskeleton and cytoskeleton
-m … meter
m- … milli
-M … molar
MEF … mouse embryonic fibroblast
min … minutes
MMP … matrix metalloproteinase
MoDC … monocyte-derived dendritic cells
mRNA … messenger RNA

MT … microtubules

MTOC … microtubule-organising centre

n … nano

NE … nuclear envelope

NELS … nuclear envelope localisation sequence

Nesprin … nuclear envelope spectrin repeat protein

NFκβ … nuclear factor κβ

NLS … nuclear localisation sequence

NMIIB … non-muscle myosin IIB

NPC … nuclear pore complex

nS … nanosecond

Nup … nucleoporin

OHC … outer hair cell

ONM … outer nuclear membrane

PA … polyacrylamide

PBS … phosphate buffer saline

PEG … poly(ethylene glycol)

PFA … paraformaldehyde

PIC … protease inhibitor cocktail

PIPES … piperazine-N,N′-bis(2-ethanesulfonic acid)

PLGA … poly(L-lactic-co-glycolic acid)

PMSF … phenylmethanesulfonylfluoride

pN … Piconewton

PNS … perinuclear space

PR- … progesterone-receptor negative

ps … Pico seconds

RNA … ribonucleaic acid

RNAi … RNA interference

rpm … revolutions per minute

RT-PCR … real time polymerase chain reaction

SDS … sodium dodecyl sulfate

SDS-PAGE … sodium dodecyl sulphate polyacrylamide gel electrophoresis

shRNA … small hairpin RNA

siRNA … small interfering RNA

SP … signal peptide

SR … spectrin repeat

ssDNA … single stranded DNA

SUMO … small ubiquitin-related modifier

SUN … Sad1 and UNC-84 homology

TAN … transmembrane actin associated nuclear

TEMED … tetramethylethylenediamine

temp … temperature

TGF … transforming growth factor

TNF … tumour necrosis factor

TRITC … Tetramethylrhodamine

TUNEL … terminal deoxynucleotidyl transferase dUTP nick end labelling

U- … units

V … volts

WT … wildtype

YAP … yes associated protein

α … alpha

β … beta

η … eta

1. Introduction

1.1 The LINC complex.

The maintenance of cell and nuclear architecture is key in maintaining normal cellular function. One key element which contributes to the maintenance of cell architecture is the cytoskeletal network, able to provide a physical link between the extra cellular matrix (ECM) and the genome through associated nuclear envelope (NE) proteins. The maintenance of nuclear architecture however is influenced heavily by its NE, consisting of a double lipid bilayer separating the nuclear interior from the cytoplasm. This compartmentalisation of the nuclear interior enables the separation of transcription and translation within eukaryotic systems, allowing the formation of a highly regulated mechanism to control gene expression [1]. The NE is an extension of the endoplasmic reticulum (ER), consisting of an inner (INM) and outer nuclear membrane (ONM), uniformly separated by the perinuclear space (PNS) of a ~50 nm width. Both the INM and ONM are fused at the nuclear pore complexes (NPC), through which macromolecular trafficking between the nuclear and cytoplasmic regions occurs [2, 3]. Further evidence is also available suggesting NPCs are not the only methods for the transport of cargoes in and out of the nucleus, with some exceptionally large nuclear cargoes able to move across the PNS through vesicular transport methods, similar to the nuclear egresses employed by herpes viruses. [4, 5].

Communication between nuclear and cytoplasmic compartments has long been known as a crucial cellular function [6]; however, understanding the mechanisms by which this physical connection enables cellular feedback is currently a growing area of interest. Mechanical coupling of the nucleus to the cytoskeleton can influence multiple cellular processes, including nuclear positioning, force transduction and cell signalling pathways [7, 8, 9]. The correct positioning of nuclei is of vital importance, especially in neuronal and muscle cell types, suggesting that this nuclear-cytoskeleton link could provide a mechanism to push and pull nuclei [10]. Forming a physical connection between the nuclear and cytoplasmic regions provide further potential for mechanotransduction across the NE, in which signal transduction from plasma membranes as a result of external stimuli can elicit a change in gene activation levels [11]. Due to this wide ranging functionality, potential roles of this nucleoskeleton-cytoskeleton coupling has been further

investigated in the onset of disease development, including muscular dystrophies, premature aging and laminopathies [12, 13].

These described connections between nucleoskeletal and cytoskeletal components are formed through Linker of Nucleoskeleton and Cytoskeleton (*LINC*) complexes [14, 15], characterised by *SUN-KASH* perinuclear interactions. The INM-resident Sad1 and UNC-84 (*SUN*) protein spans the perinuclear space, interacting with ONM-resident Klarsicht ANC-1 and *SYNE*-Nesprin-1/-2 homology (*KASH*) proteins, helping to establish a physical bridge between INM and ONM.

1.1.1 Components of the LINC complex.

The *LINC* complex is widely recognised as the major NE component able to provide the mechanical links between the nucleus and cytoskeletal network, comprising of ONM KASH domain proteins and INM SUN proteins (*Figure 1.1*). The KASH domain projects into the NE lumen, where it interacts with SUN domains. This *SUN-KASH* interaction helps to anchor KASH proteins to the NE, preventing them from diffusing into the adjoining ER. The ONM KASH proteins interact with a range of cytoskeletal components, physically tethering the nucleus to the cytoplasmic compartment [15, 16], whereas the SUN proteins physically interact with INM proteins networks such as the nuclear lamina and chromatin components [17, 18]. This complex of proteins therefore establishes a physical bridge between the cytoskeletal and nucleoskeletal networks. The formation of this two membrane adhesive assembly of proteins is capable of transmitting force across the NE, providing function in maintaining centrosome-nuclear interactions, nuclear architecture, signal transduction, DNA repair and chromosome migration [14]. This therefore suggests that the *LINC* complex must be a dynamic protein network of highly ordered protein interactions, allowing the transmission of multiple signal transductions from a variety of cytoskeletal components to the nuclear interior.

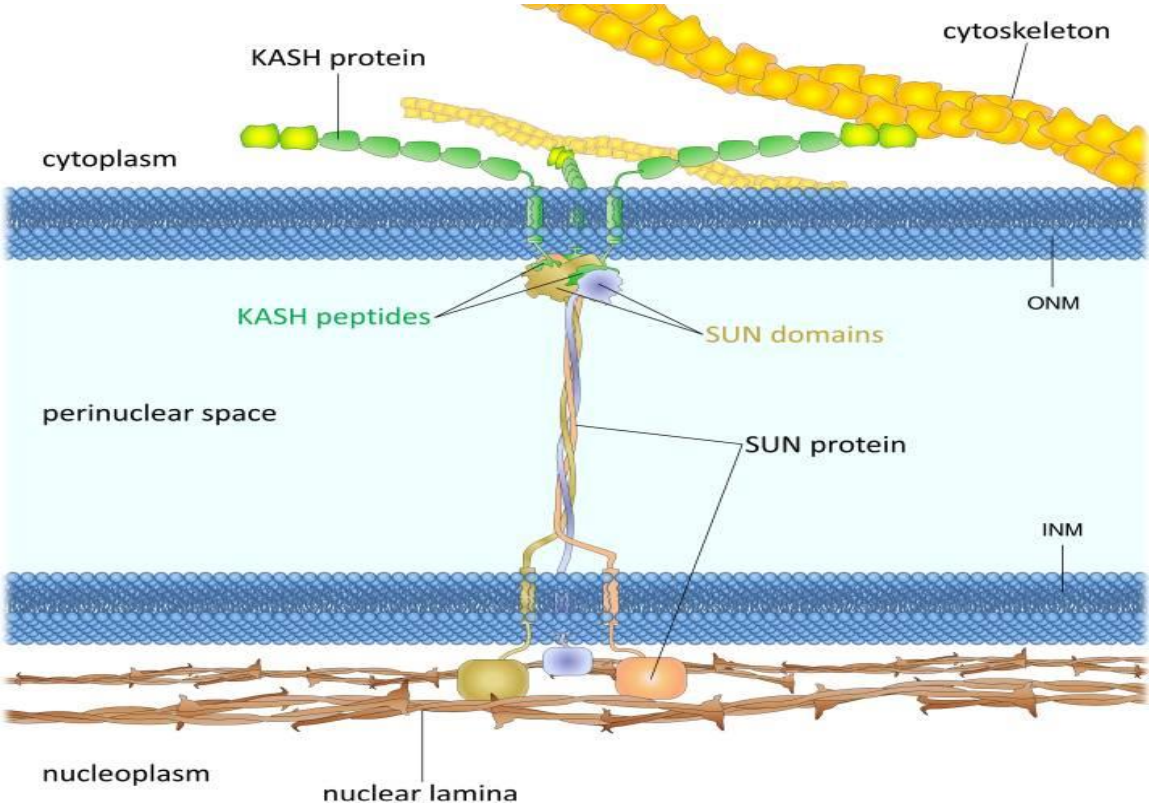

***Figure 1.1**: The LINC complex bridge across the NE; comprising of SUN and KASH interactions within the perinuclear space, alongside associated cytoskeletal and nucleoskeletal networks. [15].*

1.1.1.1 The nuclear lamina.

To efficiently position and move the nucleus through the cell, the *LINC* complex must be anchored so that the force exerted by cytoskeletal components can be transmitted directly to the nucleus. This anchoring is established through SUN interactions across the INM with nuclear lamins, composed of type V intermediate filaments (IFs), able to self-associate to form parallel coiled-coil homodimers. These homodimers then cross link, forming a higher ordered filament network across the INM (the nuclear lamina). The major components of this nuclear lamina are the A- and B-type lamin proteins, sharing similar structural homology including a central α-helical rod domain, flanked by non-helical, globular domains situated at each terminus [19].

B-type lamins, including lamin B1 and lamin B2, are encoded by the *LMNB1* and *LMNB2* genes respectively. It is interesting to note that limited mutations in B-type lamins are observed across a range of diseases, however, with implications in the development of adult onset autosomal dominant leukodystrophy (ADLD) and more recently the

development of neural tubes in spina bifida patients [20, 21], it is becoming increasingly evident that these proteins do in fact play critical roles in cellular functions. Of further interest is current evidence implicating a potential role for B-type lamins in the development of a number of cancers [22, 23]. In breast cancer for example, the decreased expression of *LMNB1* has been associated to poor patient prognosis [24], and further evidence suggests that overexpression of lamin B1 is associated with low grade differentiation in pancreatic cancers [25]. Of importance in this final study however, is the suggestion of lamin B1 for use as a potential therapeutic target against cancer progression. It was shown that the activity of the anti-cancer drug betulinic acid appears to down regulate lamin B1 as part of its anti-cancer effects. However thus far it is not known whether the down regulation of lamin B1 was a direct result of the anti-cancer effects, or a resulting side effect of drug action.

A-type lamins however, are encoded by a single gene, *LMNA*, which undergoes alternative splicing to generate the major lamins, types A and C, which are both ubiquitously expressed and developmentally regulated [26]. As lamin A/C are considered key in the maintenance of nuclear architecture across many cell types [27], mutations in the *LMNA* gene resulting in altered expression patterns of lamin A/C have been implicated across a wide range of human diseases, collectively known as 'laminopathies' [28].

These variable lamin sub-types have been shown as contributing factors in nucleoplasmic anchorage of *LINC* complex components through multiple methods. Initial investigations were able to discern that the carboxyl terminus of lamin A was able to bind with SUN1 through yeast two hybrid systems, whereas binding affinity with lamin B and C sub-types were shown to be very weak [29]. Further to this, Östlund *et al.* helped identify that SUN1 and SUN2 mobility across the INM was increased in fibroblast cells derived from lamin A knock-out mice [30]. Using *LMNA* knockout mice ($LMNA^{-/-}$), further investigations into actin-dependant nuclear movement in mouse embryonic fibroblasts (MEFs) suggested that upon lamin A loss across the INM, Nesprin-2G-SUN dependant transmembrane actin-associated nuclear (TAN*)* line orientation and anchoring was impaired [31]. This suggests that the loss of A-type lamin proteins stimulated a decreased actin binding potential across the NE through the potential loss of *LINC* connections.

Interestingly, it is suggested that lamin A binding is not essential for the correct localisation of SUN proteins to the INM, suggesting that further protein interactions must be involved in *LINC* complex anchoring to the nucleoplasmic network [32]. It was shown that limited localisation defects of SUN1 were present in COS7 cells lacking A-type, or A/B-type lamins [32]. Alongside this, SUN2 localisation was seen to be minimally miss

localised to the ER in lamin A and C deficient HeLa cells [33], suggesting alternate protein interactions aside from those displayed by lamins are contributing to *LINC* anchorage across the NE. Further mouse models have supported this claim that lamin associations are not crucial to the maintenance of *LINC* NE anchoring, by which it was observed that lamin A deficient mice were able to develop normally through early stages of development [34]. Subsequent postnatal growth however, was severely retarded, displaying the development of muscular dystrophy [34].

Potential suggestions as to alternate protein interactions involved in *LINC* complex anchoring to the NE comes from further mouse models, suggesting that B-type lamins, despite their weak interactions with SUN proteins, may be a key component. It was shown that lamin B1, lamin B2, nesprin-1/-2 and SUN1/2 deficient mice all expressed similar defects in neuronal migration [35, 36, 37], suggesting roles for lamin B in anchoring *LINC* complex components during neuronal development. These findings further suggest differential roles for lamin proteins in maintaining NE functionality, whereby A-type lamin components may provide the physical connections between the nucleoskeleton and the cytoskeleton, whereas B-type lamins may contribute to maintaining more specific *LINC* complex functions, such as maintaining nuclear stiffness [38].

Alongside lamin interactions with SUN proteins, further evidence suggests direct interactions also exist with nesprin-1 and nesprin-2 across two conserved spectrin repeats (SRs) localised to nesprin C-terminal regions [39, 40]. This direct interaction however is not suggested to influence the anchoring of *LINC* components to the nucleus, as nesprin-2G localisation across the ONM is not seen to be disrupted upon A-type lamin absence [41]. This however, does suggest further potential roles for smaller nesprin isoforms situated across the INM in lamin associated roles, such as chromatin organisation and maintaining nuclear integrity [42].

1.1.1.2 Lamin associated proteins.

Alongside the wide ranging functionality of lamin proteins, their interactions with further associated proteins provide a high degree of complex functionality within the cell. Of these associated proteins, the A-type lamin associated emerin and samp1 (NET5) have been implicated in *LINC* anchoring to the NE. Through analysing the localisation of samp1 deletion mutants, it has been shown that the samp1 localises to the INM through its cysteine rich N-terminal domain, comprising of four conserved CxxC motifs with the

potential to form Zinc fingers [43]. Its INM localisation has been shown to depend upon A-type lamin presence [44]. Initially, it was shown that samp1 displayed binding affinity to SUN1 and emerin across the INM, with post-translational silencing of samp1 in HeLa cells displaying a loss of emerin localisation across the INM, suggesting roles form samp1 in emerin localisation at the NE [43]. Subsequent investigations further displayed interacting potential with SUN2, lamin A and lamin C across the INM, however, correct localisation of these proteins was not dependent on samp1.

It was further highlighted that for correct TAN line formation to occur, samp1 was required across the NE, mediated through the further interacting potential with nesprin-2G and SUN2 during MEF migration [44]. In this study, it was suggested that samp1 helped to reinforce TAN line anchorage across the NE through providing further binding sites for SUN2 alongside A-type lamins.

Emerin is a further lamin associated protein with implicated roles in *LINC* complex anchoring. Emerin consists of an N-terminal nucleoplasmic domain and a C-terminal transmembrane domain, found localised to the INM and the ONM (where it binds MRS and the centrosome). Upon synthesis of the completed emerin protein, its small size allows it to freely diffuse into the nucleus through NPCs whilst remaining membrane anchored [45]. Once inside the nucleus, emerin binds to A-type lamins, shown to be crucial to the efficient localisation of emerin to the INM, as cells lacking A-type lamins express increased emerin mobility through the NE and the ER [46]. The ubiquitous expression of emerin across multiple cell types has been linked to its role in numerous cell functions, including regulating gene expression, cell signalling and nuclear architecture [47, 48, 49]. This ranging functionality, linked with suggestive interactions with SUN1 and SUN2 across their nucleoplasmic domains, suggests potential roles of emerin in maintaining *LINC* function across the NE. Depletion of emerin in polarising NIH3T3 fibroblasts has been shown to lead to abnormal nuclear migration and loss of TAN line organisation across the nuclear surface [50]. Thus, emerin, alongside its associated interacting partners A-type lamins and samp1, may function in maintaining *LINC* complex connections between nucleoskeletal and cytoskeletal compartments.

1.1.1.3 SUN proteins.

Forming close associations with the INM nuclear lamina, SUN proteins form the physical link between INM and ONM regions through their associations with nesprins,

enabling the establishment of *LINC* complex interactions across the NE. These Sad1/UNC-84 (SUN) proteins were originally described in fission yeast [51] and *C. elegans* (UNC-84) [52], with subsequent BLAST searches using the highly conserved C-terminal domain (SUN-domain) revealing the mammalian homologues SUN1 and SUN2. Mammalian SUN proteins consist of five family members (SUN1-5), whereas SUN1 and SUN2 are ubiquitously expressed across a range of tissues [52, 33, 53], SUN 3-5 are expressed exclusively in the testis [54, 55]. Both SUN1 and SUN2 are type II membrane proteins [56], expressing a single pass transmembrane domain, anchored to the INM through their signal-anchor sequence localised to their C-terminal region. Aside this, both SUN1 and SUN2 further express high degrees of similarity, sharing 64% homology, containing an N-terminal region localised to the nucleoplasm [29] followed by a single transmembrane domain which spans the INM [57]. The core of both SUN1 and SUN2 is comprised of the stalk region spanning the PNS, made up from coiled-coil repeats, which are essential for protein trimerisation [58, 59]. Following the coiled-coil is the most highly conserved region of SUN proteins, the C-terminal SUN-domain, composed of ~175 aa, forming the core protein region responsible for KASH interactions. Interestingly, recent studies have found 6 potential splice isoforms for SUN1 alone expressed in murine heart tissue using RT-PCR [60], through which all isoforms were shown to retain the conserved SUN-domain, coiled-coil stalk and INM transmembrane domain, but expressed varying lengths of N-terminal nucleoplasmic protrusions. This helps to suggests that through these multiple splice variants, SUN1 could display a range of tissue specific functionalities, however, it is currently unknown whether these described splice variants are actually translated into protein. For SUN2 however, there is currently no experimental evidence for isoform variants as a result of splicing [61].

Both SUN1 and SUN2 have been shown to display direct interacting potential with nuclear lamins [33, 29]. Investigations overexpressing HA-tagged SUN1 displayed co-immunoprecipitation potential with GFP-conjugated lamin A in U2OS cells, alongside further work showing that *in vitro* transcribed/translated N-terminal region of SUN1 displayed further interacting potential with *in vitro* transcribed/translated lamin A, but not lamin C, B1 or B2 [29]. Further biochemical analysis has also increased our understanding of SUN-lamin interactions through evidence suggesting that GST-bound N-terminal regions of SUN1 display preferential binding with pre-lamin A over mature lamin A, alongside further weak interacting potential with lamin C and lamin B1 subtypes [33]. Interestingly, the retention of this lamin-SUN interaction appears to be evolutionary conserved, as the localisation of both SUN1 and SUN2 homologues within *C. elegans* to the NE appears to be dependent on lamin expression [62]. Further *in vitro* work however,

highlighted that SUN retention at the NE was not solely dependent on lamin. In both lamin A/C deficient MEFs and lamin A/C or lamin B deficient HeLa cells, it was shown that SUN1 was still able to localise to the NE [63]. This therefore suggests that further SUN1 interactions must be present across the NE, enabling SUN retention across this region. In contrast, SUN2 does display some dependence on lamin A/C for NE retention, as SUN2 displayed the inability to localise to the NE within mouse embryonic fibroblast cells lacking lamin A/C, expressing diffuse staining through the ER [33].

As displayed above, much of the early research implicates lamin A/C dependant localisation of SUN proteins to the NE. However, mouse models used in these studies must be taken with caution in light of recent investigations showing that *LMNA* -/- mice were still able to produce truncated lamin A, which may retain its SUN interacting potential [64]. In the study conducted by Crisp *et al.* above, in which MEFs expressing lamin A/C absence showed retention of SUN1 across the NE, it is possible that the truncated lamin A/C retained in these cells expressed the SUN1 binding site. Upon closer inspection, it was shown that regions of lamin A proposed to bind SUN1 maps to residues 389 – 664 [29] and the truncated lamin A produced within the lamin A/C null MEF's retained 78 of these 275 aa's. It is therefore possible that the remaining 78 aa's in the truncated lamin A/C null mice may infer the SUN1 binding to truncated lamin A.

Alongside these potential lamin interactions across the NE, further lamin independent mechanisms also exist to localise both SUN1 and SUN2 to the INM. In *C. elegans*, UNC-84 requires a combination of two nuclear localisation signals (NLS) to retain its INM positioning, an INM-sorting motif and NE-localisation signal (NELS), found to be evolutionary conserved within its mammalian SUN1 homolog [56]. Alongside this, it has been further demonstrated that in addition to lamin A/C, SUN2 requires a further combination of its NLS, Golgi-retrieval sequence and the transmembrane domain for its maintained localisation across the INM [65]. Aside the requirement of classic NLS sequences for SUN retention across the NE, further evidence suggests that interactions with emerin and short nesprin isoforms may also be contributing factors to SUN localisation [66], however, it is clear that further work is required to increase our understanding of SUN interactions responsible for retaining their localisation across the NE.

As can be seen, SUN1/SUN2 localisation and connection to the nucleoskeleton requires a complex combination of protein interactions. In contrast to this, connections with cytoskeletal components are well documented, known to mediate through interactions with nesprin family members through *SUN-KASH* domain interactions [58, 67,

59]. Deriving the crystal structure of SUN2 revealed that it forms a trimer [58, 67], essential for the recruitment of KASH domains of nesprin-1 and nesprin-2 [59] (*Figure 1.2*).

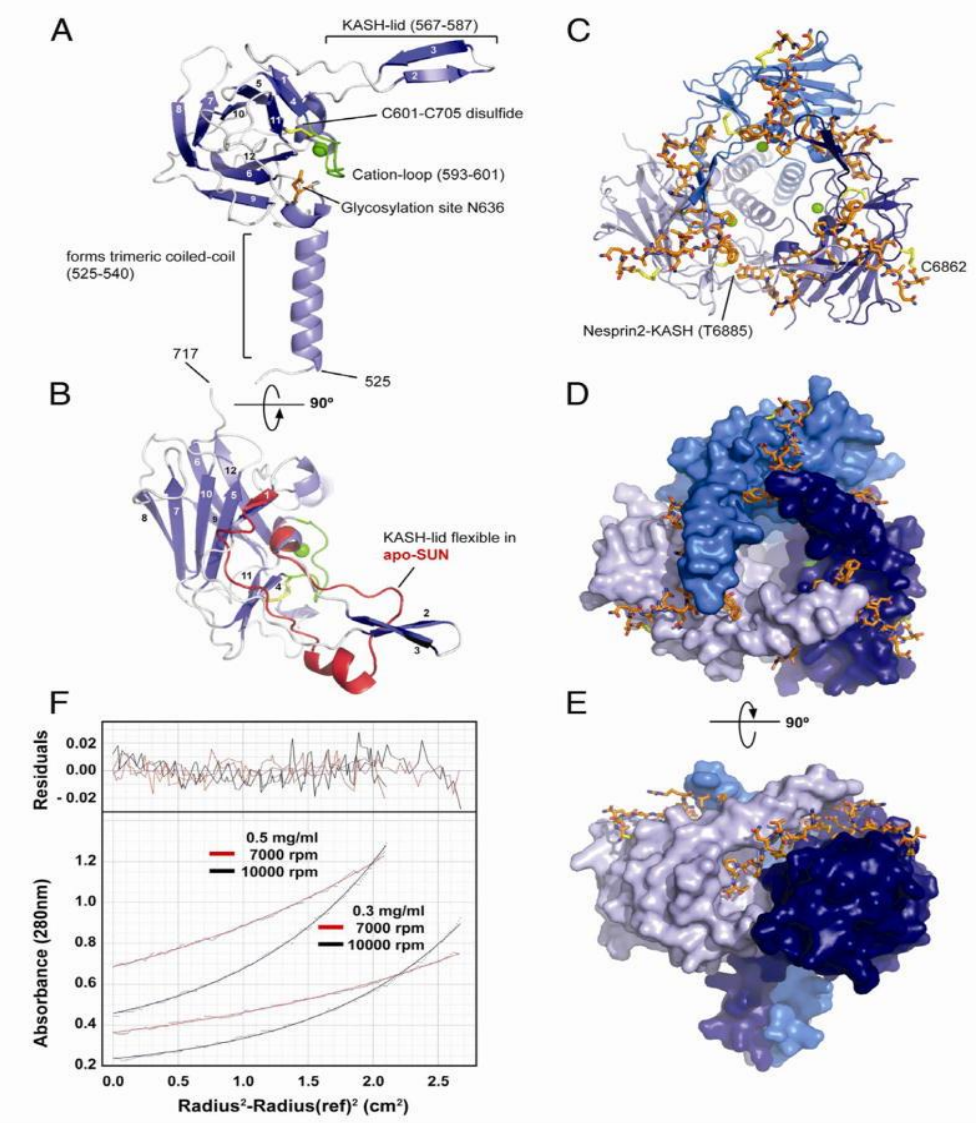

***Figure 1.2**: (A) Overview of the SUN2 protomer isolated whilst not bound to KASH binding partners. (B) Top view of the SUN2 protomer displayed in (A) (facing the outer nuclear membrane). The apo-protomer of SUN2 is superimposed in red, with the only region displaying significant conformational changes being the KASH-lid. (C) Top view of the trimeric SUN2-KASH complex. SUN2 domains are coloured in blue and the KASH peptide in orange. (D) Same view as (C), but SUN2 in surface representation, highlighting how each bound KASH peptide is clamped between two SUN2 protomers. (E) Side view of the SUN2-KASH complex, illustrating the deep binding pocket on SUN2 into which the terminal four residues of the KASH peptide bind. (F) Sedimentation equilibrium ultracentrifugation analysis of apo-SUN2 at two concentrations overlaid over primary data (red and black) for the two speeds. In the upper panel, the mass of the complete SUN2 trimer was calculated at 138 kDa. [505]*

It is envisioned that three SUN domains form a hexametric complex with three KASH domains, coordinating them through a combination of hydrogen bonds, a KASH 'lid' (a ~20 aa extension emanating from the central β-sandwich motif) and disulphide bridges. Interestingly, the KASH lid region of SUN domains was found in an unstructured, monomeric form when not bound to KASH peptides during observations by Zhao *et al.* [57], but incorporated an alpha helix in the later Sosa *et al.* study [68]. These findings suggest that the KASH lid is a dynamic structure until bound to KASH peptides. Its ability to display varying structural conformations may further reflect the ability of SUN proteins to connect to other ONM proteins aside from the KASH proteins. The incorporation of this KASH lid appears to resemble an evolutionary locking mechanism, whereby interactions between SUN domains and KASH peptides are further reinforced. This extensive arrangement of connections between the SUN and KASH domains across the perinuclear space is suggested to make up the core of *LINC* complex, able to transmit signals and force between the nucleoskeleton and cytoskeleton [69, 70].

1.1.1.4 KASH proteins.

LINC components have been identified in a wide range of organisms including plants, yeast, amoebae, worms, flies and vertebrates [71, 72, 73, 14, 74, 32]. The core of this *LINC* connection between nucleoskeletal and cytoskeletal components is formed through *SUN-KASH* perinuclear interactions. The KASH (Klarsicht, ANC-1 and Syne Homology) component is situated across the ONM, forming both direct and indirect connections between NE and cytoskeletal elements. The C-terminal KASH domain of these proteins is encompassed by a single transmembrane segment, followed by an evolutionary conserved PNS-situated short peptide, which associated directly with the luminal SUN domain [75, 14]. In contrast to their highly conserved C-terminal domains, N-terminal regions are highly variable, displaying considerable variation in both length; due to their differing SR copy numbers and domain composition; resulting in differential interacting potential with cytoskeletal structures [76, 77, 14]. For most KASH proteins, especially the large isoforms, their most prominent structural features can be found in their N-terminal cytoplasmic extensions, containing predicted regions of SRs or coiled-coil domains (*Figure 1.3*).

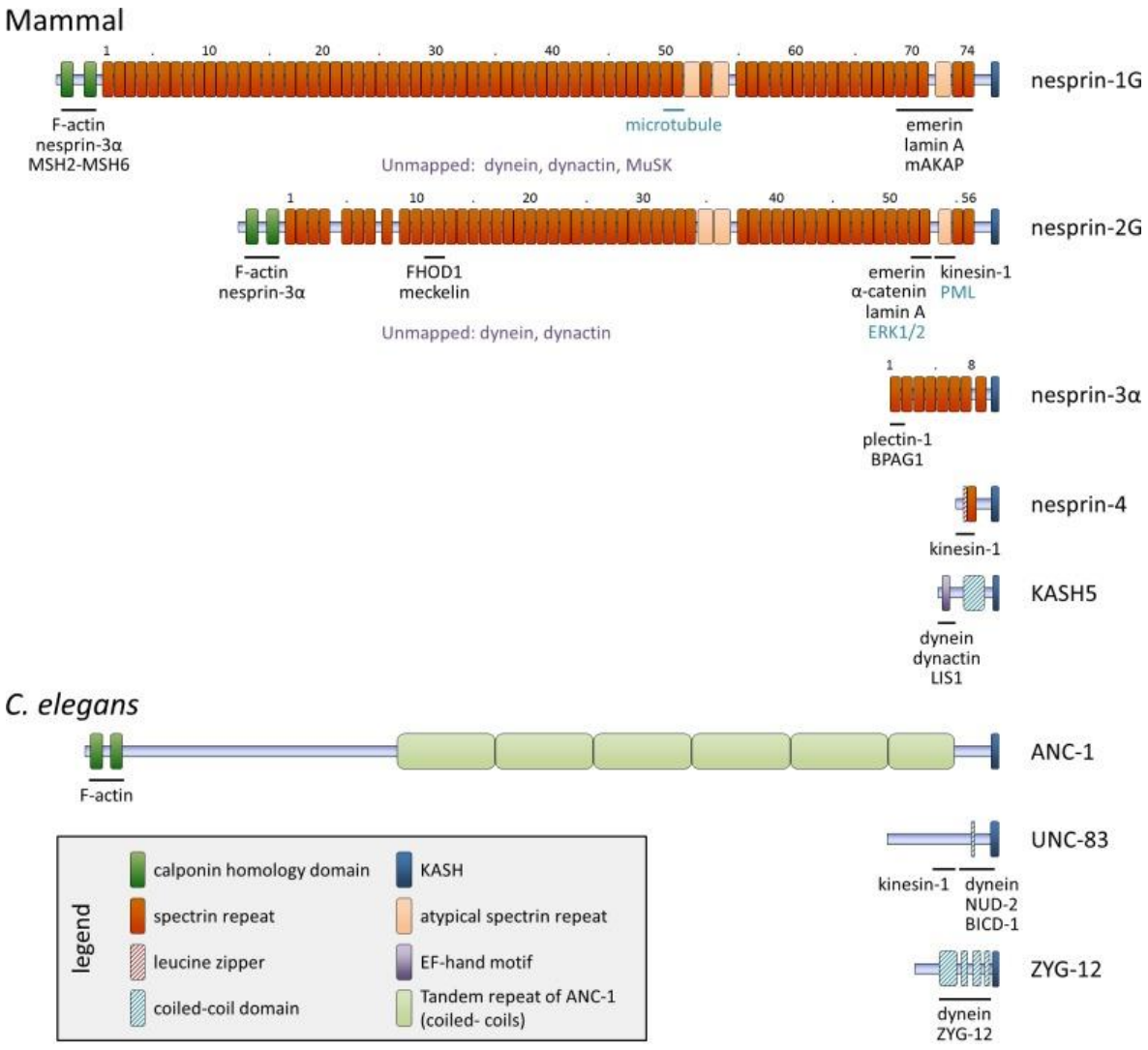

Figure 1.3: *Schematic of the major KASH proteins across mammals and C. elegans. Lines under the KASH proteins indicate known binding partners. The calponin homology domain (CH) situated across GIANT isoforms bind F-actin, and signalling protein interactions (displayed in blue) have also been identified in nesprin isoforms lacking the C-terminal KASH domain. [15].*

To date, five KASH domain-containing proteins have been identified in humans, termed nesprin 1-4 (nuclear envelope spectrin repeat proteins) and KASH5 (encoded by *SYNE1*, *SYNE2*, *SYNE3*, *SYNE4* and *CCDC155* respectively). Each of these proteins expresses unique numbers of SRs across the length of these molecules [78, 79], whereas KASH5 contains a large coiled-coil region. Alongside the range of KASH containing proteins, associated genes also contain multiple exon splice sites, forming multiple splice variants. These multiple splice variants contain variable spectrin repeat numbers,

alongside some isoforms missing the KASH domain completely [80], suggesting potential roles for further nesprin isoforms in alternate functions than maintaining *LINC* connections across the NE. Across this wide range of nesprin isoforms, N-terminal regions display interacting capabilities with cytoplasmic filament systems. This interacting potential supports early beliefs that nesprins localised to ONM regions of the NE, alongside many nesprin isoforms (*i.e.* giant, >800 kDa) being too large to migrate through outer NPC channels into the nucleus. However, shorter nesprin isoforms have now been implicated in INM functionality, suggesting a nucleoplasmic localisation [81]. More specifically, in muscle, the small-tissue specific expression of nesprin-1α and nesprin-2α have been implicated in retaining nuclear integrity, through nucleoplasmic interactions with lamin A, emerin and SUN1 [37, 82].

The cytoplasmic regions of nesprin-1G and nesprin-2G isoforms express a range of cytoplasmic binding potentials, able to directly interact with actin networks through their tandem calponin homology (CH) N-terminal domains, alongside indirectly to microtubule networks through kinesin and dynein interactions. These interactions with kinesin occur via a conserved LEWD motif comprising of a four residual tryptophan-acidic [83], which are essential for the maintenance of correct nuclear positioning in myotubes [84]. These LEWD motifs have also been identified across the short nesprin-1α and nesprin-2α isoforms, suggesting potential roles for these proteins in microtubule interactions via kinesin light chain 1 (KLC1). Further support for this microtubule (MT) interacting potential came from Schneider *et al.* [77], through which yeast two-hybrid screens and GST-pulldowns highlighted a direct interacting potential between KLC1 and nesprin-2. These investigations therefore provide strong support to suggestions that nesprins play key roles in recruiting both actin and MT networks to the NE.

It is further suggested that nesprin-4 and KASH5 also plays roles in recruiting MT networks to the NE. Nesprin-4 has been shown to interact with kinesin [78], through which experimentation shown that nesprin-4 overexpression in HeLa cells stimulated significant changes in cellular organisation, including relocation of Golgi and centrosome components away from the NE. KASH5 however, is located specifically to germ cells, where interactions have been displayed with the dynein-dynactin complex [85].

In contrast to nesprin proteins described thus far, nesprin-3 displays interactions with plectin, noted for its roles in connecting intermediate filament networks throughout the cell. Notably, plectin is further shown to mediate connections between the three major cytoskeletal networks [86]. Thus, this vast diversity of KASH proteins making up the *LINC* complex presents interacting potential between the NE and all three cytoskeletal

networks. Further to this, the varying isoforms of nesprin infer unique properties to the NE due to their associated interacting potentials and binding partners, suggesting that their relative expression could confer unique properties to the NE-cytoplasmic filament interactions.

Thus far, it has been described how interactions between SUN domains and KASH peptides across the PNS produce a physical connection between INM and ONM regions of the NE. Through associated binding of KASH proteins to cytoskeletal components and SUN interactions with the nuclear lamina, this connection is able to physically connect nucleoskeletal and cytoskeletal components, allowing a bridge for cross talk between the two subcellular compartments.

The importance of this physical bridge across the NE can be seen through its high conservation through evolution. At least one pair of SUN- and KASH- domain proteins is found across all higher eukaryotes, and although homologues are not as readily apparent in lower eukaryotes, current in-depth research is beginning to uncover these conserved protein bridges [87]. It has been identified that during evolution, multicellular eukaryotes have amplified both SUN and KASH components, but not necessarily in equal proportions. For example, mammals tend to have 4-6 KASH and 4-6 SUN domain containing proteins, whereas fish display double the number of KASH-domain containing proteins and only half the number of SUN proteins. When combined with current understanding of *LINC* associated proteins, this conservation suggests strong evidence for potential unique *LINC* functionalities, specific to different tissues, developmental stages and organisms [88]. In support of this suggestion, investigations by Göb *et al.* highlighted the existence of two distinct *LINC* complex connections established during mouse sperm development [54]. These include the spermatogenesis specific SUN3-nesprin-1, and SUN1η (a novel SUN1 isoform) -nesprin-3 interactions. Interestingly, it was shown that each *LINC* connection localised to opposite spermatid poles, likely providing sperm-specific interactions with cytoskeletal components. These investigations therefore highlights that not only are *LINC* connections required to connect the nuclear interior with cytoplasmic components, but may also infer unique region specific cytoskeletal interactions across the NE, aiding in the formulation of cell polarisation, and subsequent differentiation.

1.1.1.5 LINC mediated NE - cytoskeletal connections.

Further to KASH protein interactions with SUN proteins, forming the physical connections between INM and ONM, cytoplasmic extensions of the KASH proteins also infer connections between the NE and cytoskeletal filaments. Through these connections, the NE is linked to the cytoskeleton and its associated interactions with the extra-cellular matrix (ECM). This cytoplasmic filament system consists of three major protein networks defined by size; microfilaments (actin) (7 nm), intermediate filaments (IFs) (10 nm) and microtubules (MTs) (25 nm) (*Figure 1.4*).

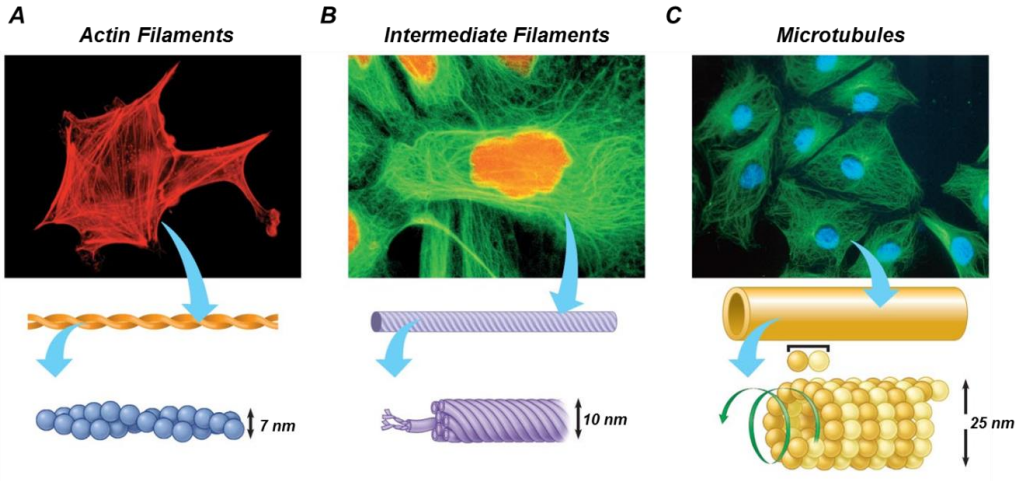

Figure 1.4: *Schematic of the major cytoskeletal filament networks in mammalian systems. (A) Shows actin filament arrangement into a right handed spiral comprised of oligermerized actin subunits, (B) displays intermediate filaments, made up from head-to-tail assembly of subunits, and (C) displays microtubule filaments, comprised of α- and β-tubulin heterodimers formed into hollow tubular structures. [506].*

Each filament network works in close association to define cell shape and structural integrity, but also maintain specific cellular functions such as maintaining cytokinesis, intracellular transport, cell signalling and cell migration [89]. Some assemblies of these filament networks display further tissue specificity, such as the formation of Z-bands in muscle between actin and desmin, the formation of actin in acrosomes or spermatozoa, alongside cilia/flagella formation in many biological systems [89, 90].

Microfilaments are formed through the oligomerisation of actin, forming two strands which further wrap around each other forming a right handed spiral, whereas MTs form through the assembly of α- and β-tubulin heterodimers, able to form linear protofilaments which in turn are able to interact laterally to form a sheet that circularises into a 25 nm

wide hollow tube [89]. In contrast to other cytoskeletal filament networks, IFs display very different properties, both through their coiled-coil rod domain making them insoluble, and through their dimers assembling into head to tail linear arrays, which further layer forming a ~10 nm diameter filament comprising of 32 molecules [91]. IF networks further differ in their cellular dynamics. Both actin and tubulin networks display dynamic assembly and disassembly in response to environmental stimuli, are stabilised by tension and are highly polarised to facilitate directional movement by associated motor proteins. In contrast, IFs are much less dynamic, confer cell stability through resistance to tension and have no polarity [89]. This helps to highlight that each filament network is able to provide unique functionality to cellular systems, through its physical properties, associated binding partners or NE connections, able to link the nucleus to various cytoplasmic functions and ECM components.

The association of actin filaments to the NE is mediated through the giant KASH proteins nesprin-1G, nesprin-2G in vertebrates and ANC-1 in *C. elegans* through their paired CH domains which closely resemble those displayed by known actin associating proteins like actinin. It has been well documented that these CH domains, situated across KASH N-terminal regions are sufficient to bind actin filaments to the NE, enabling actin dependant nuclear movement and positioning [92, 93]. However, recent studies indicate that these CH domains alone are not sufficient to resist the mechanical strain exhorted by the actin cytoskeleton during nuclear movement [94]. Polarising fibroblast cells re-position their nucleus towards the rear of the cell, resulting in re-orientation of the centrosome [95]. This movement is enabled through coupling retrograde moving actin cables to the NE through SUN2-nesprin-2G *LINC* connections, arranged into linear arrays known as transmembrane associated nuclear (TAN) lines [96]. Kutscheidt *et al.* [94] were able to show that nesprin-2G was necessary for the formation of TAN lines and resulting nuclear movement, however, required a further interaction with the formin FHOD1 actin binding proteins to perform this function. FHOD1 contains a typical formin domain structure alongside a unique second actin binding site which, in conjunction with an adjacent site that binds to SR11-13 of nesprin-2G, is able to sufficiently cross link nesprin-2G and actin across the NE. These FHOD1 interacting domains found in nesprin-2G are not present in nesprin-1G, suggesting a unique role played by nesprin-2G in resisting mechanical stress upon nuclear movement.

Aside from actin connections across the NE mediating nuclear movement, MT filament networks are also tethered to the NE through interactions with KASH proteins including nesprin-1, nesprin-2, nesprin-4 and KASH5 in mammalian systems [97]. In most cases, this interaction is mediated through association of KASH proteins with the motor proteins

kinesins or dynein or both. One exception however, comes from the KASH-less $p50^{nesp1}$ isoform, containing SRs 48-51 of nesprin-1. This isoform has been shown to display direct interacting potential with MTs through co-sedimentation assays [98]. The impact of this finding could suggest that all nesprin-1 isoforms containing SRs 48-51 could also display direct MT interactions, however, to date this hypothesis has not yet been tested. Nesprin-1, nesprin-2 and KASH5 have been shown to bind with specific subunits of the motor proteins dynein. For KASH5, this binding with dynein and dynein regulators occurs in close proximity to its KASH domain [99], whereas the interaction sites for nesprin-1/2 and dynein have not yet been resolved. Several KASH proteins also display interacting potential with kinesin-1 motors, including nesprin-2 [77] and nesprin-4 [78], mediated through direct binding between kinesin-1 light chain (KLC) tetraticopeptide repeats and sites close to the KASH domain.

Of further emerging interest are suggestions that KASH proteins are able to interact with multiple motor proteins or cytoskeletal elements. For example, across its N-terminal region, nesprin-2G display interacting potential with actin through CH domains and FHOD1 interaction sites, whereas interaction potential with kinesin is inferred at its other end. This suggests potential dual functions played by individual KASH proteins across the NE, able to confer specific functionalization based on environmental requirements. For example, nesprin-2G is involved in actin dependent nuclear movement in fibroblast cells [93], alongside MT and dynein dependant nuclear movement in developing neurones [100]. This suggests that further regulatory mechanisms must be in place to allow selection of one mechanism for nuclear movement over another dependant on the situational requirements.

The engagement of KASH proteins with MTs across the NE has also been shown to facilitate centrosome movement in number of mammalian systems. These proteins include nesprins-1-3, and KASH5, all of which have been shown to play roles in retaining close positioning between centrosomes and nuclei [99, 100]. In contrast, Roux *et al.* showed that overexpression of GFP-tagged nesprin-4 constructs into HeLa cells stimulated a detachment of centrosomes from the NE, resulting in a fivefold increase in nuclear to centrosome distance [78]. This again helps to support suggestions that a complex interplay between KASH proteins exists across the NE to maintain normal cellular function.

Nesprin-3α is the only KASH protein to date known to interact with cytoplasmic IF through a unique region situated across its N-terminal domain. This region interacts with the ABD domain of plectin, which in turn, binds IFs through its plakin domain [86]. It is also

interesting to note that further binding has been suggested between nesprin-3α and N-terminal ABD domains of nesprin-1G and nesprin-2G. This interaction has been hypothesised to control nuclear size through the formation of a nuclear cage situated across the ONM [101]. Integration between NE and IFs (mediated through nesprin-3α) has also been implicated in regulating cellular responses to shear stress, force transmission and flow induced cell polarisation [102, 103].

The described ability of KASH proteins to confer variable NE interacting potential with multiple cytoskeletal components both individually, or at the same time, highlights the complex mechanisms by which the *LINC* complex is able to relay mechanical and signal induced responses from the NE to cytoplasmic regions. Therefore providing a subtle regulatory mechanism, through which cells can dictate responses to environmental stimuli.

1.2 Roles of the LINC complex in normal cell function.

1.2.1 LINC complex roles in maintaining nuclear architecture and correct nuclear movement.

The maintenance of nuclear architecture is of great importance to the maintained functionality of many cell types due to its suggested roles as an anchoring site for many cytoskeletal components [104]. In this recent evidence, it was shown that nuclear shape changes result from peripheral cell boundary dynamics, as a result of variations in mechanical stress and strain mediated through the cytoskeleton. The nuclei of most cells display a nuclear shape of either round or oval morphology, with alterations in this nuclear shape being implicated as an important factor in the development of many disease phenotypes. Moreover, in certain specialised cell types, altered nuclear shape is important to their function, such as that found neutrophils, in which, protein composition across the NE is adapted to increase nuclear malleability, allowing increased cellular migration in and out of numerous tissue systems [105].

An essential *LINC* complex component shown to play roles in maintaining nuclear architecture is the nuclear lamina. The importance of this protein network in maintaining nuclear shape has been well characterised, with analysis of lamin A/C deficient MEFs and *LMNA1* RNA interference (RNAi) in *C. elegans* shown to lead to alterations in nuclear

shape [106, 107]. Further to this, many laminopathies are characterised by altered nuclear shapes, most notably presented in the development of the premature aging disease Hutchinson-Gilford progeria syndrome (HGPS). The mutation stimulating the formation of HGPS was mapped to the *LMNA* gene [108], stimulating the activation of a cryptic splice site, which in turn, results in the generation of an aberrant form of lamin A, called progerin which is constitutively lipid-modified across the INM [109]. It is hypothesised that this constitutive lipid-modification of lamin A stimulates the observed alterations in nuclear shape, as treatment of cells from HGPS patients with the farnesyl transferase inhibitor rac-R115777 (designed to inhibit farnesylation), reverses the abnormalities in nuclear shape [110]. More recent investigations into roles of lamin proteins in maintaining nuclear architecture have suggested further functions in maintaining the structural integrity of the nucleus, as well as conferring its sensitivity to mechanical stress. For example, lamin A/C have been shown to play key roles in defining the nuclear lamina's elastic properties; through which lamin A/C deficient HeLa cells, displayed increased numbers of misshapen nuclei and a decreased nuclear stiffness [111]. Further to this, when wildtype or mutant lamin A is overexpressed within *Xenopus* oocyte nuclei, nuclear stiffness is shown to increase proportionally to the lamin A concentration inserted [112].

Further to roles for lamin A/C in maintaining nuclear architecture, current investigations further implicate roles for lamin B in maintaining the integrity of the NE. Current investigations suggest that lamin B1 absence in MEFs results in no changes to the elastic properties of the nucleus, however stimulates severe abnormalities in nuclear morphology [113]. More recently, Ferrera *et al*. investigated the effects of lamin B1 overexpression associated with autosomal dominant leukodystrophy (ADLD) on nuclear function and mechanics [114]. It was shown that transient transfection of lamin B1 into both HEK293 and neuronal N2a cells stimulated an increased nuclear stiffness, similar to that found within ADLD cells. More importantly however, in ADLD fibroblasts, reducing lamin B1 levels through shRNA knockdowns was shown to restore elasticity values indistinguishable from those of control fibroblast cells. It was shown that isolated nuclei from ADLD fibroblasts displayed reduced nuclear ion channel open probability in voltage-step application, suggesting that the increased lamin B1 levels associated with ADLD also contribute to altered nuclear signalling cascades in somatic cells. These findings therefore help to highlight the complex roles played by lamin components of the *LINC* complex in regulating nuclear architecture.

Of further importance in maintaining nuclear architecture are the KASH proteins situated across the ONM. It has been shown that the maintenance of *LINC* connections across the NE, specifically those mediated through nesprin-2 interactions are required to

maintain normal nuclear size and shape [115]. Further work conducted by Kandert *et al.* [116] suggested that nesprin-2G is responsible for maintaining nuclear shape when correctly localised to the NE. In this investigation, it was observed that p.S143F progeria fibroblast cells (*LMNA* mutant cells) exhibited dysmorphic nuclei containing nuclear blebs and lobulations, which increased in number during cell aging in culture (*Figure 1.5*). On closer observations, it was shown that nesprin-1 displayed a slight increase in cytoplasmic distributions in mutant cells, whereas nesprin-2 appeared to be mostly reduced or absent from the NE. Interestingly however, through immunofluorescence analysis against nesprin 2 N- and C-terminal regions, it was shown that mutant fibroblast cells expressing even low levels of nesprin-2G across the NE displayed normal nuclear shapes, with significant reductions in nuclear blebs and lobulations. Observations from this work were therefore able to suggest that correct nesprin-2G localisation across the NE was able to safe-guard the nuclear architecture within *LMNA* mutant cells. Alongside this, further investigations have described the combined roles of nesprin-1G, nesprin-2G and nesprin-3 in the maintenance of nuclear shape, suggesting the complex interactions displayed across the range of nesprin proteins forms a cage across the ONM, able to control nuclear size and shape [101].

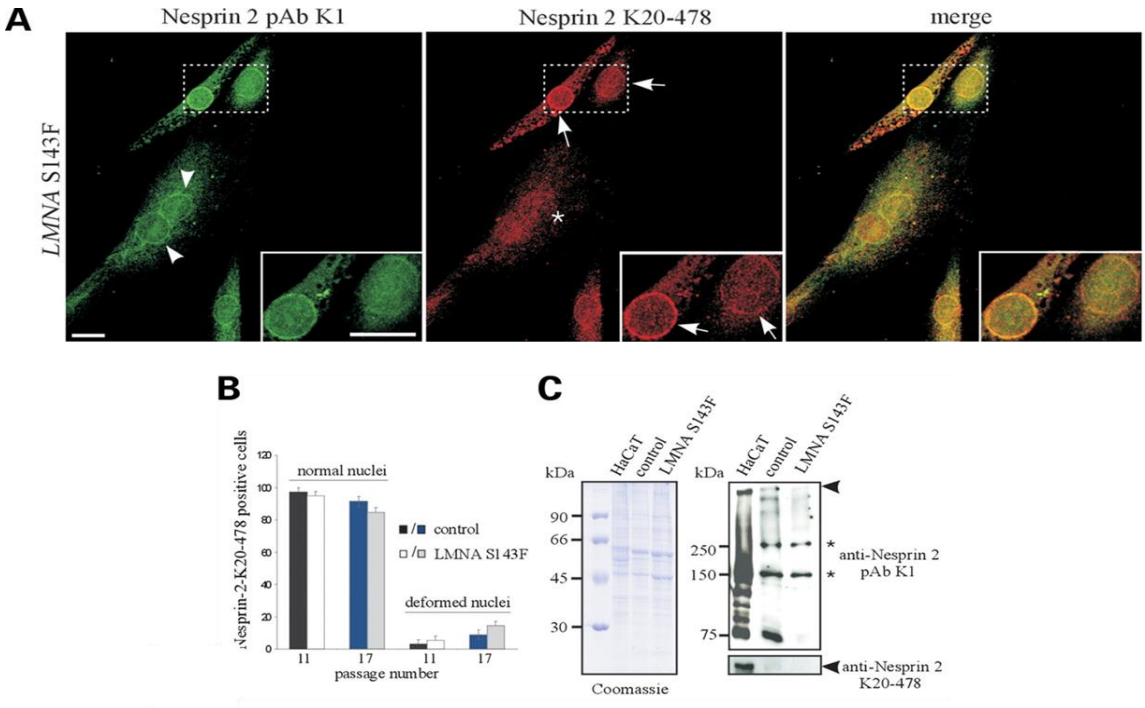

Figure 1.5: *p.S143F progeria fibroblasts display normal nuclear morphology when expressing nesprin-2G. (A) Displays indirect immunofluorescence analysis of nesprin-2 C-terminal (pAbK1), and N-terminal (K20-478) staining. Arrows present mutants expressing low C-terminal levels and asterisks display cell lacking N-terminal staining. (B) Displays histogram data of nuclear deformations in cells positive for nesprin-2 N-terminal regions, showing reduced nuclear deformations observed in both young and aged mutant cells positive for nesprin-2G. (C) Displays western blot data against nesprin-2 N- and C-terminal regions across control and mutant fibroblasts, indicating a slight reduction in nesprin-2G in mutant fibroblasts. [116]*

Aside roles in maintaining nuclear shape, size and mechanical properties, *LINC* components have been further suggested to influence the distance between INM and ONM regions of the NE [58]. However, literature views are mixed on this issue. In HeLa cells for example, disrupting the *SUN-KASH* interaction across the PNS with dominant negative versions of SUN/KASH, or siRNA knockdowns alters spacing between the two membranes [33]. However, disruptions of the SUN homologue UNC-84 in *C. elegans* only affect membrane spacing when nuclei are actively under force such as in wall muscle cells, and further deleting a large portion of the luminal domain does not appear to change the spacing [117]. As the nuclei in HeLa cells, like many other adherent cells, are under constant tension, these studies suggest the *LINC* complex may only contribute to INM and ONM spacing when the nucleus is under stress. Current views have now clarified these prevailing models, suggesting that across many cells, the SUN protein component of *LINC* complex interactions is necessary to maintain the even spacing between INM and ONM in cells under high mechanical strain [118]. However, these interactions are not required in cells not undergoing nuclear strain.

Alongside the maintenance of nuclear architecture, nuclear positioning is also an important cellular process, leading to the establishment of cell migration, cellular polarity, cell division and zygote formation. It is thought that three main protein families play roles in maintaining correct nuclear movement; the cytoskeleton, motor proteins and KASH proteins, which are all key components of the *LINC* complex.

The involvement of MT and MT-associated proteins in nuclear migration has been documented across a range of organisms. Dynein and its activator complex dynactin have been shown to control nuclear migration events in budding yeast and *Drosophila* [119] [120], with further LIS1 loss (a dynein and MT-binding protein) shown to affect neuronal migration in humans during cerebral cortex development, leading to the development of lissencephaly [121]. Alongside roles for cytoskeletal components to act alone in nuclear movement, the combined action of both MT and actin networks has also been implicated in nuclear migration [122]. In *Xenopus* for example, the MT and actin binding Myo10 facilitates nuclear anchorage and spindle assembly [123].

This coordinated action of multiple cytoskeletal components in nuclear migrations has been attributed to *LINC* connections across the NE. It has been shown that ANC-1 loss in *C. elegans* stimulates nuclear clumping, preventing the correct nuclear migration to their assigned destinations [92]. In mammalian systems, extensive mouse models have been used to demonstrate that nuclear anchorage is mediated by nesprins *in vivo*. Transgenic mice overexpressing a dominant negative nesprin-1 KASH domain under the regulation of

a muscle specific promoter display a loss of nuclear anchorage beneath neuromuscular junctions in skeletal muscle [124]. It was also suggested nesprin-1 $^{-/-\text{KASH domain}}$ knockout mice display synaptic nuclei displacement alongside extensive branching of phrenic nerves, suggesting that nesprin-1 mediated synaptic nuclear anchorage may be essential in maintaining neuronal innervation sites. In contrast, nesprin-2 $^{-/-\text{KASH domain}}$ knockout mice display no abnormalities in nuclear anchorage.

Interestingly, when all actin connections are abolished across the NE in nesprin-1/-2 $^{-/-\text{KASH domain}}$ knockout mice, a lethal phenotype is observed [125], suggesting the existence of a potential redundancy mechanism between these KASH proteins. It is not considered in these experiments however, the potential impact of these knockouts on other KASH isoforms across the NE. These animal models may additionally disrupt the function of KASH proteins which do not display direct actin interactions. For example, nesprin-1 and nesprin-2 both display interacting potential with dynein and kinesin-1, coupling the centrosome to the NE in neurons of the developing mouse brain. In the nesprin-1/-2 knockout mouse described above, the centrosome was shown to un-couple from the NE resulting in severe nucleokinesis and interkinetic nuclear migration defects [100]. As the binding motifs for these motor proteins have not yet been mapped across nesprin-1 or nesprin-2 proteins, they could interact with one or multiple SRs across the N-terminal regions or truncated KASH domain variants. This therefore suggests further investigation is required to understand the complex interplay between *LINC* components across the NE during nuclear migration and subsequent cellular processes.

Due to these observed roles of *LINC* components in maintaining correct nuclear positioning and migration, it is not surprising that the *LINC* complex is further implicated in the development of cell polarity, a crucial process responsible for directing correct cellular differentiation and tissue formation across many organisms. Nesprin-3 for example has been implicated in the establishment of flow induced polarity of human aortic endothelial cells (HAECs) through regulating nuclear-MTOC connectivity [103]. Through the application of nesprin-3 siRNA, it was shown that not only was this silencing sufficient to sever connections between the NE and MTOC, but also the HAECs ability to correctly polarise in response to environmental flow. Alongside nesprin-3, nesprin-4 has been further implicated in regulating kinesin mediated cell polarisation [78], through the regulation of both centrosome and Golgi positioning in the cell.

With more current investigations now implicating the *LINC* complex as having key functional roles in maintaining cell polarity in both fibroblast and myoblast cells [126, 127], it can be suggested that the complex interplay of protein interactions across the NE,

mediated by the *LINC* complex components, is able to infer a further regulatory component facilitating nuclear migration and the maintenance of nuclear architecture.

1.2.2 LINC roles in force transmission and mechanotransduction across the NE.

Investigating the processes by which cells are able to transmit force from peripheral cellular regions to the NE, and subsequently induce a response through alterations in signalling pathways or gene expression is an area of great interest in current cell biology fields. Initial evidence suggesting the nucleus of a cell is under tension came from Sims *et al.* in 1992 [128], through which it was shown that disrupting the actomyocin forces exerted across the nuclear surface altered both cell and nuclear shape. Further work from this research group later showed that the tugging of integrin receptors situated across the plasma membrane stimulated direct distortions across the NE [129], displaying the first indication as to direct physical links existing between the NE and plasma membrane. This established the concept that forces applied externally to the cell, such as those from the surrounding ECM, are propagated to the nuclear surface, which links closely to mechanical models suggesting physical interactions exist between cytoskeletal networks and the NE [130, 131, 132]. Current investigations further support these suggestions, showing that external cellular forces are able to induce clearly detectable nuclear deformations across a range of cells [102, 133, 8].

In recent years, the *LINC* complex has been highlighted as the only known structure by which cytoskeletal stresses can be directly transferred to the nuclear surface (*Figure 1.6*). Since the cytoskeleton has been shown to directly connect with focal adhesions and cell-cell junctions across the plasma membrane [134, 135], subsequent connections with *LINC* components across the NE therefore enable a mechanism by which the nucleus, cytoskeleton and ECM can be physically connected [14, 136]. In support of this, current understanding suggests *LINC* complex components are required for correct nuclear positioning, cell polarisation, propagation of cytoskeletal forces [137] and the efficient transfer of force between the nucleus and cytoskeleton [102, 138].

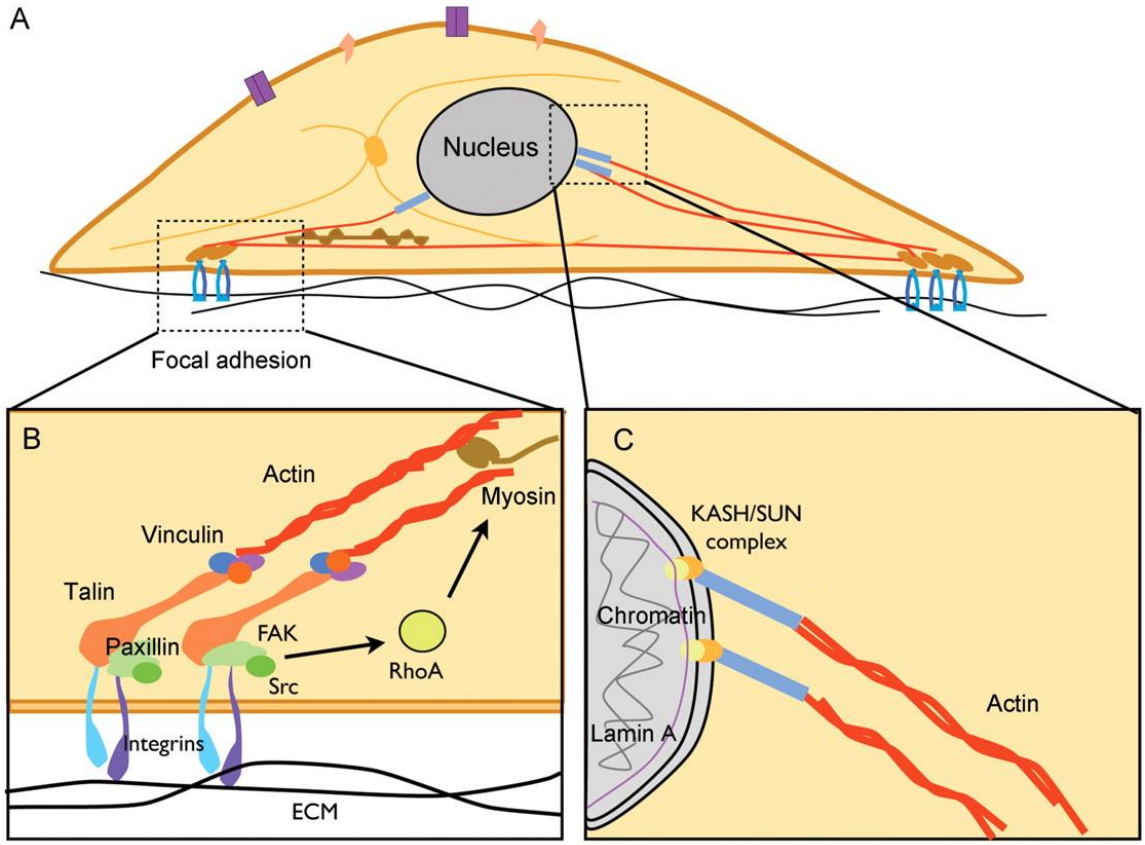

Figure 1.6: *LINC mediated mechanotransduction from the ECM to the nucleus. (A) The actin cytoskeleton links focal adhesions at the plasma membrane to the LINC connections across the NE. (B) Focal adhesions are sites of integrin clustering and adhesion to the ECM. (C) Actin filaments connect to LINC complex components situated across the ONM, stimulating signal transduction to the INM. [134]*

It has been demonstrated that forces applied to the apical surface of living cells are able to propagate through the cytoskeleton and induce a response to the nucleus in emerin deficient MEFs [69], alongside integrin manipulation able to invoke direct motion in cellular organelles in bovine capillary endothelial cells [129, 133]. It was recently shown that nesprin-1 knockdowns in human umbilical vein endothelial cells (HUVECs) through siRNA-mediated silencing were able to significantly increase the nuclear height [139], suggesting potential roles for nesprin-1 in flattening the nucleus in endothelial cells. Following this, Chancellor *et al.* was further able to show that inhibiting myosin activity in HUVECs induced similar phenotypes [140], leading to their proposed model in which actomyocin force pulls laterally on the nucleus, stimulating the observed flattened disk phenotype. In this proposed model, the nucleus is suggested to act as a scaffold to balance the actin and microtubule forces internally, whilst the extracellular substrate balances them externally. Through their investigations, the absence of nesprin-1

substantially reduces the pulling forces exerted across the nuclear surface, leading the nucleus to 'relax' vertically, forming a more rounded shape, whilst excess forces are balanced through an increased number of adhesion sites with the substratum.

Following from this, a series of recent papers were able to show that dorsal actin bundles situated across the top of the nucleus interacted with the NE through TAN line formation, mediated by nesprin-2G and SUN2 [93]. It was suggested that these TAN lines act in a similar fashion to focal adhesions situated across the plasma membrane due to both assemblies able to anchor actin cables to each respective membrane and transmit mechanical force [93, 94]. Aside this, it has been suggested that further unique actin organisations across the NE surface are also present, comprising of distinct apical stress fibres forming across the top of the nucleus, able to manipulate nuclear shape [141]. These 'Actin Caps' link to the peripheral plasma membrane through specialised focal adhesions, which have been shown to be larger than conventional focal adhesions as well as displaying faster turnover dynamics [142]. These actin caps alongside associated focal adhesions have been proposed to provide fast and efficient, physical pathways for mechano-transduction by providing a stabile connection between the ECM and nuclear regions of the cell [143, 144].

Further to actin, MTs have also been implicated in the generation of tension across the NE, mediated through *LINC* connections. It was shown that through binding the NE via cargo ends, dynein and kinesin are able to pull the nucleus either towards or away from centrosomes respectively [145]. Further work by Wu *et al.* highlighted roles for these interactions in eliciting nuclear rotation in response to environmental stimuli, alongside producing a computational model describing how this process occurs [146].

It is therefore evident that the physical links between the NE and surrounding ECM mediated by *LINC* complex components is of great importance in the maintenance of normal cell function. However, to date the exact mechanisms by which cells sense and subsequently respond to environmental stimuli is still unclear. One potential mechanism by which mechanotransduction through *LINC* components could elicit a cellular response to environmental stimuli comes from evidence suggesting that nuclear forces could potentially regulate gene expression [147]. In response to cyclic strain, lamin A/C deficient and emerin deficient mouse embryonic fibroblasts (MEFs) display impaired expression of the genes lex-1 and Egr-1 [106] alongside impaired nuclear translocation of MKL-1 transcription factor [148].

It can therefore be suggested that although the precise mechanisms by which nuclear coupling to the ECM through *LINC* associations is able to elicit a cellular responses to

external stimuli remains unknown, evidence is emerging that *LINC* components are critical in maintaining efficient mechanotransduction and force transmission across the NE.

1.2.3 The LINC complex displays functions in regulating signalling and chromatin anchorage across the NE.

As growing evidence suggests roles for *LINC* complex in maintaining mechanotransduction through the cell, further research has presented propositions as to roles of *LINC* connections in regulating cellular signalling pathways. Early investigations were able to show that nesprin-1 interacts with both muscle specific tyrosine kinase and muscle A kinase anchoring protein (mAKAP) [79, 15], known to complex signal transduction molecules such as cAMP-dependent protein kinase A and protein phosphatase 2A. More recently however, nesprin-2 has been shown to display interacting potential with α-catenin alongside the NE protein emerin [149]. Through these interactions, it was shown that nesprin-2 was able to positively regulate the nuclear localisation of active β-catenin alongside Wnt signalling [149]. Interestingly however, it has been further documented that emerin is able to bind with β-catenin and negatively regulate Wnt signalling by restricting nuclear accumulation of β-catenin [9]. When collated together with knowledge that emerin and α-catenin bind to the same region of nesprin-2, it can be suggested that both proteins compete for nesprin-2 binding, inferring roles for nesprin-2 within the regulation of Wnt signalling (*Figure 1.7*).

Of further interest is that this role of KASH proteins in the regulation of Wnt signalling may be evolutionary conserved. ANC-1 in *C. elegans* has been shown to interact with Regulator of Presynaptic Morphology 1 (RPM-1), a regulator of neuronal development and regulation [150]. Further genetic studies suggested that RPM-1, ANC-1 and β-catenin work together to regulate the formation of synapses in motor neurons and axon termination sites in mechanosensory neurons. To maintain this function, it was shown that ANC-1 retention to the NE is required, with emerin displaying a negative regulatory role similar to that found within mammalian systems [151]. This evidence supports current hypothesis that the retention of KASH proteins across the NE contributes to Wnt signalling through enhancing the perinuclear concentration of active β-catenin.

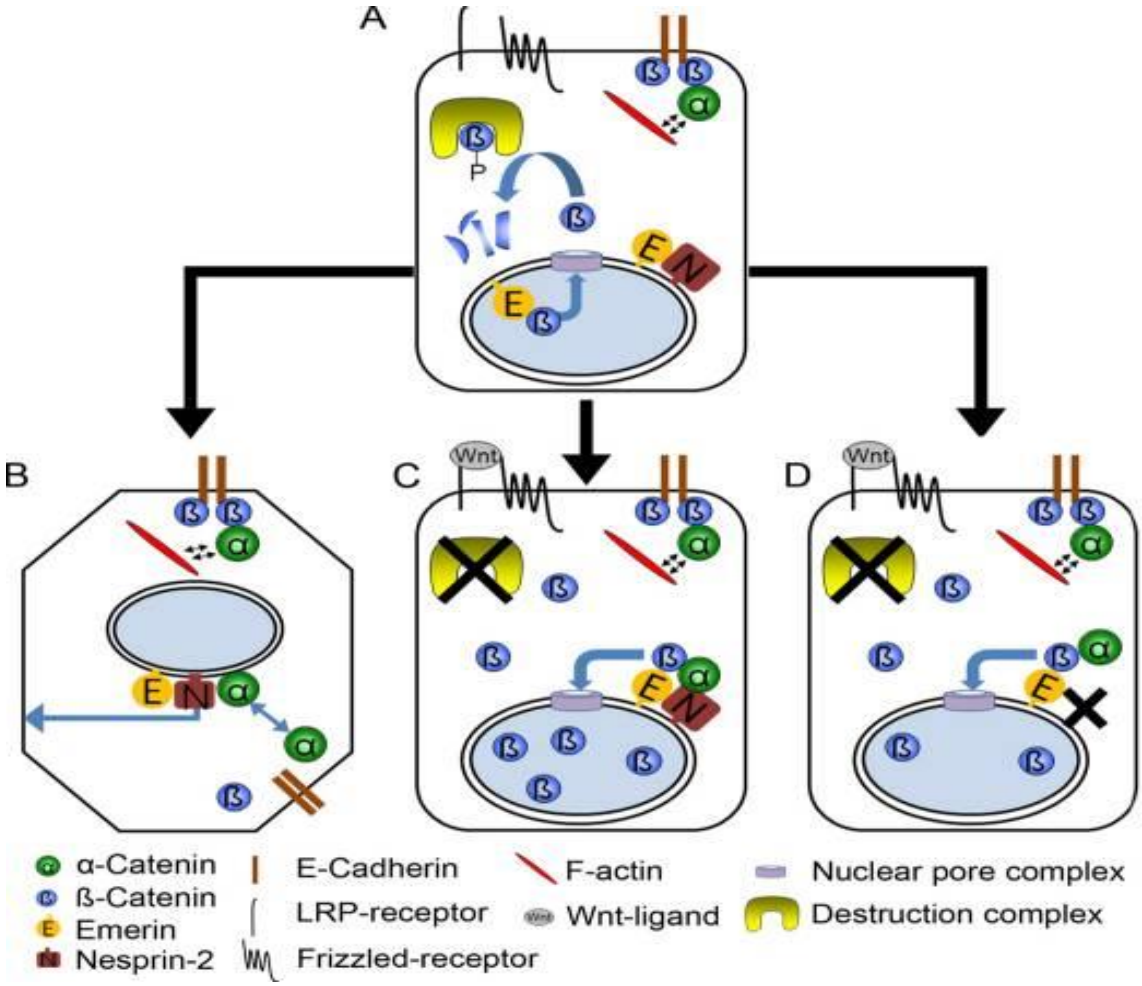

Figure 1.7: *Model of nesprin-2 and α-catenin roles in Wnt signalling. (A) α- and β-catenin localise to adherence junctions and the cell periphery, forming links with the actin cytoskeleton. Nesprin-2 and emerin are localised to the NE, where emerin across the INM supports β-catenin nuclear export. (B) α-catenin can be dislodged from the plasma membrane through reduction in cell contacts, where it then moves to the NE. (C) During Wnt pathway activation, cytoplasmic β-catenin levels increase. A quaternary complex of nespri-2, emerin, α- and β-catenin can be formed across the ONM. When this complex dismantles, β-catenin then enters the nucleus. (D) Upon loss of nesprin-2, reduced β-catenin is observed in the nucleus, hypothesised due to a loss of α- and β-catenin quaternary complexes forming at the NE. [9]*

Aside strong evidence for roles of *LINC* components in the regulation of Wnt signalling, further implications have been made between the *LINC* complex and rapid mechanochemical signalling in the nucleus [152]. It has been well documented that the nucleus responds to mechanical force sourced from extracellular regions, and that *LINC* complex components are necessary for this force transmission. However, it has proven difficult to determine whether *LINC* complex components are able to convert these mechanical stimuli into chemical signals in the nucleus. The first evidence for direct roles

of *LINC* components in mechanosensing came from Guilluy *et al.* [153], in which magnetic tweezers were used to pull on nesprin-1 antibody coated beads attached to the surface of isolated endothelial and fibroblast nuclei. This pulling force was shown to stimulate a stiffening response in the nucleus, through which increased accumulation of A-type lamins, activation of Src and tyrosine phosphorylation of emerin were observed. This helped to identify the first instance of direct correlation of KASH proteins and nuclear mechanotransduction responses.

Alongside documented interactions between *LINC* complex components and signalling molecules across the NE, further roles of the *LINC* complex in meiotic chromatin anchorage have also been speculated. During meiosis, the *LINC* complex is mobile across the NE, tethered to defined regions of chromosomes (telomeres in mice and pairing centres in *C. elegans*) [85]. This tethering is required for chromosome movement and is mediated through interactions between meiotic proteins that link regions of the chromosomal site and SUN proteins, and subsequently the cytoskeleton through *LINC* associations. In mammalian systems, associated interactions with KASH5 enable telomere associated SUN1 to engage dynactin and dynein, mediating meiotic chromosome movement [99, 154]. SUN2 has been further implicated in telomere tethering, but may not be required for meiosis [155].

The mechanism by which the *LINC* complex is modified in meiotic cells to enable force transmission directly to the chromosomes is still unclear. However, one possibility is that during meiosis, *LINC* components are post-translationally regulated. Suggestive evidence for this comes from Penkner *et al.* and Wynne *et al.* [156], through which it was shown in *C. elegans* that specific phosphorylation of Ser/Thr residues in the nucleoplasmic tail of SUN1/Matefin occurs during meiosis, which is essential for meiotic movement. Further to this, these modifications may also contribute to an increase in *LINC* complex mobility across the NE, which have been observed during the onset of meiosis [157].

A further potential mechanism by which *LINC* modifications may enable chromosome migration could reside in the formation of the nuclear lamina itself. In mammalian germ cells, a meiotic specific A-type lamin (lamin C2) is expressed, localised to sites of *LINC* mediated telomere tethering [158, 159]. This lamin sub-type lacks the amino-terminal head, alongside the central α-helical rod domain required to allow filament formation [158]. The expression of lamin C2 in somatic cells has been shown to alter the localisation of SUN proteins and lamin B1, suggesting potential roles for lamin C2 in modifying the anchoring mechanisms of *LINC* associated proteins. However, it was further shown that tethering of meiotic telomeres to *LINC* components was not altered in the absence of

lamin C2, but detachment of the telomere-*LINC* connection was affected, suggesting that the presence of lamin C2 may only be required for the efficient separation of chromosomes after migration.

It is further suggested that the *LINC* complex functions in DNA damage repair. It has been shown across both budding yeast and fission yeast systems that *LINC* components Mps3 and Sad1/Kms1 respectively are able to localise to sites of DNA double-stranded breaks and participate in repair [160, 161]. In mammalian systems, SUN1 and SUN2 are seen to interact with DNA-dependant protein kinase, which function in DNA repair, with loss of either SUN1 or SUN2 perturbing this process [161]. Further to SUN proteins, nesprin-1 has been shown to interact with DNA damage response proteins MSH2 and MSH6 through N-terminal CH domains [162], suggesting strong evidence that *LINC* components play roles in anchoring regions of damaged DNA in order to facilitate efficient repair across the NE.

It can therefore be seen that the *LINC* complex functions across a wide range of cellular activities, contributing to nuclear architecture, chromatin organisation and mechanotransduction events across the NE. This wide ranging functionality is further supported through the high degree of conservation across many *LINC* proteins, suggesting that the inferred functions of the *LINC* complex connections are fundamental in maintaining cellular homeostasis.

1.3 Roles of the LINC complex in disease development.

Due to wide ranging cell functionality displayed by the *LINC* complex, it is of no surprise that *LINC* complex components have been implicated in the development of numerous disease phenotypes. With extensive reviews covering the broad range of laminopathies deriving from mutations in both *LMNA* and *LMNB2* genes [163, 164, 165] we will focus herein on roles for KASH and SUN proteins in the development of multiple disease phenotypes.

1.3.1 LINC complex roles in neurodegenerative and musculoskeletal disease development.

As *SYNE-1*, *SYNE-2* and *SYNE-4* genes display a wide range of splice variants leading to the extensive range of nesprin protein isoforms, the roles of nesprins in the development of diseases has become an area of great interest over recent years. Current evidence suggests strong links between mutations in *SYNE-1* and the development of a number of neurodegenerative diseases including late onset ARCA1 (autosomal recessive cerebellar ataxia type 1) [166] and cerebellar ataxia [167]. Interestingly, although ARCA1 has been linked to nonsense mutations scattered along the *SYNE-1* gene in a range of populations [168, 169], little is known about the molecular etiology of its debilitating late onset phenotype. In recent work however, it has been shown that nesprin-1 expression is specific to the CNS, with an abundant expression of a KASH'less nesprin-1G isoforms (KLnes1g) highlighted in the cerebellum [170]. This KLnes1g isoform was shown to express noncanonical localisation at glomeruli of cerebellar neurons, whereas nesprin-2 retained specific staining across the NE in all tissues. Due to the specific nature of KLnes1g expression in the CNS, it was proposed that these nonsense mutations along the *SYNE-1* gene may stimulate dysfunction in KLnes1g isoforms. As KLnes1g is found most abundantly expressed in the cerebellum, this may explain why ARAC1 mutations mostly target cerebellar function and integrity. Aside alterations to the regulation of KLnes1g, further abnormal *SYNE-1* splicing or translational modification events could lead to the development of truncated or shortened nesprin-1 protein variants, which in turn, stimulate the late onset phenotypes of ARAC1 due to disruptions to the *LINC* complex [171]. With evidence also available to suggest that SUN1 deficiency may be a leading cause to the development to multiple cerebellar ataxia conditions [172], it is becoming evident that disruptions to the *SUN-KASH* NE interactions may be a causative factor in its onset.

As the maintenance of KASH proteins have been identified as a key factor in brain development, further links have also been made between this protein family and the development of a number of disorders associated with the brain, including schizophrenia, bipolar disorder, depression and autism spectrum disorders (ASD). Recent evidence has identified the *SYNE-1* gene as a potential candidate gene in the development of ASD through the application of whole-exome sequencing, through which it was shown that biallelic mutations in *SYNE-1* across both consanguineous and nonconsanguineous families were displayed [173, 174]. In further genome-wide association studies, links

between *SYNE-1* and both bipolar disorder and recurrent major depression were made [175] through which significant correlations in *SYNE-1* polymorphisms and disease onset were made. This helps to provide further support for the roles of nesprins in the development of numerous neurodegenerative diseases.

Over recent years, the *LINC* complex has been further implicated in the development of Emery Dreifuss muscular dystrophy (EDMD), characterised by progressive skeletal muscle wasting and potentially fatal cardiomyopathies. Much of the literature accredits its development to mutations in emerin (X-EDMD, EDMD1) and lamin A/C (EDMD2, AD-EDMD), however, increasing evidence is developing suggesting roles of further *LINC* complex components in its onset [37]. For example, in fibroblasts extracted from DMD suffering patients, distribution and abundance of nesprin-1 and -2 were seen to be altered compared to controls [176]. Through the use of both immunofluorescence and western blotting analysis, it was seen that nesprin-1 and -2 displayed decreased expressions across the NE of patients suffering from DMD, with the lower C-terminal containing isoforms of nesprin-1 displaying the largest decrease. Further studies also support these propositions in which lower isoforms of nesprin-1/-2 may be the leading nesprin contributor to EDMD, through evidence highlighting missense mutations residing in nesprin-1α and nesprin-2β, two small ONM and INM positioned, KASH- and SR-containing variants of *SYNE-1* and *SYNE-2* [82, 177]. It is believed that due to binding sites of nesprin-1 and nesprin-2 to emerin and lamin A/C overlapping, that disruptions to nesprin/emerin/lamin A/C interactions within the *LINC* complex lead to the development of EDMD [42].

With further links also suggesting roles for nesprin-1/-2 in the development of Duchenne muscular dystrophy (DMD) [176] and autosomal recessive myogenic arthrogryposis multiplex congenita (AMC) [178], it can be suggested that nesprins play key roles in the development of neuromuscular disorders. However, the exact mechanisms by which nesprins are able to stimulate the development of these disorders are still unclear due to the complex nature of *SYNE* genes and multiple nesprin isoform variants.

Of further interest was the identification of a down regulation of SUN2 in patient fibroblasts expressing DMD and EDMD-CMT phenotypes [176]. Upon closer inspection, the proteome of EDMD-CMT patient fibroblasts was significantly altered to that of healthy controls (*Figure 1.8*), displaying altered SUN2 interacting potential through the application of GST pulldown techniques. These findings further help to support suggestions that alterations in nesprin and SUN protein interactions across a range of EDMD patients may

be a contributing factor to disease onset, however, it is not yet known whether the observed differences in protein expression profiles are causative or resulting phenotypes from disease development.

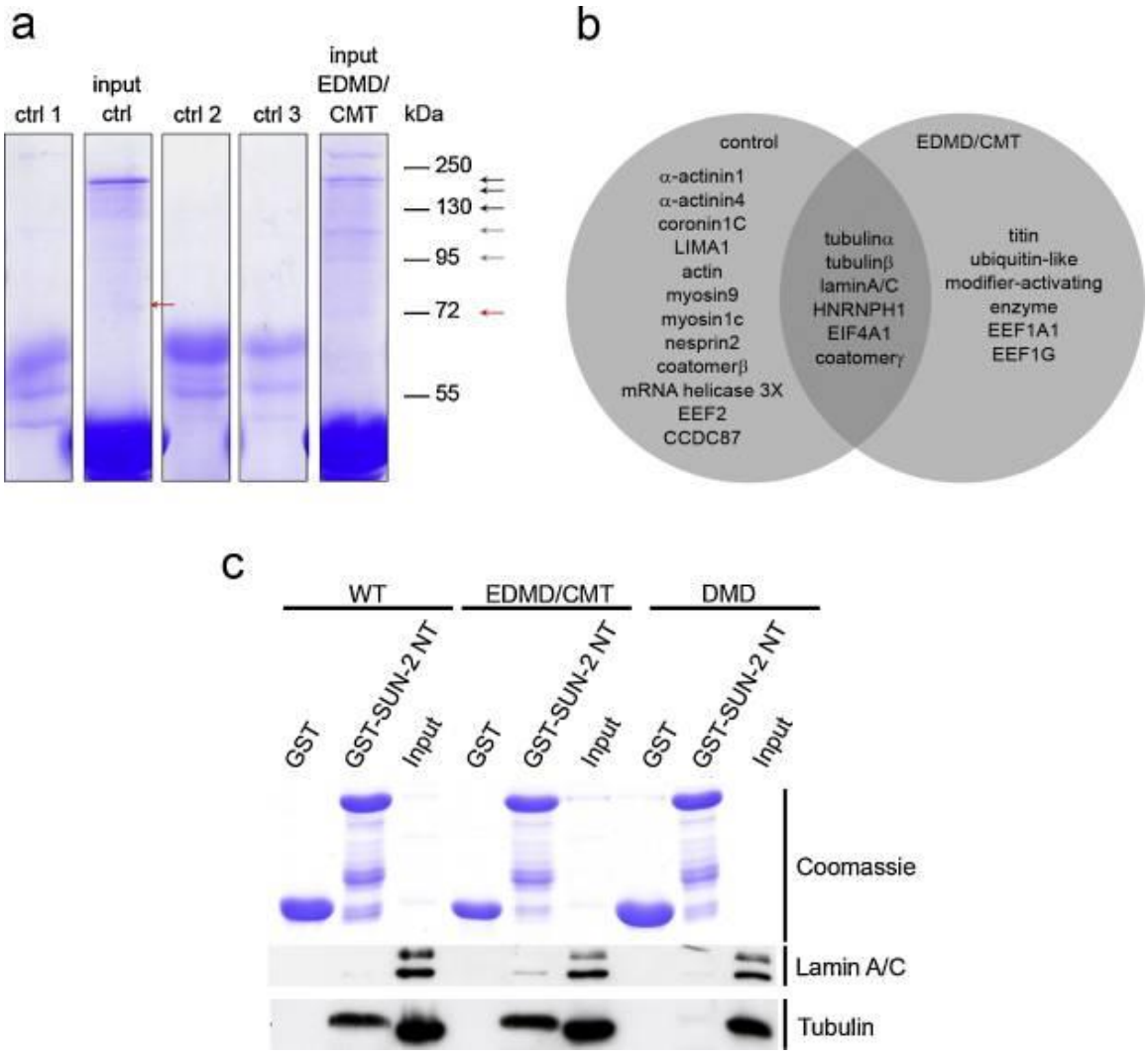

Figure 1.8: *SUN2 proteome from control and EDMD/CMT patients. (A) Displays Commassie blue staining from SDS gel electrophoresis of pulldowns using GST-SUN2Nt as bait. Ctrl 1 represents GST-SUN2Nt incubated with PBS, Ctrl 2 and 3 represent GST beads alone incubated with control and EDMD/CMT lysates respectively. Input Ctrl and Input EDMD/CMT represent GST-SUN2Nt incubation with the appropriate lysate. Red arrows display proteins only precipitated in control lysates, dark grey only the EDMD/CMT lysates and light grey controls (B) graphical representation of observed SUN2 binding partners in control and EDMD/CMT patients. (C) Pull down experiment using GST and GST-SUN2Nt, displaying precipitation of tubulin and lamin A/C [176].*

1.3.2 Roles of the LINC complex in premature aging.

The onset of accelerated aging diseases such as progeria has been well characterised over recent years, suggested to arise from defects in A-type lamin expression [179]. In many lamin A/C mediated progeria symptoms, further abnormalities have also been reported in *LINC* complex proteins such as SUNs and nesprins, in which increased expression of SUN1 alongside severe down regulation of nesprin-2G is observed [41]. Coupled with further mouse model and cell line data presented by Chi *et al*. [180], suggesting that SUN1 deletion in *LMNA* deficient mice and HGPS derived cells reduced progeric and dystrophic phenotypes, it was suggested the complex interplay between *LINC* complex proteins was central to the development of premature aging. Following from this research, Chen *et al.* was then able to verify the potential mechanism by which this SUN1 depletion reversed progeric effects of the *LMNA* mutations [181]. Through the use of light and electron microscopy techniques, it was shown that SUN1 contributes to the progerin-elicited structural defects arising across the NE and ER. Further to this, it was shown that the farnesylation of progerin enhanced its binding with SUN1, reducing SUN1s mobility across the NE. This reduced mobility resulted in the accumulation of SUN1 across the NE, resulting in the aberrant recruitment of progerin to the ER during post-mitotic re-assembly of the NE, which subsequently lead to the accumulation of SUN1 and progerin over consecutive cell divisions. It is therefore suggested that this de-regulation of SUN1 through progerin farnesylation leads to the accumulation of SUN1 across the NE, often a hallmark of Hutchinson-Guilford progeria syndrome (HGPS). This further provides an explanation as to why the observed deletion of SUN1 in progeric mice conducted by Chi *et al.* was able to revert some of the phenotypic symptoms.

1.3.3 Roles of nesprin-3/-4 in disease development.

SYNE-3 is known to code for at least two protein isoforms, termed nesprin-3α and nesprin-3β [182, 58], with nesprin-3α displaying high binding affinity to the ABD domains of plectin, MACF1 and MACF2 (MT-Actin Cross-linking Factor 1 and 2, respectively) inferred through its first unique SR. It was shown through *In vitro* siRNA silencing studies in vascular epithelium that nesprin-3 is required for the correct induction of flow induced polarity, and correct regulation of cytoskeletal-NE interactions [103]. However due to similar functionality also displayed by nesprin-2 [77], a potential redundancy mechanism

may also exist for systems displaying a loss of nesprin-3, which could explain why to date, no disease mutations have been linked directly to nesprin-3 in humans. In support of this suggestion, it was shown that in nesprin-3 knockout mice, nesprin-3 was not required for the maintenance of cell polarisation and migration in MEFs, nor the testicular morphology and efficient spermatogenesis [183], suggesting that the further mechanisms are acting to retain IF connections across the NE.

In contrast, *SYNE-4* encodes a single protein, the smallest nesprin family member nesprin 4. Unlike nesprin-1/-2/-3, nesprin 4 is found expressed exclusively in secretory epithelial cells and mechanosensory hairs of the cochlea, within which it is able to mediate NE-kinesin-1 binding across the ONM [184], dependent on SUN1 for its correct localisation. The binding function displayed by nesprin-4 and kinesin-1 has been further shown to regulate kinesin-mediated cell polarisation [185], through which overexpression of nesprin-4 leads to dramatic changes in centrosome and Golgi positioning in relation to nuclei.

It has been further suggested that nesprin-4 plays critical roles in the development of hearing due to its observed localisation across the NE of outer hair cells (OHC) [186]. It was shown by Horn *et al*. [184], that mice lacking nesprin-4 or SUN1 develop OHCs normally, however, as hearing matures, these cells begin to degrade. Further to this, it was shown that the OHC cells were unable to retain their basal nuclear positioning (*Figure 1.9*), potentially due to the loss of kinesin-1 mediated MT associations across the NE through nesprin-4 interactions. OHC cells act to amplify sound within the cochlea, through a variety of mechanisms, one of which is through the hyperpolarisation and depolarisation events, suggesting that these cells are highly mobile [187, 188]. It is believed that through an ATP dependent motility mechanism involving the modification of cytoskeletal proteins [189, 190], OHCs are able to tune and amplify large decibel sound input, whilst preventing overstimulation, which could potentially lead to cell stress and subsequent cell death [191]. As the nucleus is implicated in playing a cytoskeletal organising role in many tissues [192], it can be suggested that the inherent loss of nesprin-4 dependant coupling of MTs to the NE may result in alterations in MT dependant nuclear positioning [185], leading to the eventual loss of MT organisation and resulting ability to withstand mechanical stresses stimulated through sound input, leading to OHC death overtime and subsequent hearing loss [191].

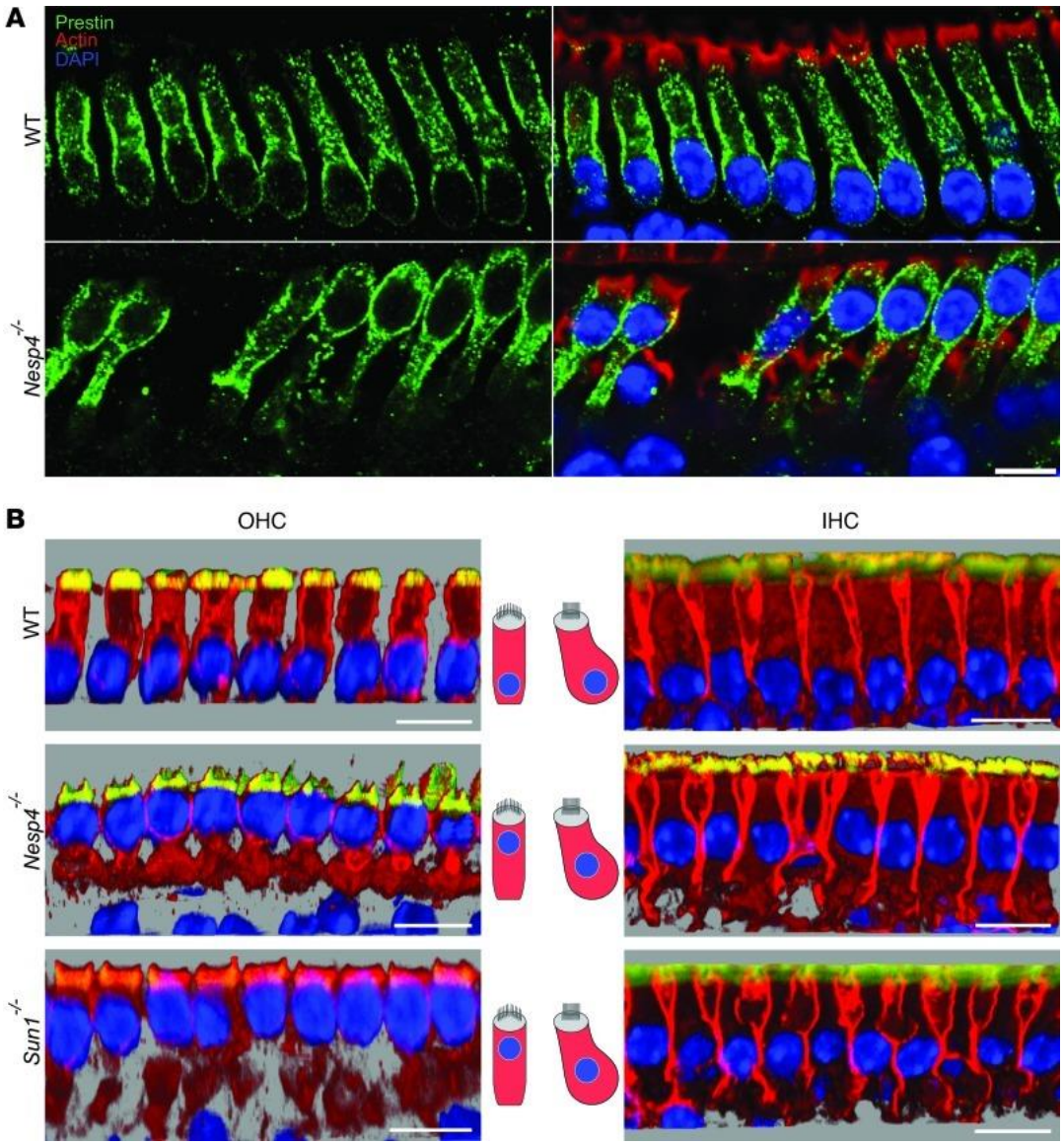

Figure 1.9: ***(A)*** *Whole mount cochlea P14 displaying nuclear localisation in WT and nesprin 4 knockout OHCs. Nuclei (blue), OHC membrane (green) and actin (red) are stained within each sample; clearly highlighting the nuclei in nesprin-4 knockout OHC's displaying a more apical localisation. (B) 3D confocal stacks depicting nuclear miss-localisation in nesprin-4 and sun1 knockout cochlea whole mounts. Staining's present include nuclei (blue), cytoplasmic membrane (red) and actin (yellow), helping to display that nuclei are miss localised in both OHC and inner hair cells (IHCs). Scale bars = 15 µm [184].*

1.3.4 Roles of the LINC complex in cancer development.

Due to our increasing understanding of the role played by the *LINC* complex in the maintenance of nuclear architecture, cell migration, mechanotransduction and cytoskeletal organisation [192, 127, 193, 194], current research is investigating whether *LINC* components play further roles in the development of cancer. Interestingly, whole genome/exome analysis has identified nesprin proteins as candidate cancer genes [195], with both *SYNE-1* and *SYNE-2* mutations implicated in the development of many cancer forms including breast [196, 197, 198], lung [199], pancreatic [195] and colorectal [200] cancers.

Although a wide range of cancers display high frequency of mutations in the *SYNE* genes, the exact mechanism by which nesprins could contribute to cancer development is still unknown. Based on current understanding that nuclei are the stiffest organelle in most cells [201] and that nesprins regulate nuclear architecture/stiffness, it can be suggested that these mutations lead to a loss of nesprin across the NE and subsequent reduction in nuclear stiffness. This increased nuclear malleability may then aid in the transmigration of cancerous cells from the primary tumour source to surrounding tissues, similar to that displayed by the highly malleable neutrophils which express very few *LINC* components [202]. This view is supported through current work by Matsumoto et al. [203], providing evidence suggesting that the *LINC* components lamin A/C, SUN1, SUN2 and nesprin-2 are all seen to be down regulated in breast cancer biopsies.

More recently, nesprins have been implicated in providing functional connections between non-muscle myosin IIB (NMIIB) and the NE, aiding in nuclear translocation during 3D MDA-MB-231 cell migration. NMIIB is a motor protein which is differentially expressed in a tissue specific and developmentally regulated fashion [204], implicated in both cell polarisation events and 2D/3D migration [205, 206]. During 2D migration, NMIIA is found at the sites of protrusions in the migratory edge, helping to stabilise nascent focal adhesions [207]. As the NMIIA filaments move rearward through actin retrograde flow, NMIIB co-assembles with the NMIIA filament and becomes the dominant isoform expressed in the cells posterior [208]. Interestingly, as mammary gland epithelial cells are driven through EMT, NMIIB expression is seen to be robustly upregulated [209]. This increased expression during EMT is suggested to contribute to the invasive behaviour of the newly formed mesenchymal like cells through its suggested roles in nuclear positioning [50]. It is now suggested however that NMIIB transmits force to the nucleus mediated through nesprin-2 interactions across the NE, which in turn aids in the nuclear

translocation required for cell migration during 3D invasion [210]. With further evidence now emerging implicating nesprins in the regulation of cell shape, malleability and migration [16, 211] it is increasingly evident that the roles of *LINC* complex in maintaining nuclear architecture, and more importantly NE integrity, is a critical factor in the development of cancer metastasis.

1.4 Current 3D culture models are becoming increasingly more relevant to the in vivo situation.

Over recent years, there has been ongoing work into the development of 3D culture models which more accurately capture aspects of the *in vivo* environment, such as the diffusion of molecules through tissues, or the effect of interstitial fluid flow on the concentration of secreted proteins [212]. Current applications of 3D materials are wide ranging, applied to the development of *in vitro* 3D tissue systems, drug screens and 3D models to study cancer development [213, 214].

1.4.1 Standard 2D cell culture imparts changes in gene expression, different to that found in vivo.

Alongside the emergence and subsequent expansion of applied 3D culture technologies, increasing evidence has been presented demonstrating the potential cellular changes associated with conventional 2D culture systems, leading to protein and genetic profiles distant from the *in vivo* situation. Alterations in 2D gene expression patterns across a range of cell lines has been increasingly noted in a wide variety of cellular functions, including proliferation and metabolism when compared back to their tissue of origin [215].

Investigations into the 3D morphology of breast cancer cell lines helps to demonstrate that there was a significant alteration in protein expression associated with signal transduction when 2D and 3D cultures were compared in addition to cells grown across different 3D growth environments [216]. Alongside these changes, it was further shown that when cultured in 3D, the cells adopted one of four distinct cell morphologies, which did not correlate to that observed under 2D growth conditions on tissue culture plastic.

Aside this, further investigations culturing hepatocellular carcinoma cells within a 3D gel also elicited changes in gene expression, shown to induce an upregulation of a range of matrix metalloproteinase (MMPs) and the focal adhesion proteins paxillin and focal adhesion kinase (FAK) [217]. This evidence demonstrated the altered localisation and expression profiles of both genes and proteins across a range of cells when compared between conventional 2D and 3D culture systems, highlighting the need for 3D culture systems.

1.4.2 Current 3D culture models are becoming increasingly more biologically relevant.

As the development of 3D culture technologies has expanded, the introduction of *in vivo* like environments has become a clear aim for these materials, with aims to provide a material able to accurately replicate a cells natural *in vivo* environment, leading to the cells displaying comparable gene and protein expression profiles. As multiple materials have been developed, the most impactful to date appear to be formed through the application of ECM hydrogel and synthetic scaffold systems.

1.4.2.1 ECM hydrogel cultures.

One current system that uses biological ECM reagents to develop novel 3D growth environments is the hydrogel. These polymeric materials have been seen to produce structures with a water content, biocompatibility and mechanical properties similar to that found within natural biological systems [218, 219]. Through adding cells to the hydrogel precursor prior to gelling, cells can be distributed homogeneously throughout the gel, leading to close cellular associations from the point of seeding. Alongside this, hydrogels are easily adapted to incorporate soluble or immobilised signalling molecules such as transforming growth factor β (TGF-β) and bone morphogenetic protein (BMP-2). This allows for the production of targeted environments that provide a supporting structure for specific cell growth and function. Numerous polymers, including natural and synthetic polymers are currently used to form hydrogels. Such natural polymers include collagen, hyaluronic acid and fibrin [220], and synthetic polymers include poly(ethylene glycol) (PEG) [221].

Whilst many of these systems can be formed through the polymerisation of a single ECM component, such as those found in the development of collagen gel systems, the microenvironment produced does not reflect the complexity of that found in normal biological systems. In contrast, systems incorporating a wide array of proteins such as in Matrigel® [220] have also been developed. However, even though the complexity of these systems is increased, closer to that of normal biological systems, they still lack the correct protein organisation as seen in the *in vivo* situation, leading to conflicting environmental cues.

A major drawback to the use of hydrogel systems as a platform to study cell migration is the weak structural rigidity exhibited by the gels. This mechanically weak polymer network may not withstand the forces exerted by the cells in order to migrate through restrictive environments.

1.4.2.2 Synthetic scaffold systems.

In addition to hydrogel systems, a wide range of porous and fibrous polymer scaffolds have also been applied to the development of novel 3D culture environments. These materials have been synthesized from a wide range of natural and synthetic polymers by a variety of fabrication techniques [222], and can be adapted to suit a range of system through tuning of the mechanical and/or chemical properties of the polymer network [223] [224]. These systems therefore provide a biologically inert environment, providing the opportunity to assess the effects of dimensionality within the 3D culturing environment in the absence of signalling cues which may arise from ECM hydrogel based systems.

Some examples of tailored scaffolds to suit the specific needs of cells grown within them include the reinforcement of skin equivalents using hyaluronic acid [225], human stem cell differentiation using poly(L-lactic-co-glycolic acid) (PLGA) [226], or ontogenesis on mPEG/hydroxyapatite scaffolds [227]. Alongside the components of the scaffold material, the fabrication methods used also introduce further functionality to the designed system. Current synthetic scaffold systems employ the numerous fabrication methods, including 3D printing, electrospinning and emulsion templating, each able to produce unique environmental conditions within which cells can adapt and respond [228].

Together, these systems help to demonstrate that over recent years, the desire for more *in vivo* like cell culturing techniques has led to the development of a wide range of 3D scaffold systems, each conferring unique properties to their biological systems.

Unfortunately however, one common trend with each system described is that as the biological relevance of the system increases, the ability to extract relevant data from the system appears to decrease.

1.5 Hypothesised Outcomes.

From the literature reviewed here, the following experimental outcomes are hypothesised:

- Chapter 3 - Disruptions to *LINC* complex connection spanning the NE will elicit NE and cellular phenotypic changes.
- Chapter 3 - The disruptions in this *SUN-KASH* bridge spanning the PNS may result in phenotypic differences emerging in migration across both 2D and 3D environments.
- *Chapter 3 - LINC-disrupted* mutant cells may exhibit increased migratory potential through challenging 3D migratory environments due to loss of NE integrity.
- Chapter 4 - Severing the connections between nuclear and cytoskeletal compartments through *LINC* complex disruptions may elicit changes in keratinocyte colony formation and subsequent differentiation potential, due to a loss of mechanotransduction between the nucleus and extracellular regions.
- Chapter 5 - Variability in *LINC* complex protein expression may be present across ranging breast cancer cell lines, of which nesprins would be suggested to display expression patterns which closely correlate to the cancer grade and aggression.
- Chapter 6 - Nesprins may further functionally interact with Nup88, a NPC protein with known links to increased cancer aggression.

1.6 Thesis Overview.

Work within this project aims to investigate the effects of *LINC* complex disruptions across the NE in both 2D and 3D culture environments. These investigations will aim to further our understandings as to roles of the *LINC* complex in maintaining directed cell

migration, cell-cell interactions and cell-substratum adhesion. Further characterisation of *LINC* complex components will then be conducted with aims to investigate whether correlation can be seen between protein expression patterns and the development of cancer aggression.

Chapter 3 will look at fully characterising the effects of disruptions to *SUN-KASH* perinuclear interactions, in relation to both 2D and 3D migration, cell colony formation, cell-substratum attachment and nuclear malleability. Further work will then be conducted to investigate whether differences in migration potential are evident between *LINC* disrupted and WT cells through both non-restrictive Alvetex® Scaffold and space-restrictive Alvetex® Strata 3D materials.

Following on from Chapter 3, work in Chapter 4 will aim to fully characterise both *LINC* protein localisation and expression patterns across a range of breast cancer cell lines, with aims to assess if correlations in expression profiles and cancer progression exist. Further work will then aim to assess migratory behaviours of representative control, low- and high-grade breast cancer cell lines within space-restrictive Alvetex® Strata scaffolds used in Chapter 3. With aims to assess whether any phenotypic similarities in migratory behaviour can be observed between the *LINC* disrupted keratinocytes characterised in Chapter 3 and high-grade breast cancer cells. In concluding sections of this chapter, immunofluorescence analysis of the key *LINC* complex protein nesprin-2 will be assessed across control, low- and high-grade primary breast biopsies, to investigate whether localisation or expression profiles appear to alter between the specimens.

Chapter 5 will aim to expand on findings from both Chapter 3 and 4, with two specified aims. The first to investigate whether *LINC* disrupted keratinocytes described in Chapter 3 displays migration advantages when co-cultured in both non-restrictive and space-restrictive 3D culture environments pre-seeded with fibroblast cells. And secondly, to assess whether the DN mutants display increased cell stacking in fibroblast co-culture conditions compared to both WT and single cultured conditions in Chapter 3. Assessment as to whether further differences exist between WT and DN HaCaT cells in their differentiation ability when lifted to the air-liquid interface will also be conducted, as the *LINC* disruptions may result in altered differentiation potential.

Finally, Chapter 6 aims to follow on from work conducted through each chapter thus far, aiming to assess whether nesprin-2 display interacting potential with the hypothesised binding partner Nup88 (component of the NPC). This theorised link between nesprin-2 and Nup88 can be implicated in the development of many forms of cancer, in which increased Nup88 levels, aside mutations in *SYNE-1/-2* are associated with increased

metastatic properties. To further our understanding of this interacting potential, assessment as to whether any functional relationships exist between nesprin-2 and Nup88 will also be conducted.

2. Materials and Methods

2.1 Routine 2D cell culture.

2.1.1 Cell Lines: COS-7, WT HaCaT, HDF, SW480, SW620 and HeLa.

The monkey derived kidney fibroblast cell line COS-7 (ATCC® CRL-1651™), human keratinocyte cell line HaCaT (AddexBio, T0020001), primary human dermal fibroblasts isolated from neonatal foreskin (HDF) (Life Technologies, C-004-5C), human adenocarcinoma cell lines SW480/SW620 (ATCC®, CCL-228™/ATCC®, CCL-2), and human cervical adenocarcinoma cell line HeLa (ATCC®, CCL-2) required the same culturing conditions. Cells were maintained in high glucose Dulbecco's modified Eagle's medium (DMEM, Sigma) supplemented with 10% v/v foetal bovine serum (FBS, Sigma), 2 mM L-glutamine (Sigma) and 100 U/ml penicillin/streptomycin (Sigma). Culturing was performed on CELLSTAR® plastic ware (Greiner Bio-one) at 37 °C in a 5% CO_2 environment and enzymatically passaged as outlined in 2.1.5, upon cells reaching 70% confluence.

2.1.2 Cell Line: DN SUN1 expressing clonal HaCaT.

Modified human keratinocyte cell line expressing luminal regions of SUN1-GFP [77] was maintained in high glucose DMEM supplemented with 10% v/v FBS, 2 mM L-glutamine, 100 U/ml penicillin/streptomycin and 400 µg/ml G418 (Geneticin, Sigma). Culturing was performed on CELLSTAR® plasticware at 37 °C in a 5% CO_2 environment and enzymatically passaged as outlined in 2.1.5, upon cells reaching 70% confluence.

2.1.3 Cell Lines: MCF 10A and MCF 12A.

The human derived mammary gland/breast cell lines MCF 10A and MCF 12A (ATCC) were maintained in DMEM: F12 (Sigma) containing 15 mM HEPES (4-(2-hydroxyethyl)-1-piperazineethanesulfonic acid) (Sigma) and $NaHCO_3$ (Sigma). Media was supplemented with 5% v/v horse serum (Invitrogen), 1 mg/ml hydrocortisone (Sigma), 100 µg/ml epidermal growth factor (EGF, Sigma), 1 mg/ml cholera toxin (Sigma), 10 mg/ml insulin (Sigma), 2 mM L-glutamine and 100 U/ml penicillin/streptomycin. Culturing was performed

on CELLSTAR® plasticware at 37 °C in a 5% CO_2 environment and enzymatically passaged as outlined in 2.1.6, upon cells reaching 70% confluence.

2.1.4 Cell Lines: MCF7, MDA-MB-231, T-47D and HCC-38.

The human mammary gland/breast adenocarcinoma cell lines MCF7 and MDA-MB-231, human mammary gland ductal carcinoma cell line T-47D and human mammary gland *TNM stage IIb* ductal carcinoma cell line HCC-38 (ATCC and Newcastle University), required the same culturing conditions. Cells were maintained in high glucose DMEM without phenol red (Sigma), supplemented with 10% v/v FBS, 2 mM L-glutamine and 100 U/ml penicillin/streptomycin. Culturing was performed on CELLSTAR® plasticware at 37 °C in a 5% CO_2 environment and enzymatically passaged as outlined in 2.1.5, upon cells reaching 70% confluence.

2.1.5 Routine passaging and propagation of cells.

All cell lines were enzymatically passaged by removing growth media, washing the adhered cells with sterile versene (phosphate buffered saline + [0.02%] EDTA (ethylenediaminetetraacetic acid) and incubating with 10% v/v trypsin (Lonza) in phosphate buffered saline (PBS, Sigma) at 37 °C. Incubation was conducted for 2 min (MCF7 and MDA-MB-231 cell lines), 5 min (COS-7, SW480, SW620, T-47D and HCC38 cell lines) and 10 min (WT HaCaT and DN HaCaT cell lines). Trypsin neutralisation was then performed with complete culturing media, followed by returning cells to the culture flask.

2.1.6 Passaging of MCF 10A and MCF 12A cell lines.

Enzymatic passaging of MCF10A and MCF 12A in a T-75 cell culture flask required more care due to increased sensitivity to trypsin. Growth media was removed followed by washing of the cells with cell culture grade PBS (Sigma). 2 ml of 10% v/v trypsin in PBS was then distributed evenly across the surface, and 1.5 ml subsequently removed leaving a thin film of trypsin. Once cells were dislodged, forming a single cell suspension, 5 ml of re-suspension media (DMEM: F12 supplemented with 20% horse serum and 100 U/ml penicillin/streptomycin) was added to neutralise the trypsin. The resulting cell suspension was then centrifuged for 5 min at 1000 rpm at 4 °C. The pellet was then re-suspended in fresh growth media and returned a T-75 culture flask.

2.1.7 Cryopreservation of cells.

All cell lines were cryopreserved at -150 °C in 1.5 ml Nunc cryovials (Thermo Scientific) following trypsinisation as described in 2.1.5, centrifugation of cell suspension at 1000 rpm for 5 min at 4 °C, and subsequent pellet re-suspension in freezing media at a density of one 70% confluent T-75 flask per 5 ml freezing media. Freezing media comprised of 10% v/v dimethyl sulfoxide (DMSO, Sigma) diluted in the specific culturing media for that cell line.

Cells were retrieved from cryopreservation by defrosting at 37 °C and diluting the freeze media in complete growth media. The suspension was centrifuged at 1000 rpm for 5 min maintained at 4 °C. The resulting supernatant was removed and the cell pellet re-suspended in fresh complete culture media. The suspension was then placed into a T-25 culture flask and incubated to obtain a monolayer culture.

2.2 Scratch wound assay.

2.2.1 Growth in 2D culture.

Cell lines were seeded into CELLSTAR® 24 well plates (Greiner Bio-one) and left to grow to 95% confluency with media changes every 2 days.

2.2.2 Scratch wound assay.

Upon obtaining 95% confluence, cells were serum starved (Incubated in normal culture media minus FBS) for 6 h, scratched using a 20-200 µl pipette tip (Greiner) and washed 3 times in cell culture grade PBS. Complete cell culture medium was then added to each well and cells were returned to an incubator at 37 °C with 5% CO_2 environment for 48 h.

2.2.3 Scratch wound assay analysis.

Phase contrast images of the wound were taken at the time of wounding, as well as 24 h and 48 h post wounding using the Leica DM1 3000 B light microscope with a Leica DFC310 FX camera attached using a 10x objective lens. Wound closure was analysed using ImageJ (v1.49s) to measure distances between the leading edge of cells across each side of the wound. At 24 h and 48 h time points, cells were fixed as described in 2.8.1 and stained with DAPI (4',6-diamidino-2-phenylindole) and phalloidin as described in

2.11.2. Fluorescence images were obtained using the Leica DM1 3000 B light microscope with a Leica DFC310 FX camera.

2.3 3D cell culture.

2.3.1 Scaffolds utilised.

We utilised two scaffolds: 12 well Alvetex® Scaffold and Alvetex® Strata inserts (Reinnervate, AVP002 and STP005). These polystyrene scaffolds were used in order to provide non-restrictive and space-restrictive 3D migratory environments respectively due to their varying void diameters.

For short term culturing (<14 days) scaffold inserts were placed into Greiner 12 well plates, with 4 mL of complete culture media. For longer term culturing (>14 days), three 12 welled inserts were placed into a triplet well insert holder in a deep well petri dish (Reinnervate, AVP015) alongside 50 mL of complete culture media.

2.3.2 Scaffold pre-treatment.

To ensure surface hydrophobicity Alvetex® Scaffolds were pre-treated with an oxygen plasma for 5 min at 40 W using the Emitech K1050X Plasma Asher. Alvetex® Strata scaffolds were subjected to oxygen plasma for 30 min at 10 W. Following treatment, scaffolds were left to cool for 10 min, then they were ready for use.

2.3.3 Preparation of cell suspensions for seeding scaffolds.

Cells cultured in 2D were trypsinised and counted as described in 2.1.5 and 2.5.1 respectively, followed by centrifugation at a 1000 rpm for 5 min at 4 °C. The resulting cell pellet was re-suspended at a cell density of 2.5 x 10^6 cells/mL.

2.3.4 Seeding cells to the scaffolds.

To seed the cells to the Alvetex® scaffold and Alvetex® Strata, 100 µl of cell suspension (2.3.3) containing 250,000 cells was applied directly to the centre of each pre-treated scaffold. The scaffolds were then placed in their respective culture dishes and moved into

a cell culture incubator for 20 min to allow cell attachment to the scaffold surface. Complete culture media was added.

2.3.5 Media changes.

To change the media during 3D culture, old media was removed through aspiration between the gaps in the insert (highlighted in *Figure 2.1*), ensuring the cells situated across the surface of the scaffold are not disturbed. New media was then place in the same gap between the insert and the culture dish.

For short-term culturing (<14 days), cell culture medium was replaced every 2-3 days in 12 well dishes. For long-term culturing (>14 days) in the deep well dishes described previously, media was replaced every 4-5 days. In addition, at 7, 14 and 21 days of culturing, cell culture dishes were replaced due to cellular build-up across the bottom of the dish.

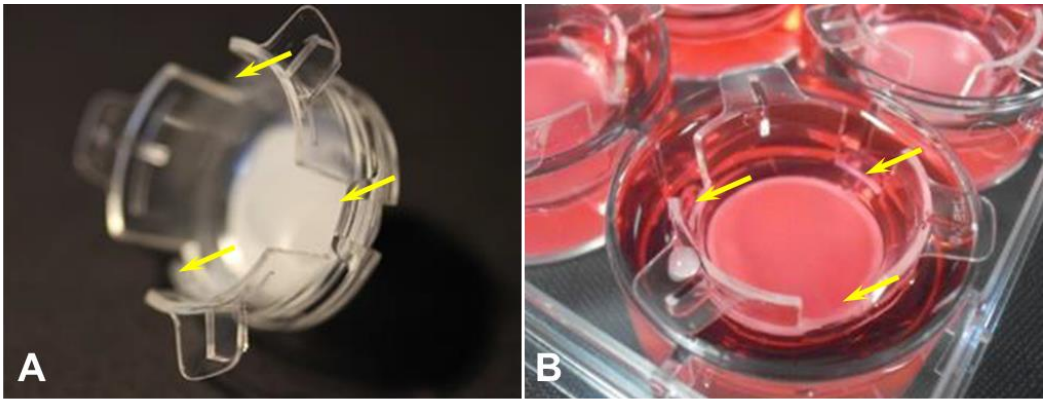

Figure 2.1: *Example images of Alvetex® scaffolds housed in their inserts. Arrows can be seen to highlight gaps in the insert to allow media flow across the scaffolds surface.*

2.3.6 Co-culture of fibroblasts and keratinocytes.

For the co-culture observations, 500,000 HDF cells at a T-75 confluence of 60% were placed onto plasma-treated scaffolds alongside complete culture medium and cultured in 12 well plates for 7 days. The scaffolds were transferred into triplet well insert holders in a deep well petri dish for a further 7 days. Either WT or DN HaCaT cells were then seeded as described in section 2.3.4, then cultured for a further 14 days. For both WT and DN cell lines, culture media described in 2.1.1 was used, as we have shown that DN HaCaT retain their phenotypic expression of DN SUN1 even after several months of drug removal.

2.4 2D culture scaffolds.

2.4.1 Rhombic micro-pillar materials.

To assess the nuclear deformity potential, a poly(L-lactic acid) (PLLA) micro-pillared polymer matrix containing protrusions of 7 µm width which extend from the surface to a height of 6 µm, was utilised [229]. The spacing between each pillar was 7 µm, and so nuclear deformity would be required for cells to settle fully within the material. These materials were kindly donated by Dr. Katrine Anselme of the Institute de Science des Materiaux de Mulhouse. Initially, cells were enzymatically passaged as described in section 2.1.5, producing a single cell suspension. 50,000 cells were then seeded onto the materials surface and cultured under normal growth conditions for 5 days.

2.4.2 Polycarbonate inserts.

To further test the migration potential of WT and DN HaCaT cell lines through restrictive void sizes of <4 µm, a commercially available polycarbonate scaffold (Corning® Costar®, Transwell™ insert) was used. This material contains a monolayer of 3 µm voids across a 24 mm diameter. Cells were enzymatically passaged as described in section 2.1.5 to produce a single cell suspension. Following this, 500,000 cells were placed onto the materials surface and maintained under normal culture conditions for 3 days.

2.5 Cell counting.

2.5.1 Neubauer Improved Haemocytometer.

To determine cell numbers for seeding within 3D cell culture experiments, 2D cultures were trypsinised into a single cell suspension as described in 2.1.5 and counted using a Neubauer improved haemocytometer (Marienfeld-Superior). To ensure consistency and accuracy of results, cell suspensions with a density between 0.5-1.5 x 10^6 were used to count the cells.

2.6 Plasmid preparation.

2.6.1 Bacterial transformation.

Plasmids used were amplified and purified by the following method: DH5α bacteria were thawed from -80 °C and a 50 µl aliquot of these competent cells was incubated with 2 µg/ml of the desired plasmid on ice for 15 min. The competent cell/DNA mixture was then heat shocked at 42 °C for 1 min and placed back on ice for a further 2 min. 500 µl of LB (lysogeny broth) broth solution (FORMEDIUM™, LMM0102) was then added to the competent cells, and the suspension was left to incubate for 1 h at 37 °C with periodic shaking. Once incubated, the suspension was then placed onto a 10 cm LB agar plate (FORMEDIUM™, LMM0203) containing the antibiotics the plasmid confers resistance to. Colonies were isolated and inoculated into 500 ml LB broth solution and incubated overnight at 37 °C with periodic shaking.

2.6.2 Plasmid purification.

To purify plasmids from the transformed bacteria described in 2.6.1, the competent cells were taken from an overnight incubation and purified using a PureYield™ plasmid midiprep system (Promega, A2492) according to manufacturer instructions. Upon plasmid purification, plasmid concentrations were calculated using a Genova spectrophotometer (Jenway, 736501). Concentration was measured at an absorbance of 260 nm followed by further measurements at 320 nm (adjustment measurement for turbidity), the output was then multiplied by the dilution factor, and using the relationship that A_{260} of 1.0 = 50 µg/ml pure dsDNA the concentration was obtained;

$$\text{Concentration (µg/ml)} = (A_{260}\text{ reading} - A_{320}\text{ reading}) \times \text{dilution factor} \times 50\ \mu g/ml$$

2.7 Plasmid transfections.

2.7.1 Cellular transfection.

Purified plasmids were incorporated into the desired cells by transfections via electroporation using an Amaxa® Nucleofector™ device, plasmids used within our investigation can be seen displayed in *Table 2.1*. Cells at a 70% confluence in a T-75 flask were dislodged from the culture flask as described in section 2.1.5, to obtain a single cell suspension. This cell suspension was then centrifuged at 1000 rpm for 5 min at 4 °C. The cell culture media was then aspirated off, and the pellet re-suspended with pre-

warmed, cell culture grade PBS. The resulting suspension was then re-centrifuged and re-pelleted as before. Transfections were then conducted using an Amaxa® Cell Line Nucleofector™ Kit V (Lonza), at a working plasmid concentration of 2 µg/µl. The Amaxa® Nucleofector™ device contains pre-programmed settings for each of the cell line used (COS7 – A-024, HaCaT – U-020, MCF7 – P-020, MDA-MB-231 – X013). Upon plasmid transfection, cells were quickly re-suspended in normal cell culture media and incubated for up to 4 days before processing. For transient transfections, protein expression deteriorates post 4 days in culture for most cell lines.

To maintain ectopic protein expression for periods >4 days, plasmids used encoded a resistance gene against a targeted drug. To establish effective drug concentrations to select for plasmid expression, kill curves were produced for each cell line, in which different drug concentrations were tested to establish the concentration required to kill 100% of cell within 1 week. This drug concentration (described in Chapter 4) was added 24 h after transfection, resulting in selection cells expressing the desired plasmid. Cells expressing the drug resistance were then selected from single colonies.

Table 2.1: *Plasmids used throughout our experimentation, detailing vectors/source of the plasmid, alongside the inferred antibiotic resistance.*

Plasmid	***Vector/Source***	***Associated antibiotic resistance***
pEGFP	*See ref.* [101]	*N/A*
pEGFP-Nup88	*Kindly donated by Dr Birthe Fahrenkrog* [230]	*Neomycin*
Nesprin-2-SR	*See ref.* [9]	*G418, Geneticin®*
Nesprin-2 siRNA	*See ref.* [101]	*N/A*
Control Nesprin-2 siRNA	*See ref.* [101]	*N/A*
Nup88 siRNA	*Santa Cruz, SC-75980*	*N/A*
Nesprin-2 mini	*See ref.* [77]	*G418, Geneticin®*
DN SUN1	*See ref.* [9]	*G418, Geneticin®*
SR-KASH	*See ref.* [9]	*G418, Geneticin®*

2.8 Sample Fixation.

2.8.1 2D monolayer cultures.

2D monolayers were fixed by growing them on glass coverslips or micro-pillar materials [229], washed for 5 min with PBS three times, and incubated for 15 min in 4% w/v paraformaldehyde (PFA, Sigma) in PBS at pH 7.4. Samples were then washed twice in PBS and stored at 4 °C for no longer than 3 days.

For the fixation of 2D monolayer cells on polycarbonate inserts, cells were washed for 5 min in cell culture grade PBS three times, and the polycarbonate membrane removed from the insert with a razor blade. The membrane was then immersed in 4% PFA in PBS, pH 7.4, and left to fix overnight at 4 °C. After fixation, the membranes were washed for 5 min in PBS twice and then stored at 4 °C until use.

2.8.2 3D cultures.

Cells cultured within Alvetex® scaffold and Alvetex® Strata were fixed as follows: inserts were rinsed once with cell culture grade PBS and carefully unclipped from the insert holder. Upon removal, scaffolds were washed a further two times in PBS for 5 min, submerged within 4% PFA in PBS, pH 7.4 and left at 4 °C overnight. After fixation, scaffolds were washed another two times in PBS and stored at 4 °C until used.

2.9 Histological processing.

2.9.1 Dehydration and Embedding.

Histological processing of Alvetex® scaffold and Alvetex® Strata materials was carried as described previously [231]. Briefly, samples fixed as described in 2.8.2 were washed in PBS for 5 min twice. Washing was then followed by 15 min incubations in varying ethanol concentrations of 30%, 50%, 70%, 80%, 90%, 95% and 100% v/v at room temperature. Scaffolds were subsequently removed from their housing inserts, cut in half across their diameter using sterilised surgical scissors and incubated for 15 min in Histoclear (Fisher, 12358637) at 60 °C. An equal volume of liquid paraffin wax (Fisher, 12624077) was added, and the scaffolds were incubated for 15 min at 60 °C. The Histoclear/liquid paraffin solution was then replaced with fresh paraffin wax, and the scaffolds were incubated for 1 h at 60 °C. Vertical embedding was then performed in which the scaffold sections were

placed into embedding moulds (Cellpath Ltd, GAD-5302-02A) with the cut side facing down. These were then topped with a labelled embedding cassette (SLS, HIS0029), and filled with fresh paraffin wax.

2.9.2 Sectioning.

Wax blocks were sectioned using a Leica RM2125RT microtome with MB Dynasharp microtome blades (Fisher, 12056679). For all cell lines, sections were cut to a thickness of 10 µm for conventional haematoxylin and eosin (H&E) staining, with subsequent 7 µm sections for antibody staining. Sections were then floated on a 42 °C water bath, mounted onto Superfrost+ microscope slides (Fisher, 10149870) and left to dry overnight on a 32 °C heated slide dryer.

2.10 Pathological samples.

Slides containing pre-paraffin embedded and sectioned pathological samples were obtained from Breast Cancer Now's tissue bank. Ethical approval was sought and approved from Breast Cancer Now's board of governance and from Durham University School of Biological and Biomedical Sciences Human Tissue Board (HTB). Samples were selected from a variety of patient sources based on their pathological phenotypes and defined grades in accordance with standard breast cancer grading systems. Approval for this work was received on 13/04/15, with a materials transfer agreement subsequently signed. Materials were received and recorded in line with legislation requirements on 16/05/15. A total of 324 sections were received. A third of which represented 18 serial sections of 6 patients derived from healthy premenopausal breast tissue obtained via breast reduction mammoplasty in pre-menopausal women. The second third was derived from ER+ (oestrogen receptor), PR- (progesterone receptor) tumours in pre-menopausal women and the final third from triple negative (ER-, PR- and HER2-) tumours in pre-menopausal women. These samples were intended for use within immuno-fluorescence analysis of *LINC* complex components.

2.11 Staining.

2.11.1 Haematoxylin and Eosin (H&E) staining.

Paraffin wax was cleared from the slides by washing with histoclear for 5 min at room temperature. Gradual sample rehydration was conducted through washes in 100% ethanol for 2 min, 95% and 70% ethanol for 1 min, and distilled water for a further 1 min. Nuclei were then stained via a 5 minute incubation in Mayer's haematoxylin (Sigma, H1532) (0.1% v/v haematoxylin, 0.02% v/v sodium iodate, 5% v/v aluminium potassium sulphate, 5% v/v chloral hydrate and 0.1% v/v citric acid in dH_2O), followed by a 1 min wash in distilled water and incubation in alkaline alcohol (3% ammonia in 70% ethanol) for 30 sec to stain nuclei. Samples were subsequently dehydrated by 30 sec incubations in 70% and 95% ethanol. Once dehydrated, cytoplasmic staining in 0.5% eosin (Sigma, E4009) in 95% ethanol for 1 min was carried out. The samples then underwent two 10 sec washes in 95% ethanol, followed by two washes in 100% ethanol, the first for 15 sec and second for 30 sec. Slides were then cleared via 2x 3 min washes in Histoclear, prior to mounting with DPX mounting media (Fisher, 10050080) and covering with a 50 x 22 mm coverslip (Fisher, 12383138).

Slides were left to dry at 4°C overnight and then imaged using a Leica DM500 light microscope with attached ICC50 HD camera at 10x and 20x magnifications utilising the LAS EZ software (Leica).

2.11.2 Immunofluorescence staining of 2D monolayers.

Cells were initially placed onto 10 mm glass coverslips (SLS) and grown to a confluence of 70% across the surface. Samples were then fixed as described in 2.8.1 and subsequently permeabilised in 0.5% v/v Triton X-100 (Fisher) in PBS for 10 min. Cells were washed for 5 min in PBS followed by 15 min blocking in 0.2% (w/v) cold water fish gelatine (Sigma), 0.5% (w/v) BSA (bovine serum albumin) in PBS (PBG). Primary antibodies were diluted in blocking buffer (PBG) to the dilutions stated in *Table 2.2* and incubated for 1 h. Samples were then washed three times in PBS for 5 min, followed by a further 1 h incubation in secondary antibodies alongside DAPI (4',6-diamidino-2-phenylindole) [20 mg/ml] (1 in 1000 dilution). The samples were then protected from light and diluted in blocking buffer to the dilutions displayed in *Table 2.3*. Post incubation, cells were washed five times in PBS for 3 min followed by mounting on Superfrost+ microscope slides (Fisher, 10149870) using Gelvatol mounting media (4.8 g Gelvatol, 24 ml glycerol,

24 ml 0.2 M Tris-HCl pH8.5 and 1.3 g DABCO [1,4-Diazabicyclo*(2,2,2)*octane]). Images were then obtained using a Leica SP5 confocal microscope with Leica LAS AF software.

Table 2.2: *Primary antibodies used for 2D immunofluorescence staining with suppliers and working concentrations.*

Antibody	***Host***	***Supplier***	***Catalogue Number***	***Working dilution***
Pan-Cytokeratin X	*Mouse*	*Millipore*	*MAB3412*	*1 in 500*
TRITC-conjugated Phalloidin	*N/A*	*Sigma*	*P1951*	*1 in 600*
β-tubulin	*Mouse*	*Sigma*	*T8328*	*1 in 100*
Nup88	*Mouse*	*BD Transduction*	*611896*	*1 in 2000*
Nesprin-1 (ABD)	*Rabbit*	*See ref. [232]*	*N/A*	*1 in 500*
Nesprin-1 (SPECII)	*Rabbit*	*See ref. [232]*	*N/A*	*1 in 100*
Nesprin-2 (pAbk1)	*Rabbit*	*See ref. [233]*	*N/A*	*1 in 300*
Nesprin-2 (K20)	*Mouse*	*See ref. [234]*	*N/A*	*1 in 1*
Nesprin-3	*Rabbit*	*In house unpublished reagent*	*Ab123031*	*1 in 5*
Nesprin-4	*Rabbit*	*See ref. [78]*	*N/A*	*1 in 100*
Mab414	*Mouse*	*Covance*	*MMS-120R*	*1 in 500*
SUN1 (282)	*Rabbit*	*abcam*	*Ab124770*	*1 in 300*
SUN1 (K71)	*Rabbit*	*abcam*	*ab74758*	*1 in 250*
SUN2	*Rabbit*	*GeneTex*	*GTX63578*	*1 in 50*
Lamin A/C	*Mouse*	*ImmuQuest*	*IQ608*	*1 in 10*
Lamin B1	*Goat*	*abcam*	*Ab16048*	*1 in 50*
Lamin B1 + B2	*Rabbit*	*Santa Cruz*	*B1913*	*1 in 50*
Vinculin	*Mouse*	*Sigma*	*V9131*	*1 in 100*

Table 2.3: *Secondary antibodies for 2D immunofluorescence staining with suppliers and working concentrations.*

Antibody	***Supplier***	***Catalogue Number***	***Working dilution***
Donkey anti mouse conjugated Alexa Fluor 488	*Molecular probes, Invitrogen*	*A21202*	*1:3000*
Goat anti mouse conjugated Alexa Fluor 568	*Molecular probes, Invitrogen*	*A11001*	*1:3000*
Chicken anti rabbit conjugated Alexa Fluor 488	*Molecular probes, Invitrogen*	*A21001*	*1:1500*
Goat anti rabbit conjugated Alexa Fluor 568	*Molecular probes, Invitrogen*	*A11011*	*1:1500*
Chicken anti goat conjugated Alexa Fluor 568	*Molecular probes, Invitrogen*	*A11041*	*1:3000*

2.11.3 Immunofluorescence staining of 3D paraffin embedded scaffolds.

Paraffin embedded scaffold sections were prepared as described in 2.9.1. Sections were then deparaffinised in Histoclear for 10 min, followed by gradual hydration through 5 min incubations in 100% ethanol, 70% ethanol and PBS. Antigen retrieval was then performed through microwave heating the samples three times for 5 min in citrate buffer (10 mM citric acid, 0.05% Tween 20, pH 6.0) with cooling at room temperature for 30 sec between each 5 min heating. The sections were then cooled to room temperature for 15 minutes, then treated with permeabilisation/blocking solution (20% normal goat serum (Sigma) in 0.4% Triton X-100 PBS) for 45 min. Primary antibody incubation was then performed overnight at 4 °C in a humidified chamber, with antibodies diluted in permeabilisation/blocking solution (20% v/v FCS and 0.4% triton x100 v/v in PBS). Antibodies used for paraffin embedded 3D scaffold sections are displayed in *Table 2.4*, alongside source and working concentrations.

Table 2.4: *Primary antibodies utilised for 3D immunofluorescence staining with suppliers and working concentrations.*

Antibody	***Host***	***Supplier***	***Catalogue Number***	***Working dilution***
E-Cadherin	*Rat*	*Sigma*	*U3254*	*1 in 100*
Keratin 14	*Rabbit*	*abcam*	*Ab7800*	*1 in 100*
YAP1	*Mouse*	*Novus biologicals*	*NB110-58358*	*1 in 100*
Keratin 10	*Rabbit*	*abcam*	*Ab76318*	*1 in 100*
Vimentin	*Rabbit*	*Kindly donated by Prof. R. Quinlan [235]*	*N/A*	*1 in 100*

Once stained with primary antibodies, the samples were then washed three times in PBS for 5 min, followed by incubation with a secondary antibody, diluted in permeabilisation/blocking solution, for 1 h at room temperature in a humidified chamber. Secondary antibody sources and working concentrations can be seen in *Table 2.5*.

Table 2.5: *Secondary antibodies utilised for 3D immunofluorescence staining with suppliers and working concentrations.*

Antibody	***Supplier***	***Catalogue number***	***Working dilution***
Donkey anti mouse conjugated Alexa Fluor 488	*Sigma*	*A21202*	*1 in 1700*
Donkey anti mouse conjugated Alexa Fluor 568	*Sigma*	*A21203*	*1 in 1700*
Donkey anti rabbit conjugated Alexa Fluor 488	*Sigma*	*A21207*	*1 in 1000*
Donkey anti rabbit conjugated Alexa Fluor 568	*Sigma*	*A21208*	*1 in 1000*

Following incubation, sections were washed a further three times in PBS for 5 min and mounted onto Superfrost+ microscope slides in *Vectashield/DAPI* hard set mounting media (Vector Labs H-1400). Slides were then left to set overnight at 4 °C and subsequently imaged using a Leica SP5 confocal microscope with Leica LAS AF software.

2.11.4 Immunofluorescence of pathological sectioned breast tissue samples.

Pathological samples were stained utilising a modified version of the protocol described in 2.11.3. Sections were deparaffinised overnight in Histoclear, followed by two 10 min washes in Histoclear. Samples were hydrated by 5 min incubations in 100% ethanol, 70% ethanol and PBS. Antigen retrieval was performed using citrate buffer (10 mM citric acid, 0.05% Tween 20, pH 6.0) pre-heated in a water bath at 95 °C. The samples were incubated in the heated citrate buffer for 20 min, then left to cool to room temperature. Once cooled, permeabilisation/blocking solution (20% normal goat serum in 0.4% triton X-100 PBS) was added. The samples were then incubated in a humidified chamber for 45 min. Primary antibodies, diluted in permeabilisation/blocking solution, were then added and the samples were left to incubate overnight at 4 °C in a humidified chamber. Details of the antibodies used for staining pathological samples are displayed in *Table 2.6*.

Table 2.6: *Primary antibodies utilised for 3D immunofluorescence staining of pathological samples, with suppliers and working concentrations.*

Antibody	Host	Supplier	Catalogue Number	Working dilution
Nesprin-2 (pAbK1)	Rabbit	See ref. [233]	N/A	1 in 100
Actin	Mouse	Sigma	A5316	1 in 100
p63	Mouse	abcam	ab53039	1 in 50

Following primary antibody incubation, samples were washed three times in PBS for 10 min, then incubated for 1 h in secondary antibodies diluted in permeabilisation/blocking solution (secondary antibodies, and dilutions used were the same as those detailed in *Table 2.5*). Samples were washed three times in PBS for 10 min, and then mounted on Superfrost+ microscope slides using *Vectashield/DAPI* hard set mounting media. The slides were then left to set at 4 °C overnight and imaged using a Leica SP5 confocal microscope.

2.11.5 Super resolution microscopy staining.

Cells were initially passaged and seeded onto (22 x 22) mm square coverslips (Fisher, 12898715), as described in 2.1.5, and then left to grow to 70% confluence. This monolayer of cells was then processed as described in 2.11.2. One difference in the protocol occurs post-incubation in secondary antibody. At this stage, cells were washed for 5 min with PBS and incubated for 15 min in a 1:1000 dilution of Hoechst (Molecular Probes, 33342) to stain the nuclei. Samples were washed a further four times in PBS for 3 min followed by mounting on Superfrost+ microscope slides using non setting *Vectashield* without DAPI. Coverslips were then sealed with nail varnish and left to set overnight at 4 °C. Images were collected using a DeltaVision OMX Blaze V4 (Ge healthcare, Applied precision) super resolution microscope under 3D SIM settings. Image analysis was conducted using ImageJ v1.49.

2.12 Western Blotting.

2.12.1 Sample preparation: from cell culture to cell lysates.

2.12.1.1 2D Lysate production.

To produce sample lysates form a single T-75 flask at 70% confluence, cells were washed three times for 1 min in cell culture grade PBS. The PBS was removed and 500 µl RIPA (Radioimmunoprecipitation assay buffer) buffer (50 mM Tris-HCl (Sigma), pH 7.5, 150 mM NaCl (Sigma), 0.1% SDS (sodium dodecyl sulphate, Sigma), 1% Nonidet P-40 (Sigma), 0.5% sodium-deoxycholate (Sigma)) containing 1% protease inhibitor cocktail (PIC, Sigma) was added and the flask cooled to 4 °C. All following procedures were conducted on ice to prevent autolysis. Cells were dislodged using a cell scraper, collected in the RIPA buffer, and transferred to a pre-cooled Eppendorf tube. The Eppendorf tube was then incubated on ice for 15 min. During the 15 min incubation, mechanical breakdown of cellular components was performed using a sterile 1 ml syringe fitted with a 24G x ¾ inch disposable hypodermic needle. Samples were syringed 15 times to ensure lysate homogenization, efficient protein extraction and genomic DNA sheering. The resulting solution was then centrifuged at 4 °C for 15 min at 12 000 x *g* to pellet the remaining cell debris. The resulting supernatant was then extracted and combined with 120 µl of 5x concentrated Laemmli sample buffer (0.25 M Tris-HCl, pH 6.8, 20% glycerol (Sigma), 4% SDS, 1.43 M β-mercaptoethanol (Sigma) and 0.2% bromophenol blue (Sigma)) and heated to 99 °C for 4 min. Samples were then stored at -20 °C until use.

2.12.1.2 3D lysate production.

To produce sample lysates from restrictive Alvetex® Strata scaffolds, cells were washed three times for 2 min in cell culture grade PBS. Scaffolds were then removed from their inserts and cut into small (~1 mm) square pieces with sterilised scissors. Scaffold pieces were then combined with 500 µl RIPA buffer containing 5 µl protease inhibitor cocktail in a pre-cooled Eppendorf and incubated on ice for 15 min. All following procedures were conducted on ice. During the 15 min incubation, the Eppendorf was vortexed every 3 min for 30 sec to dislodge cells. Following incubation, samples were sonicated for 1 min using the MSE soniprep 150 sonicator, then centrifuged at 4 °C for 15 min at 12 000 x *g* to pellet the remaining cell and scaffold debris. The resulting supernatant was then extracted and combined with 120 µl of 5x concentrated Laemmli sample buffer and boiled at 99 °C for 4 min. Samples were then stored at -20 °C until use.

2.12.2 Sodium Dodecyl Sulphate Polyacrylamide Gel Electrophoresis (SDS-PAGE).

For 10% polyacrylamide gels, we combined 9 ml of 10% polyacrylamide stock solution (375 mM Tris HCL pH 8.8, 10% v/v Protogel Acrylamide (PAA, Fisher), 0.1% w/v SDS), with 22 µl 10% ammonium persulfate (APS, Sigma) and 10 µl tetramethylethylenediamine (TEMED, Sigma). This solution was then poured into a gel caster (Hoefer Inc.) topped with isobutanol and left for 45 min to set.

For gradient gels, we used a gradient mixer system (VWR, 700-7104) to produce gels with a range of 3-15% acrylamide concentrations. 5.5 ml of 3% polyacrylamide stock solution (25 mL of 1.5 M Tris-HCl pH 8.8, 10 mL [30%] acrylamide, 1 mL of [10%] SDS and 64 mL H_2O) was mixed with a 15% polyacrylamide stock solutions (25 mL of 1.5 M Tris-HCl pH 8.8, 50 mL [30%] acrylamide, 1 mL [10%] SDS and 24 mL H_2O) as it was drawn into the gel caster. This resulted in a gradient gel, with a 15% base, decreasing in polyacrylamide concentration towards the top of the gel. The solution was topped with isobutanol after pouring, and left for 45 min to set.

Once set, the isobutanol was removed and a 4% polyacrylamide stock solution (1.7 M Tris-HCl pH 6.8, 4% v/v PAA and 1.72% w/v SDS) was combined with 30 µl APS and 16 µl TEMED, was then poured over the surface of the resolving gel. The comb was then inserted to form the wells and left for 10 min to set. Once set, sample lysates produced by the method described in 2.12.1 were thawed and loaded in equal protein concentrations alongside a standard protein ladder. Samples were then electrophoresed at a constant

voltage of 100 V for 20 min, followed by an increase in voltage to 120 V until the dye front reached the base of the gel. Glass plates were then separated, and the gel was equilibrated in transfer buffer (25 mM Tris-Base, 190 mM glycine, 0.1% SDS, 10% ethanol) for 1 min.

2.12.3 Tank (wet) western blot electro-transfer.

Following SDS-PAGE, wet electro transfer of proteins from the gel to a more stable membrane platform was carried out. Within a transfer compression cassette (VWR, CLEVSB10C), a fibre pad (VWR) was placed across the negative electrode region, followed by two layers of Whatman paper wetted with transfer buffer. The SDS-PAGE gel was then placed on top of this Whatman paper layer, followed by the activated PVDF (Polyvinylidene fluoride) membrane. The PVDF membrane was activated by washing in methanol (15 sec), distilled water (2 min), and transfer buffer (5 min). Two layers of transfer buffer wetted Whatman paper and a fibre pad layer were then placed on top of the SDS-PAGE gel, and then the compression cassette closed. The complete compression cassette was then placed into the electrophoretic transfer tank (VWR, 700-7131) filled with 2 L western blot transfer buffer ([10%] ethanol, 25 mM Tris and 190 mM glycine in H_2O) and set to a constant voltage of 10 V for 18 h, followed by an increase in voltage to 45 V for a further 2 h.

2.12.4 Membrane blocking and immuno-blotting.

Following protein transfer, the compression cassette was disassembled and protein standard positioning was labelled on the PVDF membrane for future reference. The membrane was then washed for 10 sec in methanol and left to dry sandwiched in Whatman paper for 15 min. Following this, membrane blocking was conducted through incubation in blocking solution (5% skim milk powder (Sigma) in PBS) at ambient temp for 30 min. The membrane was then rinsed twice for 15 sec in a solution of 0.1% Tween-20 in PBS, followed by a single 5 min wash in a fresh portion of the 0.1% Tween-20 in PBS solution. Primary antibody, diluted in blocking solution, was then added to the membrane and shaken overnight at 4 °C using a rocking shaker. The primary antibodies used are described in *Table 2.7*.

Following the overnight incubation in primary antibody, the membrane was washed three times for 10 min in a solution of 0.1% Tween-20 in PBS, followed by a further 1 h incubation in secondary antibody, diluted in blocking buffer, at ambient temp, on a rocking

shaker. Details of secondary antibodies used, alongside working concentrations can be seen in *Table 2.8*.

After secondary antibody incubation, membranes were washed three times, for 5 min in a solution of 0.3% Tween-20 in PBS, followed by three 5 min wash in a solution of 0.1% Tween-20 in PBS.. The washing solution was then removed from the membrane, and excess liquid removed with a paper towel. Freshly made ECL (enhanced chemiluminescence) detection solution (2.51 mM luminol (Sigma), 413.58 µM p-coumaric Acid (Sigma), 1 M Tris HCl pH 8.5 (Fisher) and 0.01% v/v hydrogen peroxide (Sigma)) was then added to the membrane and left for 1 minute. The excess ECL was then removed and membranes exposed to high performance photographic film (GE Healthcare Life Sciences), followed by film development

Table 2.7: *Primary antibodies utilised for western blot detection, with suppliers and working concentrations.*

Antibody	***Host***	***Supplier***	***Catalogue Number***	***Working dilution***
Pan-Cytokeratin X	*Mouse*	*Millipore*	*MAB3412*	*1 in 500*
β-actin	*Mouse*	*Sigma*	*A5316*	*1 in 1000*
β-tubulin	*Mouse*	*Sigma*	*T8328*	*1 in 2000*
λ-tubulin	*Mouse*	*Sigma*	*T6557*	*1 in 100*
YL ½ tubulin	*Mouse*	*Abcam*	*Ab6160*	*1 in 1000*
Acetylated Tubulin	*Mouse*	*Sigma*	*T7451*	*1 in 100*
GAPDH	*Mouse*	*Millipore*	*6C5*	*1 in 3000*
Nup88	*Mouse*	*BD Transduction*	*611896*	*1 in 500*
Nesprin-1 (ABD)	*Rabbit*	*See ref. [232]*	*N/A*	*1 in 300*
Nesprin-1 (SPECII)	*Rabbit*	*See ref. [232]*	*N/A*	*1 in 500*
Nesprin-2 (pAbk1)	*Rabbit*	*See ref. [233]*	*N/A*	*1 in 1000*
Nesprin-2 (K20)	*Mouse*	*See ref. [234]*	*N/A*	*1 in 500*
Nesprin-3	*Rabbit*	*Abcam*	*Ab123031*	*1 in 500*

Nesprin-4	*Rabbit*	*See ref. [78]*	*N/A*	*1 in 400*
E-Cadherin	*Rat*	*Sigma*	*U3254*	*1 in 1000*
Emerin	*Mouse*	*Abcam*	*Ab49499*	*1 in 500*
Mab414	*Mouse*	*Covance*	*MMS-120R*	*1 in 400*
SUN1 (282)	*Rabbit*	*Abcam*	*Ab124770*	*1 in 1000*
SUN1 (K71)	*Rabbit*	*Abcam*	*Ab74758*	*1 in 1000*
SUN2	*Rabbit*	*GeneTex*	*GTX63578*	*1 in 1000*
Lamin A/C	*Mouse*	*ImmuQuest*	*IQ608*	*1 in 350*
Lamin B1	*Goat*	*Abcam*	*Ab16048*	*1 in 4000*
Lamin B1 + B2	*Rabbit*	*Santa Cruz*	*B1913*	*1 in 500*
Lap2α	*Mouse*	*BD Transduction*	*611000*	*1 in 200*
Centrin	*Rabbit*	*Santa Cruz*	*sc-27793-R*	*1 in 500*
Peri-Centrin	*Rabbit*	*Abcam*	*Ab4448*	*1 in 500*
Vimentin	*Rabbit*	*Kindly donated by Prof. R. Quinlan [235]*	*N/A*	*1 in 400*
p53	*Mouse*	*Abcam*	*Ab7757*	*1 in 1000*
JNK	*Mouse*	*Cell signalling*	*9258S*	*1 in 1000*
Phosphorylated JNK	*Mouse*	*Cell signalling*	*4668S*	*1 in 1000*
p38 total	*Mouse*	*Cell signalling*	*9212S*	*1 in 2000*
Phosphorylated p38	*Mouse*	*Cell Signalling*	*28B10*	*1 in 1000*
82F-HSP27	*Mouse*	*Kindly donated by Prof. R. Quinlan [236]*	*N/A*	*1 in 100*
3270-GFAP	*Rabbit*	*Kindly donated by Prof. R. Quinlan [237]*	*N/A*	*1 in 250*
ACD5-HSP27	*Rabbit*	*Kindly donated by Prof. R. Quinlan [236]*	*N/A*	*1 in 250*
2D2B5-CRYAB	*Mouse*	*Kindly donated by Prof. R. Quinlan [237]*	*N/A*	*1 in 100*
3148-CRYAB	*Rabbit*	*Kindly donated by Prof. R. Quinlan [237]*	*N/A*	*1 in 200*

Table 2.8: *Secondary antibodies utilised western blot detection, with suppliers and working concentrations.*

Antibody	***Supplier***	***Catalogue Number***	***Working dilution***
Goat anti rabbit conjugated POD	*Sigma*	*A6154*	*1 in 3000*
Goat anti mouse conjugated POD	*Sigma*	*P4416*	*1 in 4000*
Goat anti rat conjugated POD	*Sigma*	*A9037*	*1 in 1500*
Rabbit anti goat conjugated POD	*Sigma*	*A5420*	*1 in 2500*

2.13 Electron microscopy imaging.

2.13.1 Transmission electron microscopy (TEM) of 2D cultured samples.

For a single T-75 culture flask at 70% confluence, fixation was performed by aspirating off the culture media and rinsing the surface with PBS. Following this, a 30 min incubation in 2% glutaraldehyde in NaHCa buffer (30 mM HEPES, 100 mM NaCl, pH adjusted to 7.4 with NaOH, followed by addition of 2 mM $CaCl_2$) was conducted. Cells were then washed a further two times for 5 min in NaHCa buffer (30 mM HEPES, 100 mM NaCl, pH'ed with NaOH followed by addition of 2 mM $CaCl_2$ in dH_2O), before a further 15 min incubation in a solution of 1% tannic acid and 0.075% saponin at room temp. The tannic acid solution was removed, and cells rinsed a further two times in NaHCa buffer for 5 min. Following this, the cells were washed twice in 0.1 M cacodylate buffer (10 ml 0.2 M sodium cacodylate pH 7.4 in 10 ml H_2O) for 10 min. Cells were then rinsed with 1.5 ml cacodylate buffer and then scraped off the surface of the flask using a cell scraper, and transferred to a 1.5 ml centrifuge tube. The cell suspension was then centrifuged at 1000 g for 4 min. The supernatant was then removed, and the resulting pellet incubated for 1 h in a solution of 0.5% osmium tetroxide in 0.1 M cacodylate buffer in a rotating mixer. A further two 5 min washes in 0.1 M cacodylate buffer then followed.

The cell pellet was then dehydrated by washing for 5 min, three times in 50%, 70% and 95% ethanol solutions, followed by three 10 min washes in 100% ethanol. The cell pellet was then transferred to a glass vial and infiltrated with a 1:1 mixture of 100% alcohol and propylene oxide for 10 min. The infiltration process was then repeated, followed by two 10 min incubations with propylene oxide. The cell pellet was then incubated for 30 min in a 1:1 mixture of propylene oxide and epoxy resin (EPON™ 828) at 60 °C. This mixture was then replaced through two 30 min washes in 100% epoxy resin at 60 °C. Finally, the pellets were orientated in embedding moulds (Agar scientific), and incubated in fresh epoxy resin at 60 °C for 24-48 h to allow the resin to polymerise.

Ultra-thin sections were cut using a Leica EM UC6 microtome. Sections were cut at 70 nm, and mounted onto Formvar coated copper grids. The grids were dried by blotting on filter paper, and then incubated in a drop of uranyl acetate for 10 min. The grids were then rinsed twice for 20 sec in distilled water, followed by 10 min incubation in lead citrate (0.4% lead citrate w/v, 0.5% sodium citrate in 0.1 N NaOH). The grids were then left to dry for 20 min and imaged using a Hitachi TEM-H7600 transmission electron microscope.

2.13.2 Transmission electron microscopy (TEM) of 3D cultured samples.

Cells were prepared as described in section 2.3 scaffolds were removed from inserts and washed three times for 5 min in PBS at room temperature. Scaffolds were then cut in half and fixed at room temp for 1 h using Karnovsky's double strength fixative (5% glutaraldehyde, 4% paraformaldehyde, 0.1 M cacodylate buffer and 50 mg $CaCl_2$/100ml). Following fixation, scaffolds were incubated in 1% Osmium tetroxide for 1 h, dehydrated through three 5 min washes in 50%, 70% and 95% ethanol solutions, and then washed three times in 100% ethanol for 10 min each time. The scaffolds were then infiltrated with 1:1 mixture of 100% ethanol: propylene oxide for three times for 10 min each time. The infiltrated scaffolds were then washed three times with propylene oxide for 10 min. Once washed, the scaffolds were cut into smaller pieces and incubated in 1:1 mixture of propylene oxide: epoxy resin overnight. Following the overnight incubation, the scaffolds were then incubated for 30 min in epoxy resin (11.75 g epon 812, 6.25 g dodecenyl succinic anhydride (DDSA), 7 g methyl nadic anhydride (MNA) and 0.375 ml benzyle dimethylamine (BDMA) twice. The scaffolds were then transferred to resin moulds with fresh epoxy resin and left to set for a further 24-48 h. Once set, samples were sectioned as described in 2.13.1 and imaged using a Hitachi TEM-H7600 transmission electron microscope.

2.13.3 Scanning electron microscopy (SEM) imaging.

Cells were cultured as described in section 2.3, and the scaffolds removed from their inserts and incubated in BRB80 buffer (80 mM PIPES, 1 mM $MgCl_2$, 1 mM EGTA, pH 6.8 with KOH) + 0.001% digitonin for 10 min. Fixation was then conducted by a 2 h incubation in a solution of 2% glutaraldehyde and 0.1% tannic acid in PHEM buffer (5 mM HEPES, 60 mM PIPES, 10 mM EGTA, 2 mM $MgCl_2$, pH 7 with KOH)). The scaffolds were then incubated in 0.1 % Osmium tetroxide for 30 min, and then dehydrated through 5 min washes in 10%, 20%, 40%, 60%, 80% ethanol, and then washed twice for 5 min in 100% ethanol. Scaffolds were then critical point dried using a Balzers CPD 030 and sputter coated with 10 nm platinum using a 328 Cressington sputter coater. The scaffolds were then fractured and placed onto silicon chips using double sided tape. Sample imaging was conducted using a Hitachi S5200 scanning electron microscope.

2.14 Atomic force microscopy (AFM) imaging.

2.14.1 AFM under non-biological conditions.

Cells were passaged as described in 2.1.5 and seeded onto glass coverslips until 70% confluence was achieved. Cells were then washed three times for 5 min in PBS, then left to air dry for 1 h at room temp. Once dried, single cells were imaged using a Bruker MM8 AFM fitted with a 70 kHz Scanasyst cantilever, expressing a 0.4 N/m spring constant and triangular tip (radios 2-12 nm, height 2.5 – 8 nm) (Bruker, Scanasyst-Air) within a (15 x 15 x 5) µm grid. Image analysis was then conducted using NanoScope Analysis 1.5 software.

2.14.2 AFM under biological conditions.

Cells were passaged as described in 2.1.5 and seeded onto 35 mm plastic petri dishes (TPP). Analysis was then performed when cells reached 60% confluence. 30 min before analysis, cells were washed three times for 1 min with sterile PBS, and 5 ml of sterile filtered CO_2 independent culture media (Fisher) was added. Cells were then analysed using a Nanowizard® 3 Bioscience AFM (JPK) using a (D)NP silicon nitride probe cantilever, expressing a spring constant of 0.06 - 0.7 N/m (Bruker, DNP-10) over a (100 x 100 x 10) µm grid. Cells were maintained at a constant temperature of 37 °C throughout image collection. Young's modulus values were then assessed across different cell regions using the Gwyddion image analysis software.

2.15 GST Pull-down.

2.15.1 GST-SR purification.

Initially, DH5α bacteria expressing the last four spectrin repeats across the C-terminal region of nesprin-2 bound to GST [77] (glutathione sepharose transferase) were inoculated into 5 ml LB broth (Formedium™) and 50 µg/ml ampicilin, and grown overnight at 37 °C with moderate shaking. 500 ml of fresh LB broth was inoculated with 4 ml of the overnight culture, and incubated for 2-4 h, until the OD at 600nm was >0.5. Protein expression was then induced through 0.5 mM IPTG (Isopropyl β-D-1-thiogalactopyranoside) addition to the culture overnight at 20 °C. Following overnight induction, the bacterial culture was centrifuged at 1500 x g for 10 min. The resulting pellet was then rinsed in STE buffer (10 mM Tris pH 8, 150 mM NaCl and 1 mM EDTA) and centrifuged at 3,500 rpm for a further 10 min. The pellet was then re-suspended in ice cold 7 ml STE buffer and 1% protease inhibitor cocktail containing 100 µm/ml Lysozyme (Sigma) and transferred to a Dounce homogenizer (Fisher) on ice. All following procedures were performed on ice. Cells were homogenized 10-20 times for 15 min, followed by the addition of sarkosyl [1.5%] v/v final concentration. The resulting solution was vortexed for 30 sec, then sonicated for 1 min. Sample was then centrifuged at 25,000 x *g* rpm for 30 min, and the resulting supernatant transferred to a separate tube, whilst the pellet was re-suspended in equal volumes of STE buffer and mixed with SDS-loading buffer (as described in 2.12.1), ready for loading as a control. To 8 ml of the transferred supernatant, 3.2 ml 10% Triton X-100 in STE buffer was added in 0.3 ml aliquots and mixed ready for GST bead incubation. To ensure successful protein purification, samples from both the pellet and supernatant were run on SDS-PAGE as described in 2.12.2 and subsequently stained using coomassie blue.

2.15.2 SR attachment to GST beads.

Following SR purification, GST beads (GE healthcare, 17, 5279-01) were cleaned through four 3 min washes in PBS, with centrifugation and supernatant removal after each wash. Incubation with 1:1 v/v ratios of GST bead slurry and isolated SR protein overnight at 4°C on a rotary shaker was then carried out. The beads were then washed a further two times for 5 min in STE buffer and stored at -20 °C until needed. A 20 µl aliquot was taken prior to storage of the beads and added to 5 µl SDS loading buffer as a control for GST-SR before cellular incubation.

2.15.3 Cell lysate production and GST-Pulldown.

To assist in protein isolation, COS7 cells were transfected as described in section 2.7 with pEGFP Nup88 in order to increase Nup88 levels, and increase protein availability for interactions with the GST-SR beads. Cells were cultured as described in section 2.1.1 until a confluence of 80% was reached in a T-75 flask. Cells were then rinsed twice, for 1 min each time, with PBS then incubated in 5 ml PBS containing a 1:100 dilution of PIC (protease inhibitor cocktail) (Sigma), 1 mM DTT (dithiothreitol) (Sigma), 1 mM benzamidine (Sigma), 1mM EGTA (Sigma) and 1 mM PMSF (phenylmethanesulfonylfluoride) (Sigma), and then scraped off the surface using a cell scraper. The cell suspension was centrifuged for 5 min at 2500 x g, and the pellet was then re-suspended in 1 ml lysis buffer (50 mM Tris-HCl pH7.5, 150 mM NaCl, 1% Nonidet P-40 and 0.5% Na-deoxycholate) and placed on ice for 15 min. During this incubation, mechanical breakdown was performed five times using a sterile 1 ml syringe fitted with a 24G x ¾ inch disposable hypodermic needle. The samples was then sonicated five times for 10 sec each time, followed by centrifugation at 16000 x *g* for 10 min at 4 °C. The resulting supernatant was then extracted and incubated with the GST-SR beads described in 2.14.2 for 2 h at 4 °C with moderate shaking. Following lysate incubation with the GST-SR beads, the beads were centrifuged at low speeds and washed six times for 1 min each with lysis buffer. The resulting solution was then centrifuged at 14000 x *g* for 2 min, and the supernatant removed and prepared as a control. The GST-SR beads were then re-suspended in 1:5 ratio of 5x concentrated Laemmli sample buffer to GST-SR beads. Samples were then run and assessed using western blotting as described in 2.12.3.

2.16 Förster resonance energy transfer (FRET) / fluorescence lifetime imaging microscopy (FLIM).

HaCaT cells were cultured and fixed onto glass coverslips as described in 2.1.2 and 2.8.1 respectively, followed by immunofluorescence staining for Nup88 and Nesprin-2's C-terminal (pAbK1) as described in 2.11.2. Within this experiment, the anti-mouse 488 secondary was used for Nup88 staining, and was considered the donor, whereas the anti-rabbit 568 secondary was used for Nesprin and considered the acceptor.

Initially, a sample of HaCaT cells stained only for Nup88 using the anti-mouse 488 secondary antibody was assessed to gain an average reading for the fluorophore's lifetime between excitation and emission without the presence of an acceptor. Once this

baseline was established, a PicoQuant event timer and TCSPC module attached to the Leica SP5 confocal microscope was used to assess the fluorescence lifetime of the anti-mouse 488 fluorophore with the acceptor present. It is widely accepted that if an fluorescence lifetime reduction greater than 0.5 ps is observed, then an association between the donor and acceptor fluorophores is suggested [238, 239], meaning that the two proteins of interest are in close association.

2.17 Statistical analysis.

Statistical analysis of data produced was carried out using Microsoft Excel and the R programming language. Where two experimental groups were directly compared, a Student's t-test was performed. For more than two experimental groups, we used a Univariate Analysis of Variance (*ANOVA*) to determine trends within the data. The type of statistical test performed can be seen stated in each experiment, with statistical significance between the groups highlighted on graphical figures as * for differences where $p \leq 0.05$ and ** for differences where $p \leq 0.005$. All error bars presented in figures represent ± standard deviation of the mean unless otherwise stated.

3. The characterisation of *LINC* complex roles within 2D and 3D growth and migration.

3.1 Introduction.

The *LINC* complex spans the double membrane of the nuclear envelope (NE), physically connecting nuclear structures to the cytoskeletal network. This protein bridge acts as a force transduction element within the cell [102, 240], facilitating cellular processes such as nuclear migration [241], cell polarity, [127] and chromatin organisation [99] in response to environmental cues. Alongside roles in maintaining cellular function, *LINC* components have been shown to maintain nuclear architecture [41, 101], which in turn influences both nuclear and cellular stiffness. Current understanding of *LINC* roles in nuclear and cellular stiffness are not well understood, however both nuclear and extracellular matrix stiffness have been shown to be key factors in influencing migratory behaviour, cellular function such as YAP signalling, and differentiation [242, 243, 244, 245]. To characterise potential *LINC* complex roles in cellular growth and migration, we employed stably transfected HaCaT lines expressing a DN SUN1 construct [77]. This mutant overexpressed the luminal domain of SUN1, which encompasses the coiled-coil region and SUN domain fused to GFP, which in turn, outcompetes endogenous full length SUN1 for KASH binding. Thus, endogenous SUN1 is no longer able to connect to the ONM due to the oversaturation of KASH domains by the DN-GFP fusion. This mutant therefore represents a severance of the link between INM and ONM, shown in *Figure 3.1*.

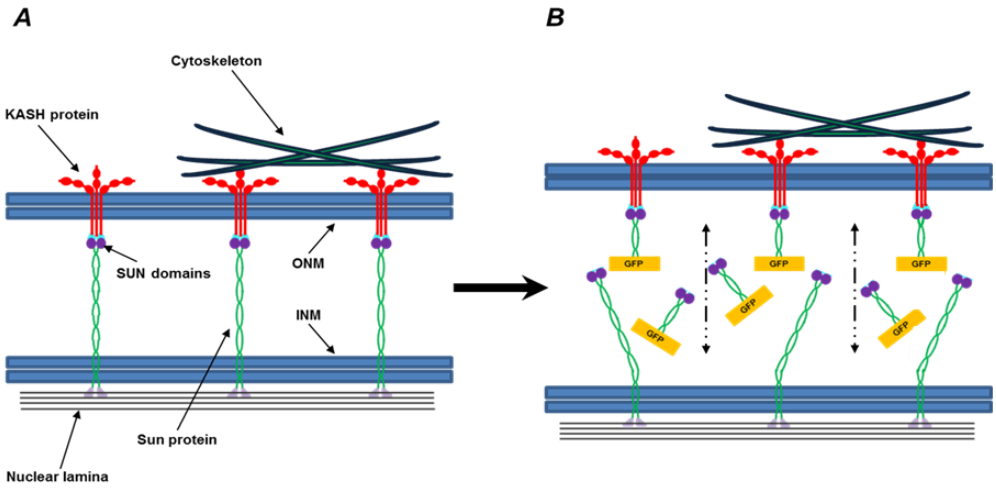

Figure 3.1: *Insertion of DN SUN1 results in the loss of KASH-SUN domain interactions. The loss of these interactions results in dilation of the nuclear membrane. DN SUN 1 constructs included the entire luminal SUN1 domain fused with GFP.*

3.1.1 LINC components function in maintaining directed cell migration, proliferation and cell signalling.

3.1.1.1 The KASH-SUN perinuclear interactions are crucial for maintaining cell polarity.

The *LINC* complex is a double membrane adhesive assembly, formed by interactions between inner NE SUN proteins and outer nuclear envelope *KASH* proteins across the perinuclear space. This connection is capable of transmitting mechanical force and signals across the NE, functioning in a wide range of cellular processes.

Cell polarisation via centrosome positioning is underpinned by *SUN-KASH* interactions across the NE helping to maintain directed cell migration, differentiation and tissue formation in many systems [246, 100]. It has been shown that the *KASH* protein nesprin-4 can influence cell polarity through Golgi and centrosome re-organisation via kinesin-1 mediated microtubule associations across the NE [78]. It was shown by Roux *et al.* that expression of nesprin-4 in non-polarised HC11 cells lead to kinesin mediated detachment of the centrosome from NE regions. These finding suggest nesprin-4-kinesin 1 interactions mediate the localisation and attachment of centrosomes across the NE. Further *KASH* containing proteins of the *LINC* complex have also been shown to play roles in the maintenance of cell polarity [103]. It was shown that loss of nesprin-3 functionality through siRNA knockdowns in human aortic endothelial cells (HAECs) caused miss-localisation of the microtubule-organising centre (*MTOC)*, resulting in the development of abnormal cell shapes. Nesprin-2 and *KLC1* depletion in the human keratinocyte HaCaT line have also been shown to alter normal centrosome positioning at the NE, resulting in loss of directed cell migration [77]. These results suggest that *LINC* components are crucial for the maintenance of cell polarity due to their role in connecting the nucleus and cytoskeleton.

3.1.1.2 LINC complex components control nuclear positioning.

Nuclear positioning plays key roles in organ physiology, tissue formation and directed cell migration [247] aiding in cellular responses to developmental and extracellular cues (*Figure 3.2*). It has been suggested that nuclear positioning is maintained through *LINC* mediated associations with the cytoskeleton, through which regulation of multiple cell

signalling pathways can be maintained including the mitogen activated protein (MAP) kinase pathway [97]. *LINC* components, such as nesprins, have been shown to regulate nuclear positioning by associating with kinesin and dynein motor proteins at the NE [84]. Microtubule dependent nuclear movement, required for skeletal muscle development in mice was shown to be impaired upon loss of Kinesin-1, leading to nuclear clustering both *in vivo* and *in vitro*. This phenotype was shown to be reversible through the accumulation of active Kinesin-1 motors at the NE via a ligand inducible dimerization system between FKBP-EGFP-KASH (FK506 binding protein chaperone fused to EGFP-KASH) embedded in the ONM and HA-Kif5B-FRB (FKBP-rapamycin binding domain fused to Kif5B-HA). This then formed a system by which the heterodimerisation of FKBP and FRB domains is induced by the cell permanent ligand rapalog. These investigations suggest strong evidence for the localisation of Kinesin-1 motor proteins across the NE to be responsible for maintaining normal nuclear migration. Nesprin-1 has been further shown to regulate nuclear anchorage within mouse skeletal muscle, with nesprin-1 loss stimulating abnormal nuclear positioning, resulting in decreased tissue stiffness and a reduction in tissue strain resistance [248, 249].

Alongside this microtubule dependent nuclear positioning, actin cytoskeletal elements are also crucial to nuclear movement. Transmembrane actin-associated nuclear (TAN*)* lines, comprising of nesprin-2G and SUN proteins anchored by A-type lamins have been suggested to influence nuclear positioning within cells [96]. Further evidence suggests the interactions between nesprin-2G and *FHOD1* (FH1/FH2 domain containing protein 1) allows the formation of these TAN lines across the NE. Disruptions in either A-type lamins, nesprin-2G or SUN proteins have been further shown to stimulate TAN line loss, resulting in abnormal nuclear positioning due to disruptions in centrosome positioning in polarising fibroblasts. [7, 94].

Alongside the nesprin family of KASH proteins, SUN proteins, located at the INM, have also been shown to affect nuclear positioning. SUN1 and SUN1/SUN2 double knockout mice display abnormal nuclear positioning within skeletal muscle [250], suggesting that the maintenance of the *SUN-KASH* bridge spanning the NE is crucial in maintaining correct nuclear positioning.

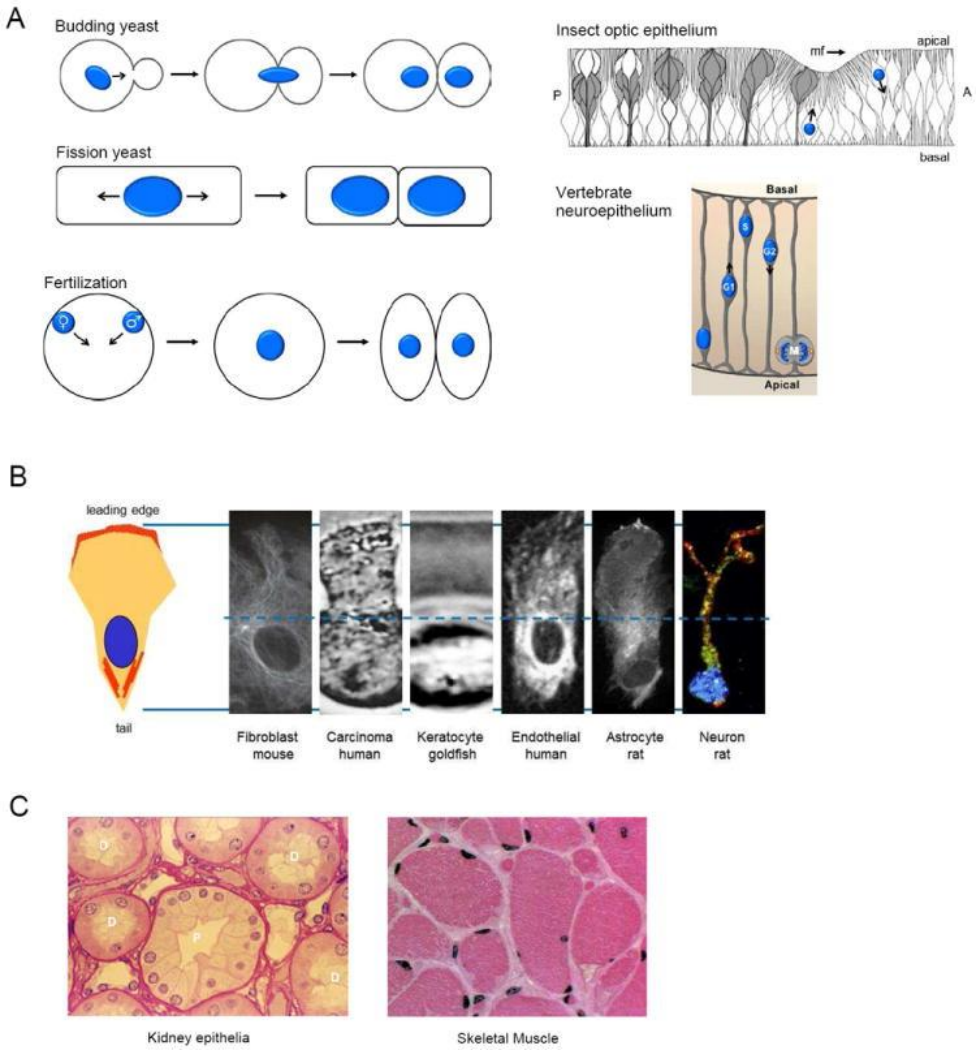

Figure 3.2: *A. Nuclear positioning in dividing cells and developing epithelium. Arrows indicate direction of nuclear movement. The nucleus is positioned relative to division plane in yeast and fertilised eggs. The diagram of insect optic epithelium represents a longitudinal section of a larval eye disc; two nuclei are shown. Nuclei anterior (A) to the morphogenetic furrow (mf), which moves anteriorly, move basally. Nuclei posterior (P) to the furrow move apically as cells are recruited into clusters comprising ommatidium (white cells, cones; grey cells, R-cells). The diagram of vertebrate neuroepithelium represents a longitudinal section of the developing cerebral cortex. Nuclei move basally during G1 and apically during G2. Mitosis (M) occurs near the apical surface. (B) Left highlights schematic of a cell with a protruding leading edge, actin filaments are highlighted in red. Right, montage of cells with the front-back dimensions normalised. Dotted line represents the midpoint between the front and back of each cell displaying nuclei are maintained at the back of the cell during migration. (C) Cross section of kidney cortex displaying nuclear positioning in the centre of each cell. In skeletal muscle, nuclei are positioned at the periphery. [97].*

3.1.1.3 LINC components play roles in proliferation and cellular signalling.

LINC complex proteins are involved in a wide variety of cellular functions. In addition to those highlighted above, nesprin-2G has been shown to play a role in both cell proliferation and wound healing [251]. Primary cells from nesprin-2G knockout (KO) mice display reduction in proliferation, and altered differentiation of keratinocytes, along with reduced cellular migration during wound healing. In addition, it was further shown that in nesprin-2 knockdown HaCaT cells (through shRNAs induced sequence specific silencing), the rate at which *TGF-β* induced *SMAD was localised to the nucleus* was reduced, suggesting that nesprins play further roles in cellular signalling.

Nesprins have been further suggested to play important roles in signalling pathways such as the *ERK1/2* (Extracellular signal-regulated kinase) and Wnt pathways [252, 9]. It was shown that nesprin-2, *ERK1/2* and *PML* (promyelocytic leukemia protein) co-localise at the NE. With nesprin 2 functionality in this pathway discerned through siRNA/DN nesprin construct insertion, stimulating an increase in *ERK1/2* function, leading to increased cellular proliferation.

3.1.2 The growing field of 3D cell culture.

Recently, 3D cell culture technologies and methods have expanded, incorporating the use of new materials that aim to replicate *in vivo* environments. It has been shown that in conventional 2D cultures, the extracellular matrix components, cell-cell and cell-matrix interactions, that are important for differentiation, proliferation and cellular functions *in vivo* are disrupted [253]. In contrast to this, 3D culture technologies have been shown to display increased expression and deposition of *in vivo* extracellular matrix components compared to their 2D monolayer counterparts [254], alongside integrated cellular signalling between cells due to their closer associations [255].

For use within this investigation, a material that provides both restrictive and non-restrictive growth environments was required in order to allow for the assessment of cell growth and migration with and without *LINC* complex disruptions. Materials with restrictive growth environments were deemed as those through which nuclear deformities would be required to migrate due to interconnects between material regions being narrower than nuclear width or height.

3.1.2.1 Potential 3D culture models to study cell behaviour and migration.

In an attempt to bridge the gap between current culturing techniques and real life systems, a wide range of biological components have been incorporated into 3D cell culture platforms [256, 257]. In the context of assessing migratory behaviour, the incorporation of features such as increased dimensionality, culture heterogeneity and close cellular associations are crucial. These factors can alter the cellular behaviours found in conventional 2D systems, directing cells to adopt migratory behaviours, which better resemble the *in vivo* phenotypes.

One current system that uses biological reagents to develop novel 3D growth environments is the hydrogel. These polymeric materials have been seen to produce structures with a water content, biocompatibility and mechanical properties similar to that found within natural biological systems [218, 219]. Through adding cells to the hydrogel precursor prior to gelling, cells can be distributed homogeneously throughout the gel, leading to close cellular associations from the point of seeding. Alongside this, hydrogels are easily adapted to incorporate soluble or immobilised signalling molecules such as transforming growth factor β (*TGF-β*) and bone morphogenetic protein (*BMP-2*). This allows for the production of targeted environments that provide a supporting structure for specific cell growth and function. Numerous polymers, including natural and synthetic polymers are currently used to form hydrogels. Such natural polymers include collagen, hyaluronic acid, fibrin and a variety of extracellular matrix proteins (Matrigel®) [220], and synthetic polymers include poly(ethylene glycol) (PEG) [221]. However, a major drawback to the use of hydrogels as a platform to study cell migration is the weak structural rigidity exhibited by the gels. This mechanically weak polymer network may not withstand the forces exerted by the cells in order to migrate through restrictive environments.

In addition to hydrogels, a wide range of porous and fibrous polymer scaffolds have been developed. These materials have been synthesized from a wide range of natural and synthetic polymers by a variety of fabrication techniques [222]. These materials can be adapted to suit a range of system through tuning of the mechanical and/or chemical properties of the polymer network [223]. Some examples of such tailored scaffolds include the reinforcement of skin equivalents using hyaluronic acid fibres [224], human stem cell differentiation using poly(L-lactic-co-glycolic acid) (PLGA) [225], or oncogenesis on mPEG/hydroxyapatite scaffolds [226]. Alongside the components of the scaffold material, the fabrication methods used also introduce further functionality to the designed system. Current synthetic scaffold systems employ the numerous fabrication methods, including

3D printing, electrospinning and emulsion templating, each able to produce unique environmental conditions within which cells can adapt and respond [227, 228, 258]. As a result of their increased mechanical integrity compared with hydrogels, a synthetic porous polymer will be used as a scaffold for 3D cell culture in this investigation.

3.1.2.2 Disadvantages of 3D migration assays.

Due to the increasing complexity of many 3D culturing systems, the means of extracting data regarding cell penetration and viability is becoming increasingly more complex, often requiring sophisticated analysis methods. 2D migration assays allow for quick and simple analysis of cell migration using single plane microscopy on either fixed or live cell systems. 3D work often requires more complex methods of tracking cells through the x, y and z planes [259]. Many cell tracking methods in 3D systems come with trade-offs between ease of use methods, which may have potential to stimulate cell damage, and process resource or time intensive methods, which in turn are less disruptive to the cells [260]. Alternative systems are available to assess 3D migration capacity in controlled systems, such as the Transwell® systems [261], however, these monolayer materials are not representative of *in vivo* systems. These factors will all have to be considered throughout this investigation to obtain accurate data with limited cellular disruption.

3.1.3 LINC complex roles in nuclear stiffness and cell migration.

Cell malleability is known to play an important role in cell migration and is partially underpinned by nuclear proteins such as *LINC* complex components [262, 263]. However, the fundamental role of nuclear malleability in this process is not well understood. With the nucleus being the largest and considered the stiffest organelle in the cell [264], it can be hypothesised that nuclear malleability, alongside cellular malleability could be a contributing factor to cellular penetration potential. Initial data suggests that in conventional 2D systems, cellular and nuclear malleability is affected upon cell migration [265]. This is also observed in many 3D migration systems. Current investigations highlight the nuclear lamina situated across the INM, as this protein network is seen as a major contributor to nuclear stiffness. Mouse embryonic fibroblasts (MEFs) derived from lamin A/C-deficient mice were observed to penetrate through a microfluidic system much

faster than their control counterparts, suggesting that the loss of lamin A/C induced a loss of nuclear stiffness, and increases cell migration potential [266]. It is further suggested that altering endogenous assemblies of A- and B-type lamins can influence migration potential through restrictive environments, as well as influence cellular resistance to migration-related stress [267]. In addition, the *SUN-KASH* interaction across the perinuclear space is also suggested to play a role in the maintenance of cell migration. It was shown that through incorporation of mutant SUN2, *SUN-KASH* interactions were disrupted, impairing cell migration, with subsequent WT SUN2 re-insertion able to promote cell migration [59]. Therefore, it can be suggested that as a complex of proteins, *LINC* components may be a major contributing factor in maintaining the mechanical properties of the cell, and in cell migration potential.

3.2 Chapter Aims.

This chapter aims to investigate the effects of *LINC* complex disruptions on normal cellular processes, such as colony formation and cellular migration in both 2D and 3D cell culture environments. To achieve this, multiple analysis techniques including scratch wound assays, western blotting, 3D scaffold technologies and atomic force microscopy will be used. From this it is aimed to provide insights into the potential roles of nuclear envelope proteins on cell migration.

3.2.1 Objectives.

- To assess the effects of *LINC* complex disruptions on the cell growth phenotypes of a human keratinocyte cell line.
- To assess whether *LINC* complex disruptions affect nuclear malleability and 2D migration potential.
- To assess whether loss of the *SUN-KASH* 'bridge' between the nucleus and cytoplasm affects other *LINC* complex associated protein levels.
- To assess the effects of *LINC* complex disruptions on the 3D migration potential in two 3D scaffold models, representing both restrictive and non-restrictive growth environments respectively.

3.3 Results.

3.3.1 Disrupting the LINC complex stimulates altered 2D growth phenotypes in culture.

3.3.1.1 DN HaCaT cells present increased cell clustering under 2D growth conditions.

It has been described previously [77] that DN HaCaT cells (expressing a DN SUN1 construct, which outcompete endogenous SUN for KASH interactions), present multiple cellular defects. These defects include reduced proliferation and migration rates, alongside nuclear deformities. Through sub-culturing, initial observations when compared to WT HaCaT cells, suggested that the DN HaCaT's further display more compact colony morphologies, as displayed through fluorescence microscopy analysis in *Figure 3.3*.

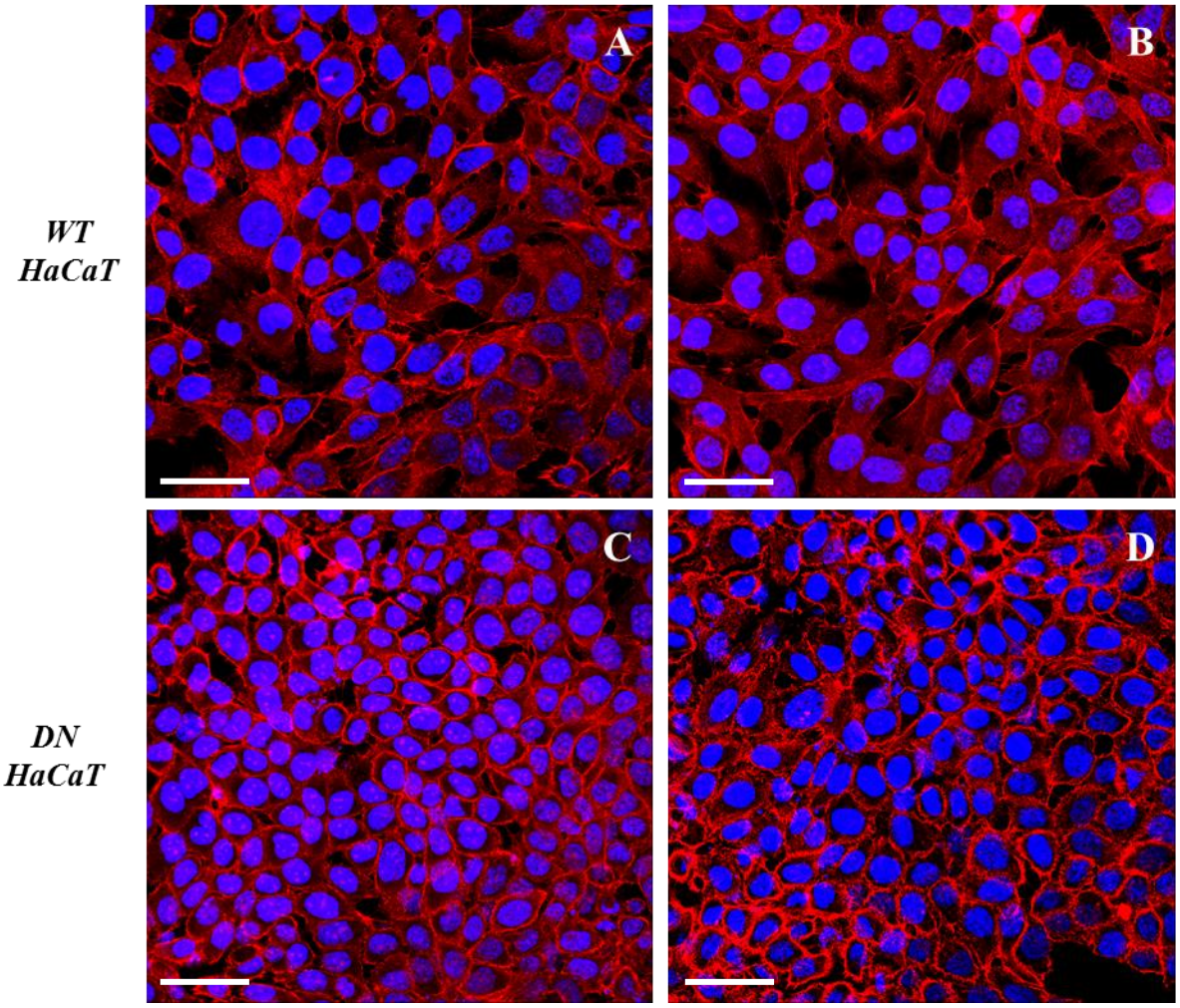

Figure 3.3: *TRITC-conjugated Phalloidin (Red) and DAPI (Blue) stained WT and DN HaCaT cells within a 70% confluence 2D culture. Scale bar = 20 µm.*

As seen in *Figure 3.3*, DN HaCaT cells appear to cluster in much more compacted colonies, displayed through *TRITC-conjugated* phalloidin staining, allowing visualisation of cytoplasmic F-actin. When collated with nuclear DAPI staining, it can be clearly seen that the DN HaCaT cells express specific accumulation of actin across regions of the cell periphery, with little space observed between each nucleus. In contrast, WT HaCaT cells appear to express more space between individual nuclei.

Quantification of this phenotype was conducted between WT and DN HaCaT cells, with measurements taken as highlighted in *Figure 3.4*. Images represent live cells at 60% confluence, providing a depiction of the cells in close association at the beginning of colony formation. Imaging of cells at high confluency was avoided due to cellular shape changes occurring due to the restricted space available. Multiple measurements were taken from 12 individual images per cell line, in order to count how many cells occupied a 100 μm^2 area. Cells situated both in and out of the analysis box were counted only if they were seen to situate across two sides of the box (*i.*e. corner regions of the square).

Observations show visual differences between the colony morphologies of both cell types. The DN HaCaT cells appear to cluster in much tighter groupings, allowing a higher number of cells to grow in the measured space in comparison to their WT counterparts. Quantification of these observations can be seen in *Figure 3.5*.

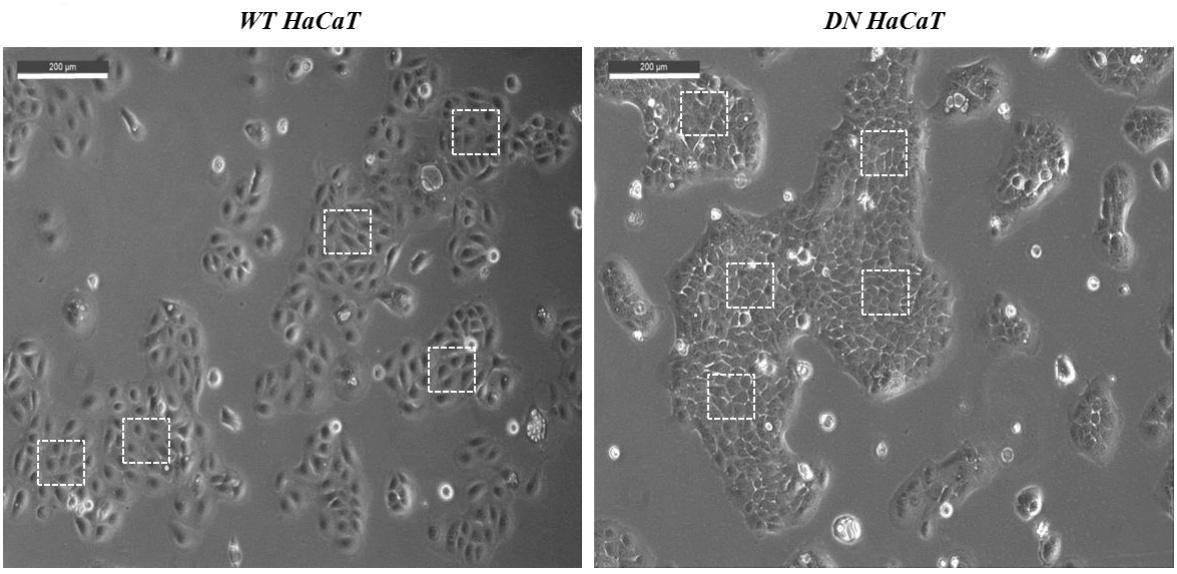

Figure 3.4: *Phase contrast images of WT and DN HaCaT's at 60% confluence under standard growth conditions. Squares depict the 100 μm^2 measurement areas. Scale bar = 200 µm.*

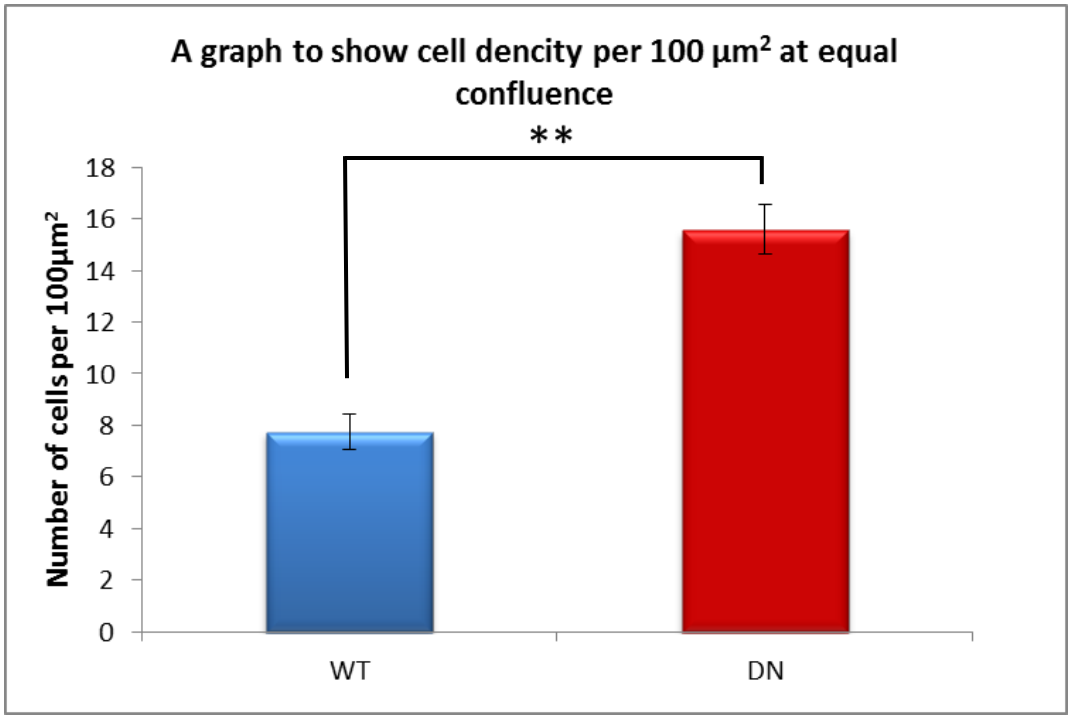

Figure 3.5: *Differences in cell numbers observed between the DN and WT HaCaT cells in a defined 2D area of 100 µm^2. Each bar represents collated data from 20 analysis grids across 3 replicates for each cell line.*

Figure 3.5 shows that DN HaCaT cells grow at a significantly higher density than WT using an unpaired student t-test where $p \leq 0.005$ was observed, suggesting an average of 7.4 cells counted per 100 µm^2 for WT HaCaT cells, whereas for DN HaCaT cells, 15.8 cells were observed. This suggests that the growth phenotype and resulting colony morphology of the HaCaT cells has been affected by the disruption of the *LINC* complex across the NE.

In order to assess if the increased density observed in DN HaCaT colonies was a result of reduced cell area, both DN and WT HaCaT cells at 70% confluence were stained with DAPI and *TRITC-conjugated phalloidin*, as shown in *Figure 3.3*. Cell area was then analysed using the Velocity® image analysis software. To obtain accurate values for each cell line, 200 WT and DN HaCaT cells were assessed using *TRITC-conjugated phalloidin* to identify the actin-rich cell cortex and peripheral cell regions. The results obtained can be seen in *Figure 3.6*.

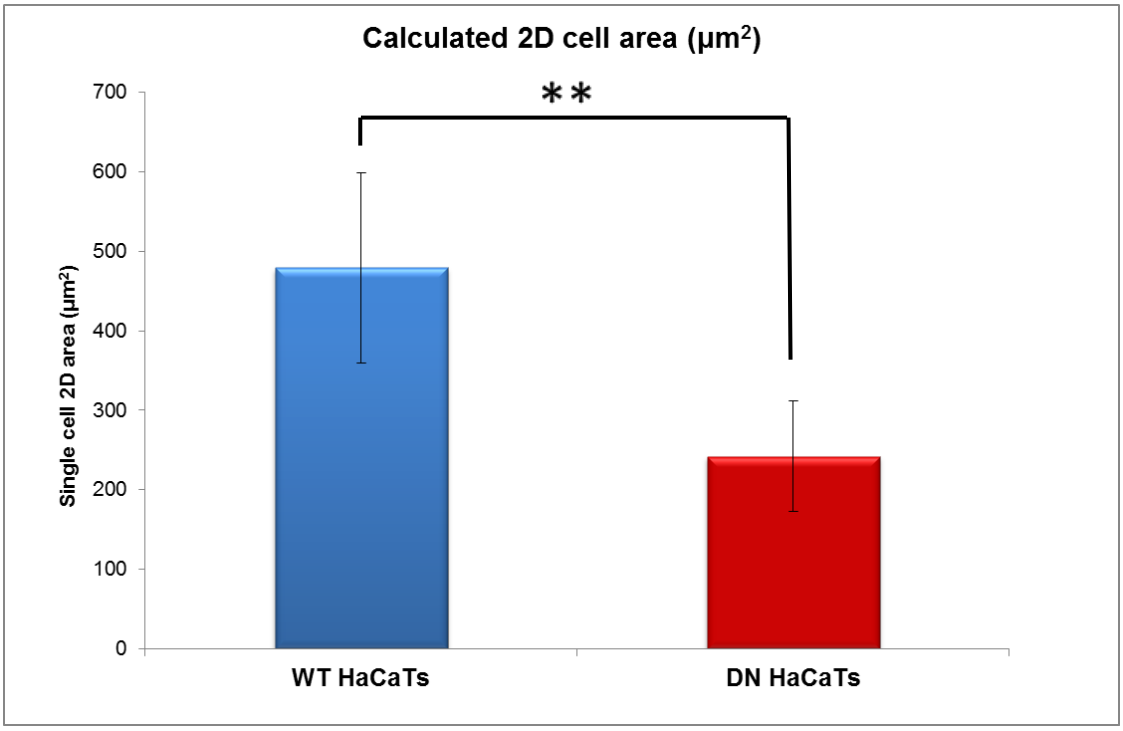

Figure 3.6: *Calculated cell area observed between the DN and WT HaCaT cells in 2D monolayer cultures.*

The data presented in *Figure 3.6* suggests that the DN HaCaT cells display a smaller cellular area of 262.33 µm^2, in comparison to a calculated cell area of 472.69 µm^2 for the WT HaCaT's. To statistically validate our findings an unpaired student t-test was used, suggesting a significant difference is observed between WT and DN HaCaT cell area, when $p \leq 0.005$. This suggests that DN HaCaT cells display a significantly smaller cell area to the WT counterparts, implicating further roles for the *SUN-KASH* interaction in maintaining normal cellular architecture and shape.

3.3.1.2 DN HaCaT cells display an altered 3D cell shape under 2D growth conditions.

As suggested in section 3.3.1.1, the DN HaCaT cells appear to grow in much closer associated colonies, occupying less space than that of the WT controls. To further understand the morphological changes undertaken by the DN HaCaT cells, the cells were analysed in 3D through Z-stack acquisition using a LEICA SP5 confocal microscope, followed by subsequent 3D rendering using the Volocity® image analysis software. This investigations aimed to assess whether DN HaCaT cells displayed a similar cellular shape

to their WT counterparts across the Z plane, or whether they have developed a more cuboidal morphology similar to that of *in vivo* keratinocytes, providing an explanation for how the cells are able to grow in such close proximity.

To test this hypothesis, DN and WT HaCaT cells were grown to 70% confluence on glass coverslips, and then stained with *TRITC-conjugated phalloidin* and DAPI in order to visualise the proximity of cell-cell positioning and cell nuclei. The acquired Z-stack 3D reconstructions are displayed in *Figure 3.7*.

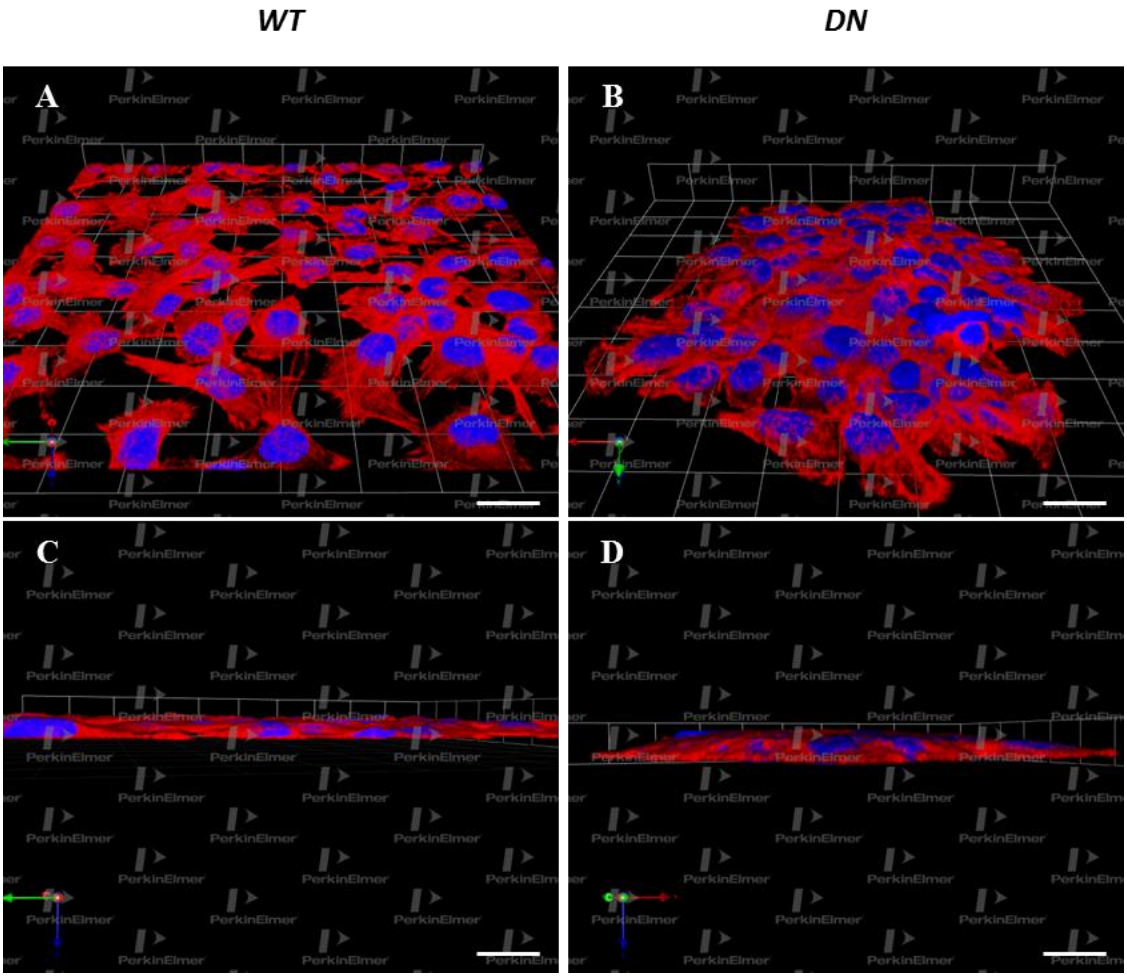

Figure 3.7: *Fluorescence images of WT and DN HaCaT Z-stacks. Images A and B display WT and DN colony morphologies. Images C and D represent WT and DN cells across the Z axel plane, allowing nuclear height to be calculated. Coloured arrows represent cell orientation across the XYZ planes. Scale bar = 10 µm.*

Differences in nuclear shape and volume were obtained through the use of Volocity® imaging software. Example data outputs can be seen displayed in *Figure 3.8*. For each cell line, the blue nuclear staining was isolated and specific cells targeted. The cell height could then be calculated across the ZY and ZX planes. Nuclear height and volumes were analysed for 150 WT and DN HaCaT cells respectively.

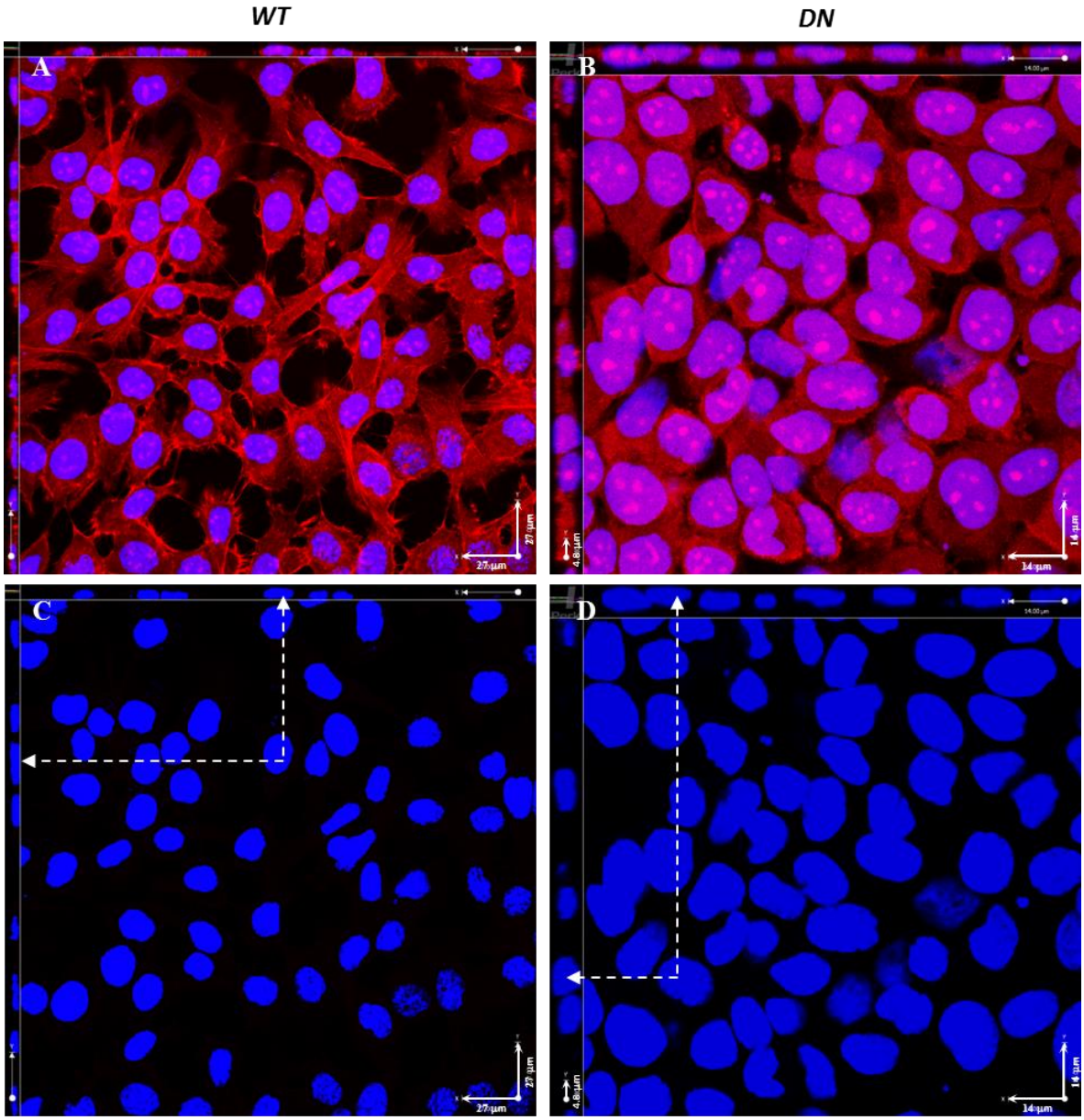

Figure 3.8: *Example output from the Volocity® image analysis software from which nuclear height was calculated. Images A and B represent WT and DN cells respectively stained with TRITC-conjugated phalloidin and DAPI. Images C and D represent WT and DN DAPI staining alone, allowing nuclear measurements to be calculated. Arrows represent the same cell across the XY plane and the ZY/ZX planes. Magnifications for each image are different; with scale bars for WT images represent 27 µm across the XY axis and 14 µm within DN images.*

A summary of the data obtained is displayed in *Figures 3.9* and *3.10.*

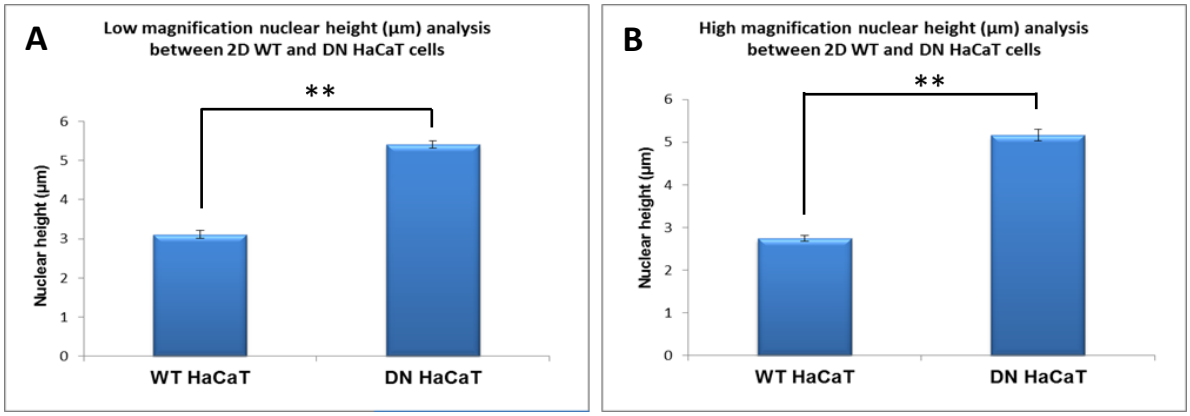

Figure 3.9: *Average nuclear heights of WT and DN HaCaT cells measured at low, 20x objective (A), and high, 40x objective (B) magnifications.*

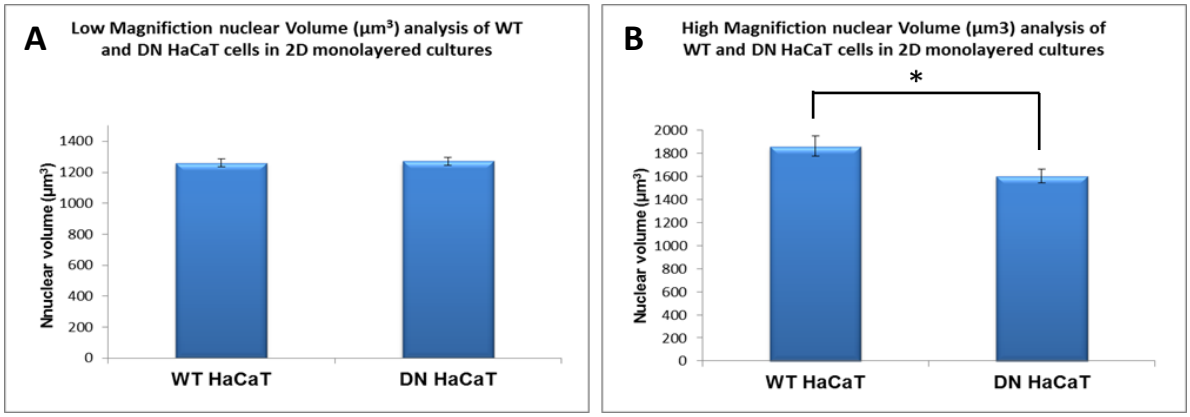

Figure 3.10: *Average nuclear volumes of WT and DN HaCaT cells measured at low, 20x objective (A), and high, 40x objective (B) magnifications. Higher magnifications elude to differences is calculated volume due to increased accuracy of Z-stack reconstructions.*

The data presented in *Figure 3.9* suggests that the DN HaCaT cells are significantly taller than the WT HaCaT cells across the Z axis. This measurement is consistent upon analysis of single cells at low (A) and high (B) magnifications using 20x and 40x objective lenses on a LEICA SP5 confocal microscope respectively. A statistical difference is observed between the WT and DN HaCaT cell lines at both magnifications using a student's t-test where $p \leq 0.005$. *Figure 3.10* displays representative data of nuclear volumes between the two cell lines at low (A) and high (B) magnifications. At low magnification, there is no significant difference between the two cell lines. However, at high magnification analysis of nuclear volume, a significant difference using an unpaired student t-test where $p \leq 0.05$ can be seen, suggesting that the DN HaCaT cells display a smaller nuclear volume than that of the WT HaCaT cells. This suggests that the observed changes in nuclear height do not directly correlate to an equal change in nuclear volume.

3.3.1.3 LINC complex disruption affects cell-substratum adhesion.

Our experimental data collected thus far suggests the DN HaCaT's appear grow in more compacted colonies compared to WT counterparts. From this, we then aimed to further investigate whether other phenotypic differences exist between the DN and WT HaCaT cells during the first few hours of cell-substratum attachment post trypsinisation. This investigation will help elucidate potential effects of *LINC* complex disruption on cell-substratum adhesion. In order to investigate phenotypic differences between the DN and WT HaCaT cells, cell-substrate attachments speed was analysed in real time. Image collection was conducted directly after cell trypsinisation, and over a period of 18 h. Images were collected over a range of Z-regions every 15 min, allowing for the assessment of flattening alongside cell-substrate attachment. The acquired images for each time point across both WT and DN HaCaT cells can be seen displayed in *Figure 3.11*.

The data presented in *Figure 3.11* suggests the DN HaCaT cells display a reduction in cell spreading upon contact with the culture substrate to that of the WT HaCaT cells. The first observation of this can be seen at 3 and 6 h time points, in which the WT HaCaT cells appear to flatten and spread across the substrate's surface, whereas the DN HaCaT cells appear to retain a more spherical phenotype. Only at later stages of cell-substrate attachment (between 15 - 18 hour time points) do the DN HaCaT cells begin to flatten out across the culture flasks surface similar to that of the WT HaCaTs. Further validation of this data is however required, in order to conclude that disruptions to the *LINC* complex do indeed reduce cell-substratum attachment speed.

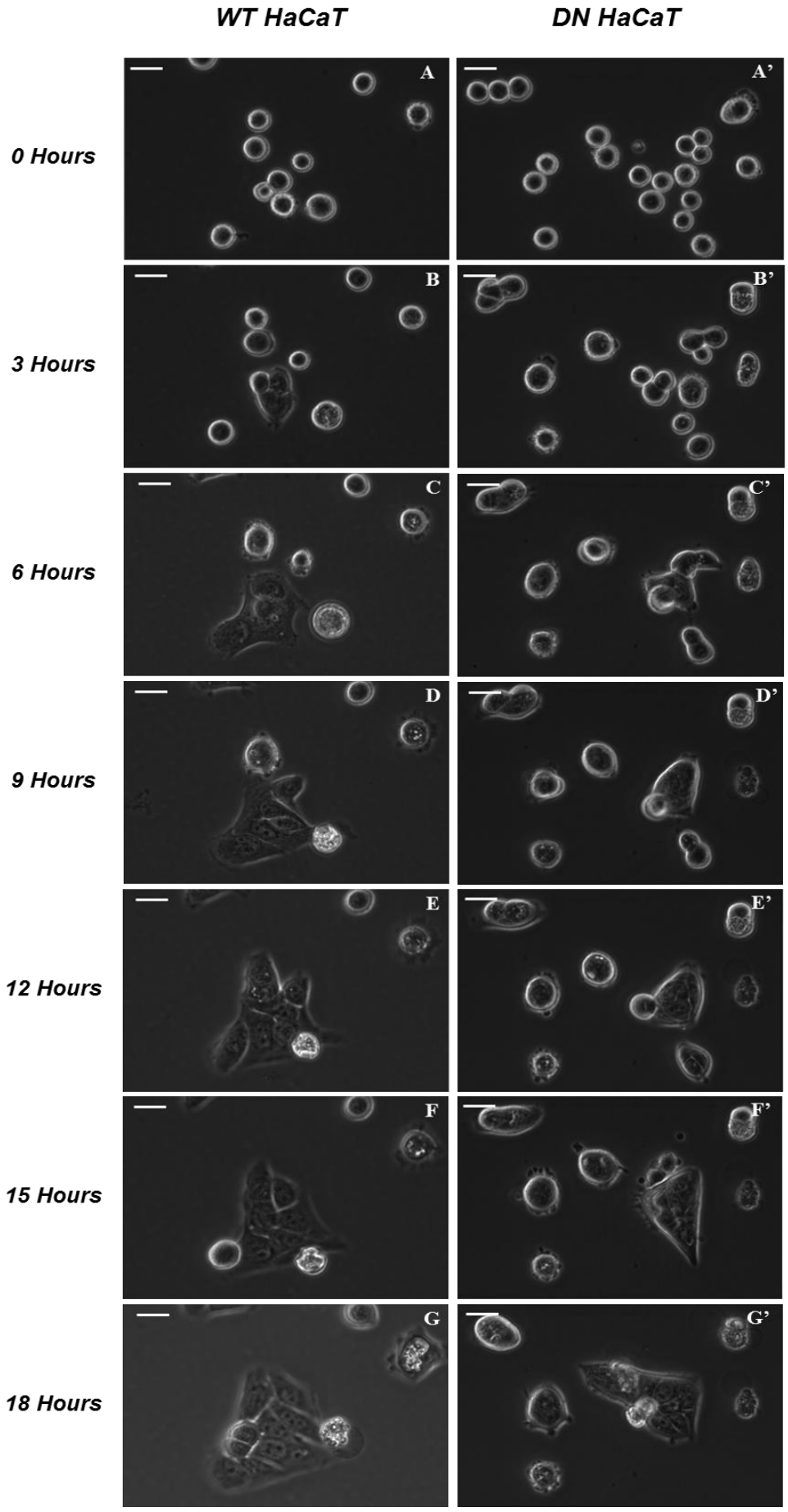

Figure 3.11: *Time course images of WT and DN HaCaT cells post trypsinisation, taken over an 18 h period. Scale bar = 25 µm.*

3.3.1.4 LINC complex disruptions stimulate differential vinculin organisation upon cell-substratum attachment.

Live cell analysis of WT and DN HaCaT cells suggests that the WT HaCaTs flatten out much faster than their DN counterparts upon contact with the cell culture substrate. To increase our understanding of the potential differences between the two cell lines stimulating this finding, further assessment of actin and vinculin organization during early stage cell-substrate attachment were assessed. Vinculin is a member of the focal adhesion complex, responsible for the connection between integrin adhesion molecules and the actin cytoskeleton, enabling the subsequent formation of cell interactions with the extracellular environment. The formation of these focal adhesions has been well documented to function in cell flattening events [268], suggesting that the function of vinculin and subsequent focal adhesion formation may be compromised in *LINC* disrupted cells.

Initial experiments aimed to investigate vinculin distribution over set time points post trypsinisation between the WT and DN HaCaT cells, therefore assessing focal adhesion formation. To assess this, both WT and DN HaCaT cells were trypsinised and placed onto glass coverslips as described in methods section 2.11.2. Cells were then incubated under normal growth conditions for a period of 24 h, with cell fixation taking place at 2, 4, 6, 8, 12 and 24 h time points. Cells were stained with *DAPI* to reveal nuclei and for vinculin in order to visualise focal adhesion sites, followed by assessment through confocal microscopy. Representative images for both cell lines at each time point can be seen in *Figure 3.12*.

From the data presented within *Figure 3.12*, observations suggest limited variation between vinculin organisation across WT and DN HaCaT cells can be seen, with potential differences in organisation observed at the 6 h time point. At this time point, WT HaCaT cells appear to begin flattening onto the culture substrate, stimulating vinculin localisation towards the cell periphery. At this same time point, DN mutants display no changes in vinculin distribution to that of 2 and 4 h time points. This observation further supports the previous finding that WT keratinocytes begin flattening between 3 - 6 h time points, with DN cells displaying a delay in cell flattening. However, at these time points, this observation is not fully clear, so alongside the 12 h time period, cells were also assessed 24 h post trypsinisation. This further analysis aimed to investigate whether focal adhesion formation and vinculin distribution is further altered upon cell attachment over extended culture periods. Representative images of this time point can be seen in *Figure 3.13*.

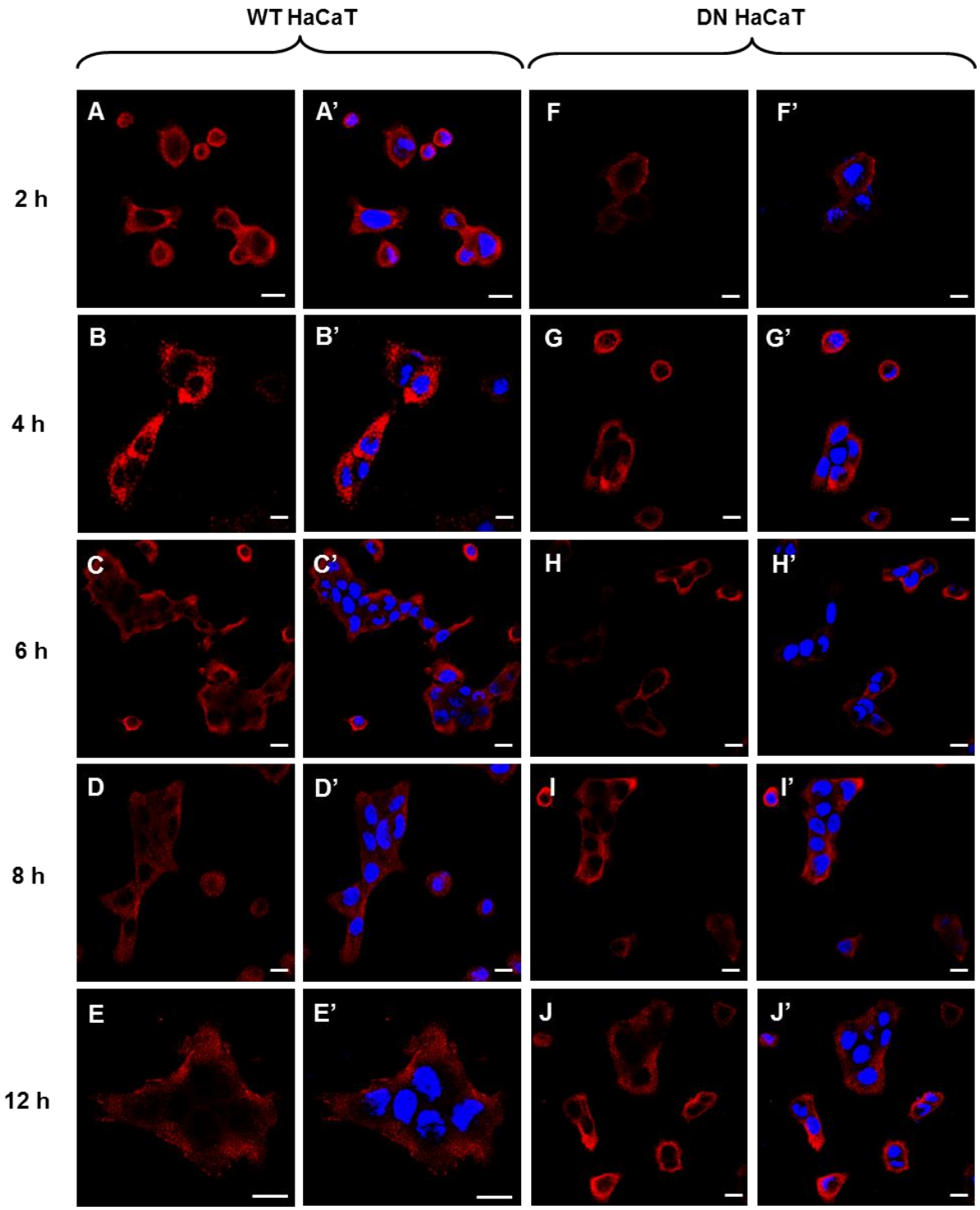

Figure 3.12: *Images of WT and DN HaCaT cells post trypsinisation. Cells are stained for DAPI (blue) and vinculin (red). Arrows at the 6 h time point display cells not yet beginning to flatten across the culture surface. Scale bar = 10 µm.*

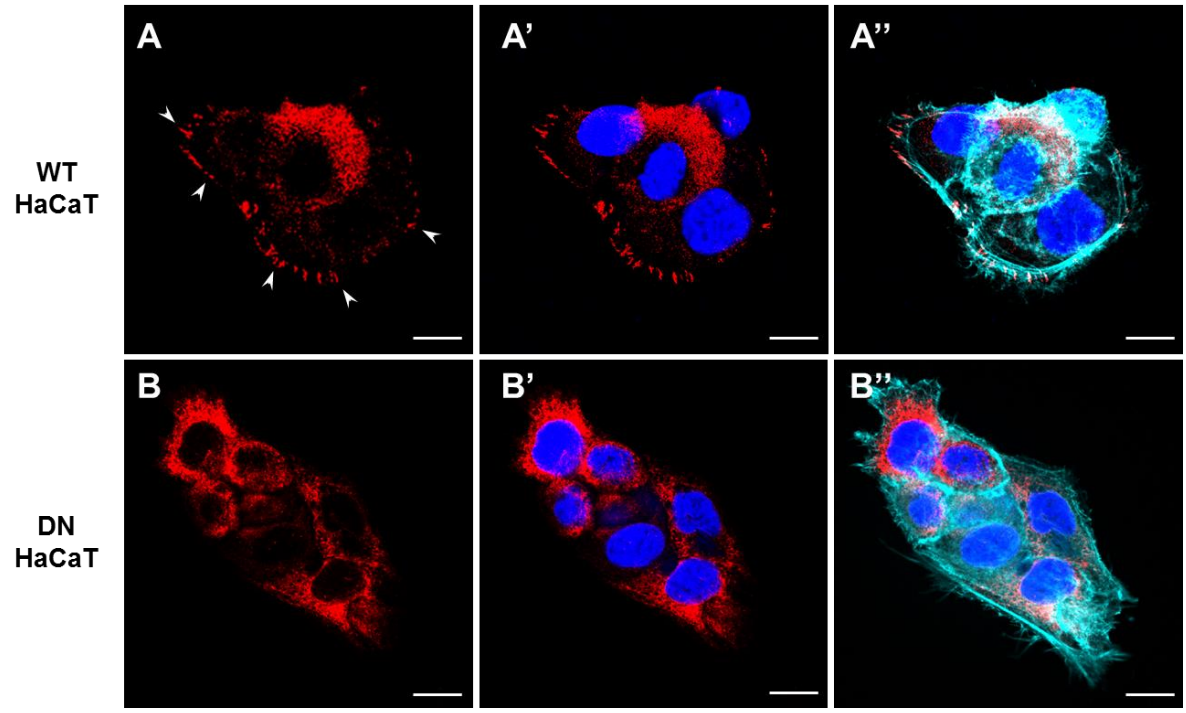

Figure 3.13: *WT and DN HaCaT cells 24 h post trypsinisation. Cells are stained for DAPI (blue), phalloidin (cyan) and vinculin (red). Arrows display sites of focal adhesion formation across the cell periphery. Scale bar = 10 µm.*

In *Figure 3.13*, a clear difference can be seen between the vinculin distribution of WT and DN HaCaT cells. It can be seen that for the WT HaCaT cell line, the majority of cellular vinculin is accumulated at the cell periphery at points of actin accumulation. This vinculin accumulation represents points of focal adhesion formation, allowing cell-substrate interactions to be established, in turn, helping the cell spread and migrate. The DN HaCaT cells however, appear to lack this vinculin accumulation at the cell periphery, retaining the majority of expression within the central cytoplasmic regions. This helps provide potential suggestions as to why DN HaCaT cells display increased nuclear height and cell clustering, suggesting the DN HaCaT cells may express less peripheral focal adhesions through which cell flattening can be aided.

In order to further investigate these observations, actin organisation during cell-substrate attachment was also monitored. It is known that actin plays vital roles in cell migration and attachment [269], thus it was hypothesized that loss of normal *SUN-KASH* interactions across the NE would affect actin organisation due to a loss of potential mechanotransduction and load bearing strength across the NE during the attachment period. Experimental set up was the same as for the vinculin investigation, with cells stained against DAPI and *TRITC-conjugated* phalloidin (*Figure 3.14)*.

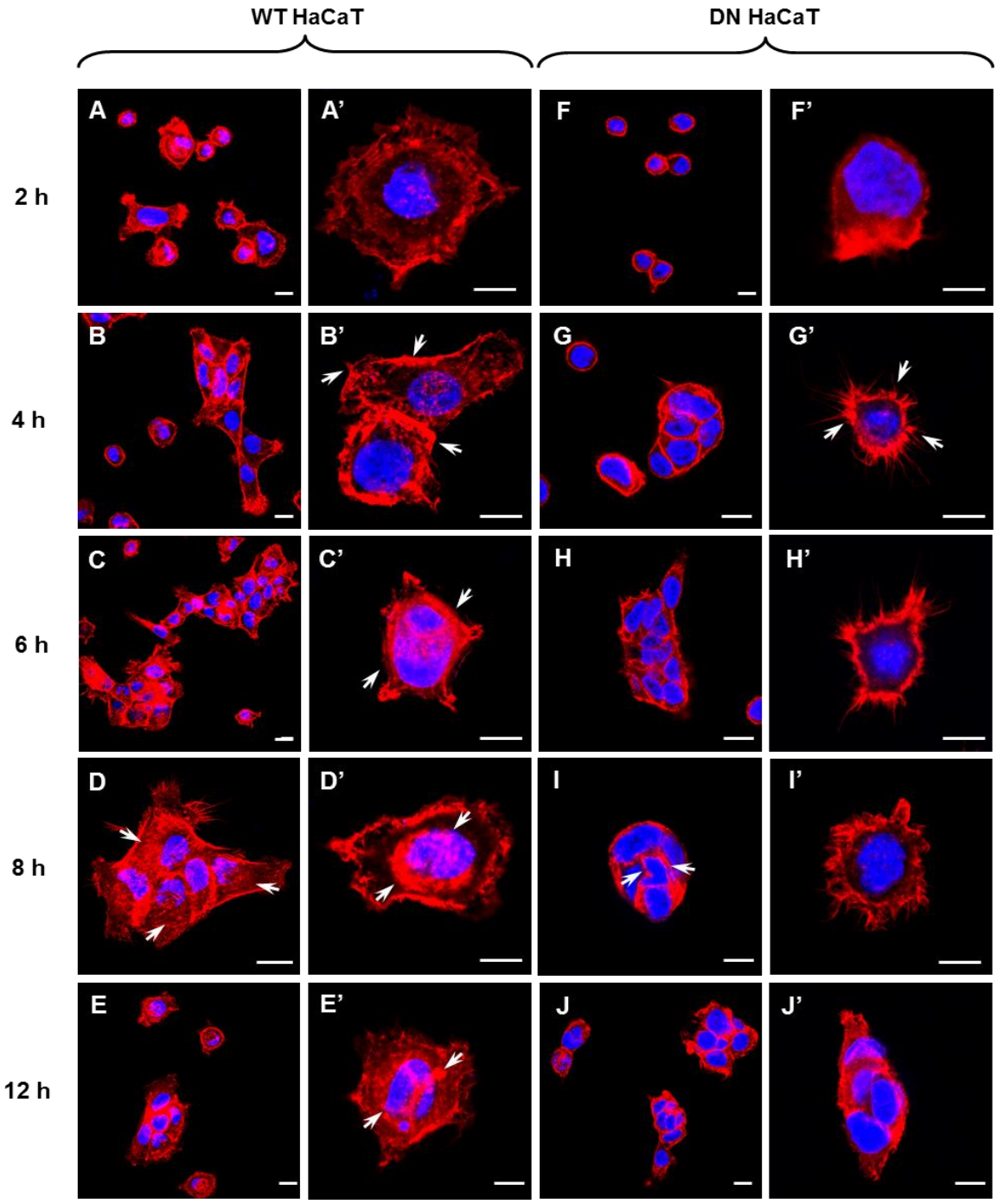

Figure 3.14: *WT and DN HaCaT cells post trypsinisation. Cells are stained for DAPI (blue) and TRITC-conjugated phalloidin (red). Arrows highlight proposed actin 'cap' (D') alongside sites of actin organisation differences between WT and DN cells. Scale bar = 10 µm.*

Figure 3.14 suggests that global actin organisation between the WT and DN HaCaT cells does appear to alter during cell-substrate attachment. Initially it can be seen that when in close proximity (A- J), the DN HaCaT cells retain the highest levels of actin within regions in contact with other cells. This differs to that of the WT HaCaT cells, which display an even distribution of actin across the cells cytoplasm and NE, with much

localised at cell-substrate interacting regions (clearly indicated in D and I). These observations support previous findings, in which WT cells appear to spread and flatten much sooner than the DN cells across the substratum, highlighted best within images D and I at the 8 h time point. For isolated cells (A'- J'), further differences in actin organisation can be seen between the two cell types. Within both cell lines, actin distribution can be seen to accumulate at the cells periphery from 4 h onwards, with DN HaCaT cells displaying more filopodia protruding into the surrounding space. Interestingly however, from 6 h onwards, the WT HaCaT cells begin to accumulate actin across the nuclear region, forming an 'actin cap' around the nucleus. This 'actin cap' is not observed in the DN HaCaT cells, which display consistent actin localisation at the cell periphery. To further quantify this observation, 100 cells for both the WT and DN HaCaT cells were analysed across the 8 – 12 h time points to assess whether a difference was observed between cell numbers expressing this nuclear actin accumulation. Cells were considered to express a nuclear actin cap when a distinct covering of actin filaments could be seen across the nuclear surface, similar to the image displayed within *Figure 3.14* (D'). The collated data from this assessment can be seen below in *Figure 3.15*.

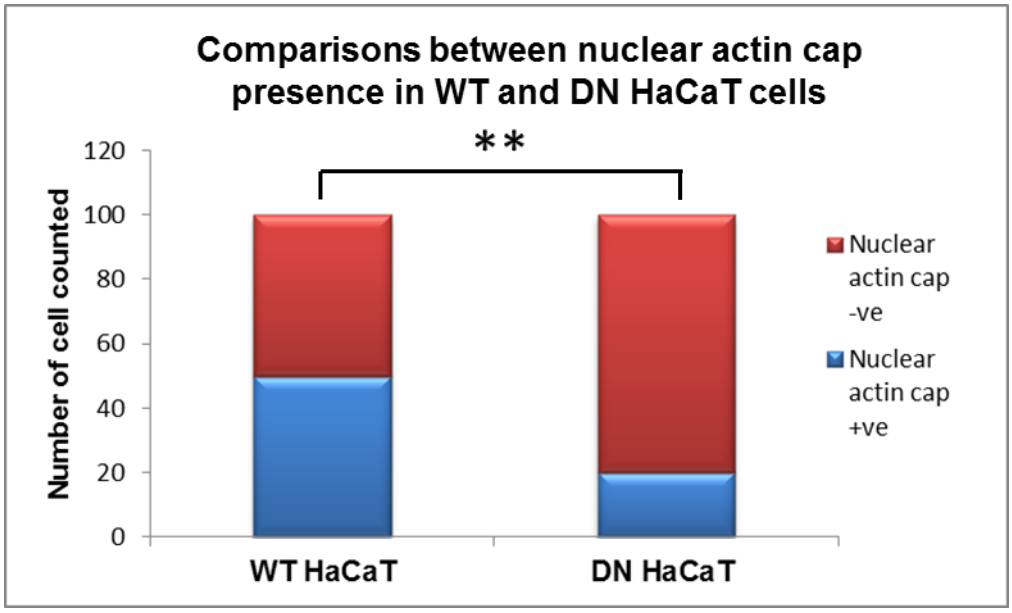

Figure 3.15: *Numbers of nuclear cap positive (+ve) and negative (-ve) cells during cell-substratum attachment between WT and DN HaCaT cells.*

The results presented in *Figure 3.15*, suggests that WT HaCaT's do indeed display significantly more nuclear actin cap positive cells compared to DN HaCaT counterparts using a student's t-test where $p \leq 0.005$, suggesting 50% of WT cells, but only 16% of DN HaCaT cells were observed to display an actin cap .

From the data presented thus far, it can be suggested that both the rate of cell attachment and flattening was less in *LINC*-disrupted compared to WT cells. Further to this, it can be seen that two major protein components of cells attachment, vinculin and actin; express differential organisation between the WT and DN HaCaT cells at varying time points post trypsinisation.

3.3.2 LINC complex disruption affects 2D directed cell migration.

3.3.2.1 LINC complex disruption reduces migration speed in 2D culture.

In order to assess the impact severing the *SUN-KASH* perinuclear interactions in the rate of cell migration in 2D culture environments a scratch wound assay was carried out. Images of wound closure were taken at 0 h, 24 h ad 48 h time points, at which phase contrast microscopy was carried out, followed by fixation and *DAPI* staining, the results of which can be seen in *Figure 3.16*.

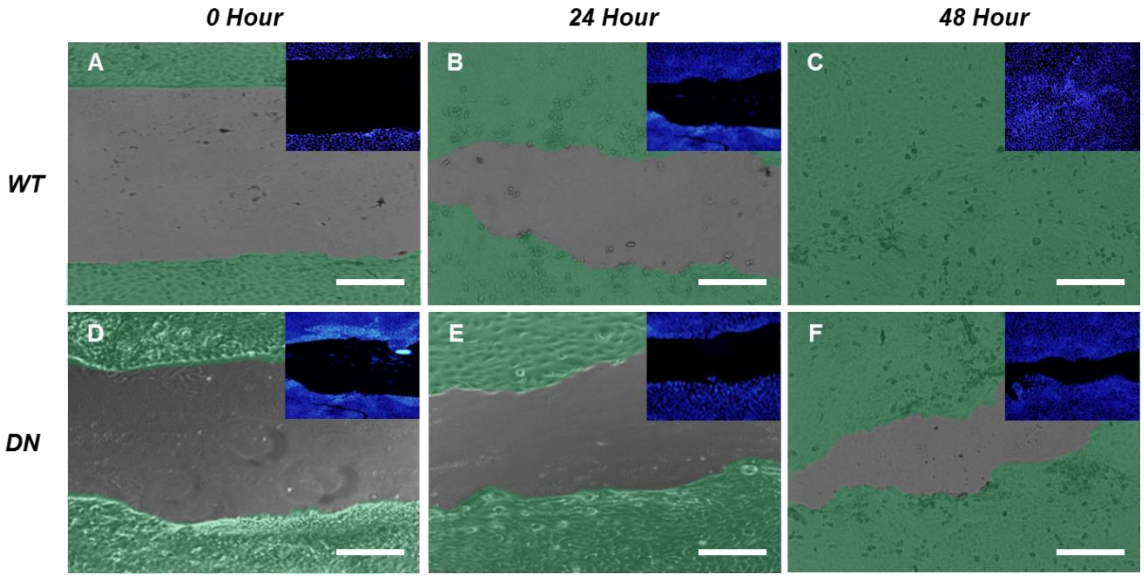

Figure 3.16: *WT and DN HaCaT at 0 h, 24 h and 48 h time points. Green phase contrast images display wound closure over time alongside DAPI staining. Green regions represent false colouring of dense cell regions either side of the wound. Scale bar = 100 µm.*

To accurately assess cell migration across the wound, 100 measurements for each cell line were taken at 100 µm intervals across three independent repeats, the results of which are shown in *Figure 3.17*.

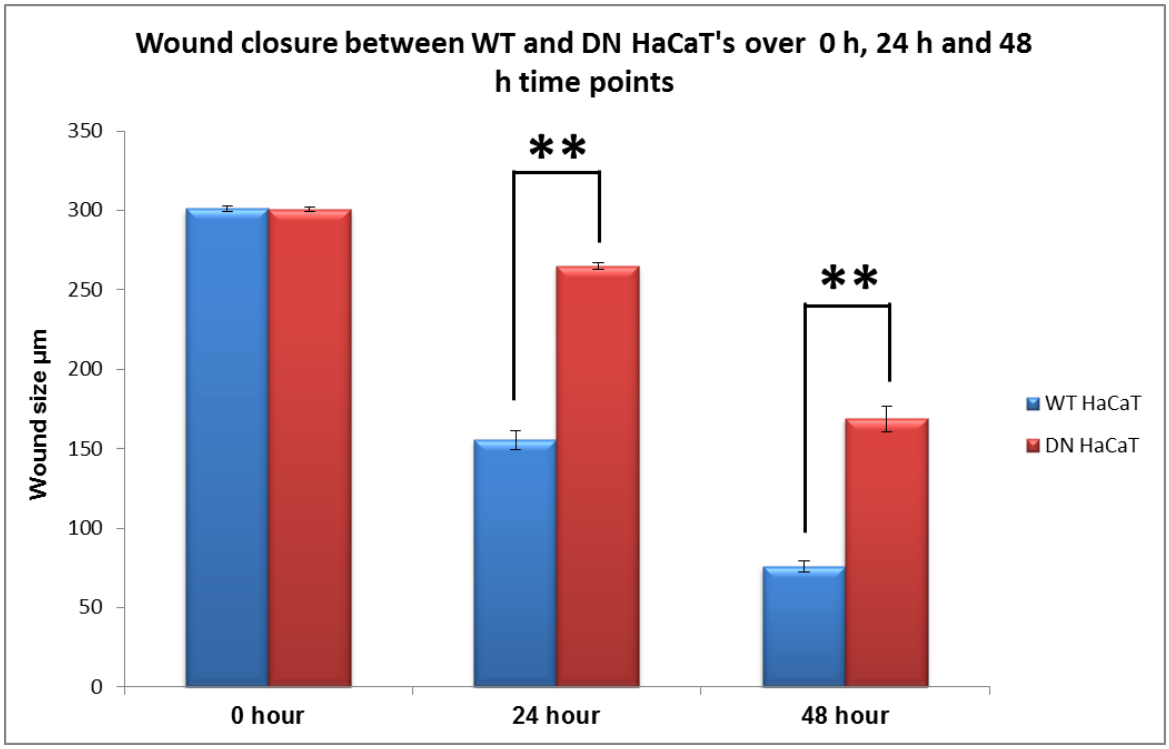

Figure 3.17: *Wound closure of WT and DN HaCaT cells over 0 h, 24 h and 48 h time points.*

The data presented within *Figure 3.17* suggests that the DN HaCaT cells display a slower migration rate in comparison to their WT counterparts. Using a student's t-test, it can be seen that there is a significant difference between the WT and DN HaCaT migration speeds at the 24 h and 48 h time points when $p \leq 0.005$.

The data obtained thus far suggest that when using conventional 2D culture systems, disrupting *LINC* complex connections through severance of *SUN-KASH* perinuclear interactions stimulates significant cellular abnormalities, ranging from reduced cell migration potential, to alterations in cell-substrate interactions. To further understand the effects of this *LINC* complex disruption in relation to more life-like settings, further characterisation of DN and WT HaCaT cell lines was then performed using a 3D culture system. This 3D environment more accurately emulated an *in vivo* growth environment, allowing observations to be made as to the effects of this *SUN-KASH* disruption on cellular behaviour/morphology in a 3D growth system.

3.3.3 DN HaCaT cells, but not WT HaCaT cells exhibit altered growth phenotypes within 3D culture to that of 2D culture.

3.3.3.1 LINC complex disruptions stimulate decreased cellular migration rates within non-restrictive 3D Alvetex® Scaffolds.

When cultured on 2D substrates, WT HaCaT cells migrate significantly faster than the DN mutants. However, when compared to 2D cultures, true biological systems often display altered cellular behaviours and movement patterns in 3D environments, allowing for more complex interactions to occur due to the nature of cellular positioning, proximity and density of packing within a confined space.

Two commercially available 3D cell culture scaffolds were used in order to investigate migration behaviour of WT and DN HaCaT cells in a 3D environment. The two systems used were Alvetex® Scaffold and Alvetex® Strata. Both materials exhibit a synthetic 3D environment produced from a highly porous polystyrene matrix. This matrix provides cells with the support and space to grow in 3D. Both materials consist of voids, interconnecting windows and pores, all working in conjunction to allow cellular migration and growth to occur throughout the scaffold. A representation of the two scaffold types and the differences between them can be seen in *Figure 3.18*. Both materials have been fabricated from the same polymer (cross-linked polystyrene), however, the manufacturing process has been modified for Alvetex® Strata in order to produce a material with much smaller voids and interconnecting windows in comparison to Alvetex® Scaffold. The observed void diameters in Alvetex® scaffold are between 15-45 µm in diameter, whereas the Alvetex® Strata scaffold void diameter is between 5-15 µm. The smaller void diameters associated with Alvetex® Strata create an environment that is more restrictive to cell migration than that of the Alvetex® Scaffold, allowing for differences in migration potential between the two cell lines to be assessed.

It has been hypothesized that the materials' high porosity allows cells to anchor to the extracellular environment, as well as migrate through the culture substrate in a manner that is more similar to that of their *in vivo* migration phenotypes. In addition, the porous nature of the material means that 'wells' of media will remain available throughout the scaffold, allowing for areas of the cell in contact with the scaffold surface to remain in contact with media. This therefore provides the ability of cells in these 3D matrices to uptake media across an increased surface area in comparison to their 2D culture counterparts.

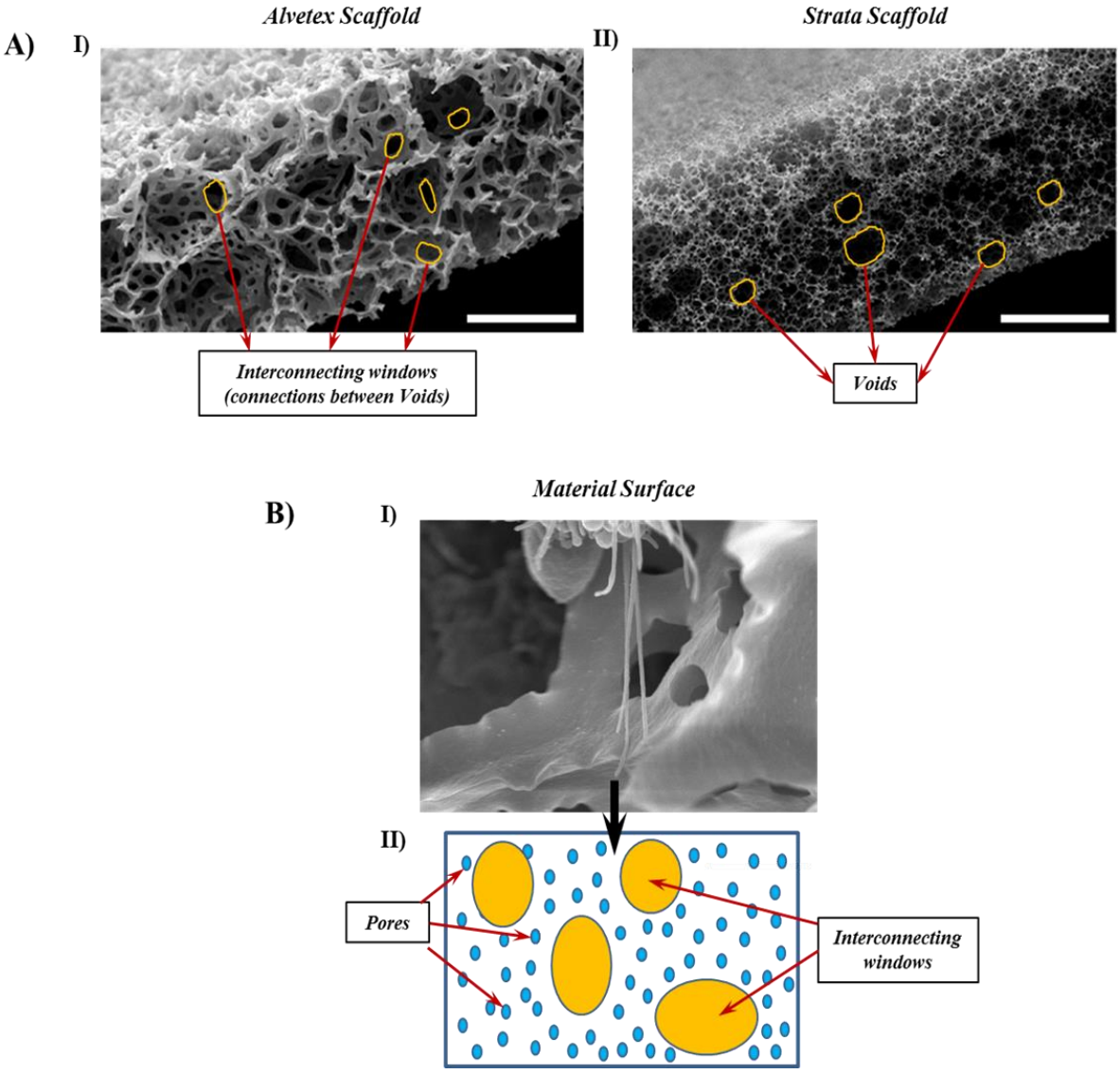

Figure 3.18: *Differences between Alvetex® Scaffold and Alvetex® Strata materials. A) I) SEM micrograph of Alvetex Scaffold, highlighting the larger void diameters (~15-45 µm) and the interconnecting windows. II) SEM micrograph of Alvetex® Strata material, highlighting much smaller void sizes (~5-15 µm). Scale bar = 40 µm. B) I) SEM micrograph material's surface, demonstrating how cells use the pores as attachment points to aid migration through the scaffolds, with II) Representation of the microstructure of the materials surface.*

To test the differences in migration and penetration potential between the WT and DN HaCaT cell lines, 250,000 cells were seeded onto each scaffold type for an observation period of 14 days. Migration was analysed at 2, 4, 6, 8, 10 and 14 day time points, allowing sufficient time for cell penetration to occur. At each time point, cells were fixed and paraffin embedded, sectioned, and H & E stained (Materials and Methods). Micrographs of the full length of Alvetex® Scaffolds containing WT and DN HaCaTs can be found below in *Figure 3.19*.

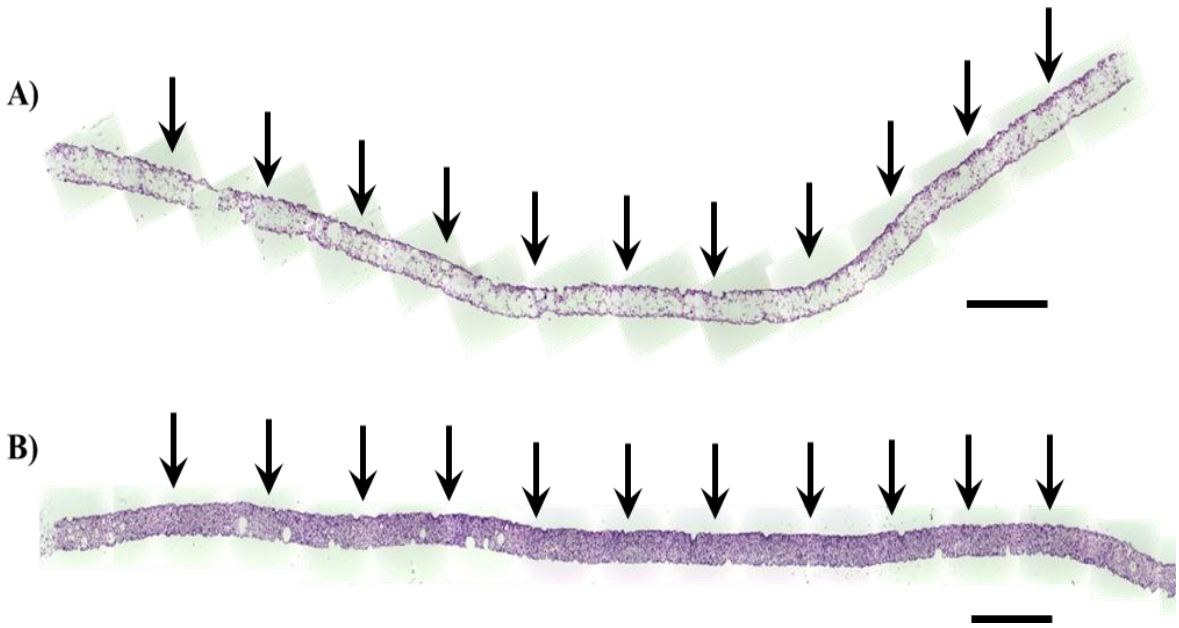

Figure 3.19: *H & E stained Alvetex® Scaffold 14 days after cell seeding. A) Alvetex® scaffold seeded with WT HaCaT cells, B) Alvetex® scaffold seeded with DN HaCaT cells. Arrows represent the surface of initial cell seeding. Scale bar = 300 µm.*

Images in *Figure 3.19* show that there is a large difference in cell packing density between the DN and WT cell lines after 14 days of culture. The DN HaCaT cells appear to pack more densely throughout the width of the material, whereas the WT HaCaT cells appear to form two dense cell layers, one on the side of seeding, and another on the opposite side of the scaffold. This result agrees with observed differences between these two cell lines in 2D systems, in which the DN HaCaT cells exhibit much closer associations.

The rate at which each cell line penetrated into Alvetex® Scaffold was assessed over a 14 day period, with sampling taking place at 2, 4, 6, 8, 10 and 14 day time points. An objective analysis method described in *Figure 3.20*, was developed in order to remove bias.

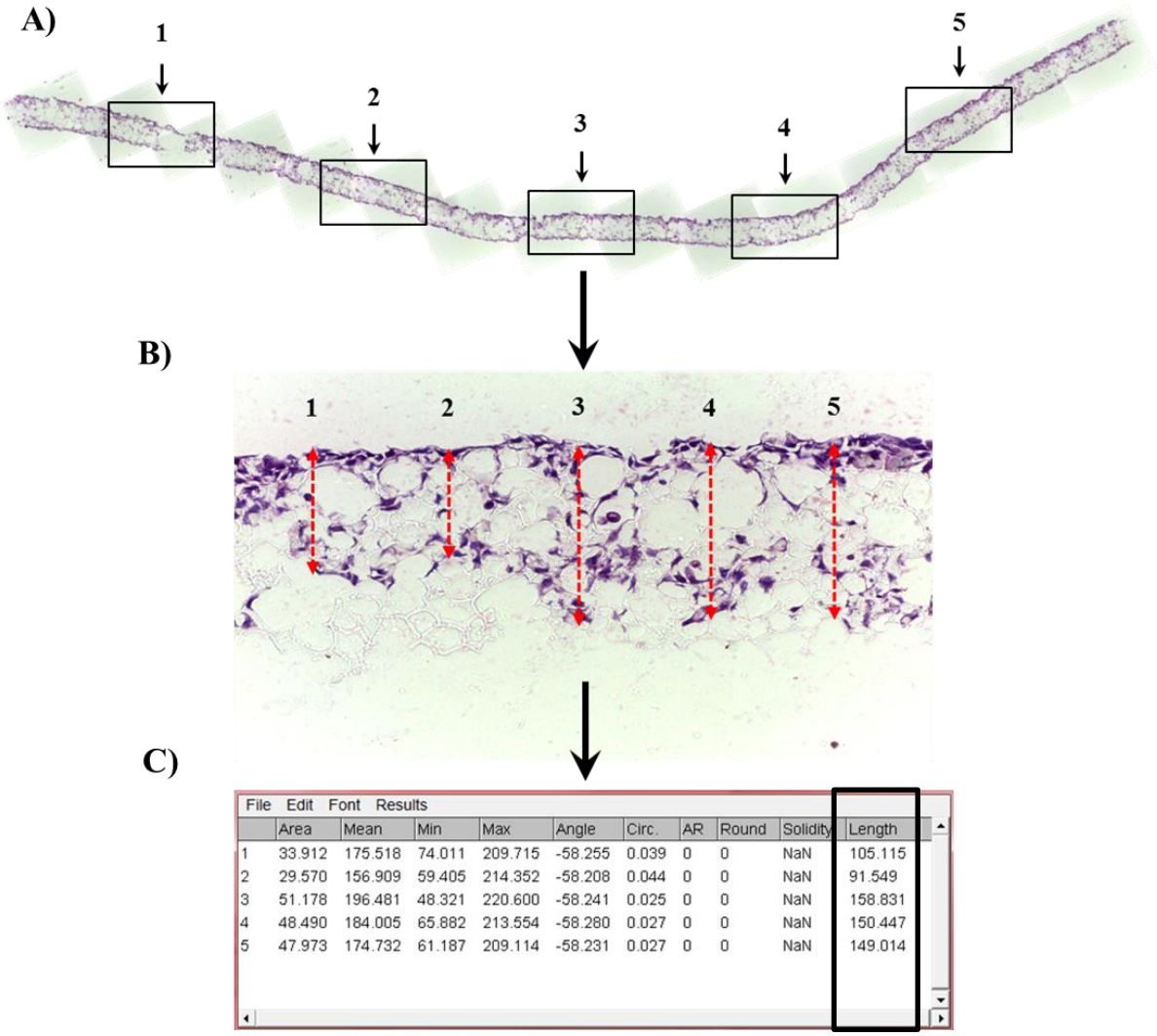

	Area	Mean	Min	Max	Angle	Circ.	AR	Round	Solidity	Length
1	33.912	175.518	74.011	209.715	-58.255	0.039	0	0	NaN	105.115
2	29.570	156.909	59.405	214.352	-58.208	0.044	0	0	NaN	91.549
3	51.178	196.481	48.321	220.600	-58.241	0.025	0	0	NaN	158.831
4	48.490	184.005	65.882	213.554	-58.280	0.027	0	0	NaN	150.447
5	47.973	174.732	61.187	209.114	-58.231	0.027	0	0	NaN	149.014

Figure 3.20: *Analysis of cell penetration into Alvetex® Scaffold. 5 sections were taken through varying depths to get a representation of penetration across the whole scaffold. Each section was then H & E stained and imaged at 100x magnification A) Full length scaffold with regions imaged. B) 5 measurements across the scaffold. C) Obtained output.*

The rules used when measuring penetration into the scaffolds were deemed strict enough to remove as much subjectivity as possible from data collection. Across each full length scaffold, images were taken at intervals of 250 µm. Penetration was then measured at 100 µm intervals across these images. Micrographs of H & E stained scaffolds at each time point can be seen in *Figure 3.21*.

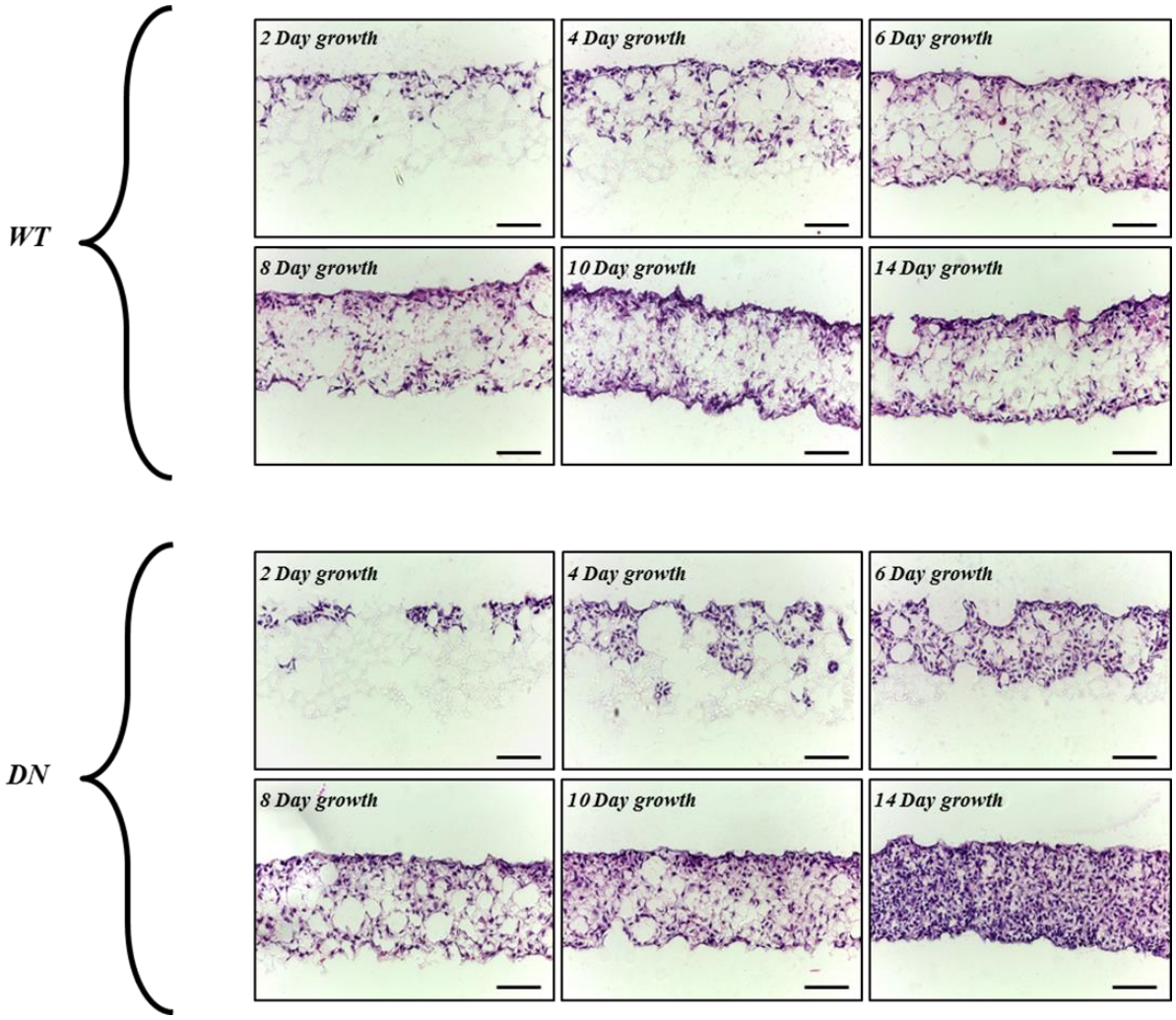

Figure 3.21: *H & E staining of both WT and DN HaCaT cells in Alvetex® scaffolds at 2, 4, 6, 8, 10 and 14 day time points post seeding. Scale bar = 100 µm.*

The data presented in *Figure 3.21* suggests that both cell lines behave differently in the non-restrictive 3D culture environment. The images suggest that the WT HaCaT cells appear to migrate through the Alvetex® scaffold faster than the DN mutants, penetrating through the whole 200 µm scaffold within 6 days. In addition, the DN HaCaTs appear to pack more densely in the voids of the material in comparison to their WT counterparts. The collated data from across all three repeats can be seen presented in *Figure 3.22*.

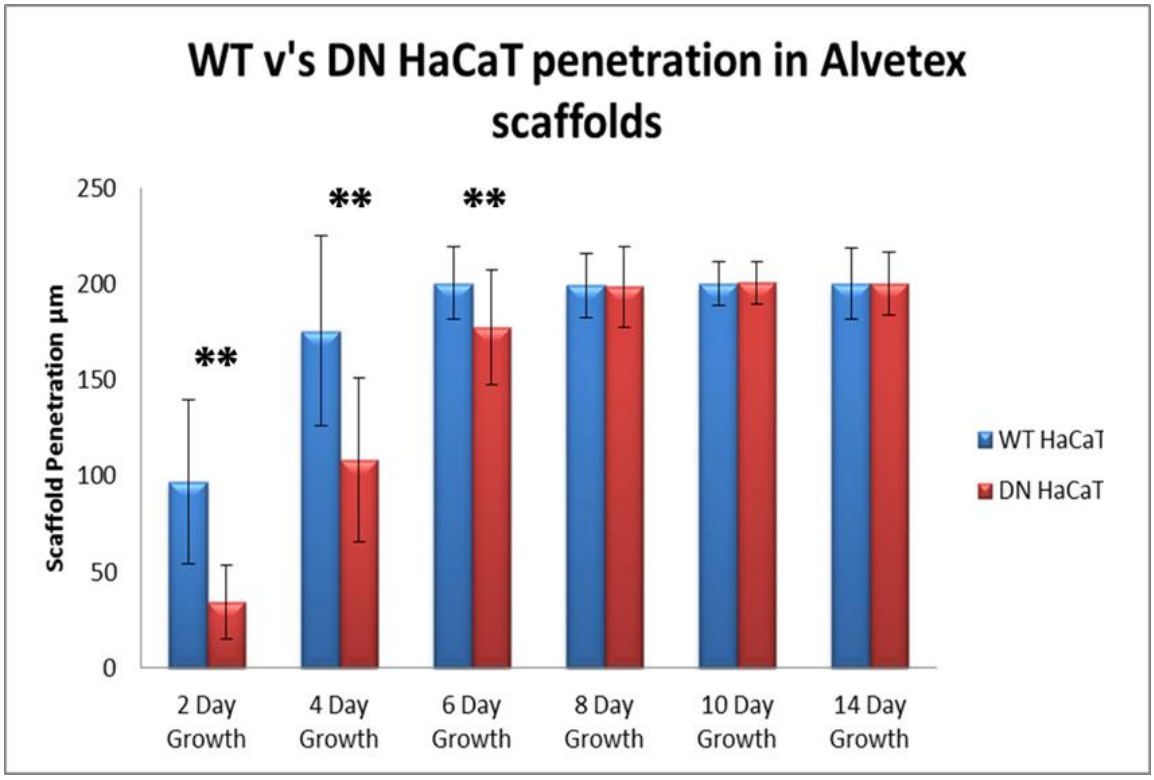

Figure 3.22: *Differences in Alvetex® scaffold penetration between WT and DN HaCaT cells over a 14 day period post-seeding.*

As shown in *Figure 3.22*, the WT HaCaTs migrate through the less restrictive Alvetex scaffolds much faster than the DN HaCaTs, showing complete penetration through the 200 µm scaffold between 4 and 6 day time points. The DN HaCaT cells show complete penetration between the 6 and 8 day time points. Statistical analysis using an unpaired student's t-test suggest that the differences observed between the WT and DN HaCaT penetrations at the 2, 4 and 6 day time points are statistically significant when $p \leq 0.005$. The 8, 10 and 14 day time points show no significant difference between penetration rates of both cell lines, as both have fully penetrated through the material. Due to the use of multiple t-tests, a Bonferroni test was also carried out as seen through p-values of 0.005, in order to reduce the occurrences of type 1 errors and therefore increase the validity of statistical data obtained.

These observations suggest that disrupting the connection between the nucleus and the cytoplasm through this *SUN-KASH* bridge effects cellular packing density of these cells within a 3D system, similar to that found in 2D environments. In addition, the WT HaCaT cells migrate through the less restrictive Alvetex® Scaffold significantly faster than the DN mutants.

3.3.3.2 Disrupting the LINC complex provides cells with a migration advantage within physical restrictive 3D Alvetex Strata inserts.

To further investigate the roles of *LINC* complex disruptions on migration behaviour, the rate of migration of both WT and DN HaCaT cells in the space-restrictive cell culture environment of Alvetex® Strata was investigated. During cancer metastasis, cancerous cells migrate away from the source tumour via extravasation and intravasation. In order to migrate away from the source tumour, cancer cells must possess the ability to migrate through highly restrictive environments. It was envisaged that the highly restrictive nature of the Alvetex® Strata material would mimic this environment, providing a platform to study the impact of *LINC* complex disruptions, and hence, nuclear deformations, on cell migration.

The same preparation and analysis methods used for the Alvetex® Scaffold materials were employed for the Alvetex® Strata scaffolds, with cells being seeded at a density of 250,000 cells after plasma treatment. Examples of full length H & E stained scaffolds containing WT and DN HaCaT cells can be seen in *Figure 3.23*.

Initial observations from *Figure 3.23* suggest the DN HaCaTs appear to penetrate consistently across the length of the scaffold, whereas their WT counterparts display a more sporadic migration pattern. Further observations suggest the restrictive nature of the material stimulates cellular build up at the seeding site. The DN HaCaTs appear to produce a much denser cell layer across the scaffold's surface, causing the scaffold to curl. In comparison to this, the WT HaCaTs appear to produce a much less dense layer of cells. Micrographs of H&E stained scaffolds at each time point are displayed in *Figure 3.24*.

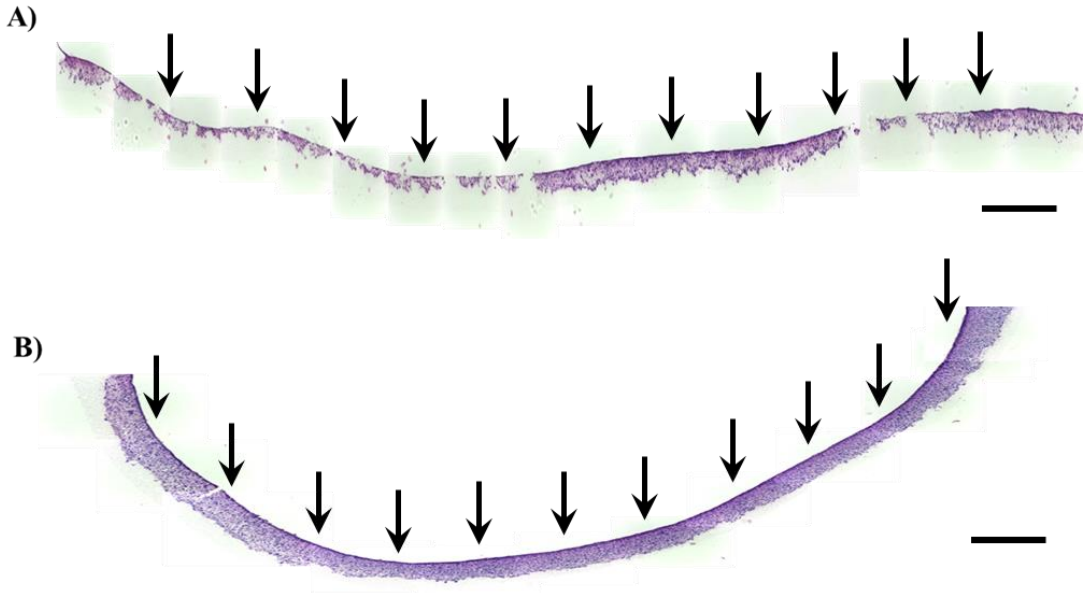

Figure 3.23: *H&E stained Alvetex® Strata scaffolds 14 days after cell seeding. A) Scaffold seeded with WT HaCaT cells, B) Alvetex® Strata scaffold seeded with DN HaCaT cells. Arrows represent the side of initial cell seeding. Scale bar = 300 µm.*

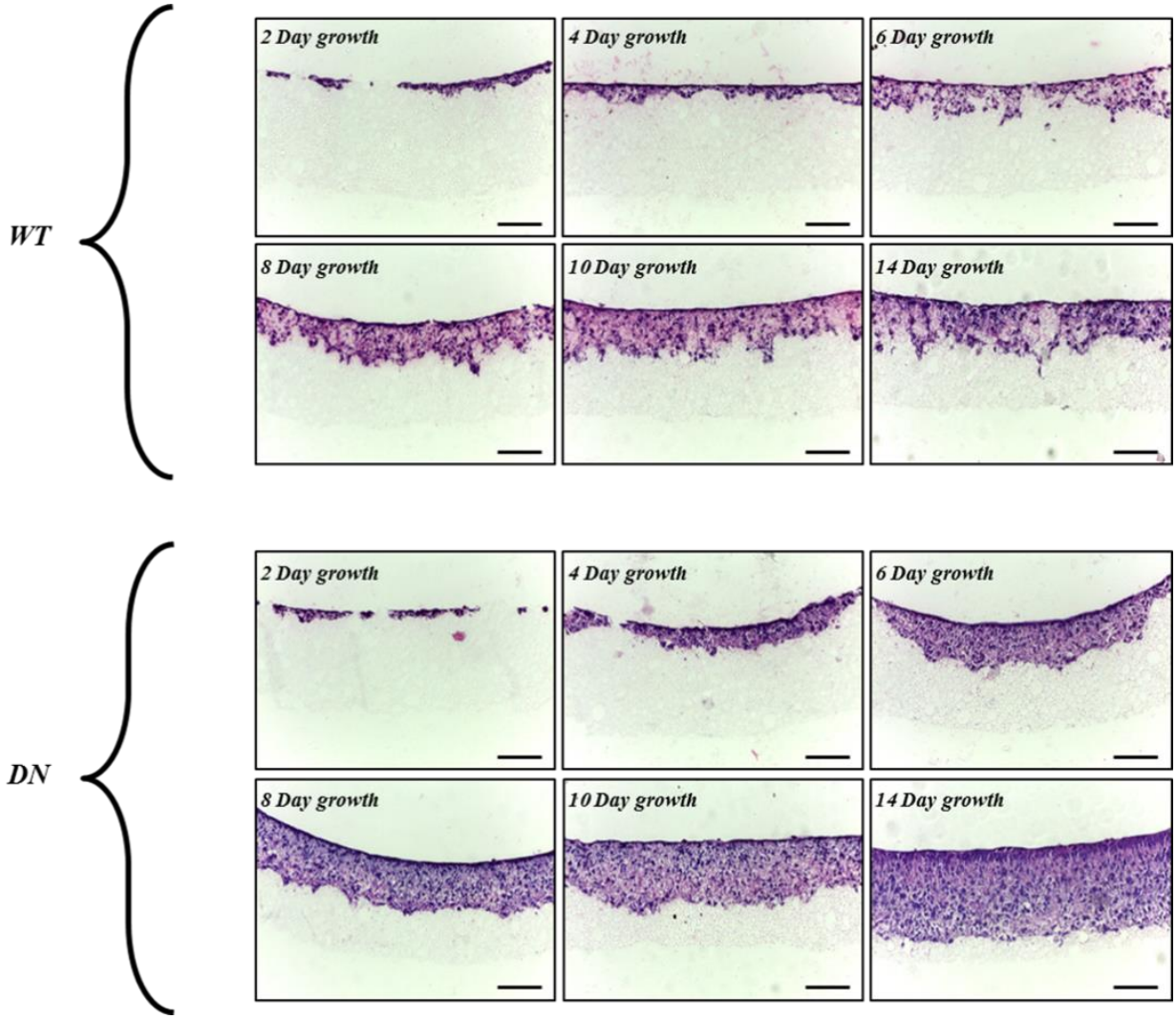

Figure 3.24: *H&E staining of both WT and DN HaCaT cells in Alvetex® Strata scaffolds at 2, 4, 6, 8, 10 and 14 day time points post seeding. Scale bar = 100 µm.*

The data presented within *Figure 3.24* suggest that there is a large variation in growth patterns observed between the non-restrictive Alvetex® Scaffold and space-restrictive Alvetex® Strata, with neither cell line penetrating fully through the scaffold. In addition, it appears that the WT HaCaTs migrate up to half way through the scaffold, then plateau, whereas the DN HaCaTs retain their slower migration speed, migrating further into the scaffold by day 10. Data collated from 3 repeats is shown in *Figure 3.25*.

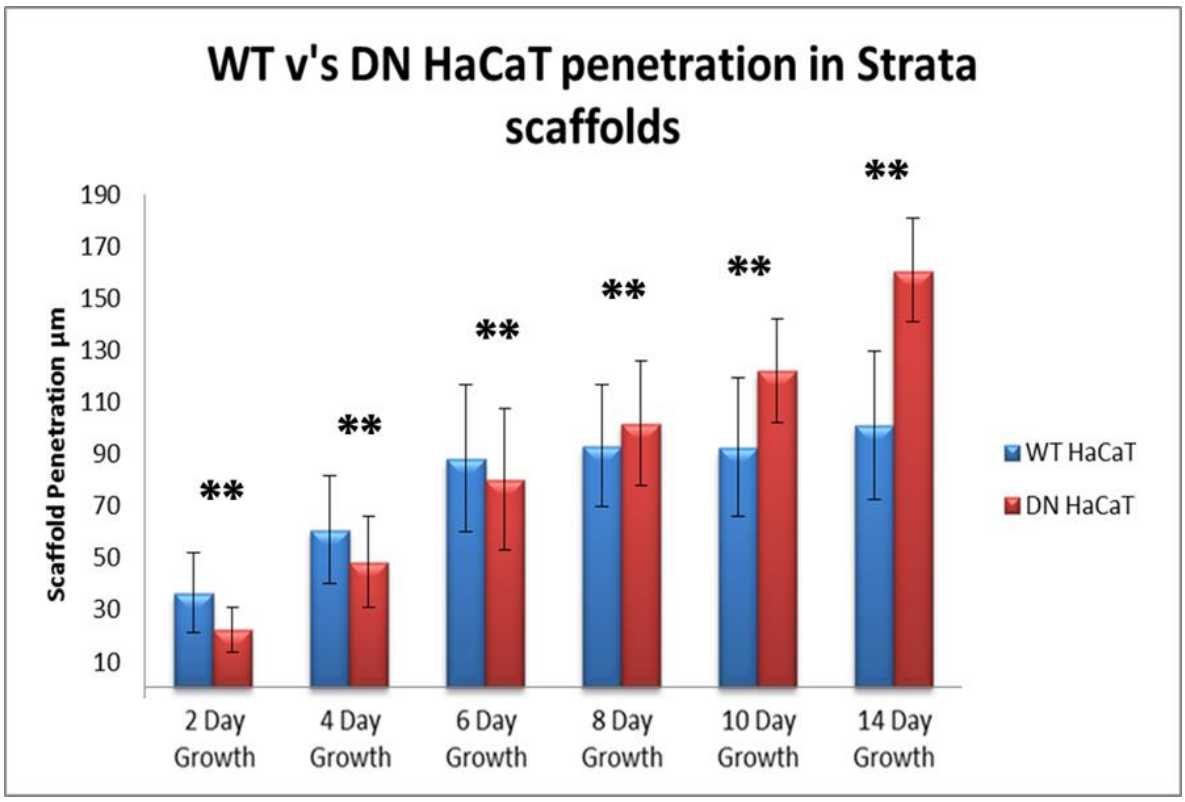

Figure 3.25: *Differences in Alvetex® Strata scaffold penetration between WT and DN HaCaTs over a 14 days period post-seeding.*

The data presented in *Figure 3.25* suggest that both cells lines exhibit different penetration properties in the restrictive scaffold. As observed previously, the WT HaCaT cells appear to migrate faster than the DN HaCaT cells over the first 6 days of growth, however, upon reaching the central region of the scaffold (~100 µm) their migration appears to halt. In comparison, the DN HaCaTs appear to maintain a constant growth rate over the course of the experiment, migrating deeper into the scaffold than the WT HaCaTs around the 8 - 10 day time point. This suggests that the DN HaCaTs have a migration advantage in the highly space-restrictive Strata® environment, in which cellular and nuclear morphology changes will be required in order to migrate and penetrate into the material. Further statistical analysis between WT and DN HaCaT penetrations at each

time point suggests that each observed difference in cell penetration is statistically significant when $p \leq 0.005$.

This initial investigation suggests that through disrupting this link between nucleoplasmic and cytoplasmic networks in the DN HaCaT cells, abnormalities in cell behaviour have occurred The properties exhibited by the DN mutants contain some similar migration phenotypes to that exhibited by many high grade cancer cells during metastasis, in which cells are able to migrate through challenging, space-restrictive environments, similar to that found in many tissue systems.

3.3.3.3 The DN HaCaT cells exhibit a more uniform penetration phenotype within restrictive Strata® Scaffolds.

It can be seen that migratory behaviour differs between the WT and DN HaCaT cells in the restrictive Strata® scaffolds, in which the DN HaCaT cells display a more uniform leading edge in comparison to the WT HaCaT cells. To quantify these observed differences, H&E staining was performed on both cell lines in these space-restrictive scaffolds at the 6 day time point. This time point was selected as it represents a time point at which both cell lines migrate equal distance through the scaffold. Measurements were then taken along the leading edge of the scaffold as highlighted in *Figure 3.26*. The leading edge was measured between two set points at 200 µm apart, allowing comparisons to be made between the cell lines regarding their migratory behaviours. Cells which migrate as a uniform group will, theoretically, produce a measurement close to the known distance of 200 µm, whereas cells that display a less uniform migratory behaviour should produce a measurement larger than that of the known distance.

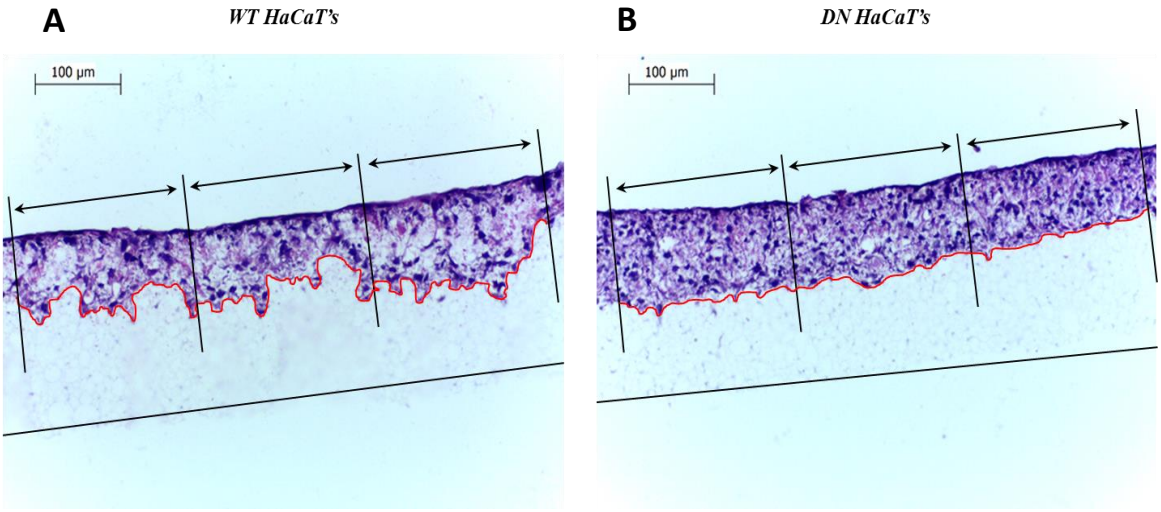

Figure 3.26: *Migratory behaviour across the leading edge. H&E stained Alvetex® Strata scaffold seeded with WT (A) and DN (B) HaCaT cells, examined 6 days post seeding. Arrows represent a known distance of 200 µm, and the red line across the leading migratory edge represents the measured distance. Scale bar = 100 µm.*

The data presented in *Figure 3.26* suggests a difference between the penetration behaviours of WT and DN HaCaT cells in the space-restrictive scaffolds. Collated data using this technique across 25 scaffolds for both the WT and DN HaCaTs can be seen displayed within *Figure 3.27*.

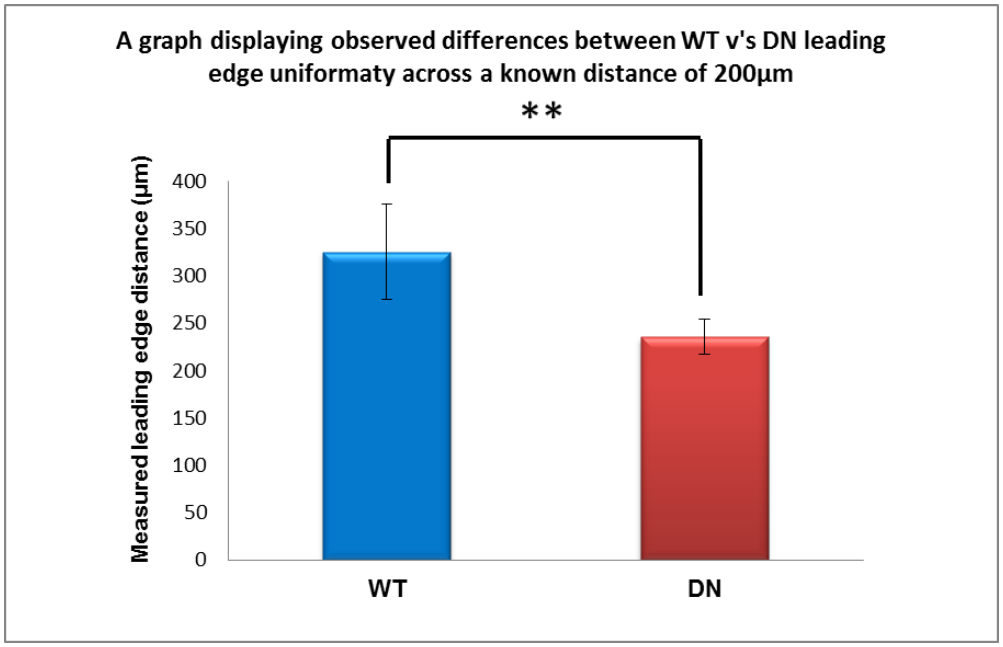

Figure 3.27: *Differences observed between the WT and DN HaCaT leading edge migration uniformity within the space-restrictive Strata® scaffolds at the 6 day time point.*

Data presented in *Figure 3.27* suggests there is a significant difference between leading edge migration uniformity in WT and DN HaCaTs using an unpaired students t-test where $p \leq 0.005$. The WT HaCaTs appear to display a less uniform migratory behaviour in the restrictive Strata® Scaffold producing an average leading edge distance of 335.5 µm. In contrast, the average DN HaCaT leading edge was measured at 235.5 µm, which is much closer to measurement distance of 200 µm. This data, therefore, suggests that the *LINC* complex disruptions present in DN HaCaT cells, stimulates a more uniform migration phenotype when faced with restrictive 3D environments.

3.3.3.4 DN HaCaT cells display cell stacking, alongside shape changes across surface regions of space restrictive scaffolds.

In addition to leading edge morphology differences highlighted in section 3.3.3.3, further observations were made as to the cellular changes occurring across both the surface and within the centre of the space-restrictive Strata® scaffolds.

Initial observations were conducted on H&E stained WT and DN HaCaT cells grown for 4 days submerged in growth media, followed by an 8 day culture period at the air-liquid interface. The use of this air-liquid interface is known to stimulate the differentiation of HaCaT cells *in vitro* [270]. It is therefore hypothesised that due to the cytoskeleton playing a key role in keratinocyte differentiation during skin development [271], alongside further evidence that *LINC* components control cytoskeletal organisation [81], the *LINC*-disruptions present in DN HaCaT cells may stimulate alterations in this process.

From this experiment, morphological differences were observed between the WT and DN HaCaT cells across space-restrictive Strata® scaffolds, in which WT HaCaT cells appeared to produce a single cell layer across the surface of the scaffold with the remainder of the cells migrating and proliferating into the scaffold. The DN HaCaT cells, however, appeared to produce a thick layer of ~2-3 cells across the scaffolds surface. This observed cell stacking displayed a layer of cuboidal and/or columnar cells in direct contact with the scaffold, while upper layers displayed a more flattened phenotypic shape. These observed phenotypes resemble cellular shape changes seen during initial stages of cellular stratification in the epidermal layer of skin. Images of this observed phenotype can be seen in *Figure 3.28*, with examples of keratinocyte morphology in human skin shown in *Figure 3.29*.

The data displayed in *Figure 3.28* and *3.29* suggest that DN HaCaTs appear to display some phenotypic similarities to that of differentiating keratinocytes in human skin. This is evident across the scaffolds surface, in which cell shapes change from a flattened to a more cuboidal phenotype. In *Figure 3.29*, the area of interest highlighted by *X* in images *A* and *B,* helps highlight that these cuboidal cell shape changes are present in both the DN HaCaT cells and human skin samples. Images *C* and *D,* however, displays the cellular flattening phenotypes across the surface of both the human skin sample and the surface layer of the Strata® Scaffolds, highlighted with *XX* in each image. This data suggests that even though the cell shape changes present within the Strata® Scaffolds seeded with DN HaCaTs are not as extensive as those found within the primary human skin, there are still some similarities in morphology.

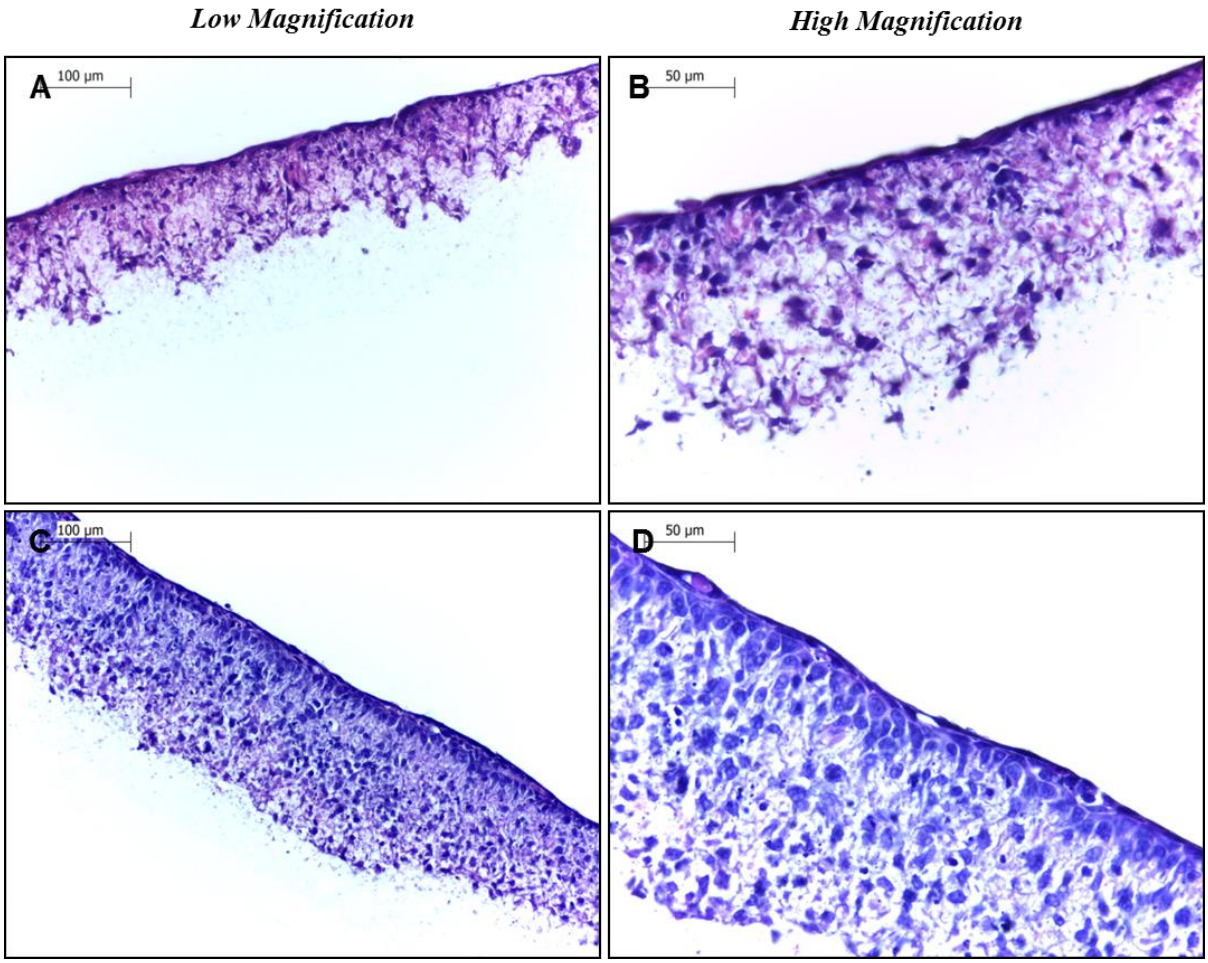

Figure 3.28: *H&E staining of (A, B) WT HaCaT, and DN HaCaT cells grown at the air-liquid interface for 8 days in the Strata scaffold. Images obtained at both (A, C) low magnification, scale bar = 100 µm, and (B, D) high magnification, scale bar = 50 µm.*

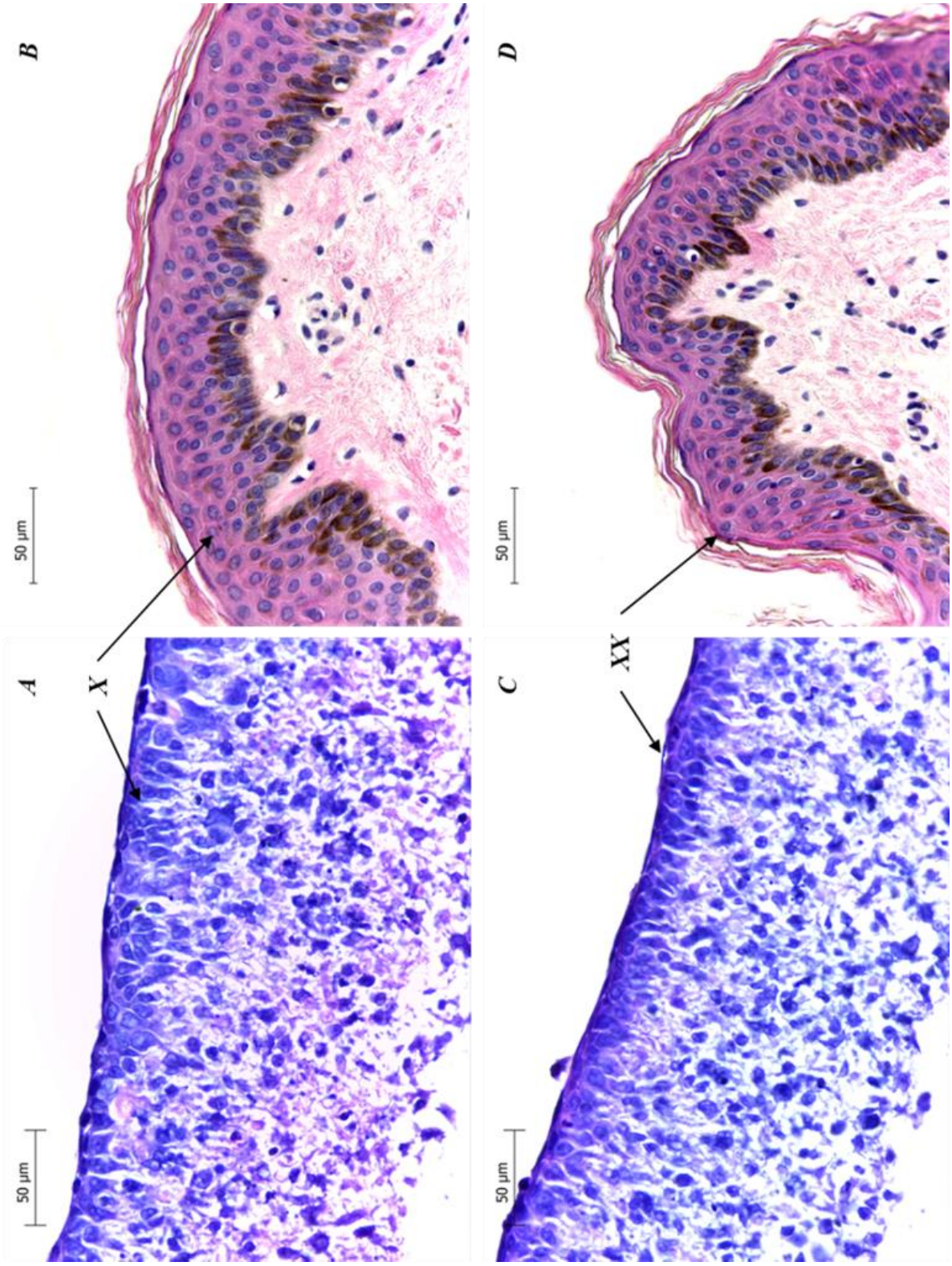

Figure 3.29: *(A, C) H&E stained DN HaCaT cells grown at the air interface in restrictive Strata® Scaffolds. (B, D) H&E stained human skin samples displaying epidermal regions. X highlights the cuboidal cell shapes change observed in both systems. XX highlights the flattened cellular layer of cells positioned across the surface layer of cells. Scale bars = 50 µm.*

3.3.3.5 DN HaCaTs display altered nuclear and cellular phenotypes across the surface and within the centre of the 3D scaffolds.

Thus far, H&E staining in section 3.3.3.4 suggest that DN HaCaTs exhibit an altered cell shape across the surface of the space-restrictive Strata® Scaffold. However, it is not clear as to whether these observed differences are occurring across the surface or within the scaffolds. To investigate this, DN HaCaT cells grown at the air-liquid interface in space-restrictive Strata® scaffolds were co-stained using *Nile* red (to stain the scaffolds), cytokeratin 1 (to visualise keratinocytes) and DAPI (to observe the nuclei). This staining allows for the clear identification between scaffold regions and cell positioning, allowing the assessment of whether this cell stacking observed previously is within, or across the surface of the scaffold (*Figure 3.30)*.

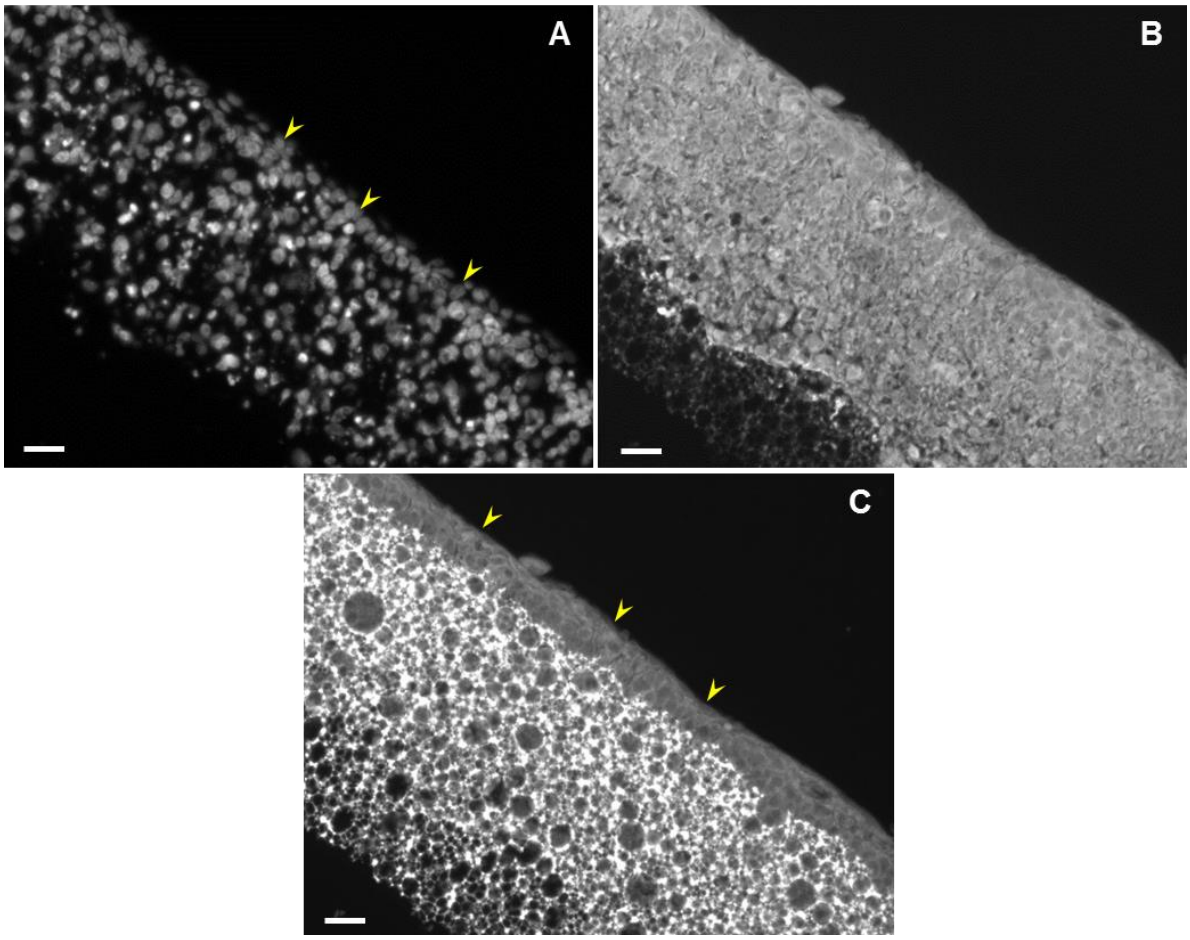

Figure 3.30: *Images of DN HaCaT cells in Strata scaffolds.(A) DAPI staining, (B) the DN GFP signal (as the DN SUN1 construct contains a GFP tag), (C) Nile Red and cytokeratin 1. Arrows display regions of cell stacking (A) and regions of cell accumulation above the scaffold (C). Scale bar = 25 µm.*

The data displayed in *Figure 3.30* suggests that the shape changes observed in DN HaCaT cells are occurring across the surface of the scaffold, rather than within the voids of the first 10-50 µm. This can be clearly observed in images *A* and *B*, showing the GFP and DAPI stains, highlighting a tightly associated network of cells across the scaffolds surface. Alongside this, *C* displays further scaffold and cell staining with Nile red and cytokeratin 1, suggesting that the layer of cells associated with the cuboidal shape changes in the initial H & E staining, can be seen above the scaffolds surface, in a layer ~2-4 cells thick.

Due to these observations, further investigation aimed to assess whether shape changes between WT and DN HaCaT cells could be seen in both space-restrictive and non-restrictive scaffolds environments when cultured at the air-liquid interface using confocal microscopy analysis. It was hypothesized that DN HaCaT cells may express abnormal nuclear shapes in central scaffold regions compared to both surface regions of the same scaffold, and their WT counterparts, due to known roles of the *LINC* complex in maintaining nuclear architecture. This inferred disruption to nuclear shape in DN mutants may therefore be the contributing factor to their observed surface shape changes and increased penetration potential into space-restrictive scaffolds. The results of this can be seen in *Figure 3.31*.

As seen in *Figure 3.31*, the cell packing densities appear to differ between the WT and DN HaCaT cells in central regions of the non-restrictive scaffolds (Image sequence C and D). It is seen that more cells are observed in close proximity across each void for the DN HaCaT mutants in comparison to their WT counterparts, similar to phenotypes observed under 2D culturing conditions (*Figure 3.3)*. These observations further support previous H&E analysis (*Figure 3.28*), suggesting that the DN HaCaT mutants appear to colonise central scaffold regions in much more dense cell colonies, displaying closer cell-cell proximity compared to WT cells.

Further to this, image sequences *A* and *B* suggests differences also exist between cell packing density across surface scaffold regions between each cell line, in which DN HaCaTs appear to produce a 1-2 cell thick layer of flattened cells. In contrast, WT HaCaT cells appear to migrate into the scaffold without any cellular stacking occurring across the scaffolds surface.

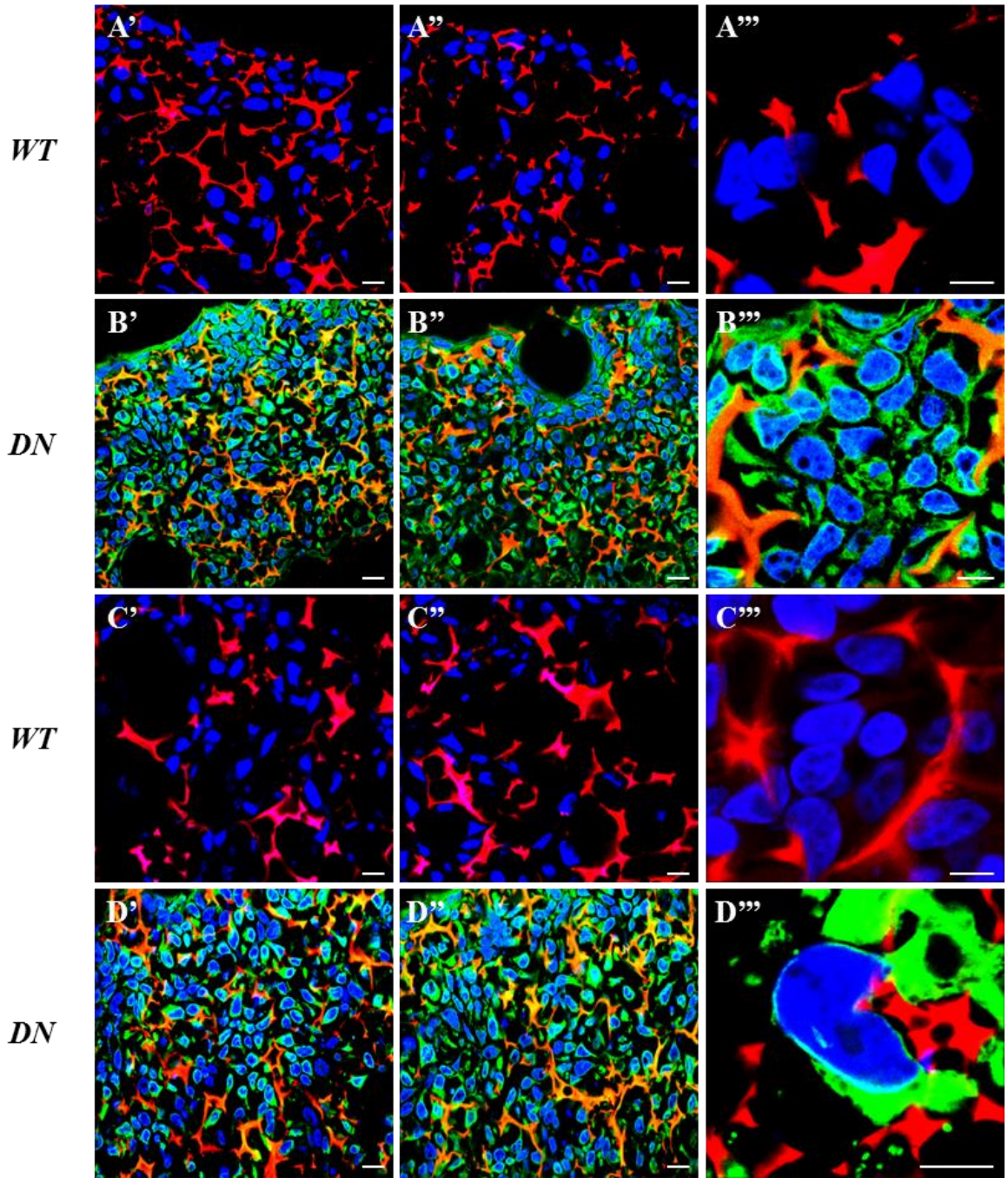

Figure 3.31: *Fluorescence images displaying both WT (A',A''A''' and C', C'',C''') and DN (B',B'',B''' and D',D'',D''') HaCaTs in the Alvetex® scaffold after 8 days at the air interface. Images A and B highlight both cell types across the surface of the scaffold. C and D highlight cellular morphology across the central scaffold regions at various magnifications. Staining's present include DAPI (blue), Scaffold (red) and GFP (green). Scale bar = 10 µm.*

Cells cultured in Alvetex® Scaffolds displayed morphological differences between WT and DN HaCaT cells in both central and surface scaffold regions. To expand on this, confocal analysis was also conducted on the space-restrictive Strata® Scaffolds under the same air-liquid interface conditions for each cell type. The aims of this investigations was

to assess whether further differences existed in cell/nuclear morphology, alongside cell behaviour between WT and DN cells in central/surface scaffold regions compared to the non-restrictive environments, with results displayed in *Figure 3.32*.

The data presented in *Figure 3.32* suggests the morphology of both cell lines appears to vary more than observed previously in the less restrictive Alvetex® Scaffold. Initial surface analysis suggests WT HaCaTs display no obvious differences to phenotypes observed in the Alvetex® Scaffold, in which cells appear to settle within the first 5 µm of the scaffold, rather than flatten across the surface. In contrast, the DN HaCaTs display large morphology differences to that of both the WT cells in the Strata® scaffold, and to that of the DN HaCaT cells grown within the Alvetex® scaffold. It can be seen that DN HaCaTs form a 2-3 cell thick layer across the scaffold's surface, similar to that seen within the non-restrictive scaffold. However, in addition to this, the DN HaCaTs appear to undergo morphological changes, displaying a much more cuboidal like phenotype, not dissimilar to that displayed by *in vivo* keratinocytes. In addition to these observed cell shape changes, it is also evident that cells situated across the surface of this 2-3 cell thick layer appear to have flattened nuclei and elongated cell shapes, similar to that found in the differentiated epidermal layers of skin (*Figure 3.29*). Further to this, the distribution of *GFP* SUN1 across the surface layer of DN HaCaT cells appears to form a more defined structure, potentially corresponding to cytoplasmic staining of the ER (*Figure 3.32* (B)). These observations suggest that DN HaCaT cells across these surface regions of space-restrictive scaffolds undergo significant changes in cellular morphology compared to their WT counterparts.

Alongside cellular differences observed across surface regions of the space-restrictive scaffold, further variation in cellular phenotypes can also be seen in central scaffold regions for both cell lines, when compared to the less restrictive Alvetex® counterparts. As suggested in *Figures 3.24* and *3.25*, the WT HaCaTs appear to exhibit a reduced migration speed in the space-restrictive Strata® scaffold, with migration appearing to halt at the centre of the scaffold (~100 µm into the scaffold). Fluorescence staining in this central region suggests a sparse cell distribution for WT HaCaT cells compared to that observed for the Alvetex® scaffold. DN HaCaTs appear to exhibit similar cellular packing densities to that found in the Alvetex® scaffolds (*Figure 3.31* (D)). However, the more restrictive Strata® Scaffold appears to stimulate an increased occurrence of nuclear morphology changes (more specifically shown in images D'' and D''', with observed nuclear constrictions measuring at 5 µm and 2 µm respectively). These observations therefore suggest that for both WT and DN HaCaT migration through space-restrictive Strata® scaffolds, but not the Alvetex® scaffolds, nuclear deformities are required.

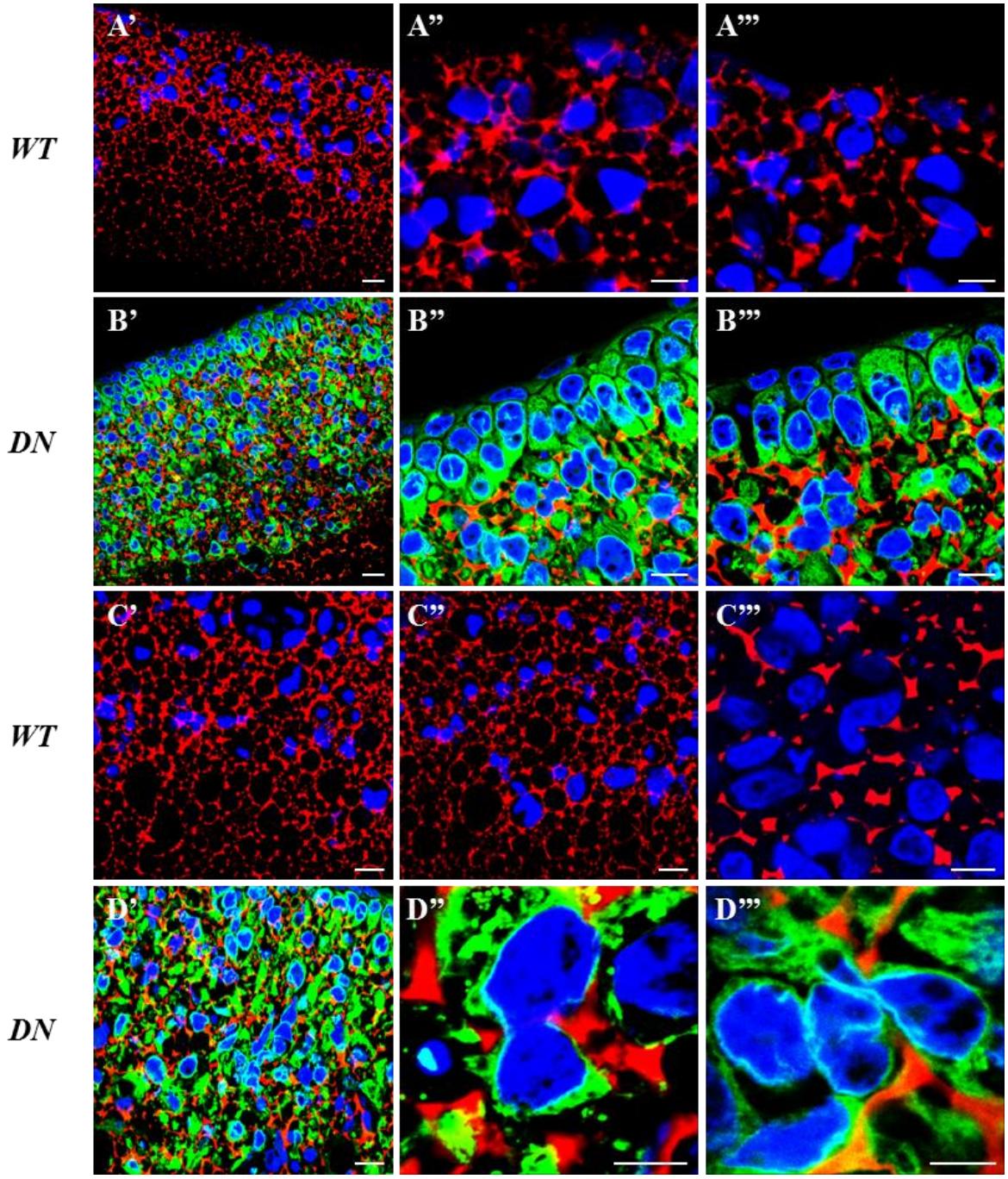

Figure 3.32: *Fluorescence images displaying both WT (A',A''A''' and C', C'',C''') and DN (B',B'',B''' and D',D'',D''') HaCaTs in the Alvetex® Strata after 8 days at the air interface. Images A and B highlight both cell types across the surface of the scaffold. C and D highlight cellular morphology across the central scaffold regions at various magnifications. Staining's present include DAPI (blue), Scaffold (red) and GFP (green). Scale bar = 10 µm.*

Due to the nature of morphological changes observed between the two cell lines, and more specifically between the DN HaCaT cells in both scaffold types, further investigations into the cell/nuclear morphological changes observed were conducted using

TEM and SEM techniques. With the use of these techniques, it was possible to more accurately assess and characterise the cellular and nuclear deformities occurring in these differing scaffold environments.

SEM imaging was used in order to investigate how both WT and DN HaCaT cells interact with space-restrictive scaffolds across surface and central regions. Due to previous H&E observations, it was chosen to examine the cell growth patterns in a submerged Strata® scaffold, at a time point of 14 days. These conditions were chosen due to previous observations suggesting the greatest degree of difference between migration potential and cell morphology occurred between WT and DN HaCaT cells under these settings. Scaffolds were processed as described in the methods and sputter coated with a 5 nm platinum layer to maintain image resolution whilst preventing sample charging. SEM micrographs of both WT and DN HaCaT cells in the restrictive Strata® scaffolds can be seen in *Figure 3.33.*

The data displayed in *Figure 3.33* suggests that the space-restrictive 3D scaffolds provide a matrix in which the cells can move freely in all directions. It can also be seen that both cell types appear to interact with the scaffolds surface in a similar manner to that of 2D culture plastic, with cellular projections reaching out in multiple directions. Alongside these initial observations, images *A* and *B* suggest the DN HaCaT cells are more densely packed at the surface of the scaffold (*B*), whereas WT HaCaTs appear to 'sink' into the surface and integrate into the porous network, resulting in more 'bare' scaffold surface (*A*). This observation is in agreement with the differences observed in previous H&E and fluorescence staining, in which the DN HaCaTs, but not the WT HaCaTs were seen to stack at the scaffold's surface.

The data displayed in *C*, *D*, *E* and *F* highlight the cell phenotypes observed in the centre of the scaffold. To gain access to these regions, scaffolds were fractured and imaged from the side, allowing a view of cell morphology in these central regions. It can be seen that in this region, cells are forced into much closer association and display numerous cellular protrusions reaching out to the surrounding scaffold. No obvious differences can be seen between WT and DN HaCaTs in this central region using this imaging technique, however, it does help provide a visual representation of how the cells interact with the 3D growth environment, which other techniques used thus far have been unable to show with as much clarity.

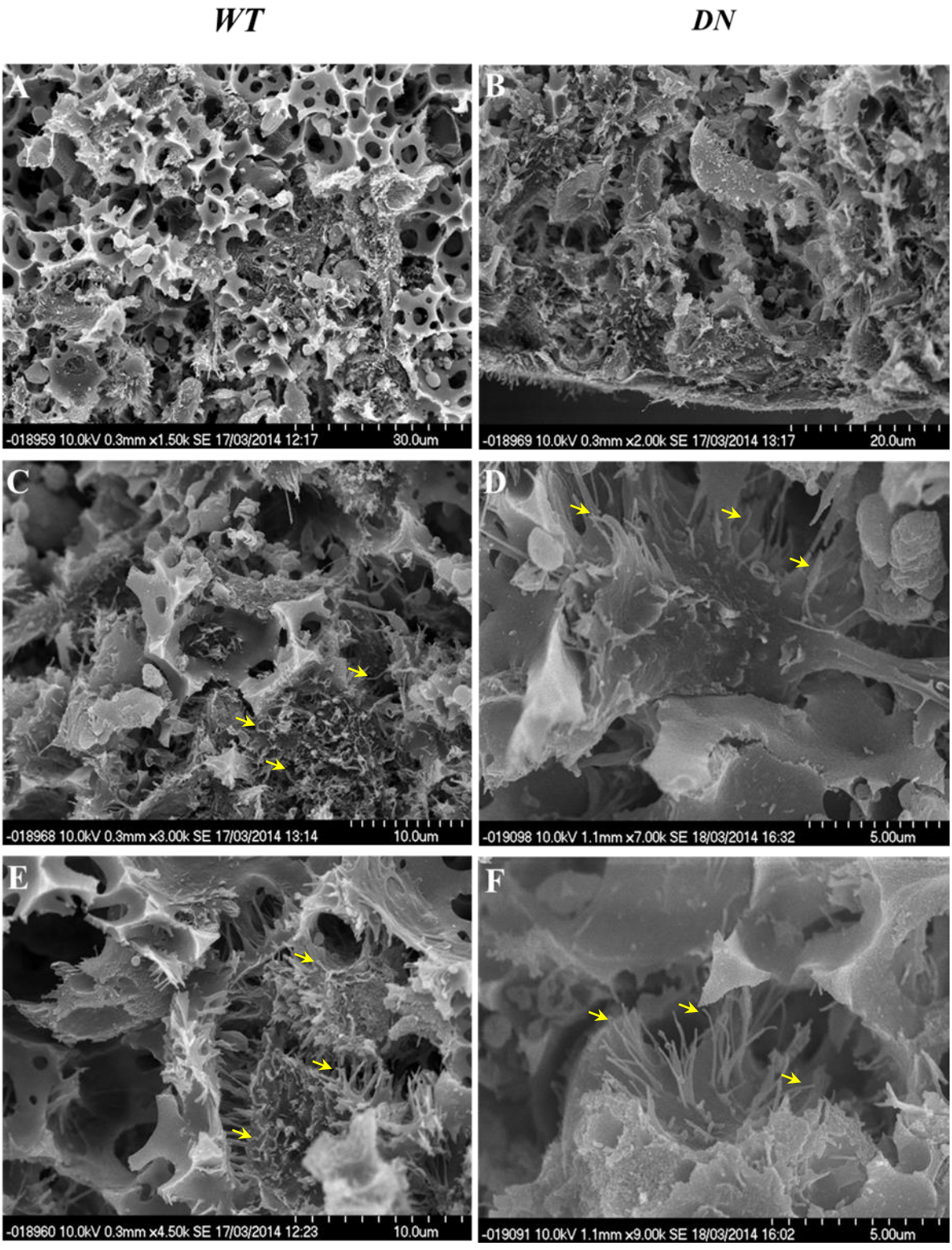

Figure 3.33: *SEM images displaying WT (A, C and E) and DN (B, D and F) HaCaT cells within Alvetex® Strata after 14 days of growth. A and B display surface scaffold regions. Images C, D, E and F highlight cell morphology in central scaffold regions. To consider cell in central scaffold regions, penetration must have exceeded 25 µm from the initial seeding surface. Arrows highlight areas of cellular projections.*

In addition to SEM analysis, further investigations were performed using high-powered TEM. Using this technique, the differences in cell ultrastructure between WT and DN HaCaT cells across the surface and in the centre of the space-restrictive scaffolds were investigated, at the 14 day time point. Cells were cultured, fixed and imaged as described in the methods, with resulting images seen displayed in *Figure 3.34*.

The data presented in *Figure 3.34* displays WT (*A*) and DN HaCaT cells (*E*) across the surface scaffold regions through under TEM analysis. The cell phenotypes observed appear to support data found from the previous H&E staining, in which the DN HaCaT cells displayed a thicker layer of cells across the scaffolds surface of space-restrictive scaffolds (*Figure 3.28*). (*A*) Highlights that the WT cells appear to flatten out and sink into the voids, with little to no cellular stacking occurring at the surface the scaffold. In contrast, (*E)* highlights DN HaCaT cells forming a 1-2 cell thick layer at the scaffold's surface, displaying nuclear deformities. Images (*B*) and (*F*) further display cells in central scaffold regions, suggesting little to no difference observed between the WT and DN HaCaT cells. Both cell types display similar nuclear deformities when passing through non-restrictive areas of this region. However, differences can be observed between the WT and DN HaCaTs as they pass through the more restrictive interconnecting windows as displayed in (*C*), (*D*), (*G*) and (*H*). It can be seen that the DN HaCaT cells appear to display more irregular nuclear projections when faced with these restrictive interconnects, whereas the WT HaCaT cells appear to maintain an elongated, smooth nuclear projection. Classification for a restrictive interconnecting window was deemed any window with a diameter < 2 µm, through which nuclear deformation would be required to pass through.

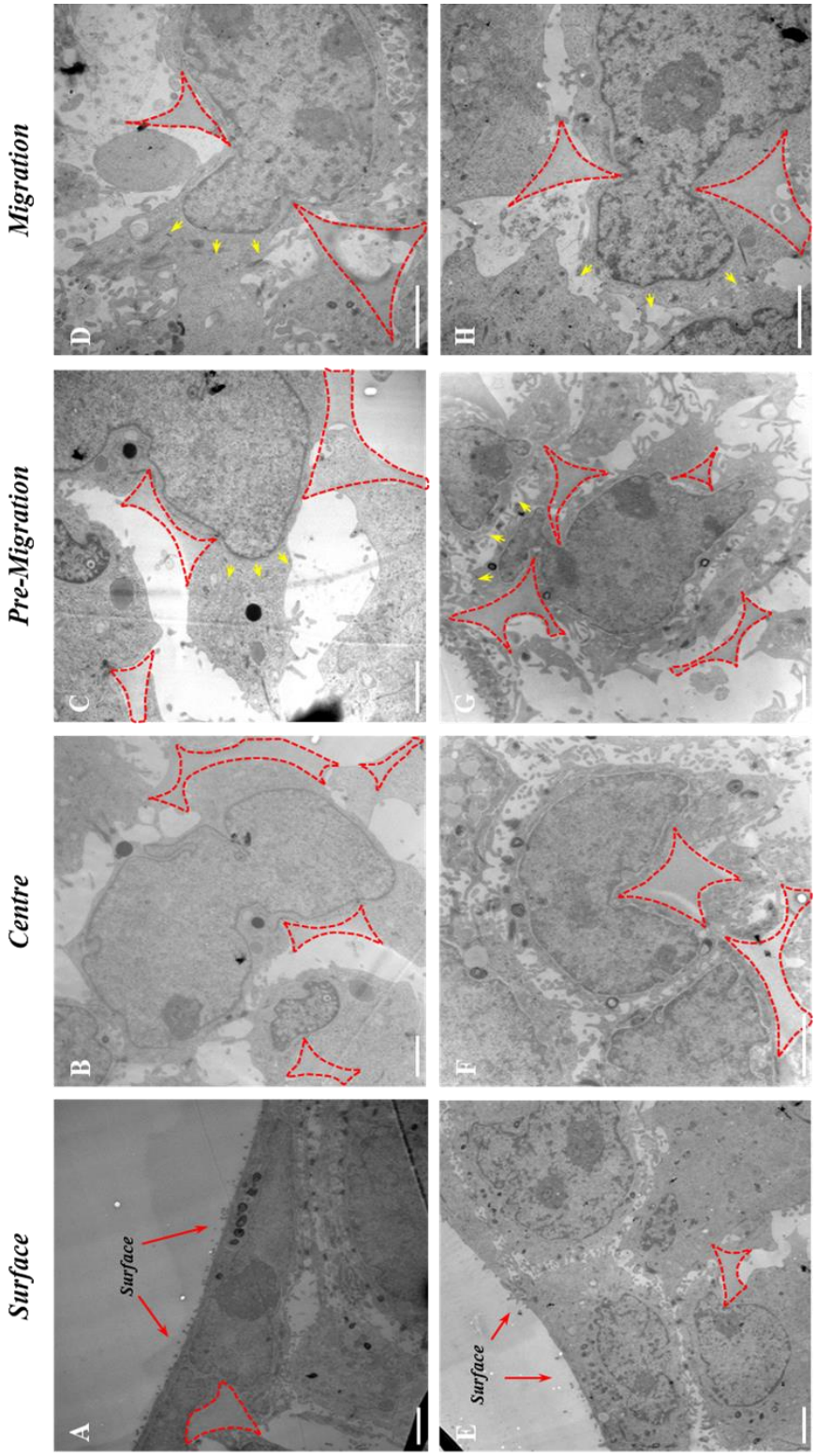

Figure 3.34: *TEM images of WT (A, B, C and D) and DN (E, F, G and H) HaCaT cells in various regions of the Strata® Scaffolds. A and E depict the two cell types across surface regions, whereas B and F display both cells in central scaffold regions. C and G further highlight phenotypic differences observed between both cell types as they are preparing to migrate through restrictive interconnecting windows (Through gaps of 2 µm or smaller). D and H display cell phenotypes observed during migration through these restrictive windows. Arrows highlight hypothesised nuclear migration direction. Scale bar = 25 µm.*

On closer observation, it was further seen that WT HaCaT cells appear to re-localise a greater proportion of their cytoplasm through the voids prior to nuclear migration in comparison to the DN HaCaTs. Migration direction was assumed through observation of Golgi orientation alongside proposed suggestions that, under normal conditions, cells will accumulate their cytoplasm through the restrictive interconnects due to the nucleus requiring deformation to migrate [272, 267]. To further quantify this, the cytoplasmic positioning of 50 WT and DN HaCaT cells respectively were analysed during migration through restrictive interconnecting windows, with aims to assess whether the migration behaviour of *LINC* disrupted cells in space-restrictive 3D environments differs from WT cells. Representative images displaying analysis technique, alongside collated data can be seen in *Figures 3.35* and *3.36*

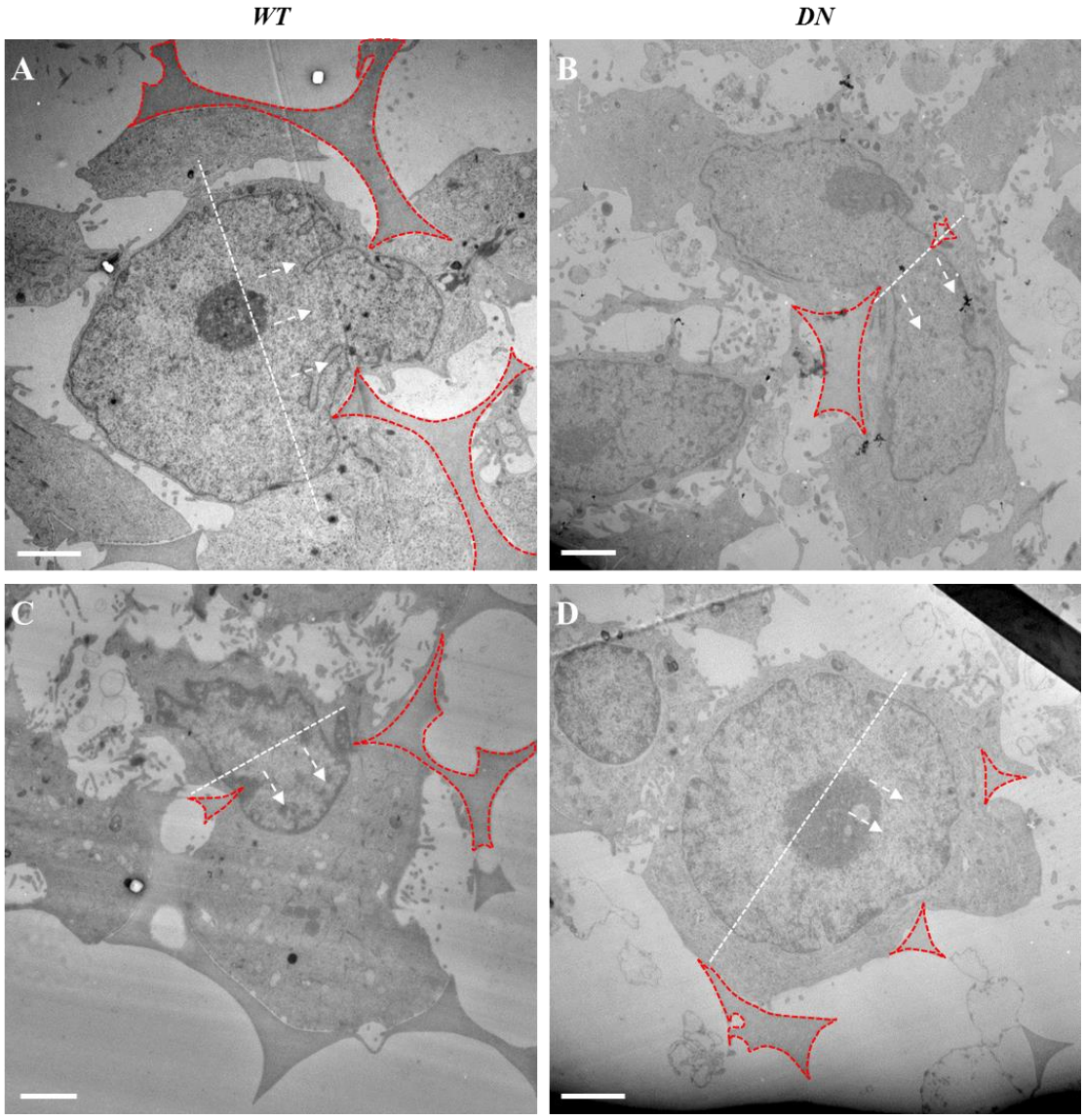

Figure 3.35: *TEM images depicting assessment criteria for cytoplasmic distribution analysis. (A) and (C) display WT HaCaT's, Images (B) and (D) display DN HaCaT cells. Arrows display hypothesised migration direction, dashed lines highlight nuclear centre. Scale bar = 2 µm.*

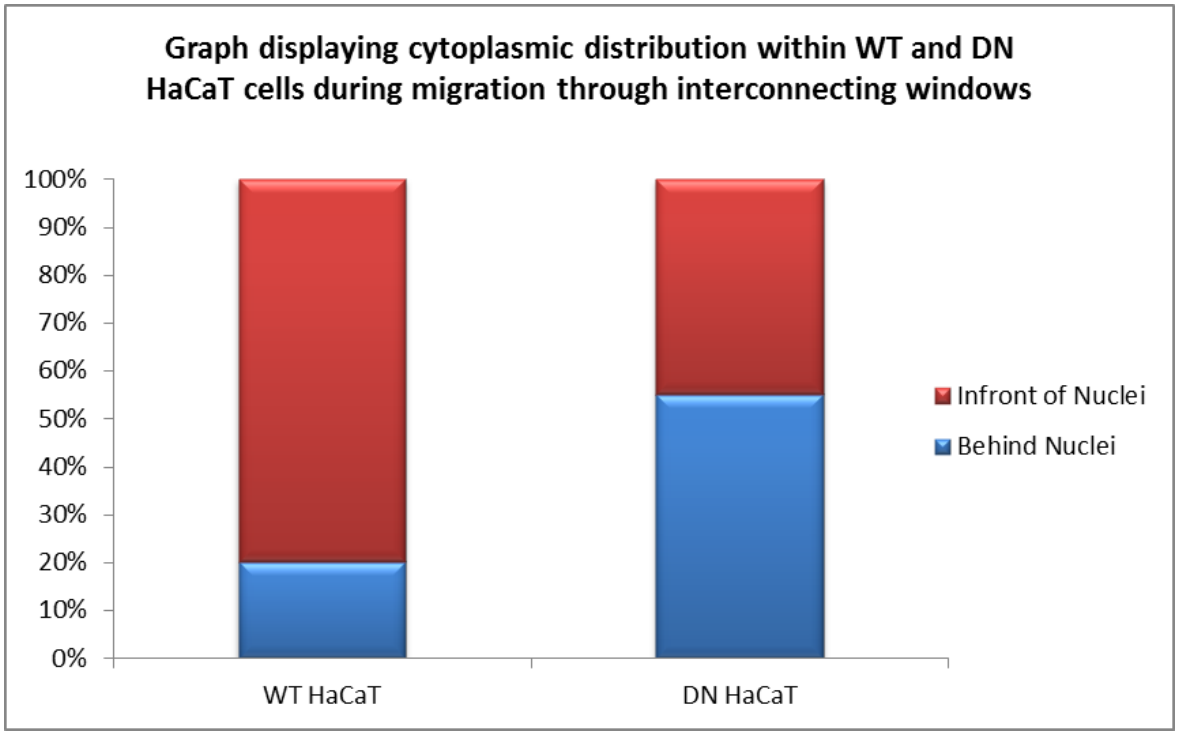

Figure 3.36: *Percentage cytoplasmic distribution across WT and DN HaCaT cells during migration through restrictive interconnecting windows. The data summarises analysis of 50 cells both WT and DN HaCaTs.*

The data presented in *Figure 3.35* helps define how the cytoplasmic distribution was assessed during cell migration through interconnects. A central line was placed in the middle of the nucleus horizontal to the direction of migration; the cytoplasmic volume was then calculated on either side of the central line using the freehand tool in image J. If a higher percentage of the cytoplasm was situated behind the line, the cytoplasmic distribution was labelled as behind the nucleus and vice versa.

Using this measurement technique, the graphical data displayed within *Figure 3.36* was obtained. This data suggests that a difference between cytoplasmic distributions in WT and DN HaCaT cells during their migration through interconnects exists. It was seen that 80% of WT HaCaTs assessed displayed a cytoplasmic distribution in front of the nuclei, whereas only 55% of DN HaCaTs assessed displayed this phenotype. This data, therefore, suggests that the *LINC* complex disruptions present in DN HaCaT cells stimulates a reduction in cytoplasmic distribution ahead of nuclei during cell migration through restrictive interconnecting windows, compared to that of the WT controls.

Alongside cellular shape and cytoplasmic distribution variations between WT and DN HaCaT cells, further differences in nuclear shape were also observed (*Figure 3.34 D* and *H*). It appears that during migration through restrictive interconnects (< 2 µm) the WT HaCaTs maintain a similar nuclear width to that of the interconnecting window during early stages of post migration. In contrast to this, DN HaCaT cells appear to spread out their nuclear structure as soon as they pass through the interconnecting window, displaying a nuclear width and shape similar to that of the pre-migration nuclear segment. This difference between the two cell types was statistically analysed, based on the frequency of this hourglass phenotype occurring during migration through a restrictive interconnecting window (< 2 µm). The criteria to define the hourglass and constrictive phenotypic shapes are highlighted in *Figure 3.37*.

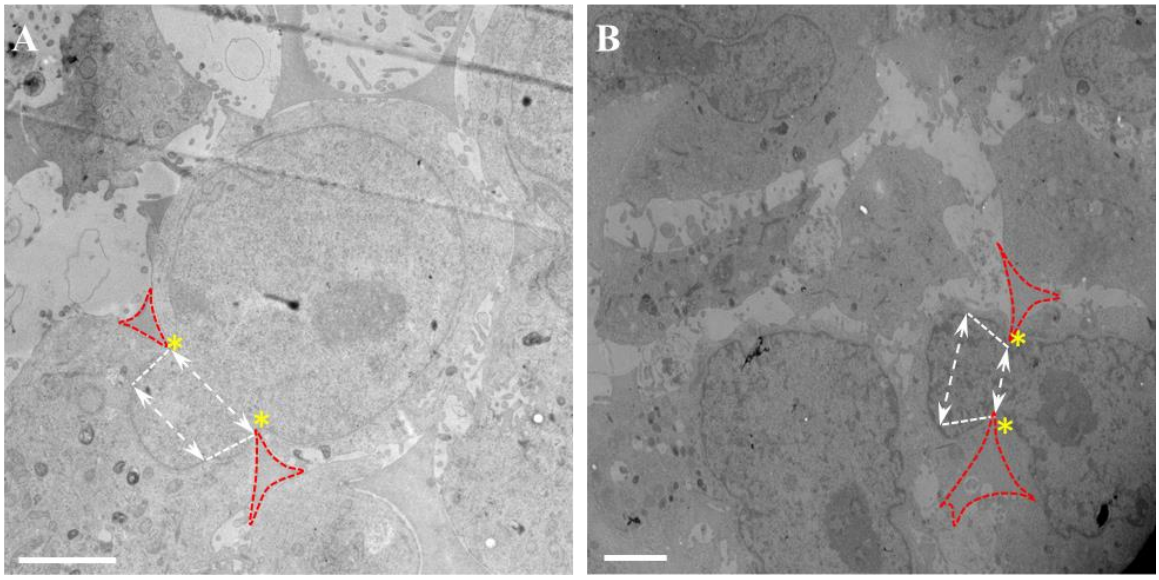

Figure 3.37: *TEM images depicting the criteria for Hourglass (B) or Constricted (A) phenotypes. (A) Displays WT HaCaT cells, scale bar = 1.5 µm, (B) displays DN HaCaT cells, scale bar = 2 µm. Cells were only analysed if migrating through restrictive (< 2 µm) interconnecting windows. Arrows help identify width of nuclei during migration through restrictive interconnect (yellow stars) and post migration. Scaffold is outlined in red.*

Hourglass phenotypes were defined by having a nuclear width of > 1.5x greater than that of the interconnecting window that the cell was migrating through 1.5 µm after the maximum constrictive point (points of maximum constriction can be seen highlighted with yellow stars in *Figure 3.37*). The collated data obtained using these analysis criteria on 50 WT and DN HaCaT cells respectively can be seen presented in *Figure 3.38*.

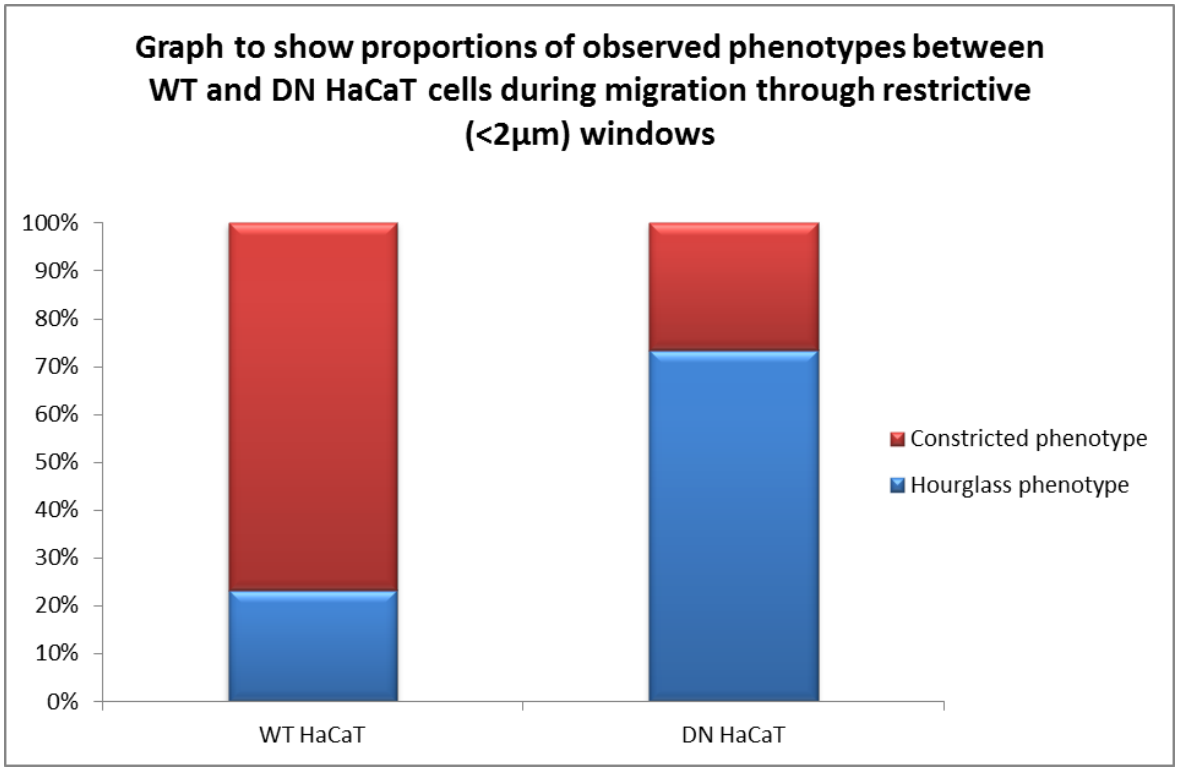

Figure 3.38: *Nuclear phenotypes observed in WT and DN HaCaT cells during migration through restrictive interconnecting windows. The data summarised analysis form 50 WT and DN HaCaTs respectively.*

The data presented in *Figure 3.38* suggests that there is a difference in nuclear phenotype between WT and DN HaCaT evident during migration through restrictive interconnecting windows. It can be seen that around 75% of WT HaCaTs display a much more 'constricted' phenotype post-migration; displaying a nuclear width equal to or less than that of the size of the interconnect. In contrast, roughly 70% of DN HaCaTs appear to display a more 'hourglass' like phenotype, displaying nuclear widths greater than 1.5x the width of the interconnecting window 1.5 µm post-migration.

The data collected through this section, including H&E staining, immunofluorescence and EM data, suggests that the WT and DN HaCaT cells display distinctly unique characteristics when placed in restrictive 3D culture environments. This further suggests that disrupting the *SUN-KASH* interaction across the nuclear envelope stimulates changes in cell behaviour in both 2D and 3D growth conditions.

3.3.4 Both Alvetex® scaffold and Alvetex® Strata environments produce cellular stresses not experienced in 2D culture systems.

3.3.4.1 Interconnecting windows provide stressful migration paths, resulting in cellular responses not observed within normal 2D cell culture.

Through further analysis of TEM micrographs of cells cultured in Alvetex Strata® and Alvetex® Scaffold, it was observed that the scaffold's interconnecting windows possessed sharp edges, and indentations across the cell periphery were observed at these points. It was further observed that filamentous accumulations occurred at the sites of indentation in close proximity to the NE, highlighted in *Figure 3.39*.

As can be seen in *Figure 3.39*, the indentations are often deep. Image (*A*) displays an indentation that appears to be in the process of scraping a fragment of cytoplasm away from the cell during migration. The tip of the scaffold in this image was ~5 nm thick, which is sharp enough to perforate the plasma membrane. Further to this, some indentations were deeper than others, as highlighted in (*B*), (*C*), (*D*) and (*E*), in which scaffold indentations were observed in close proximity to the NE. These deeper indentations appear to alter nuclear shape, resulting in NE deformations. In addition, when sharp scaffold sections come into close association with NE regions, a large accumulation of filaments (hypothesised to be keratin based on filament thickness and morphology) is observed around the point of indentation, as seen most clearly in (*D*). It is therefore hypothesized that these sharp edges create a stressful environment for the cells, able to elicit a cellular response through potential keratin accumulation. However, to further validate these observations, further immuno-gold labelling would be needed to identify the filamentous accumulations.

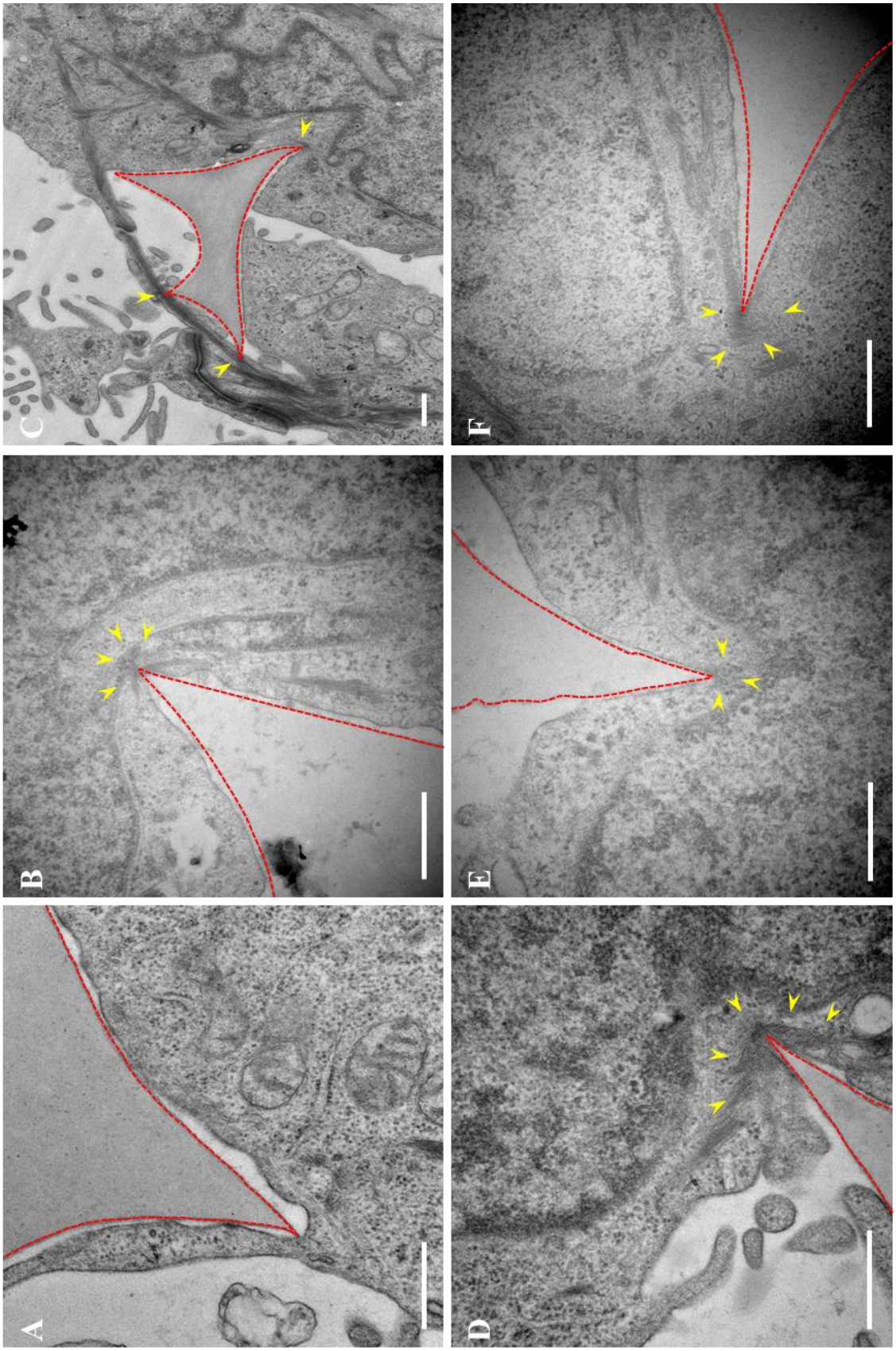

Figure 3.39: *TEM images displaying cell indentations and keratin accumulation (highlighted with arrows). Images represent 14 day growth points of WT (A, B and C) and DN (D, E and F) HaCaTs in Alvetex® Strata. Scaffold regions are outlined in red. Scale bars = 500 nm.*

3.3.4.2 Restrictive interconnecting windows stimulate cytoskeletal accumulation during nuclear migration.

As both the WT and DN HaCaT cells migrate through the space-restrictive Strata® Scaffolds, observations suggest an accumulation of cytoskeletal components develop across the leading edge of the nucleus when faced with restrictive interconnects. Representative images highlighting this observation can be seen in *Figure 3.40*.

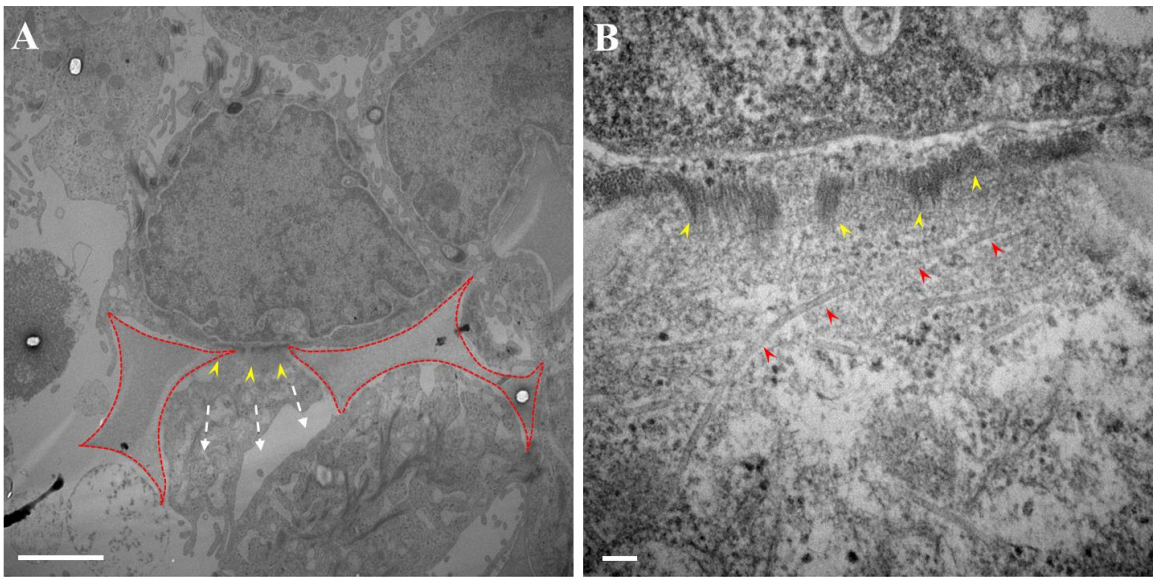

Figure 3.40: *TEM images showing cytoskeletal accumulation across the NE upon restrictive interconnect migration. Image display 14 day grown WT HaCaT cells in central Alvetex® Strata scaffold regions. In (A) white arrows display nuclear migration direction, yellow arrows highlight observed filamentous accumulation across NE. Scaffold is outlined in red. In (B), yellow arrows highlight suspected keratin accumulation, red arrows highlight suggested MTs. Scale bars = 2 µm (A) and 100 nm (B).*

The data displayed in *Figure 3.40* highlight the accumulation of cytoskeletal filaments across the NE upon migration through restrictive interconnects. It can be seen that the cytoskeletal accumulation (suggested to be keratin) highlighted in B with yellow arrows is uniform across the NE in regions directly facing the interconnecting window, whereas further accumulation cannot be found across other nuclear regions. This suggests that cytoskeletal accumulation may be required to 'pull' the nucleus through the restrictive gap, providing further support for roles of cytoskeletal components in nuclear migration. Closer observations, displayed in (*B*), further suggest that this accumulation may not be directly attached to the NE surface, but remains at a distance of 50-100 nm from the nuclear surface; however this could also be due to the plane of sectioning. This could be a result

of cytoskeletal proteins, such as nesprins, providing a link between cytoskeletal components and the NE, however, further investigations using immuno-TEM techniques would be required to validate this hypothesis.

These observations help to further support the hypothesis that the nature of the deformation exhibited by the NE and adjacent cytoskeleton are suggestive of a mechanism that pulls nuclei through the restrictive 3D environment, rather than through passive nuclear movement. This could therefore highlight potential pressures unique to such restrictive 3D culture environments, which are not present in conventional 2D culture systems.

3.3.5 SUN-KASH bridge disruption in keratinocytes increases 3D migration potential by decreasing nuclear stiffness.

3.3.5.1 DN HaCaTs display a decreased circularity index within central regions of the restrictive Strata Scaffolds compared to surface regions.

DN HaCaT cells are able to migrate deeper into the Strata® scaffold than their WT counterparts, it is believed that this is due to the DN mutation effectively disrupting the link between the INM and ONM, resulting in increased nuclear malleability. This phenotype may allow DN HaCaT cell an increased capacity to squeeze through restrictive interconnecting windows, whilst using less energy to de-stabilise the proteins that govern NE architecture. To assess whether the nuclear malleability of DN HaCaT cells is indeed higher than that of the WT controls, nuclear circularity indexes in various regions of both the Alvetex® Scaffold and Alvetex Strata® scaffolds were assessed. This allows for accurate and direct comparisons to previous penetration investigations conducted in these materials. The 14 day growth time point at the air-liquid interface was identified as the most suitable for this investigation as cells can be found across both the surface and central regions of the scaffold in high numbers. The use of confocal microscopy to visualise sections of these scaffolds allowed for the analysis of specific Z axis regions, allowing for the majority of in-focus cells to be imaged. An example of the images obtained along with the measurement criteria used can be seen in *Figure 3.41* and *Figure 3.42* respectively.

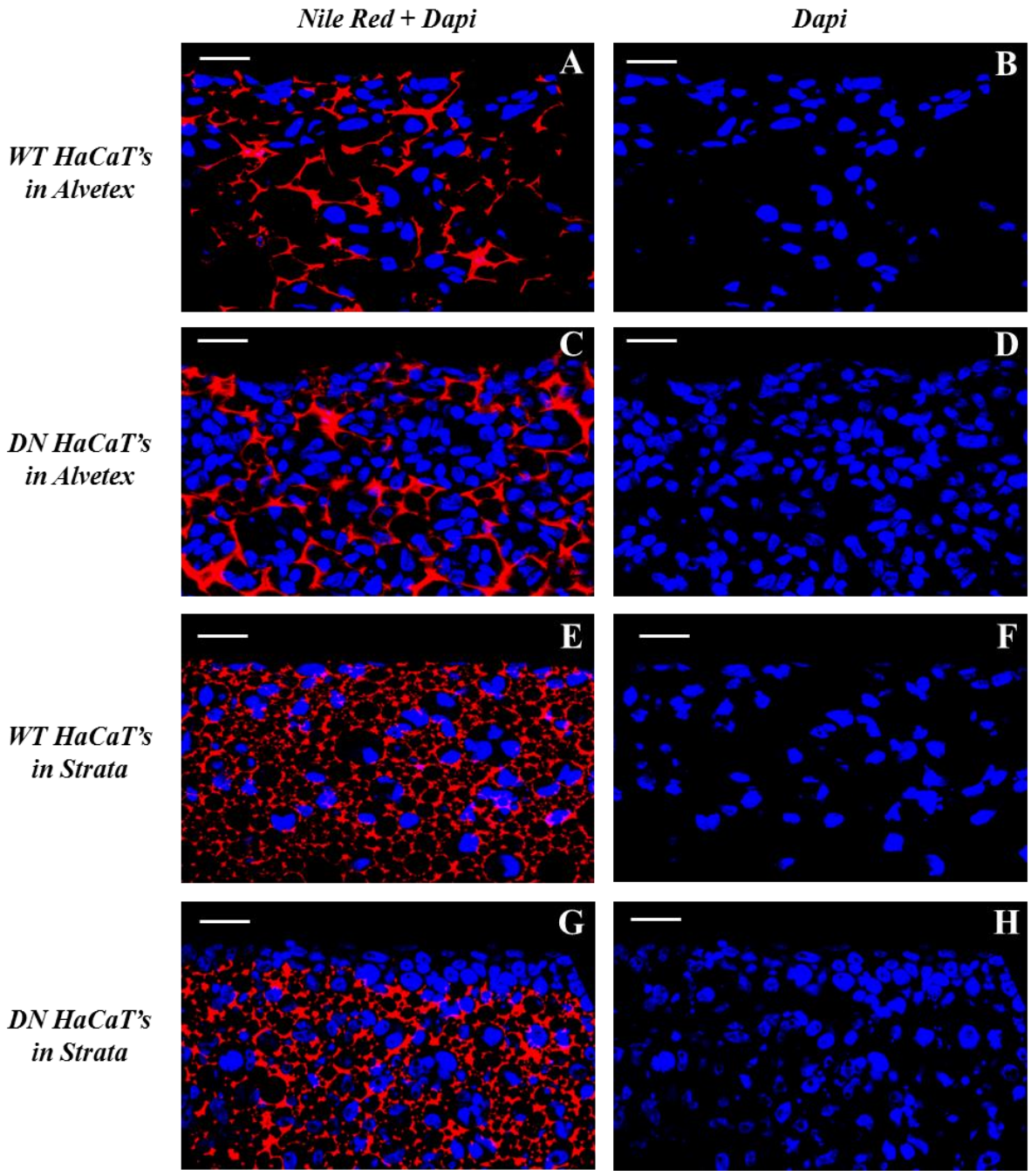

Figure 3.41: *Images displaying 14 day grown WT and DN HaCaT cells in Alvetex® Scaffold (A-D) and Alvetex® Strata (E-H). Cells are stained for DAPI (Blue) and scaffolds for Nile red (Red). Scale bar = 25 µm.*

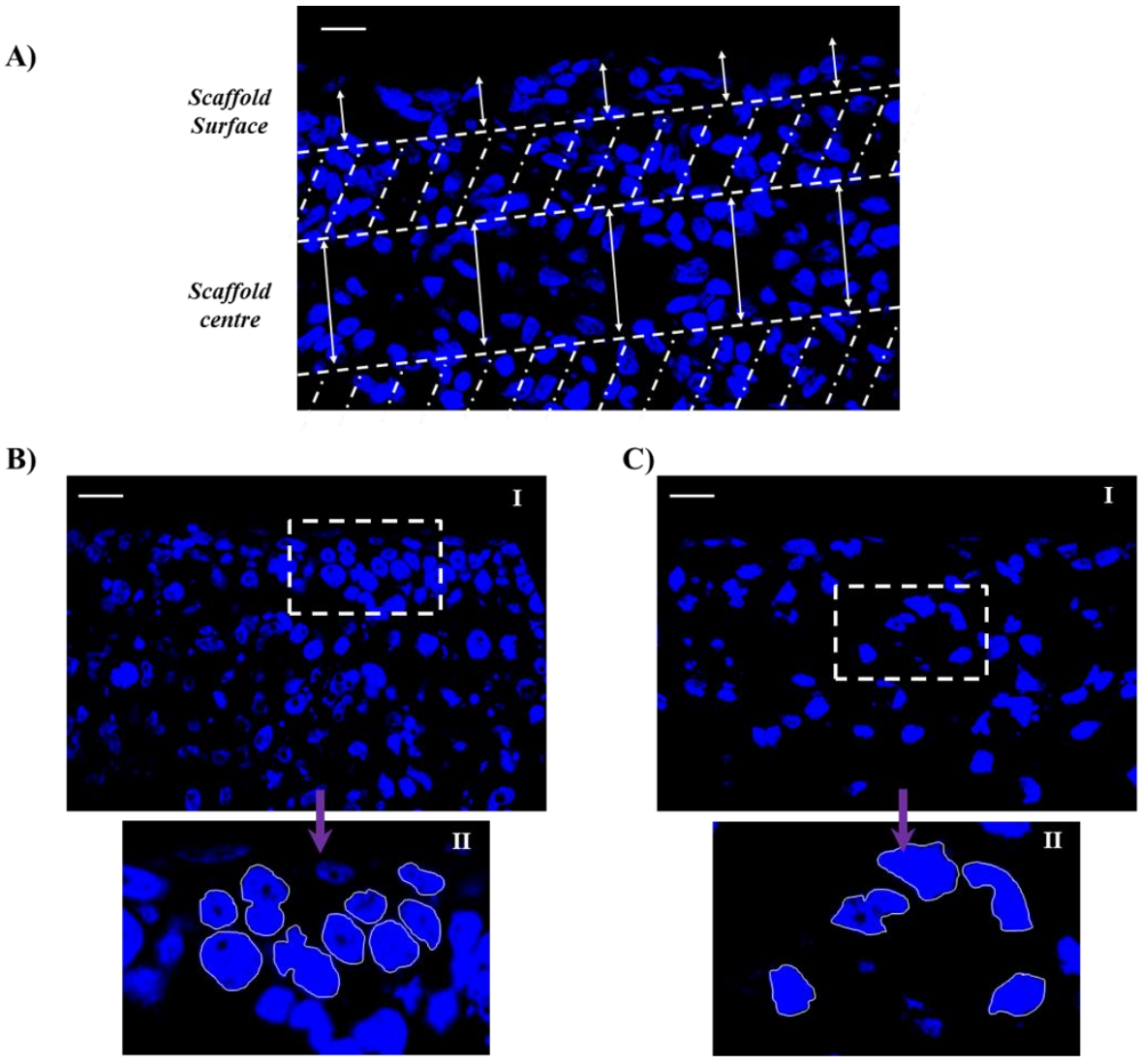

D)

File	Edit	Font	Results					
	Area	Mean	Min	Max	Circ.	AR	Round	Solidity
4	57.973	83.621	5	87	0.590	1.228	0.814	0.886
5	22.085	59.855	0	85	0.473	1.749	0.572	0.846
6	29.019	33.305	0	85	0.716	2.408	0.415	0.956
7	51.232	77.555	0	85	0.731	1.490	0.671	0.926
8	34.219	82.308	15	90	0.649	1.382	0.723	0.934
9	63.238	73.793	4	86	0.392	3.046	0.328	0.817
10	82.113	80.952	0	132	0.599	2.320	0.431	0.823

Figure 3.42: *Image series displaying assessment criteria. A) Highlights measurements for cells on the scaffolds surface were taken within the top 25 µm, whereas measurements for the scaffolds centre were taken from 75-150 µm into the scaffold. B) and C) display examples of how the measurements were taken. Within each region, in focus nuclei were highlighted using the free hand tool in ImageJ and then measured. D) displays an example output. Cells were stained for DAPI (blue). Scale bars = 25 µm.*

The data presented in *Figure 3.41* highlights differences in cell packing density between the two cell lines across the two scaffolds, with the DN HaCaT cells showing a higher cell density per μm^2 in comparison to their WT counterparts, as shown by H&E (*Figure 3.19* and *3.21).* The initial number of cells seeded to each scaffold for both cell lines was the same (250,000 cells), and so even though it is known that the WT HaCaTs replicate faster, it appears the DN HaCaT colonise both 3D scaffold systems more densely. In addition, DN HaCaT cells seeded onto space-restrictive Strata® scaffolds produce a layer of ~2-3 cell across surface scaffold regions, further supporting previous observations at the air-liquid interface for this cell line (*Figure 3.28* and *Figure 3.29)*.

Figure 3.42 (*A*) displays the defined regions from which the nuclear circularity index measurements were obtained. Measurements were taken across the scaffold's surface and in its centre, to investigate whether nuclear circularity changes exist between the two environments. The 'surface' of the scaffold for the purposes of these measurements was considered as the first 25 µm from the top layer of cells. This, therefore, helps to provide an indication of nuclear circularity before the cells begin to adapt to the new environment within the scaffold, in which space is more limited and media flow is at a much lower rate. The central region measurements were taken from 75-150 µm into the scaffold. This region was selected due limitations in cell penetration depth, and so a maximum depth of 150 µm allows for accurate comparisons to be made between both cell lines in each scaffold. Alongside this, the selected central region is far enough from the surface to ensure cell deformities have occurred, allowing for speculations on nuclear malleability to be made. (*B*) and (*C*) highlight two examples of how cells were analysed at the various scaffold regions. Nuclei were individually traced to ensure that only in focus nuclei were analysed and measured using ImageJ. An example of the output produced can be seen in (*D*), in which the circularity index of the traced nuclei can be seen in the highlighted area labelled Circ. This measurement technique provides an accurate estimation tool to decipher if differences exist between the DN and WT HaCaT nuclear circularity in different scaffold regions. The data collected via this method is shown in *Figures 3.43 – 3.46*

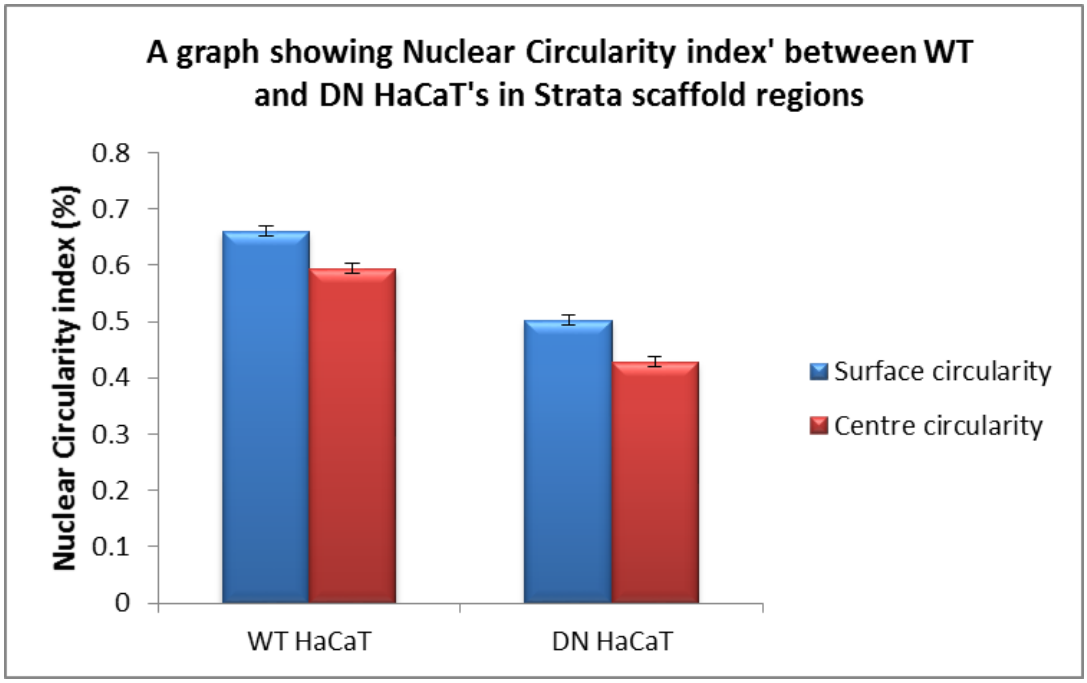

Figure 3.43: *Differences observed between nuclear circularity index of WT and DN HaCaT cells across surface and central Alvetex® Strata regions.*

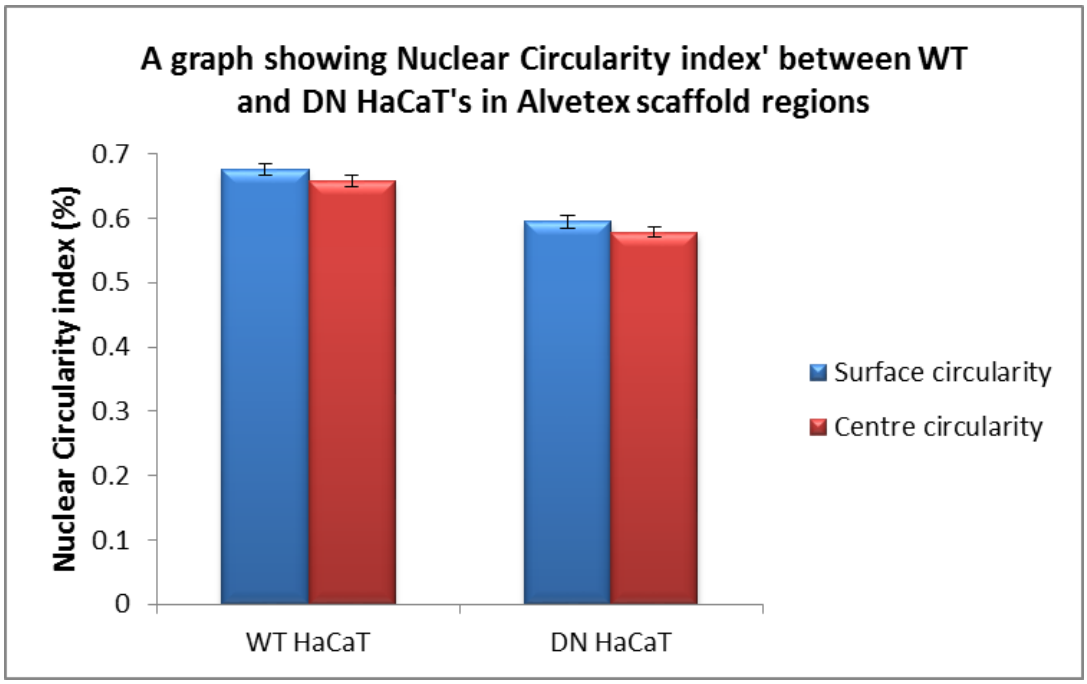

Figure 3.44: *Differences observed between nuclear circularity index of WT and DN HaCaT cells across surface and central Alvetex® Scaffold regions.*

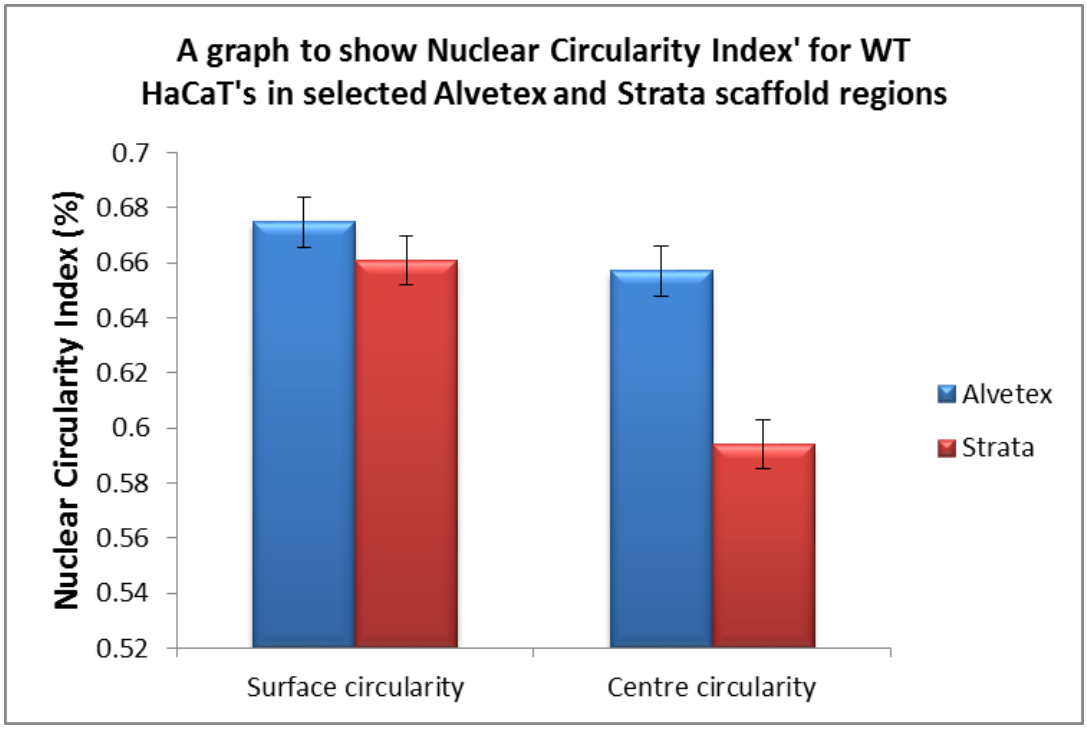

Figure 3.45: *Differences observed between nuclear circularity index of WT HaCaT cells across surface and central Alvetex® Strata and Alvetex® Scaffold regions.*

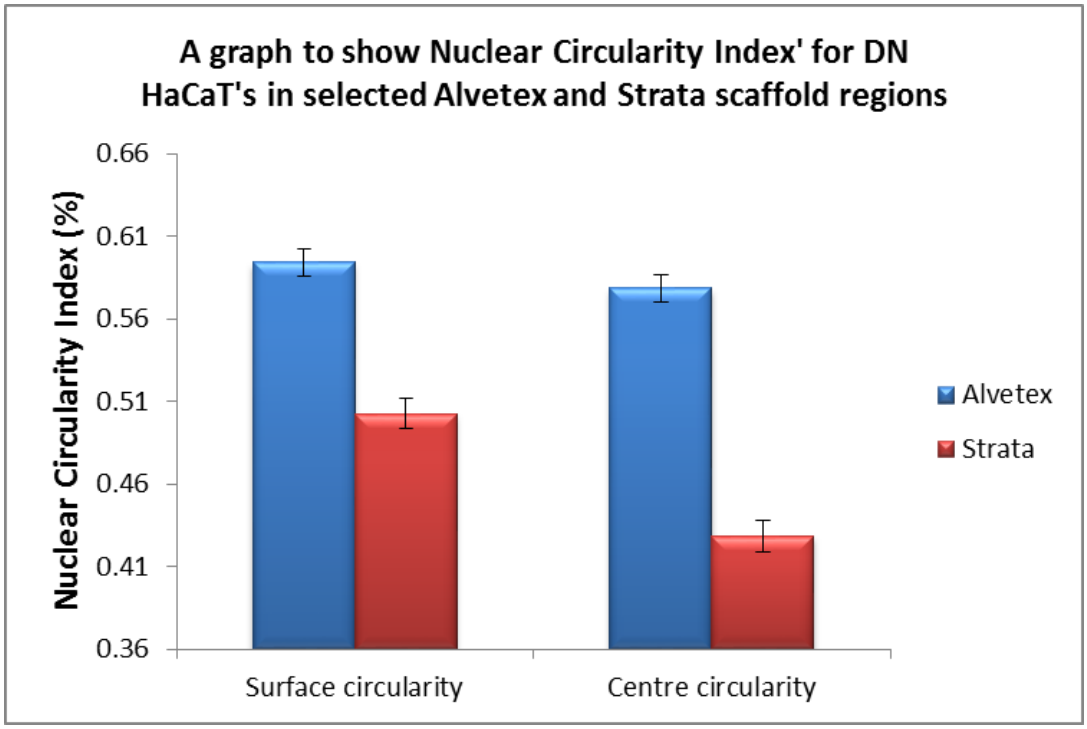

Figure 3.46: *Differences observed between nuclear circularity index of DN HaCaT cells across surface and central Alvetex® Strata and Alvetex® Scaffold regions.*

The data presented in *Figure 3.43* suggests that both the WT and DN HaCaT cells display a significant difference between their nuclear circularity at the surface and central scaffold regions in the Strata® scaffolds using an unpaired t-test at a p-value of ≤ 0.005. The Strata® Scaffold's restrictive void sizes (~5-15 µm) and interconnecting windows (~4 µm) appear to stimulate nuclear deformities, suggesting that these deformities are required in order to pass from void to void. This requirement of nuclei to deform in order to migrate could be the reason why nuclear circularity is greatly reduced in central scaffold regions in comparison to surface regions. Further observations also suggest that the nuclei of the DN HaCaTs display a lower circularity index than their WT counterparts in both regions of the scaffold. This supports the observations in 2D culture systems previously discussed, in which the DN mutants also displayed nuclear abnormalities, such as increased nuclear heights to that of the WT HaCaTs (*Figure 3.9*).

The data presented in *Figure 3.44* suggest there is no observable difference between the DN and WT HaCaT nuclear circularity across both the surface and central regions of the non-restrictive scaffolds. In the Alvetex® Scaffold, void diameters range from ~15-45 µm, resulting in little to no restriction on movement between voids during migration, resulting in less nuclear deformation occurring during migration through interconnecting windows. However, the data does suggest that DN HaCaTs, again, display a significantly lower circularity index value to their WT counterparts in both surface and central scaffold regions.

Figures 3.45 and *3.46* look at comparisons between the central and surface scaffold region impact on cell circularity in both Alvetex® Scaffold and Alvetex® Strata for each cell line. The data suggests that for the WT HaCaT cells, circularity changes are observed in central scaffold regions of both materials, with Strata scaffolds stimulating the lowest nuclear circularity values. However, across the surface of both scaffold materials, no significant difference in WT HaCaT nuclear circularity was observed. For the DN HaCaTs, it can be seen that in both central and surface scaffold regions, the DN HaCaT cells display a much lower circularity index value when grown within the restrictive Strata scaffolds. This suggests that the DN HaCaT cells display an increased capacity to adapt to their environmental surroundings, displaying nuclear deformation as soon as scaffold penetration commences, whereas the WT HaCaT cells only appear to display changes in nuclear circularity after migration of ~75 µm into the scaffolds.

From these investigations, it can be seen that the DN HaCaTs appear to display an altered nuclear circularity index compared to that of the WT HaCaTs in all regions of both scaffold types. In addition, it has been shown that the nuclear circularity index significantly

reduces upon migration into the more restrictive Strata® scaffold for both cell lines, however, this difference appears to be greater for the DN HaCaT cells due to their lower initial circularity index. This indicates that decreased nuclear circularity and increased nuclear malleability could be providing the DN HaCaT cells with an advantage when migrating through restrictive environments; however, further investigations are required as the investigations thus far present only a suggestion of increased nuclear malleability in the DN HaCaT cells. To fully verify whether nuclear stiffness is indeed different between WT and DN HaCaT cells, mechanical testing of the NE is needed directly, through the application of atomic force microscopy (AFM) for example.

3.3.5.2 DN HaCaT cells display an increased nuclear malleability upon external nuclear pressure from osmotic stress.

Previous investigations suggest that the DN HaCaTs display a reduced nuclear circularity index in comparison to their WT counterparts upon migration through restrictive 3D culture environments. Coupled with further 3D migration analysis data displayed in section 3.3.3, it is suggested that an increased ability to deform the nuclear architecture (nuclear malleability) displayed within the DN HaCaT cells could be a crucial factor in increasing the migration potential through restrictive environments. However, the circularity index only suggest that the nuclei are more deformed and does not provide information as to their ability to deform their nuclei in direct response to an external factor over a set time.

To expand current knowledge of nuclear malleability between the WT and DN HaCaT cells, a follow up experiment using osmotic stress [273, 274] in the surrounding media as a controllable external factor to analyse nuclear deformation was conducted. It has been suggested that in a hypertonic solution, cells will lose most of their cytoplasmic volume due to osmosis of liquid into the surrounding solution. Due to this decreased volume within the cytoplasm, cytoplasmic area will shrink causing pressure from the organelles to be exerted on the nuclear envelope. This pressure, if great enough will stimulate nuclear deformation based on the stiffness/malleability of the nuclear envelope. If the nuclear envelope is more malleable in the DN HaCaT cells, a decreased nuclear circularity index compared to the WT HaCaT cells as the osmotic stress increases in the surrounding environment would be expected. The results of this study can be seen in Figure 3.47.

To conduct this experiment, we incubated both WT and DN HaCaT cells at a confluence of 70% in a range of hypertonic sucrose concentrations (0 mM, 40 mM, 80 mM, 160 mM, 320 mM, and 640 mM) added to normal growth media for a period of 30 min under normal growth conditions. Cells were then fixed and immuno-fluorescently stained for lamin A/C (nuclear envelope marker) and with DAPI (nuclei). The literature suggests that a longer time point of over 30-40 minutes could provide cells time to adapt to the exerted stress and revert to a pre-stress phenotype. Images were obtained utilising the *LEICA SP5* confocal microscope, with representative images for both cell types displayed in *Figure 3.47*.

The data displayed in *Figure 3.47* shows fluorescence images from the control condition (0 mM sucrose) and the highest level of osmotic stress exerted (640 mM sucrose). Very few differences in nuclear circularity can be observed, with both cell lines displaying little variability in nuclear shape before and after osmotic stress. To quantify if any differences exists between the two cell lines over the course of osmotic stress, nuclear circularity of 200 cells at each sucrose concentration was carried out, the results of which are shown in *Figure 3.48*.

The data presented in *Figure 3.48* displays the nuclear circularity deformation trends upon introducing the cells to varying hypertonic sucrose concentrations. The data presented in both (*A*) and (*B*) suggests that the increasing sucrose concentrations correspond to a decrease in calculated nuclear circularity for both cell types. Within R, a two way *ANOVA* was used to calculate whether a difference existed between the effects of sucrose on the WT and DN HaCaT nuclear circularity. The results obtained show evidence of a relationship between increasing levels of sucrose and observed nuclear malleability for both cell types (*ANOVA,* $F_{5.2388} = 3.02$, $P = 0.010$). However, the graphical data displayed in *Figure 3.48* clearly shows that the DN HaCaT cells have a lower nuclear circularity index in the control condition without sucrose addition. Further statistical analysis supports this, showing strong evidence that the nuclear circularity differs between the control conditions for each cell type (*ANOVA,* $F_{1.398} = 127.12$, $P < 0.001$). To look for evidence that the relative effect of increasing sucrose concentrations on nuclear circularity differs between the two cell types, The data was normalize, making the control circularity index value obtained for both the WT and DN HaCaT cells the baseline to which other values were compared. This was performed through giving the control circularity a value of 1 (Representing a perfect circle), from which the effect of increasing sucrose concentration could be directly compared between the cell lines. The resulting normalised graphical data can be seen in *Figure 3.49*.

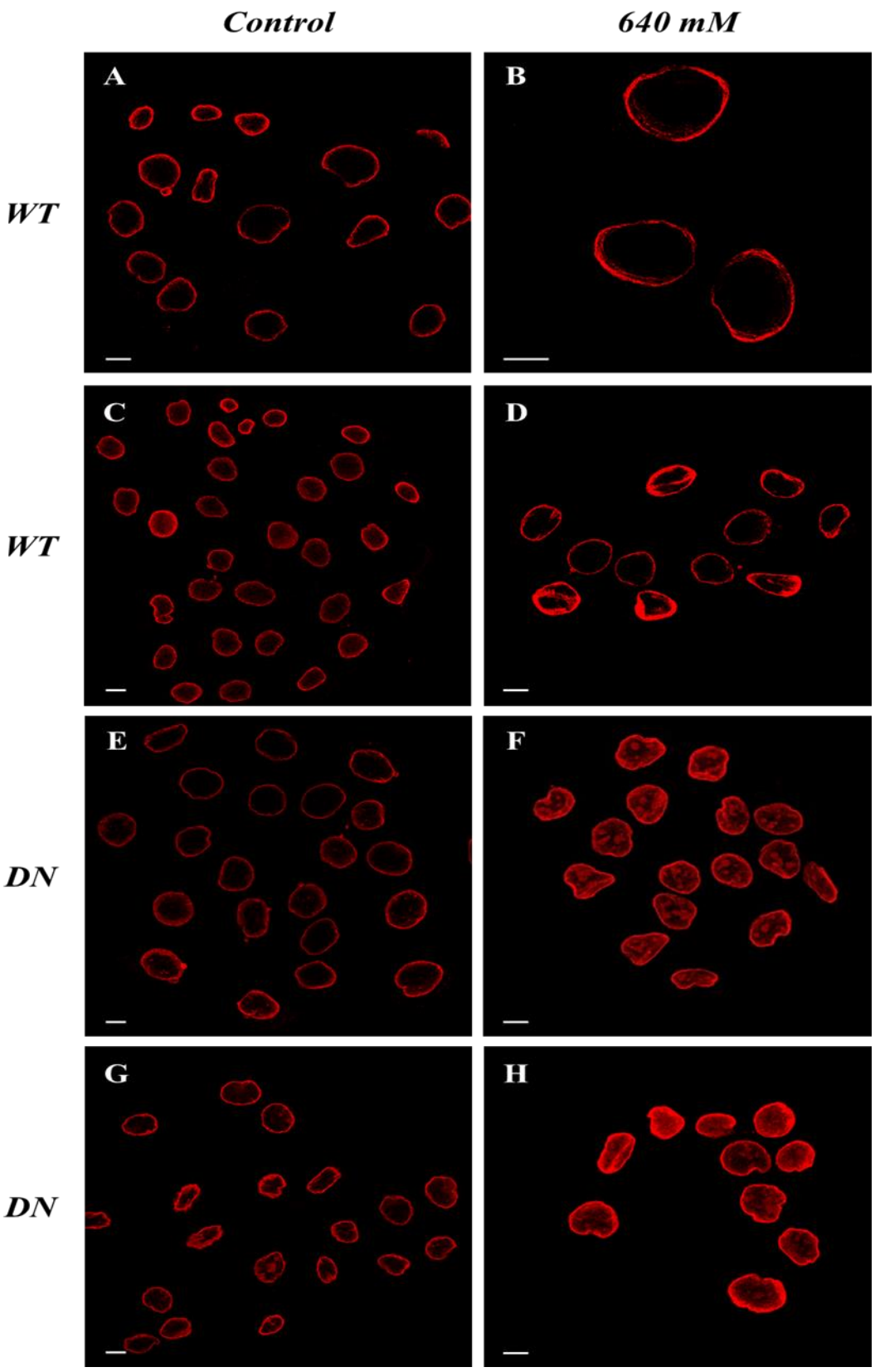

Figure 3.47: *Image series displaying WT and DN HaCaTs incubated in both normal growth media (A, C, E and G) and growth media + 640 mM Sucrose (B, D, F and H). Cells are stained for lamin A/C (red). Scale bars = 5 µm.*

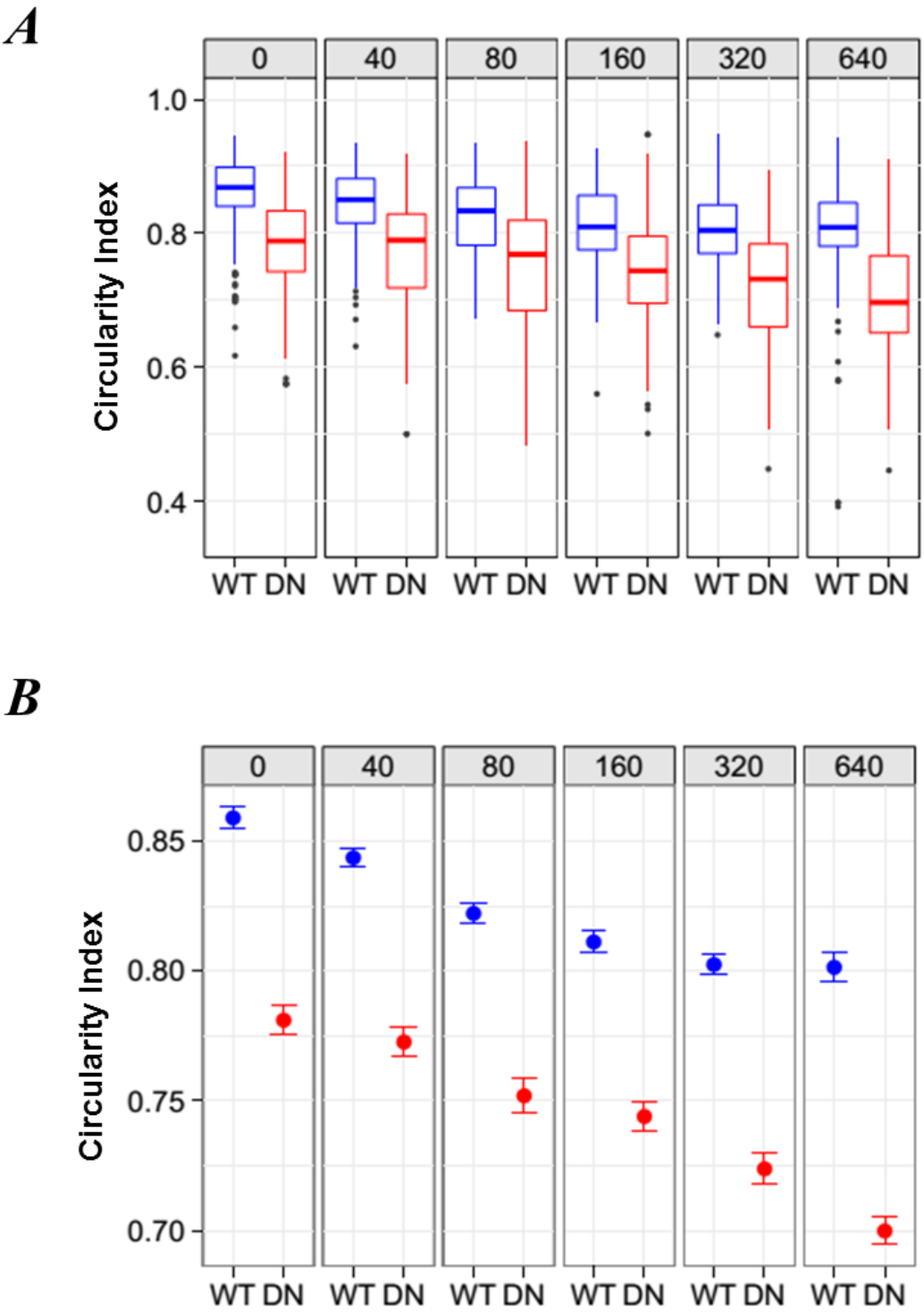

Figure 3.48: *Nuclear circularity across WT and DN HaCaT cells. A) Displays raw data alongside the mean and standard deviation plotted using 'R'. B) Displays the refined data displaying the means for both the WT (Blue) and DN (Red) HaCaT cells.*

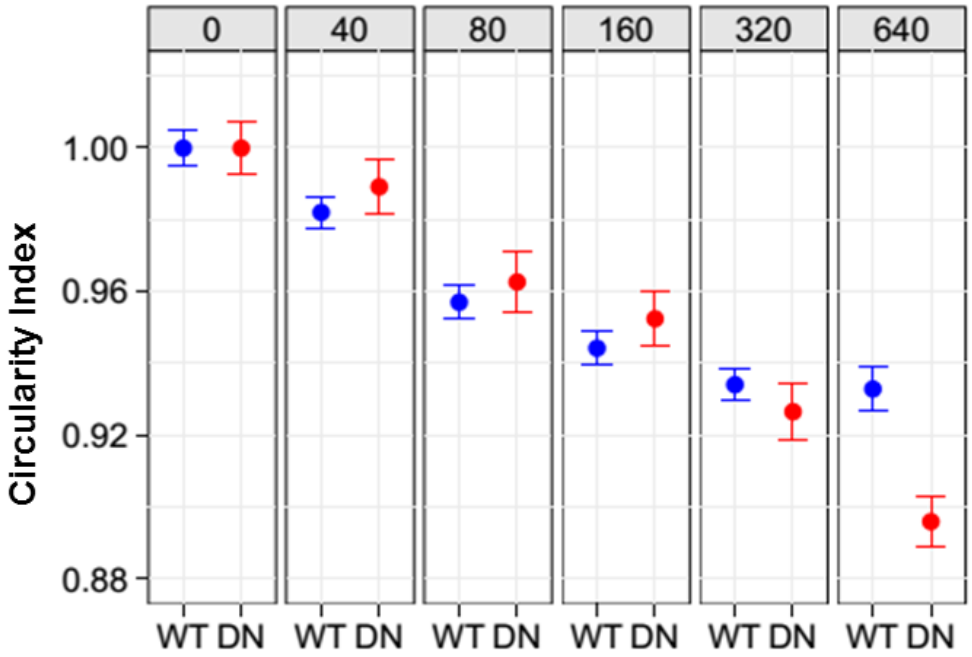

Figure 3.49: *Normalised nuclear circularity across each sucrose concentration plotted using 'R', displaying the means for both the WT (Blue) and DN (Red) HaCaT cells. Control conditions for each cell line were given a value of 1, allowing the effects of increasing sucrose concentrations to be directly compared.*

The graphical data presented in *Figure 3.49* suggests that as sucrose concentrations are increased, the nuclear circularity values for each cell type decrease. However, at a sucrose concentration of 640 mM, it is seen that the DN HaCaT cells exhibit a greater decrease in nuclear circularity than that of the WT HaCaT cells. To support this, *F-tests* were performed for each sucrose concentration (excluding the control) to test for differences between the nuclear circularity between the WT and DN HaCaT cells. Five F-tests were performed in order to ensure the test is statistically significant when a P-value less than 0.05 / 1 = 0.01 is obtained. Of the 5 statistical tests performed, a significant change in the effect of sucrose between the WT and DN HaCaT cells was only detected when sucrose concentration was at 640 mM. This result is consistent with the trends observed from the plot of means and standard errors presented in *Figure 3.48*. This, therefore, suggests that the DN HaCaTs display a decreased nuclear circularity to that of WT HaCaTs at sucrose concentrations of 640 mM, suggesting that under high osmotic stress conditions, the DN HaCaT cells display an increased ability to deform their nuclei than that of the WT HaCaT cells.

3.3.5.3. DN HaCaT cells display softer nuclei and decreased nuclear stiffness under biological and non-biological conditions.

Results thus far indicate that DN HaCaT cells express an increased penetration potential into space-restrictive scaffolds, alongside an increase in nuclear malleability when compared to WT cells. However, during the osmotic stress experiment conducted previously, it was not taken into consideration, the possible alternate cellular features which could be affecting the deformation potential of the NE under these experimental conditions osmotic stresses. To validate this data, further investigation into the nuclear malleability differences between the WT and DN HaCaT cells was conducted using Atomic Force Microscopy (AFM). The Young's modulus, and hence nuclear stiffness, can be directly measured via AFM [275].

Initially the two cell types were analysed under dry, non-biological conditions (not under normal growth conditions for specific cells as described in 2.14.1 of the methods section), in order to assess whether cellular AFM analysis was feasible using the instrument available. Cells were processed as described in the methods section and imaged using a Bruker MM8 AFM fitted with a 70 kHz scanasyst cantilever. Initial observations from this pilot experiment can be seen in *Figure 3.50*.

The initial data from the pilot investigation displayed in *Figure 3.50* highlights cellular differences observed between the two cell types under these experimental conditions. It can be seen that initially, the 15 µm x 15 µm analysis grid allows single cells to be observed. As can be seen from the WT HaCaTs displayed within images (*A*) and (*B*), the drying process after fixation stimulates a collapse across an area corresponding to the nucleus, leaving behind a crater in the cell, lower than the surrounding cytoplasmic environment. In comparison to this, the DN HaCaT cells displayed in images (*C*) and (*D*) do not appear to undergo this nuclear collapse, displaying a nuclear protrusion higher to that of the surrounding cytoplasm, corresponding to the expected nuclear positioning.

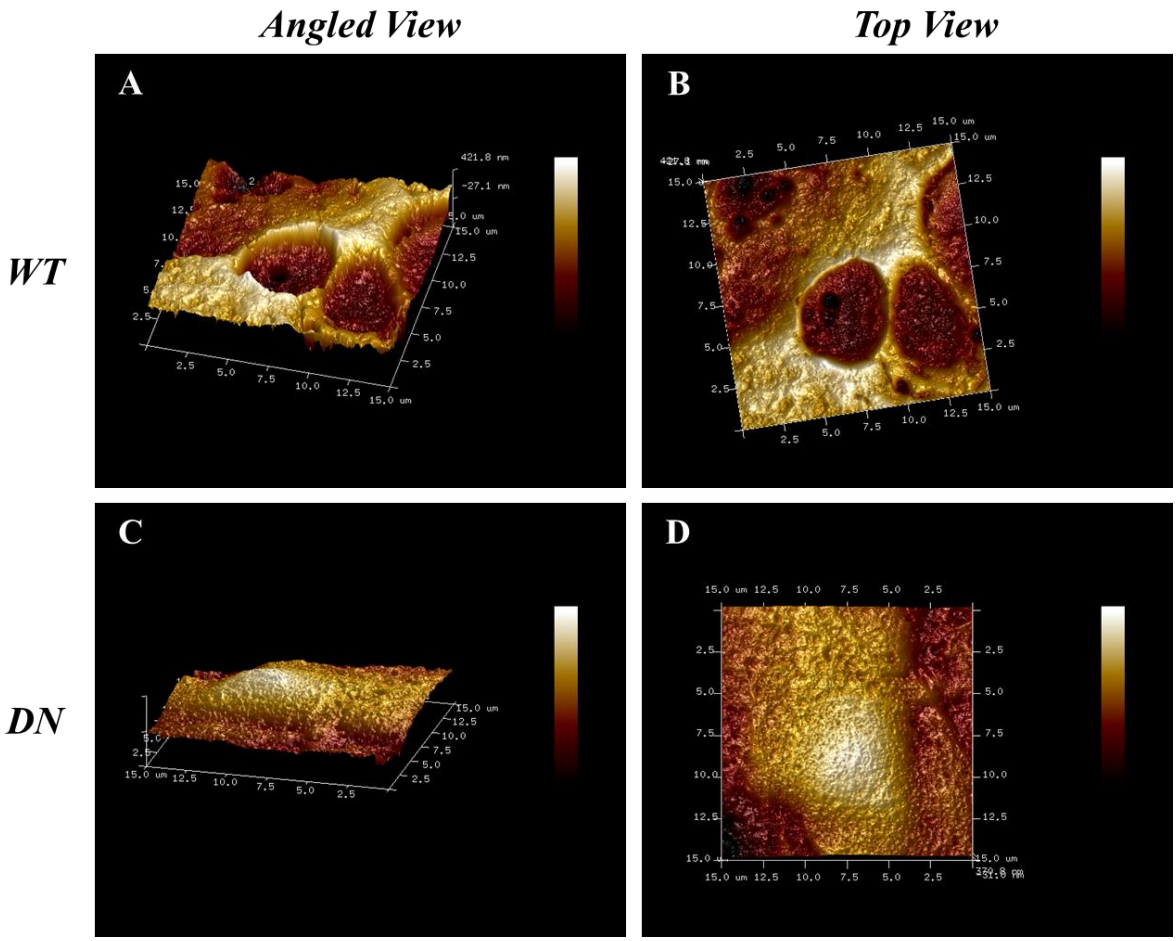

Figure 3.50: *AFM height maps for WT (A and B) and DN (C and D) HaCaT cells under non-biological conditions. Scale bars = cell height, with light shading representing the highest region of the cell.*

The AFM used in this pilot study was not sensitive enough to give a Young's modulus value for the cell nuclei; however, differences between the DN and WT HaCaT nuclei can be seen. These differences could arise from the WT cells exhibiting stiffer nuclear properties, and are therefore unable to withstand the compression pressures of drying, thus undergoing complete nuclear collapse. As a result, further analysis using a more sensitive AFM (NanoWizard 3 Bioscience AFM) that has been designed to analyse cells under biological conditions. Both DN and WT HaCaTs were grown on glass bottom petri dishes with a known modulus, so as not to affect the readings under experimental conditions. Analysis was performed on 15 WT and 15 DN HaCaT cells, consisting of both single and grouped cell morphologies. The AFM's cantilever was aligned and run in a raster configuration across the cells surface, providing detailed information on the Young's modulus and height, the results of which can be seen in *Figure 3.51.*

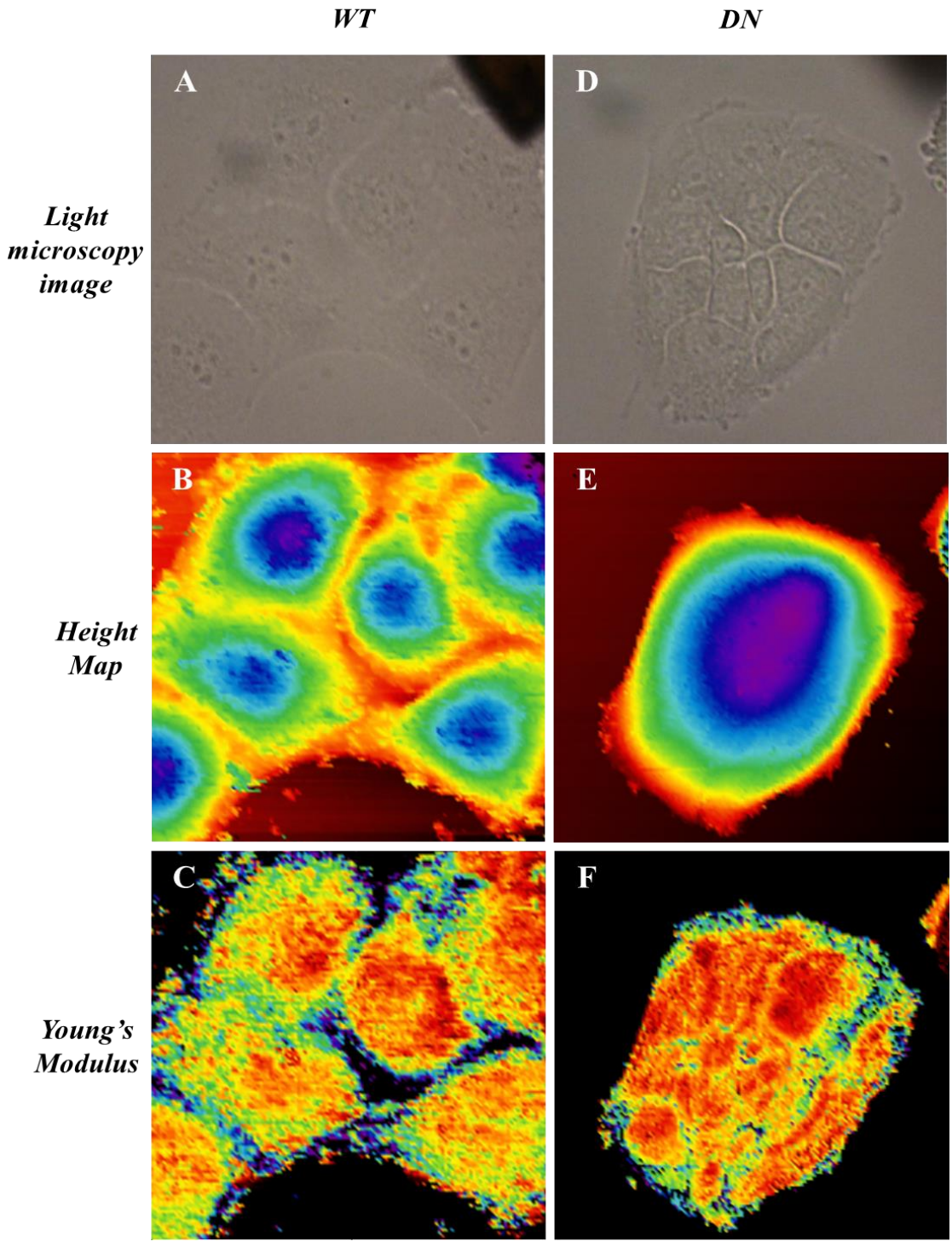

Figure 3.51: *Phase contrast (A, D), height map (B, E) and Young's Modulus (C, F) analysis for both WT and DN HaCaT's under biological conditions. Cold shading (Blue) in B and E represent the highest cellular regions points, whereas the hot shading (Red) in C and F represents areas with the lowest Young's Modulus values. Images represent 15 x 15 μm^2 analysis areas.*

The data presented in *Figure 3.51* shows that differences can be observed between nuclear stiffness in both the WT and DN HaCaT cells. Initially, light microscopy images (*A* and *D*) support the previous findings that DN HaCaT cells cluster in tighter associations,

rather than form spaced colonies like their WT counterparts. Information provided in the height map (*B* and *E*) suggests that the DN HaCaTs display a more uniform colony morphology, appearing as a single dome with the highest point at the centre of the colony. In contrast, the WT HaCaT cells display a more dispersed colony morphology, with multiple peaks corresponding to nuclear localisation within each cell. The Young's modulus measurements displayed in images *C* and *F* further show the variability of stiffness across the different cell regions, with the DN HaCaT cells displaying a decreased stiffness across cell regions correlating to nuclear localisation. Collated graphical data for these measurements can be seen in *Figure 3.52*.

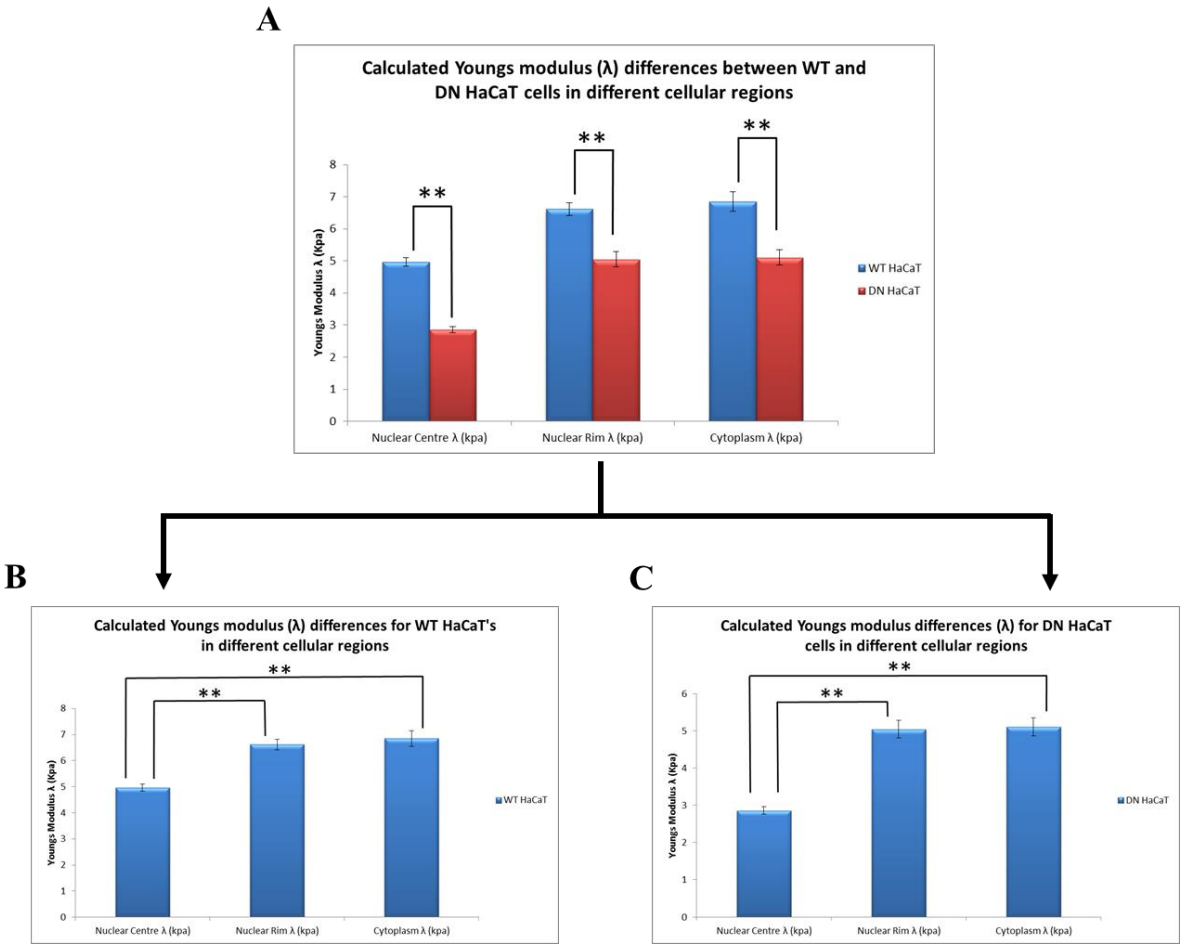

Figure 3.52: *Calculated young's moduli across three selected cellular regions of WT and DN HaCaT cells. (A) Displays comparisons between both WT and DN HaCaT cells across each cellular region. (B) and (C) represent comparisons between cellular regions in the same cell line.*

The collated data displayed in *Figure 3.52* initially suggests that the DN HaCaT cells are softer in each of the three cellular areas assessed. The data shows a central nuclear Young's modulus of 4.97 kPa in the WT HaCaT cells compared to the 2.86 kPa value for

DN HaCaT cells. This suggests that the central regions of WT HaCaT cells are much stiffer than that of the DN HaCaTs.

Interestingly, it was observed that the calculated Young's modulus values in both WT and DN HaCaTs were much higher at the nuclear periphery and cytoplasmic regions than that of the nuclear centre. This appears to contradict current knowledge and publications, which state that the nucleus is the stiffest organelle of the cell. At the peripheral nuclear regions, the WT HaCaT cells displayed an average Young's modulus value of 6.61 kPa in comparison to the value of 5.05 kPa found for the DN HaCaTs. Similar readings were observed in cytoplasmic cell regions, with WT HaCaT cells displaying a modulus value of 6.85 kPa compared to the DN HaCaTs 5.11 kPa. However, it is possible that due to the cellular region assessed being thinner further away from the nucleus that the stiffness of the coverslip may have an increased influence on the readings obtained. From this data it is possible to suggest that the loss of *SUN-KASH* interactions in the DN HaCaT cells stimulates nuclear architectural changes, leading to a decrease in nuclear stiffness.

One remaining flaw within this investigation is however, that to investigate the Young's modulus of the nucleus within each cell line, we probed the cellular surface. Due to this, the AFM's cantilever will have had to indent the plasma membranes surface far enough to indent the NE. In addition, there is currently little available data regarding the known distance between the plasma membrane and nuclear envelope within WT HaCaT cells. To validate the obtained results, further analysis is required.

Initially, the compression forces used by the cantilever and the maximum penetration observed during cellular analysis were assessed. An example of cantilever compression distances (cantilever indentation across the surface of the cell) observed for DN HaCaT cells can be seen in *Figure 3.53*, alongside collated data from across 30 WT and DN HaCaT cells respectively.

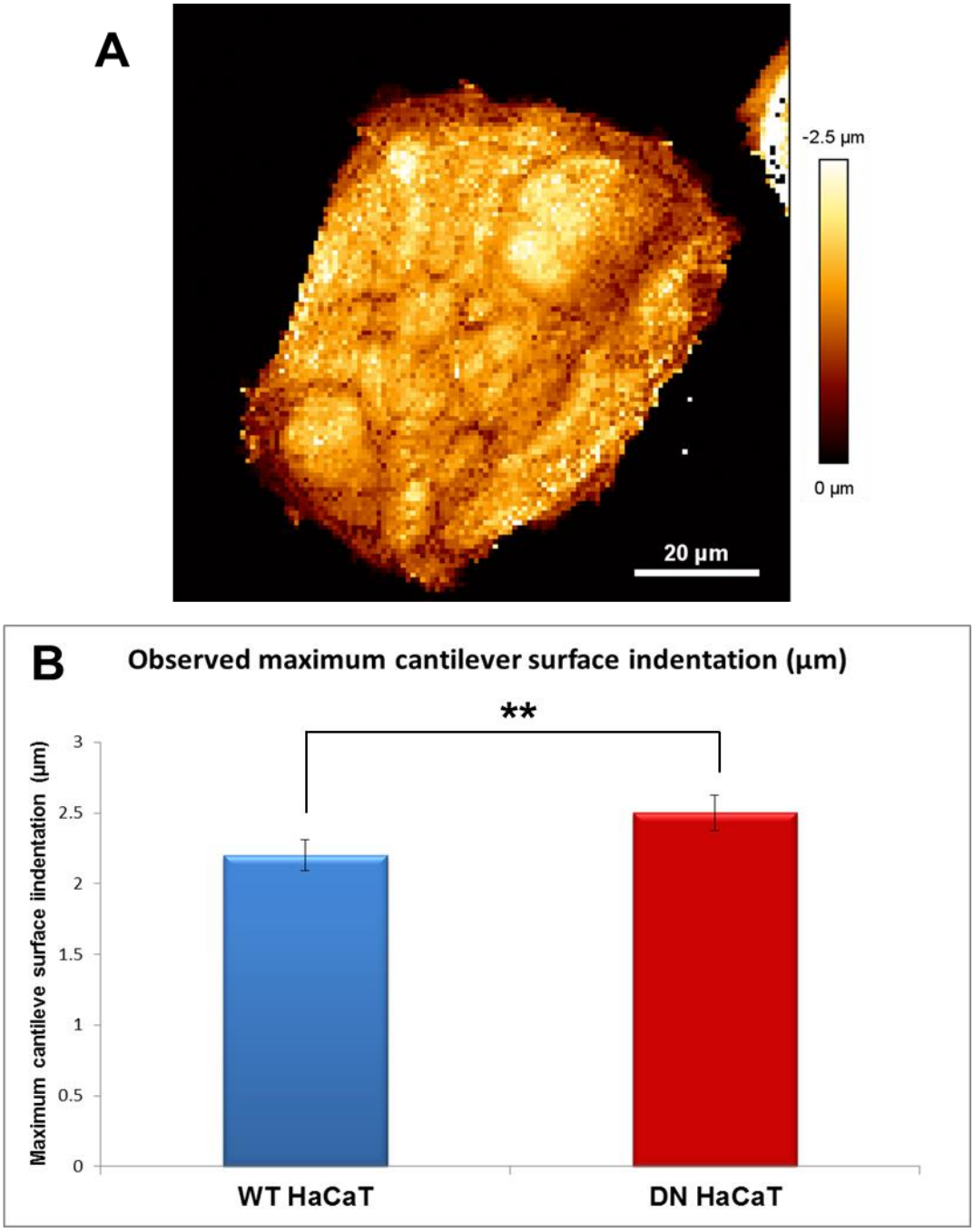

Figure 3.53: *Observed compression output data. (A) DN HaCaT cells displayed the highest indentation across both cell lines under a cantilever force of 150 pN. Scale bar displays areas of highest compression in white, and areas of low compression in dark. (B) Collated indentation data from across 30 WT and DN HaCaT cells respectively.*

The data presented within *Figure 3.53* displays an example indentation map using a cantilever force of 150 pN. The image highlights that in the DN HaCaT cells the average maximum indentation observed was 2.5 µm at the central nuclear region. This region was previously seen to exhibit the lowest Young's modulus for both cell lines assessed,

suggesting that the DN HaCaT cells display the largest indentation across nuclear regions using this applied force. The average maximum observed indentation for WT HaCaTs was calculated to be 2.2 µm supporting the previous observations that WT HaCaTs display a much less malleable central cellular area, corresponding to nuclear localisation.

It is now known that the cantilever was able to assess modulus values between 2 and 2.5 µm below the plasma membranes surface; however it is still unclear whether the nuclear envelope resides at this depth below the plasma membrane. To assess whether the nuclear envelope was within this cantilever indentation zone, TEM on both WT and DN HaCaT cells was performed, with the aim to assess the distance between plasma and nuclear envelope membranes. The 2D TEM culture processing method described in the methods allows cells to retain their 2D phenotypic shapes, therefore, allowing cross sections to be taken through central cellular regions, allowing nuclear-plasma membrane distances to be assessed. A representation of how measurements were performed can be seen in *Figure 3.54*.

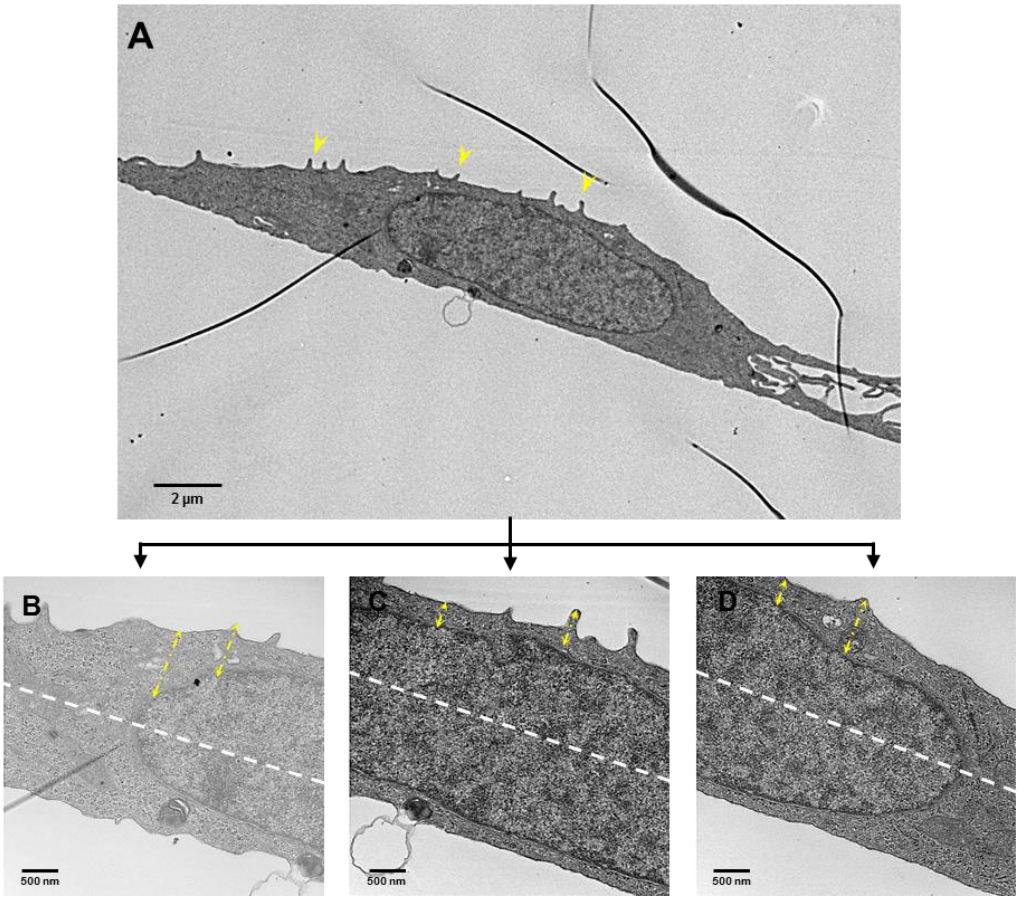

Figure 3.54: *TEM images displaying measurement techniques used to assess nuclear envelope to plasma membrane distances. A) displays the cell overview with surface protrusions (highlighted with arrows) defining the cell surface. B), C) and D) further display how measurements were taken at 90° angles from the central dashed line. Scale bars = 500 nm.*

Using the measurement technique described in *Figure 3.54*, a total of 40 individual cells for both the WT and DN HaCaTs were assessed. For each cell, high magnification images were taken across the length of nuclear envelope and plasma membrane regions along the cells surface, with 5 measurements being taken at 90° angles to the central plane of the cell, the results of which can be seen in *Figure 3.55*.

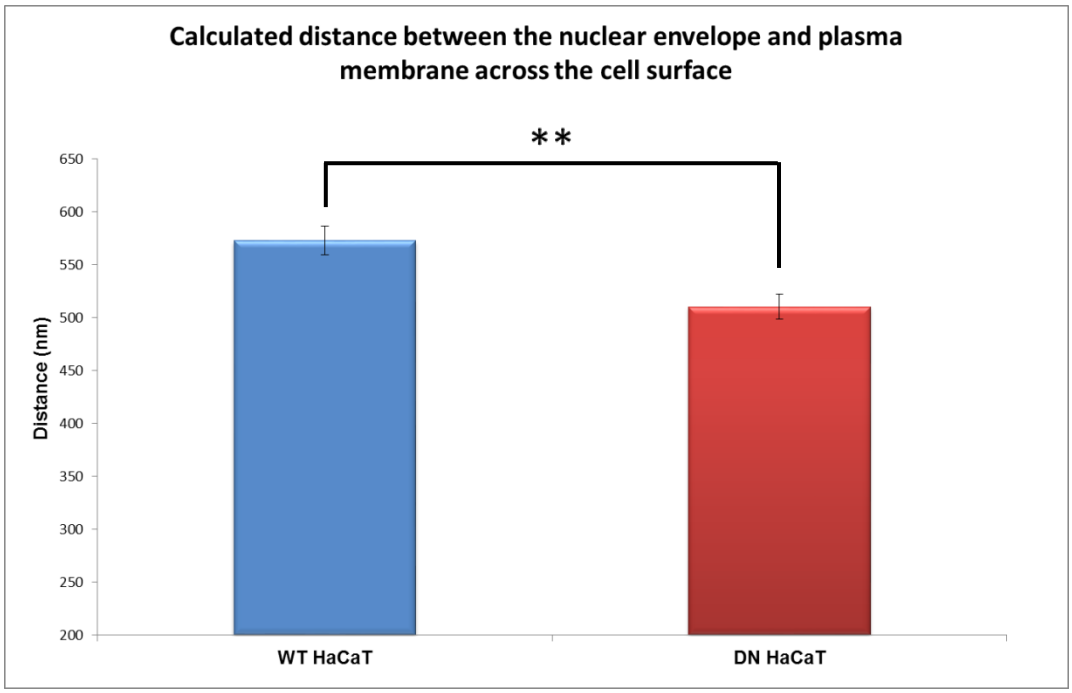

Figure 3.55: *Calculated distance between nuclear envelope and plasma membrane in WT and DN HaCaT cells. The data represent averages of 600 measurements taken across 40 cells for each cell line.*

The data displayed within *Figure 3.55* suggests that the average distance between nuclear envelope and plasma membrane in both cell lines is less than the measured cantilever indentation during AFM analysis. Interestingly, the data suggest the WT HaCaT cells display a significantly larger distance between nuclear and plasma membranes of 572 nm in comparison to a distance of 510 nm calculated for the DN HaCaT cells using a student's t-test where $p \leq 0.005$. This observation could suggest that the associations between KASH proteins and cytoskeletal components may be perturbed in the DN HaCaT cells, resulting in a displacement of cytoskeletal components across the NE surface. It can be further suggested that *LINC* disruptions present in DN HaCaT cells may stimulate abnormal nuclear positioning. This again could arise through disruptions in NE-cytoskeletal linkages mediated by the *LINC* complex, resulting in less 'scaffolding' by the cytoskeleton to hold the nucleus in place, therefore due to gravity or other cellular forces,

the nucleus may be forced closer the cells basal region. From this analysis, it can be concluded that in the AFM investigation, the cantilever indentation did indeed penetrate far enough into the cell to assess differences between nuclear malleability's of both WT and DN HaCaT cells.

The data gathered in this investigation suggests that under both biological and non-biological conditions, the WT and DN HaCaT cells display significant differences in their biomechanical properties. In addition, the data suggests that *LINC* complex disruptions reduce the observed nuclear stiffness alongside cytoplasmic stiffness, suggesting further roles for *SUN-KASH* connections in maintaining nuclear architecture and cellular stiffness.

3.3.6 SUN-KASH disruptions have variable effects on LINC associated protein organisation and expression patterns.

3.3.6.2 Loss of SUN-KASH interactions does not appear to alter F-actin organisation.

As previous data suggests loss of the *SUN-KASH* connection across the perinuclear space stimulates a decrease in nuclear stiffness, we further aimed to assess whether further disruptions could be identified in actin or lamin protein networks, which have both been implicated in the maintenance of nuclear stiffness. Actin networks have been suggested to play roles in maintaining nuclear structure, aiding nuclear migration and cellular migration, all of which are functions in which DN HaCaT cells have displayed abnormalities. To assess the phenotypic differences in actin organisation in the WT and DN HaCaT cell lines, super resolution microscopy was used. This high-powered imaging technique allows fine structural details to be assessed for each cell line. Cells stained with *TRITC-conjugated* phalloidin as described, and then imaged using the OMX super resolution microscope. Images for both WT and DN HaCaT cells lines can be seen in *Figure 3.56*.

The images presented in *Figure 3.56* depict both WT and DN HaCaT cells at a confluence of 70%. The data suggests that the actin organisation displays minimal variation between the WT and DN HaCaT cells which varies to that presented in *Figure 3.14*, suggesting that the formation of a clear actin cap is more prevalent in WT HaCaT cells. However, due to the experiment described in *Figure 3.14* presenting actin formation

upon early stage cell-substratum attachment, it is possible that following 24 h substratum attachment, the DN HaCaTs are able to form similar actin arrangements spanning the nucleus. It can be seen through this super resolution analysis of 20 cells for both WT and DN HaCaT cells that stress fibre formation across the nuclear surface and actin organisation across the cellular periphery appear to be similar, suggesting that the loss of *LINC* connections spanning the NE does not affect cortical and cytoplasmic F-actin organisation.

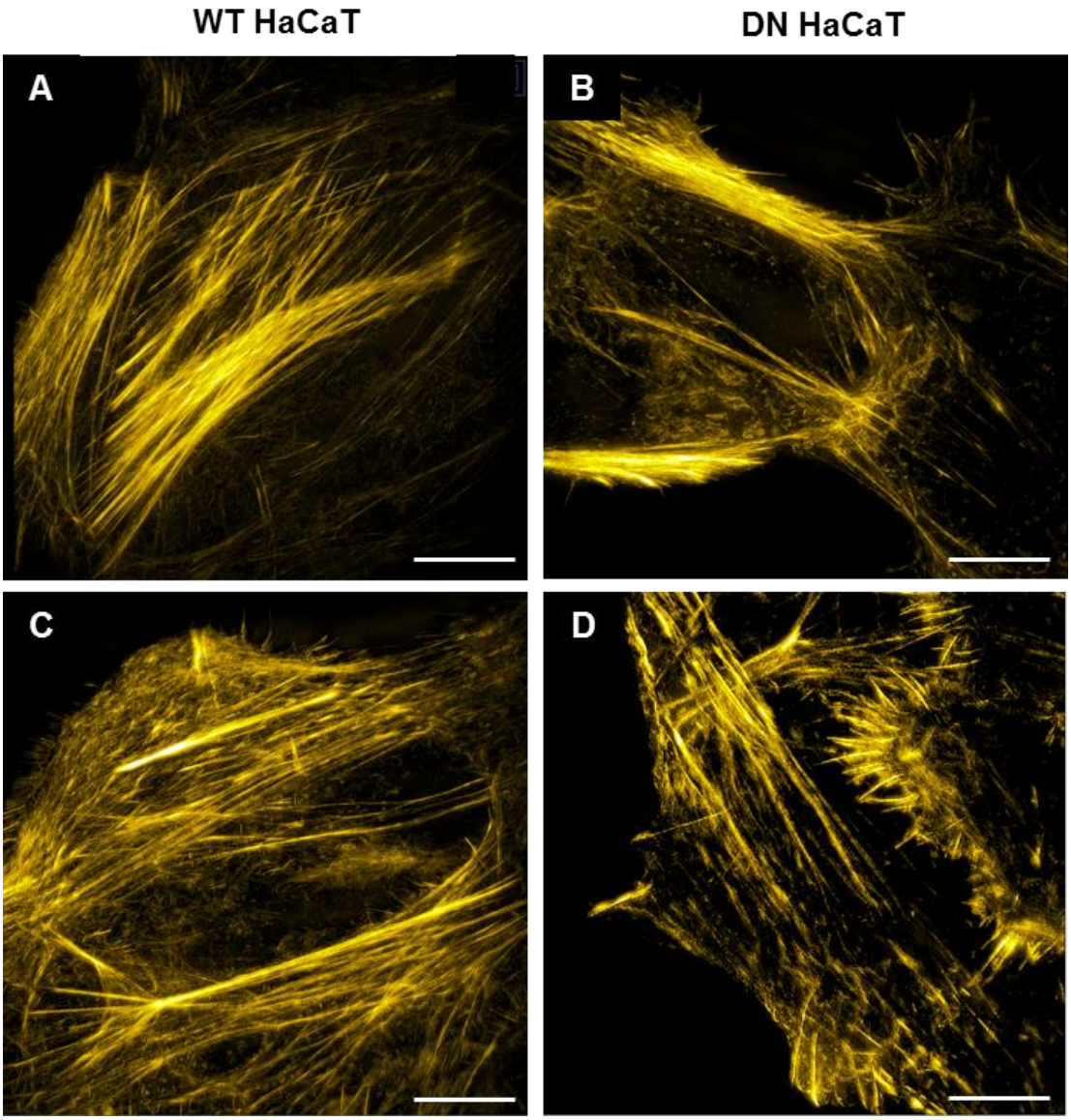

Figure 3.56: *Images of TRITC-conjugated Phalloidin staining in WT (A and C) and DN (B and D) HaCaT cells. Scale bars = 10 µm.*

3.3.6.3 Disruptions in SUN-KASH perinuclear interactions stimulate variable lamin B, but not lamin A/C organisational changes.

As suggested in *Figure 3.56*, F-actin cytoskeletal organisation does not appear to be altered between DN and WT HaCaT cell lines. To further investigate why the DN HaCaT cells display phenotypic differences in nuclear malleability, the lamin protein network was assessed using super resolution microscopy. Alongside actin, it is suggested that the lamin network is a further key component of nuclear stiffness; therefore we aimed to assess whether any structural or organisational changes to lamin A/C or lamin B networks could be observed between WT and DN HaCaT cells. Cells were processed and stained for lamin A/C and lamin B as described in the methods section. The obtained super resolution images of lamin A/C stained cells can be seen in *Figure 3.57*, with lamin B staining displayed in *Figure 3.58*.

The data displayed in *Figure 3.57* suggests that in both the WT and DN HaCaT cells, lamin A/C distribution remains constant across the surface and central regions of the nuclei. It can be seen that the surface distribution of lamin A/C appears to form filament like structures in both cell lines. Central nuclear analysis further shows clear nuclear rim staining in both cell lines, suggesting that lamin A/C distribution and positioning in the nucleus has not been altered through the disruption of SUN-KASH interactions across the nuclear envelope.

Alongside lamin A/C, the distribution of lamin B within both cell lines was assessed. As lamin B is seen to remain constant through numerous disease phenotypes deriving from lamin alterations, it was hypothesised that no differences would be seen in lamin B organisation and distribution between the WT and DN HaCaT cells. However, the data presented in *Figure 3.58* suggests that differences between lamin B distributions in the DN HaCaT cells exist. At the nuclear surface, spherical staining can be seen within the WT HaCaT cells, but not the DN HaCaT cells. Further to this, these circular structures appear to form channels protruding into the central regions of the nucleus, only visualised through lamin B staining for the WT HaCaT cells, but not the DN HaCaTs. This suggests that these structures observed express no lamin A/C, however further more in-depth investigation would be needed using TEM analysis to conclude this.

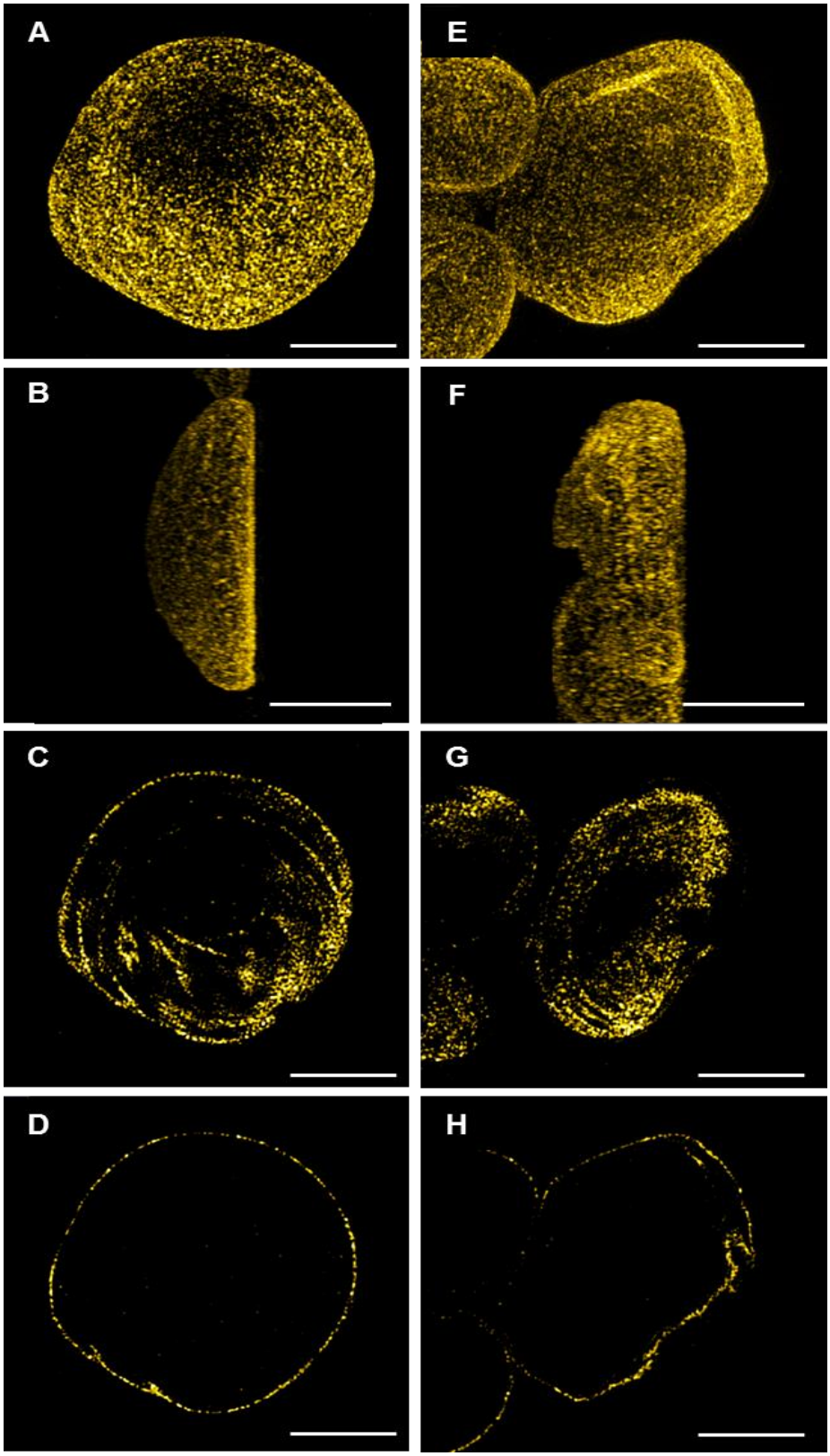

Figure 3.57: *Lamin A/C staining within WT (A, B, C and D) and DN (E, F, G and H) HaCaT cells. Images C and G display nuclear surface staining, whereas D and H display central nuclear staining. Scale bars = 5 µm.*

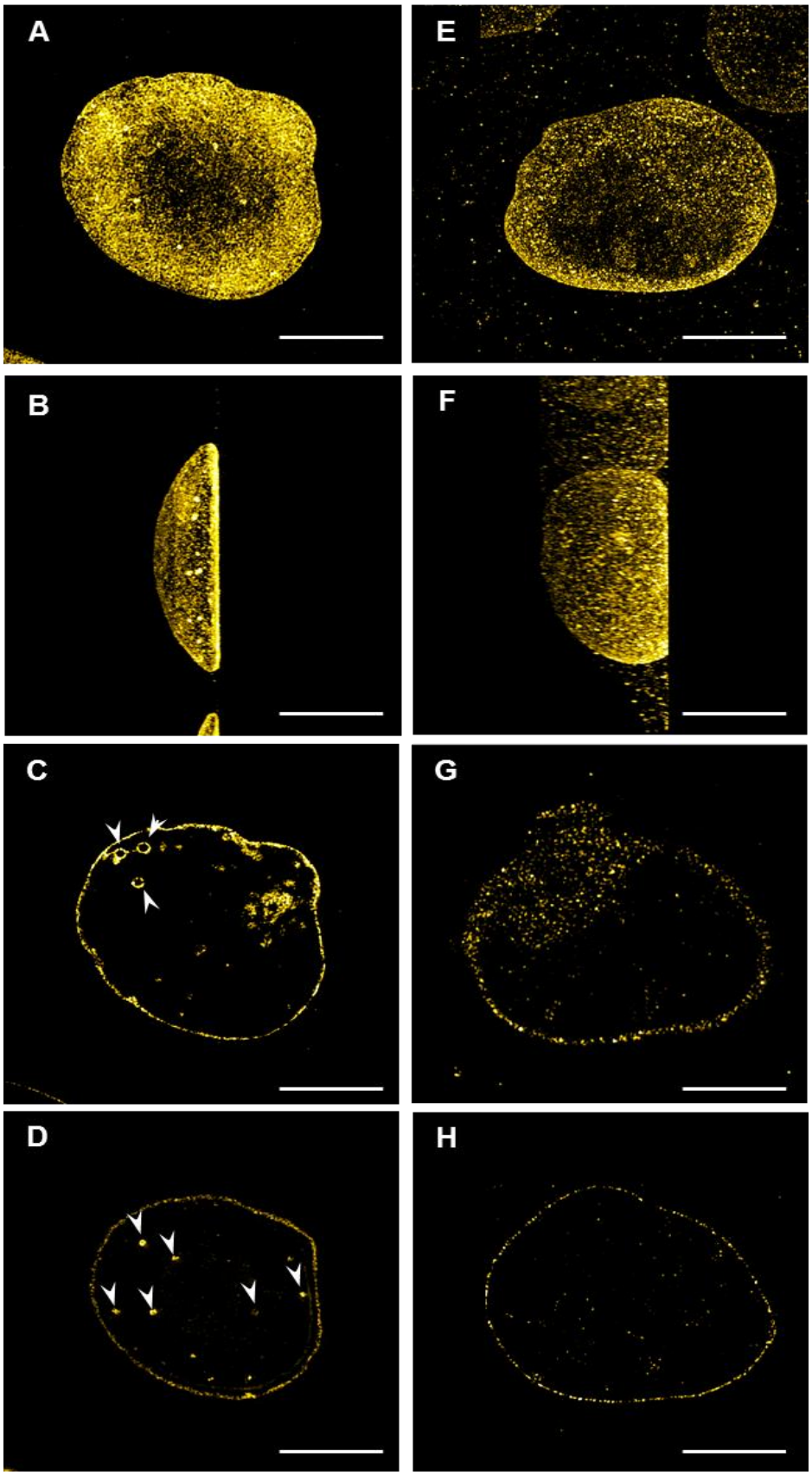

Figure 3.58: *Lamin B staining within WT (A, B, C and D) and DN (E, F, G and H) HaCaT cells. Images C and G display nuclear surface staining, whereas D and H display central nuclear staining. Scale bars = 5 µm.*

3.3.6.4 Analysis of LINC complex proteome expression in WT and DN HaCaT cells grown in 2D and 3D environments.

Disrupting the link between inner and outer nuclear envelope through severing the *SUN-KASH* perinuclear interaction stimulates numerous phenotypic abnormalities. Significantly, this disruption appears to induce a migration advantage in space-restrictive 3D environments and decreased nuclear stiffness in DN HaCaT cells, whilst displaying little to no abnormalities in lamin and actin organisation within the cell. To further investigate why these phenotypes are observed upon *LINC* complex disruptions, western blotting was employed to assess protein expression levels of various *LINC* complex proteins and binding partners. This investigation, therefore, aims to assess whether any expression variations in *LINC* complex proteins exist in these DN HaCaT cells that could be inductive factors to the phenotypes observed.

The presence of *LINC* complex variations was assessed in 6 samples; 2D cultured WT HaCaTs, 2D cultured DN HaCaTs, 3D cultured WT HaCaTs, 3D cultured DN HaCaTs and 2x 2D DN revertant mutants (DN HaCaT cells maintained without G418 selection drug). The 3D cultured samples were grown in Alvetex® Strata scaffolds for 9 days due to both cell lines displaying similar migration distances into the scaffold at this stage. The DN revertant mutants represent the DN HaCaT cells with the selection drug (G418) removed from the growth media for 2 months to assess that the phenotypes observed in DN HaCaT cells are indeed the direct consequence of DN SUN1 expression.

Initial western blotting for three standard equal loading markers; β-actin, β-tubulin and GAPDH was performed. For each protein assessed, results represent data from 3x repeats with new lysates during each repeat. Western blot results, alongside densitometry analysis, can be seen in *Figure 3.59*.

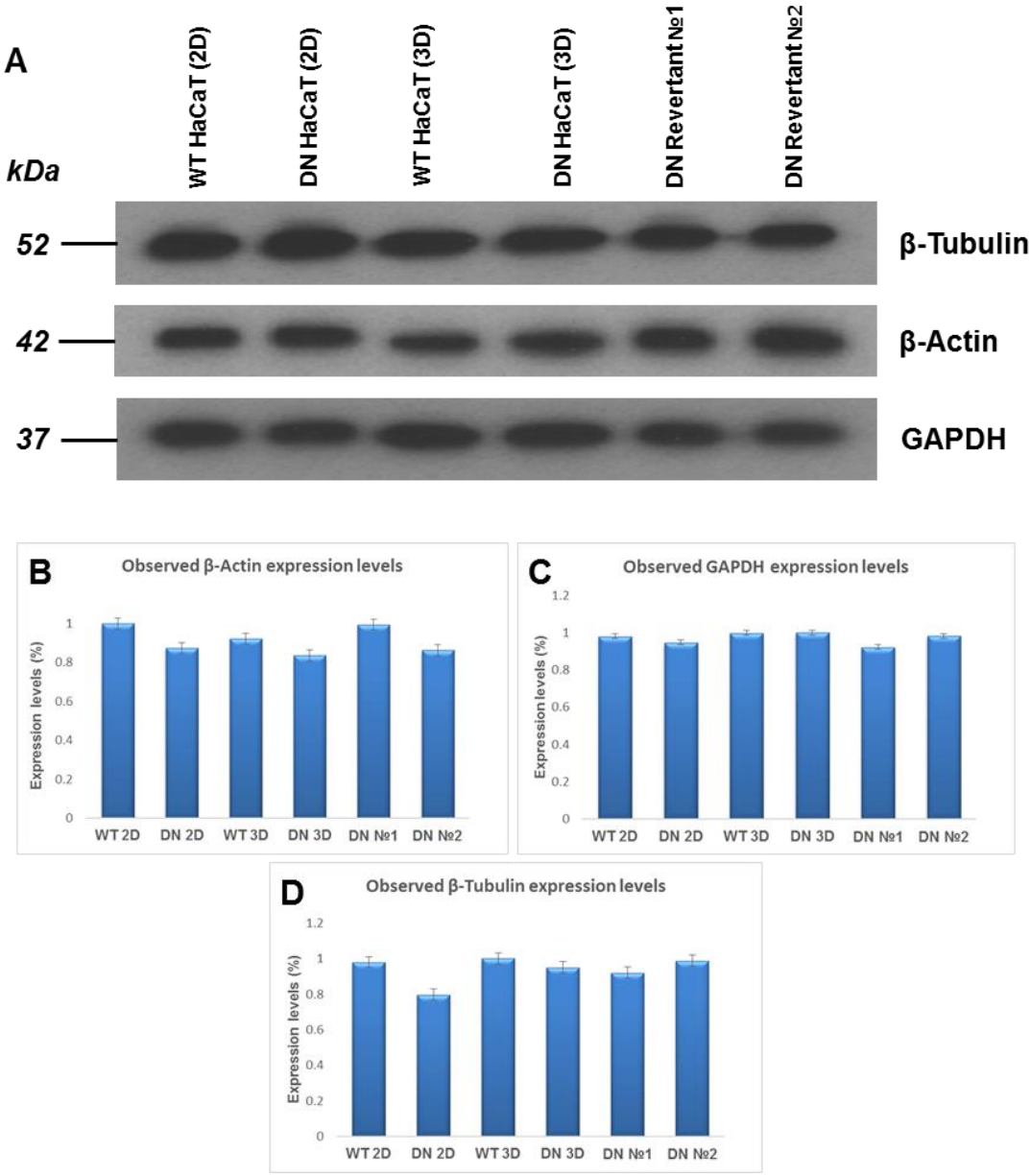

Figure 3.59: *Equal loading marker expression across our samples. (A) Displays western blot data observed upon loading of equal protein concentrations (B), (C) and (D) represent densitometry analysis across three repeats for each protein. 3D lysates represent Strata® scaffolds.*

As can be seen from data displayed in *Figure 3.59,* equal loading has been achieved across all three markers, indicating that each lane contains equal concentrations of each protein. The data suggest no statistical difference between each of the equal loading markers using a two way *ANOVA* where $p \leq 0.05$. This suggest that levels of β-tubulin, β-actin and GAPDH remain constant between the WT and DN HaCaT cell lysates, in both 2D and 3D culture environments.

Following this initial analysis, the variation in expression levels of inner nuclear envelope proteins of the *LINC* complex upon *LINC* complex disruptions was assessed. The proteins analysed included SUN1, SUN2, emerin, lamin A/C and lamin B, and the results can be seen in *Figure 3.60*.

The data presented in *Figure 3.60* suggests that there are statistical differences using a two way *ANOVA* where $p \leq 0.05$, between expression levels of some *LINC* complex proteins situated across the INM. To validate these observed differences, post hoc F-tests were applied between lanes in the data to investigate where these differences lie. It can be seen in (*B*) that SUN1 expression levels appear to remain consistent across each sample, with a significant increase in expression levels observed in 3D WT HaCaT cells ($p \leq 0.001$). In comparison, (*C*) suggests that levels of SUN2 within 3D restrictive cultures appears to significantly reduce in comparison to that of 2D culture conditions ($p \leq 0.001$), whereas little to no variation can be seen between the WT and DN HaCaT cells in both environments. Alongside this, cellular levels of emerin and lamin A/C appear to be different. For emerin, the data presented in (*F*) suggests that there is a significant increase in expression levels across 3D restrictive culture environments compared to that of the 2D ($p \leq 0.001$), again with little variation observed between the WT and DN HaCaTs in both environments. Lamin A/C however displays large differences in expression levels. It can be seen from (*D*) that in 2D culture environments, lamin A/C expression appears to remain constant between the two cell lines, however, within 3D culture systems, it can be seen that the WT HaCaTs express a significant increase in lamin A/C protein levels ($p \leq 0.001$). Data for lamin B levels can be seen displayed within (*E*), suggesting that no significant difference is observed between the WT and DN HaCaT cells in both 2D and 3D environments.

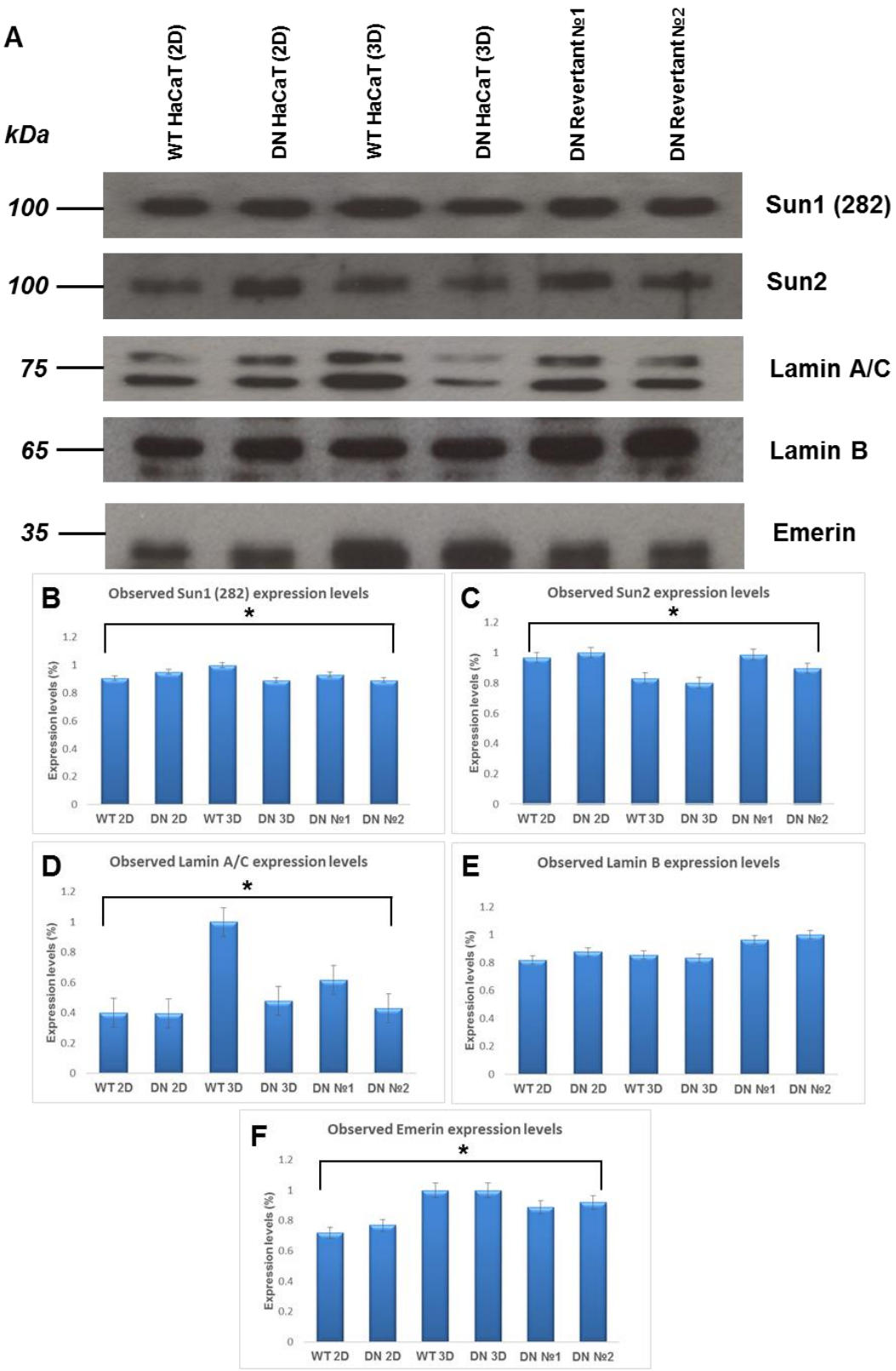

Figure 3.60: *Western blot data for each analysed protein across our samples. (A) Displays western blot data observed upon loading of equal protein concentrations. (B), (C), (D), (E), and (F) represent densitometry analysis across three repeats for each protein. 3D lysates represent Strata® scaffolds.*

Following assessment of key *LINC* complex proteins across the INM, two *KASH* containing outer nuclear envelope proteins, both crucial for the maintenance of *LINC* connections across the perinuclear space, were investigated. These proteins were nesprin-1 and nesprin-2. Antibodies targeted to the N-terminal actin binding domain (*ABD*) of each protein were used in order to assess the range of nesprin isoforms containing this region. Representative data displaying nesprin-1 and nesprin-2 isoform levels across both WT and DN HaCaT cells in 2D and 3D environments can be seen in *Figure 3.61*.

The data presented in *Figure 3.61* suggests that significant differences are present across the full range of nesprin-1 and nesprin-2 isoforms which retain the N-terminal *ABD*. As shown in (*B*) and (*C*), significant differences using a two way *ANOVA* at a p-value of 0.05, are seen between nesprin-2 isoforms across the entire range of molecular weights assessed. Using post hoc F-tests, the protein expression levels of nesprin-2 isoforms above 250 kDa can be seen to significantly decrease in DN HaCaT cells ($p \leq 0.001$) when placed into restrictive 3D environments, where as in 2D culture systems, WT and DN HaCaT cells appear to express similar levels. Further significant differences are observed in nesprin-2 isoforms below 250 kDa ($p \leq 0.001$), in which isoform levels appear to increase in 2D DN HaCaT cells compared to other conditions.

Alongside this observed data for nesprin-2 isoforms, nesprin-1 proteins also present significant isoform variability between different conditions. It can be seen that for isoforms above 250 kDa (*F*), nesprin-1 expression levels remain constant across all samples other than the DN HaCaT cells grown in restrictive 3D culture environments, in which significantly reduced expression levels are observed ($p \leq 0.001$) using post hoc f-tests. For isoforms between 75 – 250 kDa, wider variability can be seen, in which WT HaCaT cells express significantly increased levels of nesprin-1 isoforms in both 2D and 3D culture systems in comparison to that of DN HaCaT cells ($p \leq 0.001$). For isoforms less than 75 kDa (D), it can be seen that WT HaCaTs significantly express increased nesprin-1 levels under conventional 2D growth conditions compared to that of DN HaCaT cells ($p \leq 0.001$). The DN and WT HaCaT cells also appear to express significantly reduced levels of these nesprin-1 isoforms in restrictive 3D culture systems compared to that of 2D systems ($p \leq 0.001$).

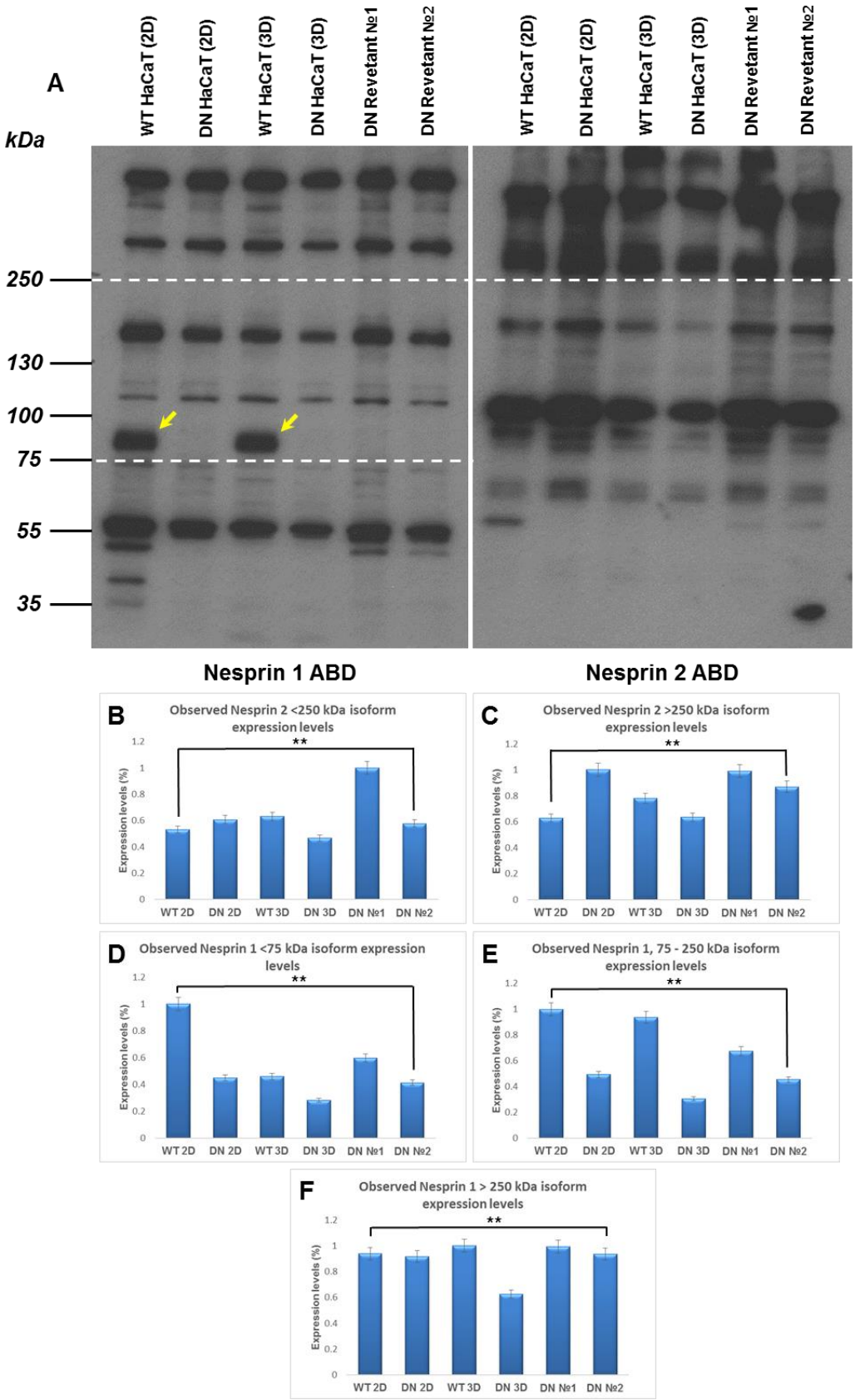

Figure 3.61: *Western blot data for each analysed protein across our samples. (A) Displays western blot data observed upon loading of equal protein concentrations. (B), (C), (D), (E), and (F) represent densitometry analysis across three repeats for each protein. 3D lysates represent Strata® scaffolds. Arrows highlight variability between WT and DN HaCaT expression patterns.*

To further assess roles of *LINC* complex disruptions on normal cellular function, we next examined expression profiles of cytokeratin's, lap2α and E-cadherin. These proteins were selected due to their noted roles in cell architecture, cell cycle regulation and cell-cell adhesion, respectively, aside further roles in maintaining cell/nuclear structure, all of which have been shown thus far to be altered in the DN HaCaT cell line. Representative western blotting data is presented in *Figure 3.62*.

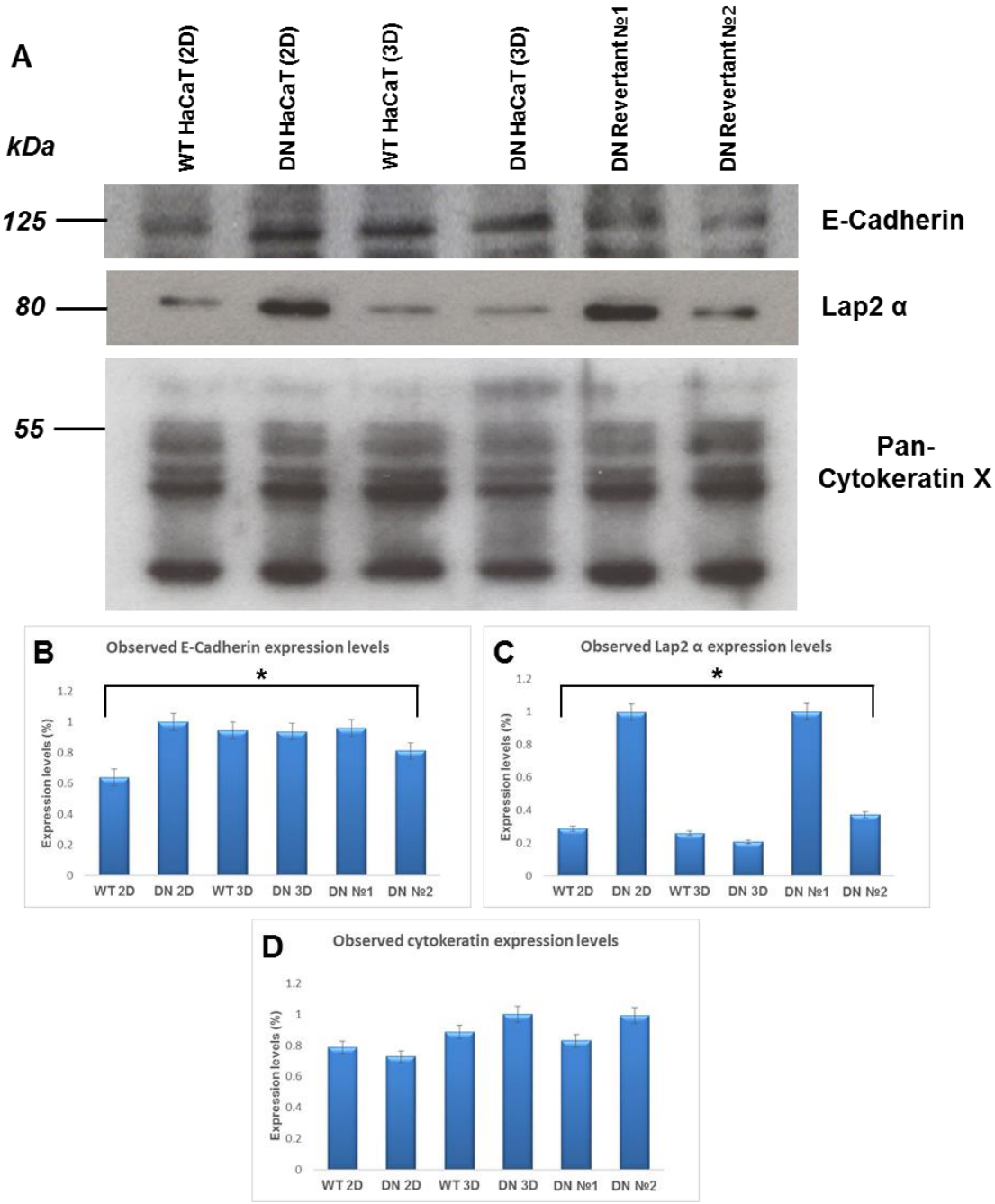

Figure 3.62: *Western blot data for each analysed protein across our samples. (A) Displays western blot data observed upon loading of equal protein concentrations. (B), (C) and (D) represent densitometry analysis across three repeats for each protein. 3D lysates represent Strata® scaffolds.*

The data presented in *Figure 3.62* suggests that there are significant differences between *LINC* associated proteins in the WT and DN HaCaT cell lines. Using further post hoc F-tests, it can be seen that in (*B*) the DN HaCaT cells appear to express significantly higher E-cadherin levels in 2D culture systems compared to that of the WT HaCaT cells ($p \leq 0.001$). Interestingly though, it appears that both cell lines express similar levels in restrictive 3D culture systems, with no significant difference observed between them. The data presented in (*C*) displays significant changes in expression levels of lap2α ($p \leq 0.001$) in which DN HaCaTs display a significant increase in expression levels across 2D culture systems compared to that of WT cells. Finally, the data presented in (*D*) represents the sum total of all bands detected suggesting that no significant difference can be observed between the levels of cytokeratin in the 2D and 3D culture systems between the WT and DN HaCaT cell lines.

As previous data has suggested that *LINC* complex disruptions stimulate a loss of cell polarity and directed nuclear migration, we aimed to assess whether the levels of tubulin were changed between the WT and DN HaCaT cell lines when grown in 2D and 3D culture systems. As microtubule networks are one controlling factor of cell polarity, acetylated tubulin levels in comparison to dynamic tubulin present in each sample were assessed, as can be seen in *Figure 3.63*. Tubulin acetylation is a modification acting to regulate both MT structural and functional properties in the cell.

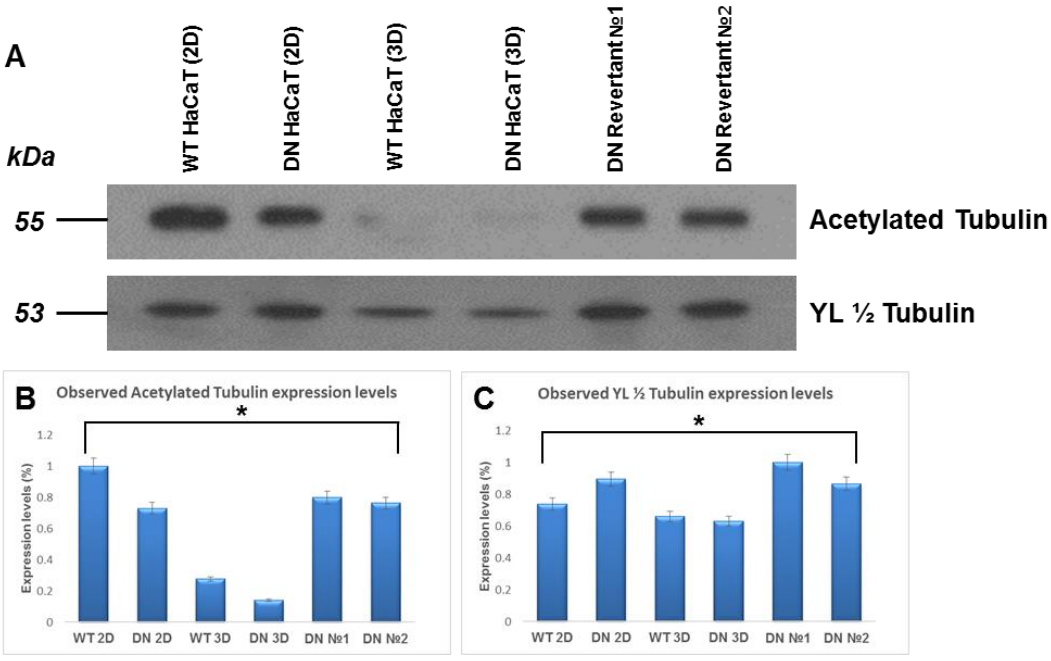

Figure 3.63: *Western blot data for each analysed protein across our samples. (A) Displays western blot data observed upon loading of equal protein concentrations. (B) and (C) represent densitometry analysis across three repeats for each protein. 3D lysates represent Strata® scaffolds.*

The data displayed in *Figure 3.63* suggests that through the use of a two way *ANOVA* where $p \leq 0.05$, significant differences can be seen between levels of acetylated tubulin in 2D and 3D culture environments (B). Through the application of post hoc f-tests, it was shown that DN HaCaT cells express significantly lower levels of acetylated tubulin than WT HaCaTs in conventional 2D culture ($p \leq 0.001$). However, the levels of acetylated tubulin are seen to reduce significantly when placed into 3D growth systems for both cell lines ($p \leq 0.001$). Alongside this, dynamic tubulin detected with antibodies against YL ½ (tyrosinated) tubulin (*C*) levels appear to be significantly lower in the restrictive 3D environments for both cell lines compared to conventional 2D growth environments ($p \leq 0.001$).

Throughout this chapter, presented information suggests that the 3D scaffold environments used could be inducing cell stress. Indications for this can be seen within section 3.3.3 in which cells colonise surface regions of the scaffolds, and section 3.3.4.1 in which sharp scaffold sections from the central region can be seen indenting the plasma membrane, inducing keratin accumulation when in close proximity to NE. To test whether cells are indeed stressed within this environment, two known stress markers [276], JNK and p38, were assessed. Phosphorylation of these two proteins indicates cellular stress, suggesting the cell is acting to reduce the damaging effects of surrounding stressful factors. These western blots can be seen in *Figure 3.64*.

The data presented in *Figure 3.64* suggests that the levels of total p38 (*D*) and JNK (*B*) remain consistent in each cell line in both 2D and 3D growth systems. However, significant differences between each sample can be seen for the phosphorylated form of both proteins using a two way *ANOVA* with a p-value of 0.05. It can be seen that both phosphorylated JNK and phosphorylated p38 levels significantly increase in WT HaCaT cells grown in restrictive 3D growth environments upon the application of post hoc f-tests ($p \leq 0.001$). This may therefore suggest that these cells are under increased stress in comparison to other samples assessed.

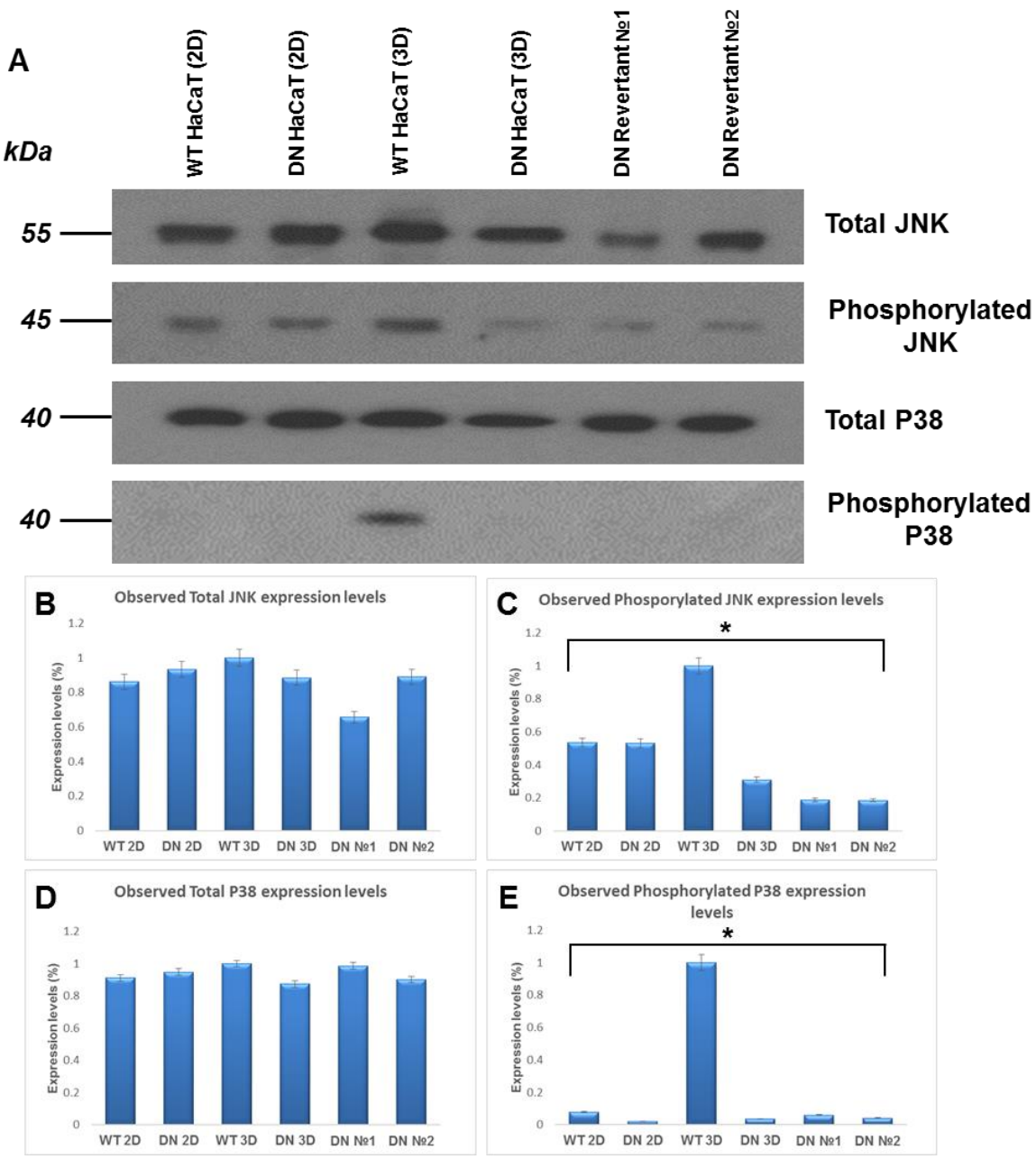

Figure 3.64: *Western blot data for each analysed protein across our samples. (A) Displays western blot data observed. (B), (C), (D) and (E) represent densitometry analysis across three repeats for each protein. 3D lysates represent Strata® scaffolds.*

The data gathered through western blot analysis of both WT and DN HaCaT cells grown in conventional 2D and restrictive 3D culture environments suggests that a wide variety of *LINC* components are altered between each cell line and each growth condition. It appears that even though statistically significant, some *LINC* components display minor expression level changes, such as SUN1, SUN2 and emerin. Whereas the nesprins and lamin A/C networks alongside cytoskeletal components and associated proteins display

larger variations in expression levels between WT and DN HaCaT cells. Of these alterations in expression levels, lower nesprin-1 isoforms express the most striking expression variations, in which the isoform produced at ~90 kDa appears to be completely absent in DN HaCaT cells across both 2D and 3D environments. When collated with AFM data, showing the DN HaCaT cells express a softer NE, it can be suggested that this isoform may play a role in the maintenance of nuclear integrity and stiffness. However, further assessment and identification of this isoform would be required to verify this. A collated view of all western blot analysis conducted thus far can be seen summarised in *Table 3.1*.

Table 3.1: *Summarised data of western blot analysis across WT and DN HaCaTs in both 2D and 3D culture environments. Increasing arrow numbers = increased expression.*

	WT HaCaT (2D)	DN HaCaT (2D)	WT HaCaT (3D)	DN HaCaT (3D)	Revertant No1	Revertant No2
β-actin	–	–	–	–	–	–
β-tubulin	–	–	–	–	–	–
GAPDH	–	–	–	–	–	–
SUN1 (282)	–	–	–	–	–	–
SUN2	↓	–	↓	↓	–	–
Lamin A/C	–	–	↑	↓	–	–
Lamin B	–	–	–	–	–	–
Emerin	–	–	↑	↑	–	–
N2 <250 kDa	–	–	–	↓	↑	–
N2 >250 kDa	–	↑↑↑	↑	–	↑↑↑	↑↑
N1 <75 kDa	↑↑	–	–	↓	↑	–
N1 75-250 kDa	↑↑	–	↑↑	–	↑	–
N1 >250 kDa	–	–	–	↓	–	–
E-cadherin	↓	–	–	–	–	↓
Lap2α	–	↑	–	–	↑	–
Cytokeratin	–	–	↑	↑	–	↑
Acetyl Tubulin	–	–	↓	↓	–	–
YL ½ Tubulin	–	–	↓	↓	–	–
Total JNK	–	–	–	–	↓	–
Phospho JNK	↑	↑	↑↑	–	–	–
Total p38	–	–	–	–	–	–
Phospho p38	–	–	↑	–	–	–

3.3.7 DN and WT HaCaTs display variable phenotypes when applied to alternate biomaterial models.

3.3.7.1 Both DN and WT HaCaT cells retain phenotypes expressed under 2D growth condition when applied to commercially available polycarbonate scaffolds.

Through the use of a variety of techniques, it has been established that the DN HaCaT cells display a decreased nuclear stiffness. To further assess the nuclear malleability potential between both the WT and DN HaCaT cells, cells were cultured on another commercially available scaffold in order to evaluate their migration potential through a highly restrictive pore size of 3 µm. The material chosen for this investigation is the Transwell® polycarbonate scaffold, which presents a single layered, porous material for the cells to migrate through. This material does not show the same pore diameter variability as observed in the Alvetex® Strata material, however, due to its monolayer structure; it does not represent a true 3D cell growth environment.

500,000 WT and DN HaCaT cells respectively, were seeded onto individual polycarbonate scaffolds and cultured for 3 days and then processed and H&E stained. The resulting images are displayed in *Figure 3.65*.

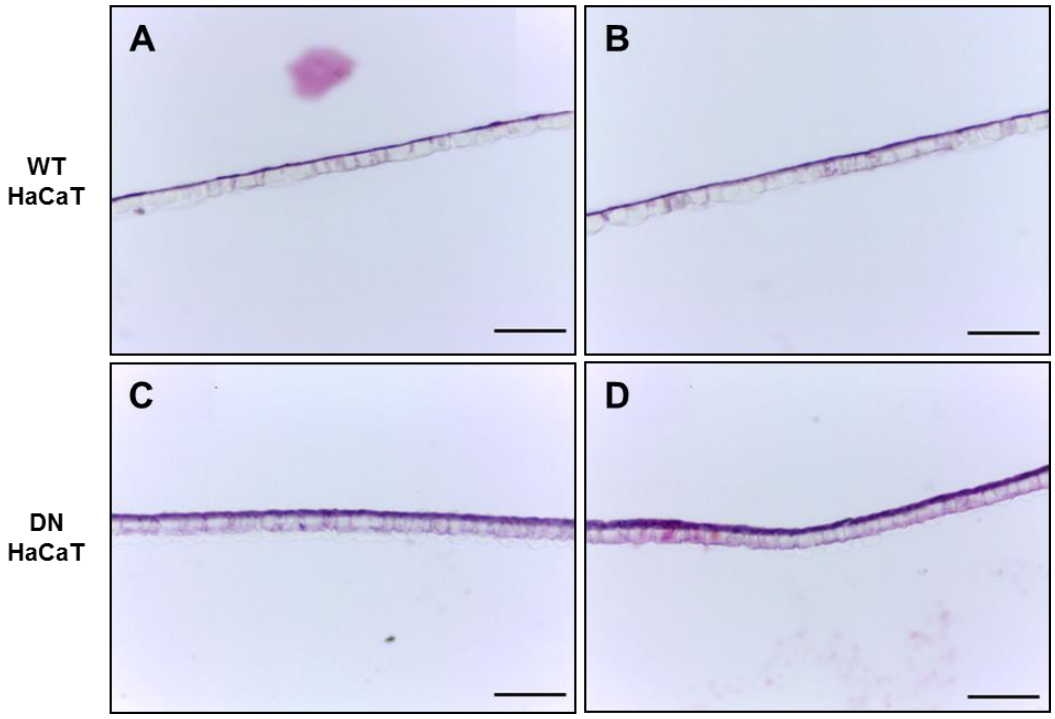

Figure 3.65: *H&E images of polycarbonate scaffolds 3 days post-seeding with WT and DN HaCaT cells. Scale bars = 50 µm.*

The low magnification images displayed in *Figure 3.65* suggest that both cell lines are unable to fully penetrate into the restrictive void diameters during the 3 day growth period. However, it can be seen that the DN HaCaT cells display a thicker layer of cells across the surface of the scaffolds. Further high-magnification images displayed in *Figure 3.66*, helps to support this.

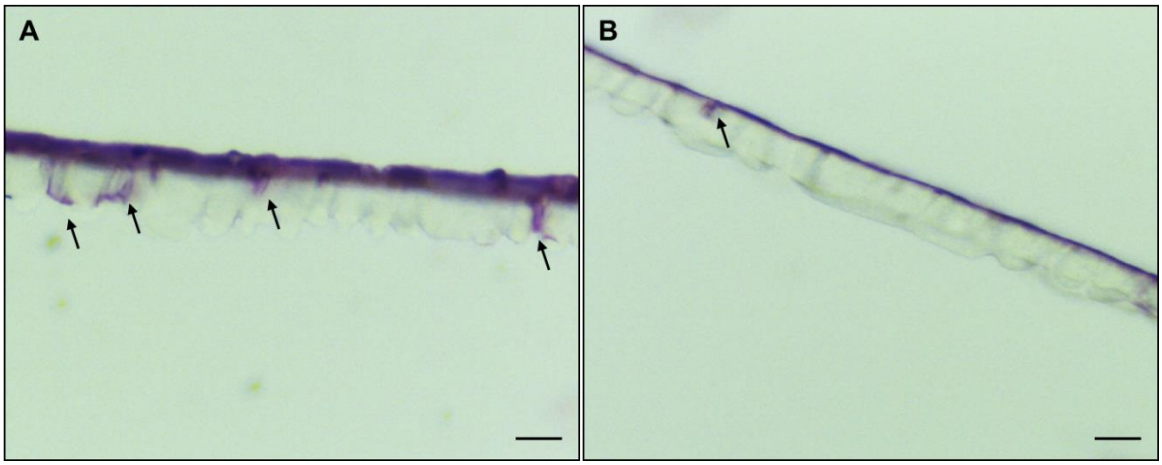

Figure 3.66: *High magnification images of 3 day H&E stained polycarbonate scaffolds seeded with WT (B) and DN (A) HaCaT cells. Arrows highlight areas of observed cell penetration. Scale bars = 10 µm.*

From the data presented in *Figure 3.66*, it can be seen that the thick cell layer produced by DN HaCaT cells appears similar to the layer observed when cultured in the Alvetex® Strata scaffolds. This cellular accumulation is not observed for the WT HaCaT cells. Under high magnification, it can also be seen that bot cell lines are in fact displaying migration potential through the scaffold. It can also be seen that a larger number of the DN HaCaT cells migrate through the restrictive pores within the scaffold compared to WT cells, as highlighted with arrows in *A* and *B*.

To further quantify these observations for cellular accumulation across the scaffold surface and number of cellular protrusions into the restrictive pores observed for each cell line, 5 sections of 5 scaffolds from 3 repeats were assessed, as seen in *Figure 3.67*.

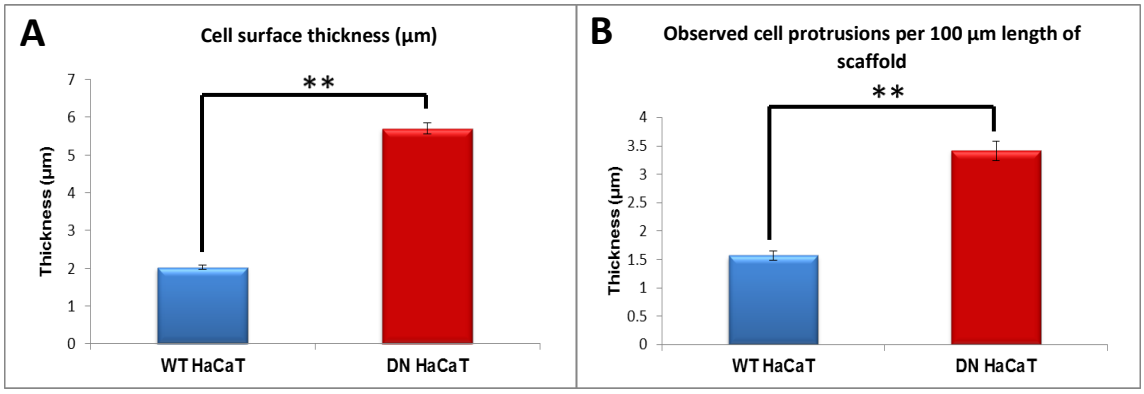

Figure 3.67: *Collated data displaying height differences between WT and DN HaCaT cells across the surface of polycarbonate scaffolds (A) alongside observed cellular protrusions per 100 µm across the length of scaffold (B).*

As can be seen from *Figure 3.67*, the data presented in (*A*) suggests there is a significant difference between the DN and WT HaCaT cell height across the surface of polycarbonate scaffolds, using a student's t-test where $p \leq 0.005$. The DN HaCaT cells express a calculated height of 5.7 µm across the scaffold, whereas the WT HaCaT cells express a much smaller height of 2.1 µm. Further statistical significance can also be seen in the number of cellular protrusions into the polycarbonate scaffolds, in which DN HaCaT cells appear to produce more than that of the WT HaCaT cells.

The data collected within this investigation therefore suggests that when placed into alternative scaffold environments to that of those previously used, the majority of cellular phenotypes are retained for both the WT and DN HaCaT cells lines. The DN HaCaT cells maintain their denser cell packing and increased surface height compared to WT counterparts. Both DN and WT HaCaTs display signs of cell penetration through the materials, however more cellular protrusions into the polycarbonate scaffold can be observed for DN HaCaT cells compared to that of WT HaCaTs.

3.3.7.2 No phenotypic differences in nuclear morphology can be observed using the 2D micro-pillared material.

To further assess the nuclear malleability between the DN and WT HaCaT cells lines in a 2D environment, a novel micro-pillared surface was used (material details described in the methods [229]. The aim of this investigation was to assess whether both cell lines were able to attach between the micro-pillars protruding from the materials surface, and in

turn assess whether the nuclear deformities induced by this attachment were variable between the two cell lines. Cells were seeded onto the materials and processed as described previously upon growth over a 5 day period. Following this, fluorescence staining was performed for *TRITC-conjugated* phalloidin and *DAPI*. Representative images can be seen displayed in *Figure 3.68*.

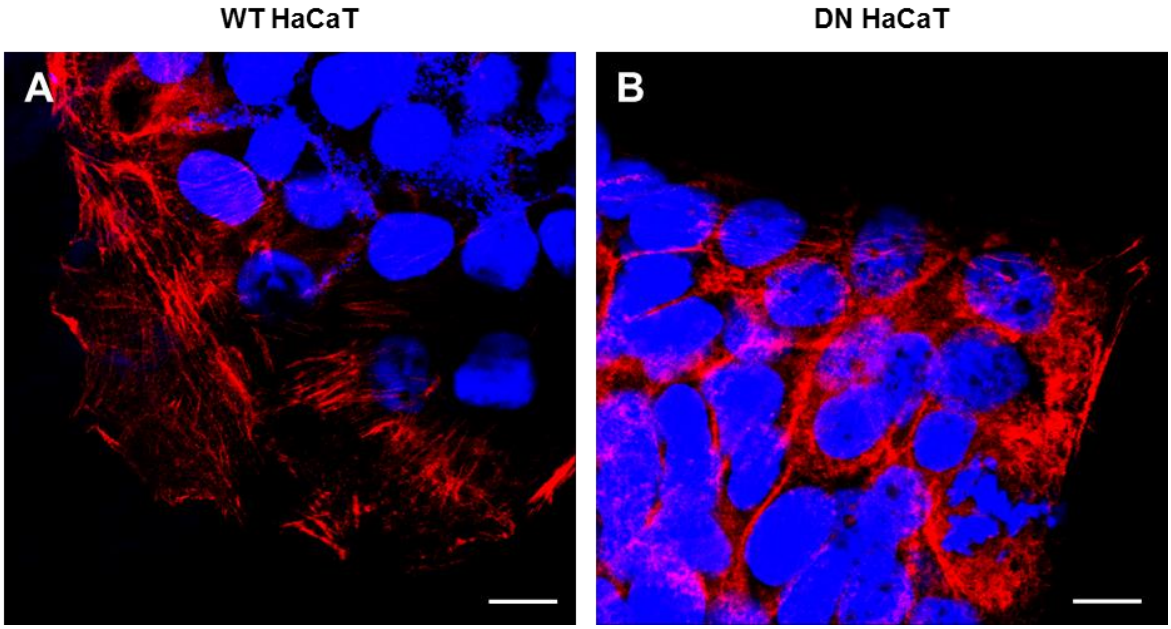

Figure 3.68: *Immunofluorescence images of both WT (A) and DN (B) HaCaT cells adhered to micro-pillared materials. Actin cytoskeleton is stained in Red and nuclei in Blue Scale bars = 10 µm.*

As can be seen from images presented in *Figure 3.68*, little difference can be observed between the WT and DN HaCaT cells when placed onto this material. It can be seen that both cell lines display actin accumulation and cellular packing as previously identified in conventional 2D culture systems. This data, therefore, suggests that both the cell lines appear grow across the surface of the pillars, rather than settle between the 7 x 7 µm spaces between each pillar. However, the imaging technique used is unable to display the pillars across the materials surface, meaning that our current assumptions would need further validation through the incorporation of a surface imaging technique such as AFM or SEM. This would allow the identification of not only the cells situated across the surface, but also the pillars, displaying whether the cells do indeed grow across the surface of these micro-pillars. To validate this; nuclear circularity was assessed between both WT and DN HaCaT cells, as displayed in *Figure 3.69*.

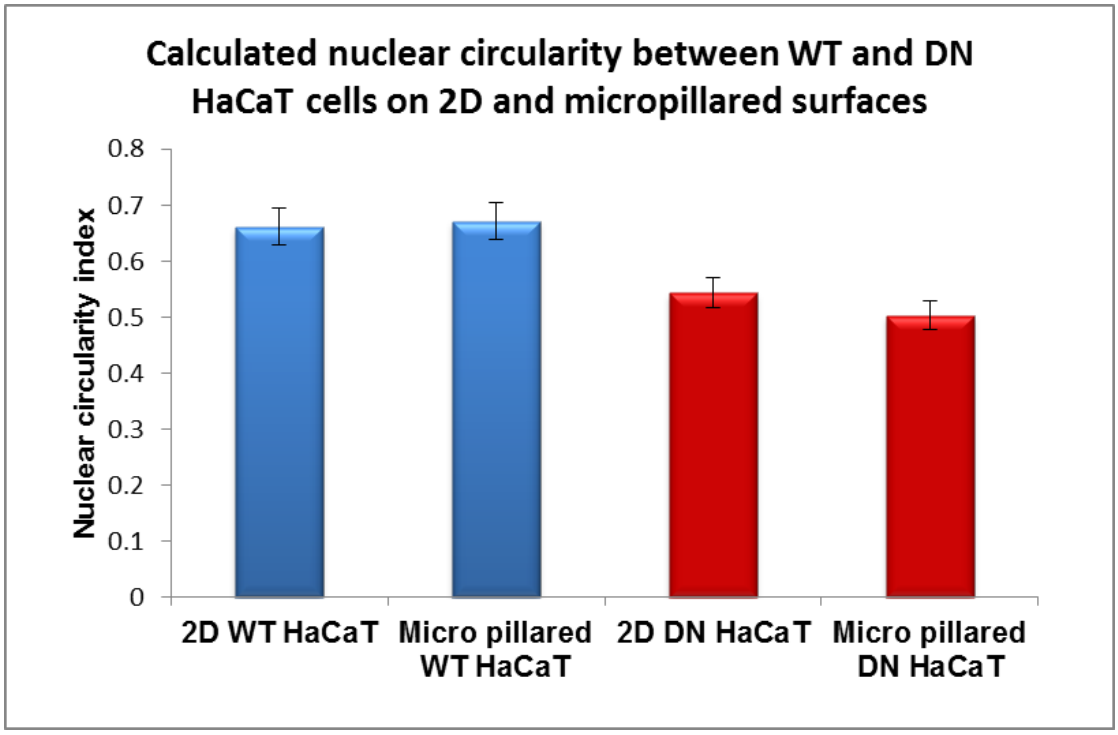

Figure 3.69: *Collated data displaying calculated nuclear circularity index values in conventional 2D culture and micro pillared materials for WT and DN HaCaT cells.*

The data presented in *Figure 3.69* suggests that there is no difference between the calculated nuclear circularity index values obtained for both cell lines between conventional 2D and micro pillared surfaces. The graph further supports the previous data suggesting that the nuclear circularity index is different between the WT and DN HaCaT cells lines in in both culturing environments.

The data presented in this investigation therefore suggests that the WT and DN HaCaT cells were unable to penetrate into the spaces between the micro-pillars, resulting in the cells forming colonies across the pillar surface. In addition, the circularity index remained consistent with conventional 2D culture systems, suggesting that the material was not able to stimulate nuclear deformities within either cell line during our investigation period.

3.4 Summary of Experimental Findings.

Work in this chapter has sought to investigate the effects of severing *SUN-KASH* protein interactions within the PNS on cellular functionality and behaviour. This protein impairment through the incorporation of DN SUN1 acts to disrupt the *LINC* complex, which has been shown to play roles in multiple cellular functions [102, 241, 99, 41].

3.4.1 DN SUN1 overexpression results in phenotypic abnormalities, including increased nuclear height, decreased cell-substratum attachment and reduced 2D migration in scratch-wound assays.

Initial investigations showed that the *LINC* complex disruptions present in DN HaCaT cells stimulated increased cellular cohesion within the colonies. It was found that the DN HaCaT cells exhibited a smaller cellular area to that of WT HaCaT cells, allowing more cells to fill the same 100 x 100 μm^2 area (*Figure 3.5 and 3.6*). Possible explanations for this observation arise from further investigations showing that the DN HaCaT cells present a larger nuclear height and a slightly reduced nuclear volume. This phenotype suggests the DN HaCaT cells are able to occupy a smaller area to that of the WT HaCaT cells, allowing for the closer association between cells. Further evidence has also been provided by western blot analysis between 2D cultured WT and DN HaCaT cells (*Figure 3.62*). It appears that the DN HaCaT cell lines display an increase in E-cadherin levels, which in turn, may increase the DN HaCaT binding affinity to surrounding cells due to E-cadherin's roles in maintaining cell-cell attachments [277]. This combination of increased E-cadherin alongside increased cell-cell proximity (cell crowding) may also suggest the DN HaCaT cells are presenting a columnar epithelium morphology, similar to that of keratinocytes situated across the basal layer in normal skin epithelium [278].

Thus far it has been found that disrupting this *SUN-KASH* perinuclear bridge (and therefore *LINC* complex connections) stimulates 2D phenotypic abnormalities in cellular/nuclear shape and cell-cell attachment. It has been shown that siRNA knockdowns of nesprin-1 are able to stimulate an increase in nuclear height [140] due to a decrease in actin attachment points across the NE, therefore reducing the forces applied by the actin cytoskeletal network across the nuclear surface. Data presented in *Figure 3.9*

supports this, suggesting the displacement if KASH protein across the NE in DN mutant cells, stimulates an increase in nuclear height. However, super-resolution microscopy data for actin organisation across the NE did not reveal any discernible differences in actin topology between WT and DN HaCaT cells (*Figure 3.56*). This suggests that either, the DN insertion impairs the ability of NE actin arrangements to withstand extracellular mechanical forces, but does not alter its cellular localisation, or that the nuclear height increase may result from disruptions to alternate protein networks such as the MT or lamin network systems, which are also implicated in maintaining nuclear height [279].

To validate this, further investigation would therefore be required to directly assess whether the actin cytoskeleton does indeed possess altered mechanical properties. To test this, AFM analysis could be used to test the mechanical properties of isolated NEs both with and without nuclear actin associations between each cell line. This would allow the direct assessment as to whether mechanical properties inferred by NE-associated actin differs between WT and DN HaCaT cells, and therefore whether the observed nuclear height increase can be attributed to this.

Subsequent investigations assessed functional differences expressed between the WT and DN HaCaT cells lines regarding cell-substratum attachment and migration potential. It has been shown through time course analysis and live cell imaging that the DN HaCaT cells appeared to flatten much slower post trypsinisation than the WT HaCaT cells (*Figure 3.11*). Further investigations lead to suggestions that this could be a result of variations in vinculin and cytoplasmic actin organisation between the two cell lines. It was shown that the vinculin organisation remained similar for both cell lines up to 12 h post trypsinisation, however, at the 24 h time point, it can be clearly seen that the WT HaCaT cells display an accumulation of vinculin across the cellular periphery in focal adhesions. In contrast, DN HaCaT cells retain similar cytoplasmic localisation to the pre 12 h time points (*Figure 3.12 and 3.13*). Aside from this, actin organisation was further shown to accumulate at peripheral cell areas in the DN HaCaT cells lines, whereas the WT cells displayed a more even actin distribution between the cell's nucleus, cytoplasm and periphery. This contradicts the super resolution data of actin presented in *Figure 3.56* in which no difference in actin organisation was observed. Potential reasoning behind this however comes from DN HaCaT cells presenting a decreased attachment rate to the cellular substratum as described in this investigation. As the actin assessments conducted in this investigation were taken 24 h post seeding, the super resolution images display the same cells 72 h post seeding. This suggests that the DN HaCaT cells may accumulate the same actin arrangement, however due to their reduced cell-substratum flattening rate; this

process may take significantly longer as a result of *LINC* complex disruptions across the NE.

Following this, investigations aimed to assess whether the *LINC* disruptions present in DN HaCaT cells stimulated any further phenotypic differences in 2D migration potential through the use of a conventional scratch wound assays. Resulting data presented in *Figure 3.17* shows that the DN HaCaT cells migrate significantly slower than their WT counterparts. In contrast to WT, DN cells are unable to completely close the wound 48 h post wounding. It has been previously suggested that the loss of *SUN-KASH* interactions across the NE leads to a loss of cell polarity [59], which subsequently leads to the loss of directed cell migration. Based on this evidence, findings within this investigation may suggest that the reduced wound closure displayed by DN HaCaT cells may be a cumulative outcome of cell-substratum and -polarisation defects.

3.4.2 LINC complex disruption in HaCaT cells increases penetration into space-restrictive 3D culture environments.

The use of two commercially available 3D culture scaffolds; Alvetex® Scaffold and Alvetex® Strata, allowed us to investigate the ability of WT and DN HaCaT cell lines to migrate through space-restrictive and non-restrictive 3D environments. For the non-restrictive Alvetex® Scaffold environment, it was shown that the phenotypic observations were similar to that of the 2D wound healing assay. Specifically, WT HaCaTs were shown to migrate faster through the scaffolds, alongside DN HaCaTs displaying a more compact grouping of cells across the full depth of the scaffold (*Figure 3.21*). Further to this, WT HaCaT cells displayed a preferred growth across the two extreme surface regions of the scaffold, whereas the DN HaCaT cells maintained their tightly packed cell morphology throughout the material (*Figure 3.19*).

It was speculated that the WT but not the DN HaCaT cells did not colonise the central scaffold regions due to this region presenting a stressful environment for the cells. One potential explanation for this observation comes from the DN HaCaT cells potentially displaying a loss of contact inhibition due to the severance of *LINC* connections across the NE. This could result in their increased clustering observed. However, further assessment of this hypothesis would be required to validate this. It can be further suggested that due to the high porosity of the material, media flow would be limited within the central region of the scaffold, meaning that cell accumulation in this region could result

in hypoxic and acidic conditions developing over longer culture periods. Testing the conditions in the central region of the scaffold would, however, be difficult due to the fragility of the material and its limited thickness of 200 µm.

Interestingly however, further data supported suggestions that central regions of the scaffold may provide stressful environments for the cells (*Figure 3.39*). Through the use TEM imaging, it was shown that interconnects between the voids present sharp edges of ~1 nm. Cells were seen to be heavily indented by these edges, but crucially, when indentations were in close proximity to nuclear regions, potential keratin accumulation was observed around the point of indentation, in which the cells appeared to protect their nuclei. To verify whether cells were under stress within these space-restrictive scaffolds, western blot analysis for known stress markers JNK and p38 was further conducted. It was observed that phosphorylation levels for both proteins were seen to be significantly upregulated for WT HaCaT cells within the space-restrictive 3D scaffolds in comparison to DN HaCaT cells (*Figure 3.64*), suggesting that these cells are indeed responding to stresses from their environment.

All of the potential stresses described above could be reasons why WT HaCaT cells are unable to colonise central regions of the scaffold. However, the DN HaCaT cells retain their 2D phenotypic growth patterns (*i.e.* cell crowding) and appear to colonise these regions. This observation could be a result of either the DN HaCaT cells expressing an increased resistance to environmental stress, or an inability to detect and respond to surrounding stresses due to a loss of mechano-transduction across the NE.

Both cell lines were also cultured in the space-restrictive Alvetex® Strata scaffolds (*Figure 3.24*). Interestingly, it was found that over the first 7 days of growth, WT HaCaT cells displayed faster migration potential; however, they then appeared to remain in the central regions of the scaffold with little to no further migration post 9 days. In contrast, the DN HaCaT cells continually migrated through the scaffold at a much slower rate than the WT HaCaTs, passing them at the 9-day time point (*Figure 3.25*). It can be suggested that this increased migration potential may arise from the stresses described in non-restrictive scaffolds, in which reduced media flow and sharp interconnecting windows may damage cells during migration. In these more space-restrictive Strata® Scaffolds, these stresses would be amplified as a result of decreased void diameters, subsequently leading to reduced media flow and more restrictive interconnecting windows. As it was suggested that DN HaCaT cells appear to resist these stresses (through colonising central scaffold regions in non-restrictive scaffolds) due to a potential loss of mechanotransduction, these

cells may display a migration advantage, in which cells may continue to migrate even though cell damage is obtained.

One further suggestion as to why WT migration appears to halt in central scaffold regions could arise from the increased cell density observed as cells migrate through the restrictive scaffolds (shown in *Figure 3.24* where WT HaCaT cells appear to display a more compact morphology due to the scaffolds decreased void diameters). This could lead to increased media consumption within central scaffold regions, alongside increased cellular damage due to migration through restrictive interconnecting windows, leading to subsequent cell damage and migration arrest.

In addition, it was shown that the *LINC* disruptions present in the DN HaCaT cells stimulated alterations in cell behaviours across the seeding surface of the restrictive Strata® scaffolds, and the leading migratory edge of cells in the centre. The DN HaCaT cells appeared to display an increased cell density and stratification across the seeding surface of the scaffold compared to WT counterparts; which presented a single cellular layer upon air/liquid interface induction (*Figure 3.28*). These observed shape changes in DN HaCaT cells appear to reflect the organisation of keratinocytes *in vivo*, in which serial differentiation across the epidermal layer of skin leads to significant morphological changes in cell shape [271] (*Figure 3.28*, *3.29* and *3.30*).

It was further shown in *Figures 3.26 and 3.27* that the DN HaCaT cells migrated through the scaffold as a cohesive unit across the leading edge, whereas the WT HaCaT cells display much more variability in penetration rates across this edge. Coupled with the 2D phenotypic observations and non-restrictive 3D migration data, this observation could suggest that the WT HaCaTs express increased proliferation rates to that of the DN HaCaT cells in these space-restrictive scaffolds. However, with data suggesting *LINC* complex disruptions stimulate loss of cell polarity and therefore directed movement in 2D environments, the increased cohesion of cell migration across the leading migratory edge may arise from DN HaCaT cells being unable to select for 'the easiest route' through the scaffold. The restrictive scaffold material used presents variable void diameters and interconnect sizes, leading to assumptions that when presented with a large and small interconnect size, the WT HaCaTs could be able to selectively migrate through the less restrictive interconnect which will not require nuclear deformities to pass through. The DN HaCaT cells on the other hand would be unable to select for the easiest route, therefore leading to a more uniform migration pattern. One alternate explanation is that the increased expression levels of E-cadherin in DN HaCaT cells influences their migratory behaviour. However, increased E-cadherin levels were not observed for the DN HaCaTs

when cultured in the restrictive Strata® Scaffold (*Figure 3.62*). This therefore supports our initial suggestions that the inability of DN HaCaT cells to direct migration may be the main contributing factor to their observed migratory behaviour.

This migratory edge analysis lead to further investigations using high-powered TEM to investigate whether any behavioural differences existed between the two cell types in central regions of the space-restrictive Strata® scaffold. Two main phenotypic differences were observed, the WT HaCaTs displayed significantly increased cytoplasmic redistribution ahead of nuclei during migration through restrictive (<4 μm) interconnect sizes (*Figure 3.34*) compared to DN HaCaT cells. Alongside HaCaT cells exhibited a more 'hourglass' nuclear shape when compared to WT nuclei upon migration through these restrictive interconnecting windows (*Figure 3.38*).

3.4.3 LINC complex disruption in HaCaT keratinocytes significantly decreases nuclear stiffness.

From the data gathered thus far, it has been shown that the DN HaCaT cells exhibit numerous phenotypic changes, the most distinct of these being the increased penetration potential into space-restrictive 3D culture scaffolds. This phenotype closely resembles those exhibited by highly metastatic cancer cells upon migration from their source to other areas of the body. These cells often exhibit increased nuclear malleability, in turn, increasing the ability of cells to squeeze between gaps smaller than that of the nuclei [283].

It was therefore investigated whether the disruption in *SUN-KASH* interactions present in DN HaCaT cells resulted in a decrease in nuclear stiffness, stimulating the observed migration advantage in space-restrictive 3D environments. It was initially observed that both WT and DN HaCaT cells display a decreased nuclear circularity index in central regions of the scaffold compared to surface regions (*Figure 3.43 – 3.46*). This suggests that nuclear shape changes are required to penetrate into these restrictive scaffolds. To gain an increased understanding of the effects of *LINC* disruptions on the mechanical properties of nuclei, we applied the use of AFM (Atomic Force Microscopy), Transwell assays and osmotic stress analysis techniques to assess; 1) whether *LINC* disruptions stimulated a significant decrease in nuclear stiffness, and 2) whether this increased nuclear malleability inferred a migration advantage when nuclear deformation is required

for migration (*Figure 3.49, 3.52* and *3.67*). It was found that the DN HaCaT cells did indeed exhibit a decreased nuclear stiffness. It has been shown that down regulation of nesprins across the NE leads to an increase in nuclear size, which in turn can be reversed through the incorporation of nesprin mini (rod-less) engineered isoforms [101]. This suggests that nesprins may form a cage like network across the ONM anchored by *SUN-KASH* protein interactions, able to provide structural rigidity to the nucleus. When this cage is disrupted, as in the DN HaCaT cells, this structural rigidity/nuclear cage may be lost, leading to a reduction in nuclear stiffness.

3.4.4 DN SUN1 induced LINC complex disruption induces altered expression patterns for multiple LINC proteins, notably nesprin-1/-2 across both 2D and restrictive 3D culture conditions.

The final investigations in this section aimed to validate that the previous observations were due to a severed link between *SUN-KASH* proteins across the perinuclear space. Current views on nuclear stiffness suggest lamins and actin play the crucial roles in maintaining nuclear stiffness [114, ,267]. It was therefore aimed to assess protein expression levels of lamin A/C, lamin B and actin alongside cellular organisation, in order to assess if any differences exist DN and WT HaCaT cells lines. Using super-resolution microscopy, little variation between the actin and lamin A/C protein networks in the cells (*Figure 3.56* and *3.57*) was observed. However, lamin B distribution did appear to be altered (*Figure 3.58*), with DN HaCaT cells displaying a loss of what appears to be lamin B invaginations into the nucleus. When coupled with protein expression data for each protein, it can be seen that lamin A/C levels appear to be increased in 3D WT cells in comparison to their 2D counterparts, whereas lamin B and actin levels remain consistent.

This observed difference in lamin A/C expression across DN and WT HaCaT cells in restrictive 3D culture environments could be due to the direct interactions present between lamin A and SUN proteins [29, 66]. As endogenous SUN proteins are outcompeted for interactions with KASH proteins in DN HaCaT cells, it is possible that this loss of *SUN-KASH* interaction may elicit alterations in lamin A/C expression as a redundancy mechanism to retain nuclear integrity. It is already known that upon lamin A/C dysregulation in HGPS, SUN1 accumulation across the NE is increased, so a potential mechanism may also exist for lamin A/C expression to safeguard the nuclear integrity upon the detection of a severed link between INM and ONM.

Through the application of western blot analysis of further *LINC* associated proteins, it was shown that disrupting the *SUN-KASH* bridge across the perinuclear space alters emerin and SUN2 expression patterns, but does not appear to affect expression of SUN1. For both WT and DN HaCaT cells, SUN1 expression remained consistent across the 2D and 3D culture environments, whereas emerin expression appeared to increase when both DN and WT HaCaTs were subjected to the space-restrictive 3D environments. A further decrease in SUN2 protein expression was observed across WT and DN HaCaT cells compared to their 2D counterparts (*Figure 3.60*). These observations in emerin expression could be a result of the cells natural response to stresses in their environment. It was shown by Hadden *et al*. that when HeLa S3 cells were subject to both mild and severe hyperthermia stress, a spiked increase in emerin levels was observed, followed by a subsequent decrease [290]. The functional attributes of these observed variations in emerin expression have not yet been ascertained, however, it does help to underline the complexity of cellular responses to cellular stress, suggesting further research to increase our understanding of this process is required. The observed differences in SUN protein expression could arise in differential levels of pre-lamin A within 2D and 3D cultured cells. It is known that pre-lamin A is closely associated to emerin and Lap2α across the nuclear envelope [291] and is able to stimulate the up regulation of SUN1 [292]. As a result of the above data also displaying a reduction in Lap2α expression levels within restrictive 3D environments, it is possible that levels of pre-lamin A may be reduced in the 3D cultured systems, leading to the observed alterations in emerin and SUN expression levels. To validate this, future work should be conducted into assessing levels of pre-lamin A present within cells grown in 2D and restrictive 3D growth environments.

Further western blot analysis revealed that the levels of nesprin-1 and nesprin-2 isoforms appeared to vary greatly between the WT and DN HaCaT cell lines. Their isoform expression levels appeared to remain consistent in both the 2D and 3D culture environments, however, isoform expression differences could be observed between the two cell lines across both environments (*Figure 3.61*). The most striking observation is the differences observed in the nesprin-1 western blot across the 90 kDa range. It can be seen that the WT HaCaT cells express a clear band in this region that is not present in the DN HaCaT cells. The precise identity and roles of this nesprin isoform are currently unknown; however it can be speculated that this isoform could regulate nuclear structure and mechanical properties. In order to validate this hypothesis however, future work could aim to isolate this isoform and attempt to rescue nuclear stiffness through its re-incorporation back into the DN HaCaT cells, to see if nuclear stiffness is increased.

Finally, the levels of acetylated tubulin in both the WT and DN HaCaT cells grown within both environmental conditions were assessed due to increasing evidence suggesting that tubulin acetylation is a potential factor in cellular invasion and metastasis [293]. The obtained data suggests that the DN HaCaT cells exhibit a reduction in acetylated tubulin levels alongside a large reduction in acetylation levels in restrictive 3D environments (*Figure 3.63*). This data does not correlate with current opinions in cancer biology, suggesting that increased tubulin acetylation levels in metastatic and basal like breast cancer cells is able to promote microtenticle formation, adhesion and invasive migration into surrounding tissue [293]. However, it is often an accumulation of multiple phenotypes that leads to cancer development and metastasis, suggesting that the DN mutant may not represent the whole picture behind increasing metastatic potential within cells.

Through the data presented in this chapter, it has been shown that severing the link between *SUN-KASH* interactions across the perinuclear space stimulates cell abnormalities in both 2D, space-restrictive and non-restrictive 3D culture environments. It has also been highlighted that nuclear malleability is a potential avenue to investigate 3D cellular migration potential through restrictive environments. Due to this, following work will aim to increase the understanding of the roles of *LINC* complex proteins in cancer metastasis, in particular whether similar phenotypes in protein expression or cell behaviour can be observed in various cancer cell lines in addition to the DN HaCaT cells used in this work.

4. Assessing the roles of LINC complex disrupted keratinocytes using 3D fibroblast co-culture models

4.1 Introduction.

The development of *in vitro* 3D cultures which closely mimic the *in vivo* environment of tissues is a current venture to produce more accurate biological models [370]. Results thus far have been obtained using non-physiological polystyrene models, which replicate conditions far from that of the *in vivo* situation, as in the body, keratinocytes do not exist in single culture environments, or display close contact with plastic. To tackle this limitation of experiments conducted thus far, we aimed to replicate a more *in vivo* like 3D culture environment in which to test our keratinocyte cell lines.

HaCaT cells are derived from the epidermal layer of human skin, situated above the dermis. This dermal region consists mainly of connective tissue, comprising of three main cellular subtypes; fibroblasts, macrophages and adipocytes, working in close association to maintain tissue integrity and resistance to stress and strain [371]. These close associations between dermal fibroblast and keratinocytes are of great importance in tissue development due to the complex interplay of cellular signalling and associated protein interactions occurring between the two layers [372]. With this in mind, to increase the biological relevance of our models, we aimed to co-culture HaCaT cells used thus far with dermal fibroblast cells, to more closely replicate the *in vivo* situation. Using these models, we aim to tackle two questions; 1) whether fibroblast incorporation into the 3D scaffolds stimulates alterations in WT and DN HaCaT cells penetration potential, and 2) whether any differences can be observed previously in cell stacking observed during DN culture in space-restrictive scaffolds.

4.1.1 Keratinocytes and fibroblasts mediate numerous tissue functions in human skin through complex cross talk between dermal and epidermal regions.

4.1.1.1 Human keratinocytes change keratin expression profiles during differentiation in epidermal skin layers, stimulating changes in cell function and tissue properties.

The epidermis, a keratinized stratified squamous epithelium can be found across the bodily surface of terrestrial vertebrates, functioning to protect against pathogen, allergen or toxic substance entry. The epidermis comprises mostly of keratinocytes, which are organized into five main cellular layers; the Stratum Basale (SB), the Stratum Spinosum (SS), the Stratum Granulosum (SG), the Stratum Lucidum (SL) and the Stratum Corneum (SC) (*Figure 4.1*).

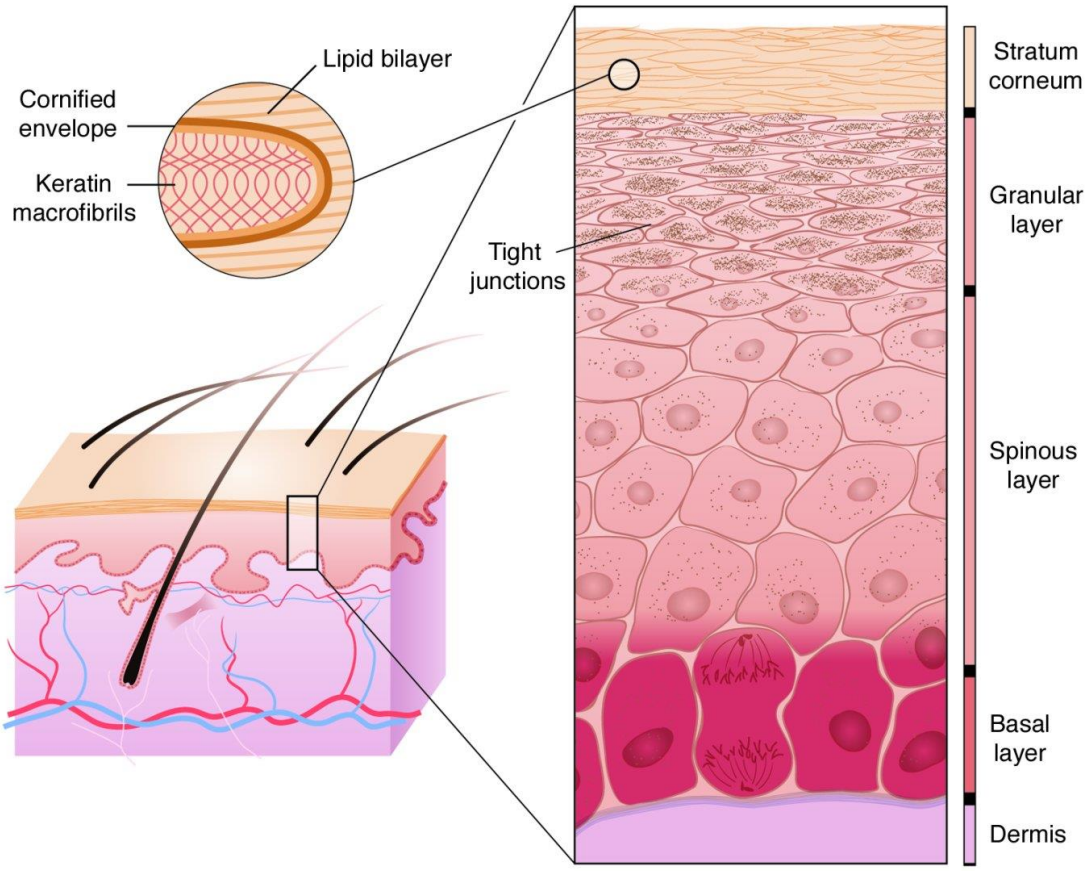

Figure 4.1: *Schematic of the stages of epidermal differentiation in human skin, highlighting relative size and regions of each associated region. The SL is situated between SG and SC layers, [507].*

The dermal region of skin is a connective tissue containing collagen and elastic fibres, working in close association with fibroblasts to provide a structural framework. Situated directly above this cellular layer is the SB, the deepest epidermal region comprising of a single keratinocyte layer. From this region, terminal proliferation and differentiation of keratinocytes occurs, leading to the development of the subsequent cellular layers [271, 278].

Keratinocytes situated across each epidermal layer express unique sets of keratin intermediate filaments. In the SB layer, keratinocytes express keratin 5 (A basic, Type II intermediate filament protein) and keratin 14 (An acidic, Type I intermediate filament protein) [373]. This keratin pair is strongly associated with regions of stem cell localisation, often found down regulated in further differentiated layers [374]. The K5/K14 keratin filaments are found bundled as tonofilaments associated with desmosomes and hemidesmosomes. The functional importance of this keratin pair across the basal layer of the epidermis has been well documented through the use of genetic studies [375], in which the dominant negative loss of K5/K14 function across basal skin keratinocytes is often associated with the development of hereditary skin blistering diseases, such as epidermolysis bullosa simplex (EBS). The loss of K5/K14 function leads to the subsequent development of fragility within the basal layers of the epidermis, meaning that through the application of mechanical force, intraepidermal blistering can develop [376].

This keratin pair has displayed further importance in the assessment of cancer progression, with the expression pattern of both K5 and K14 suggested to remain constant during cancer development across many tissues. Keratin 5 for example is present in the basal layer of both keratinized and non-keratinized epithelium, due to this, Vasca *et al*. suggested K5 as a potential diagnostic marker for the detection of differentiated and undifferentiated regions of tumours from the oral cavity, oropharynx, hypopharynx and larynx [377]. Further evidence also highlights roles for K5 in assessing breast pathology, including the identification of myoepithelial cells, the classification of proliferative lesions and the recognition of specific subtypes of invasive ductal breast carcinomas [378].

The transition of keratinocytes from the proliferative basal cell layer to the post mitotic spinous layer is characterised by a change in keratin expression, such as the exchange of K5 and K14 for suprabasal epidermal keratins like the Type II keratin K1 and the Type I keratin K10 [379, 380]. The pairing of K10 and K1 elicits an increase in mechanical integrity to the surrounding tissue due to the formation of dense intermediate filament bundles. Further to these structural roles, it has been identified that this keratin switch,

most notably the expression of K10 is able to inhibit cell proliferation and cell cycle progression [381], with further loss of K10 expression associated with increased keratinocyte turnover [382], suggesting functional roles played by this keratin switch during terminal keratinocyte differentiation. Serial differentiation then continues from the SS to the SG, in which cells begin to develop a more flattened morphology. Following this layer is the SC, consisting of a mixture of lipids and dead keratinocytes, forming a flattened, water resistant barrier across the surface of the epidermis. During the final stages of keratinocyte differentiation into this layer, keratin proteins align into highly ordered arrays through interactions with the matrix protein filaggrin. This protein is able to aggregate with keratin filaments, forming tight bundles, which subsequently stimulates cellular collapse into this observed flattened cell shape [383].

It is suggested that this process of serial differentiation in human keratinocytes aids in the development of a wide range of cellular functions throughout the epidermis, due to the associated cellular changes with each differentiation step. Aside these alterations in keratin expression patterns, cell-cell interactions between keratinocytes and other cellular populations also vary during terminal differentiation [384]. For example, in healthy human skin, the cross talk between keratinocytes and melanocytes situated across the basil epidermal layer is important for tissue maintenance. Keratinocyte cells are able to regulate the proliferation and cellular behaviours exhibited by melanocytes via interconnections through E-cadherin. The extracellular domains of these E-cadherin proteins form stabile connections between actin cytoskeletal networks within each cell through associated α- and β-catenins [385]. This cellular linking between cytoskeletal elements across cells was then further suggested to infer the ability of multiple cells to act as one across the tissue, able to resist mechanical forces which would tear single cells apart [386].

It is therefore evident that the complex differentiation and cellular interaction patterns expressed by keratinocytes within the epidermis allow the formation of a complex network of cellular functions. In comparison to this however, it has been continually documented that keratinocytes grown in synthetic 2D and 3D culture systems do not express this complexity in cell-cell interactions or differentiation potential without the implication of external factors [387, 388, 389]. This helps to highlight the need for a more *in vivo* like model to assess whether differences in WT and DN HaCaT cells displayed thus far reflect how they would behave *in vivo*.

4.1.1.2 Human dermal fibroblasts display a wide range of functions, including maintaining tissue integrity, re-modelling the ECM and organising epidermal function.

Dermal regions of the skin are located below the basement membrane of the epidermis, consisting of multiple cell types working in conjunction to maintain organ homeostasis. One major component of this dermal layer are the fibroblast cells. These resident mesenchymal cells produce collagen and other ECM proteins including laminin-1, laminin-5 and fibronectin [390, 391, ,392], shown to function in maintaining skin structure and integrity. Alongside its roles in creating and re-engineering the surrounding extracellular matrix, dermal fibroblasts have also been implicated in further tissue functions. In recent *in vitro* investigations, it was shown that complex cross talk between dermal fibroblasts and monocyte-derived dendritic cells (MoDC) was required for the efficient migration through the surrounding ECM [393]. In this study, it was shown that innate-immune activation stimulated the activation of MoDC's. This in turn stimulates the release of TNFα (tumour necrosis factor alpha) and IL-1β (interleukin-1β), which subsequently stimulated the release of MMP1 (human collagenase) and PGE_2 from neighbouring dermal fibroblasts, resulting in a re-modelling of the ECM. This ECM remodelling was further shown to increase the migratory potential of MoDCs through the tissue environment, helping to highlight further roles of dermal fibroblasts in remodelling the ECM as a method of controlling the cutaneous immune response.

Dermal fibroblast cross talk has also been implicated in the remodelling phase of wound healing. This phase of wound healing is considered the longest process, continuing from a period of weeks to months. One of the main characterising features of this stage is the active re-organisation of the ECM by the dermal fibroblast population. Through the accumulation of collagenase and MMPs, Type III collagen secreted by the myofibroblast population is gradually replaced by the Type I collagen [394]. During this process, dermal fibroblasts help to facilitate an increase in crosslinking between collagen, reduction in fibronectin and an increase in localised proteoglycans, helping to increase overall the strength of the resulting scar. This therefore, highlights that dermal fibroblasts help to re-organise the EMC of the scar, developing a composition more similar to that observed in non-wounded tissue [395].

It has been shown thus far that dermal fibroblasts exhibit a wide range of functionality through the re-organisation of ECM components in response to various environmental cues. Aside these roles, current investigations suggest further roles for fibroblasts in

organising epidermal function through cellular cross talk between epidermal and dermal tissue regions. This link between keratinocyte and fibroblast regions is controlled by both paracrine and autocrine linkage. Initial *in vitro* investigations suggest fibroblast cells secrete soluble factors that diffuse to the overlaying epidermis, influencing keratinocytes in a paracrine manner [396, 397]. This was shown through investigating keratinocyte growth behaviours under fibroblast co-culture conditions *in vitro.* Using this system, it was shown that under single culture conditions, keratinocyte cells appear to produce a thin epidermal layer and become apoptotic ~2 weeks post seeding in collagen gels [396]. However, the introduction of a fibroblast cell layer before keratinocyte seeding, followed by growth at the air-liquid interface (similar to conditions found under *in vivo* conditions) resulted in a much more defined epidermal layer, displaying clear SB, SS, SG and SC layers. This highlighted the potential for cross-talk existing between the keratinocyte and fibroblast cells within the system, allowing the formation of a more defined keratinocyte organisation and differentiation pattern to that observed in single cultures.

Furthering these findings, follow on investigations highlighted the importance of fibroblast secreted cytokines and growth factors, revealed both autocrine and paracrine effects of these secreted factors on epidermal keratinocytes. Autocrine activity is displayed by the TGF-β induced secretion of connective tissue growth factor (CTGF), which helps promote the synthesis of collagen into the ECM, alongside increase neighbouring fibroblast proliferation [398]. Paracrine activity displayed by dermal fibroblast cells affects keratinocyte growth and proliferation directly, through the secretion of keratinocyte growth factor (KGF), IL-6 and fibroblast growth factor (FGF) [399, 400, 397]. In response to these external signals, keratinocytes increase expression levels of IL-1 compared to that of monoculture cells [401], which in turn, stimulates increased KGF expression by the fibroblast cells, suggesting the existence of a double paracrine loop [402, 403, 404].

Further work now suggests roles for this keratinocyte-fibroblast paracrine linkage within mechanisms of UVB-induced wrinkling in skin, suggesting a complex interplay exists between keratinocyte cytokine release and subsequent increased elastase expression by dermal fibroblasts [405]. More interestingly however, there is current speculation that the production of keratinocyte microvesicles, stimulated under wound healing conditions regulates the expression of multiple genes in dermal fibroblasts [406]. It was found that when keratinocyte microvesicles derived from wounding skin were added to dermal fibroblast cultures, expression of 21 genes was significantly regulated, including those associated with the production of MMP1, MMP3, IL-6, IL-8 and genes associated with TFG-β signalling.

Current data therefore suggests that not only do both keratinocyte and fibroblast cells play important individual roles in the maintenance of skin functions, but that they also possess complex interactions across dermal and epidermal regions, allowing a diverse range of functional responses to environmental cues to be implemented. These findings help to provide further support for the inclusion of fibroblast cells into our simplified model, as the complex interactions between keratinocytes and fibroblasts may induce altered phenotypic behaviours by the WT and DN HaCaT cells in comparison to their single culture conditions.

4.1.1.3 ECM composition can alter cell behaviours, including cell-substratum adhesion, cell migration and cell spreading both in vivo and in vitro.

The incorporation of keratinocytes and dermal fibroblasts into simplified 3D models should help to more accurately emulate cellular environments which closer resemble the normal *in vivo* system. Fibroblast introduction will stimulate complex interplay between keratinocyte and fibroblast cells through the secreted ECM. Current literature suggests that in both *in vivo* and *in vitro* culturing systems, the secretion of ECM and its composition is heavily influenced by its surrounding environment [407]. This produced ECM infers a wide variety of biochemical and mechanical stimuli to surrounding cells, with perturbation stimulating drastic phenotypic and behavioural abnormalities.

As current understanding suggests that the mechanical stiffness of the growth environment influences cellular growth properties, current investigations apply the use polyacrylamide (PA) gels with increasing and decreasing Bis-acrylamide content, to assess the effects of environmental stiffness on cellular morphology [408]. In this study, It was shown that through the incorporation of both NRK-52E and 3T3 fibroblast into the 'hard' polyacrylamide substrate, cell spreading was increased, whereas cells applied to the 'softer' material displayed an increased variability in lamellipodia in the NRK cells, alongside an increased motility in the 3T3's. This investigation therefore provides insight into the cells ability to adapt to environmental composition.

The modulation of ECM environmental stiffness has been shown to be a key component in aiding cellular migration through localised tissue environments. *In vivo* mouse models have demonstrated that the tissue stiffness in mammary gland regions of the breast increases upon type-1 interferon receptor loss [409]. This increased stiffness

was attributed to an increase in collagen expression, alongside an increase in liberalisation and cross-linking between these collagen fibres. The identification of increased crosslinking between collagen fibres was further correlated to an increase in lysyl oxidase expression, an amine oxidase which acts as a collagen cross-link initiator. To further this work, MCF 10A cells were grown in *in vitro* collagen gels displaying varying cross-linking densities [410]. It was found that as the collagen matrix stiffness was increased through increased cross-linking, structural organisation of acini formation was disturbed, alongside an increase in colony size. This suggests that an increase in environmental stiffness is sufficient to elicit structural abnormalities and altered cell behaviours in model 3D systems.

In papers described thus far, variability between cellular responses to these varying matrix conditions is observed based on the cell line applied. For example, it has been demonstrated that varying grades of cancer cells display adaptable cell behaviours in response to substrate rigidity [411]. In this study, a variety of cancer cell lines (including MDA-MB-231, MCF7, HPSC and VMM18 cells) were assessed for their ability to grow within collagen coated PA gels displaying elastic moduli ranging from 150 – 9600 Pa. Variability in cellular mobility was observed across the range of cell lines tested, however, it was found that in cells displaying increased mobility on rigid surfaces (such as the A549 and MDA-MB-231 cells), the same cells displayed a cell-cycle blockade or increased apoptotic events when grown on softer surfaces. Interestingly however, it was further demonstrated that some cells (Such as the mPanc-96 cells) displayed no preference of increased growth or motility to any Pa range tested, suggesting that the environmental stiffness may affect cells in different ways. This investigation however, clearly suggests that for some cell types, the mechanical properties of the ECM can play a large role in the attachment and migration potential through environmental substrates.

The presence of specific ECM components within the cellular growth environments has also been implicated in enhancing cellular behaviours when grown on model 3D matrices. The presence of fibronectin in 3D collagen I gels *in vitro* has been implicated in increasing the cellular migration potential of Chinese hamster ovary (CHO) cells [412]. It was shown that in control collagen I substrates, CHO cells displayed delayed substrate attachment whilst retaining a spherical morphology up to 2 h post seeding. In contrast, those cells seeded onto matrices coated with fibronectin adopted a more characteristic flattened cellular morphology in this time frame. This observed difference in attachment potential was lost by the 24 h time point, by which time both cellular conditions displayed no significant difference in cell flattening. Interestingly, further observations in this study suggested fibronectin introduction did not display any significant effects on cellular

proliferation potential; however, it did appear to drastically enhance cellular penetration into the collagen I gel. After the initial 3 days of culturing, 12.4% of the CHO cells cultured with fibronectin were found integrated into the collagen matrix, whereas without the fibronectin presence, only 6.1% of the cells were found to have integrated into the gels.

Together, these investigations help to demonstrate that the composition of ECM microenvironments is able to help drive cellular behaviours. The introduction of fibroblast cells, known to secrete ECM components into surrounding microenvironments to 3D migration experiments conducted in this thesis may therefore help to infer similar protein environments closer to those found under normal biological conditions.

4.1.2 Current In vitro models are able to accurately replicate the in vivo tissue conditions, allowing the assessment of cell migration and metastasis.

In the development of 3D *in vitro* models, a growing field is emerging to develop model systems that more closely reflect the cellular environment in primary tissue systems. The majority of this research focuses on the development of 3D models, which more accurately reflect tumour environments found within a variety of cancers [413, 414, 415], with aims to increase our understanding of the complex cellular defects leading to cancer development, as well as for use as drug screening models.

However, for the purpose of our investigations, we aim to look more closely at the migratory potential of keratinocyte cells across *in vitro* systems, which closely resemble normal human skin. Collagen gel systems appear to make up the vast majority of models in this area due to their close associations to the normal ECM found within human skin [416, 417]. The fibroblast mediated synthesis of protocollagen molecules into surrounding tissue environments *in vivo*, helps to provide physical and mechanical stability to the connective tissue within skin, acting like a scaffold to which other ECM components such as fibronectin and glycosaminoglycans can connect. Current college matrices are aiming to replicate this scaffold environment to interstitially study cellular migration and invasion under controlled *in vitro* conditions [418, 419]. In each of these systems, re-organisation of the ECM equivalent collagen matrix was adapted to investigate the migratory potential of various cell types, in order to increase our understanding of the complex interplay of the role of cell-environment interactions on migratory behaviour.

Interestingly, current investigations are now expanding these models, with intentions to develop model matrix systems derived solely from cellular components. One such system has been able to produce a synthetic skin model via self-assembly of autologous cultured cells without the addition of exogenous antigenic growth factors or scaffold matrices, able to produce its own vascularisation [420]. This micro vascularised reconstructed skin model (MRS) was formed through the *in vitro* culture of neonatal HDF cells for 4 weeks, followed by the subsequent addition of HUVEC and keratinocyte cell sheets. The system was then moved to the air interface to allow keratinocyte differentiation. Using this developed system, the group was further able to investigate the migratory behaviour of melanoma cells within their vascularised environment [421]. They were able to show that not only did the melanoma display similar migratory characteristics as to those found *in vivo*, displaying migratory behaviour through the epidermal-dermal barrier, but was also able to re-organise the vasculature of the model system.

It can therefore be suggested that even though a vast array of *in vitro* models to assess cellular migration and metastatic potential exist, the production and re-organisation of ECM components through fibroblast function may provide more accurate representations of the *in vivo* system. With this in mind, we aim to co-culture human keratinocytes on a sub-population of human dermal fibroblasts, to assess cell penetration potential through a simplified dermal equivalent alongside the effects of fibroblast inclusion on both WT and DN HaCaT cell morphology and differentiation potential.

4.2 Chapter Aims.

This chapter aims to expand current understanding of both WT and DN HaCaT migration properties through the 3D culture environments assed thus far, by introducing a co-culture system of fibroblast cells. The introduction of HDF (Human Dermal Fibroblast) cells into both space-restrictive and non-restrictive scaffold systems allows the assessment of *LINC* disruptions on cellular penetration in a more ECM-rich *in vivo* like environment. Further to this, due to *LINC* roles in many aspects of cell biology including cell polarity, migration, cell-cell and cell-substratum attachment, we further aimed to assess its roles in epidermal tissue formation *in vitro*. To achieve this, histological techniques alongside immunofluorescence analysis will be applied to assess whether differences in penetration, alongside expression of known epidermal differentiation markers like K10 exist between WT and DN HaCaT cells in these systems.

4.2.1 Objectives.

- To assess the roles of *LINC* disruptions on cellular penetration potential through space-restrictive and non-restrictive 3D fibroblast-HaCaT co-culture scaffold systems.

- To assess whether *LINC* disruptions affect stratification potential of HaCaT cells in co-culture *in vitro* systems.

4.3 Results.

4.3.1 Fibroblast introduction into space-restrictive and non-restrictive scaffolds reduces penetration potential of WT but not DN HaCaT cells.

4.3.1.1 Human dermal fibroblasts colonise both scaffold environments within 14 days of growth.

Previous investigations in Chapter 3 were able to highlight that *LINC* disruption inferred a migration advantage in restrictive 3D growth systems. It was further shown that this migration advantage could be potentially attributed to a decreased nuclear stiffness. Current investigations therefore aimed to further assess the migration ability of *LINC* disrupted HaCaT cell in a further, more *in vivo* like migration model.

As keratinocytes and fibroblast cells display a complex array of intercellular interactions in human epidermis, alongside basement membranes forming a physical barrier to cell migration, current investigations aim to assess whether producing a simplified co-culture model of HDFs cultured alongside WT and DN HaCaT cells would stimulate altered phenotypes to those observed in Chapter 3.

Initially, a devised experimental plan incorporating the use of HDF cells alongside the WT and DN HaCaT cells into both scaffold environments was employed, displayed in *Figure 4.2*.

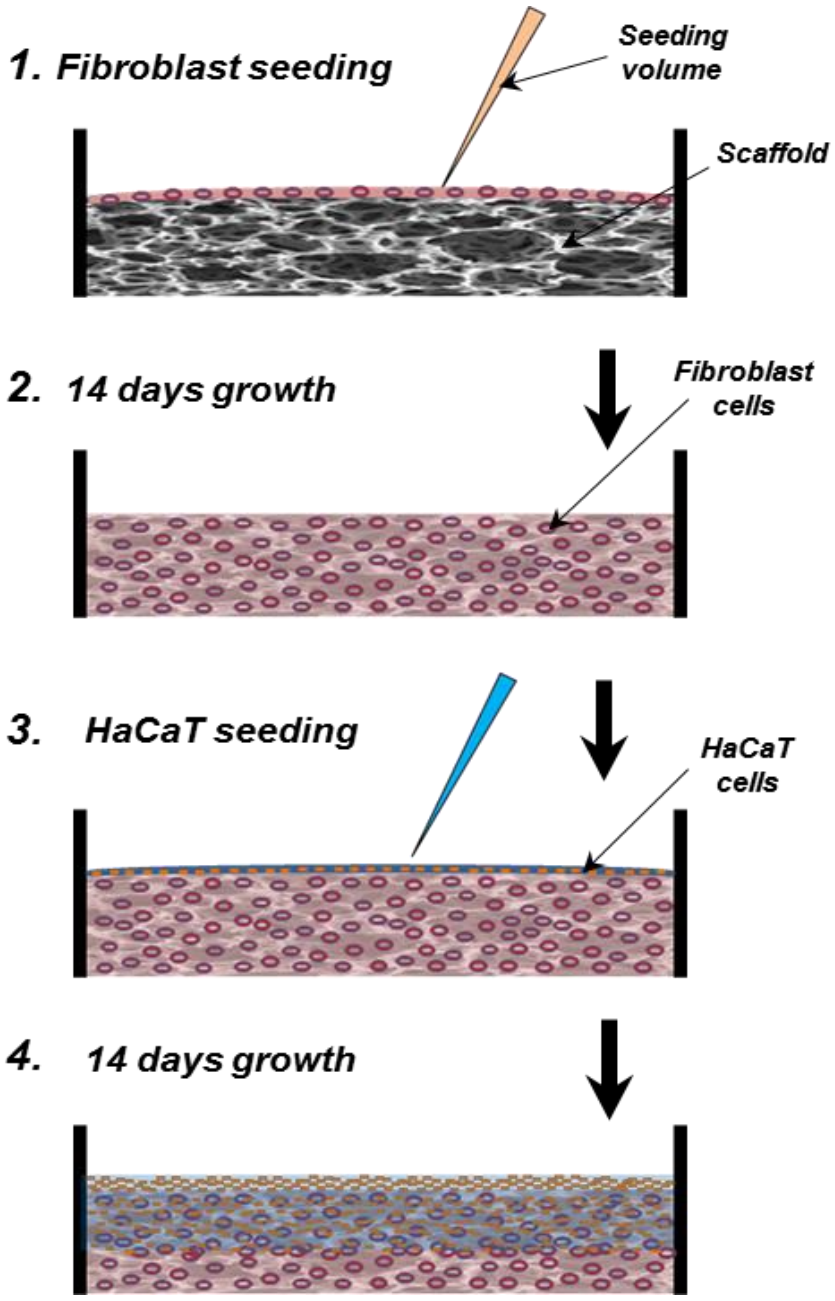

Figure 4.2: *Experimental design for the fibroblast + HaCaT co-culture penetration assessment in both restrictive and non-restrictive scaffolds.*

As described in *Figure 4.2*, both Alvetex® Scaffold and Alvetex® Strata were seeded with 250,000 HDF cells, then left to grow under submerged conditions in standard growth media. Samples were then extracted and fixed at the 14 d time point and processed through H&E (*Figure 4.3*).

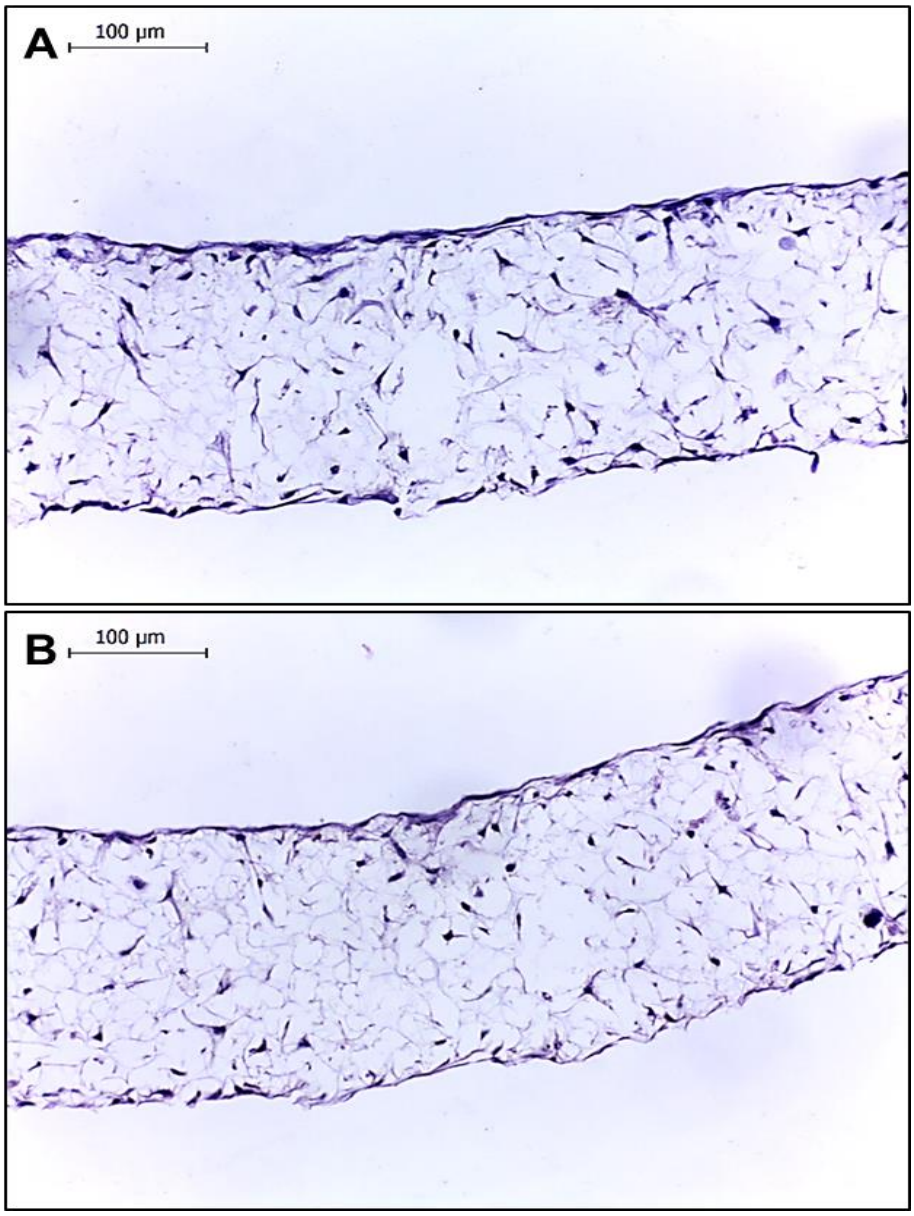

Figure 4.3: *Non-restrictive Alvetex® scaffold (A), and restrictive Alvetex® Strata (B) environments seeded with 250,000 HDF cells and grown for 14 days under submerged culture conditions.*

Figure 4.3 suggests fibroblast cells colonise the whole 200 µm area of both 3D scaffolds. The uniformity of fibroblast coverage appears to resemble that of WT HaCaT cells, displaying a reduction in cell density across central scaffolds regions. Interestingly, further observations highlight weak eosin staining of potential extracellular matrix components lining the surface of voids throughout the material, suggesting that fibroblasts appear to maintain normal cellular functionality, able to secrete large amounts of extracellular matrix components into their environment.

4.3.1.2 WT and DN HaCaT cells display reduced migration speeds in both restrictive and non-restrictive scaffold environments pre-seeded with fibroblasts.

Following successful fibroblast culture over the first 14 days, 250,000 WT and DN HaCaTs, respectively, were seeded to the fibroblast coated Alvetex® Scaffold and Alvetex® Strata environments. HaCaT cells were then left to grow in the co-culture for a further 14 day period under submerged growth conditions as described in both the methods and Chapter 3, with time points taken at 2, 4, 6, 8, 10 and 14 days of growth, allowing direct comparisons to previous observations in non-co-culture conditions to be made. H&E stained images for each time point of both WT and DN HaCaT cells in can be seen displayed in *Figures 4.4* and *4.5*.

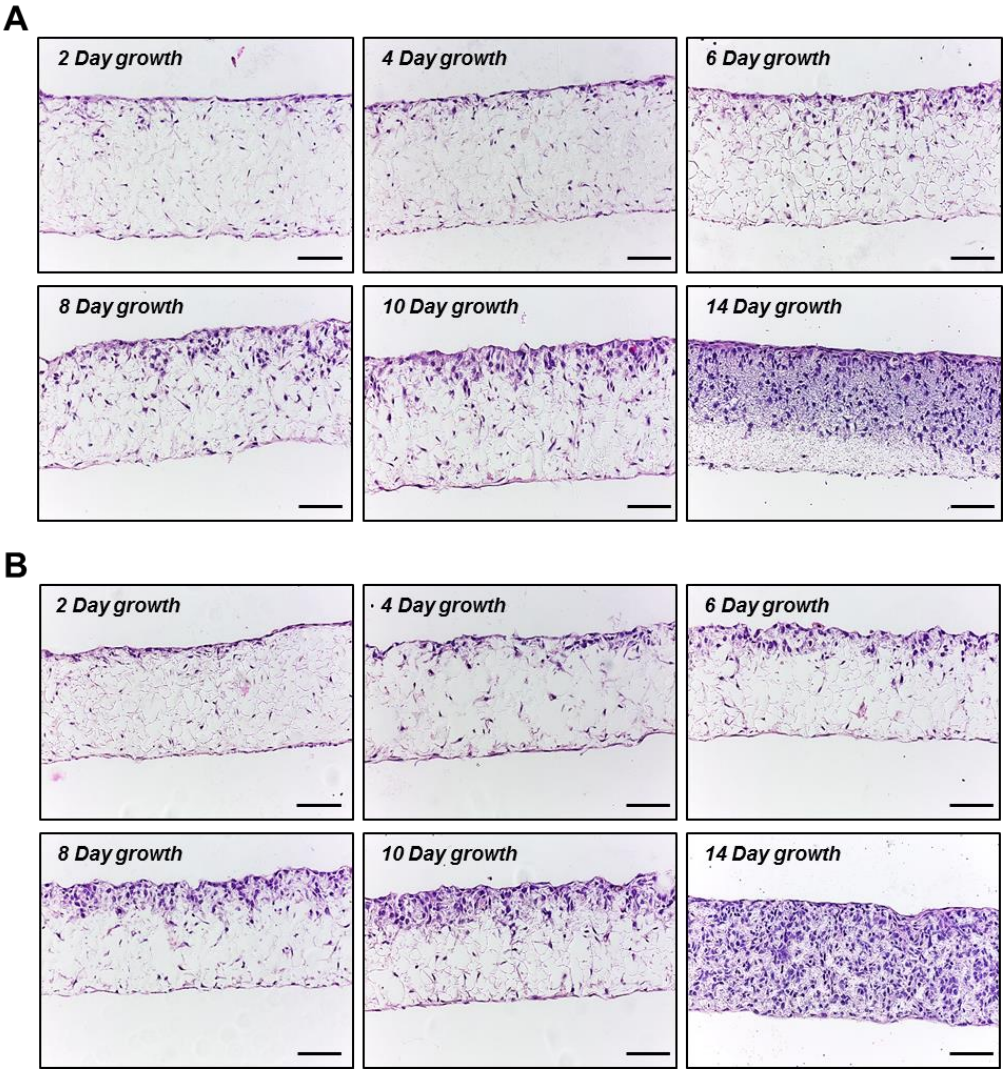

Figure 4.4: *H&E staining of both WT (A) and DN (B) HaCaT cells in Alvetex® co-cultures at 2, 4, 6, 8, 10 and 14 day time points post HaCaT seeding. Scale bars = 100 µm.*

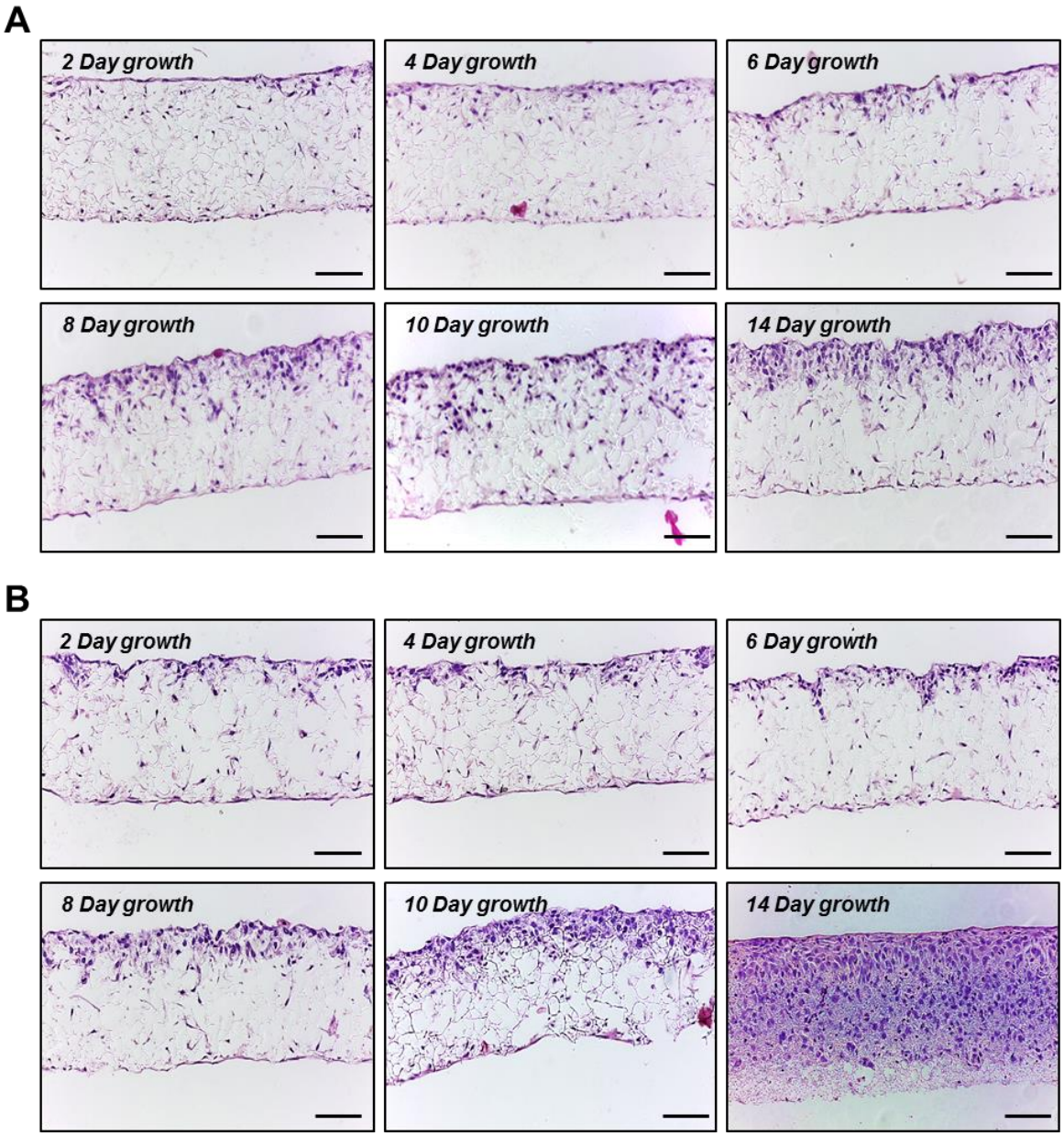

Figure 4.5: *H&E staining of both WT (A) and DN (B) HaCaT cells within Strata® co-cultures at 2, 4, 6, 8, 10 and 14 day time points post HaCaT seeding. Scale bars = 100 µm.*

Figure 4.4 displays both WT and DN HaCaT cells grown submerged in co-culture conditions across non-restrictive Alvetex® scaffold environments. It can be seen that both cell types are able to penetrate into the co-culture environment. WT HaCaT cells appear to display a 1-2 cell thick layer across the scaffolds surface from 6 d growth onwards. As no such layer was observed in the Alvetex only condition presented in Chapter 3, it can be suggested that fibroblast insertion may be creating a more restrictive environment. However, the most obvious difference observed in cell penetration between WT and DN HaCaT cells in this co-culture system comes between 10 and 14 d time points. It appears that to the 10 d time point, both cells express similar penetration potentials, however,

upon experiment completion after 14 days, DN HaCaT cells appear to have migrated through the full scaffold region, whereas WT HaCaT cells appear to migrate only half way through the full length of the scaffold.

Data presented in *Figure 4.5* displays similar cell migration phenotypes as to that observed in non-restrictive co-culture conditions for both cell lines assessed. Initial cellular penetration for both WT and DN HaCaT cells appears to be reduced in comparison to the non-restrictive system, however, it again appears that the DN HaCaT cells were able to penetrate deeper into the scaffold at the 14 day time point in comparison to their WT HaCaT counterparts.

From this acquired data set alone, it is difficult to accurately assess WT and DN HaCaT penetration potential in both adapted co-culture systems due to the incorporation of a further fibroblast cell line. This makes it difficult to accurately select for keratinocytes or fibroblasts across the heterogeneous cell population using H&E staining alone. Due to this limitation, the use of immuno-fluorescence techniques was applied, in which staining for specific fibroblast markers and keratinocyte markers will allow the accurate quantification of HaCaT penetration into these 3D systems to be assessed. Sections from each time point were processed through immunofluorescence staining against keratin 14 (K14; keratinocyte marker) and vimentin (fibroblast marker). Images for the 14 day time points can be seen displayed in *Figure 4.6*, displaying a representation of how we differentiated between the fibroblast and HaCaT cells across the same culture environment.

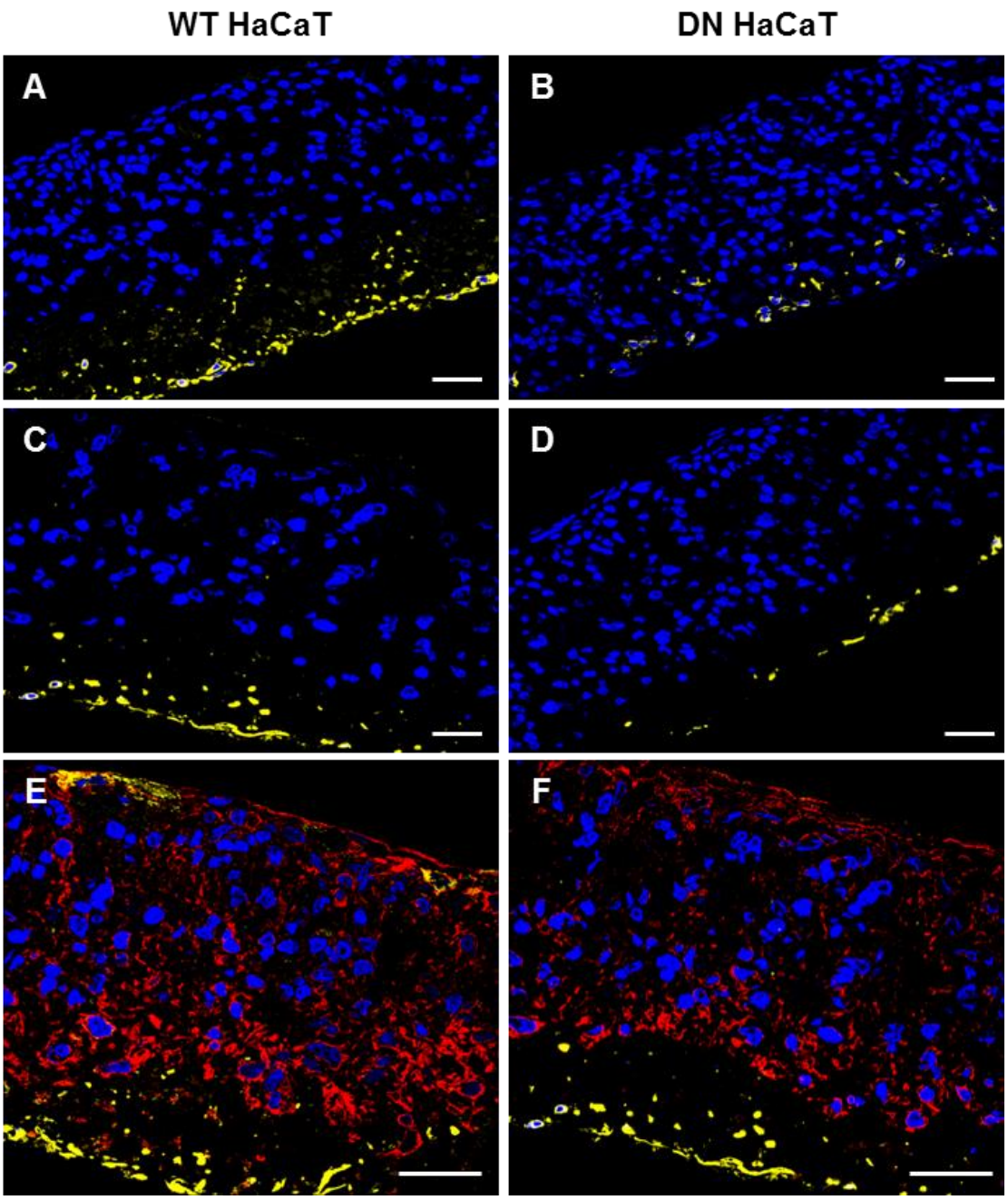

Figure 4.6: *Immunofluorescence staining of DAPI (blue) and vimentin (yellow) in Alvetex® (A, B) and Strata® (C, D) scaffolds for both WT and DN HaCaT cells at the 14 d time point. (E) and (F) display K14 (red)/vimentin (green) and DAPI co-staining in Strata® Scaffolds. Scale bar = 20 µm.*

Figure 4.6 highlights how K14 and vimentin staining allowed the specific localisation of HaCaT and fibroblast cells across the co-cultures. Interestingly, it is shown that when stained against vimentin, staining appeared to localise in front of the leading edge of HaCaT cells, across the opposite surface to that of seeding. When co-staining with K14, both WT and DN HaCaT cells are easily detected across the system. Regions of K14 positive staining appears to be distinct from that of vimentin staining, leading to potential

suggestions that as the HaCaT cells migrate through the co-culture environment, they may be pushing the fibroblast cells through the scaffold. This would account for the distinct vimentin staining observed across the leading edge of migrating HaCaT cells.

As shown in *Figure 4.6*, the use of vimentin and K14 counter staining in the co-culture models allowed both WT and DN HaCaT cells to be distinguished from the heterogeneous population of cells. Using this staining, cell penetration was assessed across each time point, with collated data displayed in *Figures 4.7* and 4.*8*.

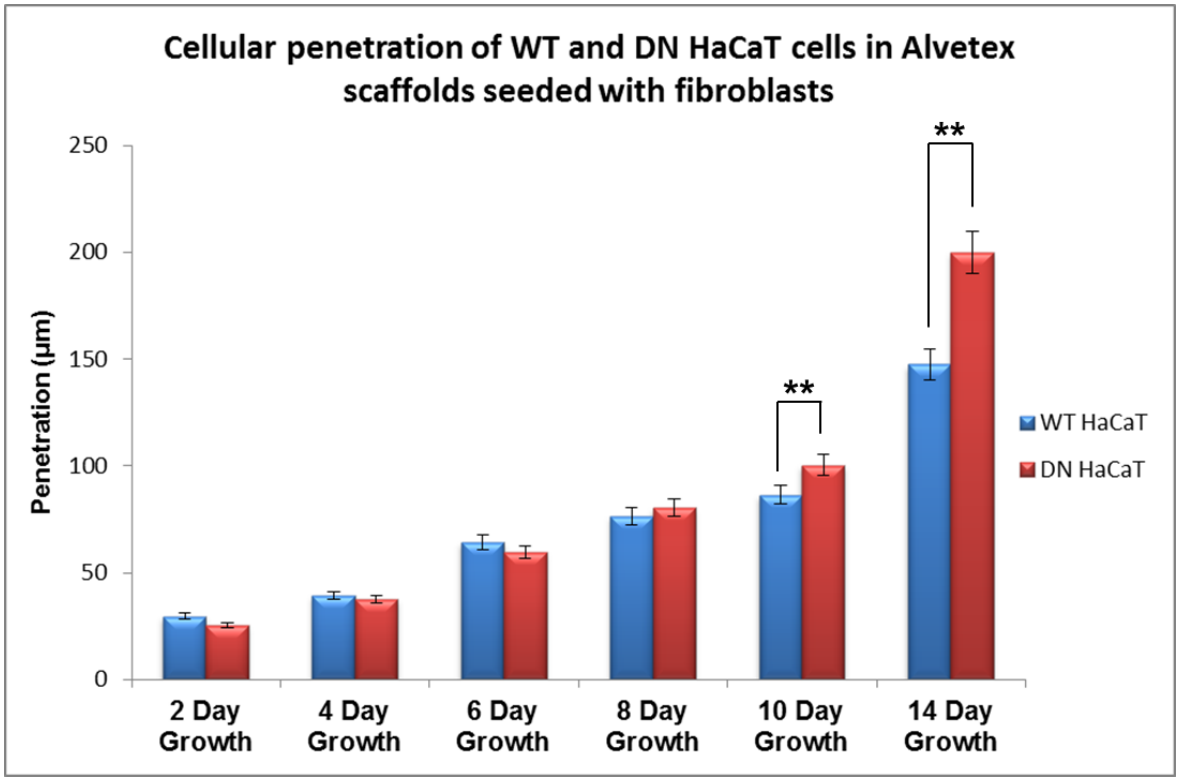

Figure 4.7: *Alvetex® Scaffold co-culture penetration between WT and DN HaCaT's over a 14 days period post-seeding. This data is collated from across three independent repeats.*

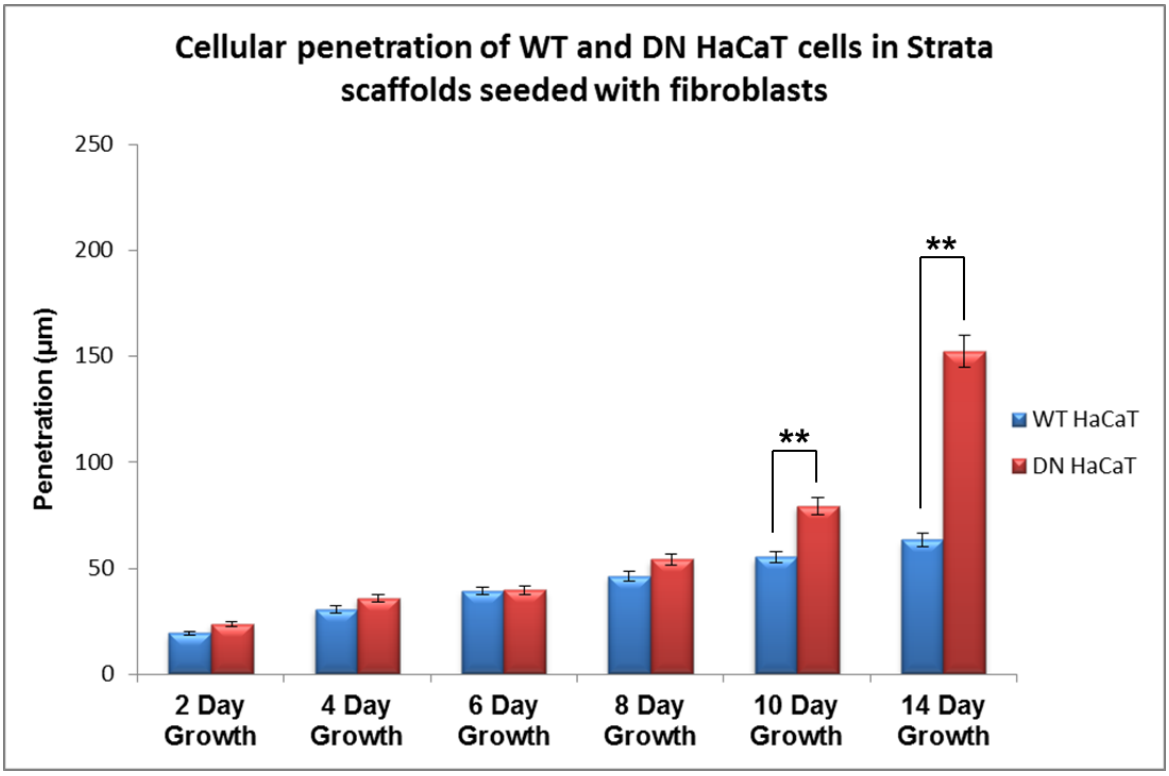

Figure 4.8 *Alvetex Strata® co-culture penetration between WT and DN HaCaT's over a 14 days period post-seeding. This data is collated from across three independent repeats.*

Data presented in *Figure 4.7* suggests that over the first 8 days of growth, differences in cell penetration appear to be minimal between WT and DN HaCaTs, displaying migration of up to ~100 µm into the scaffold. Upon reaching 10 and 14 day time points, it appears that the DN HaCaT cells display an increased penetration potential compared to that of the WT HaCaT cells, able to migrate the full length of the scaffold in the 14 day experimental set up. This migration potential is not emulated by the WT HaCaT counterparts, which appear to display a reduced migration speed through this co-culture environment. Upon statistical analysis using a student's t-test, significant differences were only observed between the WT and DN HaCaT penetration at 10 and 14 d time points when $p \leq 0.005$. This data therefore suggests that the insertion of fibroblast cells into the non-restrictive Alvetex® Scaffold reduces the penetration potential of WT HaCaT cells compared to their *LINC* disrupted counterparts.

Alongside this, data presented in *Figure 4.8* suggests that again, there is little difference between the WT and DN HaCaT cells penetration up to the 8 day time point, after which, the DN HaCaT cells appear to display an increased penetration potential to that of the WT HaCaT cells. Interestingly however, neither cell line was able to migrate through the complete 200 µm length of the co-culture scaffolds, suggesting that even in

this more restrictive scaffold environment, the fibroblast inclusion appears to reduce penetration potential of both cell lines compared to that of the non-restrictive scaffold environment. Further statistical analysis using a student's t-test helps to show that the differences observed in scaffold migration across the 10 and 14 day time points were statistically significant where $p \leq 0.005$.

As the collated data presented thus far suggests that the incorporation of fibroblasts into Alvetex® Scaffold and Alvetex® Strata environments appears to display clear differences between DN and WT HaCaT cell penetrations potential, we further compared migration potential across each scaffold between co-culture and single culture conditions conducted in chapter 3. The aim of this direct comparison is to more accurately assess the effects of fibroblast co-cultures on the migration potential of each cell line in each scaffold system, as displayed in *Figure 4.9*.

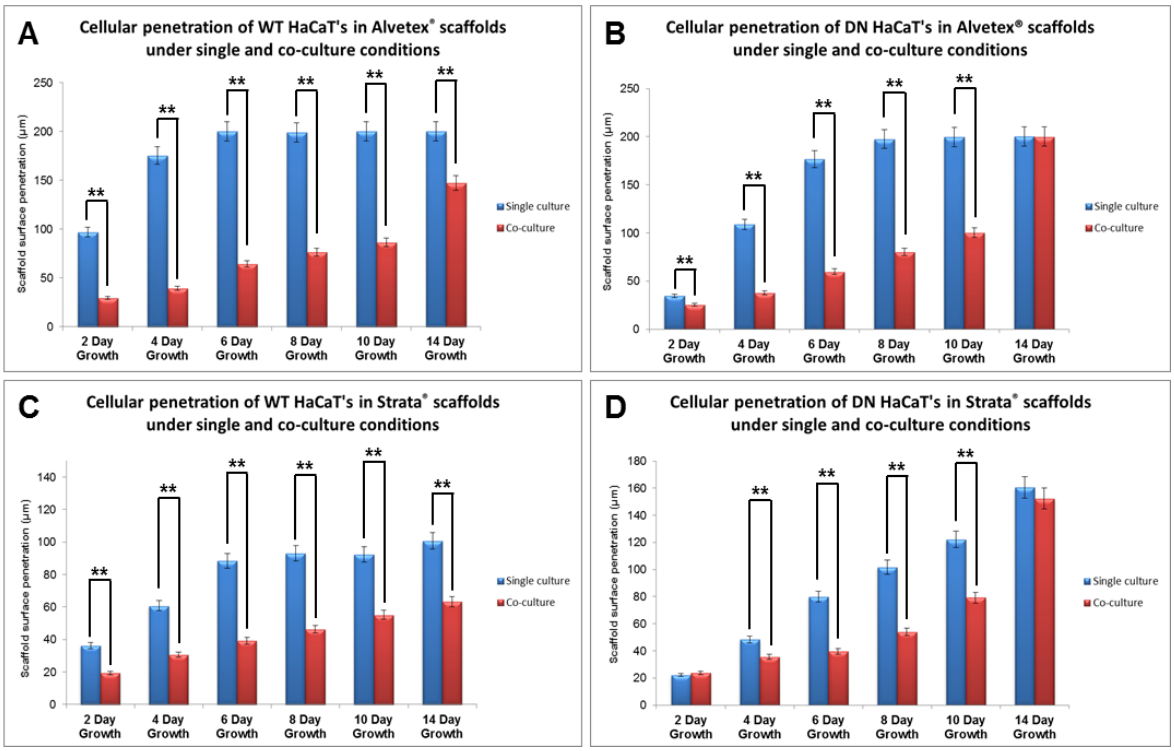

Figure 4.9: *Differences between WT and DN HaCaT penetration through Alvetex® Scaffold and Alvetex® Strata scaffolds, under single and co-culture conditions over a 14 days period post-seeding.*

Data presented in *Figure 4.9* suggest the introduction of fibroblast co-culture systems appears to have more drastic effects on WT HaCaT penetration in both restrictive and non-restrictive scaffold systems. The data presented in (A) highlights WT HaCaT penetration in non-restrictive scaffolds under single and co-culture conditions. These

experimental conditions present the most drastic differences observed, suggesting that the fibroblast introduction reduces migration speeds through the scaffold across each time point assessed. (B) Displays the same experimental set up with the DN HaCaT cells, showing again that the fibroblast introduction to non-restrictive scaffolds appears to reduce penetration speed. However, the DN HaCaT cells are able to penetrate the through the full length of the scaffold, suggesting that these cells may present a migration advantage over their WT counterparts. Data presented in (A) and (B) helps to suggest that the introduction of fibroblast cells to the non-restrictive scaffolds increases its restrictiveness to cellular migration. This could arise due to either the fibroblast cells or their ECM secretions adding a further layer of migration inhibition, forming a 'barrier' through which the HaCaT cells will have to migrate in order to penetrate further into the material.

Data presented in (C) and (D) highlights once again, that fibroblast introduction into restrictive scaffold environments appears to reduce migration potential for both WT and DN HaCaT cells compared to their single culture counterparts. Interestingly however, it can be seen that for DN HaCaT cells, the 2 day and 14 day time points appear to be similar between single and co-culture conditions. This suggests that even though significant differences between single and co-culture conditions are observed across the intermediate time points, DN HaCaT migration behaviour remains the same at the experimental beginning and end time points. This could suggest that these DN HaCaT cells may present adaptive behaviours, in which over time and exposure to the restrictive and potentially damaging environment, cells may adapt to their surroundings, and be able to migrate at a faster rate. However, to fully conclude this, further investigation would be required.

All of the differences observed were statistically quantified using a student's t-test where $p \leq 0.005$, suggesting statistical differences exist in migration potential between WT and DN HaCaT cells across both scaffold environments for single and co-culture systems.

4.3.2 DN HaCaT cells display increased cellular stacking across the surface of co-culture Strata Scaffold systems.

Alongside differences in cell migration through the restrictive and non-restrictive scaffold systems upon co-culture formation, further investigations aimed to assess whether the introduction of fibroblast cells to the co-culture environments would affect the

morphology of cells stacking across surface scaffold regions for WT and DN HaCaT cells. Previous investigations suggested that the DN HaCaT cells displayed cellular stacking above the restrictive strata scaffold during air-liquid interface induction, with suggestions that the restrictive nature of the scaffold, coupled with cell polarity defects lead DN HaCaT cells to develop this phenotype. This experimental set up was therefore repeated with co-culture systems in both restrictive and non-restrictive scaffolds.

HDF cells were cultured in both scaffold environments for 14 days as described previously, followed by seeding of WT and DN HaCaT cells, respectively. These HaCaT cells were grown submerged in culture for 4 days, followed by a further 8 days grown at the air-liquid interface. Images for both WT and DN HaCaT cells grown under these conditions can be seen displayed within *Figure 4.10*.

As suggested in *Figure 4.10*, DN HaCaT cells grown in non-restrictive co-culture conditions do not appear to undergo any cell stacking across surface regions (B), whereas WT HaCaT cells appear to produce a 1-2 cell thick layer (A). In contrast to this, restrictive Strata Scaffolds appear to induce no cellular stacking for the WT HaCaT cells (D), but a drastic cellular accumulation across the surface for DN HaCaTs (C), displaying cellular shape changes alongside cell flattening across the cell layer. Under closer observation, DN HaCaTs appear to display a layer of ~3-4 cells presenting a more cuboidal like cellular shape, with a flattened layer of 2-3 cells situated on top of these cells in the restrictive Strata co-culture conditions (E).

To further quantify these observed differences, the size of this cellular accumulation was analysed above the scaffold, with measurement techniques alongside collated data displayed in *Figure 4.11*.

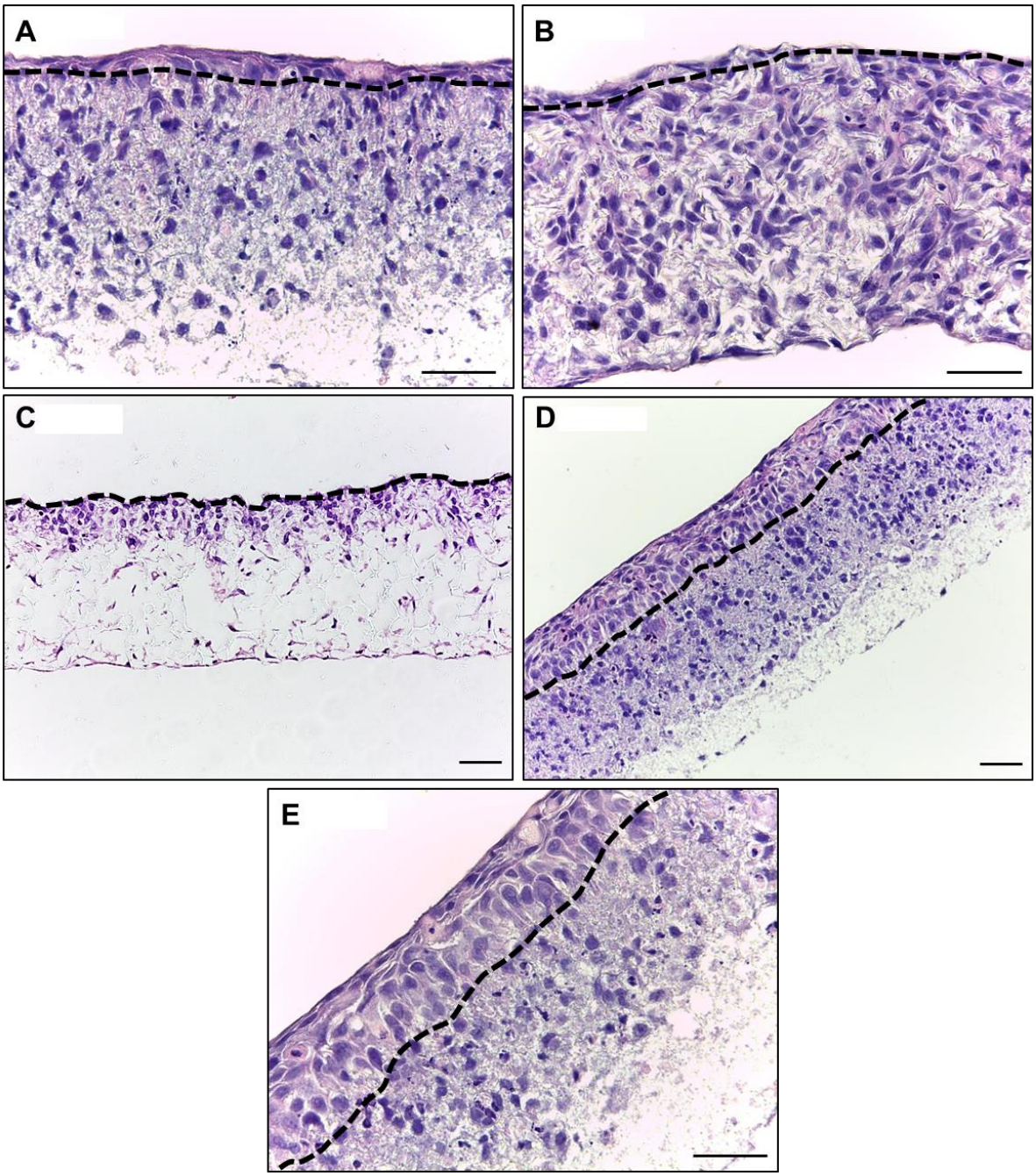

Figure 4.10: *H&E stained Alvetex® and Strata® co-culture scaffolds after 8 days at the air-liquid interface. Images (A) and (B) display WT and DN HaCaT cells, respectively in Alvetex® Scaffolds. Images (C) and (D) represent DN and WT HaCaT cells in Strata® Scaffolds respectively. (E) Displays increased magnification of DN HaCaT cells in Strata® scaffolds. Scale bars = 50 µm.*

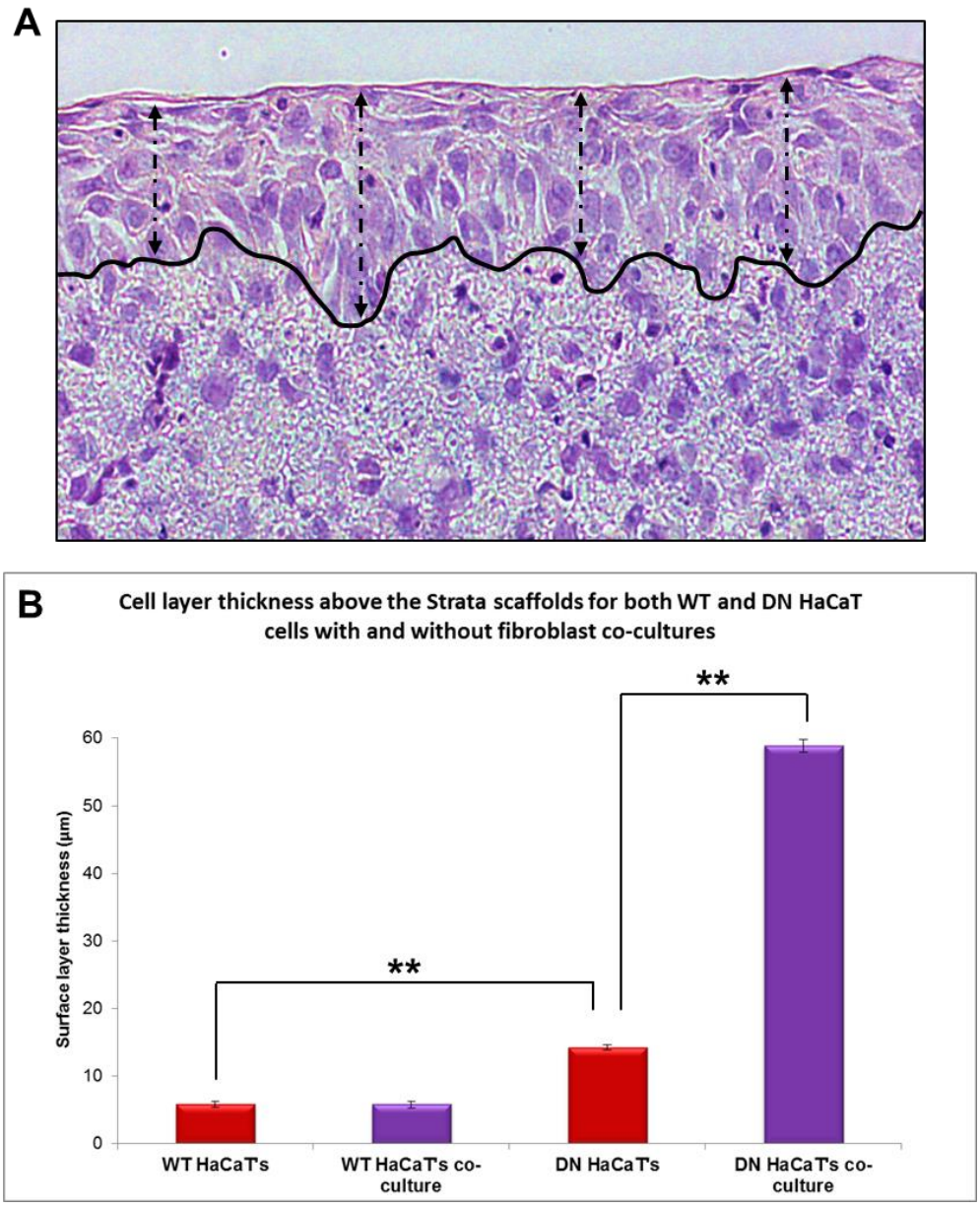

Figure 4.11: *(A) displays measurement technique used for the assessment of cellular stacking above the scaffolds seeding surface. Measurements were taken using the Image J software as described in chapter 3. (B) Represents graphical data of 375 measurements across 3 repeats, comparing cell surface thickness between WT and DN HaCaT cells in Strata® scaffolds under single and co-culture conditions.*

Data presented in *Figure 4.11* suggests that the calculated thickness for DN HaCaT cells in single culture Strata® Scaffolds were 14 µm, whereas the calculated thickness in the co-culture system was shown to be ~59 µm. This suggests that the introduction of fibroblasts into restrictive scaffold systems stimulated an increased surface thickness of nearly five times. Further statistical quantification using a student's t-test suggests this observed difference is statistically significant where $p \leq 0.005$, showing that fibroblast introduction

stimulates an increase in cellular stacking across the scaffold surface. In contrast, it can be seen that no significant difference between the cellular stacking above Strata® Scaffolds can be seen for the WT HaCaT cells, between both single and co-culture conditions. A further statistically significant difference is further observed between WT and DN HaCaT cells grown on single culture systems using a student's t-test where $p \leq 0.005$, suggesting the DN HaCaT cells display an increased thickness of cell stacking.

The data presented in this section reveals that the introduction of fibroblasts to the 3D scaffold systems appears to affect the cellular stacking potential of DN HaCaT cells more than that of the WT HaCaT cells. The observed results could represent the effects of *LINC* disruptions stimulating a loss of cellular polarity in the DN HaCaT cells. This loss of directed cell migration, may allow the cells to migrate more freely in all directions without the effects of contact inhibition reducing cell stacking potential. Further to this, an increased cell crowding effect could also be an important factor in the observed phenotype. As both keratinocytes and fibroblasts colonise the surface voids in the material, the limited space available may for cell to migrate and proliferate in the only direction available, up. However, due to data from WT HaCaT observations in non-restrictive co-cultures displaying no cell stacking, suggestions as to alternate signalling cues or environmental factors can be implicated due to the cellular stacking observed under co-culture conditions in the same scaffold, similar to that observed in keratinocyte differentiation and stratification.

4.3.3 WT and DN HaCaT cells display varied expression patterns of differentiation markers across single and co-culture systems.

4.3.3.1 Both WT and DN HaCaT cells express similar basal layer markers across both single and co-cultures scaffold systems.

To further investigate the observed stacking phenotypes displayed thus far, subsequent experimentation aimed to assess whether differences in known skin differentiation marker expression were present between the single and co-culture conditions. These investigations will therefore discern whether this observed cell stacking is indeed a result of differentiation as suggested in Chapter 3.

Staining for the basal skin marker (K14) was initially used to assess whether any differences in expression could be seen across restrictive and non-restrictive, single and co-cultured conditions. This staining can be seen displayed in *Figures 4.12 and 4.13*.

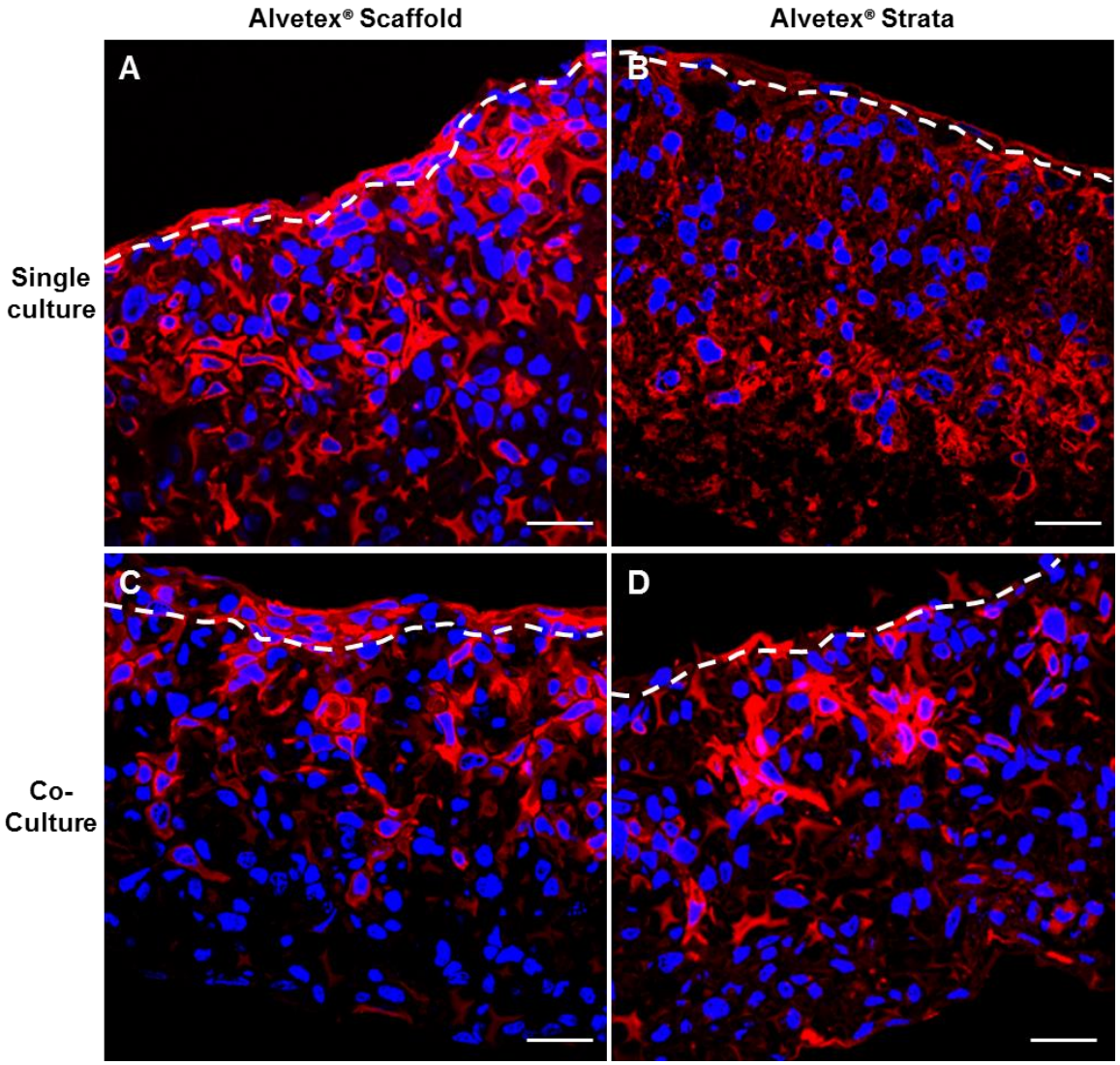

Figure 4.12: *Immunofluorescence staining of WT HaCaT cells for K14 (red) and DAPI (blue) across single (A, B) and co-culture (C, D), Alvetex Scaffold (A, C) and Alvetex Strata (B, D) systems. Scale bars = 25 µm.*

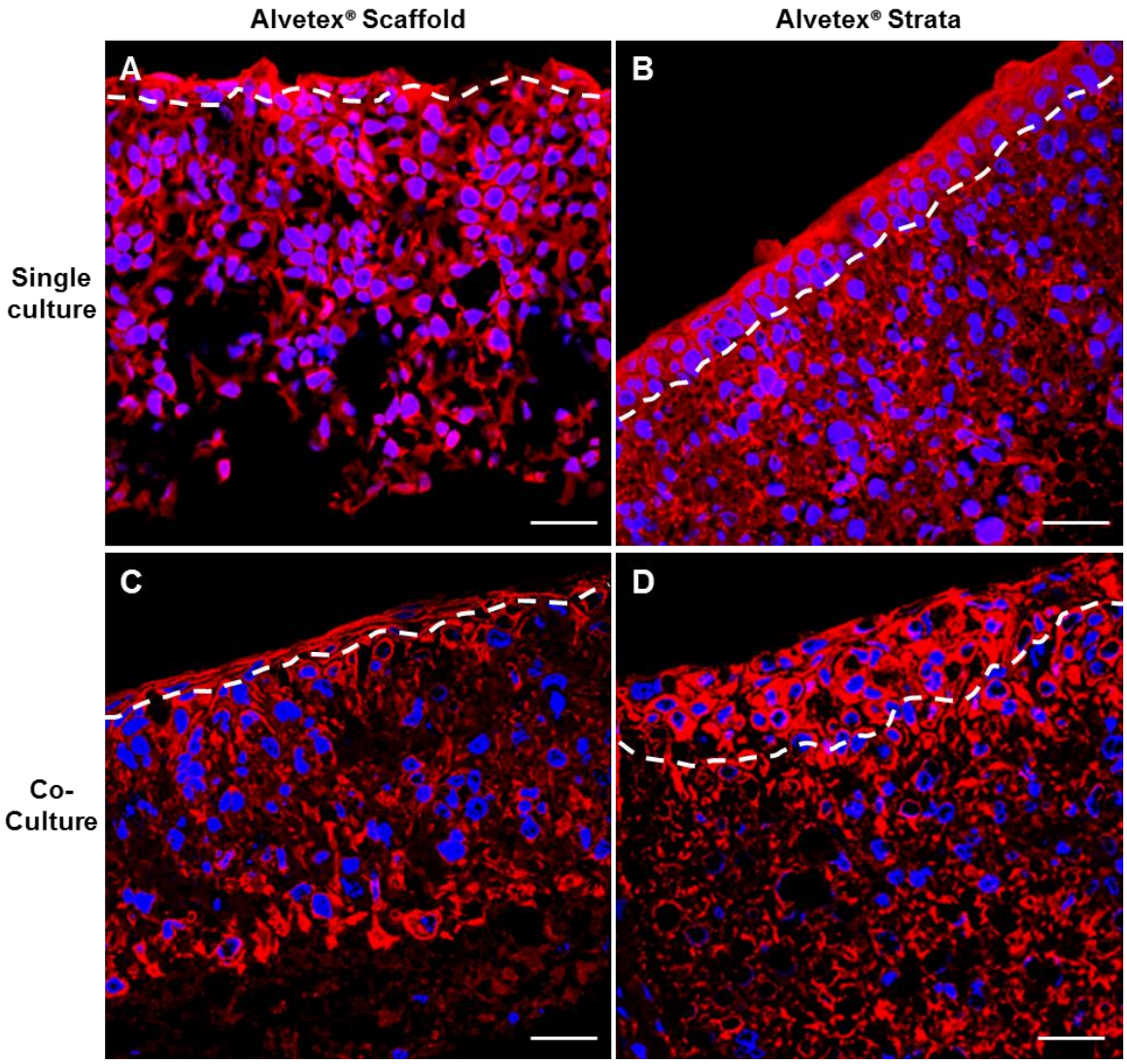

Figure 4.13: *Immunofluorescence staining of DN HaCaT cells for K14 (Red) and DAPI (Blue) across single (A, B) and co-culture (C, D), Alvetex Scaffold (A, C) and Alvetex Strata (B, D) systems. Scale bars = 25 µm.*

As displayed in *Figure 4.12*, WT HaCaT cells appear to show positive staining for K14, helping to distinguish these keratinocytes from the fibroblast cells in the co-culture. Alongside this, K14 expression appears to be reduced in Strata single culture conditions. However, accurate indications as to protein levels across individual cells cannot be ascertained through immunofluorescence alone, meaning further protein analysis through techniques such as western blotting would be required to verify this.

The data presented in *Figure 4.13* suggests the DN HaCaT cells also stain positively for the K14 basal marker. Within the Alvetex scaffolds, expression appears uniform across all scaffold regions, in contrast however, cells across surface regions of restrictive Strata scaffolds appear to present an increased expression of K14 in both single and co-culture conditions.

Through this investigation it has been shown that limited variation in expression of K14 is observed between WT and DN HaCaT cells under single and co-culture. This suggests that disruptions to the *LINC* complex expressed by the DN HaCaT cells do not appear to limit the expression profile of K14 markers.

4.3.3.2 LINC disruptions stimulate increased cell differentiation across restrictive scaffold surface regions.

To expand on previous findings through K14 staining, following investigations aimed to assess whether cellular differentiation is occurring across the layer of observed cell stacking found in the restrictive strata scaffolds. To do this, the differentiation marker chosen was K10, allowing the detection of early keratinocyte differentiation from a basal like phenotype, to that closely resembling regions of the stratum spinosum. This resulting staining can be seen displayed in *Figure 4.14 and 4.15*.

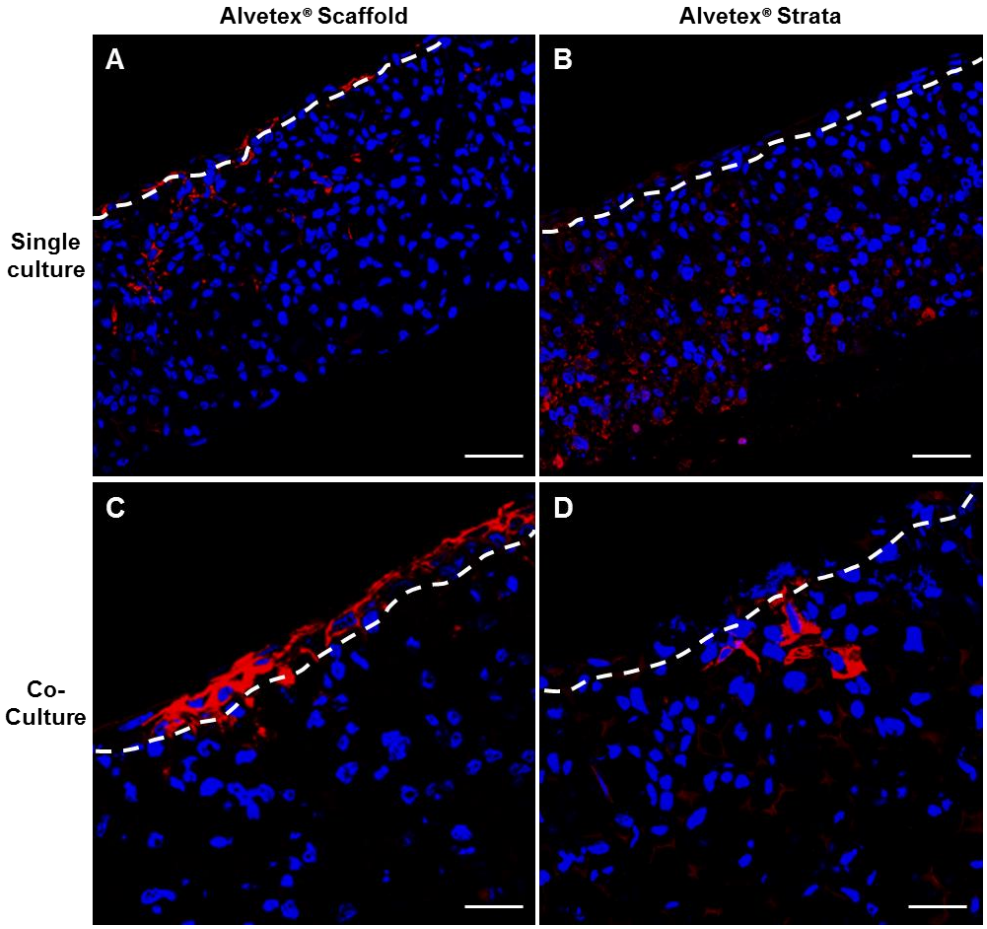

Figure 4.14: *Immunofluorescence staining of WT HaCaT cells for K10 (red) and DAPI (blue) across single (A, B) and co-culture (C, D), Alvetex Scaffold (A, C) and Alvetex Strata (B, D) systems. Scale bars = 25 µm.*

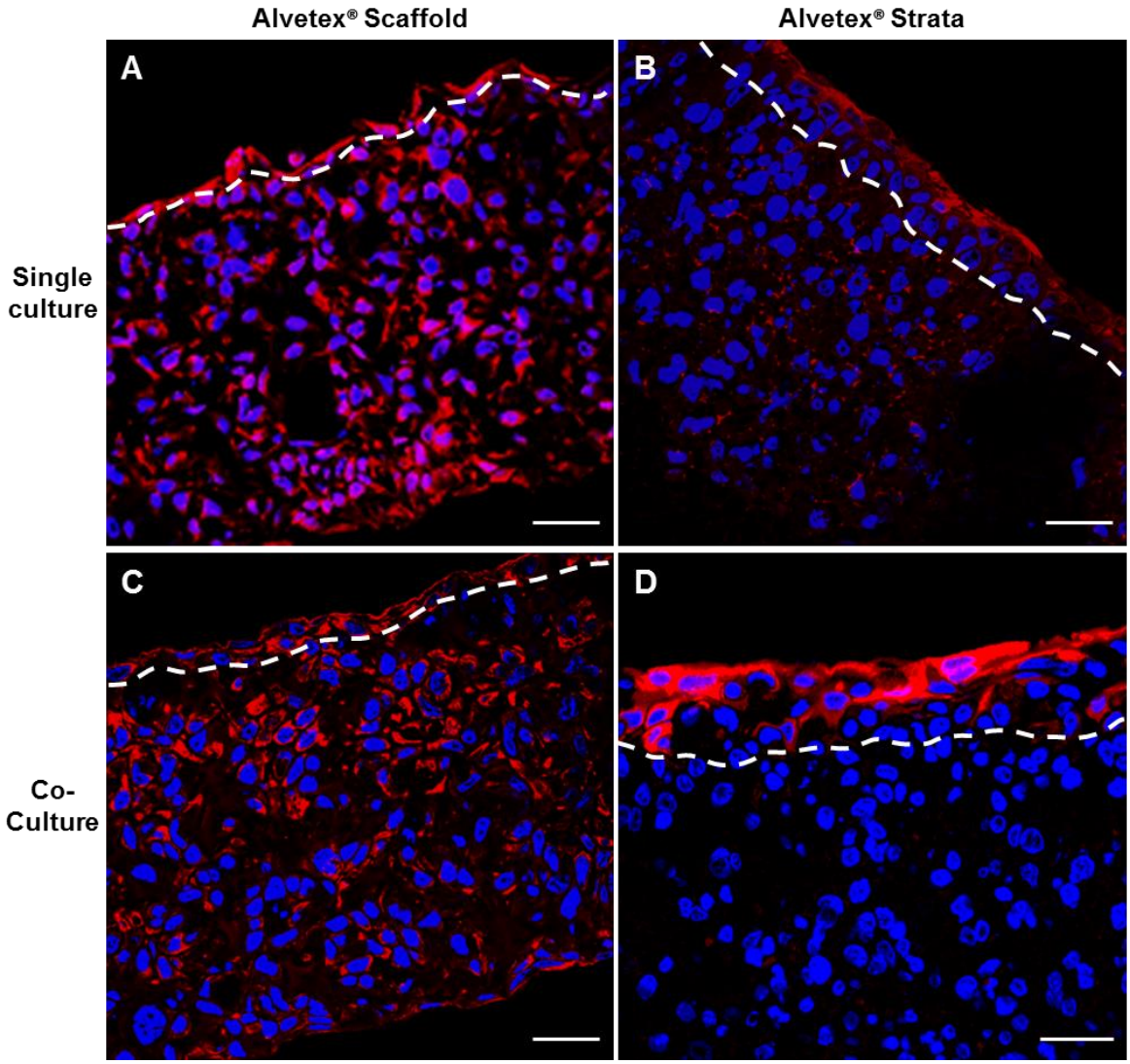

Figure 4.15: *Immunofluorescence staining of DN HaCaT cells for K10 (red) and DAPI (blue) across single (A, B) and co-culture (C, D), Alvetex Scaffold (A, C) and Alvetex Strata (B, D) systems. Scale bars = 25 µm.*

The data presented in *Figure 4.14* suggests a low level of K10 expression can be seen across both single culture systems and the Strata co-culture system, suggesting the WT HaCaTs across these conditions are not undergoing early stages of cellular differentiation, often associated with skin stratification. Interestingly however, positive K10 staining is presented across the surface cell layer in the Alvetex scaffold co-culture system (C), suggesting that these cells are undergoing differentiation. This therefore helps to suggest that in the non-restrictive scaffold environment, fibroblast presence appears to stimulate cellular differentiation under an air-liquid interface.

Alongside these observations, *Figure 4.15* displays further variations in K10 expression between experimental conditions. Initial observations suggest DN HaCaT cells display K10 positivity at varying degrees throughout the non-restrictive Alvetex scaffold under

both single and co-culture conditions. It can be further seen that in the more restrictive Strata Scaffold systems, K10 expression appears to be localised across the surface layer of cells where cellular stacking was previously observed. This observed signal appears to be further increased across the fibroblast co-culture condition in restrictive scaffolds, suggesting that the increased thickness of cell stacking could be a result of increased early stage cellular differentiation as a result of fibroblast influence.

Thus far investigations have shown that under varying experimental conditions, both the DN and WT HaCaT cells express early stage differentiation markers. For the WT HaCaT cells, this could derive from the associations established between keratinocytes and fibroblasts in the non-restrictive scaffold environments. Whereas for the DN HaCaT cells, the region of highest K10 expression are observed across surface regions of restrictive scaffolds, displaying high levels of cellular stacking. The introduction of fibroblast cells to these restrictive scaffolds appeared to stimulate an increase in K10 expression in comparison to single culture counterparts. However, whether the expression of early differentiation markers by DN HaCaT cells in regions of increased cellular stacking is a causative or resulting factor of the cell stacking phenotype still remains unknown.

4.3.3.3 Expression levels of YAP and E-cadherin correlate within regions of early differentiation for both WT and DN HaCaT cells.

One final avenue of investigation across these co-culture systems was to assess whether levels of E-cadherin and YAP expression are altered between WT and DN HaCaTs in restrictive and non-restrictive systems. YAP is a crucial component of the Hippo pathway, responsible for cellular proliferation and contact inhibition, suggesting that increased YAP signalling could indicate regions of altered contact inhibition. E-cadherin on the other hand was previously shown in Chapter 3 to display higher expression in 2D DN HaCaT cells, but equal levels between DN and WT HaCaT's in 3D systems. Experimentation therefore aims to assess whether further expression variation is observed upon fibroblast introduction to both restrictive and non-restrictive 3D culture systems.

Under the same experimental conditions, double staining against YAP and E-cadherin was conducted as described in the methods. Resulting images from both WT and DN

HaCaT cells across each experimental condition can be seen displayed in *Figures 4.16* and *4.17*.

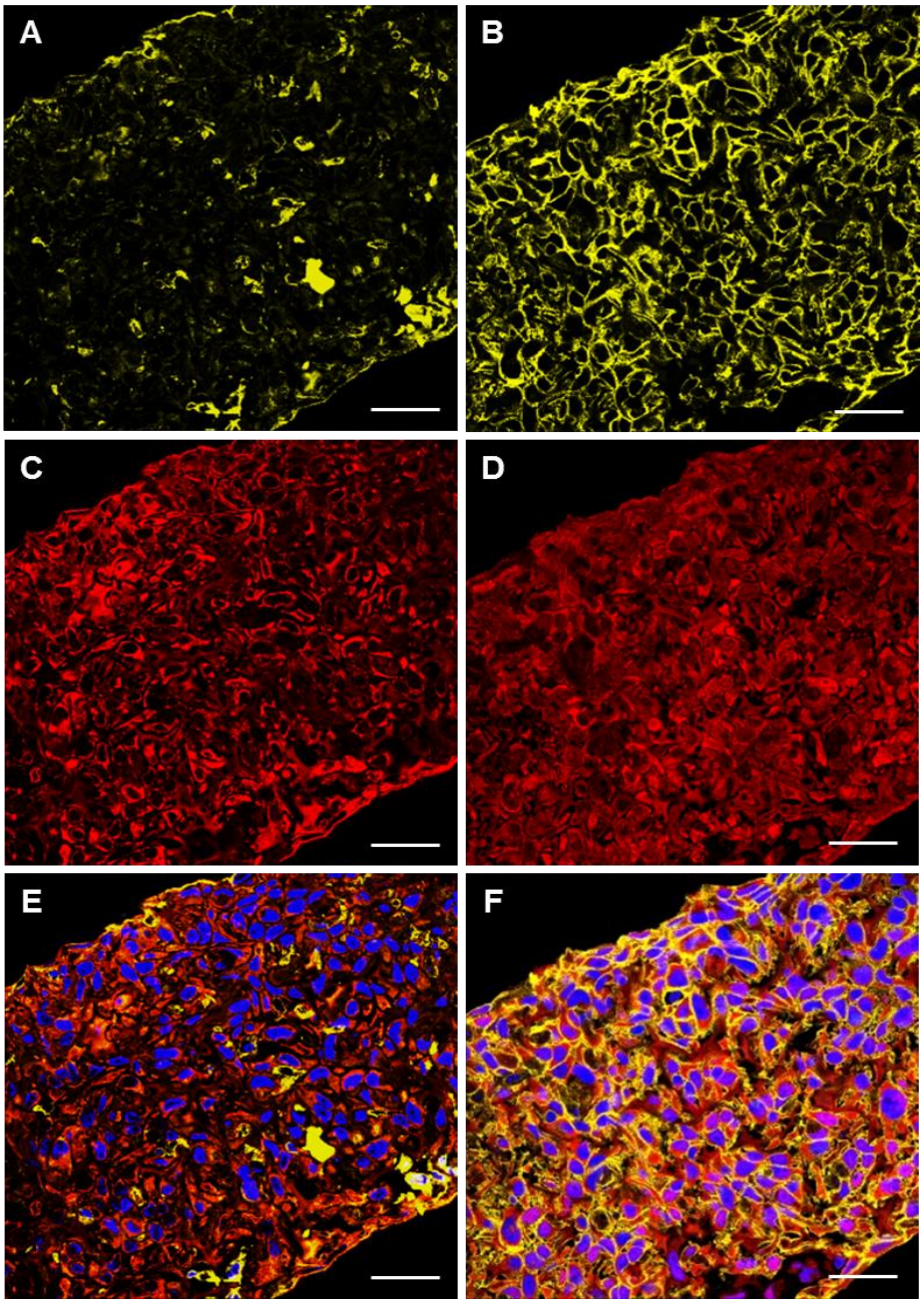

Figure 4.16: *Immunofluorescence staining of both WT (A, C and E) and DN (B, D and F) HaCaT cells for E-cadherin (Yellow), YAP (Red) and DAPI (Blue) across co-culture Alvetex® Scaffold systems. Scale bars = 25 µm.*

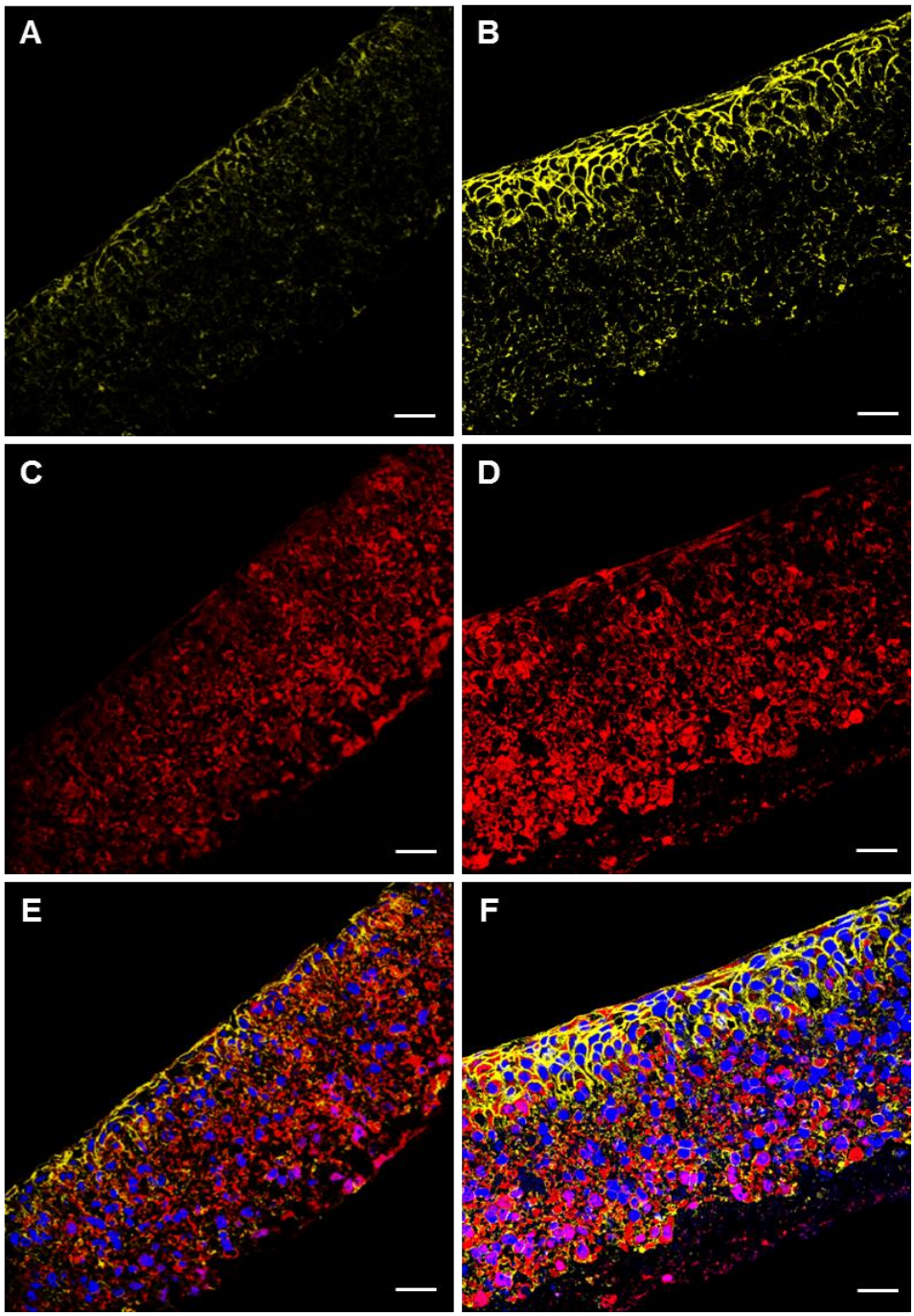

Figure 4.17: *Immunofluorescence staining of WT (A, C and E) and DN (B, D and F) HaCaT cells for E-cadherin (Yellow), YAP (Red) and DAPI (blue) across co-culture Strata® scaffold systems. Scale bars = 25 µm.*

The data provided in *Figure 4.16* suggests that the WT HaCaT cells express reduced levels of E-cadherin expression compared to their DN counterparts. Alongside this, YAP expression appears to remain consisted across the full length of scaffold for both WT and DN HaCaT cells; however the DN HaCaT cells appear to display an increased nuclear accumulation in comparison to WT cells, however, due to these images representing Z

slices through the scaffolds, this cannot be fully concluded from these images due to it being unknown whether we are viewing peripheral or central cell areas. In contrast however, data presented in *Figure 4.17* suggests that in restrictive Strata® Scaffold co-cultures, E-cadherin expression appears to be much weaker for WT HaCaT cells in comparison to the DN HaCaT's. Both cell lines express an accumulation of E-cadherin staining across the seeding surface of the scaffolds, with DN cells expressing higher levels. Of further interest is the co-staining with YAP in both WT and DN HaCaT cells. In regions of high E-cadherin expression, YAP expression appears to be reduced, seen most clearly in the DN HaCaT cells. In these cells, regions of intense E-cadherin staining further correlated with regions of increased cell stacking and differentiation. To fully assess this observed relationship between YAP and E-cadherin expression however, further protein quantification would need to be conducted through the use of western blot analysis.

This investigation has aimed to assess whether WT and DN HaCaT cells display any variations in YAP or E-Cadherin expression across the co-culture restrictive and non-restrictive models. Through the use of immunofluorescence analysis, it is shown that WT HaCaT cells appear to express reduced levels of E-cadherin across both restrictive and non-restrictive co-culture systems compared to that of DN HaCaT cells. With further analysis suggesting that the observed accumulation of E-cadherin across the restrictive scaffold surface, correlated not only with regions of high cell stacking behaviour, but also with reductions in YAP expression. This observation suggests that the observed cell differentiation displayed by the DN HaCaTs in *Figure 4.17* may be a result of complex interplay between cellular adhesion, cell proliferation and contact inhibition. However, to fully validate these observations, total protein expression would need to be assessed through western blotting techniques, as immunofluorescence analysis only provides an indication as to expression levels.

4.4 Summary of Experimental Findings.

This chapter has sought to investigate the effects of *LINC* complex disruptions on cellular migration in more *in vivo* like 3D culture environments. To implement this, a sub-culture of HDF cells were inserted into both Alvetex® Scaffold and Alvetex® Strata. The insertion of dermal fibroblasts into these scaffold environments could potentially alter the chemical composition of the materials surface due to the production of ECM components by the fibroblast cells based on environmental stimuli [396]. This new chemical environments could potentially stimulate variations in cellular migration potential due to further suggestions as to chemical cross talk between endogenous keratinocytes and fibroblasts in *in vivo* skin environments [399]. Further aims in this chapter were to assess the effects implementing this co-culture system into both scaffold environments on keratinocyte behaviour across surface scaffold regions, more specifically, whether fibroblast incorporation was able to alter cell packing and keratinocyte differentiation potential. It has been well documented in the literature that fibroblast inclusion into keratinocyte cultures increases differentiation potential due to the cross talk between each cell line [422], with current evidence further suggesting that mesenchymal-derived signals are essential for correct epidermal morphogenesis, homeostasis and differentiation [423]. We therefore hypothesise that inclusion of these HDF cells will stimulate altered cell stacking phenotypes to those observed in Chapter 3.

4.4.1 Fibroblast inclusion into both Alvetex® Scaffold and Alvetex® Strata environments reduces migration potential of WT, but not DN HaCaT cells.

Initial investigations were able to show that the human dermal fibroblast cells are able to colonise all regions of both the space-restrictive and non-restrictive scaffolds environments within a 14 d period. The ability of these fibroblast cells to migrate through the entire length of both the restrictive and non-restrictive environments comes as no surprise due to their mesenchymal cell origin. Mesenchymal cells often adopt spindle shaped morphologies, dependant on integrin mediated adhesion dynamics and high cytoskeletal traction forces, resulting in an increased plasticity to migration in more challenging environments [424, 425]. This is further exemplified through the classic

epithelial to mesenchymal transition (EMT) mechanism employed by many high-grade cancers to migrate from the tumour source, and through surrounding tissue to other bodily areas [426]. The exchange of E- for N- cadherin subtypes alongside protein expression variations of keratin proteins (often associated with epithelial cells) for vimentin allows cancer cells to alter their epithelial cell-cell adhesion junction composition to a more mesenchymal form, aiding the migration through surrounding tissues [427, 428].

Analysis of the scaffolds using standard histology stains highlighted the presence of weak eosin staining across the scaffold surface regions, potentially denoting ECM protein deposition in *Figure 4.3*. This staining could suggest the deposition of ECM components such as collagen, which could in turn, stimulate alterations to behaviour of HaCaT cells within these 3D scaffold environments as it is well noted in the literature that *in vivo* like microenvironments and ECM composition are key to *in vivo* like development and differentiation of keratinocytes in *in vitro* skin equivalent models [429]. However, the eosin component of this staining technique only provides a general stain for certain ECM components. To further validate whether fibroblast cells are indeed secreting ECM into their surrounding environments, further more specific staining techniques can be used including Masson's trichome and Herovici staining techniques, allowing the differentiation between cells and ECM, alongside both young and mature collagen, respectively [430] [431]. Investigations could further employ the use of immunofluorescence analysis for targeted ECM components to increase our understanding of the ECM composition.

Following the establishment of a fibroblast sub-culture, both WT and DH HaCaT cells were seeded onto both space-restrictive and non-restrictive scaffold environments for 14 days in submerged growth. Initial observations of the vimentin staining (used to display fibroblast cells in the environment) displayed in *Figure 4.6,* suggested that that the fibroblast cells were collecting across the bottom of both scaffold environments. When co-stained with K14, it was further shown that this accumulation of vimentin staining can be seen to localise in front of the leading edge of HaCaT cells, providing potential suggestions that both HaCaT cells lines may be physically pushing the fibroblast cells deeper into the scaffold during their migration.

As the use of both K14 and vimentin staining in co-culture system allowed the accurate identification of HaCaT cells localisation in the scaffold environments, migration analysis was conducted to assess penetration potential between WT and DN HaCaT cells. The collated data presented in *Figures 4.7* and 4.*8* helps to show that in both scaffold systems, DN HaCaT cells display an increased penetration potential over the 14 day investigation. It was further shown that the only significant differences in penetration potential between

WT and DN cells were found at the 10 d and 14 d time points across both co-culture scaffold systems.

Interestingly however, when compared with single culture migration assessed in Chapter 3, it can be seen that the incorporation of fibroblast cells to both scaffold environments stimulates a significant impact on 3D cellular migration potential (*Figure 4.9*). It can be seen that for the WT HaCaT cells, total migration potential in both restrictive and non-restrictive scaffold environments has been reduced through fibroblast incorporation, with cells being unable to migrate completely through the non-restrictive environments. This implies that the introduction of fibroblast cells to the system increases the restrictiveness of the Alvetex® Scaffold environment, more closely resembling those displayed by the space-restrictive Alvetex® Strata single cultures. The DN HaCaT cells also display a reduced migration potential during early time points in both scaffold environments. However, no significant differences between the final penetration distance displayed for both DN single and co-culture systems could be seen. This suggests that even though the ECM deposited by fibroblast cells potentially poses an increased restriction to cellular migration into the scaffolds, the DN cells are still able to migrate through these restrictive environments, potentially due to the increased nuclear malleability described in Chapter 3.

4.4.2 Inclusion of fibroblast cells into both scaffold systems stimulates increased cell stacking across surface regions for WT and DN HaCaT cells under air-liquid interface conditions.

Although it was difficult to distinguish between HaCaT and fibroblast cells through H&E staining alone, closer observations of surface scaffold regions of these co-cultures under air-liquid interface conditions (*Figures 4.10* and *4.11)* display obvious phenotypic differences between WT and DN HaCaTs. It can be seen that the WT HaCaT cells grown in Alvetex® Scaffold co-cultures display a small layer of flattened cells above the scaffolds surface, alongside a much more compact cellular morphology. In contrast, when placed into the space-restrictive Strata® Scaffold, a similar cellular flattening phenotype can be observed alongside an obvious reduction in cellular penetration. These observations suggest that the introduction of fibroblast cells into these systems may infer an increase in restrictiveness, alongside potential fibroblast-keratinocyte communication, resulting in stratification events similar to that found in the epidermis [437].

In comparison, the DN HaCaT cells displayed significant phenotypic differences under higher magnifications, including increased cell stacking alongside potential cell shape change associated with keratinocyte differentiation. It can be seen that in the Alvetex® Scaffold co-cultures, DN mutants colonise all regions of the scaffold, alongside producing a single cellular layer across the surface similar to that observed in WT cells in the same system. The DN HaCaT cells however, displayed an increased cellular accumulation across the surface, ~5-6 cells thick when grown in the more restrictive Strata® co-culture environments. Initial observations of this cellular stacking identifies cell shape changes to more cuboidal like phenotypes in regions closest to the scaffolds surface, slowly changing to a more flattened phenotype across cell surface regions. This observation could potentially arise from the fibroblast incorporation producing a more restrictive environment. Upon closer analysis, this increase in cellular stacking was increased fivefold compared to that found within the single culture systems.

4.4.3 DN HaCaT cells display increased expression of keratin 10, often associated with keratinocyte differentiation upon introduction to fibroblast co-culture systems.

Due to data thus far suggesting cell stacking is increased for DN HaCaT cells in space-restrictive co-culture conditions in comparison to single culture conditions, further investigation aimed to assess whether differences in keratin differentiation markers could be observed across each culture systems between WT and DN HaCaT cells under air-liquid interface conditions. Initial staining against the basal keratinocyte marker K14, displayed little variability between the WT and DN HaCaT cells grown in both the single and co-culture conditions (*Figures 4.12* and *4.13*). Due to these observations, it is suggested that the incorporation of fibroblast cells into each culture condition does not display any significant differences in K14 expression, suggesting that both HaCaT cell lines appear to maintain a basal like keratin expression profile [441]. However, as immunofluorescence analysis only provides an indication as to protein expression profiles, further western blotting would be needed to verify that no significant changes in K14 expression is observed between each cell line in each experimental condition.

In contrast however, when stained for K10, a known early keratinocyte differentiation marker, differential expression patterns can be observed between both WT and DN HaCaT cells across single and co-culture systems. It can be seen that for WT cells, K10

expression appears to be very low across each scaffold condition other than the non-restrictive co-culture system, in which specific K10 staining can be seen localised across the single layer of flattened cells situated across the scaffolds surface. This suggests that cells in these regions are undergoing early stages of the keratin differentiation as a result of fibroblast introduction. Interestingly, it is further suggested that the increased restrictiveness of the scaffold is a further contributing factor to this observed differentiation phenotype due to no presence of K10 staining observed in the non-restrictive scaffold co-culture.

In comparison, DN HaCaT cells displayed an overall increase in K10 staining across each experimental condition. It was shown that in both the single and co-culture non-restrictive Alvetex® Scaffold environments, K10 positive staining could be seen across all regions of the scaffold, however, its expression was not detected in every cell. Within the more restrictive Strata® Scaffold single and co-culture conditions, localised expression of K10 could be identified across the region of cellular stacking situated across the scaffolds surface. It is however difficult to discern whether this K10 accumulation across the scaffolds surface is in fact a causative or resulting factor of the cellular stacking, meaning that further experimental investigations would be required in order to validate potential mechanisms behind this observation. The results do however display some similarities to observations found in mice lacking the ABD domain of nesprin-2. In these mice, it was shown that significant epidermal thickening resulting from increased nuclear size in keratinocytes occurred, however no further alterations in differentiation or proliferation were shown [171]. These results suggest that the increased cell stacking and subsequent differentiation of DN HaCaT cells in co-cultured space-restrictive scaffolds may result from the *LINC* disruption altering nuclear shape. It was reported in Chapter 3 that the DN mutants display an increased nuclear height and that in restrictive Strata® Scaffolds, displayed cellular stacking. However, why the DN HaCaT cells display increased cellular stacking and differentiation potential in co-culture conditions is unknown thus far. It may result from further implications of *LINC* complex disruption to than that of maintaining NE integrity, which will require future investigation.

Final investigations aimed to assess the potential differences in E-Cadherin and YAP (Yes Associated Protein) expression across co-culture systems for both WT and DN HaCaT cells. E-Cadherin is a transmembrane protein involved in cell-cell adhesion whereas YAP is a crucial component of the Hippo signalling pathway, known control organ size through regulating cellular proliferation and apoptosis. YAP represents one of the mammalian orthologues of Yki (Yorki), which works in conjunction with TAZ (PDZ-binding motif) to bind several transcription factors upon activation [443]. YAP has also

been shown to regulate the expression of both Hoxa1 and Hoxc13 genes [444], known to regulate gene expression, morphogenesis and cellular differentiation.

From our staining's, it can be seen that in non-restrictive co-culture systems, WT HaCaT cells appeared to display low levels of E-cadherin staining across all scaffold regions, correlated with uniform YAP staining. In contrast however, the DN HaCaT cells appeared to display an increased E-cadherin expression, alongside a further increase in YAP expression (*Figure 4.16*). This increased E-cadherin expression for DN HaCaT cells could potentially infer the observed increased migration potential displayed in *Figures 4.7* and 4*.8.*

The data within this chapter suggests that introduction of fibroblast cells to the space-restrictive and non-restrictive scaffolds are able to stimulate a reduction in cellular migration potential for WT HaCaT cells. Alongside this, the incorporation of HDF cells appears to stimulate the formation of drastic phenotypic differences in DN HaCaT cells as to those observed in single culture conditions as a potential result of alterations in YAP and E-Cadherin expression profiles. This therefore helps to suggest that the formation of a simplified skin model through fibroblast incorporation has shown that DN HaCaT cells retain their increased migration potential, whilst WT HaCaT cells display a reduction in penetration potential. This presents further support to the hypothesis that increased nuclear malleability in DN HaCaT cells may be the contributing factor to their increased penetration potential through restrictive 3D environments.

It was difficult however to assess whether the loss of *LINC* connections affected the cellular responses to potential ECM components secreted by the fibroblast during co-culture conditions. To further investigate whether *LINC* disruptions present in DN HaCaT cells could alter cellular responses to these cues through loss of mechanotransduction mechanisms, application of fractionated western blot techniques allowing the separate assessment of both nuclear and cytoplasmic protein composition could be used. This would allow the assessment and quantification of transcription factor localisation in the cell such as YAP, helping to indicate whether cells are indeed sensing, and responding to external stimuli.

5. Assessing *LINC* protein roles in cancer progression and metastatic potential

5.1 Introduction.

From roles in maintaining cell signalling pathways (*e.g.* mechano-transduction, MAPK, Wnt) [294, 295, 252, 9], chromatin organisation [296], chromosome movement [85] and DNA damage repair [161], *LINC* components display fundamental roles in maintaining the normal function of healthy tissues. Due to this wide ranging functionality within the cell, it is no wonder that the *LINC* complex plays suggested roles in multiple human diseases, including Emery-Dreifuss muscular dystrophy (EDMD) [176], hearing loss [184] and progeria [297]. Current understanding of roles for *LINC* components in cancer development however, is still not well understood. Present views suggest roles for nuclear deformability as a rate limiting step in cellular migration [266], to which *SUN-KASH* perinuclear interactions alongside the INM lamin network plays key roles in maintaining nuclear architecture. Further to this, a recent study has highlighted significant down regulation of SUN, nesprin and lamin proteins within high grade breast cancer tissues [203]. These findings suggest *LINC* components could potentially play fundamental pathological roles in breast cancer development.

5.1.1 LINC roles in cancer development.

As the *LINC* complex displays connections to multiple disease phenotypes often characterised by nuclear abnormalities, it is not surprising that further roles in cancer development are also suggested due to many early diagnostic methods using nuclear structure as a prognostic tool [298]. One protein network key to maintaining *LINC* connections across the NE is the lamin network. This type V intermediate filament network situates across the INM in the form of highly ordered filamentous structures. B-type lamins, including lamin B1 and lamin B2, are encoded by the *LMNB1* and *LMNB2* genes respectively [299, 300]. It is interesting to note that limited mutations in B-type lamins are observed across a range of diseases, potentially due to these mutations leading to early lethality, shown through mouse knock-downs of lamin B1 and knock-outs of lamin B2 [301, 20]. This suggests B-type lamins are essential to cellular function. Current work,

however, suggests potential roles for B-type lamins in the development of chromatin instability, often associated as a hallmark of cancer development [302]. Through shRNA-mediated silencing of lamin B1 in cancer cell lines, it was shown that cells exhibited a delay within the S phase of the cell cycle. This delay was attributed to the stalling and collapse of replication forks, which in turn resulted in inefficient repair of double stranded DNA breaks. This inefficient repair resulted in persistent DNA damage signalling and assembly of extensive repair foci on the chromatin. This data, coupled with further investigation displaying lamin B1 interactions with promoters of DNA damage repair like *BRCA1* and *RAD51*, suggests that the maintenance of lamin B1 is required for efficient DNA replication and repair.

In contrast, A-type lamins are encoded by a single gene, *LMNA*, which undergoes alternative splicing to generate the major A- and C- type lamins. The expression pattern of lamins is ubiquitous and developmentally regulated, with expression only detected within differentiated cells [26]. Due to their known roles in maintaining nuclear architecture and chromatin organisation, mutations in the *LMNA* gene stimulates a broad range of human diseases, collectively known as 'laminopathies' [28]. This group of mutations comprises of multiple clinical disorders, including several forms of muscular dystrophies, such as autosomal dominant (AD)-EDMD [303] and LMNA-related congenital muscular dystrophy (L-CMD) [304]. De-regulation of lamin expression levels have also been observed in various cancers. It has been reported that loss of lamin A/C expression can be seen within colon cancer [305], small cell lung cancer [306], leukaemias [307], ovarian cancer [308] and breast cancers [309, 24]. Interestingly however, overexpression of lamin A/C has been further reported in ovarian cancers [310], colorectal cancers [311], prostate cancers [312] and skin cancers [313]. This therefore suggests associations between lamin A/C expression and cancer severity involves a complex interplay of up and down regulations, which are not yet fully understood.

Alongside lamins, *SUN* proteins also display connections to the development of numerous disease phenotypes. *SUN* proteins localise to the INM through interactions with lamins and emerin [33, 66], enabling the formation of trimetric *SUN* structures [67]. These *SUN* trimers form probable hexametric complexes with three nesprin *KASH* domains across the perinuclear space, which is shown to recruit nesprins across the nuclear envelope [59]. This physical interaction provides a platform to transmit mechanical forces between the cytoskeleton and nucleoskeleton [57]. The implications of the localisation of *SUN1* and *SUN2* across the inner nuclear envelope, alongside its wide range of binding partners makes it a likely candidate for potential roles in diseases such as cardiomyopathies and X-linked EDMD [180, 250]. In both investigations, the phenotypes

produced upon dysregulation of lamin A/C or emerin respectively, affected *SUN* expression profiles. The cardiomyopathy phenotype was partially rescuable through the down regulation of *SUN1*, whereas in EDMD, *SUN1/SUN2*-emerin binding affinity was observed to be weakened. Further observations link *SUN1* to the maintenance of genome integrity, through roles in regulating telomere tethering to the nuclear envelope during post mitotic nuclear assembly [314]. However, the neoplastic regulation and expression of *LINC* components, including *SUN* proteins, alongside their clinical significance within difference cancers is not yet fully understood.

To date, nuclear structural defects have been attributed to loss of lamin A/C expression within cells [309, 24]. However, Matsumoto *et al.* [203] was able to show that previously observed lamin A/C loss within various breast cancers, was accompanied by loss of further crucial *LINC* components, including nesprin-2. Nesprins are vertebrate spectrin-repeat (SR) containing proteins, expressing an evolutionary conserved C-terminal KASH domain, able to maintain nuclear architecture through *SUN-KASH* perinuclear interactions. One hallmark of this protein family is its drastic variability in cellular function. Specifically, the *SYNE-1* and *SYNE-2* genes each have enormous complexity due to their multiple exon splice sites. The *SYNE-1* gene for example displays a predicted 16 *KASH* containing and 14 *ABD* containing isoform variants within mammalian systems alone [177]. This large isoform variability leads to potential implications in the development of multiple disease phenotypes. Nesprin-1 and nesprin-2 have been implicated in a range of disease phenotypes including musculoskeletal diseases like EDMD and arthrogryposis multiplex congenita (AMC), alongside premature aging diseases [303, 178, 315].

Recent investigations are now implicating suggestive roles for nesprins in cancer development. High-throughput genome sequencing studies have identified nesprins as potential candidate genes [200, 316]. Alongside this, the *SYNE-1* region has been identified as a susceptibility locus for breast and lung cancers [197], with *SYNE-1* promoter hypermethylation being shown to impair nesprin-1 expression in various lung cancer cell lines [199]. Further nesprin-1 polymorphism have also been associated with an increased risk of invasive ovarian cancer development [317]. Specific links to cancer metastasis have also been described, in which *SYNE-1* genetic abnormalities are absent from pancreatic tumour sources, but present upon subclone metastasis to the liver and lungs [195]. This suggests mutations in the nesprin-1 gene may occur during metastasis. Further to this, mutations in the *SYNE-2* gene have also been detected in breast cancers [200]; leading to suggestions that nesprins may play further roles in cancer development.

The exact mechanisms by which nesprins and alternate *LINC* complex components contribute to the development of cancer phenotypes are thus far, unknown; however, suggestions are emerging that nuclear stiffness could be a rate limiting factor in cellular migration. Coupled with knowledge that the nucleus is the stiffest organelle, alongside nesprin roles within maintaining nuclear architecture and integrity, it has been suggested that these nesprin mutations allow an increase in nuclear malleability. These mutations in turn, may allow cells to penetrate through the restrictive tissue environments, enabling intravasation and extravasation [318].

5.1.2 Current understanding of breast cancer development and metastatic mechanisms.

Worldwide, breast cancer is the most common cancer form within women, displaying a reported 1.68 million new cases diagnosed in 2012 alone. Mortality attributed to breast cancer is currently the second leading cause of death for women in developed regions [319]. Of tissue systems in both males and females, the breast region is one of the most susceptible to genetic instability, arising through permanent mutations in tumour suppressor genes and proto-oncogenes. This increased susceptibility arises due to delayed tissue maturation until the completion of the first full term of pregnancy. Within this un-differentiated breast tissue, it has been shown that binding affinity to carcinogens is increased, leading to increased potential of mutations arising from DNA damage.

In normal breast pathology, tissue consists of epithelial and stromal components, with the milk producing ductolobular system forming from a dual layered epithelium, resting on a basement membrane (basal lamina) enveloped by stroma. Both normal and cancerous pathology of breast tissue can be seen in *Figure 5.1*, highlighting the observed differences in cellular organisation upon cancer development.

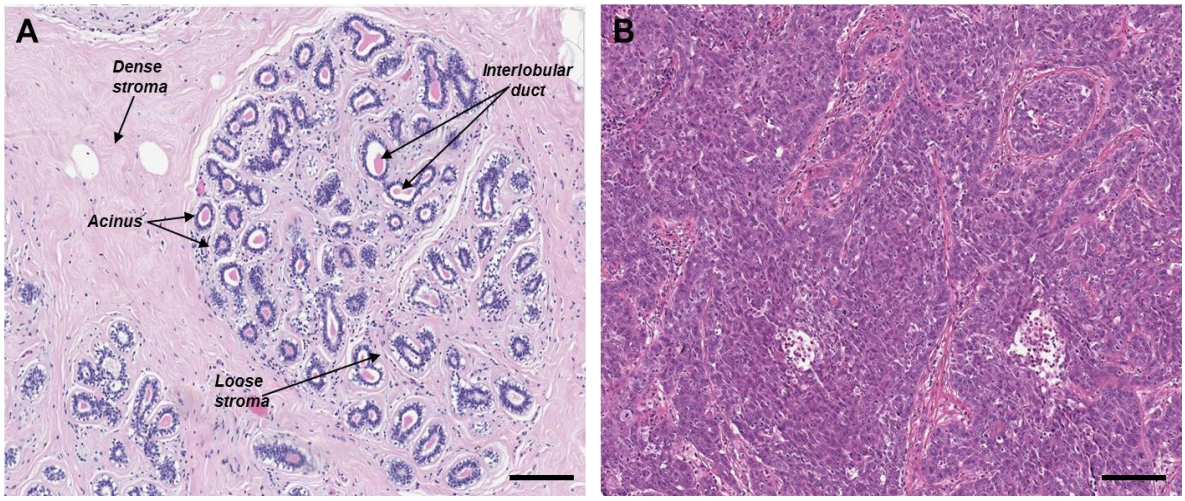

Figure 5.1: *Pathological examples of normal breast tissue (A) and high grade triple negative breast tissue (B). Images highlight loss of normal tissue structure as a result of uncontrolled proliferation. Scale bars = 100 µm*

As shown in *Figure 5.1*, one hallmark of breast cancer development is the uncontrolled cell proliferation, leading to a loss of structural organisation arising from mutations in oncogenes or tumour suppressor genes.

Oncogenes refer to genes through which inappropriate activations can lead to cancer development, one of which includes *HER-2,* often displaying gene amplification upon cancer development. This amplification leads to increased levels of signalling cascades though a variety of cellular signalling pathways, including the mitogen activated protein (MAP) kinase and Phosphodyl Inositol 3-kinase (PI3K)/Akt pathways, leading to increase cell motility, apoptosis resistance and metastasis [320]. Alongside oncogenes, mutations in tumour suppressor genes can also stimulate uncontrolled cell growth and increased cancer malignancies, such as that found upon abnormal p53 expression. p53 is considered a guardian of the genome, responsible for maintaining DNA integrity via regulating DNA damage repair, able to halt cellular proliferation until the acquired DNA damage is repaired, or apoptosis is activated. Mutations in p53 make up the most common genetic abnormality within breast cancer, with links to poor prognosis [321] and estrogen receptor (ER) negativity [322].

A further hallmark within high grade breast cancer development is the development of uncontrolled cell cycle progression, induced by dysregulation of cyclin-dependant kinases (CDKs). When activated, CDKs promote phosphorylation of target proteins such as retinoblastoma proteins (pRb), a primary gatekeeper controlling cell cycle passage from resting G_0 to active cycling states and mitosis. These CDKs are regulated positively by

cyclins and negatively by cyclin dependent kinase inhibitors (CKIs). Of specific importance within breast tissue is the function of cyclin D1. Cyclin D1 is known to oscillate in expression levels according to the stage of the cell cycle, playing key roles in cell cycle progression from the G_1 to S phase [323]. This protein is found to be overexpressed in 40-50% of invasive breast cancers [324], with further evidence suggesting that high cyclin D1 expression levels can be positively correlated to ER positivity and increased proliferation rates [325, 326], similar to those phenotypes expressed within many high grade breast cancers.

As highlighted so far, a multitude of hallmarks are present within breast cancers, resulting from alterations in cell cycle progression as a result of oncogene mutations. The development of breast cancers can be grouped into different stages, depending on tumour size, tissue occupation and metastatic properties. The specific staging category assigned to individual tumours depends on the combination of these factors. A simplified example of breast cancer tumour staging can be seen displayed within *Figure 5.2* and *Table 5.1*.

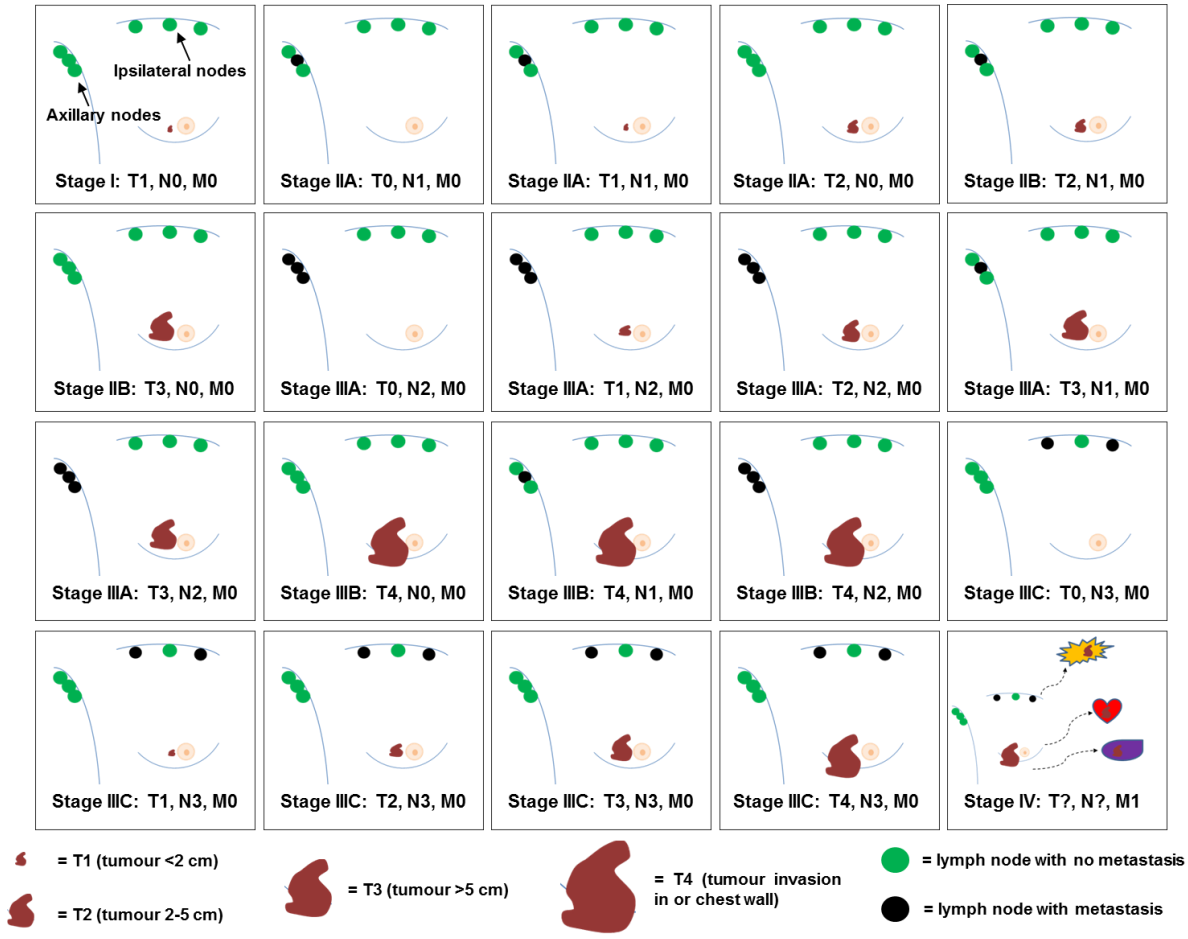

Figure 5.2: *Pathological examples of each stage in breast cancer development, alongside associated severity of each stage.*

Table 5.1: *Defined breast cancer staging categories through tumour development.*

Tumour Size ***T***	*Tumour size <2 cm* T1	*Tumour size 2 – 5 cm* T2	*Tumour size >5 cm* T3	*Tumour extends to skin or chest wall* T4
Lymph Nodes ***N***	*N0 – no lymph node metastasis*	*N1 – metastasis to ipsilateral, movable, axillary LNs*	*N2 – metastasis to ipsilateral fixed axillary, or IM LNs*	*N3 – metastasis to infraclavicular/ supraclavicular LN, or to axillary and IM LNs*
Metastasis ***M***	*M0 – no distant metastasis*	*M1 – Distant metastasis*		

As can be seen, a multitude of categories exist based on tumour phenotypes, migration patterns and metastatic potential. Cancer severity can also be influenced by regions of cancer development within the breast and alternate bodily regions post metastasis. This complexity in phenotypic expression patterns is leading current research to investigate potential markers specifically altered within breast cancer, to not only devise targeted therapies, but also monitor and track the invasive nature of cancers post metastasis, with aims to increase patient prognosis.

5.1.3 Current understanding of breast cancer migration and applications of 3D scaffold environments.

The high mortality rates associated with many cancer forms derives not only from the source and site of primary tumour formation, but also from the ability of the tumour cells to invade surrounding tissue environments and metastasise to distant bodily areas [327]. One major model by which cancer cells are proposed to acquire their invasive motility is through the epithelial-mesenchymal transition (EMT), characterised by the exchange of epithelial markers such as E-cadherin for mesenchymal markers like N-Cadherin and vimentin [328]. In breast cancers, the core EMT gene signature is associated with the claudin-low molecular subtype, displaying reduced expression levels of tight and adherens junction proteins [329]. This subtype is most prevalent in highly aggressive triple negative breast cancers (ER-, PR-, HER2-), which often display poor prognosis for the patient.

However, these claudin low subtypes of breast cancer are also the least common subtype, accounting for ~12% of tumours [330]. This suggests that even though the core EMT phenotype is present in some aggressive breast cancer forms, the majority of human breast cancers do not express this core EMT signature. The correlated assumption that E-cadherin levels are uniformly lost within cancerous tissues due to this EMT transition means that cell cohesion within many breast cancer tumours is often overlooked.

Current investigations now suggest E-cadherin expression levels vary significantly between histological subtypes. With ~75% of all breast cancer cases deriving from invasive ductal carcinomas [331], it is interesting to note that membrane E-cadherin expression levels are absent in <10% of these tumours [332]. Further evidence also suggests membrane E-cadherin levels within metastatic breast cancers is equal to, or in some cases higher than that found within the primary tumour source [333]. Taken together, these investigations suggest breast tumours are typically cohesive; expressing membrane bound E-cadherin in both primary and metastatic tumour sources. This potentially implicates strong cell-cell interactions, leading to breast cancer cells migrating as a collective unit.

Over the past few years, multiple theories of how breast cancer cells are able to cohesively migrate from the tumour source to distant bodily areas have been proposed, including the fibroblast leader's model and cancer cell leader's model. Employing novel 3D scaffold environments, these suggested theories display the attachment of breast cancer cells to either stromal fibroblasts (which are intrinsically mesenchymal and excel in extracellular matrix remodelling) [334], or cancer cells expressing high levels of metastatic markers [335, 336] as a means of metastasising from the primary tumour site. Further suggestive roles for macrophage-tumour cell interactions are also proposed, due to macrophage accumulation at the site of tumour inflammation being closely linked to a decrease in patient prognosis [337]. Using 3D Matrigel models, two potential mechanisms by which tumour cells can use macrophages to exit the tissue source are suggested. For one mechanism, macrophages remodelling of the extracellular matrix is suggested to form channels in the tissue, through which tumour cells can migrate and leave the source tissue [338]. Alongside this, a second mechanism using an *in vitro* intravasation model, displayed that direct interactions between macrophages and tumour cells triggered RhoA dependent invadopodia formation in the tumour cells, leading to migration through the endothelium [339].

This collated data therefore helps to highlight the variable complexity displayed by breast cancers upon metastasis, alongside current attempts to gain insights into these

mechanisms using novel 3D environments. It is however suggested that due to limitations in current 3D technologies available thus far, these technologies are unable to provide clinical grade observations, comparable to those found within mouse models used to study the invasive nature of cancerous tumours.

5.2 Chapter Aims.

This chapter aims to characterise both expression levels and architectural positioning of selected *LINC* complex proteins across a range of breast cancer cell lines. To achieve this, multiple analysis techniques including western blotting, immunofluorescence, primary tissue staining and plasmid transfections will be used. From this it is aimed to provide insights into potential roles of *LINC* complex proteins in the development of metastatic phenotypes.

5.2.1 Objectives.

- To assess expression levels and arrangement of various *LINC* components across a range of breast cancer cell lines.

- To assess differences in migration potential across a range of breast cancer cell lines through restrictive 3D growth environments.

- To establish whether migration behaviour of low and high grade breast cancer lines can be altered through alterations in *SUN-KASH* interactions and nuclear architecture.

- To assess whether nesprins could provide a novel target for highly metastatic breast cancer grading.

5.3 Results.

5.3.1 LINC complex components vary drastically across low-, medium- and high-grade breast cancer cell lines.

5.3.1.1 LINC expression levels vary drastically between different cancer cell lines.

LINC components are suggested to play multiple cellular roles, affecting cell migration in both 2D and 3D culture systems, alongside nuclear and cellular stiffness. In multiple cancers, metastasis is the leading cause of mortality, in which cells migrate from the source tissue to alternate areas of the body. Although multiple mechanistic phenotypes have been suggested to contribute to this process, we suggest that nuclear malleability is a crucial factor in allowing the cell to 'squeeze' through surrounding tissue environments. With links between *LINC* components and nuclear stiffness, initial pilot investigations were conducted to assess *LINC* proteins expression across various cancer cell lines.

Lysates were produced as described in the methods section, from; MCF7 and MDA-MB-231 cell lines (low- and high-grade breast cancer cells, respectively), SW480 and SW620 cell lines (low- and high-grade colorectal cancer cells, respectively), and HeLa cells (representing high grade cervical cancer cells). The human keratinocyte HaCaT cell line was further included as well as the monkey kidney fibroblast COS7 cell line as non-cancerous controls. Initial data for *LINC* protein expression levels can be seen in *Figure 5.3*.

Figure 5.3 suggests variations exist between *LINC* complex components assessed across varying cell lines. Interestingly, expression levels of β-actin, lamin A/C and SUN1 appear to remain constant across each cell line. In contrast, variable expression is displayed for nesprin-2 and Nup88 levels, in which for both proteins, expression levels appear to reduce in the high-grade cancers. This data, coupled with centrin, emerin and lamin B staining showing further sample variability, suggests that *LINC* components do appear to vary drastically between cancer cell lines. However, due to the complexity of differences observed, it is difficult to discern whether any functional relationships can be seen whilst using limited numbers of samples from numerous cancer sources.

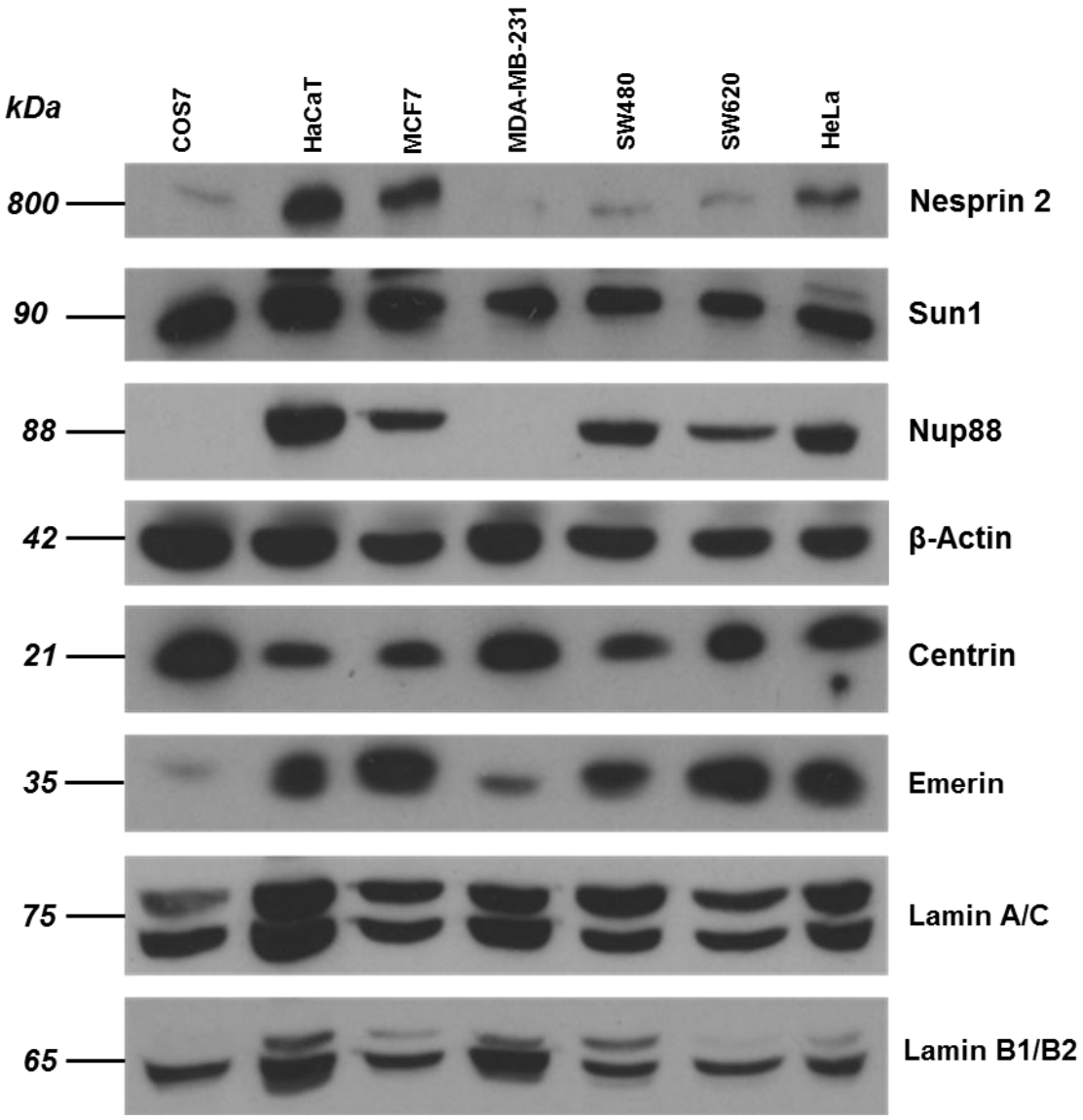

Figure 5.3: *Western blot data for LINC complex proteins across a range of both cancerous and non-cancerous cell lines.*

5.3.1.2 Standard equal loading markers display variable expression patterns across breast cancer cell lines.

As suggested in section 5.3.1.1, the selected *LINC* components analysed appear to vary drastically across the cell lines assessed, however, it is difficult to discern whether these differences exist due to the variability in cancer grades, or due to the natural expression variability between tissue sources (*i.e.* colorectal expression of *LINC* components may vary to that of breast epithelium). To further characterise *LINC* component roles in the development of high-grade cancers, further investigations were conducted, with aims to characterise *LINC* complex protein expression patterns and

cellular positioning in breast cancer. To do this, we employed six cell lines representing various breast cancer grades. As controls, we used MCF 10A and MCF 12A cell lines, alongside MCF7, HCC-38 and T47D lines to represent low to medium grades. The MDA-MB-231 cell line was used as a triple negative (PR, ER and HER2 negative) breast cancer representative, displaying highly metastatic properties in both in-vitro and in-vivo environments.

Lysates were produced and run through SDS-PAGE to separate proteins based on weight. Equal loading was assessed through Coomassie Blue staining to visualise total protein levels in each sample, as shown in *Figure 5.4*.

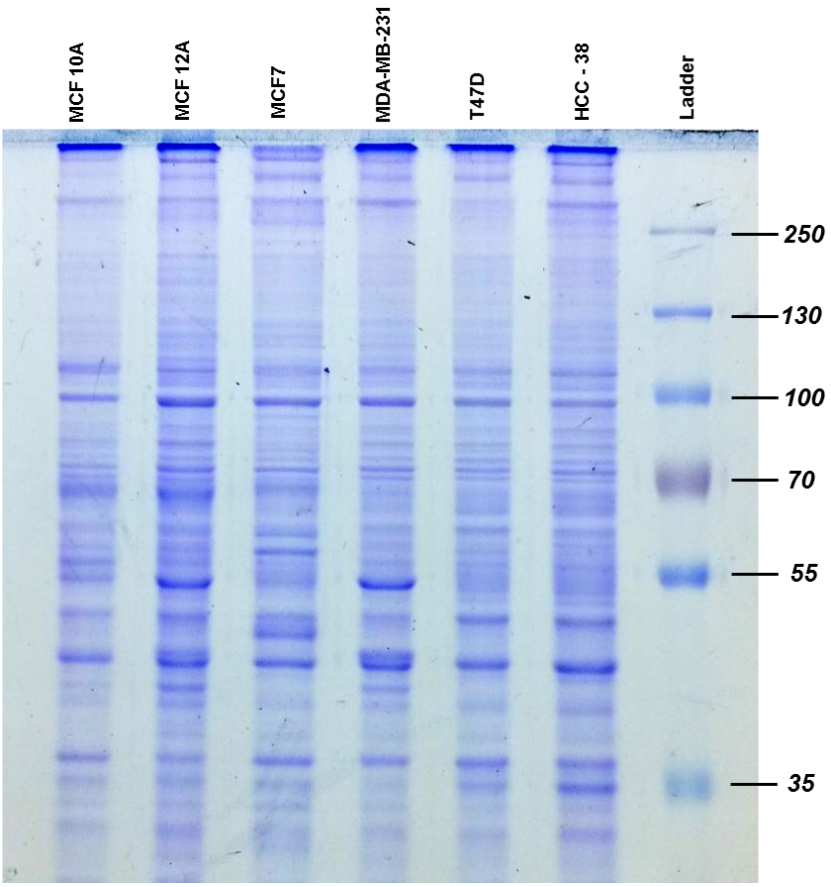

Figure 5.4: *Coomassie Blue staining of breast cancer cell lines following SDS-PAGE.*

As shown in *Figure 5.4*, the protein loading is constant between each lane, with slight variability arising from natural protein expression differences across each cell line. To validate equal loading, further western blot analysis was conducted for three standard equal loading markers, β-tubulin, β-actin and GAPDH, with resulting staining displayed in *Figure 5.5*.

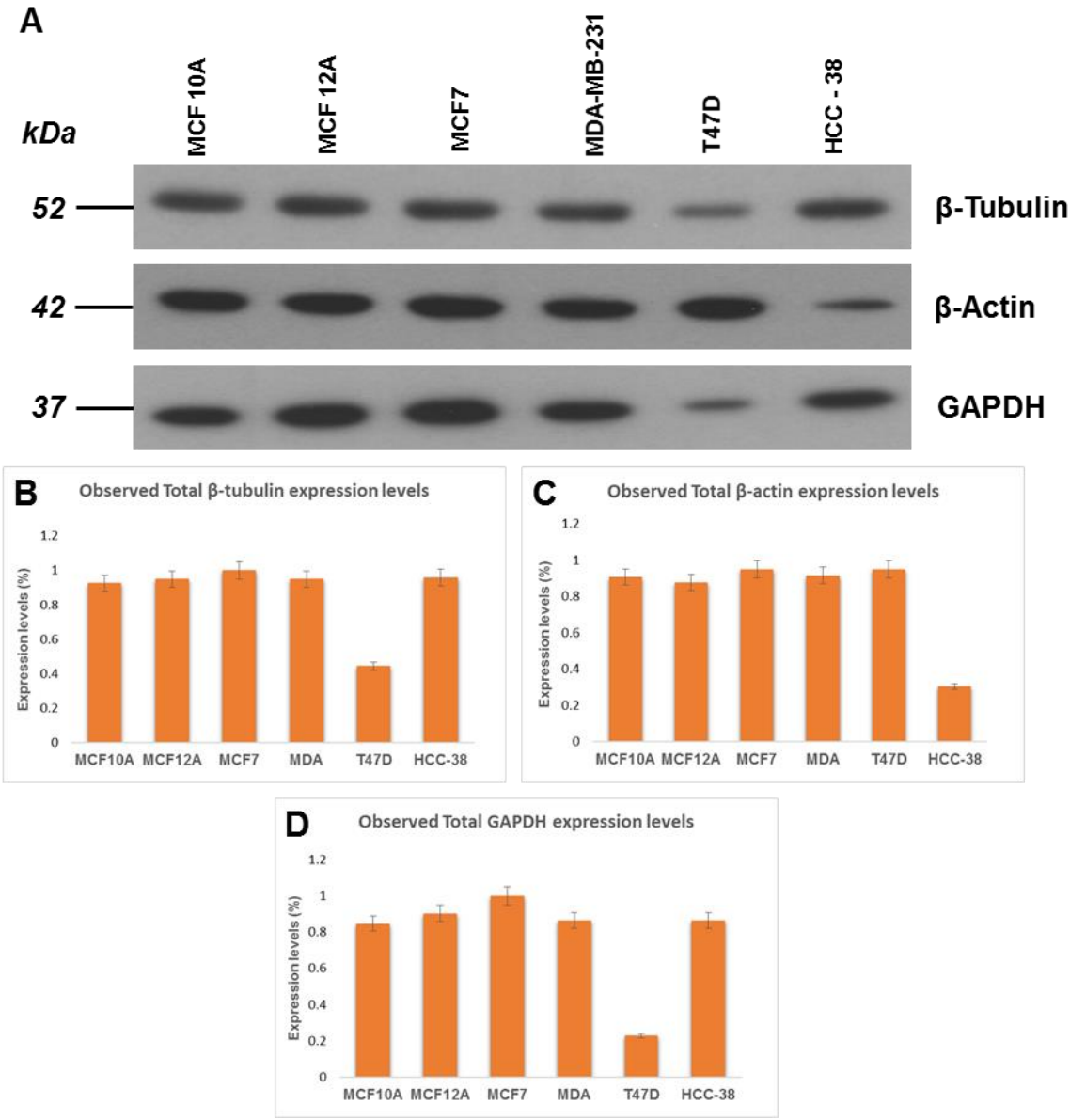

Figure 5.5: *Western blot data for equal loading markers (A) Displays western blot staining observed. (B), (C) and (D) represent collated densitometry analysis across three repeats for each protein.*

The data presented in *Figure 5.5* suggests equal protein loading is present across the majority of samples. Interestingly for both β-tubulin and GAPDH, the T47D cell line displays a reduction in protein expression, which initially suggests that less protein is present within this sample. Subsequent β-actin analysis however, displays that lower protein levels can be found within the HCC-38 cell line, whereas as the T47D cells now present equal protein levels. These observations suggest variability exists between standard equal loading markers across the cancer cell lines. However, when combined with Coomassie Blue staining, the three standards do suggest equal loading has been achieved.

5.3.1.3 Cytoskeletal protein positioning and expression levels vary between low-, medium- and high-grade breast cancer cell lines.

Once equal loading was established, cytoskeletal component expression levels were assessed due to their known roles regulating cell/nuclear migration and nuclear stiffness. These cytoskeletal proteins analysed include intermediate filament, microtubule and actin components. To assess whether cellular localisation defects arise within these cytoskeletal components from increasing cancer severity, immunofluorescence analysis was performed on 70% confluent MCF 10A, MCF7 and MDA-MB-231 cell lines. Initial actin staining across these cell lines can be seen in *Figure 5.6*.

The data displayed in *Figure 5.6* suggests that variations exist in actin organisation across these cancer cell lines. It is shown that control MCF 10A cells display actin localisation evenly throughout the cytoplasm and across the nuclear and cellular periphery. These observations can also be seen in the MCF7 cells, however, there does appear to be a more prominent nuclear absence of actin. In contrast to both the MCF 10A and MCF7 cell lines, the high-grade MDA-MB-231 cells appear to express the majority of their actin components across the cellular periphery in filapodia. Closer inspection of this observation is shown in more detail in *Figure 5.7*.

As shown in *Figure 5.7*, MDA-MB-231 cells appear display the majority of their actin across peripheral cell projections, potentially aiding their well characterised increase migratory potential. It is further shown that MCF7 cells appear to accumulate actin across cytoplasmic regions, producing a defined ring of actin around the NE. The MCF 10A cells appear to display an even distribution of actin between regions of the cytoplasm and cell periphery. When coupled with β-actin expression levels presented in *Figure 5.5*, our data suggests that variation in organisation, but not protein expression is observed between the low-, medium- and high-grade breast cancer cell lines.

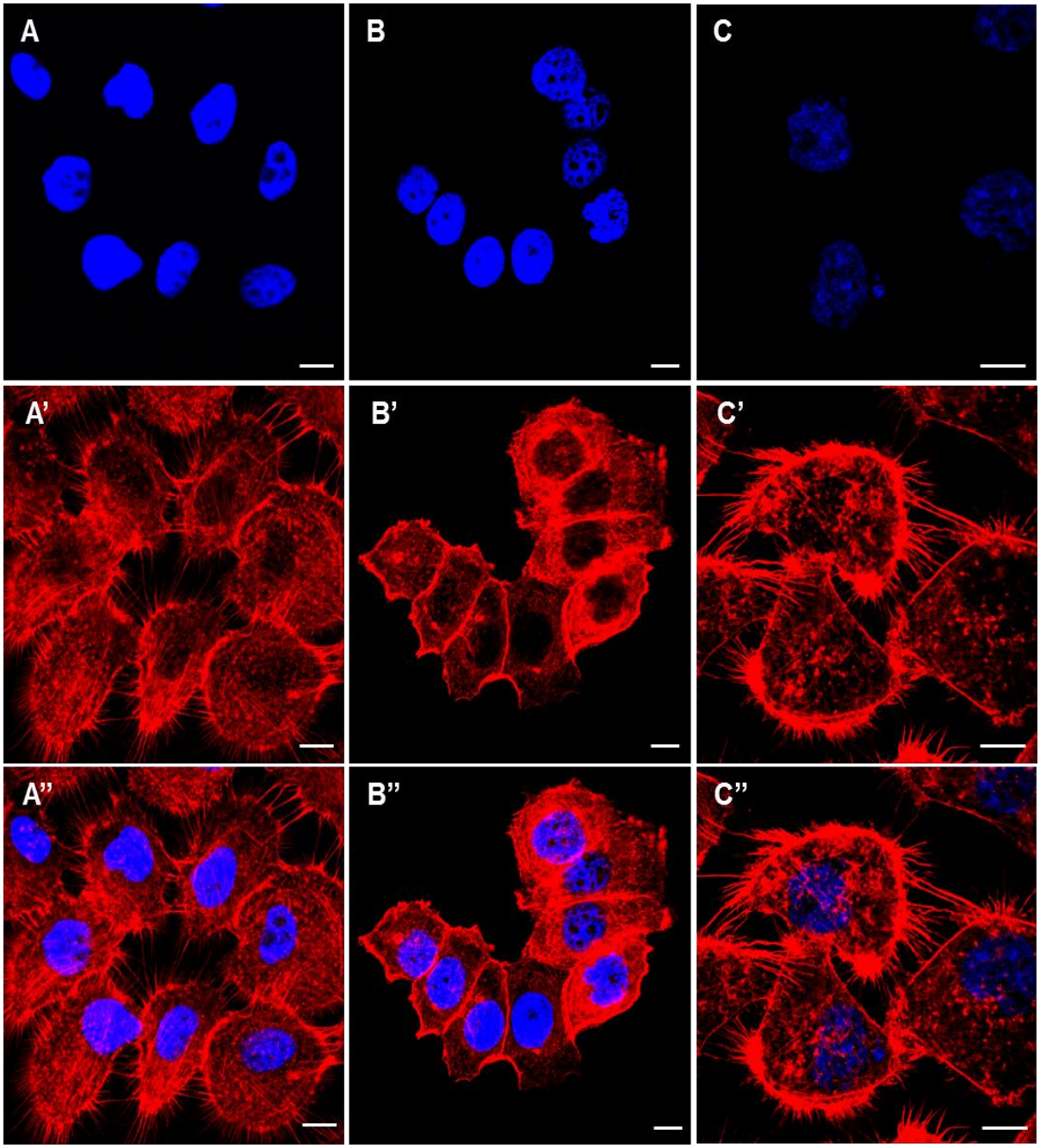

Figure 5.6: *TRITC-conjugated phalloidin (Red) stained MCF 10A (A, A', A''), MCF7 (B, B', B'') and MDA-MB-231 (C, C', C'') cells displaying F-actin organisation. Nuclei were further stained with DAPI (Blue). Scale bars = 10 µm.*

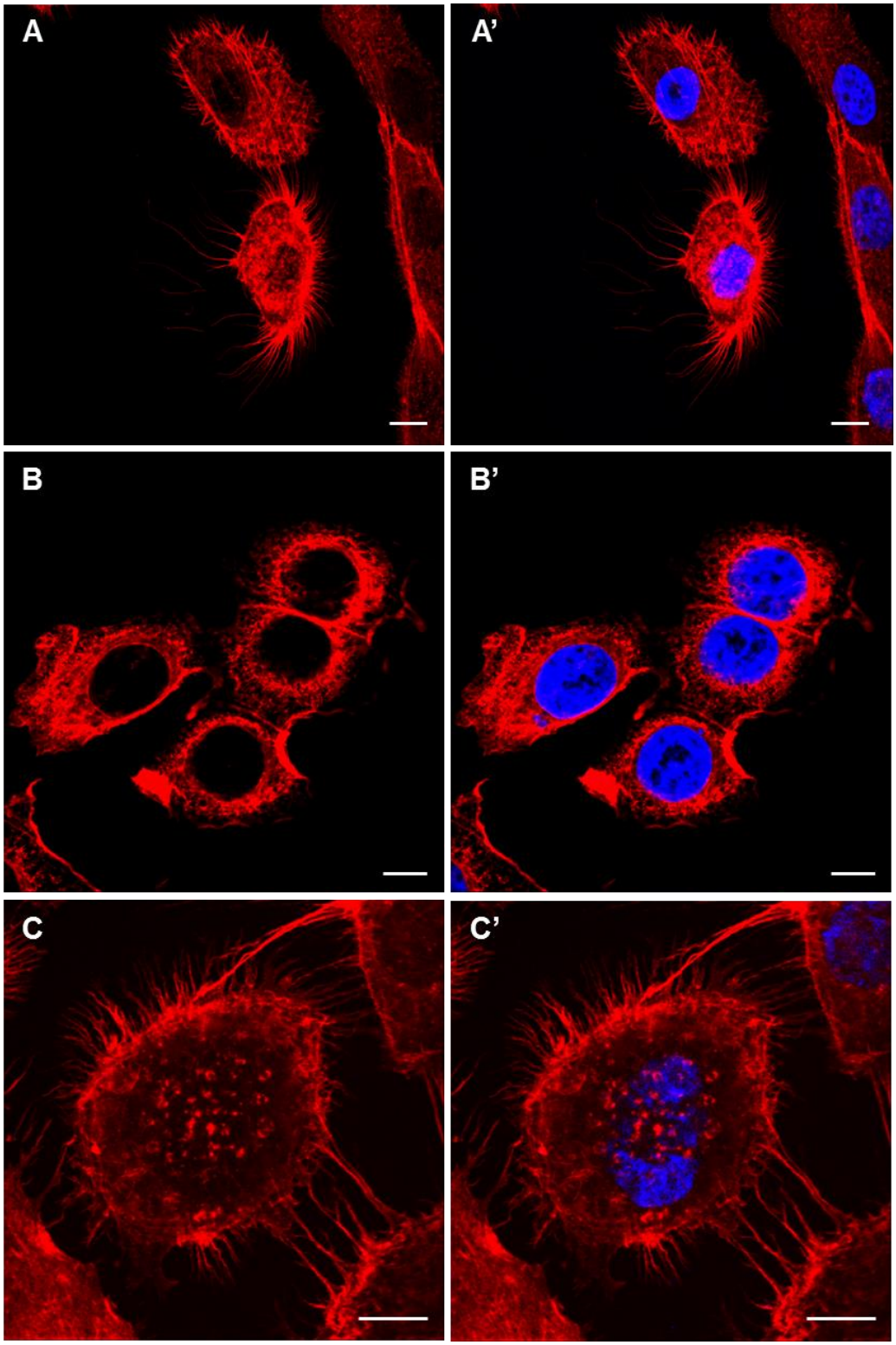

Figure 5.7: *TRITC-conjugated phalloidin (Red) stained MCF 10A (A, A'), MCF7 (B, B') and MDA-MB-231 (C, C') cells displaying F-actin organisation. Nuclei were further stained with DAPI (Blue). Scale bars = 10 µm.*

As previous data suggests the actin cytoskeletal organisation appears different between control, low- and high-grade breast cancer cells, further investigations aimed to assess whether differences were present between MT and IF networks, with resulting images displayed in *Figures 5.8* and 5.*9*.

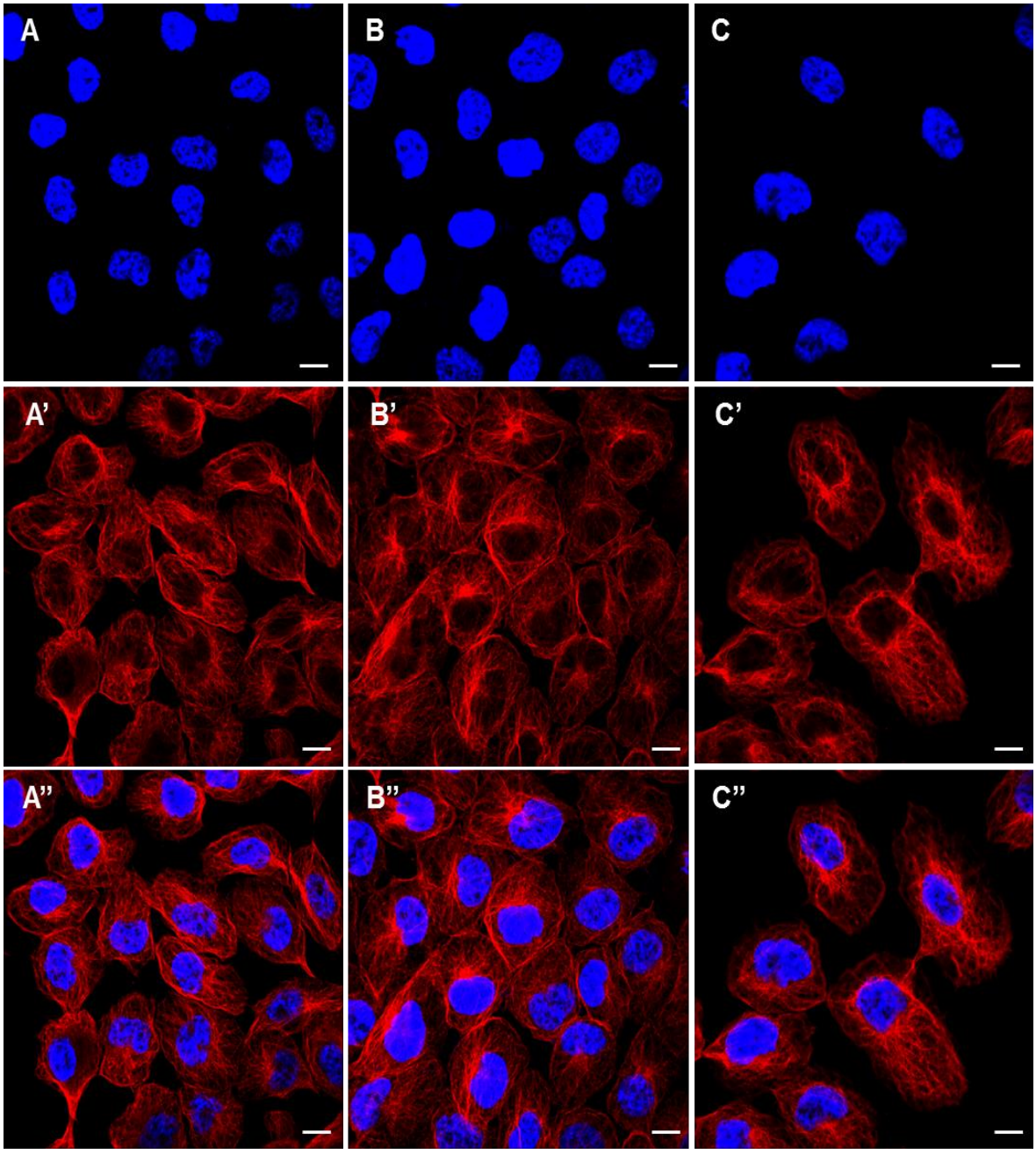

Figure 5.8: *β-tubulin (Red) stained MCF 10A (A, A', A''), MCF7 (B, B', B'') and MDA-MB-231 (C, C', C'') cells displaying microtubule organisation. Nuclei were further stained with DAPI (Blue). Scale bars = 10 µm.*

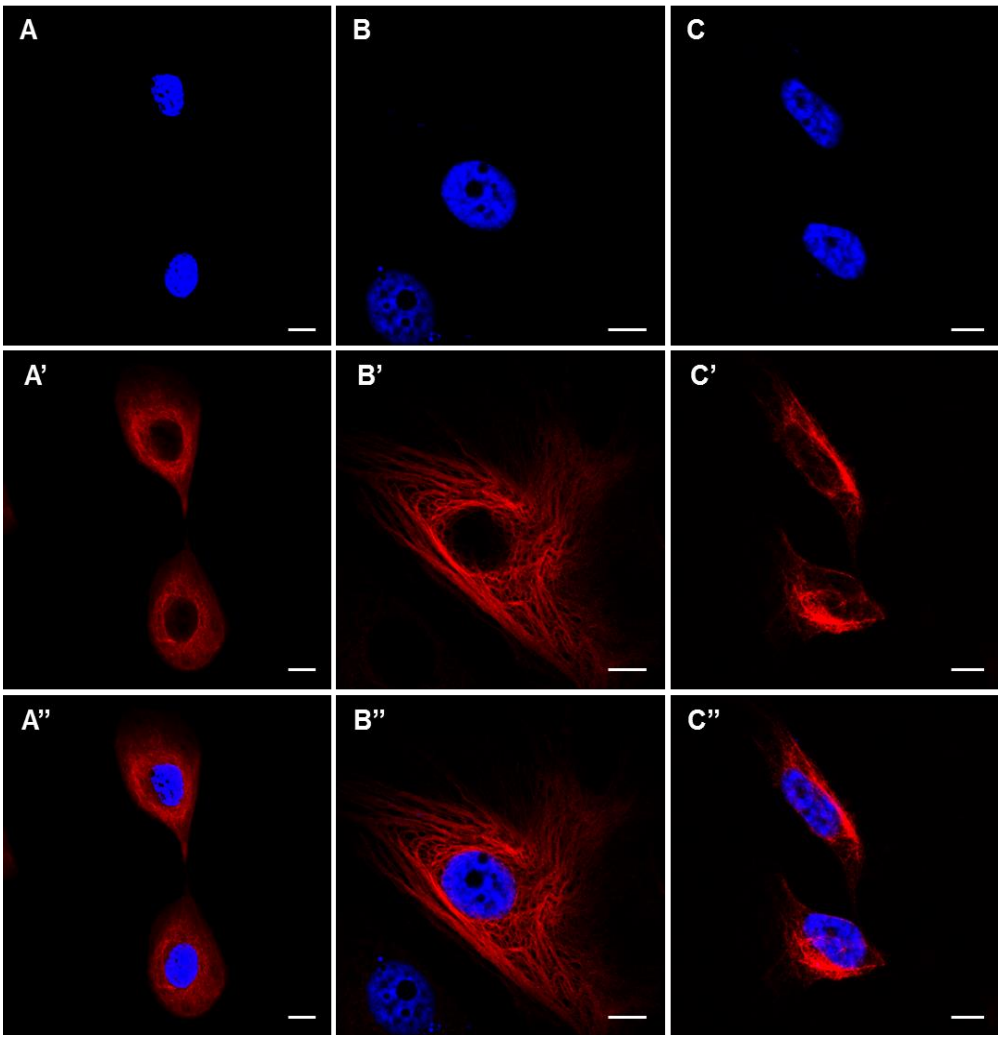

Figure 5.9: *Cytokeratin (Red) stained MCF 10A (A, A', A''), MCF7 (B, B', B'') and MDA-MB-231 (C, C', C'') cells displaying cytokeratin organisation. Nuclei were further stained with DAPI (Blue). Scale bars = 10 µm.*

Figure 5.8 displays microtubule network organisation across the three breast cancer cells analysed. It appears that under closer observation, no difference is observed in organisation across the cells, suggesting that the microtubule network organisation remains unaltered across the range of cell lines investigated. In contrast, *Figure 5.9* suggests variation exists in cytokeratin organisation across these cells. It appears that the MCF7 cells display a more defined organisation of cytokeratin distributed throughout the cytoplasm compared to the MCF 10A cells. The MDA-MB-231 cells however, appear to display a more nuclear envelope specific accumulation of cytokeratin, with further observation suggesting these cells express lower levels in comparison to MCF7 and MCF 10A cells.

To further investigate the observed differences in IF and microtubule organisation, western blotting technique was applied to assess whether these fluorescence

observations correlated to variations in protein expression levels across a range of breast cancer cell lines. Collated western blot staining is displayed in *Figure 5.10*.

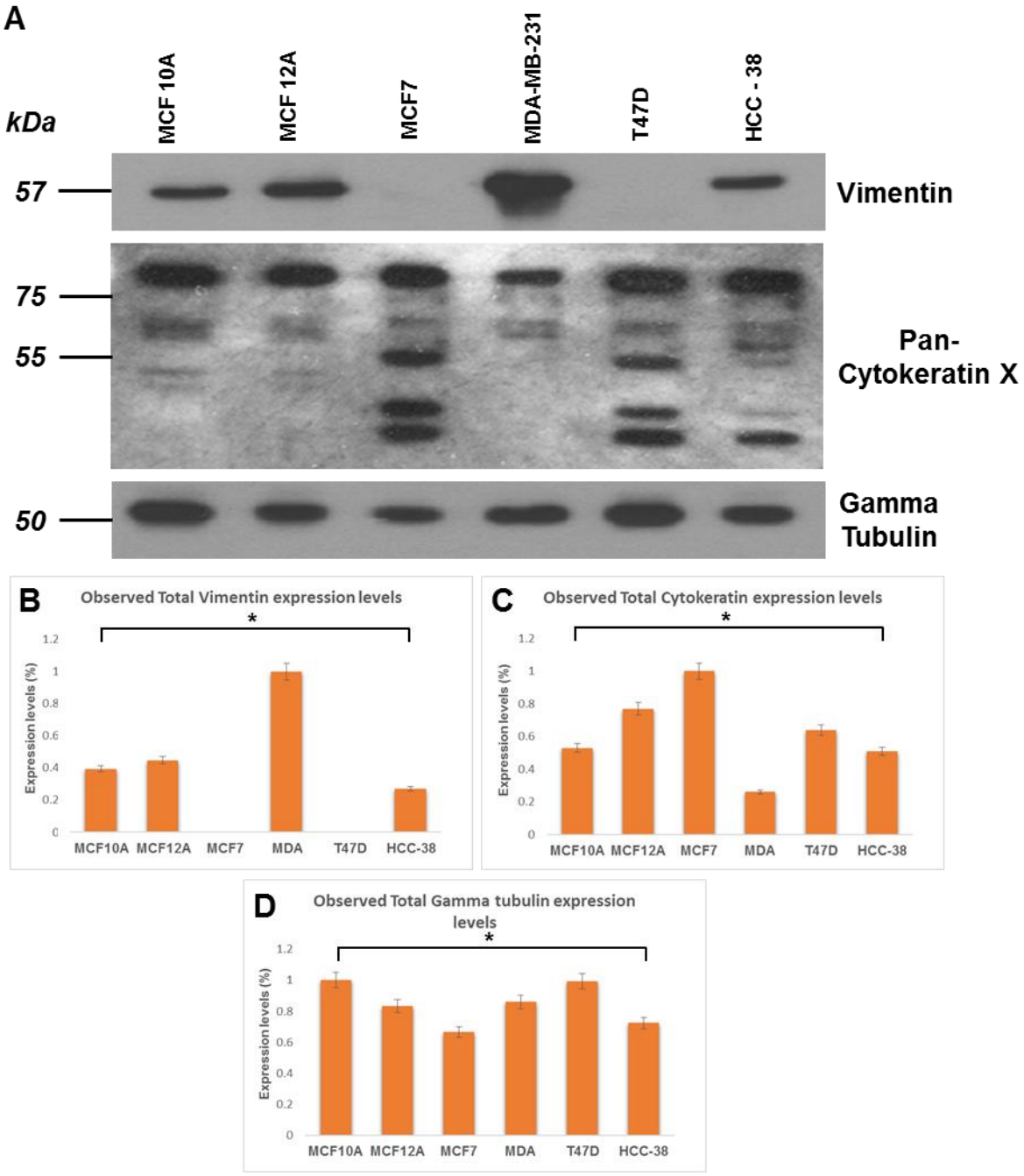

Figure 5.10: *Western blot staining for cytoskeletal proteins across breast cancer cells. (A) Displays western blot staining observed. (B), (C) and (D) display collated densitometry analysis across three repeats for each protein.*

Data presented in *Figure 5.10* suggests that IF and gamma-tubulin expression varies across the range of cell lines analysed (*ANOVA,* $F_{8.2536} = 4.64$, $P = 0.010$ *and* $F_{7.1138} = 3.98$, $P =$

0.010 respectively). Using post hoc F-tests, it was shown that vimentin expression appears to be significantly increased in MDA-MB-231 cells, whereas cytokeratin expression appears to significantly reduce in the high-grade MDA-MB-231 when compared to their low-grade MCF7 counterparts (where $p \leq 0.001$). This correlates with observations in immunofluorescence staining, in which MCF7 cells displayed a greater level of cytoplasmic organisation to that of both the MCF 10A and MDA-MB-231 cells. Further variability is also observed in gamma tubulin levels, suggesting a significant reduction in the low-grade MCF7 and HCC-38 cell lines (*ANOVA,* $F_{7.3125} = 4.01, P = 0.010,$ followed by F-test post hoc analysis where $p \leq 0.001$), suggesting contrasting results to that observed for β-tubulin expression levels in *Figure 5.5*.

The use of both fluorescence and western blotting analysis techniques suggests that although differences can be observed between cytoskeletal networks across low- and high-grade breast cancer cells, the variability observed makes it difficult to approach any solid conclusions. However, observations were able to suggest that a correlation may exist between decreased expression levels of IF proteins such as cytokeratin, alongside an increase in vimentin levels, and increased metastatic phenotypes. This appears to support current views in the literature which suggest that increased vimentin expression is associated with characteristic EMT transition [340] and subsequent metastatic potential. Further evidence however suggests that further investigation will be needed to verify this finding, as it has been documented that 2D growth environments may stimulate cancer cell lines to alter their protein expression patterns [341]. It was shown that MCF7 cells were shown to decrease vimentin expression levels when placed into novel 3D culture systems. This suggests further factors may also be influencing protein expression profiles across each cell line, other than just the cancer grade.

5.3.1.4 LINC associated proteins situated across the INM display variability in expression patterns across breast cancer cell lines.

To further examine *LINC* complex connections to breast cancer development, further investigations aimed to assess localisation and expression levels of select INM proteins, known to display *LINC* complex associations. Initial experimentation aimed to investigate whether SUN protein positioning was displaced across breast cancer cells of varying pathological grades. To assess this, immunofluorescence analysis using a LEICA SP5

confocal microscope was conducted for both SUN1 and SUN2 in MCF 10A, MCF7 and MDA-MB-231 cell lines, the result of which can be seen in *Figures 5.11 and 5.12*.

Data presented in *Figures 5.11* and 5.*12* suggest that both SUN1 and SUN2 expression remains localised across the NE. SUN1 localisation appears to remain consistent between the control and low-grade cells across NE regions, with an apparent increase in intra-nuclear staining observed for the MCF 10A cells. However for the high-grade MDA-MB-231 cells, it appears that expression of SUN1 increases in cytoplasmic regions of the cell. SUN2 however, displays no variation in cell positioning across each cell line assessed. Staining for SUN proteins also reveals one further cancer hallmark, an increase in nuclear deformities upon cancer progression, as the high-grade MDA-MB-231 representative cell line displays significant abnormalities in nuclear shape to that of control and low-grade counterparts.

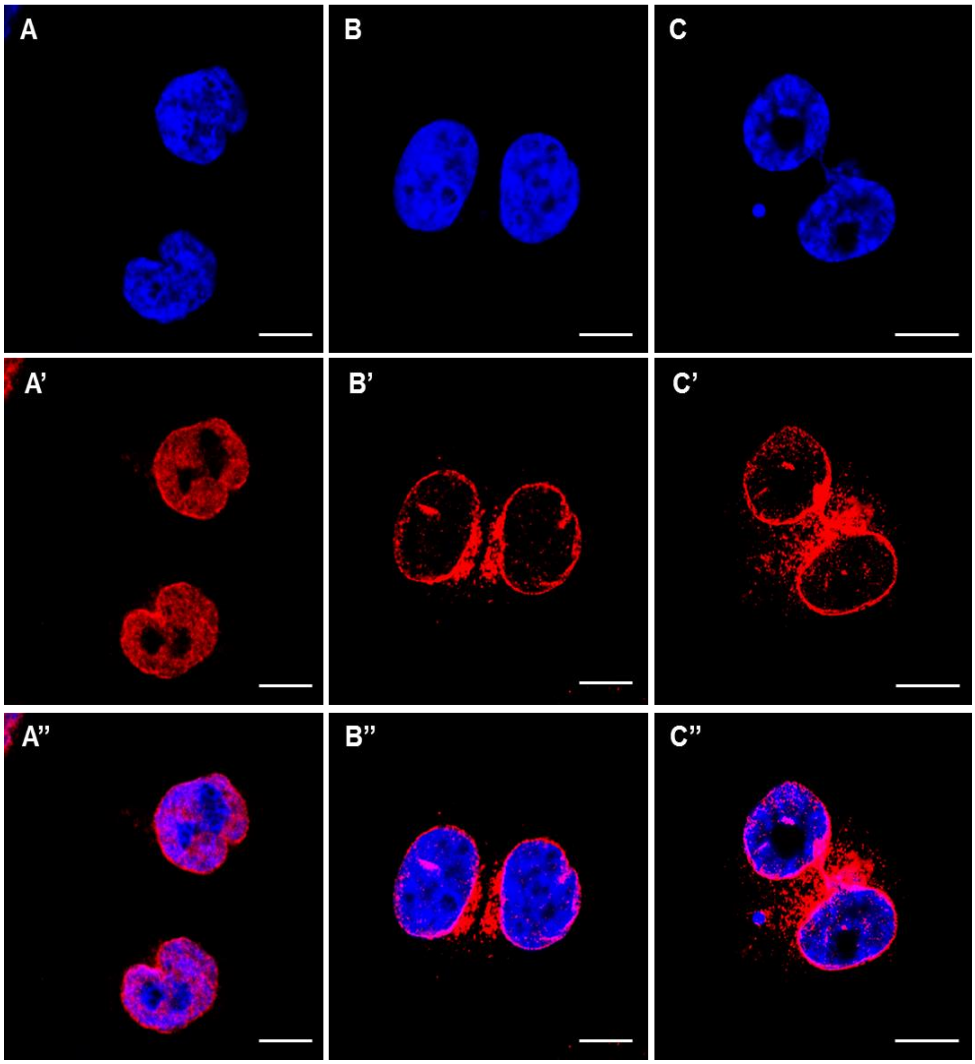

Figure 5.11: *SUN1 (Red) stained MCF 10A (A, A', A''), MCF7 (B, B', B'') and MDA-MB-231 (C, C', C'') cell lines displaying inner nuclear envelope organisation. Nuclei were further stained with DAPI (Blue). Scale bars = 10 µm.*

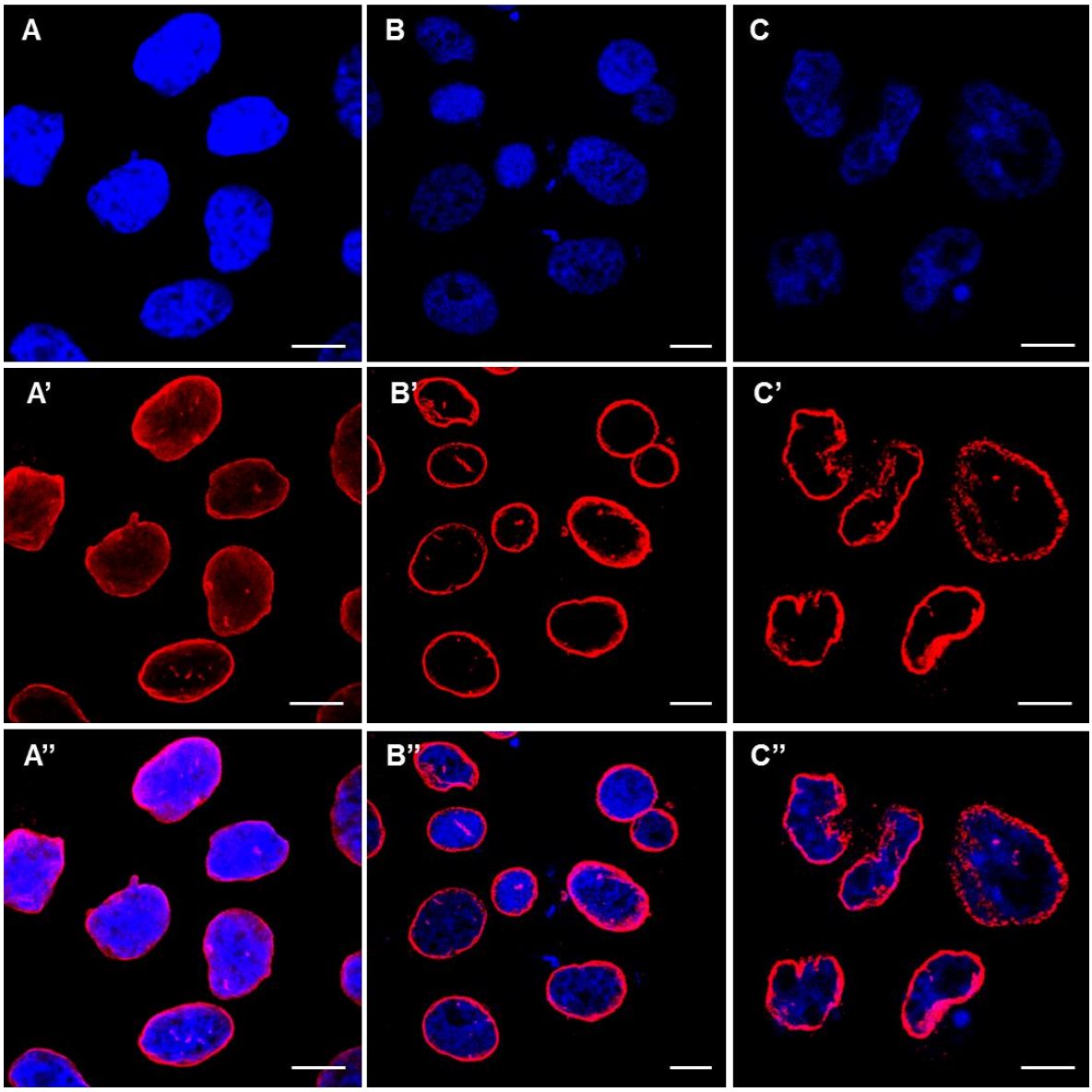

Figure 5.12: *SUN2 (Red) stained MCF 10A (A, A', A''), MCF7 (B, B', B'') and MDA-MB-231 (C, C', C'') cell lines displaying inner nuclear envelope organisation. Nuclei were further stained with DAPI (Blue). Scale bars = 10 µm.*

Alongside SUN protein localisation, further analysis of lamin A/C and lamin B positioning across the INM was assessed. Much of the literature suggests that lamin A/C expression levels vary between low- and high-grade cancers, whereas lamin B levels remain constant. Aims were therefore to assess whether their topographical positioning in control, low- and high-grade cell lines through immunofluorescence staining, results of which can be seen displayed in *Figures 5.13* and 5.*14*.

The data presented in *Figures 5.13* and 5*.14*, suggest that the localisation of both lamin A/C and lamin B appear to remain constant across the NE between control, low- and high-grade breast cancer cells. However, it can once again be seen that lamin A/C and lamin B staining highlights the drastic nuclear deformities present in the high-grade MDA-MB-231 cell lines in comparison to the low-grade and control cells.

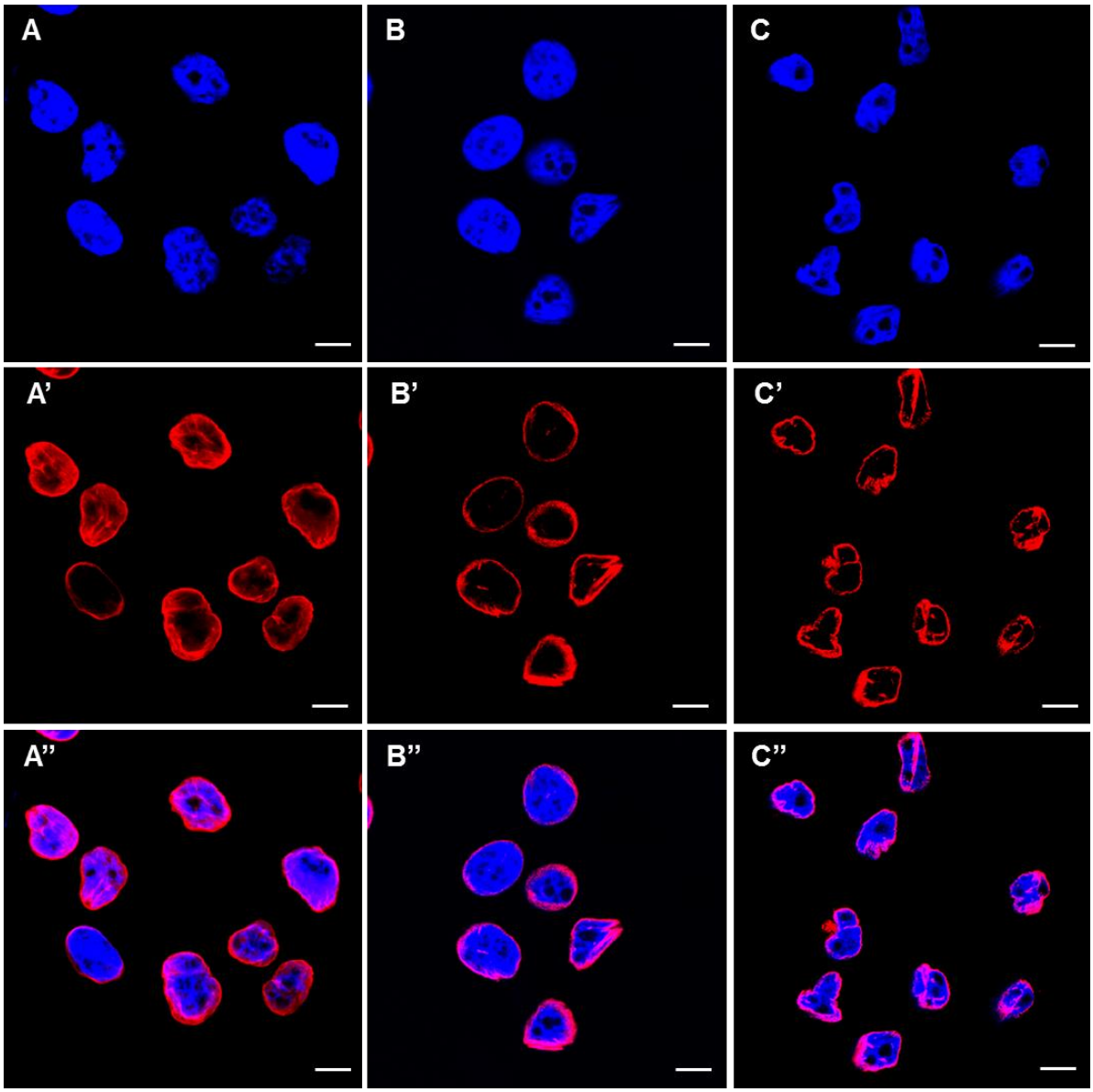

Figure 5.13: *Lamin A/C (Red) stained MCF 10A (A, A', A''), MCF7 (B, B', B'') and MDA-MB-231 (C, C', C'') cell lines displaying inner nuclear envelope organisation. Nuclei were further stained with DAPI (Blue). Scale bars = 10 µm.*

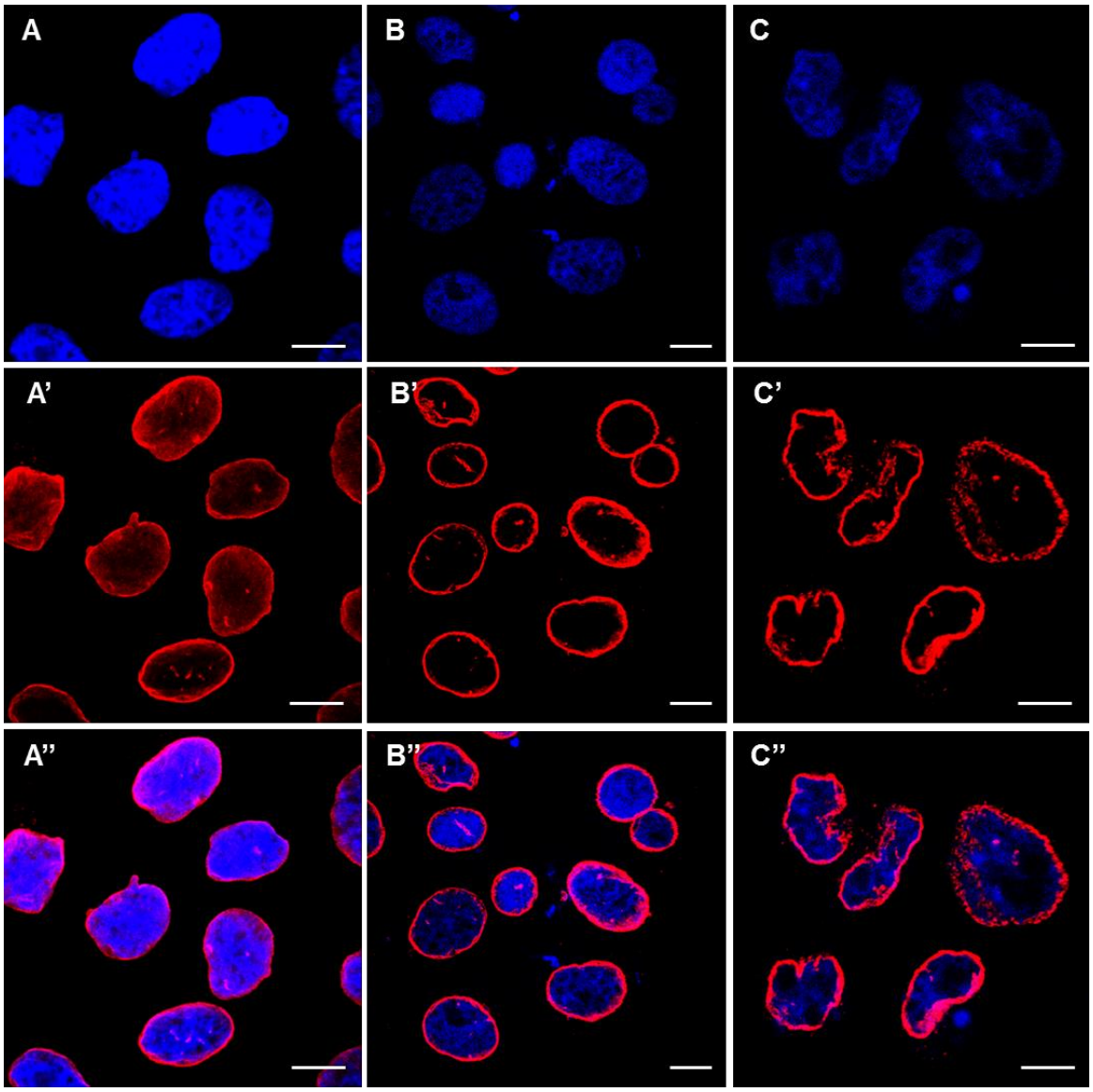

Figure 5.14: *Lamin B (Red) stained MCF 10A (A, A', A''), MCF7 (B, B', B'') and MDA-MB-231 (C, C', C'') cell lines displaying inner nuclear envelope organisation. Nuclei were further stained with DAPI (Blue). Scale bars = 10 µm.*

Following staining against SUN and lamin proteins across the INM, we further aimed to assess whether further variability existed in emerin protein localisation across control-, low- grade and high-grade breast cancer cell lines. Images of this staining can be seen in *Figure 5.15*.

The data presented in *Figure 5.15* suggests that emerin organisation, like that of the lamin A/C and lamin B, appears to remain consistent across the NE of breast cancer cells assessed, displaying specific localisation to the NE. It can be seen however, that some intra-nuclear staining is observed in control MCF 10A cells but not in MCF7 or MDA-MB-231 cells, potentially suggesting miss-localisation of emerin upon cancer development.

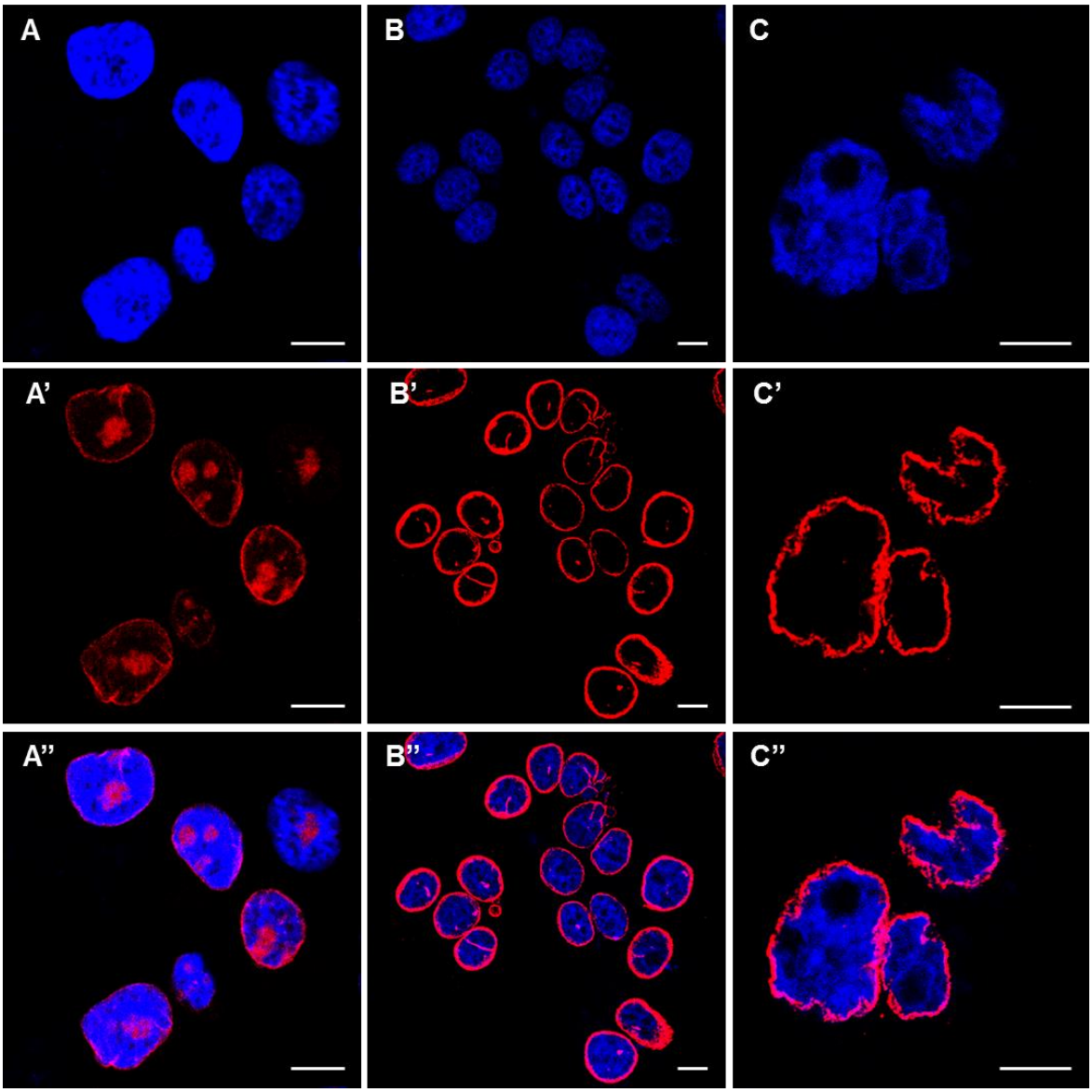

Figure 5.15: *Emerin (Red) stained MCF 10A (A, A', A''), MCF7 (B, B', B'') and MDA-MB-231 (C, C', C'') cell lines displaying inner nuclear envelope emerin organisational differences. Nuclei were further stained with DAPI (Blue). Scale bars represent 10 µm.*

Next we used western blotting to quantitatively compare expression levels of lamins, SUNs and emerin across the varying grades of breast cancer cell lines (*Figure 5.16)*.

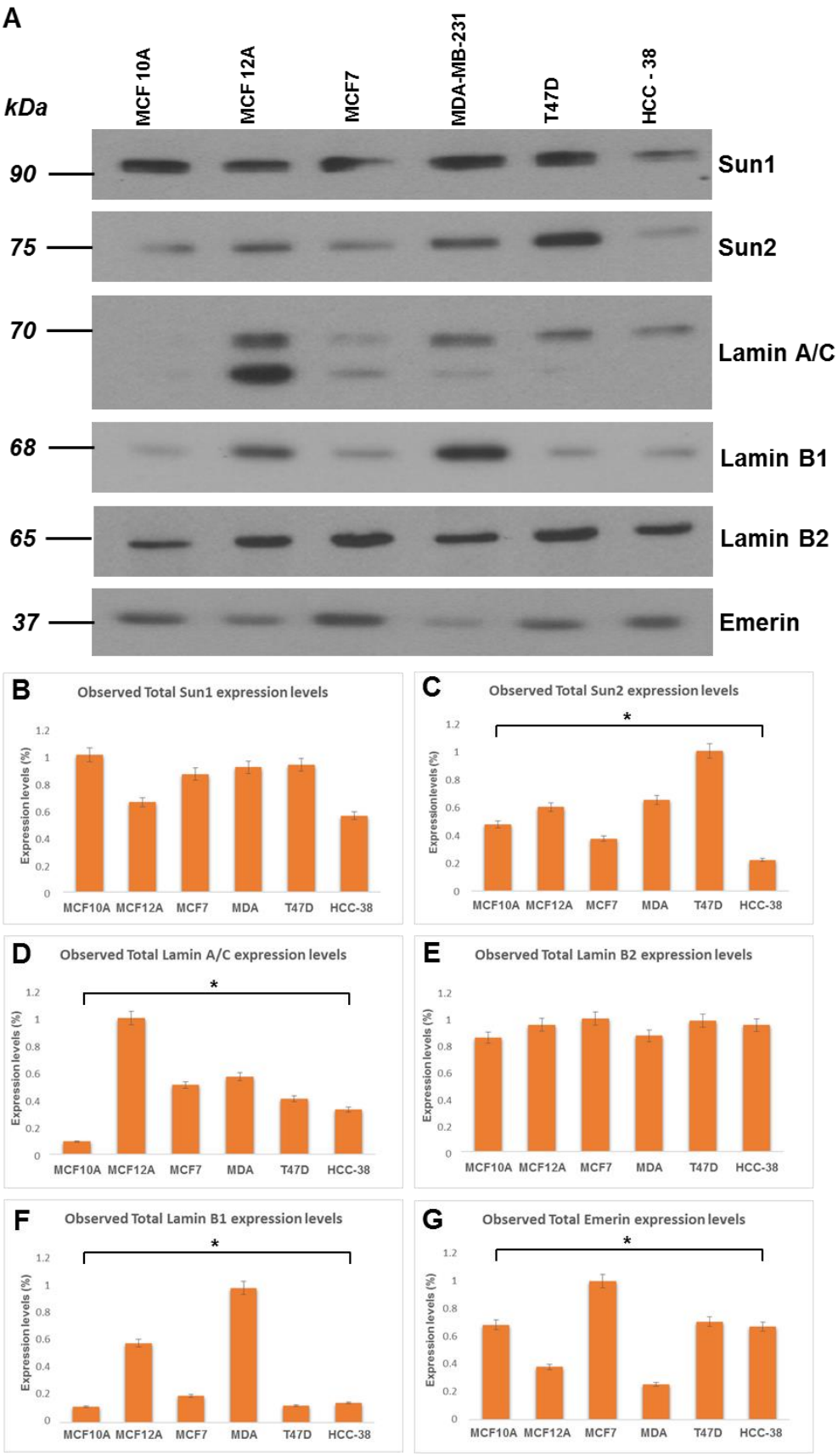

Figure 5.16: *Western blot analysis of INM proteins across breast cancer cell lines. (A) Displays western blot staining observed. (B), (C), (D), (E), (F) and (G) displays collated densitometry analysis across three repeats for each protein.*

Figure 5.16 suggests that variability can be seen between INM protein expression across the breast cancer cells assessed. It is shown that expression of SUN1 and Lamin B1 remain consistent across the various cancer grades, with little variability observed between samples. However, variability between SUN2 levels can be seen across the ranging breast cancer cells, in which significant up regulation in T47D cell lines are observed, alongside a significant reduction in expression across MCF 10A and MCF7 cell lines (*ANOVA,* $F_{5.3752} = 3.56$, $P = 0.010$ followed by subsequent F-test post hoc analysis where $p \leq 0.001$). Although variability is observed, it is difficult to discern if correlations exist between SUN2 expression levels and cancer progression due to the differential expression patterns displayed between control cell lines. This variation in protein expression across control cells could arise due to the unique history of the cells. Although from the same tissue region, these cells were isolated from different patients of differing ages (60 year old and 35 year old), suggesting that patient variability, alongside genetic changes resulting from cell line establishment, may stimulate protein expression profiles which vary between cells from the same tissue region.

Further observations suggest lamin B1 expression levels also appear to display significant variability across the samples (*ANOVA,* $F_{6.5488} = 2.92$, $P = 0.010$). Further post hoc F-test analysis where $p \leq 0.001$ suggests lamin B2 expression appears to be significantly upregulated in MCF 12A and MDA-MB-231 cell lines compared to MCF 10A and MCF7 cell lines, suggesting that lamin B1 expression could be associated with late stage development of cancerous phenotypes. It is further shown that variability in lamin A/C and emerin expression patterns also exists, in which lamin A/C is significantly upregulated in MCF 12A cells (*ANOVA,* $F_{3.6388} = 4.95$, $P = 0.010$, followed by subsequent F-test post hoc analysis where $p \leq 0.001$), whereas emerin is significantly upregulated within the MCF7 cells (*ANOVA,* $F_{4.2379} = 3.62$, $P = 0.010$, followed by F-test post hoc analysis where $p \leq 0.001$).

Thus far, collated data suggests that *LINC* components associated to the INM display differential variability across the breast cancer cells analysed. However, this variability appears to display little correlation to the specific cancer grade, suggesting these observed differences may be a result of downstream effects from further cellular alterations, which remain thus far undetected.

5.3.1.5 Nesprin proteins display drastic variability between control and cancerous breast cell lines.

Following observations in Chapter 3, in which *LINC* complex disruptions stimulated a reduction in nuclear stiffness alongside increased migration potential through restrictive scaffolds, current investigations aim to characterise *nesprin* protein organisation alongside expression levels across a range of breast cancer cell lines. At first, immunofluorescence analysis for nesprin-1's ABD domain (staining all nesprin-1 isoforms retaining the N-terminal ABD region) was conducted, to assess whether correlations exist between cellular localisation and cancer progression. Data from this staining is displayed in *Figure 5.17*.

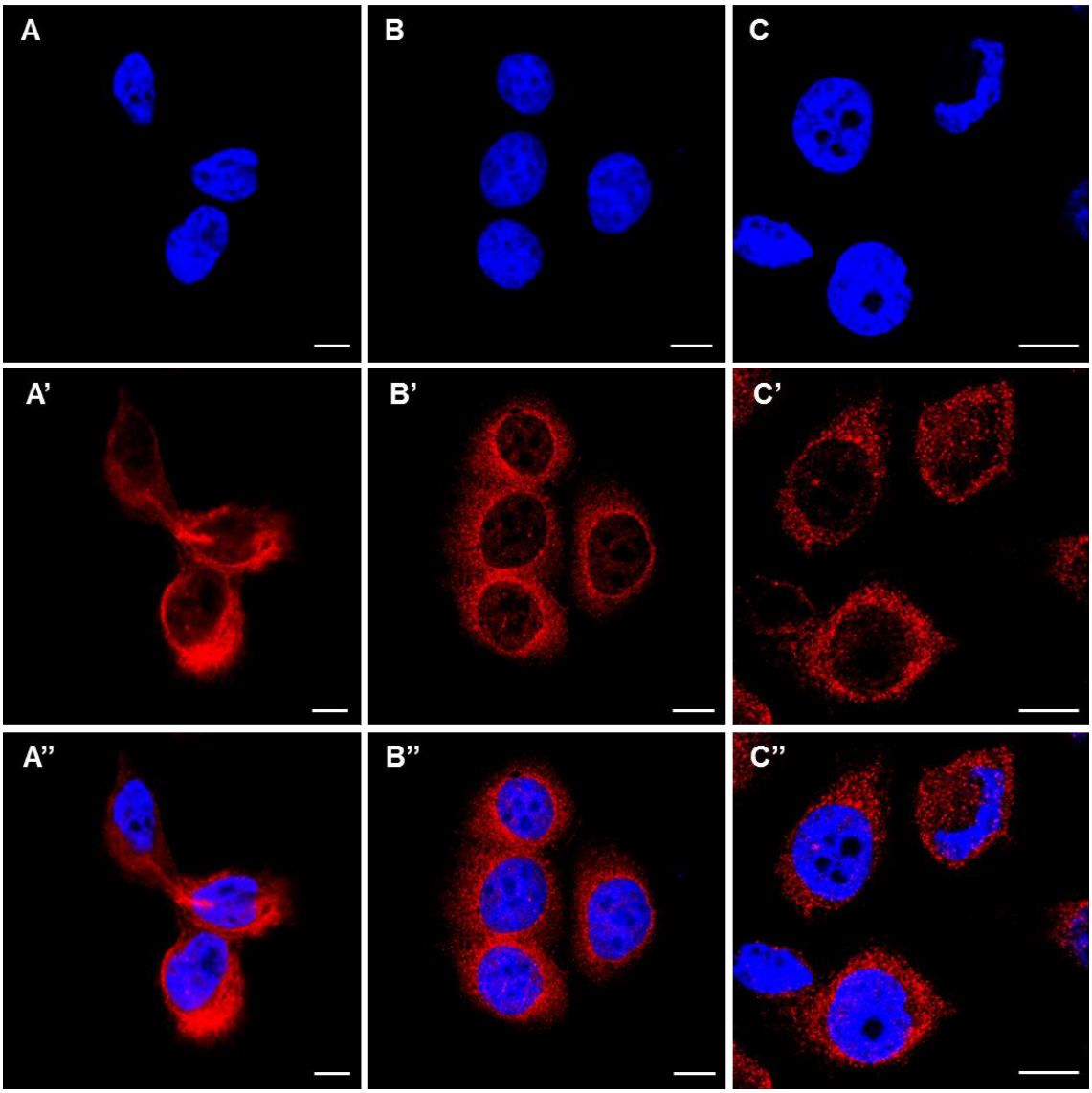

Figure 5.17: *Nesprin-1 (ABD) (Red) stained MCF 10A (A, A', A''), MCF7 (B, B', B'') and MDA-MB-231 (C, C', C'') cell lines displaying Nesprin-1 isoforms containing the N-terminal ABD domain. Nuclei were further stained with DAPI (Blue). Scale bars = 10 µm.*

Data shown in *Figure 5.17* suggests nesprin-1 ABD staining appears to be in closer associations across defined cellular regions which could correlate to the ER in MCF 10A cells, compared to low and high grade breast cancer representative cells. In MCF 10A and MCF7 cells, nesprin-1 ABD staining appears specifically localised to the NE with diffuse cytoplasmic staining. In the MDA-MB-231 cells however, staining reveals a potential loss in direct NE staining, with resulting images displaying a punctate staining pattern across cellular regions potentially correlating to ER. These observations could potentially suggest that expression levels of nesprin-1 ABD domain containing isoforms could be lost under cancer progression, resulting in the more diffuse staining observed in the MCF7 and MDA-MB-231 cells lines, however, quantitative protein analysis techniques would be required to verify this, such as PCR and western blotting approaches.

As the nesprin-1 ABD fluorescence staining suggests a potential variability in organisation across breast cancer samples, further protein analysis was performed to investigate whether correlations could be seen with protein expression levels. This will allow the assessment of whether observed alterations in nesprin-1 ABD localisation is a direct result of miss-localisation across the NE, or a result of variability in ABD containing isoform expression differences across the breast cancer lines. Resulting western blot analysis alongside staining for both nesprin-1 N- and C-terminal region is displayed in *Figure 5.18*.

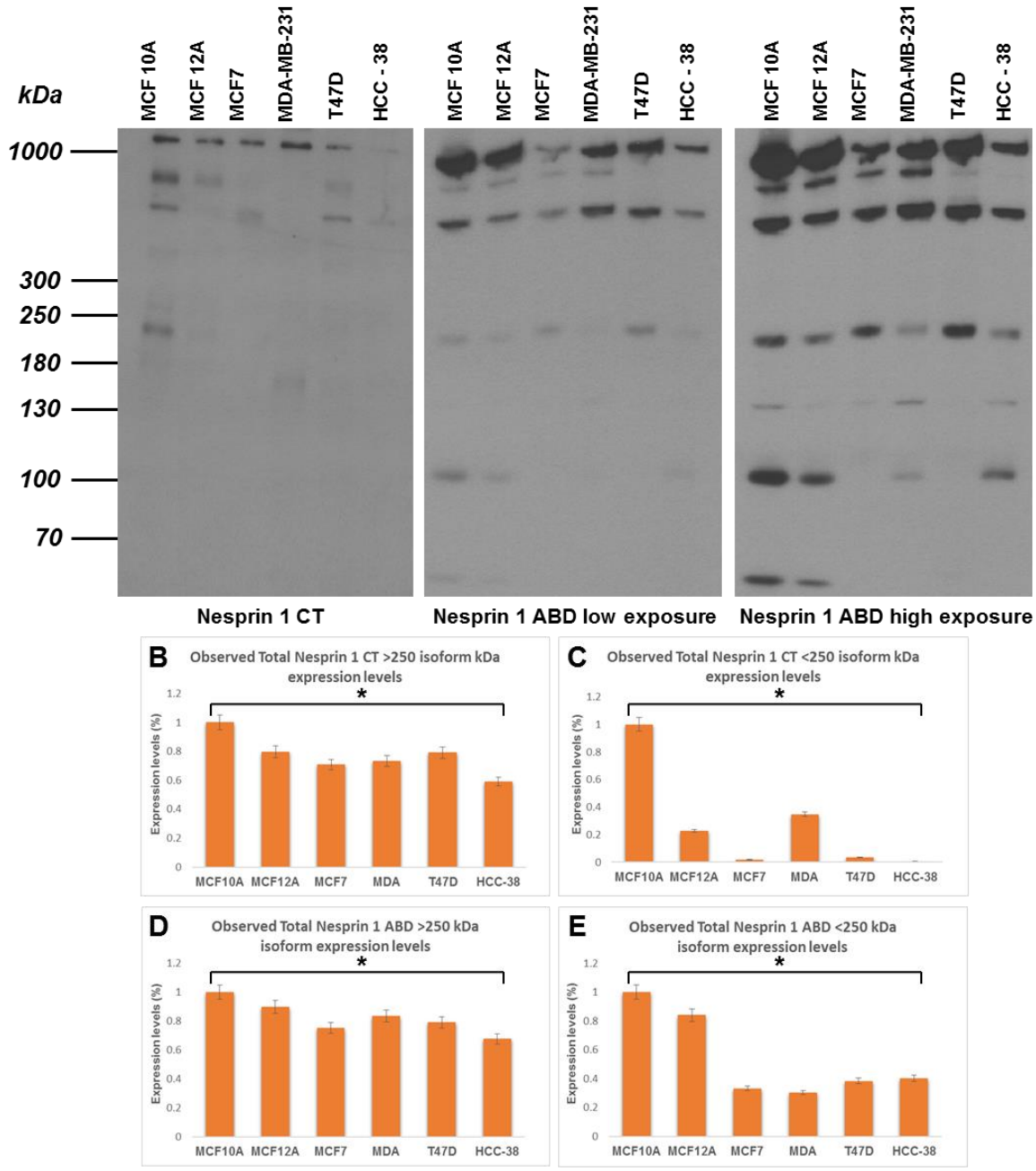

Figure 5.18: *Western blot data for Nesprin-1 C-terminal KASH and N-terminal ABD domains across breast cancer cell lines. (A) Displays western blot staining observed. (B), (C), (D) and (E) represent collated densitometry analysis from across three repeats.*

The data presented within *Figure 5.18* suggests significant variability in nesprin-1 isoform expression levels does exist across the range of breast cancer cell lines (*ANOVA,* $F_{5.1165} = 3.91$, $P = 0.010$). It can be seen that across the 1000 kDa giant nesprin-1 isoform, no observable relationships can be discerned. However, when observing the lower isoforms of nesprin-1 N- and C-terminal regions (<250 kDa), it appears that the lower nesprin-1

isoforms are expressed to a significantly higher level within the two non-cancerous control cell lines for isoforms exhibiting both C-terminal and N-terminal regions using post hoc F-tests where $p \leq 0.001$. Alongside this, levels appear to significantly reduce upon cancer development, suggesting that the lower isoforms for nesprin-1 could be a potential factor within the development of cancerous phenotypes, rather than the more commonly analysed *GIANT* isoform.

Following these observations, further investigations aimed to assess whether similar organisation and expression trends existed for alternate KASH proteins across breast cancer cell lines. To do this, immunofluorescence studies were performed using antibodies against N and C-terminal nesprin-2 epitopes, from which data can be seen presented in *Figures 5.19 and 5.20*.

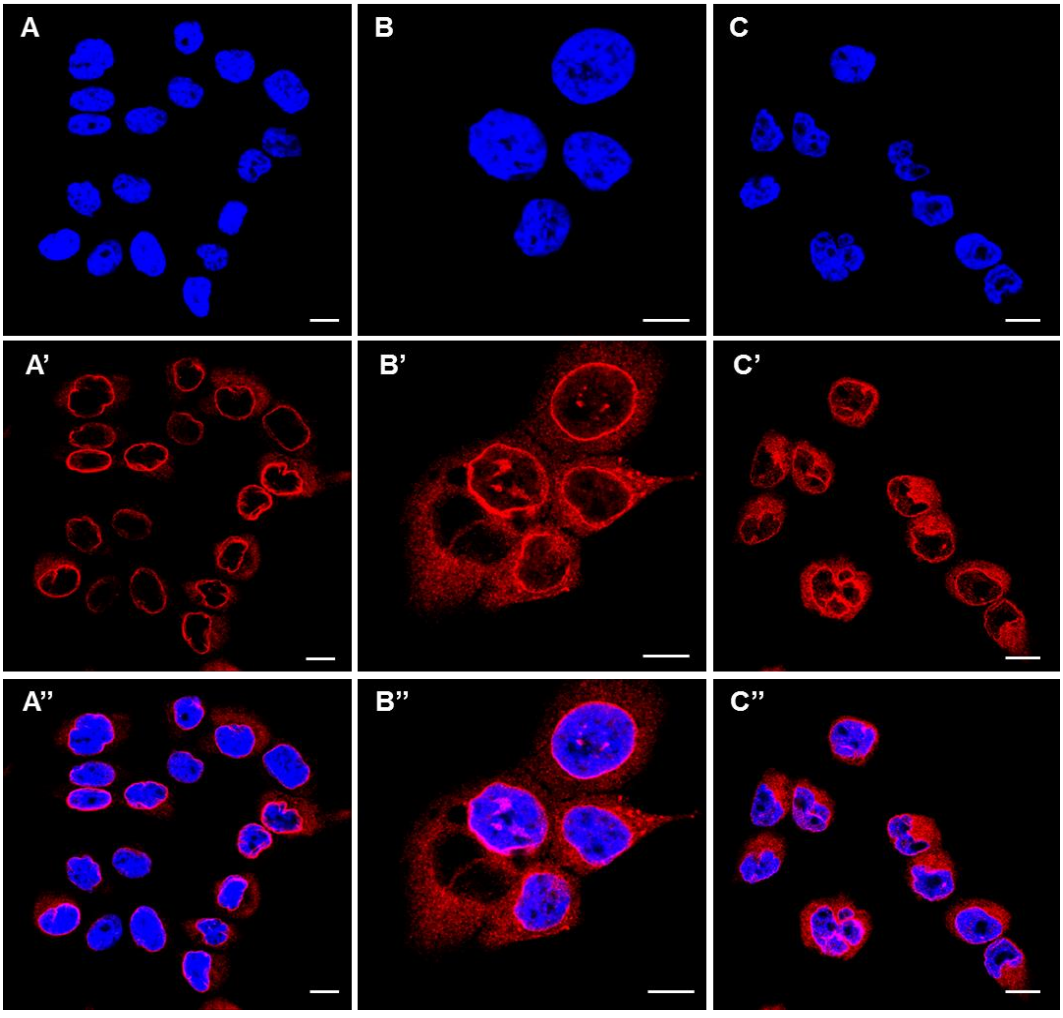

Figure 5.19: *Nesprin-2 C-terminal (Red) stained MCF 10A (A, A', A''), MCF7 (B, B', B'') and MDA-MB-231 (C, C', C'') cell lines displaying isoforms containing the C-terminal KASH domain. Nuclei were further stained with DAPI (Blue). Scale bars = 10 µm.*

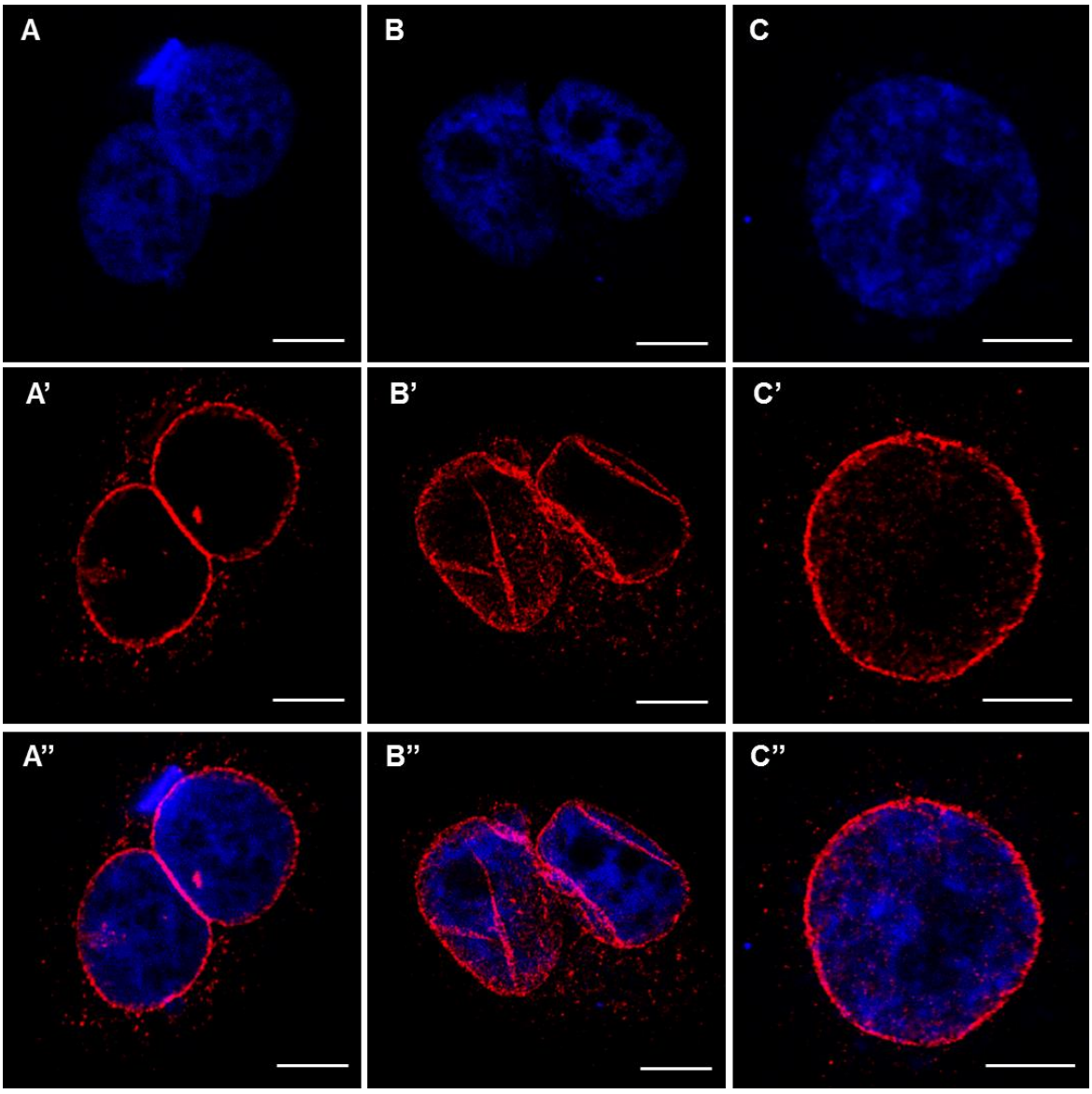

Figure 5.20: *Nesprin-2 N-terminal (Red) stained MCF 10A (A, A', A''), MCF7 (B, B', B'') and MDA-MB-231 (C, C', C'') cell lines displaying isoforms containing the N-terminal ABD domain. Nuclei were further stained with DAPI (Blue). Scale bars = 10 µm.*

The data presented in *Figures 5.19* and 5.*20* suggest that some organisational differences exist between the cancer cells assessed for nesprin isoforms containing the C-terminal KASH domain but not the N-terminal *ABD* domain. It is shown that the C-terminal staining appears to become more cytoplasmic as the cancer grade increases, with the control MCF 10A cells displaying specific nuclear envelope staining and MCF7 and MDA-MB-231 lines expressing increasing cytoplasmic distribution. In contrast, nesprin-2 N-terminal *ABD* localisation retains mainly specific NE localisation across each cell line.

To validate observations suggesting nesprin-2 C-terminal regions appears to become more cytoplasmic as the breast cancer grade increases, quantitative analysis of pixel intensities across the whole length of MCF 10A, MCF7 and MDA-MB-231 cell lines was performed, to assess cell regions in which staining could be observed. Images alongside graphical data collated from across triplicate measurements of 50 cells are displayed in *Figures 5.21* and 5.*22*.

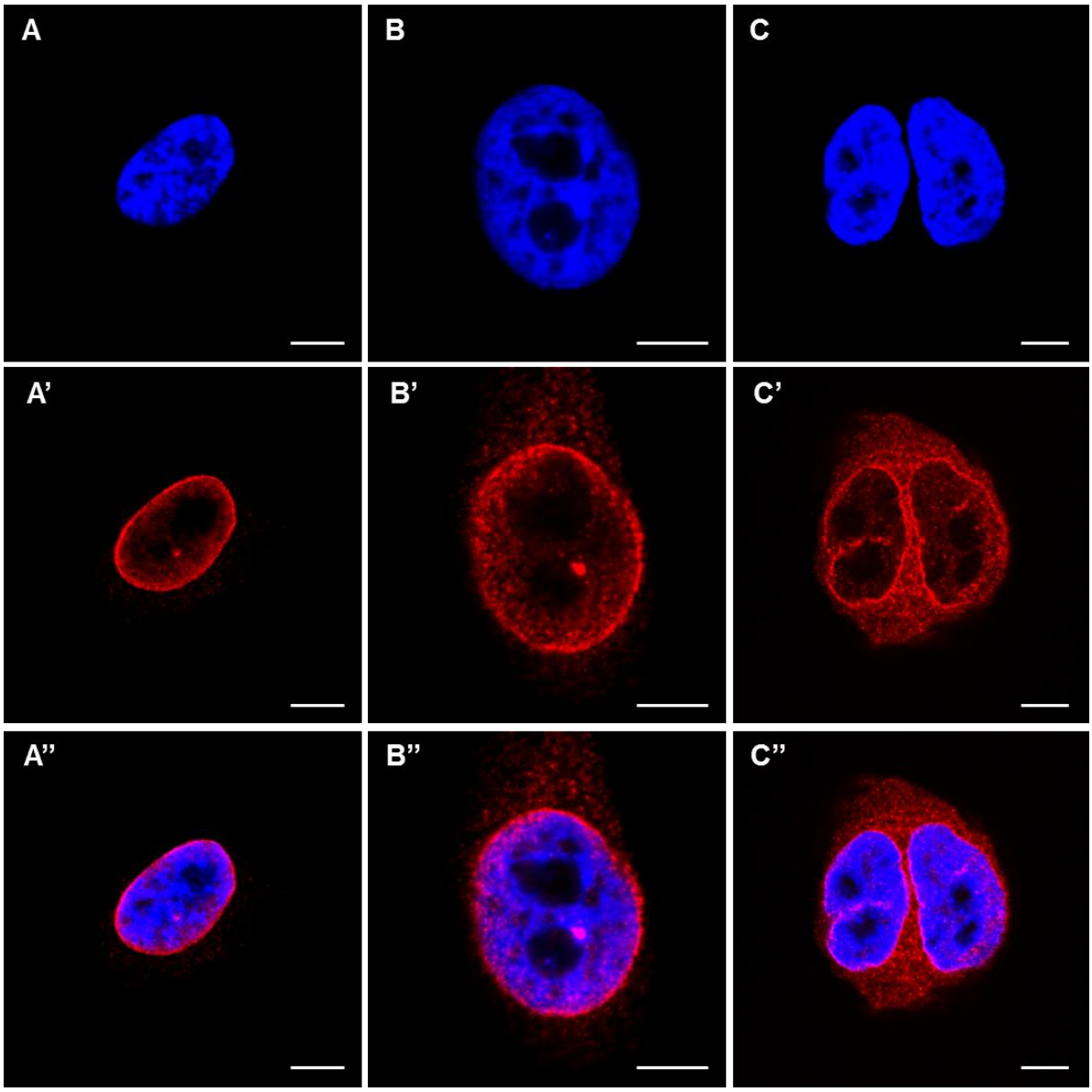

Figure 5.21: *Nesprin 2 C-terminal (Red) stained MCF 10A (A, A', A''), MCF7 (B, B', B'') and MDA-MB-231 (C, C', C'') cell lines. Displaying increased cytoplasmic staining as cancer grade increases. Nuclei were further stained with DAPI (Blue). Scale bars = 10 µm.*

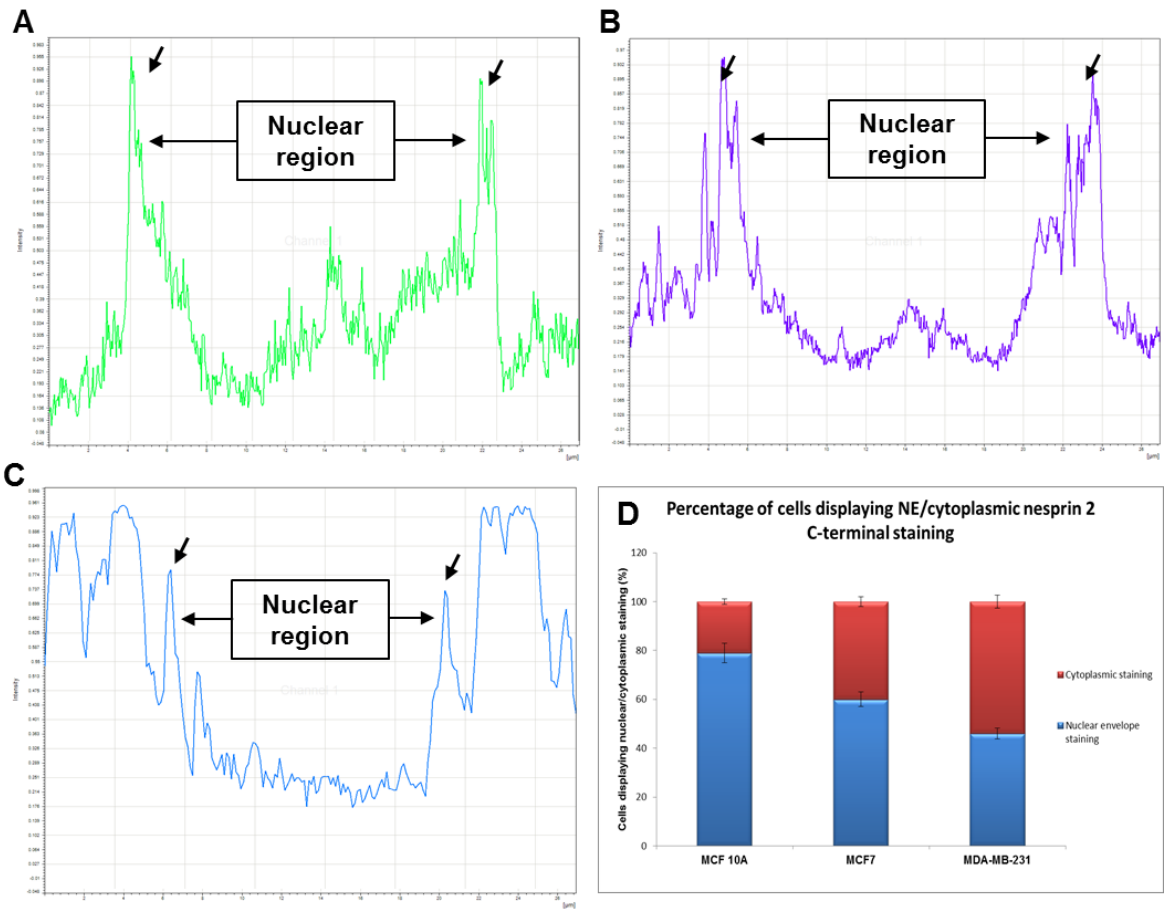

Figure 5.22: *Pixel intensity map of Nesprin-2 C-terminal stained MCF10A (A), MCF7 (B) and MDA-MB-231 (C) cell lines. Images display pixel intensity across the whole cell. Arrows display nuclear envelope staining regions. (D) Displays percentage NE/cytoplasmic nesprin-2 C-terminal staining, collated from across 50 cells of each cell line, repeated three times.*

From the data presented within *Figures 5.21*, it is suggested that nesprin-2 C-terminal staining (antibody binding to the last two SRs that precede KASH domains) appears to disperse from the nuclear envelope within high grade breast cancer cell lines, stimulating an increase in cytoplasmic staining. Further pixel mapping data displayed in *Figure 5.22*, highlights that in both control and low grade breast cell lines (A and B), pixel intensity appears to peak at the NE, followed by a reduced signal correlating to central nuclear and cytoplasmic regions. In contrast, MDA-MB-231 cell lines display an increase in cytoplasmic signal retention, whilst retaining low expression levels within central nuclear regions. (D) Further supports this observation, suggesting a significant increase in cytoplasmic accumulation of nesprin-2 C-terminal staining in the MDA-MB-231 cells (*ANOVA,* $F_{4.2253} = 5.09$, $P = 0.010$). It can therefore be suggested that the localisation of nesprin-2 C-terminal KASH domain isoforms may be disrupted within high-grade breast cancers, leading to a potential dissociation from the nuclear envelope into the surrounding cytoplasm.

To further assess whether observed organisational differences between control, low and high grade breast cancer cells were due to disruptions in protein interactions, or alterations in protein expression levels, further western blot analysis was conducted. Staining against nesprin-2 N- and C-terminal regions alongside quantification analysis can be seen in *Figure 5.23*.

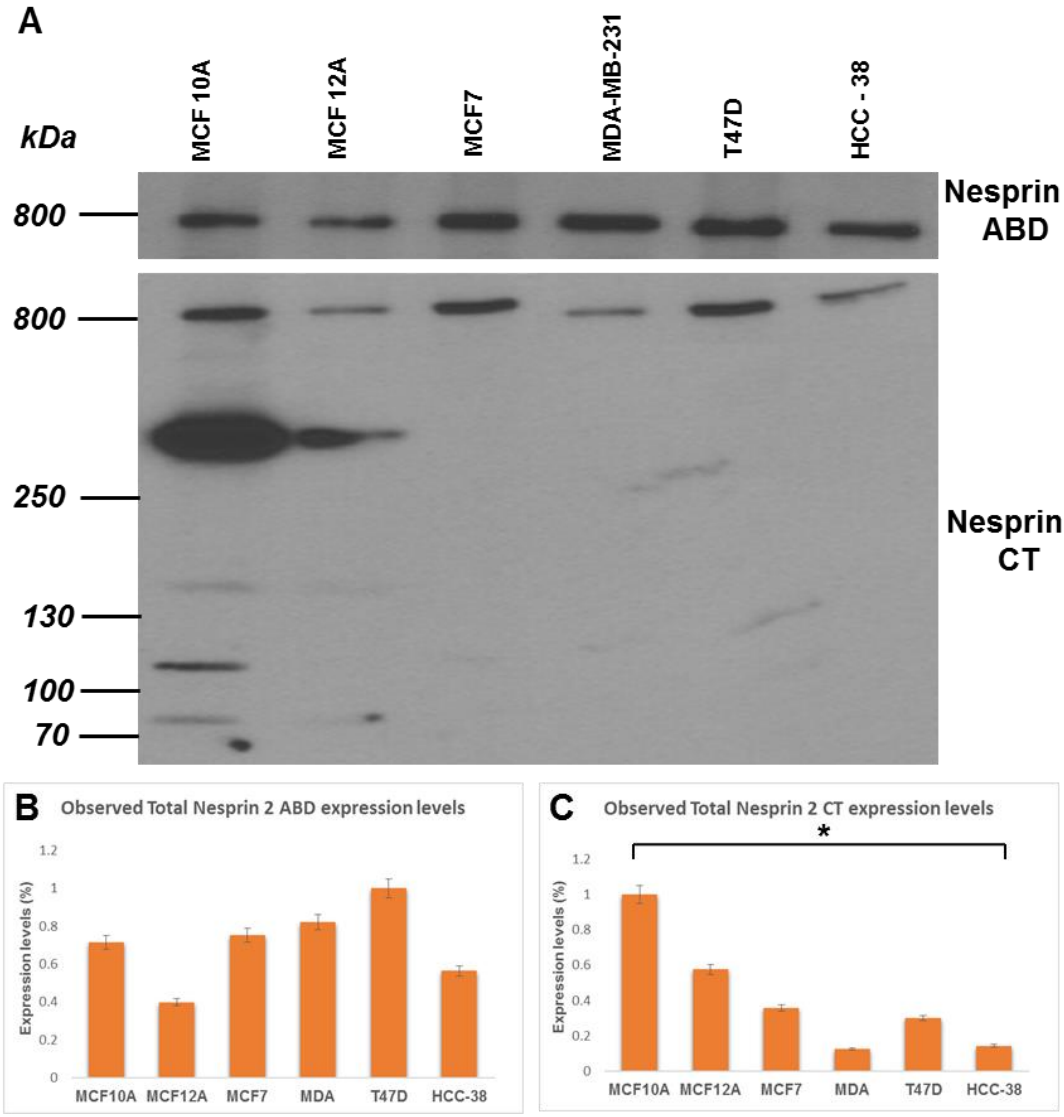

Figure 5.23: *Western blot data for Nesprin-2 C-terminal KASH and N-terminal ABD domains across breast cancer cell lines. (A) Displays western blot staining observed. (B) and (C) represent collated densitometry analysis across three repeats for each protein.*

Figure 5.23 suggests that similar trends to that observed within nesprin-1 isoform analysis can be seen in which the lower nesprin-2 isoforms are down-regulated in the cancerous cell lines in comparison to control cell lines. It is shown that the *GIANT* isoforms of nesprin-2 situated at 800 kDa display limited variability across the breast

cancer cell lines for N-terminal ABD domain. However, significant variability is observed across the C-terminal *KASH* domain isoform expression levels, in both high and low isoform variants (*ANOVA,* $F_{4.5387} = 4.12$, $P = 0.010$). Further post hoc analysis through the application of F-tests where $p \leq 0.001$ suggests the most obvious of these differences is in the reduction of lower nesprin-2 isoforms in cancerous cell lines, in which little to no expression of lower C-terminal containing isoforms are detected across the cancerous cell lines. This data, coupled with fluorescence analysis could suggest that lower C-terminal *KASH* containing isoforms of nesprin-2 could provide a potential anchor for the larger nesprin-2G isoform across the NE. This is suggested due to breast cancer cell lines displaying a reduced expression of these lower isoforms, alongside an increased cytoplasmic accumulation of nesprin-2 C-terminal staining. This nesprin diffusion from the NE to cytoplasm could result in a loss of nuclear stiffness due to a disruption in *LINC* connections across the NE (Chapter 3). This resulting loss of nuclear stiffness may in turn aid in the development of metastatic behaviours, due to suggestive evidence linking nuclear stiffness to cancer metastasis [272].

Following observations for nesprin-1 and nesprin-2 isoforms, further assessment of the KASH containing protein nesprin-3 cell positioning across different breast cancer grades was conducted. Cells were stained for nesprin-3 as described in the methods section, from which data can be seen, displayed in *Figure 5.24*.

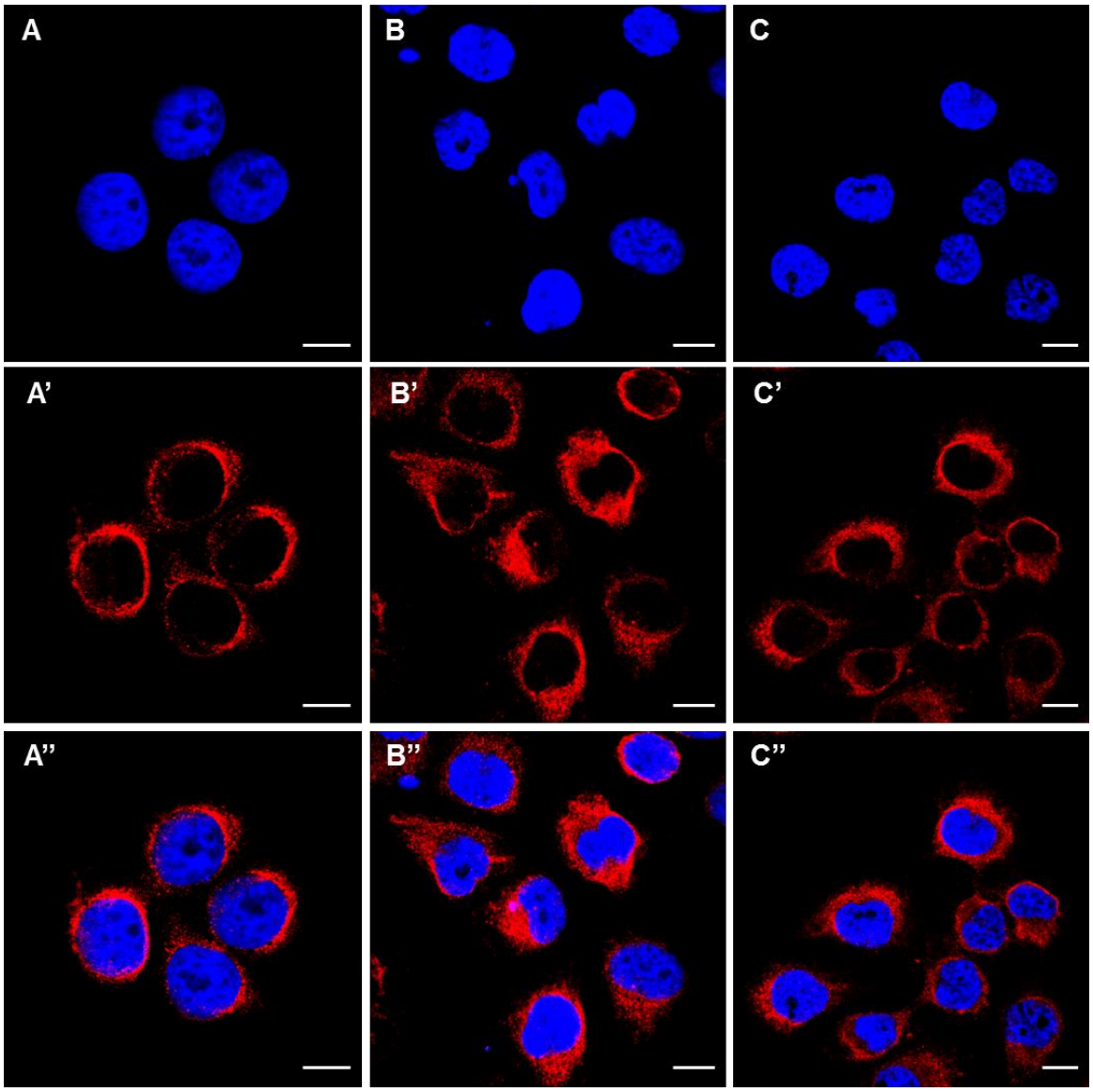

Figure 5.24: *Nesprin-3 stained MCF 10A (A, A', A''), MCF7 (B, B', B'') and MDA-MB-231 (C, C', C'') cell lines. Nuclei were further stained with DAPI (Blue). Scale bars = 10 µm.*

Data displayed in *Figure 5.24* suggests no obvious localisation differences are observed for nesprin-3 across the control, low grade and high grade breast cancer cell lines. The staining suggests specific nesprin3 localisation across the NE and potential ER, with no intra-nuclear staining.

Further analysis of nesprin-3 and nesprin-4 expression levels across a range of breast cancer cell lines was then conducted, with aims to investigate whether correlations exist between nesprin-3/-4 expression levels and cancer progression. Experimental data alongside densitometry analysis is displayed in *Figure 5.25*.

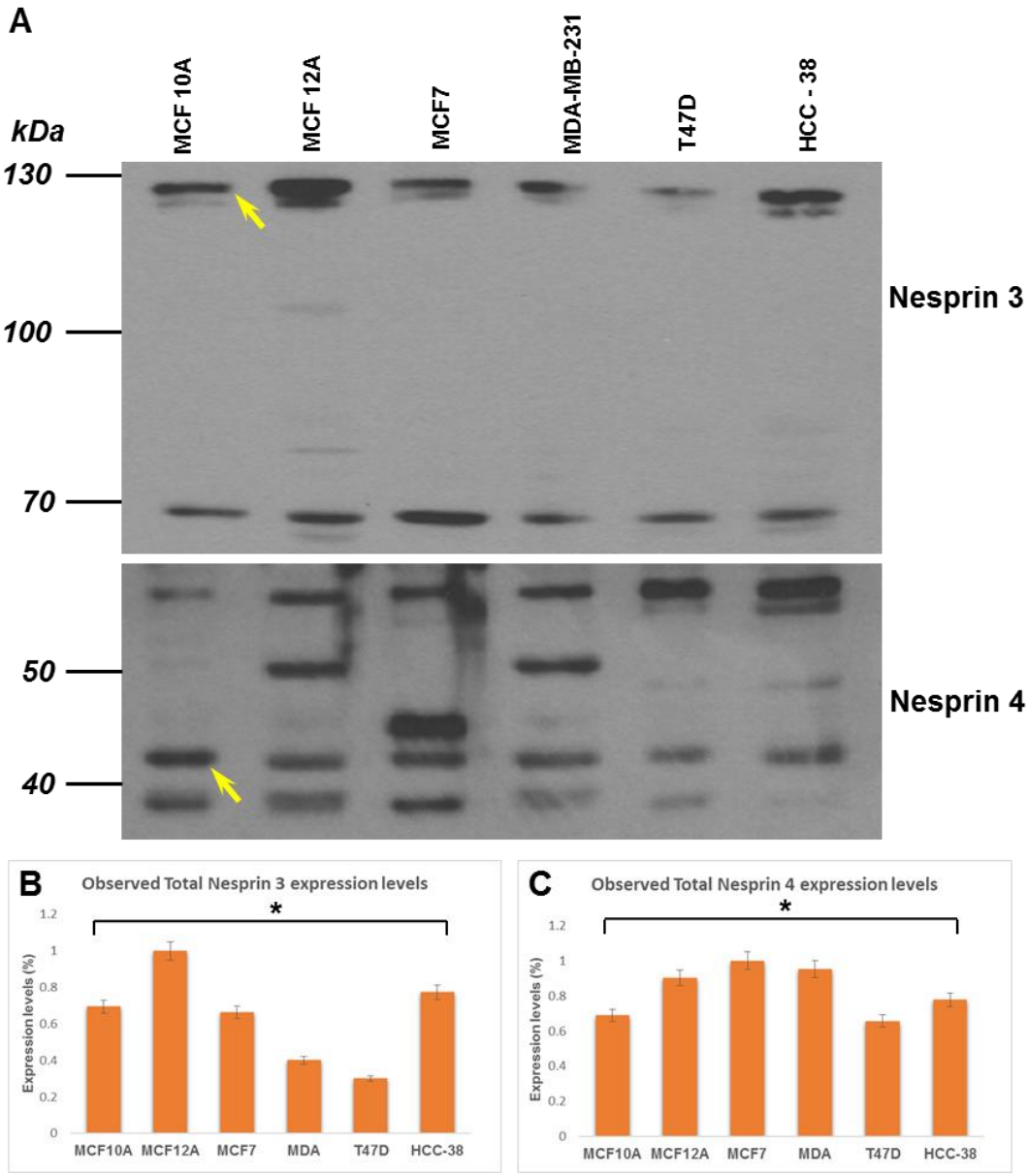

Figure 5.25: *Western blot data for nesprin-3 and nesprin-4 expressions across breast cancer cell lines. (A) Displays western blot staining observed. (B) and (C) displays collated densitometry analysis across three repeats for each protein. Arrows highlight predicted bands correlating to nesprin-3 and nesprin-4 respectively.*

The data presented in *Figure 5.25* suggests that significant variability is observed across the range of breast cancer cell lines for both nesprin-3 (*ANOVA,* $F_{6.2188} = 3.62$, $P = 0.010$, followed by subsequent F-test post hoc analysis where $p \leq 0.001$) and nesprin-4 (*ANOVA,* $F4_{.5365} = 4.32$, $P = 0.010$, followed by subsequent F-test post hoc analysis where $p \leq 0.001$) isoform expression levels. For nesprin-3, it can be seen that both the full length isoform can be seen (~120 kDa) alongside a lower isoform variant. To assess nesprin-3 expression across each cell line, densitometry analysis was performed across the whole

lane for each cell line. Aside this, nesprin-4 staining displayed the expected band at ~42 kDa, however, further non-specific staining was also observed. These further detected isoforms may be a result of non-specific antibody binding, or not yet characterised nesprin-4 isoforms. To maintain objectivity, the total signal from within each lane was assessed, as in the nesprin-3 analysis. Although significant differences are observed however, the variations do not appear to correlate with increased cancer severity. This therefore suggests the observed variability in nesprin-3 and nesprin-4 expression patterns may arise from cell specific variation, rather than the cancer severity.

5.3.1.6 Further proteins involved in maintaining cell polarity, nuclear architecture and cell-cell interactions display variability across breast cancer cell lines.

Due to levels of nesprin-1 and -2 isoforms decreasing upon increasing cancer cell line severity, further investigations aimed to assess the expression patterns of known associated proteins to nesprin-1 and -2, alongside known cancer markers across a range of breast cancer cell lines. Western blot staining was performed against centrin and pericentrin (known centrosome markers), E-cadherin and lap2α (proteins involved in maintaining cell-cell adhesion and cell-cycle regulation/chromatin organisation respectively) and p53 (a protein known to play roles in cancer progression). Data from this investigation is shown in *Figure 5.26*.

Figure 5.26 suggests further significant differences can be observed for pericentrin expression across the range of breast cancer cells; however, this variability in expression does not appear to correlate with an increase in cancer severity (*ANOVA,* $F_{3.2669} = 3.01$, $P = 0.010$, followed by subsequent F-test post hoc analysis where $p \leq 0.001$). However, for centrin, it appears that protein expression increases from control, to low then high grade cell lines (*ANOVA,* $F_{3.0021} = 2.92$, $P = 0.010$, followed by subsequent F-test post hoc analysis where $p \leq 0.001$). This observed correlation however is not true for all cell lines assessed, as the T47D and HCC-38 cell lines (representing medium grade cancers) display reduced centrin levels, further suggesting that these observations may be cell specific rather than cancer grade specific.

Alongside these observations, it is further shown that levels of both p53 and lap2α proteins increase as the cancer severity increases. Highest p53 expression is observed in medium and high grade breast cancer cells, whereas lap2α expression peaks in all

cancerous cells. Protein expression levels for E-cadherin also vary drastically across the range of cell lines assessed, with lowest expression observed in MCF 12A and MDA-MB-231, representing control and high grade breast cancers respectively suggesting variability in E-cadherin expression may be cell line specific.

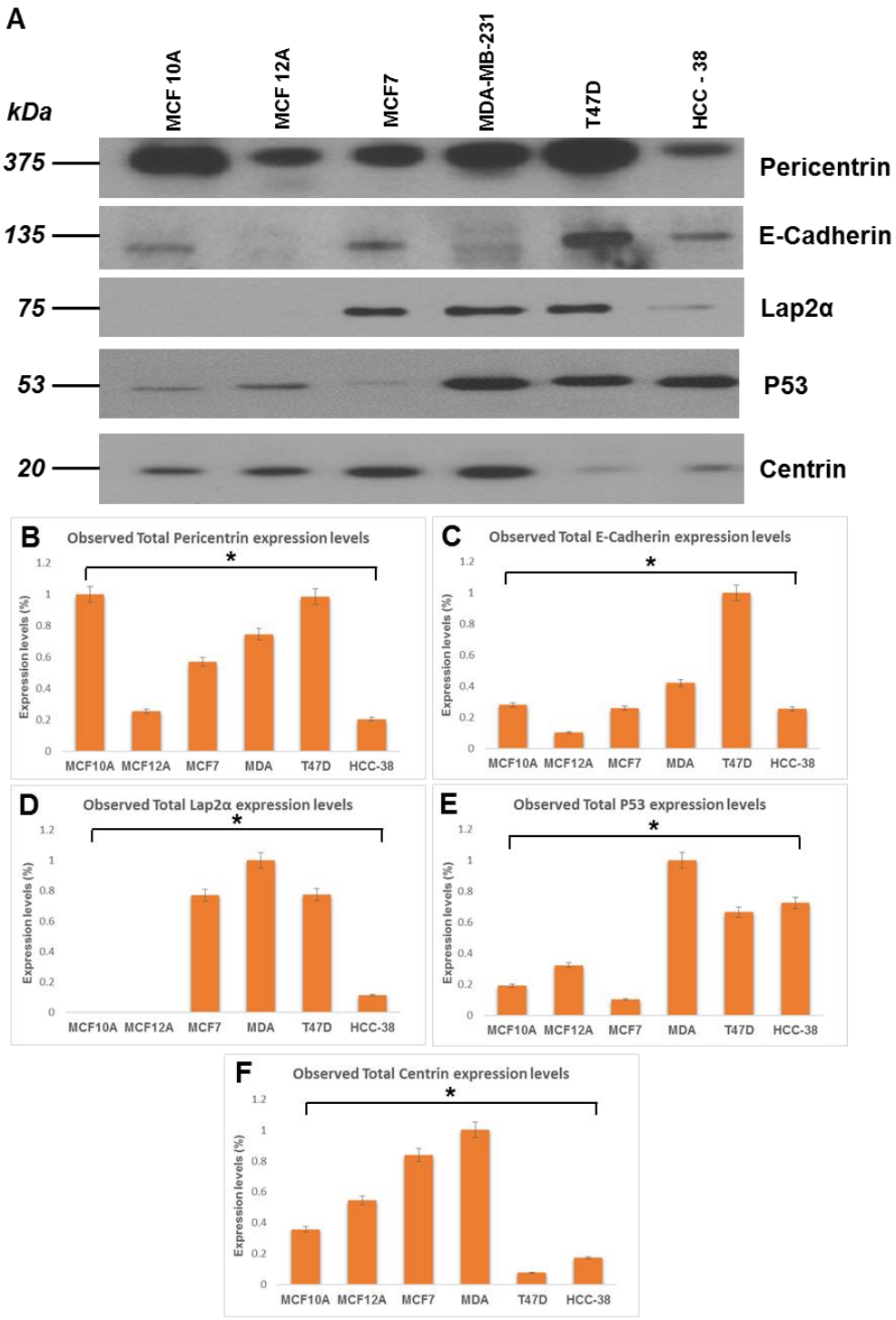

Figure 5.26: *Western blot data for LINC associated proteins and known cancer marker expression across breast cancer cell lines. (A) Displays western blot staining observed. (B), (C), (D), (E) and (F) displays collated densitometry analysis across three repeats for each protein.*

These observations therefore suggest that correlations can be seen between lap2α and p53 expression levels and cancer severity. However for the further *LINC* associated proteins analysed it is difficult to discern whether expression levels correlate to the breast cancer severity, potentially due to further variables in alternate gene/protein expression patterns specifically present within each cell line.

5.3.1.7 Nuclear pore complex proteins display differential expression patterns across a range of breast cancer cell lines.

As previous data presented in Chapter 3 suggests loss of *SUN-KASH* connections across the perinuclear space stimulates alterations in nuclear architecture, further investigations aimed to assess positioning and expression levels of known nuclear pore complex proteins. The nuclear pore complex, alongside the *LINC* complex plays an important role in maintaining nuclear architecture, helping to form anchor points connecting inner and outer nuclear membranes. As data thus far suggests *LINC* complex disruptions lead to a decrease in nuclear stiffness, and that specific *LINC* components such as lower nesprin isoforms appear to be down regulated in high grade cancers, further work aims to investigate whether NPC variations also exist in high grade breast cancers, and whether NPC defects could be crucial components for the development of highly metastatic phenotypes.

Initial investigations aimed to assess the organisation of select NPC proteins across control, low grade and high grade breast cancer cell lines using immunofluorescence techniques. Cells were stained for Mab414 (NPC marker) and Nup88 (NPC protein) as described within the methods, with resulting staining displayed in *Figures 5.27* and 5*.28*.

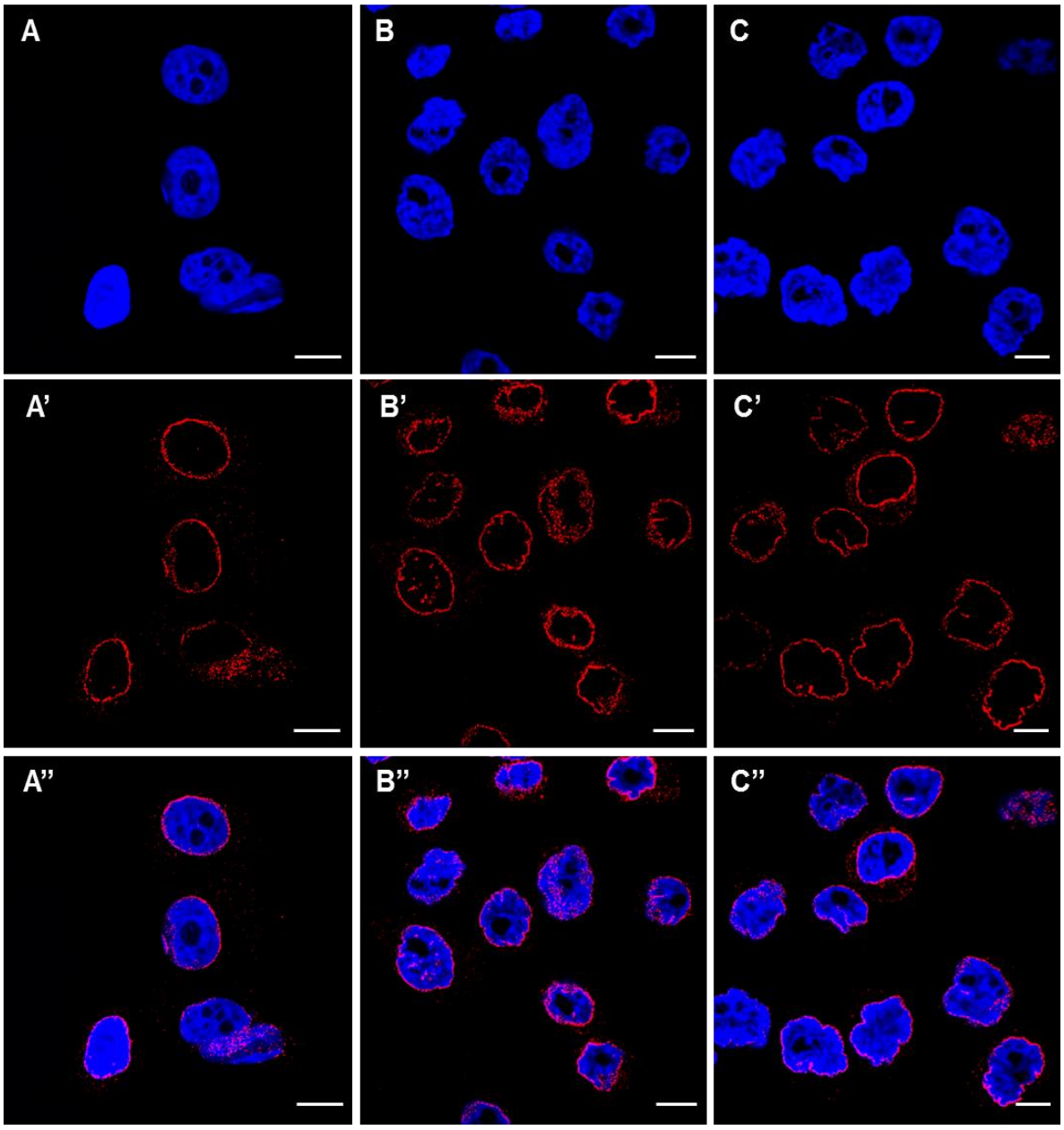

Figure 5.27: *Mab414 (Red) stained MCF 10A (A, A', A''), MCF7 (B, B', B'') and MDA-MB-231 (C, C', C'') cell lines. Images display NPC organisation across the NE. Nuclei was further stained with DAPI (Blue). Scale bars = 10 µm.*

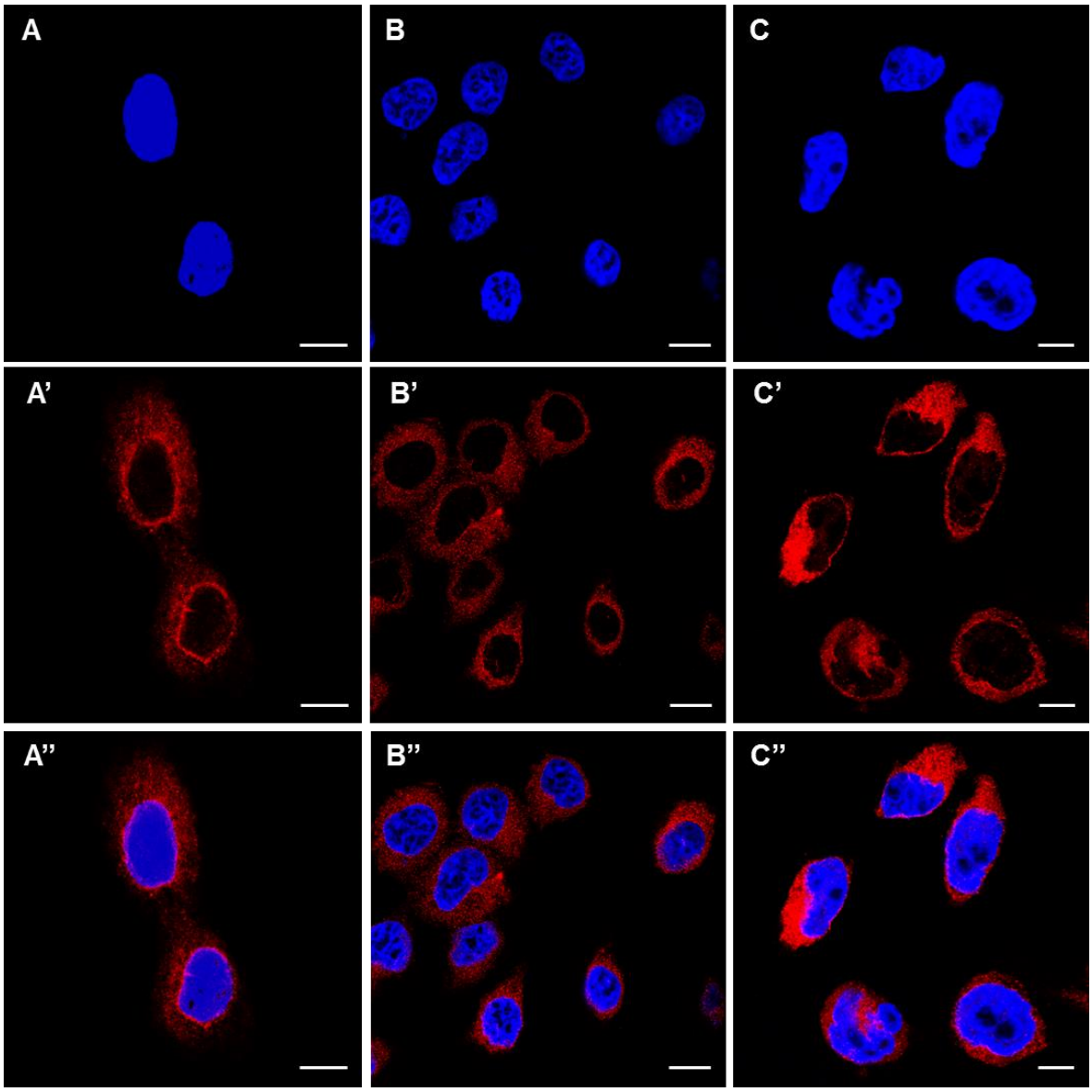

Figure 5.28: *Nup88 (Red) stained MCF 10A (A, A', A''), MCF7 (B, B', B'') and MDA-MB-231 (C, C', C'') cell lines. Nuclei were further stained with DAPI (Blue). Scale bars = 10 µm.*

Data presented in *Figures 5.27* and 5*.28* suggest that the organisation of Mab414 and Nup88 across the range of breast cancer cells appears to remain consistent. It is shown that Mab414 displays specific NE staining across control, low and high grade cell lines. In contrast, Nup88 staining displays both NE and cytoplasmic staining (potentially correlating with ER) across all cell lines analysed. One observed difference however, is a possible increase in cytoplasmic staining of Nup88 in high grade MDA-MB-231 cells, however, further protein analysis would need to be conducted to verify this.

As it is difficult to assess whether protein expression levels are indeed altered within the cell lines based on immunofluorescence staining alone, further western blot analysis

for Mab414 (antibody targeted against FG nucleoporins) and Nup88 protein expression levels was conducted. This will allow the verification as to whether the observed differences from *Figure 5.28* are indeed due to an increase in Nup88 expression, or due to abnormalities in protein organisation. This western blot analysis can be seen displayed in *Figure 5.29*.

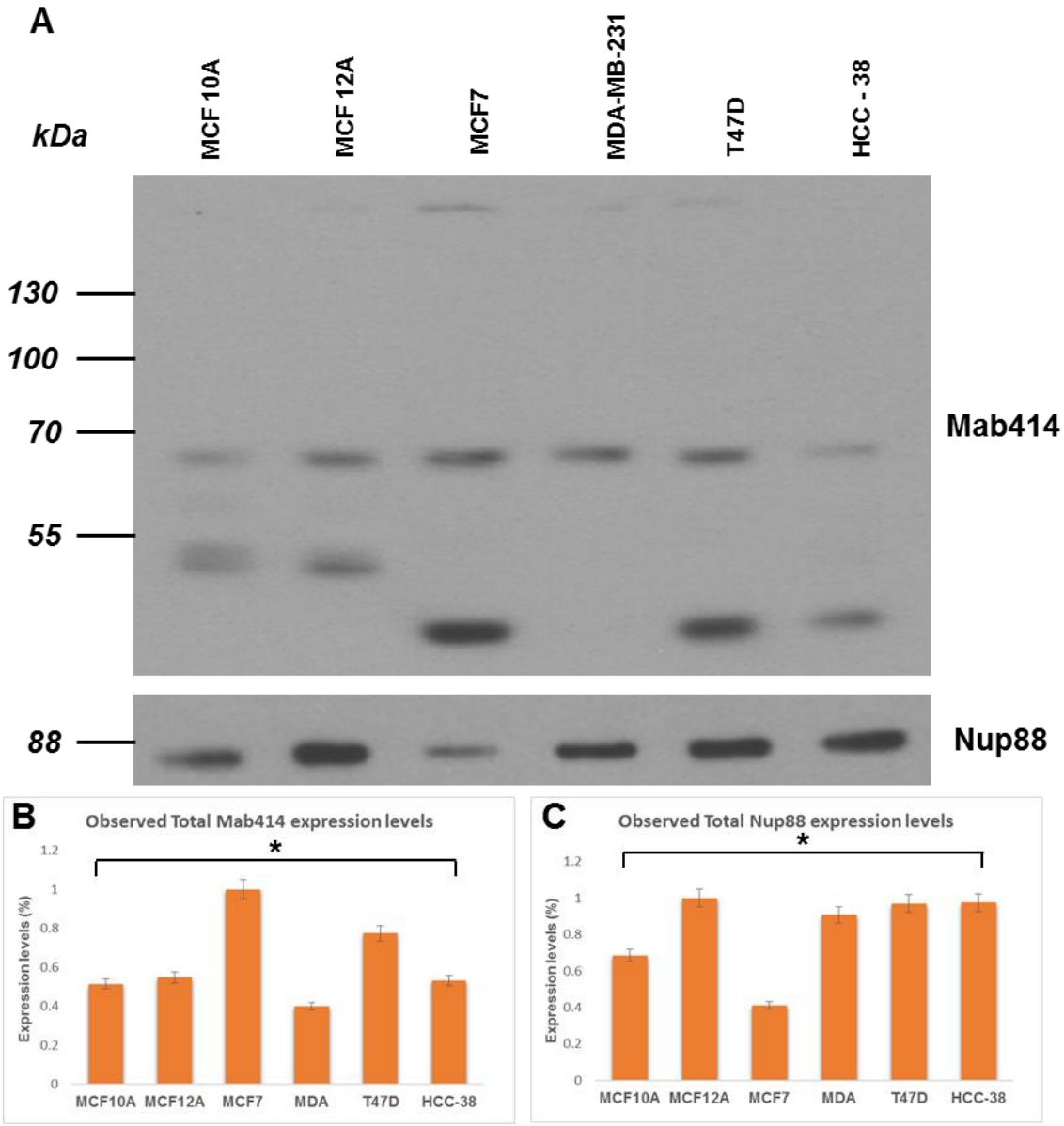

Figure 5.29: *Western blot data for NPC protein expressions across breast cancer cell lines. (A) Displays western blot staining observed. (B) and (C) represent collated densitometry analysis across three repeats for each protein.*

The data presented in *Figure 5.29* suggests significant variability exist between expression profiles of both Mab414 (*ANOVA,* $F_{4.1152} = 4.13$, $P = 0.010$, followed by subsequent F-test post hoc analysis where $p \leq 0.001$) and Nup88 (*ANOVA,* $F_{3.6498} = 3.23$, $P = 0.010$,

followed by subsequent F-test post hoc analysis where $p \leq 0.001$) across the range of breast cancer cell lines. However, it is difficult to discern whether correlations exist between the variability in expression levels and grade of cancer, suggesting that the observed protein expression differences may be a result of cell specific variability. Mab414 expression appears to remain constant across the ~70 kDa band, which can be potentially identified as Nup62 in each sample. Further to this, the band displayed in MCF 10A and MCF 12A at ~50 kDa could represent Nup50, showing reduced expression upon cancer progression. Of further interest is the band expressed at ~35 kDa, in which expression is only present in low and medium grade breast cancer cell lines, suggesting that expression profiles of this protein may correlate to early stages of cancer progression, before high grade metastasis develops. In contrast, Nup88 levels appear to display reduced expression in MCF7 cells. This data further supports observations from *Figure 5.28*, in which Nup88 cytoplasmic accumulation appeared to be constricted in MDA-MB-231 cells, suggesting this observation is due to increased Nup88 expression observed in MDA-MB-231 cells compared with MCF 10A and MCF7 cell lines.

5.3.1.8 Heat shock protein expression displays variability across breast cancer cell lines.

To further investigate potential links between observations highlighted thus far, and stress signalling pathways linked closely to cancer development, following investigations aimed to analyse expression levels of known chaperones, including HSP27, CRYAB and GFAP. These investigations therefore aim to increase understanding of links between cancer severity, nesprin expression and chaperone expression patterns within breast cancer. Western blotting across the range of breast cancer cell lines was conducted with multiple antibodies against CRYAB and HSP27, alongside a single antibody for GFAP. Results obtained from this western blot data can be seen displayed in *Figures 5.30* and *5.31*.

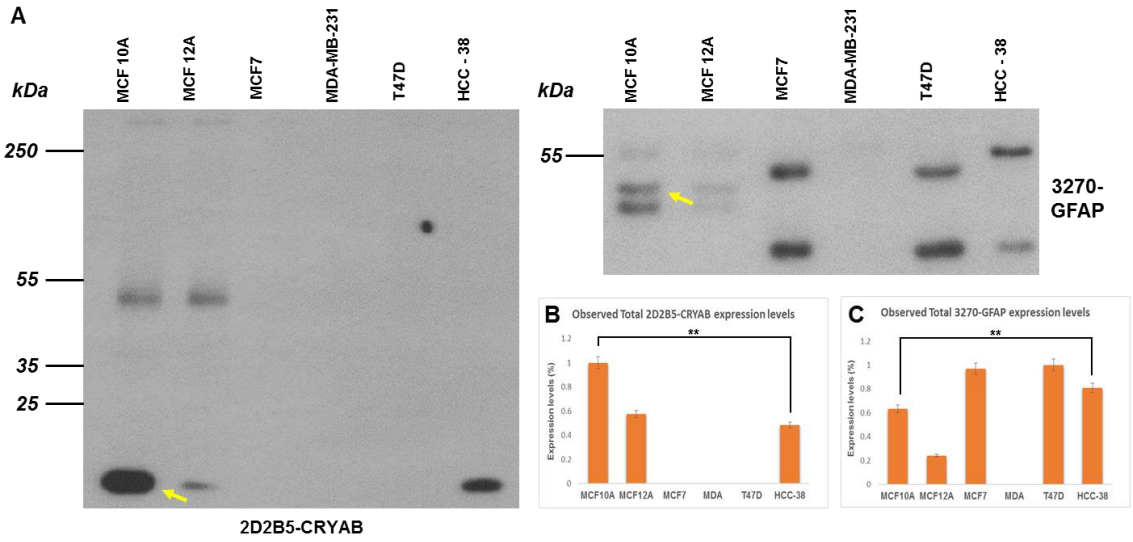

Figure 5.30: *Western blot data for heat shock protein expressions across breast cancer cell lines. (A) Displays western blot staining observed. (B), (C) and (D) displays collated densitometry analysis across three repeats for each protein.*

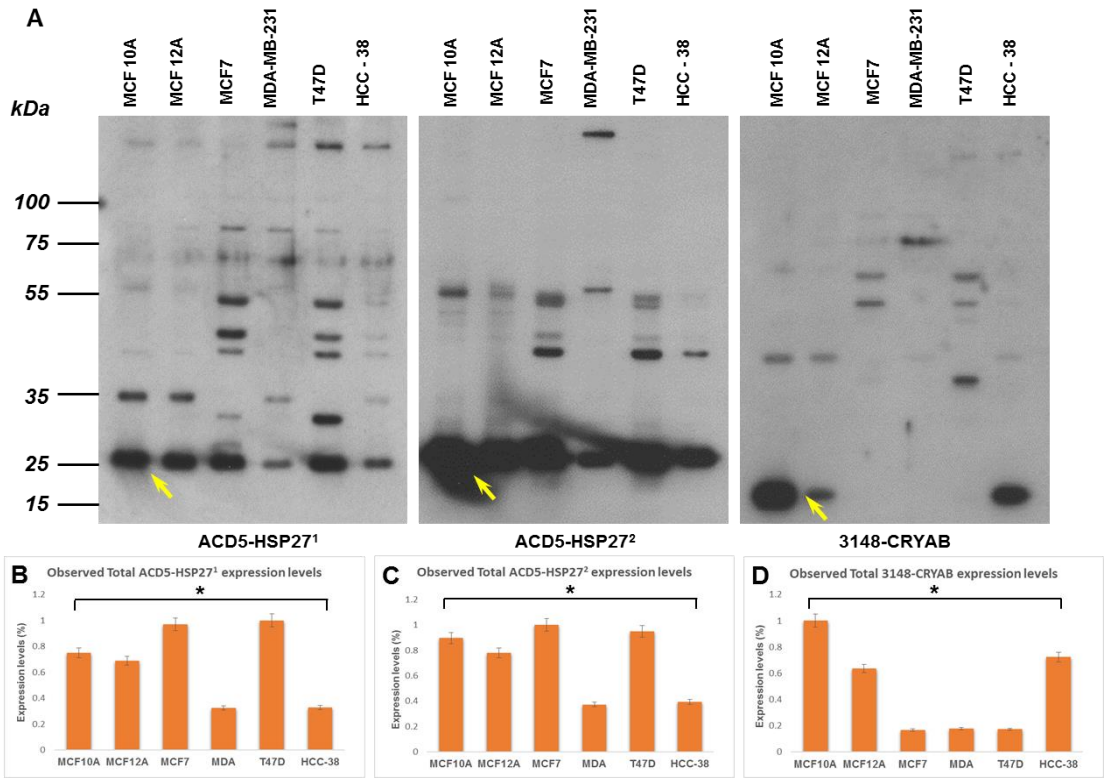

Figure 5.31: *Western blot data for heat shock protein expressions across breast cancer cell lines. (A) Displays western blot staining observed. (B), (C) and (D) displays collated densitometry analysis across three repeats for each protein.*

From data presented in *Figures 5.30* and *5.31*, variations in chaperone expression can be seen (*ANOVA, $F_{4.3789} = 5.62$, $P = 0.010$*). For both CRYAB antibodies used the predicted band correlating to ~16 kDa was the assessed using densitometry, suggesting that expression appears to significantly decrease upon cancer development when post hoc F-tests were applied where $p \leq 0.001$. However, further bands were also observed at higher kDa (Detected by the 3148-CRYAB), but due to the potential of these bands being unspecific binding, they were not assessed. However, these bands could also represent differences in protein variants arising from gene mutations expressed within each cell line, leading to alterations in post-translational modifications of the proteins.

Further to this, HSP27 protein expression is also shown to vary across the breast cancer cells (*ANOVA, $F_{5.2679} = 4.82$, $P = 0.010$*). The predicted band at ~20 kDa was assessed for densitometry. The data suggests expression appears to remain consistent in MCF7 and T47D cells in comparison to control cells. Alongside this, expression patterns using the ACD5-HSP27 antibody appear to significantly decrease in the MDA-MB-231 and HCC-38 cell lines in comparison to the control cell lines when subjected to post hoc F-test analysis where $p \leq 0.001$.

Alongside these two chaperones, GFAP expression also displayed variation across the breast cancer cell lines assessed. For the purpose of densitometry, total protein in each lane was compared due to known differences in isoform expression between cell lines. It is shown that expression patterns presented in both control cell lines differ to that expressed within cancerous lines. MDA-MB-231 cells appear to display a loss of detected GFAP, with remaining cell lines displaying expression of alternate molecular weight bands. These observations could arise due to the varying cancer grades expressing different GFAP isoforms [342]; however, this would need further investigation through PCR and western blot analysis against known GFAP isoforms to confirm.

These investigations have aimed to characterise *LINC* protein expression levels and organisation across a variety of breast cancer cell lines. Through the use of immunofluorescence and western blotting techniques, it is suggested that between the ranges of control, low- and high-grade breast cancer cell lines analysed, variations are observed across multiple *LINC* components. However, many of these observed differences do not directly correlate to and increase or decrease in the cancer grade, and therefore may be a result of cell specific expression patterns.

One interesting observation however, was found in nesprin-1 and -2 protein expression patterns. It was shown that lower nesprin-1 and -2 isoforms decrease in low/high cancer

cell lines in comparison to the two control lines. This is also correlated to an increase in cytoplasmic staining for the nesprin-2 C-terminal *KASH* domain as the grade of cancer increases. This observation, coupled with data presented in Chapter 3 suggests nesprin proteins may hold functional roles within the development of cancerous phenotypes such as metastatic properties. This data therefore suggests further investigation is needed into the potential roles of nesprin-1 and nesprin-2 (specifically the lower isoforms) in the development of cancerous phenotypes.

5.3.2 Control, low- and high-grade breast cancer cell lines express differential migration potential through restrictive 3D environments.

5.3.2.1 High-grade MDA-MB-231 breast cancer cell lines display enhanced migration through restrictive 3D scaffolds compared to control MCF10A and low-grade MCF7 cells.

When collated data thus far is linked to data presented in Chapter 3; suggesting *LINC* disruptions decrease nuclear stiffness and increase migration potential through restrictive 3D scaffold, it can be hypothesised that the loss of these lower nesprin-1/-2 isoforms could be a potential causative factor to the observed migration potential of multiple cancers due to suggestions that nuclear stiffness is a rate limiting step in migration through 3D environments [272]. To investigate this, current investigations aim to assess control, low and high grade cancer migration potential through restrictive 3D Strata scaffolds, to observe if differences exist. MCF 10A, MCF7 and MDA-MB-231 cells were grown within individual Strata® scaffolds and maintained submerged in normal growth media for 14 days as described in the methods section. Scaffolds were fixed at the 2, 4, 6, 8, 10 and 14 d time points to assess penetration rate, with the resulting data displayed in *Figure 5.32*.

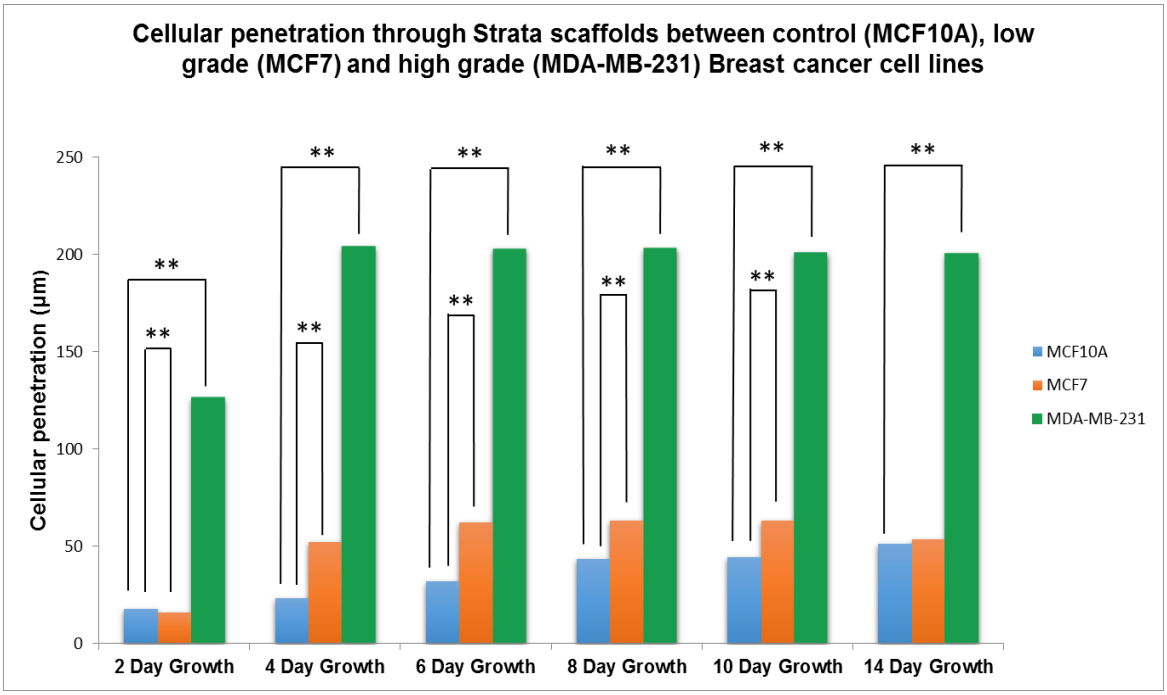

Figure 5.32: *Cell penetration of MCF 10A (Control), MCF7 (Low grade) and MDA-MB-231 (High grade) cancer cell lines through restrictive Strata® scaffold environments. Data represents collation of measurements from across three independent repeats.*

The data presented in *Figure 5.32* suggests MDA-MB-231 cells display a significantly increased migration potential through restrictive Strata® Scaffold environments compared to control and low grade counterparts. It is shown that MDA-MB-231 cells were able to migrate through the full scaffold length between the 2 and 4 d time points, whereas the MCF7 and MCF 10A cells penetrated a maximum of 50 µm into the scaffold by the 14 d time point. Further observations also suggest MCF7 cells displayed a faster migration potential over the first 6 days of growth in comparison to MCF 10A cells, with both cell lines then displaying a reduction in scaffold penetration when ~50 µm penetration was achieved. Through the use of a student's t-test, we were able to show that the observed differences in migration potential between MCF 10A and MCF7, alongside MCF 10A and MDA-MB-231 were statistically significant when $p \leq 0.005$ across all-time points except 14 d. At this time point, no significant difference between scaffold penetrations could be seen between the MCF 10A and MCF7 cell lines.

The data presented in this investigation therefore suggests that the high grade MDA-MB-231 cell lines display an increased migration potential through the restrictive 3D Strata® scaffolds compared to the low grade MCF7 and control MCF 10A cell lines. One potential contribution to this could be an increased nuclear malleability within the high grade MDA-MB-231 cells due to their altered nesprin distribution and expression levels highlighted in *Figures 5.17* – 5*.23*.

5.3.2.2 MCF7 and MDA-MB-231 breast cancer cell lines display similar cell phenotypes in restrictive 3D scaffolds.

Thus far, data suggests as the cancer grade increases, the cellular migration speed through restrictive Strata scaffolds also increases, however it is unclear as to whether any further differences between low and high grade breast cancer cell lines exist. Protein expression analysis suggests lower nesprin-1/-2 isoforms expression decreases in high cancerous cell lines compared to controls (*Figure 5.18* and *5.23*), however little variation is observed between the cancerous cell lines. Therefore to further investigate why such a drastic difference between low and high grade breast cancer penetration exists, high powered TEM and SEM analysis on both 2D and 3D grown MCF7 and MDA-MB-231 cell lines was conducted, with aims to decipher whether any differences in migration behaviour and cellular/nuclear shape could be observed.

Initial investigations aimed to assess whether cell surface properties varied between the two cell lines, in both 2D and multiple regions of the 3D scaffolds through SEM analysis. Cells were grown for 6 days, fixed and imaged as described in the methods section on both 2D silicon chips and in 3D space-restrictive Strata® scaffolds. Images can be seen displayed in *Figure 5.33*.

Data provided in *Figure 5.33* shows that both the MDA-MB-231 and MCF7 cells display differences in cell surface phenotypes between 3D scaffold environments and conventional 2D culture systems. It is shown that for both cell lines, when grown on 2D silicone chips, the leading edge of the cell displays filapodia formation. Across this migratory edge cell projections can be seen. However these projections are not observed across any other cell regions than the leading migratory edge. In contrast, for both cell lines, the plasma membrane appears to display an increase in cellular projections across the whole cell, alongside displaying a much more spherical cell shape within 3D culture systems. These cellular projections, best highlighted within images E and F, suggest that these increased numbers of projections could be a result of increased cell surface area in contact with the surrounding material, helping the cell migrate through the scaffold environment. No differences in surface properties can be observed between MCF7 and MDA-MB-231 cells within each growth environment, suggesting that the observations are a result of environmental influence, and not cell line variation.

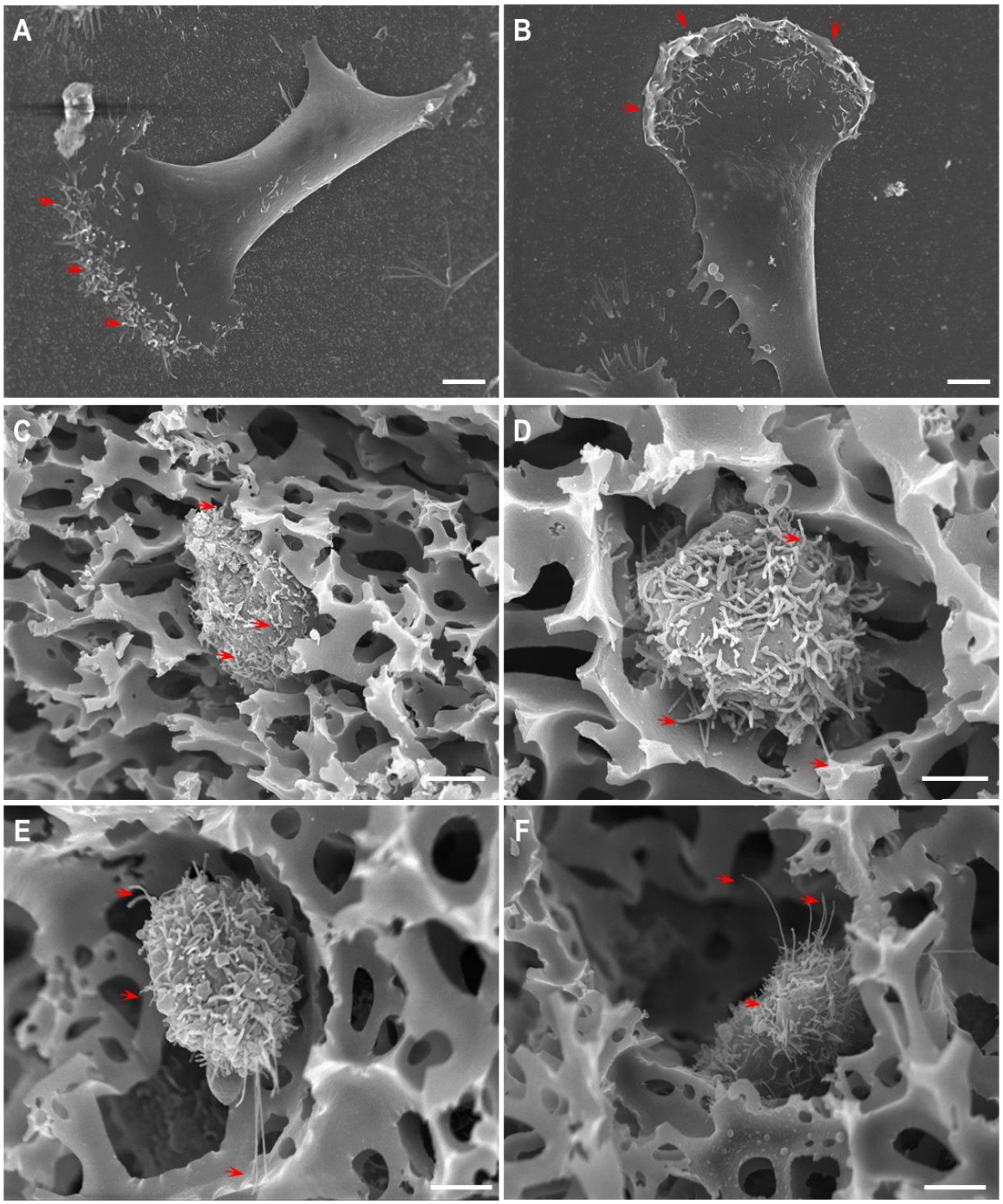

Figure 5.33: *Scanning electron microscopy images of MDA-MB-231 (A, C and E) and MCF7 (B, D and F) breast cancer cell lines. Images A and B display cells grown on 2D silicon chips. C and D represent cells situated across the restrictive scaffolds surface. E and F display cellular morphologies in central scaffolds regions. Arrows highlight the observed cellular projections. Scale bars = 2.5 µm*

Alongside SEM analysis, TEM analysis was also conducted to investigate how the low and high grade breast cancer cell lines respond to the restrictive scaffold environment on

a sub-cellular level. Cells were grown in the restrictive scaffolds for 6 days and processed as described in the methods section. Initial observations suggest that both low and high grade breast cancer cell lines displayed similar migration phenotypes through the scaffold. It was shown that each cell line was able to migrate through restrictive interconnects (interconnecting windows smaller than nuclear diameters), with mitochondrial accumulation occurring at the perceived front of the nucleus. Representative images alongside quantification of this phenotype are displayed in *Figure 5.34*.

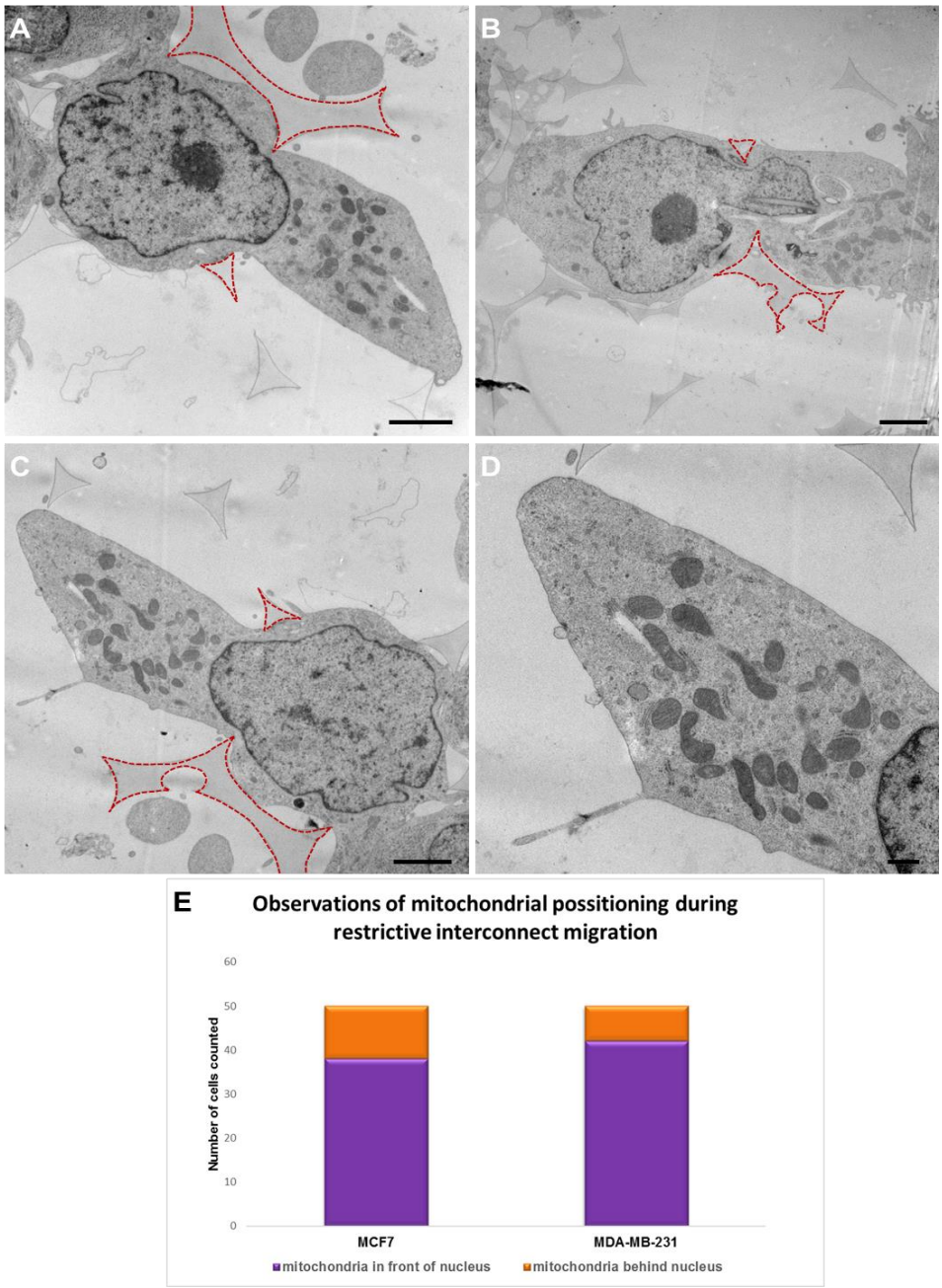

Figure 5.34: *TEM images of MDA-MB-231 (A) and MCF7 (B) breast cancer cell lines displaying mitochondrial positioning during restrictive interconnect migration. (E) Displays quantification of mitochondrial positioning across 50 cells for each cell line assessed. Scale bars = 2 µm.*

Figure 5.34 suggests both MCF7 and MDA-MB-231 cell lines display mitochondrial re-positioning in front of the nucleus during migration through the restrictive interconnecting windows. Quantification displayed in (E) further suggests ~80% of both MCF7 and MDA-MB-231 cell lines displayed this mitochondrial re-positioning in front of the nucleus during migration through restrictive interconnecting windows. These observations suggest that as the nucleus is the largest organelle, it may act as the restrictive component during migration through tight spaces, delaying migration due to nuclear deformities being required to pass through the windows.

Further investigations were then conducted to see if further nuclear and NE phenotypes abnormalities were present in MCF7 and MDA-MB-231 cell lines during migration through restrictive interconnects. Interestingly, it was found that within both cell lines, drastic nuclear deformities could be seen upon migration through restrictive interconnecting windows, alongside differences between INM and ONM distance on either side of the restriction (*i.e.* pre and post migration). Images of these observed nuclear deformities alongside quantification of NE dilations pre and post migration can be seen displayed in *Figures 5.35* and 5*.36*.

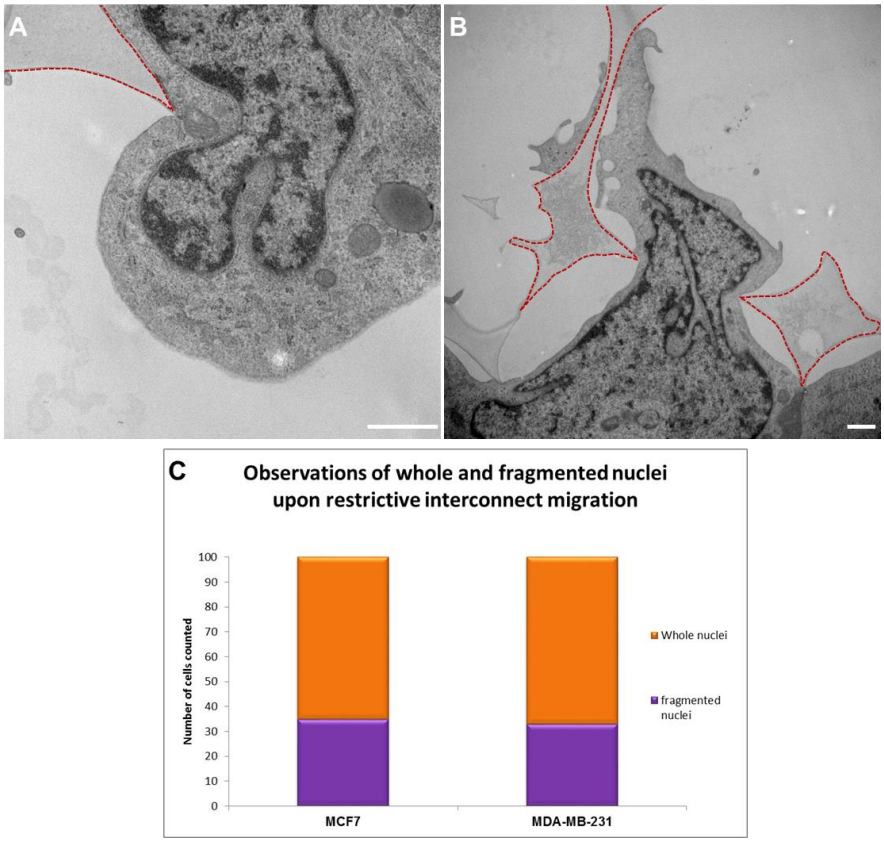

Figure 5.35: *TEM images of MDA-MB-231 (A) and MCF7 (B) breast cancer cell lines displaying nuclear deformities during restrictive interconnect migration. (C) Displays quantification of nuclear phenotypes during restrictive interconnect migration. Scale bars = 500 nm.*

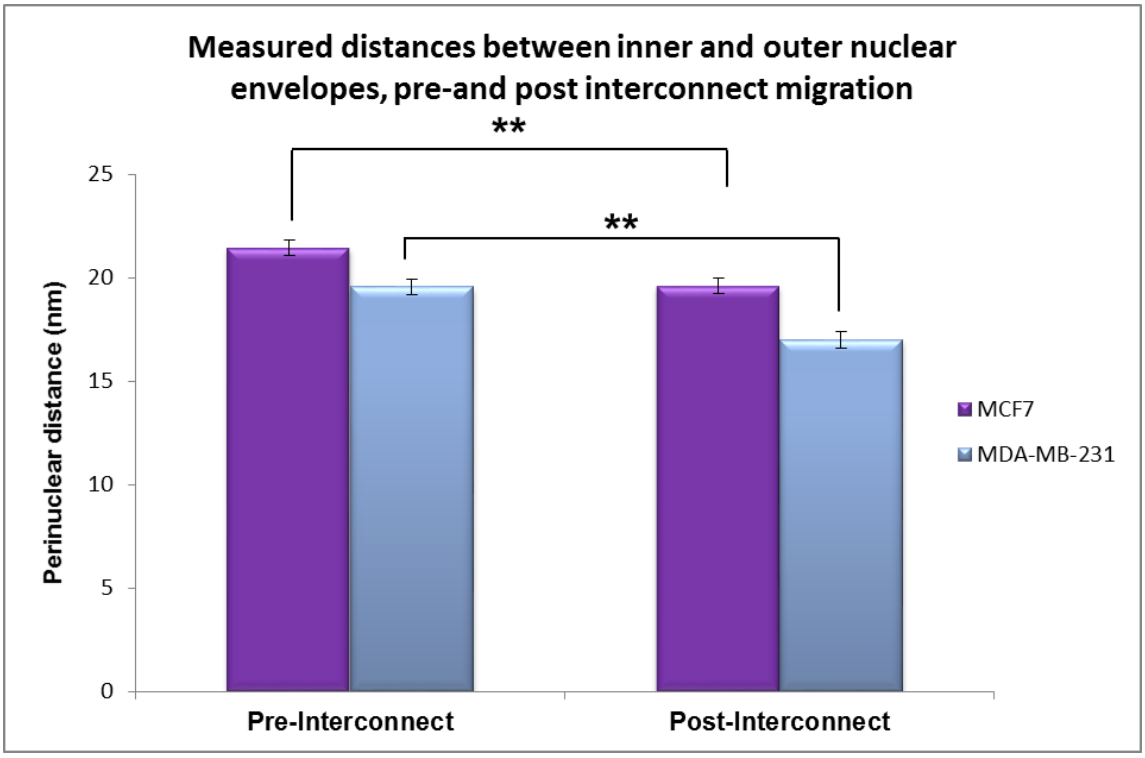

Figure 5.36: *Quantification of MDA-MB-231 and MCF7 NE dilations pre and post restrictive interconnect migration.*

The data presented in *Figure 5.35* suggests both MCF7 and MDA-MB-231 cells display similar nuclear deformities upon migration through restrictive interconnects. Initially, it is shown that both cell lines infrequently display drastic nuclear shape abnormalities upon migration through restrictive spaces, suggesting support for the need of nuclear deformities during cell migration through these materials. Further analysis displayed in *Figure 5.36* suggests that differences are also seen between INM and ONM before and after migration through restrictive spaces for both cell lines. This investigation aimed to assess whether variation in PNS spacing could be observed before and after restricting interconnect migration, to gain insight into whether *SUN-KASH* interactions may be altered. The data suggests NE dilation significantly decreases post interconnect migration using a student's t-test where $p \leq 0.005$ for both cell lines assessed. These result further supports suggestions that both MCF7 and MDA-MB-231 cells display defects in NE spacing during restrictive interconnect migration.

One final observation of interest found during TEM analysis of both MCF7 and MDA-MB-231 cell lines in restrictive Strata® scaffolds was that the cancer cells appear to express differences in phenotypic responses to proposed stressful regions of the scaffold displayed in Chapter 3. In this chapter, edges of interconnecting windows were shown to

penetrate HaCaT cells during migration, leading to suspected intermediate filament accumulation across the region of penetration when in close nuclear proximity. Representative images of these same penetration events in cancer cell lines can be seen displayed in *Figure 5.37*.

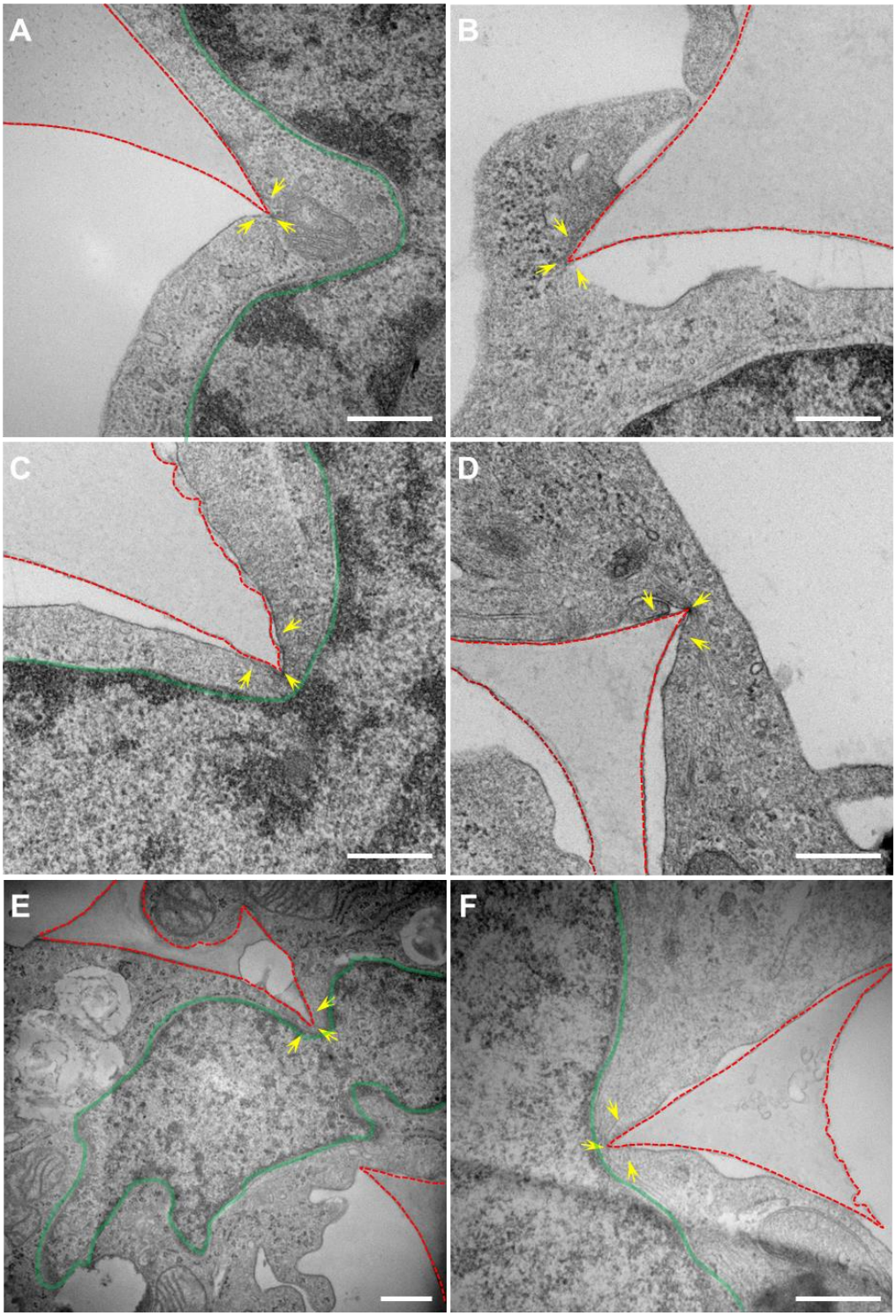

Figure 5.37: *TEM images of MDA-MB-231 (A, C and E) and MCF7 (B, D and F) breast cancer cell lines displaying cellular indentations during restrictive interconnect migration. Green outlines highlight NE. Scale bars = 500 nm.*

Figure 5.37 suggests both MCF7 and MDA-MB-231 cells do not appear to respond to the cellular indentations in the same way as HaCaT cells. It is shown that in both nuclear proximity and cellular extremities, breast cancer cells display limited cytoskeletal accumulation across the indentation. One potential suggestion for this lack of filamentous accumulation may be due to these cells may being unable to detect or respond to these surrounding environmental stresses in the correct manner, however, further analysis into stress response pathways and cell behaviour would be required to verify this hypothesis.

Data presented in this investigation helps suggest that MCF7 and MDA-MB-231 cell lines display similar cellular phenotypes in both 2D and 3D culture environments. However, these observations vary drastically from those of alternate cell lines placed in these environments such as the HaCaT cell lines. Observed differences between these cell lines could be a result of *LINC* disruptions across the nuclear envelope, leading to loss of mechano-transduction, and therefore the cells ability to respond to environmental stimuli. However, this is thus far speculation and further investigation would be required to verify this potential theory as current data provides only potential support for this due to the drastic nuclear deformities displayed upon migration through the restrictive 3D environments, suggesting that the nuclear envelopes structural integrity may be compromised as a result of this restrictive environment.

5.3.3 Manipulating LINC complex connections stimulates altered cellular phenotypes in breast cancer cell lines.

5.3.3.1 The incorporation of DN Sun1, but not nesprin-2 mini stimulates phenotypic difference in low-grade breast cancer cell lines.

To further investigate potential roles of nesprin-2 within the metastatic phenotypes observed by the MDA-MB-231 cells and DN HaCaT cells in Chapter 3, further investigations aim to test whether disruption or re-insertion of *LINC* components into low- and high-grade breast cancer cell lines is able to alter their phenotypes within 3D environments. This will therefore shed light on whether disruptions in *SUN-KASH* interaction across the nuclear envelope are a functional requirement for the increased migration potential displayed in high grade breast cancer cell lines.

To test this, a range of transfections in both MCF7 and MDA-MB-231 cell lines was conducted. MDA-MB-231 cells were transfected with nesprin-2 mini constructs, with the intention of re-localising nesprin-2 proteins across the NE, therefore increasing NE integrity. This mini construct [101] contains the ABD and KASH domain of nesprin-2G, but lacks the large rod domain, making the protein much smaller. We further transfected MCF7 cells with dominant negative (DN) SUN1 and DN KASH constructs (ONM bound fragment of nesprin-2 retaining the transmembrane and KASH domain). The DN SUN1 construct severs the link between *SUN-KASH* interactions spanning the perinuclear space by out-competing endogenous SUN proteins for KASH interactions. The DN KASH construct however, displaces KASH proteins situated across the NE, maintaining the *SUN-KASH* interactions within the PNS, but displacing endogenous KASH proteins across the NE. A further pEGFP control was also used to test that the resulting phenotypes were not a direct result of transfection, but rather the constructs inserted. Images displaying transfection efficiency alongside observed phenotypes are displayed in *Figure 5.38*.

The data presented in *Figure 5.38* helps suggest the transfection efficiency for each construct was above 50%, suggesting that any results obtained from experimentation using this material will be a result of the alterations in *LINC* components.

Following transfections, cells were placed into two experimental set ups, a hanging drop experiment (in which 200 cells were suspended upside down in a 100 µl drop of media) to assess whether cell-cell interaction potential was altered upon *LINC* disruptions (similar to that displayed by the DN HaCaT cells), alongside a 3 day migration experiment through the restrictive 3D Strata® scaffolds. It has been shown that MDA-MB-231 cells are able to migrate completely through Strata® scaffolds between 2 and 4 day time points. As transient transfections last up to 2-3 days, experiments aimed to test whether the disruption or re-insertion of *LINC* components affects the migration potential of cells through restrictive environments. Experimental data for both hanging drop and restrictive scaffold penetration investigations can be seen displayed in *Figures 5.39* and 5*.40*.

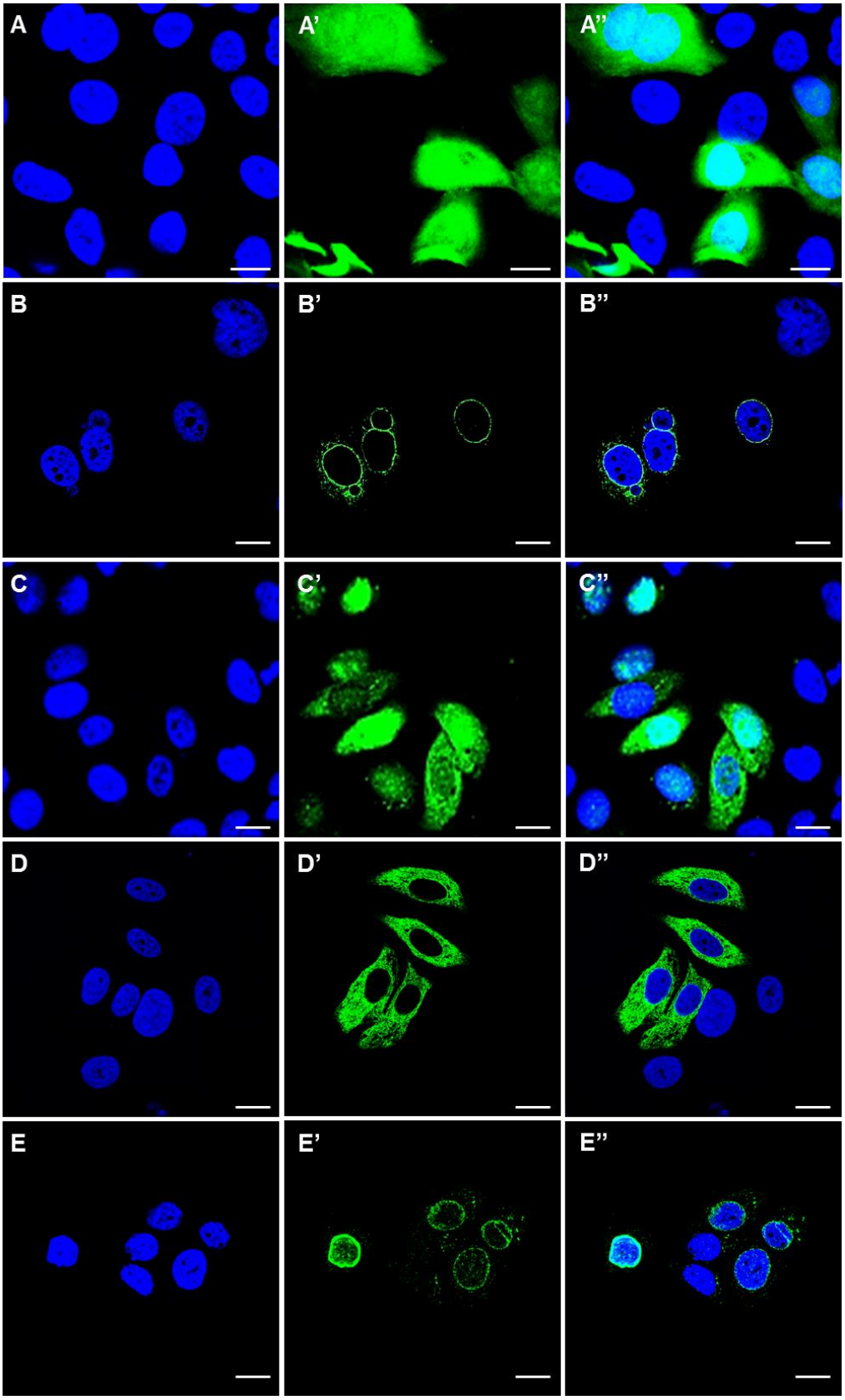

Figure 5.38: *Fluorescence images displaying transfection efficiency across MCF7 and MDA-MB-231 cell lines. (A) and (B) display MDA-MB-231 cells transfected with pEGFP and nesprin-2 mini respectively. (C), (D) and (E) display MCF7 cells transfected with pEGFP, DN SUN1 and DN KASH respectively. Scale bars = 10 µm.*

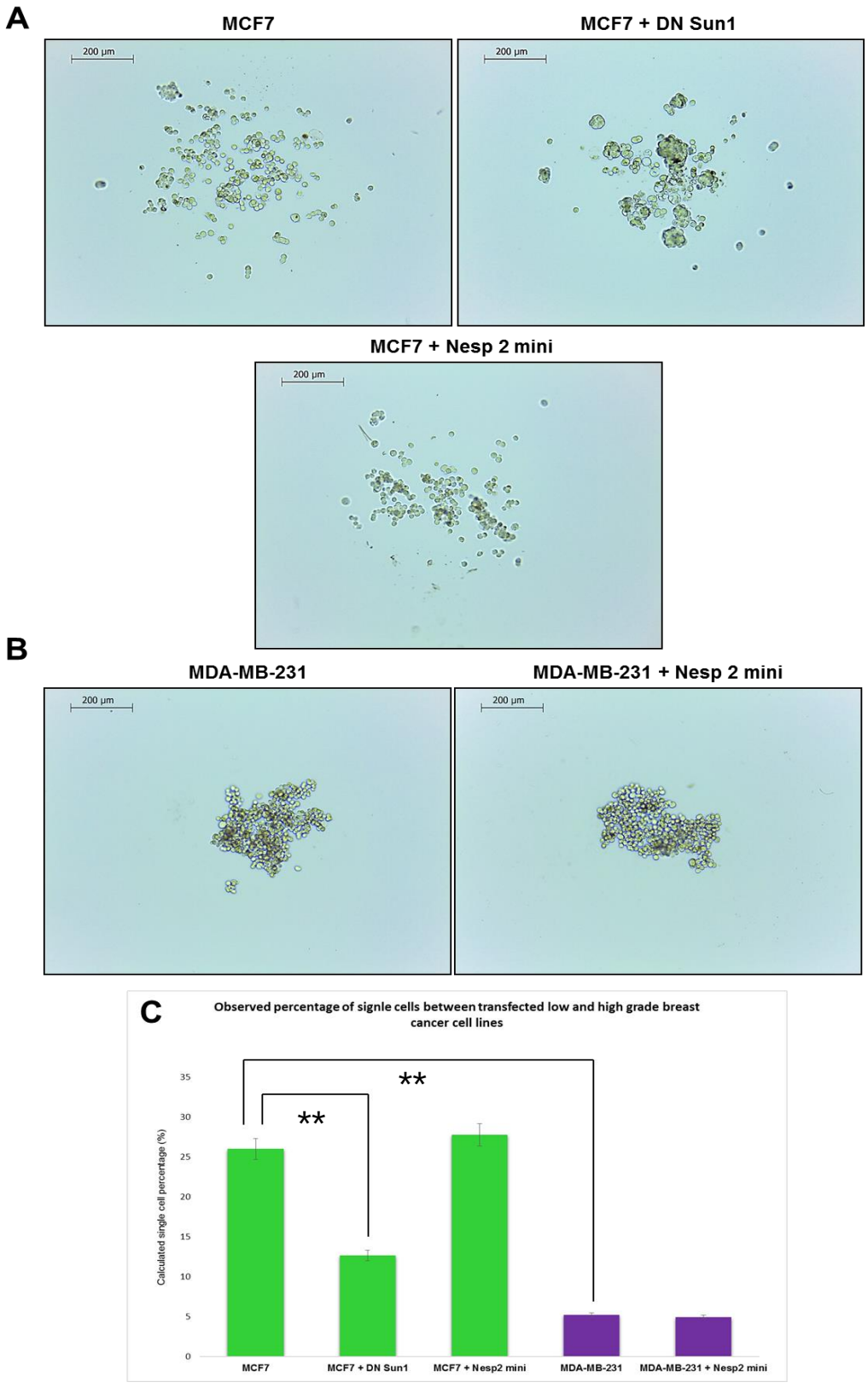

Figure 5.39: *Images displaying hanging drop experimental analysis following LINC complex manipulation. (A) Displays cellular packing of MCF7 cells between DN KASH, DN SUN1 and non-transfected cells. (B) Shows packing phenotypes of MDA-MB-231 and cells transfected with nesprin-2 mini. Further quantification from across 20 experimental replicates can be seen displayed in (C). Scale bars = 200 µm*

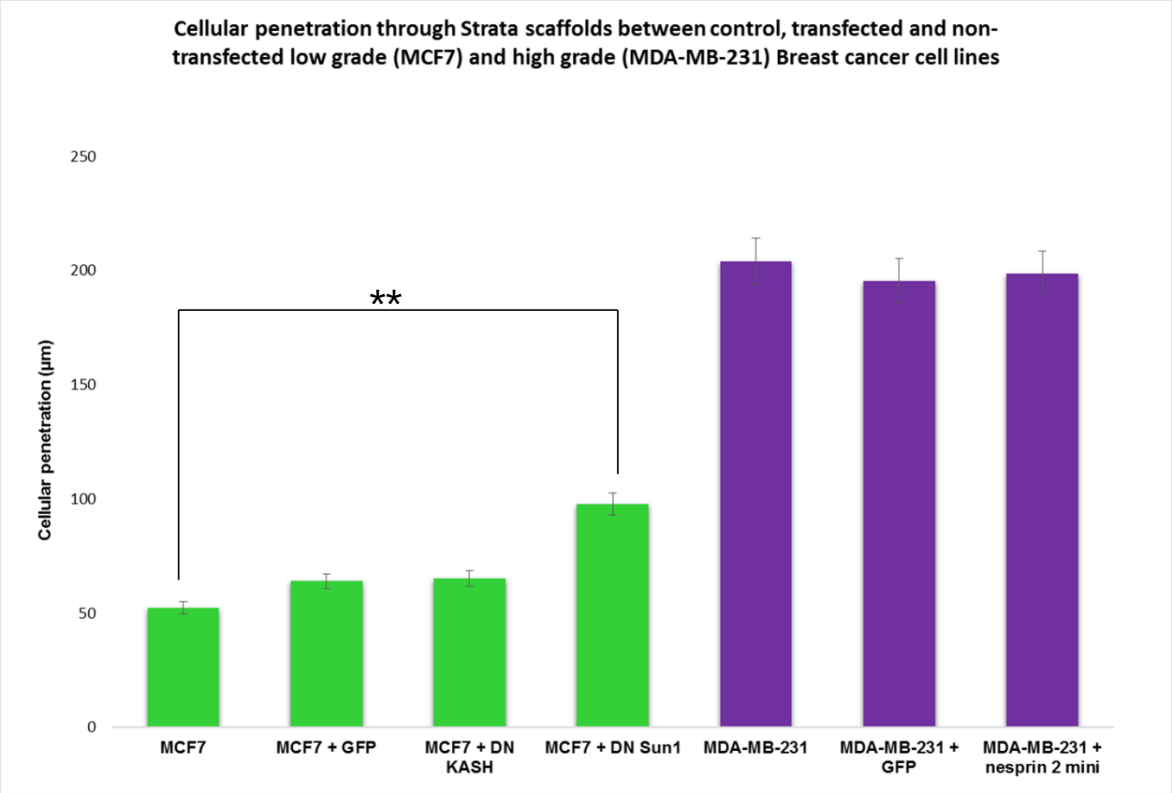

Figure 5.40: *Quantification of restrictive scaffold penetration between MCF7, MCF7 + pEGFP, MCF7 + DN KASH, MCF7 + DN SUN1, MDA-MB-231, Mda-MB-231 + pEGFP and MDA-MB-231 + nesprin-2 mini, 3 days post seeding.*

Figure 5.39 suggests that the disruption of *LINC* connections across the NE in MCF7 cells stimulates altered colony phenotypes. It is shown that upon transfection of MCF7 cells with DN SUN1, the total single cell population within the hanging drop significantly decreases using a student's t-test where $p \leq 0.005$. Alongside this, further differences were observed between single cell numbers of MCF7 and MDA-MB-231 cell lines, in which MDA-MB-231 presented a more cohesive cell population, with less single cells observed. The incorporation of nesprin-2 mini constructs into both MCF7 and MDA-MB-231 cells simulated no change in the number of single cells observed. These observations therefore suggest the disruption of *SUN-KASH* interactions across the NE through DN SUN1 insertion, could potentially stimulate a more cohesive colony phenotype, similar to those observed within the DN HaCaT cells in Chapter 3.

The data presented within *Figure 5.40* suggests that the disruption of *SUN-KASH* connections across the NE in low grade MCF7 cells stimulates increased cell migration potential through restrictive 3D scaffolds. It is shown that DN SUN1 incorporation, the penetration depth significantly increases to ~100 µm, in comparison to ~55 µm displayed by control MCF7 cells using a student's t-test where $p \leq 0.005$. It was further shown that

insertion of control GFP signal peptides alongside DN *KASH* displayed no significant effect on cellular migration through the scaffold environment. This suggests the destabilisation of *SUN-KASH* interactions across the perinuclear space, leading to a loss of NE structural integrity, may be critical for increasing cell penetration potential through restrictive environments. Further to this, the experimental data also suggests the insertion of nesprin-2 mini and GFP signal peptide into the high grade MDA-MB-231 cells was unable to stimulate any alterations in migration potential through the restrictive strata scaffolds.

Through data presented in this investigation, it can be suggested that the *SUN-KASH* interaction may potentially provide a limiting factor in the migration potential of cells through restrictive 3D scaffolds. With further evidence suggesting that the re-organisation of nesprin-2 across the NE being unable to reduce the penetration speed of high grade cancer cells. This helps highlight that nuclear architecture defects are not the only factor stimulating the increased cellular penetration potential present within the high grade breast cancer cell lines.

Due to the use of transient transfections within this investigation, the data obtained may not represent the true nature of this *SUN-KASH* disruption in real scenarios. This is due to a number of limiting factors such as the increase in cell death post transfection, plasmid maintenance deteriorating within 3-4 days post transfection and the fact that the transfected population of cells is not homogeneous. This therefore means that further investigations into this SUN-KASH interaction in cancer migration potential should be conducted through the production of stable transfected cell lines.

5.3.3.2 Stabile transfection of DN SUN1 into MCF7 cells stimulates increased nuclear abnormalities and subsequent cell death.

Due to the limitations of assessing cell penetration potential within the first few days post transfection as described in 5.3.3.1, further experiments aimed to produce a stably transfected MCF7 cell line expression DN SUN1, as this was the only construct to display migration differences within 3D restrictive Strata scaffolds. Before cell line production, the concentration of Geneticin®/G418 (The drug to which the DN SUN1 plasmid encodes resistance against) required to kill all MCF7 cells within 7 days was investigated. This concentration ensures that sufficient selection pressure is maintained within the transfected culture, positively selecting for cells expressing the desired construct post 7

days of transfection, allowing subsequent cloning to be performed. Data from kill curve investigations can be seen in *Figure 5.41* displaying cells stained using the LIVE/DEAD® fixable red dead stain kit.

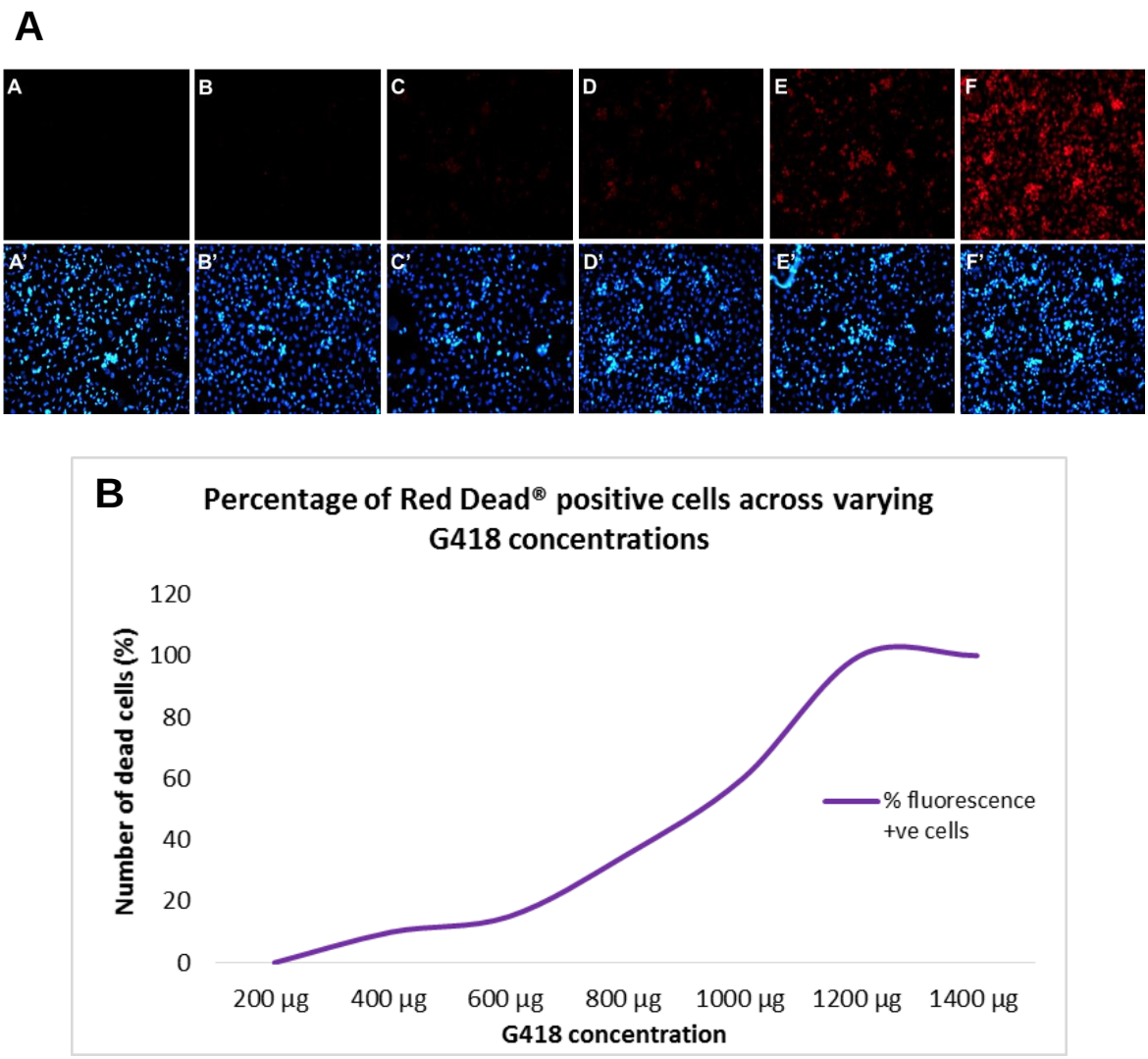

Figure 5.41: *LIVE/DEAD® Red Dead staining within MCF7 cells under varying cell G418 concentrations, to assess drug concentration required to kill 100% of cell in 7 days. In (A) Panel (A-F) represents incrementing G418 concentrations of 100, 200, 400, 800, 1000, 1200 and 1500 µg/ml respectively. Red staining display the resulting Red Dead staining and blue staining represents nuclear DAPI staining. (B) Displays collated kill curve data.*

The data presented in *Figure 5.41* suggests that 100% cell death was achieved at the 7 day time point using a G418 concentration of 1200 µg/ml. The staining kit used acts through binding with free amines, upon cell death, cell membranes are compromised, losing the ability to regulate transport of compounds across the plasma membrane, resulting in free diffusion of the dye into cytoplasmic regions of the cell. This dye then

displays an increased fluorescence signal in dead cells due to the dyes ability to react with both cell surface and cytoplasmic amines. The data presented in (B) highlights that MCF7 cells displayed limited death up to a concentration of 400 µg/ml, following which further increase in concentration displayed a significant increase in cell death percentage.

It was established that for plasmid selection in MCF7 cells, a concentration of 1200 µg/ml of G418 was sufficient. Using this information, MCF7 transfections were performed through electroporation as described in the methods, with aims to investigate whether the destabilisation of *SUN-KASH* interactions across the NE was able to increase the migration potential of MCF7 cells.

Following transfection, cells were maintained in conventional culture conditions alongside 1200 µg/ml of G418 in order to actively select for the cells expressing the desired plasmid. Interestingly however, 5 days post transfection, 70% of cells died within the culture flask, with the remaining cells displaying reduced replication rates. Upon closer analysis of the remaining cells, it was seen that cells displayed abnormal nuclear architecture alongside multi-nucleated cells. Quantification of these observations from across three independent repeats can be seen in *Figure 5.42*.

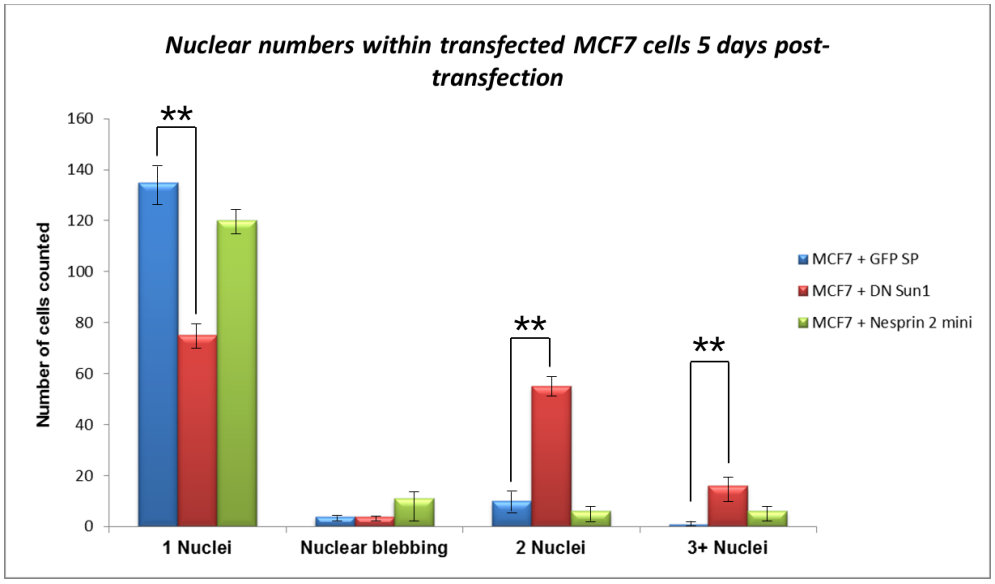

Figure 5.42: *Nuclear analysis across MCF7cells transfected with GFP signal peptide, DN Sun1 and nesprin-2 mini. Data presented represents analysis of 150 cells within each transfection.*

Data presented in *Figure 5.42* suggests transfection with DN SUN1 stimulates drastic nuclear abnormalities alongside increase frequency of multi-nucleated cell formation. It can be seen that significant differences between nuclear numbers present post transfection can only be seen within MCF7 cells transfected with DN SUN1 using a

student's t-test where $p \leq 0.005$. Continual observation of the transfected cells suggested that this multi-nucleated phenotype stimulated cell death before cloning could be conducted. Interestingly however, this data does suggest that the DN introduction stimulates cellular phenotypes different to that observed in HaCaT cells, as the formation of multi-nucleated cells is not observed within the DN HaCaT cells described in Chapter 3.

5.3.4 Nesprin-2 C-terminal polyclonal antibody staining displays differential expression patterns between primary control, ER+ and triple negative breast cancers.

5.3.4.1 Nesprin-2 C-terminal KASH domain isoforms display localised expression within luminal epithelial cells in healthy breast ducts.

Thus far, investigations have shown that high grade breast cancer cell lines are able to penetrate into restrictive 3D scaffolds much faster than their low grade and control counterparts. With further suggestions that this increased migration potential could be attributed to altered expression patterns and cellular organisation of nesprin proteins, with disruptions of *SUN-KASH* interactions potentially increasing migration potential. This collated data does suggest that the *KASH* containing nesprin proteins may play key roles in the development of metastatic phenotypes observed across many aggressive breast cancers. However, thus far, cell line data has been used to establish whether links exist between nesprin organisation and cancer metastasis. To further validate this hypothesis that nesprins do indeed play roles within cancer metastasis development, further investigations aimed to characterise the expression patterns of nesprin-2 across various grades of primary breast tissues.

Initially, control breast tissue obtained through breast reduction mammoplasty was sourced from Breast Cancer Now in the form of pre-embedded and pre-sectioned material from a range of 6 patients. Staining for nesprin-2 C-terminal domains was conducted, as previous work within section 5.3.1.5, suggests significant loss of nesprin-2 C-terminal organisation and protein expression within cancerous breast cancer cell lines. Sections were processed and stained as described in the methods section, with images of nesprin C-terminal and actin staining displayed in *Figure 5.43*.

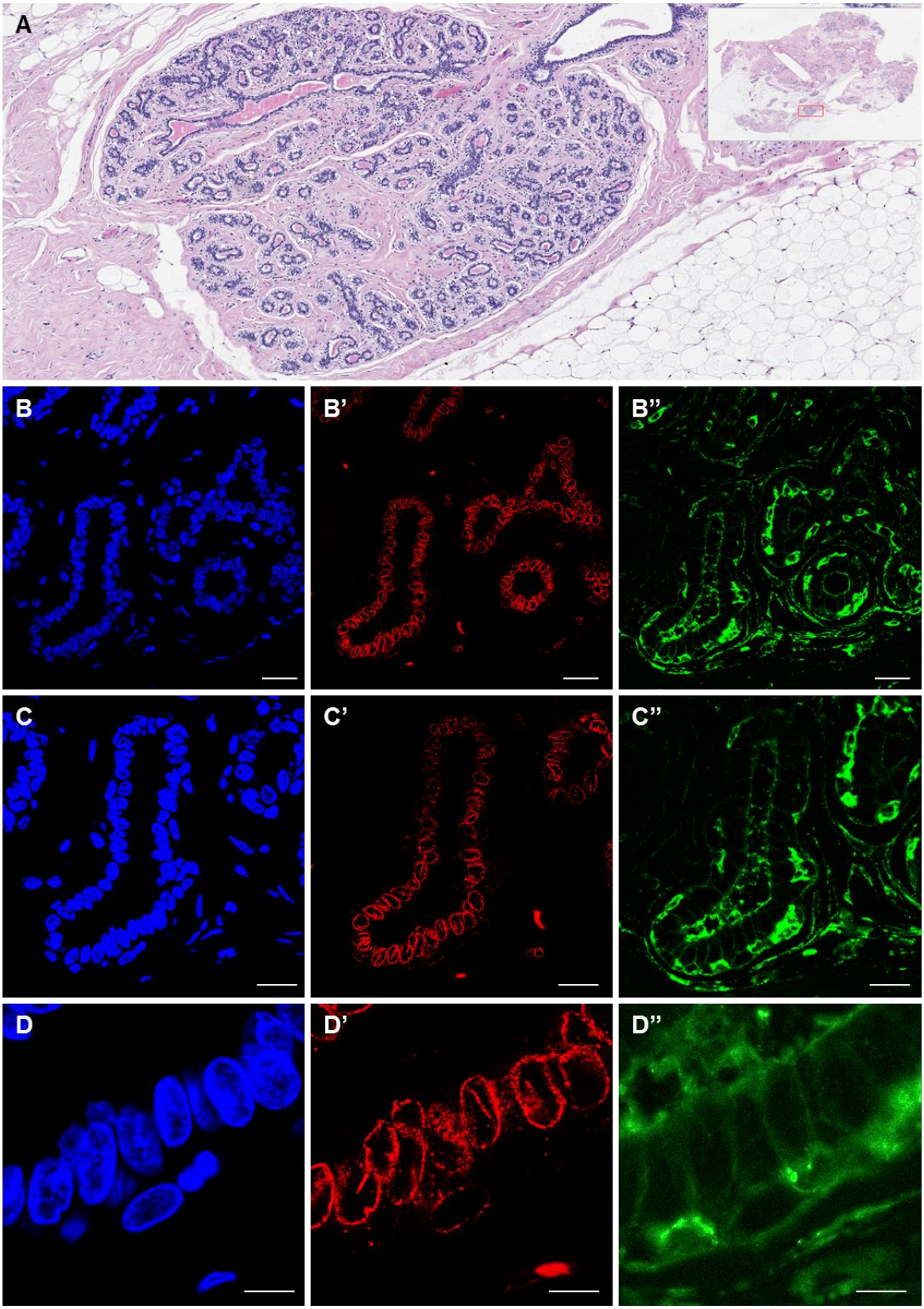

Figure 5.43: *Control pre-menopausal breast tissue. (A) displays H&E staining across the analysed section of tissue. (B, C and D) display DAPI staining across varying magnifications of the same structure. (B', C' and D') shows nesprin-2 C-terminal KASH domain staining. And images highlighted in (B'', C'' and D'') show actin staining. Scale bars = 30 µm (B), 20 µm (C) and 10 µm (D).*

The data presented within *Figure 5.43* suggests that the expression pattern of nesprin-2 C-terminal KASH domains remains localised to the luminal epithelial cells of the ducts. It can be seen that specific nuclear envelope staining is seen within the cells in closest proximity to the central duct, with reductions in nesprin-2 expression in more peripheral myoepithelial cells. The staining also helps to show that the ductal regions appear to be the only nesprin positive areas of the sample, suggesting nesprin presence within these structures may be crucial to maintaining their complex structural arrangements.

So far, fluorescence data has suggested that the ductal regions of the control breast tissue present nesprin-2 C-terminal KASH domain positive staining. Further speculation can be made as to the localisation of positive cells within this region correlating to the luminal epithelial cells. However, due to the complexity of tissue organisation, it is difficult to conclusively state whether these cells are indeed luminal cells. To validate this, further staining was performed within control breast tissue using the myoepithelial marker p63 [343] in order to increase our understanding of cellular arrangements within the structures present. Cells were processed and stained for nesprin-2 C-terminal and p63 as described within the methods section, with images displayed in *Figure 5.44*.

Figure 5.44 helps to highlight the cellular organisation present in the observed ductal regions of control breast tissue, through p63 labelling of myoepithelial cells found across peripheral basal layer of the duct. The data suggests that nesprin-2 C-terminal counterstaining is localised to the luminal epithelial cells, with much weaker staining observed in the peripheral myoepithelial cells. This collated data therefore suggests that within non-cancerous breast tissue, nesprin-2 C-terminal staining appears to localise across luminal epithelial cells of the duct, with much weaker staining present in the myofibroblast, myoepithelial and basal cells present in the tissue.

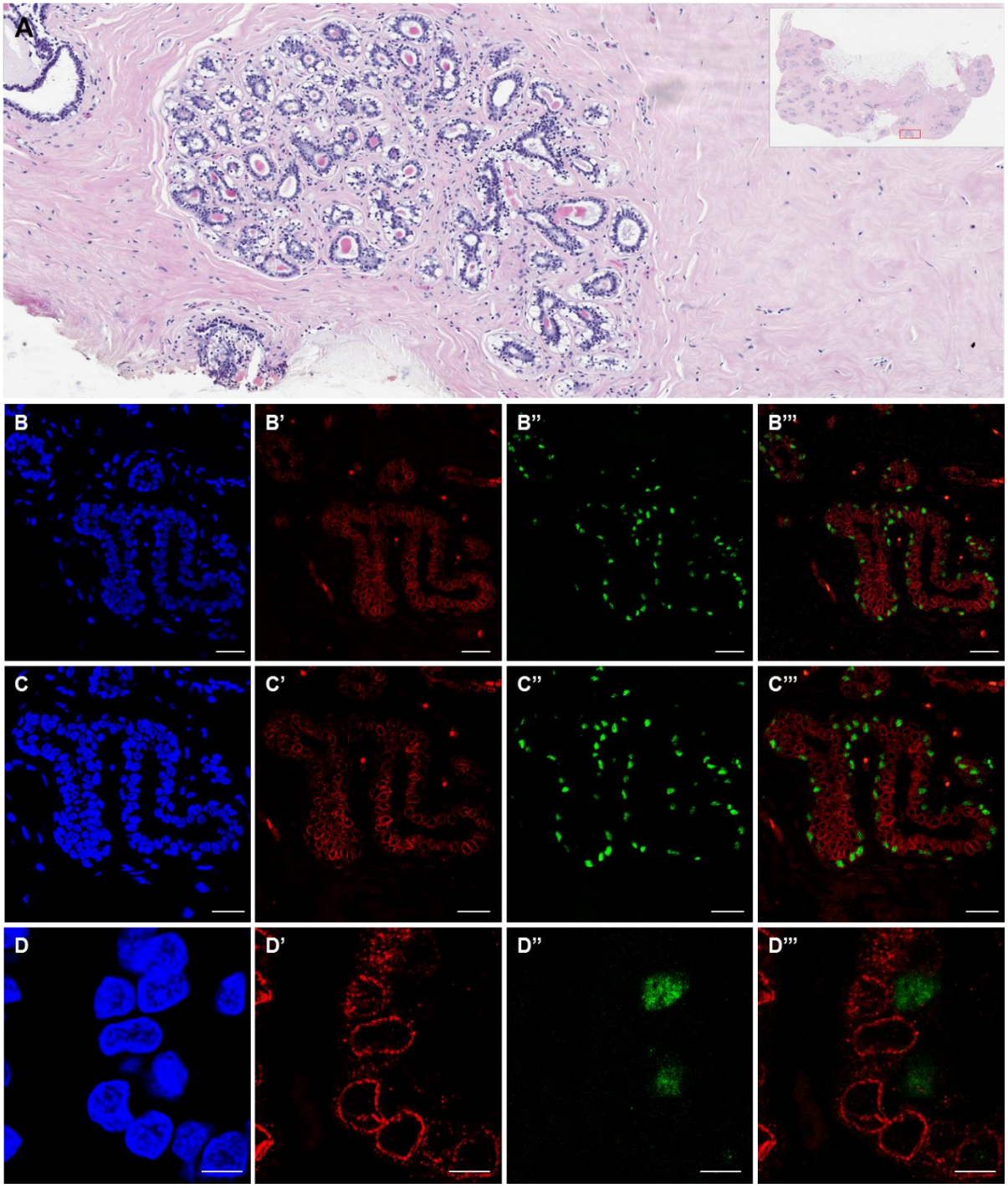

Figure 5.44: *Control pre-menopausal breast tissue. (A) Displays H&E staining across the analysed section of tissue. (B, C and D) display DAPI staining across varying magnifications of the same structure. (B', C' and D') shows nesprin-2 C-terminal KASH domain staining. Images highlighted in (B'', C'' and D'') show p63 staining and images (B''', C''' and D''') display merged p63 and nesprin-2 staining. Scale bars = 30 µm (B), 20 µm (C) and 10 µm (D).*

5.3.4.2 Nesprin-2 C-terminal KASH domain isoforms display an altered cytoplasmic cellular localisation and decreased expression within ER+ and triple negative breast cancers.

Following initial investigations into nesprin expression patterns across non-cancerous breast tissue, further investigations aimed to test whether any alterations in nesprin-2 expression levels were present across varying grades of breast cancer. To assess this, tissue sections from ER+ and triple negative breast cancer patients were obtained from Breast Cancer Now and stained for nesprin-2 C-terminal domains as described before, with resulting images for each condition displayed in *Figures 5.45 and 5.46 respectively*.

Figures 5.45 and 5*.46* helps highlight the drastic morphological differences in tissue architecture found upon cancer development within the breast. H&E staining in *Figure 5.45* displays how uncontrolled cell proliferation rates stimulate an increase in cellular packing density across the tissue, drastically deforming the observed ductal structures found in healthy tissue. Immunofluorescence staining further supports these observations, through increased cell proximity and packing density observed through DAPI and actin staining. Interestingly however, it can be seen under high magnifications nesprin-C-terminal expression levels appear to be less nuclear envelope specific and correlate heavily with the cytoplasmic actin staining. This suggests that the nesprin staining may be displaced from the nuclear envelope upon cancer development. To further assess nesprin staining within both non-cancerous and ER+ breast cancer tissues, we used the pixel distribution analysis tool within the LEICA LAS AF imaging software to quantify nesprin distribution across the cell (*Figure 5.47*).

Alongside ER+ tissues samples, the data presented within *Figure 5.46* further displays nesprin staining within triple negative tissue. Interestingly however, it can be seen that nesprin 2-C-terminal expression levels appear to be reduced in the cancerous regions of the tissue. This evidence suggests that nesprin-2 C-terminal KASH domain loss may be a crucial factor within the progression of cancer phenotypes, however, with our current evidence, we are unable to state whether this observation is a cause or result of the cancer progression. To further assess this, future investigations should aim to analyse protein and gene expression levels through western blotting and PCR techniques, to gain a greater understanding as to whether nesprin-2 C-terminal KASH domains are indeed down-regulated in highly metastatic cancers.

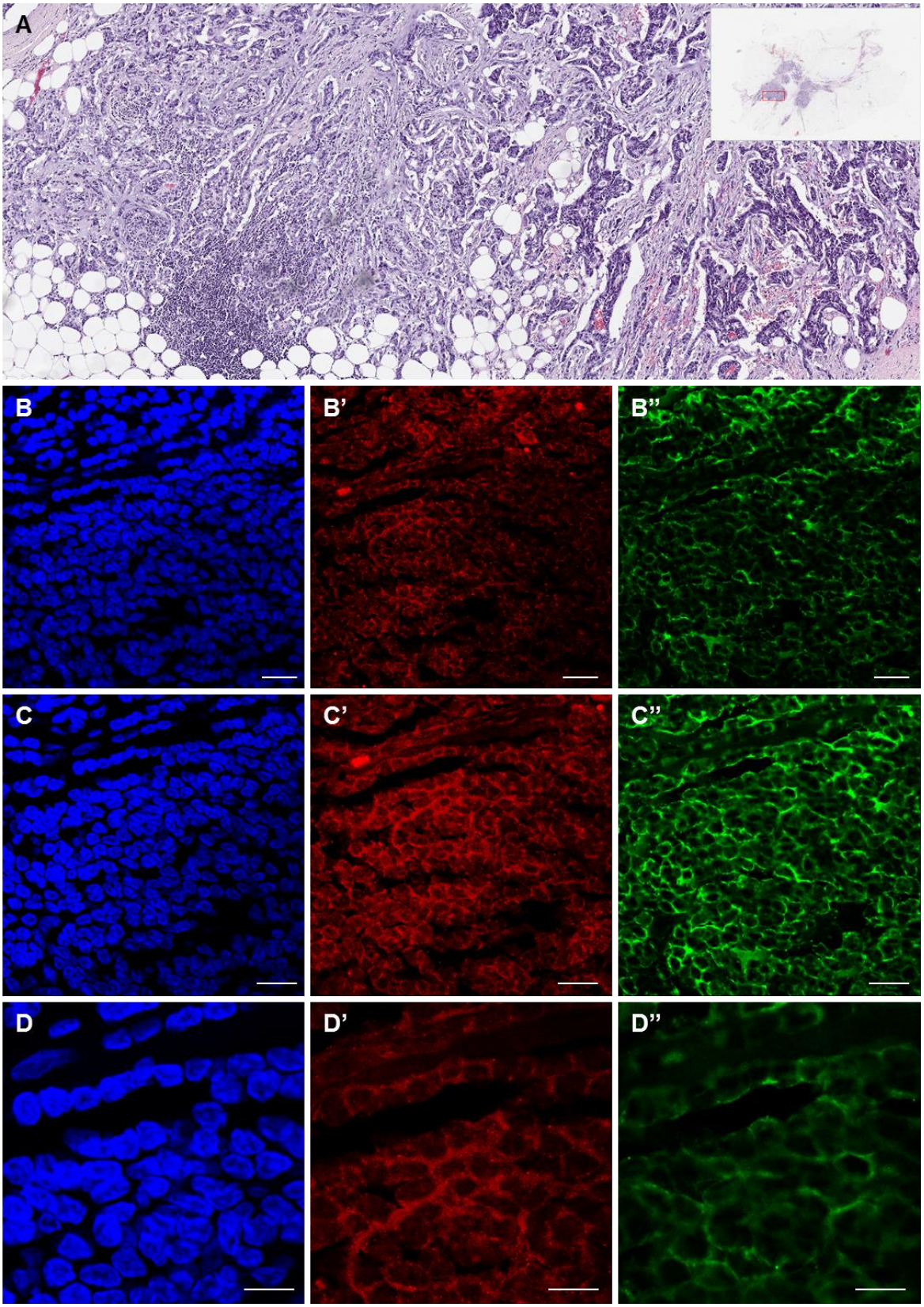

Figure 5.45: *ER+ pre-menopausal breast cancer tissue. (A) Displays H&E staining across the analysed section of tissue. (B, C and D) display DAPI staining across varying magnifications of the same structure. (B', C' and D') shows nesprin-2 C-terminal KASH domain staining. Images highlighted in (B'', C'' and D'') further display actin staining. Scale bars = 40 µm (B), 30 µm (C) and 20 µm (D).*

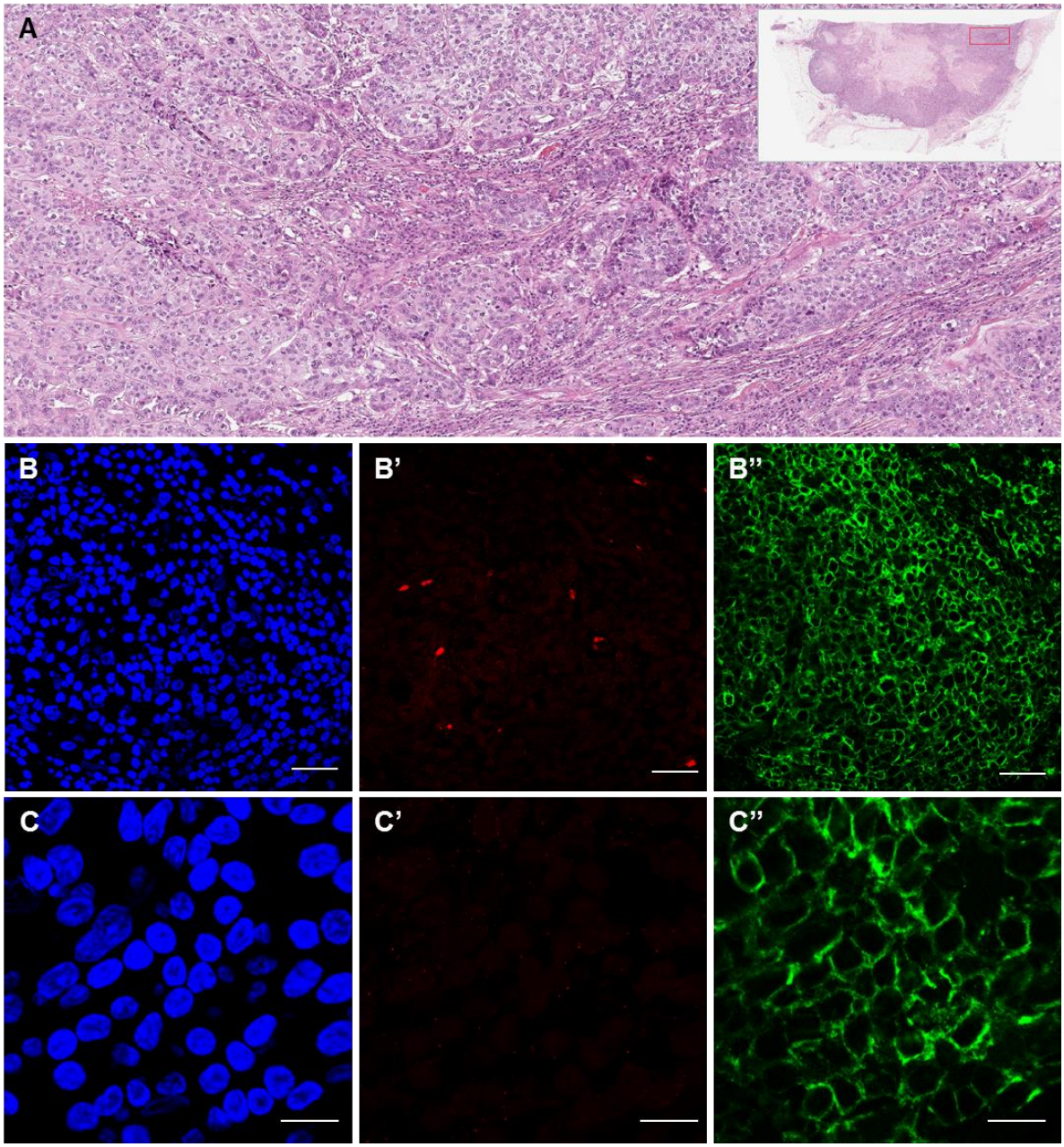

Figure 5.46: *Triple negative pre-menopausal breast cancer tissue. (A) Displays H&E staining across the analysed section of tissue. (B, and C) display DAPI staining across varying magnifications of the same structure. (B' and C') shows nesprin-2 C-terminal KASH domain staining. Images highlighted in (B'' and C'') further display actin staining. Scale bars = 30 µm (B), 20 µm (C).*

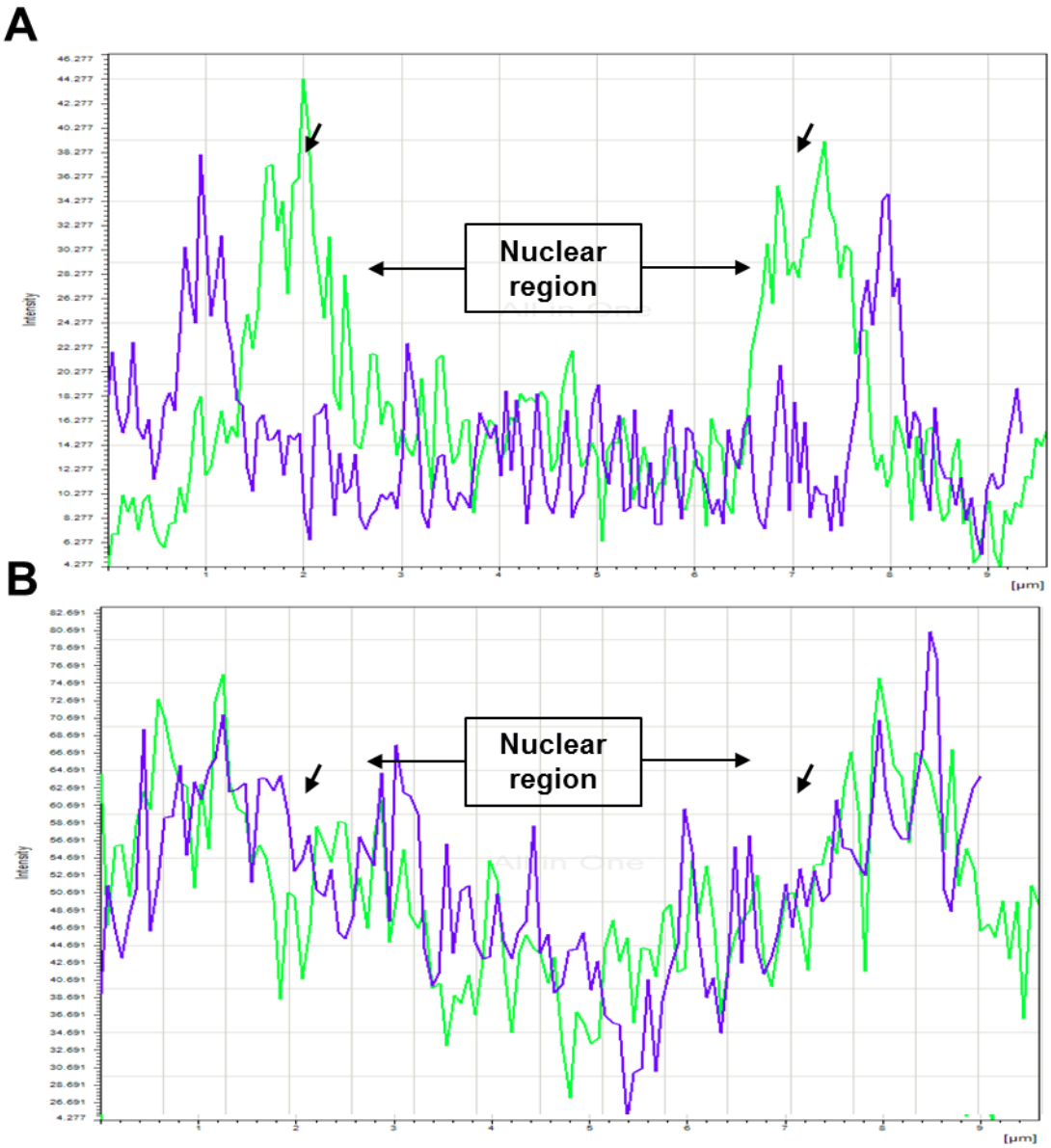

Figure 5.47: *Pixel topology analysis of nesprin-2 C-terminal domain staining (Green) and actin staining (Blue) within non-cancerous breast tissue (A) and ER+ cancerous breast tissue. Nuclear envelope positioning is displayed with arrows.*

Figure 5.47 displays collated data from 50 individual cells within each tissue type, helping to support suggestions that nesprin 2-C-terminal staining within the ER+ breast cancer tissue expresses variable cellular topology. It can be seen from (A) that the peaks of highest nesprin-2 pixel intensity can be seen at nuclear envelope regions, whereas the actin peaks are found within more distant cellular regions at the plasma membrane. In contrast to this, the peaks for both actin and nesprin 2 staining in ER+ cells appear to localise to peripheral cellular regions. This result therefore suggests that nesprin-2 localisation is drastically altered, leading to a more cytoplasmic distribution, which further correlates with previous nesprin-2 C-terminal staining observations across control, low

and high grade breast cancer cell lines in section 5.3.1.5. However, to further asses this data, more detailed observations would need to be conducted, as the ER+ cancer cells appear to cluster in much closer associated cellular colonies. This could result in a reduced distance between nuclear envelope and plasma membranes, leading to more observations of nesprin-2 staining across the cellular periphery. Therefore to validate these findings, further TEM analysis can be performed to assess nesprin-2 C-terminal localisation in relation to NE and plasma membranes.

5.4 Summary of Experimental Findings.

Throughout this chapter, investigations have aimed to characterise the cellular organisation and expression levels of various *LINC* complex proteins across a wide range of breast cancer cell lines.

5.4.1 LINC complex proteins display variable expression patterns across breast, cervical and colorectal cancer cell lines.

Initial pilot data, investigating select *LINC* complex protein expression levels across a range of cancer types (*Figure 5.3)*, displayed complex protein variability across the varying cancers assessed. More specifically, variability in emerin, nesprin-2G isoforms, lamin B1/B2 and Nup88 expression was observed. However, within each representative cancer form, it is difficult to establish whether any functional relationships exist between the low and high grade cancer samples. Nesprin-2G expression for example appears to be reduced in MDA-MB-231 cells compared to their low grade counterparts MCF7's, whereas little variation can be seen between the low- and high-grade colorectal cancer cell lines SW480 and SW620. These observations highlight potential cell line specific variability in *LINC* complex protein expression. Whereas current understanding of the tissue specificity for many *LINC* components is limited, current literature suggests nesprin proteins present tissue specific isoform expression, with smaller isoforms able to induce potential tissue specific functions not present in other bodily regions [80]. This potential for different bodily tissues to express various nesprin isoform levels suggests that to effectively assess the role of *LINC* components in cancer progression through the assessment of cell lines, multiple cell lines must be assessed from within the same cancer type, originating from similar regions of the tissue source.

Due to these observations, following experimentation was conducted in breast cancer cell lines, due to its high importance within current clinical investigation, alongside its ease of investigations due to the availability of a wide range of model cell lines for the disease.

5.4.2 Variation in LINC protein expression is observed across breast cancer cell lines, alongside localisation defects in both cell lines and primary breast tissue samples; most significantly in low molecular weight nesprin-1/-2 isoforms.

Initial investigations into the expression of *LINC* proteins between these breast cancer cell lines lead to an interesting observation. It was observed that through Coomassie Blue staining, sample loading within the blot appeared equal (*Figure 5.4*), however, variations between HCC-38 and T47D cell lines across each standard loading marker were found (*Figure 5.5*). It was shown that the HCC-38 cells expressed a reduction in β-actin, whereas the T47D cell line displayed reductions in both GAPDH and β-tubulin expression. Potential explanations for these observations come from our increasing understanding of cell specific protein expression levels, in which drastic variability in supposed equal loading markers can vary between cell lines [344]. With this knowledge, collated data from the equal loading markers employed, alongside initial Coomassie Blue staining lead to the assumption that loading was equal across each breast cancer protein sample.

Following investigations aimed to investigate cytoskeletal organisation between MCF 10A, MCF7 and MDA-MB-231 cell lines (representing control, low- and high-grade breast cancers). It was shown in *Figures 5.6 - 5.9* that microtubule organisation was retained across each cell line assessed. In contrast however, the actin and cytokeratin networks expressed drastic organisational differences, with actin displaying an observed peripheral localisation at cellular projections. In MCF7 and MCF 10A cells, actin appeared more evenly distributed across the nuclear, cytoplasmic and cell periphery regions.

It was further shown that cytokeratin appeared to be much less abundant within control and high-grade breast cancers compared to the low-grade MCF7 cells, which displayed a highly ordered structural arrangement of cytokeratin through its cytoplasm. This is further supported through protein expression analysis (*Figure 5.10*), through which specific keratin proteins like vimentin were shown to display reduced expression profiles in high-grade MDA-MB-231 cells in comparison to low-grade MCF7 cells.

Further investigations into expression patterns and organisation of core *LINC* complex components including SUN, KASH and lamin protein family members were then conducted. Interestingly, the gathered data appears to support current suggestions that a loss of core NE proteins which are crucial for maintaining nuclear architecture is more prevalent in highly metastatic cancers. Evidence in the literature suggests in high-grade

breast cancers (similar to those represented by MDA-MB-231 cell lines) a down regulation in lamin A/C, lamin B2 and SUN2 is observed, which supports findings within our investigations suggesting loss of expression for each protein in the high-grade cell lines [203]. It is suggested that loss of NE protein functionality could stimulate chromatin instability and increased oncogene expression [302], metastatic phenotype development [353] and malignancy in various cancer types [354].

Aside functional defects arising from loss of key *LINC* components, it is also suggest that the loss of these *LINC* connections across the nuclear envelope impairs nuclear integrity, and therefore increases nuclear malleability. It is known that loss of *LINC* components such as nesprins and lamins compromises nuclear architecture [14]. Coupled with data from Chapter 3 and protein expression patterns displayed in *Figures 5.18* and 5.23 suggesting loss of low molecular weight nesprin-1/-2 C-terminal isoform expression in high-grade cell lines, it can be suggested that this observed loss of lower nesprin isoforms stimulates an increase in nuclear malleability, allowing 'softer' nuclei to migrate through more restrictive environments.

It is further suggested that displacement of nesprin-2 C-terminal *KASH* domains from the NE is also present within high-grade breast cancer cell lines (*Figures 5.21* and 5*.22*). When further applied to primary pathological breast tissue samples, implications for the use of nesprin-2 -C-terminal antibody staining as potential markers for cancer grading is apparent. It can be seen that nesprin-2 C-terminal *KASH* domains appear to dissociate from the NE upon cancer development in ductal epithelial cells specifically (*Figures 5.43 – 5.46*). As the cancer progresses to a triple negative phenotype, nesprin-2 C-terminal staining further reduces, suggesting potential use for this protein region as an early staging marker for breast cancer biopsies.

Current understanding of the functionality of lower nesprin-1 and nesprin-2 isoforms is limited due to the difficulty in isolating and distinguishing between the potential protein variants. This means that conclusive effects of nesprin roles in cancer development remain unknown thus far; however, the data presented here does suggest that the lower nesprin isoforms may be a crucial future target to investigate the relationships between nuclear stiffness and cancer metastasis in breast cancer.

5.4.3 LINC associated proteins including lap2α, E-cadherin and Nup88, alongside the protein chaperones HSP27, GFAP and CRYAB display variability in protein expression profiles across breast cancer cell lines.

Further observations in protein variations came through analysing *LINC* associated proteins, including NPC proteins, and centrosome markers, relative to p53, E-cadherin and lap2α. Interestingly, although significant differences were observed in centrosome marker expression levels, no obvious correlations were displayed between expression levels and breast cancer severity (*Figure 5.26*). For example, we saw a significant increase in pericentrin levels in MDA-MB-231 cells in comparison to the low-grade MCF7 cells, which correlated directly with the literature. It is suggested that increased pericentrin levels would stimulate an increase in centrosome number, which in turn would result in altered mitotic spindle formation and function, leading to genome instability [355, 356, 357]. This would then lead the development of aneuploidy (a known cancer hallmark). However, alongside our high-grade cancer cells expressing increased pericentrin levels, the control MCF 10A cells also present similar expression levels, leading to a conflict to this suggestion.

Aside this, further variations in expression levels were observed in Mab414, a nuclear pore complex marker, in which the high-grade MDA-MB-231 displayed a reduced total protein expression of lower nuclear pore proteins (*Figure 5.29*). Alongside its roles in regulating nuclear transport and chromatin organisation, knowledge on potential roles of nuclear pore proteins within cancer development is limited to only a few components such as Nup88 [358]. However, current evidence presented by Martignetti *et al*. highlight the nuclear pore complex as a future target in cancer research using algorithmic analysis of key miRNAs contributing to the development of triple negative breast cancers [359]. Within these investigations, key miRNA and gene expression levels were identified across a range of triple negative breast cancer tissues, suggesting correlations in miRNA expression profiles which regulate NPC function. Collectively, these data suggest that the NPC function could be compromised in high-grade breast cancer patients.

Further investigations were conducted into expression levels of oncogenic markers like p53, cell proliferation markers and cell-cell adhesion proteins. Observations suggest p53 and lap2α levels appear to increase during increased cancer cell lines severity, whereas E-cadherin levels appear varied across cell lines (*Figure 5.26*).

As already stated, genomic mutations leading to disruptions in known oncogenes pose a sever risk within the human population. Due to this fact, multiple avenues are being perused in order to increase our understanding of the development of cancer in order to design more specific treatment methods. One such area is the investigation as to cellular disruptions in chaperone proteins, responsible for regulating protein folding ensuring protein functionality is retained. To validate whether a correlative variation in heat shock expression levels exist across varying breast cancer cell lines, the assessment of HSP27, CRYAB and GFAP was conducted (*Figures 5.30* and *5.31*). Our data suggested that the levels of CRYAB appear to be down-regulated across many breast cancer cell lines. Interestingly however, the 3148-CRYAB (Polyclonal) antibody further displayed bands at alternate molecular weights, which could correlate to unspecific binding, or alternatively may display alternate protein variants which vary across the breast cancer cell lines. .Aside this, further variations in HSP27 and GFAP were also identified, in which high grade breast cancer cell lines were shown to express reduced expression levels of HSP27, alongside increased expression of GFAP in all lines except the triple negative MDA-MB-231 cell lines.

5.4.4 High-grade MDA-MB-231 cells display significantly increased migration potential through space-restrictive 3D environments which is not reversible through nesprin-2 mini insertion.

As much of the literature thus far suggests that an increase in breast cancer severity correlates with an increase in migratory potential, further investigations aimed to assess the migration potential of control (MCF 10A), low-grade (MCF7) and high-grade (MDA-MB-231) breast cancer cell lines in the restrictive Strata® scaffolds. This investigation therefore aims to assess whether any associations between *LINC* proteins expression assessed thus far and migration behaviour in space-restrictive environments can be observed. It was shown that MDA-MB-231 cells displayed the greatest migration potential through the space-restrictive scaffold environments, with further EM analysis displaying little variation in cellular morphologies across the different scaffold regions between cell lines. When collated with protein analysis data, it can be suggested that this observed migration advantage could be attributed to a decrease in nuclear stiffness, similar to that observed within *LINC* disrupted DN HaCaT cells in Chapter 3.

It has been shown that the high-grade MDA-MB-231 cells express reduced levels of *LINC* components responsible for maintaining NE integrity (*Figures 5.9 – 5.26*) including lamin A/C, lamin B and lower nesprin-1 and -2 isoforms. These observations suggest a disruption to the *LINC* complex, and subsequent loss of NE integrity present in MDA-MB-231 cells, which in turn may provide them with their increased migration potential through space-restrictive environments. This is supported by suggestions in the literature that nuclear size and deformability may be a rate limiting step in cellular migration through restrictive environments [272].

In an attempt to validate whether nuclear malleability is indeed a contributing factor in the migration potential of high-grade breast cancer cell lines through restrictive environments, further experimentation aimed to disrupt and re-introduce *LINC* components across low- and high-grade breast cancer cell lines respectively. Interestingly, we found that the incorporation of DN SUN1 constructs into low-grade breast cancer cell lines stimulated a significant increase in cellular clustering alongside an increased penetration potential through restrictive Strata® scaffolds. However, it was further shown that the incorporation of a nesprin-2 mini construct into the high-grade MDA-MB-231 cell lines was unable to revert the increased cell clustering or migration potential phenotypes expressed (*Figures 5.39* and *5.40*).

These observations suggest that the disruption of *SUN-KASH* interactions across the perinuclear space is able to incite a migration advantage in the low-grade breast cancer cell lines. However, this increased migration potential still remains lower than that of the high-grade breast cancer cell lines, suggesting that further gene and protein expression differences exist between the low- and high-grade cell lines, inferring the difference in migration potential. On the other hand however, the DN SUN1 population was heterogeneous in its expression of the DN SUN1 construct, meaning that further repeats of this experiment with a homogeneous population would be required to increase the validity of these findings.

Of further interest were observations suggesting that the incorporation of DN KASH constructs into the low-grade breast cancer cell lines inferred no migration changes. This construct is considered a milder *LINC* disruption to that displayed by the DN SUN1 construct. DN KASH maintains the *SUN-KASH* perinuclear linkage whilst displacing KASH proteins from the ONM, therefore severing cytoskeletal interactions to the NE surface. This data therefore hints to the potential that this inferred migration advantage displayed by the DN SUN1 construct insertion, could result from the loss of *SUN-KASH* interactions across the NE, rather that the loss of ONM protein associations. Potential reasoning for

this observation may come from evidence presented by Wang *et al*. [59]. They were able to show that the upregulation of SUN2 in Ovcar-3 cell was able to increase migration potential, with final remarks suggesting a potential regulatory role played by SUN2 coiled-coil motifs in cell migration. It is therefore possible that as our system targets *SUN-KASH* binding, the regulatory roles played by SUN2 coiled-coil domains may be perturbed, leading to an altered cell response in pathways involved in cell migration.

It was further shown that the incorporation of nesprin-2 mini into the high-grade breast cancer cell lines was unable to produce a slower migration phenotype. One potential explanation for this however, is the use of nesprin-2 mini as a means of re-establishing NE integrity. This mini construct is much smaller than the endogenous nesprin-2G protein due to the removal of the vast majority of spectrin repeat proteins situated between N- and C-terminal regions. The decrease in nuclear size attributed to mini insertion may counteract the potential increased nuclear stiffness, meaning that the nuclei are now small enough to migrate through the restrictive interconnects without the need of nuclear deformities. However, to fully validate this, further investigations will be needed to assess the effects of incorporating numerous *LINC* complex components within these high-grade cancer cells, to see if re-establishment of nuclear stiffness without altering nuclear size does indeed affect migration potential.

One further potential flaw within this investigation was the use of transient transfections to assess the effects of *LINC* disruptions on migratory behaviours across various cell lines. The process of transient transfection using electroporation does not elicit 100% transfection efficiency, alongside inducing cellular stresses. These combined factors could contribute to alterations in cellular migration potential irrespective of the components inserted into the genome. To combat this experimental weakness, we attempted to produce a new cell line of stably transfected MCF7 + DN SUN1, in order to produce a cloned population of cells expressing the desired plasmid. However, we found that the expression of DN SUN1 in these cells stimulated an increase in multi-nucleated cells, suggesting that within these cells, the mechanisms behind maintaining efficient DNA replication or separation during mitosis was disrupted, leading to eventual cell death. However, this observation does provide further indications as to potential roles of nesprins within cancer development, as multi-nucleation alongside abnormalities in DNA replication, centrosome amplification and chromatin splitting are considered hallmarks of cancer development [369].

Through the assessment of a range of *LINC* complex proteins and associated proteins, correlations have been observed between expression levels in specific components

responsible for maintaining nuclear architecture, such as the lamin and nesprin proteins and breast cancer cell lines severity. With further primary tissue analysis suggesting further protein organisational defects arising during breast cancer development, we suggest that key components of the *LINC* complex, including nesprins, SUN proteins and lamins are vitally important within breast cancer progression. Specifically, nesprin-2 C-terminal containing isoforms display the greatest potential for use as an early prognosis marker for high-grade breast cancer development. To further validate this however, future investigations should assess gene and protein expression levels within primary tissues correlating to the staining work conducted here using PCR and western blotting techniques. This will help to further validate whether the expression of C-terminal regions of nesprin-2 are indeed reduced within high-grade breast cancers, alongside providing insights to the levels of lower nesprin-1 and nesprin-2 isoforms within the tissue.

6. Investigating binding potential between C-terminal regions of nesprin-2 and Nup88

6.1 Introduction.

As described previously, five proteins containing KASH-domains have been identified to date, termed nesprin-1, -2, -3, -4 and KASH5 [78, 452, 234]. Each nesprin is encoded by a separate gene, giving rise to a multitude of structurally and functionally diverse isoforms [452]. Of these nesprin isoforms, the largest are termed nesprin-1 and nesprin-2G, and comprise an N-terminal actin binding domain and a C-terminal transmembrane domain, separated by a large spectrin repeat (SR) rod segment [234, 232]. One hallmark of these nesprin proteins is the retention of the evolutionary conserved C-terminal KASH domains across the majority of isoforms. This domain encompasses a single transmembrane segment, followed by a conserved PNS localised peptide which associates directly with SUN protein luminal domains [32, 33]. This interaction helps to link the ONM to the INM through further interactions between SUN and lamin proteins [29]. Unlike the high conservation of C-terminal regions, nesprin N-terminal regions display complex diversity due to the differing spectrin repeat compositions. They also contain distinct protein binding regions, imparting further roles for nesprins in maintaining ONM connections with cytoskeletal components such as actin through Nesprin-1 and -2G [14, 76, 77], microtubule motor proteins (*i.e.* kinesin 1) through nesprin-4 [78], and intermediate filaments through nesprin-3 [86, 182] (*Figure 6.1*).

The specific maintenance of NE connections between INM and ONM regions through nesprin-2G interactions have been shown to play further functional roles in maintaining nuclear architecture [101]. It was shown that specific interference of nesprin-2G N-terminal interactions with nesprin-3, alongside C-terminal interactions across the NE resulted in an increase in nuclear size. More importantly, this nuclear defect was able to be rescued and reversed through the re-incorporation of nesprin-2 mini (nesprin-2 -C and -N-terminal regions connected by a smaller interconnecting rod domain), producing a smaller nuclear size. This data, therefore, suggests that the interacting potential of both N and C-terminal domains of nesprin-2 plays crucial roles in maintaining normal cellular architecture.

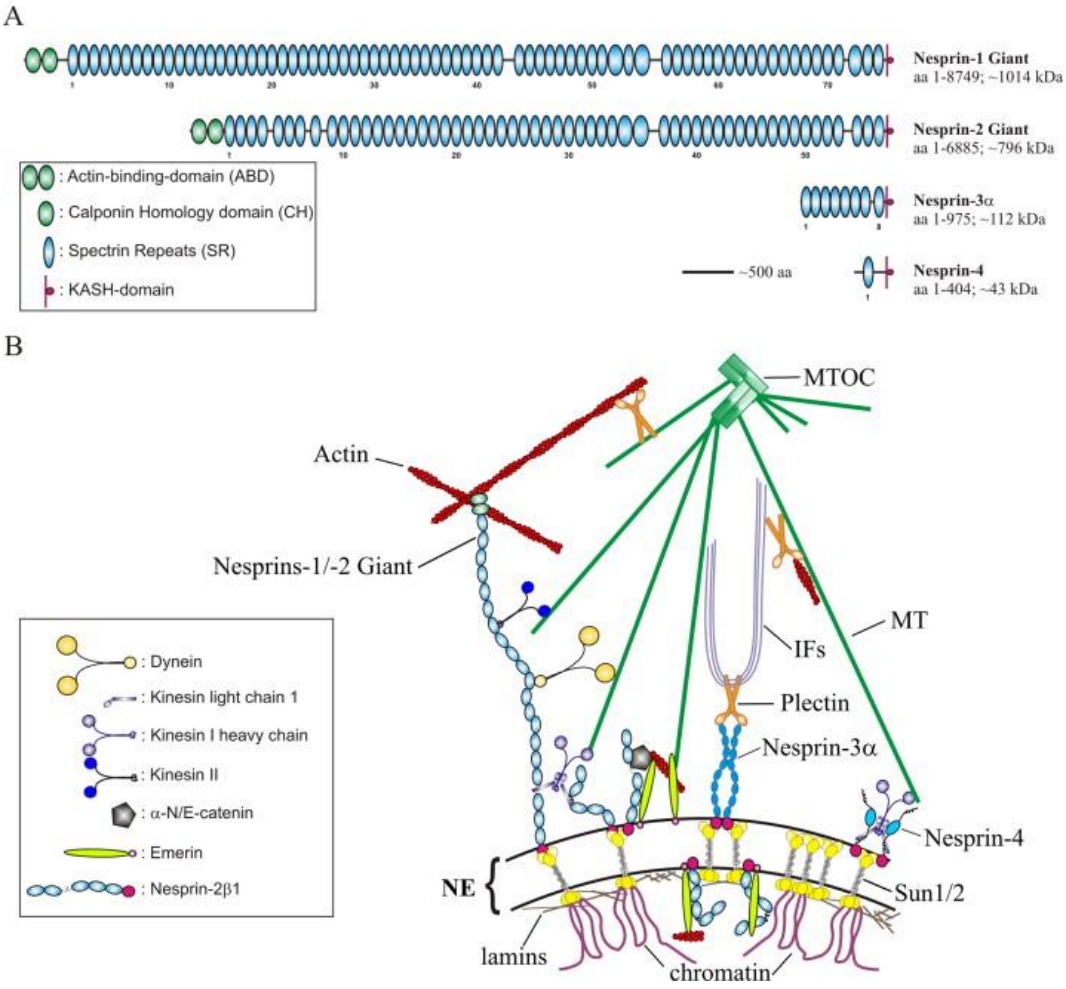

Figure 6.1: *A) Domain architecture of the largest nesprin family members in humans. B) Direct and indirect protein interactions displayed by nesprin-1, -2, -3 and -4 across the NE. Nesprin-1 and -2 giant interact directly with F-actin, and indirectly to microtubules via kinesin and dynein across the ONM. Nesprin-3α indirectly binds IFs through plectin, which is further able to crosslink multiple cytoskeletal networks. Nesprin-4 associates indirectly to MTs through kinesin 1. [508]*

Interestingly, further research suggests that, not only are -N and -C-terminal interactions with NE components crucial for maintaining nuclear architecture through *LINC* connections, but are also crucial for the recruitment of functional proteins to the NE surface. Recruitment of the diaphanous related formin (DRF) FHOD1 to the nuclear envelope and its roles in actin binding and the formation of TAN lines across the NE have been well characterised [453]. Recent investigations have shown that the recruitment of FHOD1, and subsequent TAN line formation across the NE, is mediated by interactions with nesprin 2G across the N-terminal residuals 1340-1678 corresponding to spectrin repeats 10-12 [94]. In this paper, Kutscheidt *et al.* identified the binding interaction

between Nesprin-2 and FHOD1 through yeast two hybrid screening accompanied by GST pulldowns. Subsequent assessment of these interactions displayed that the nesprin-2G/FHOD1 interaction provides a second connection between the NE and actin cables. This second connection is essential for the formation of TAN lines and thus nuclear movement in the cells.

In addition, further interacting potential has been suggested between nesprin-2 and α-catenin across the nuclear envelope [9]. This, in turn, suggests roles for nesprin 2 in the regulation of Wnt signalling across the NE. Through the use of yeast two-hybrid screening, alongside immunoprecipitation, it has been shown that the -C-terminal region of nesprin-2 displays interacting potential with α-N-catenin. It was further shown that this nesprin-2/α-catenin interaction is able to regulate β-catenin dependent transcription. Through the use of SP-GFP-SUN-1-C (construct able to sever KASH-SUN protein interactions in the NE lumen) incorporation into HaCaT cells, resulting in the disruption of nesprin-2 across the NE, nuclear accumulation of β-catenin was seen to reduce. From this work it is suggested that nesprin-2 complexes with emerin, α- and β- catenin upon Wnt signal activation, forming a quaternary protein complex, from which β-catenin can sequester into the nucleus and undergo its normal transcriptional functions.

6.1.2 Nup88, a potential nesprin-2 binding partner.

As described thus far, the N- and C-terminal regions of nesprin-2 display functional roles in both maintaining nuclear architecture and in the recruitment of proteins across the NE. Of further importance are interactions between nesprin-2 C-terminal domains and KLC1. This KLC1 interacting potential was identified through isolation of the last 4 C-terminal spectrin repeats (termed N2-SR) [77], followed by subsequent yeast two hybrid and GST-pulldowns. An illustration of nesprin-2G, alongside the N2-SR construct and spectrin repeat structural representations can be seen in *Figure 6.2*. Interestingly however, the unpublished data from this yeast two-hybrid screen suggests further interacting potential with multiple proteins, one of which is the NPC protein Nup88.

The NPC mediates molecular exchange across the NE with the aid of ~30 different nucleoporins. These nucleoporins are organised into distinct sub complexes able to form the major building blocks of the NPC, displaying an octagonal core formed from a central framework connecting INM and ONM rings [454, 455]. The nucleoporin Nup88 resides across the cytoplasmic face of the NPC, found in a complex with the nucleoporins Nup214

and Nup358, as well as the nuclear export factor CRM1 [456, 457]. Nup88 has been found to localise to intranuclear regions displaying chromatin associations, suggesting potential roles of Nup88 in gene regulation [458].

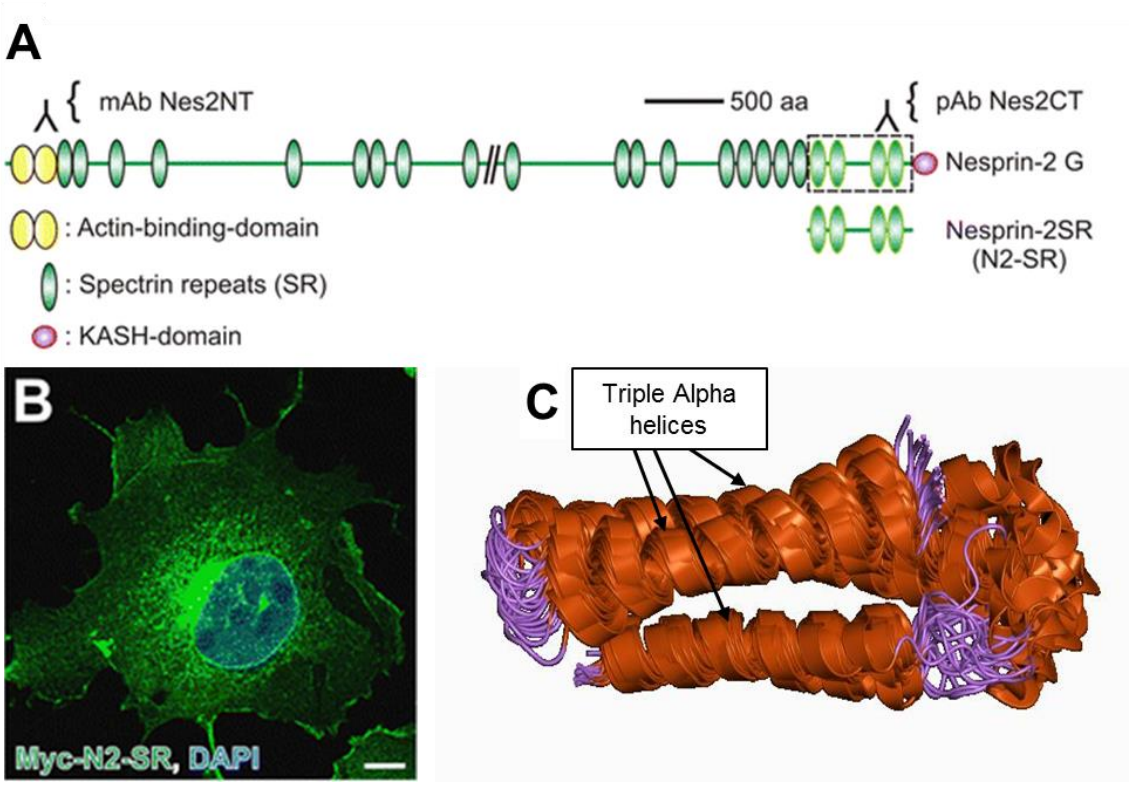

Figure 6.2: *A) Nesprin-2G and N2-SR structural features, alongside NT and CT antibody binding regions. B) Myc-tagged N2-SR transfected into COS7 cells, displaying both NE and ER staining, with cells stained for Myc (green) and DAPI (blue). Scale bar = 10 µm. C) Hypothesised crystal structure of the left handed antiparallel triple-helical-coiled coil spectrin repeats [77, 509].*

Nup88 is composed of two structural domains: an N-terminal β-propeller making up two thirds of the proteins (residuals 1-584 in humans); and a C-terminal alpha helical coiled coil (residuals 585-741) [459]. This observed coiled-coil domain mediates the interactions with Nup214 [460], whereas the N-terminal β-propeller domain interacts with the NPC-targeting domain of the nucleoporin Nup98, thought to localise across both the cytoplasmic and nucleoplasmic face of the NPC [461]. This wide range of interacting partners, alongside both its cytoplasmic and nucleoplasmic localisation suggests complex functionality for Nup88. It has been shown that the formation of Nup88-Nup214 complexes are not directly required for the import of proteins through the NPC, but is, however, crucial for CRM1-mediated nuclear export [462]. This suggests that Nup88 function across the NPC is required in the maintenance of nuclear transport. Further roles have been

identified for Nup88 in the maintenance of NFκB activation across the NE [463]. In this investigation, it was shown that overexpression of the Nup214-Nup88 complex sequestered CRM1 to the cytoplasmic foci of the NPC, resulting in the inhibition of protein export. This investigation therefore suggests regulating Nup88-Nup214 interactions, could act to regulate the duration and strength of NFκB signal responses. However, further investigations have now verified Nup88 as a regulating component of nucleoplasmic NFκB transport [464]. Through the application of a small interfering RNA (siRNA) against Nup88 NFκB dependent reporter gene activation was inhibited, and nuclear accumulation of NFκB was observed. In contrast, nuclear import of alternate factors, including glucocorticoid, was not affected. This suggests that specific regulatory interactions exist between NFκB and Nup88 across the NE. Interestingly, in many highly metastatic cancers, NFκB displays constitutive activation in both nuclear and cytoplasmic regions of the cell [465], however, depletion of Nup88 in these cells was shown to reduce TNF-induced nuclear accumulation of these NFκB subunits.

Investigations into the roles of nucleoporins in cancer development have shown that a small number of nucleoporins display tumorigenic properties, including Nup62, Nup214, Nup358, and Nup88 [466]. Although the exact roles of Nup88 in cancer development are not well understood, the expression levels of both Nup88 protein and mRNA are seen to be increased in highly metastatic cancers [467, 468, 469]. For example, increases in serum levels of Nup88 correlate to the development of highly aggressive colorectal cancer phenotypes [470]. Quantitative sandwich enzyme-like immunosorbent assay (ELISA) analysis on blood serum of pre- and post-operative colorectal cancer patients, show that levels of Nup88 were higher in pre-operative patients in comparison to post-operative patients. Further positive correlations between Nup88 serum levels and depth of tumour penetration were also observed, suggesting that not only are Nup88 correlated with increased cancer metastasis, but they may also provide novel biomarkers for use in the early grading of tumours.

These hypothesised interactions between Nup88 and nesprin-2 through yeast two-hybrid investigations could provide implications for functional relationships existing between these two proteins in the development of cancer phenotypes.

6.2 Chapter Aims.

In this chapter the roles of *LINC* complex proteins in the development of highly metastatic cancer phenotypes will be investigated. It has been shown previously that nesprins play key functional roles in the maintenance of LINC connections across the NE. Disruptions in the SUN-KASH bridge lead to increased migration potential due to an increase in nuclear malleability. It is aimed to assess whether relationships exist between nesprins and binding partners (*e.g.* Nup88) in relation to the development of cancerous phenotypes. To achieve this, a range of cell biology and biochemistry techniques, including cellular transfections and GST-pulldowns, and advanced microscopy techniques, will be used in order to validate whether physical interactions exist between these two proteins.

6.2.1 Objectives.

- To assess whether nesprin-2 and Nup88 co-localise *in vitro*.

- To validate whether a physical interaction exists between the SR region of nesprin-2 and Nup88.

- To establish whether functional relationships exist between Nup88 and nesprin-2 in simplified cellular models.

6.3 Results.

6.3.1 Nesprin 2 CT domain displays strong co-localisation with the nuclear pore protein Nup88.

6.3.1.1 The C-terminal domain of nesprin-2 and Nup88 display strong co-staining across the NEs of multiple cell types.

Maintaining *LINC* connections across the NE is an important factor in retaining nuclear stability through *SUN-KASH* interactions across the peri-nuclear space. Alongside *SUN-KASH* interactions, nesprins display further interacting potential with the NPC protein Nup88. It was shown through yeast-two hybrid screening, that nesprin C-terminal SR regions displayed binding affinity with kinesin light chain 1 (KLC1) [77], alongside further unpublished interacting potential with Nup88. As both of these proteins have been shown to display abnormal expression patterns in high grade cancers, investigations aimed to validate these potential Nup88 and nesprin-2 C-terminal interactions through *in vitro* cell systems.

Initial investigations assessed whether nesprin-2 C-terminal regions and Nup88 displayed co-localisation across HaCaT, SW480 and SW620 cell lines. HaCaT cells were chosen due to their known high expression profiles of *LINC* proteins, whereas SW480 and SW620 lines were selected due to their representation of both low and high grade colorectal cancers [471]. Cells were cultured, processed and stained through immunofluorescence as described within the methods section, with images displayed in *Figure 6.3*.

Data presented in *Figure 6.3* suggests expression levels of nesprin-2 C-terminal regions appears to be uniform across the NE for each cell line, with SW620 cells displaying more punctate NE staining to that observed in SW480. Interestingly, Nup88 staining appears to display strong co-localised NE staining with nesprin-2 C-terminal regions across each cell line assessed, alongside more dispersed Nup88 cytoplasmic staining, suggesting Nup88 function may not solely reside across the NE. From these observations, it is evident that each of these cell lines analysed could act as a good model system to investigate Nup88 and nesprin-2 C-terminal domain interacting potential. However, HaCaT cells were chosen to maintain consistency with previous work through this thesis.

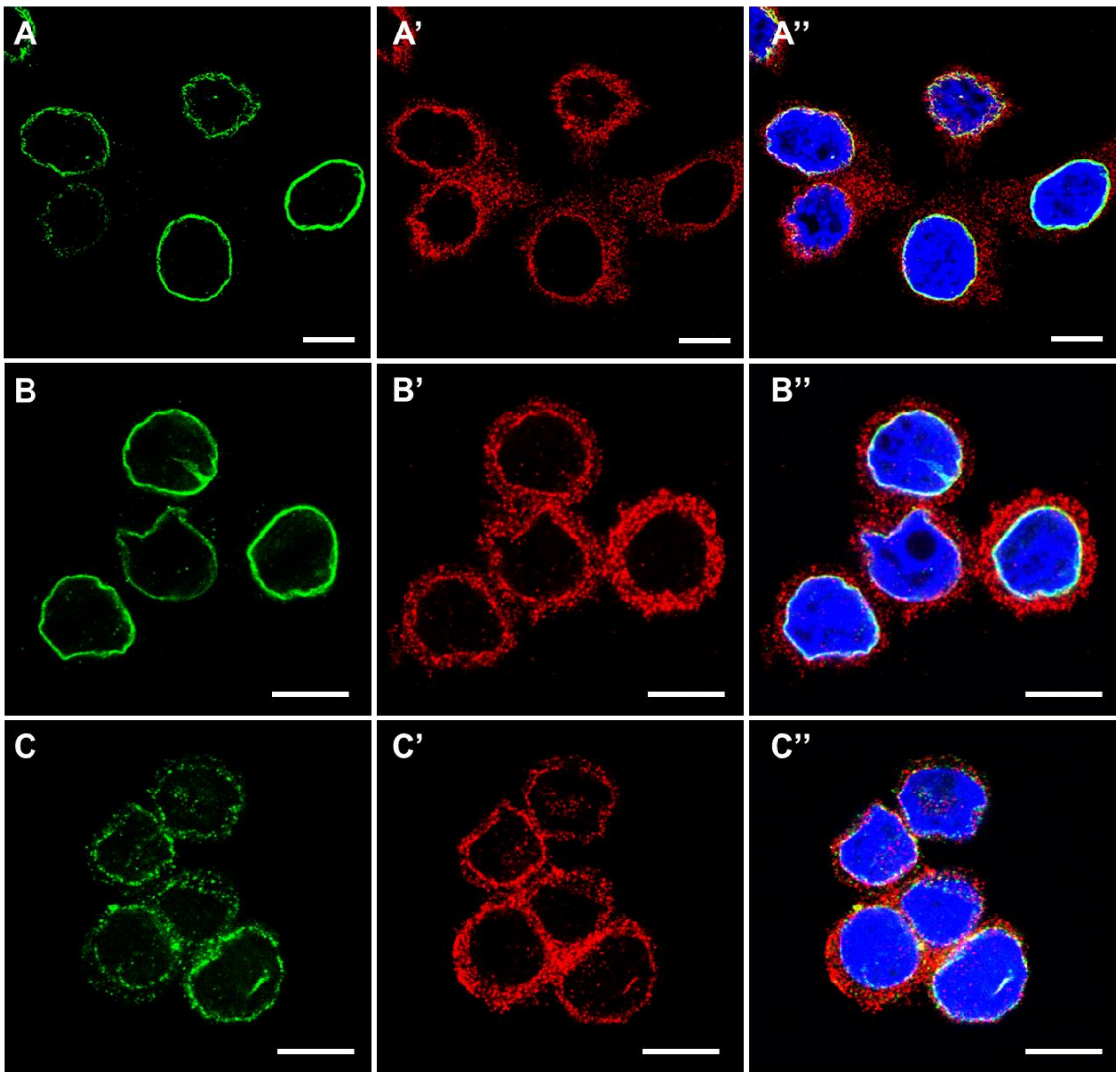

Figure 6.3: *Immunofluorescence staining against nesprin-2 C-terminal domain (A, B and C), Nup88 (A', B' and C') and DAPI (Blue). Images represent HaCaT (A), SW480 (B) and SW620 (C). Scale bars = 10 µm.*

6.3.2 Nup88 and the C-terminal region of nesprin-2 display co-localisation within HaCaT cells across the NE.

6.3.2.1 Indirect immunofluorescence suggests Nup88 and nesprin 2 C-terminal display close associations across the NE.

As displayed thus far, HaCaT cells display strong expression of both Nup88 and nesprin 2 under normal biological conditions, making them highly suited for the assessment of co-localisation potential between these two proteins. Initial investigations then aimed to optimise staining conditions for each protein to provide high specificity of

staining. The results of this optimisation lead to the clear identification of both Nup88 and nesprin-2 C-terminal (using the pAbk1 antibody and the Nup88 antibody defined in the methods section) attached fluorophores across the NE, as displayed in *Figure 6.4*.

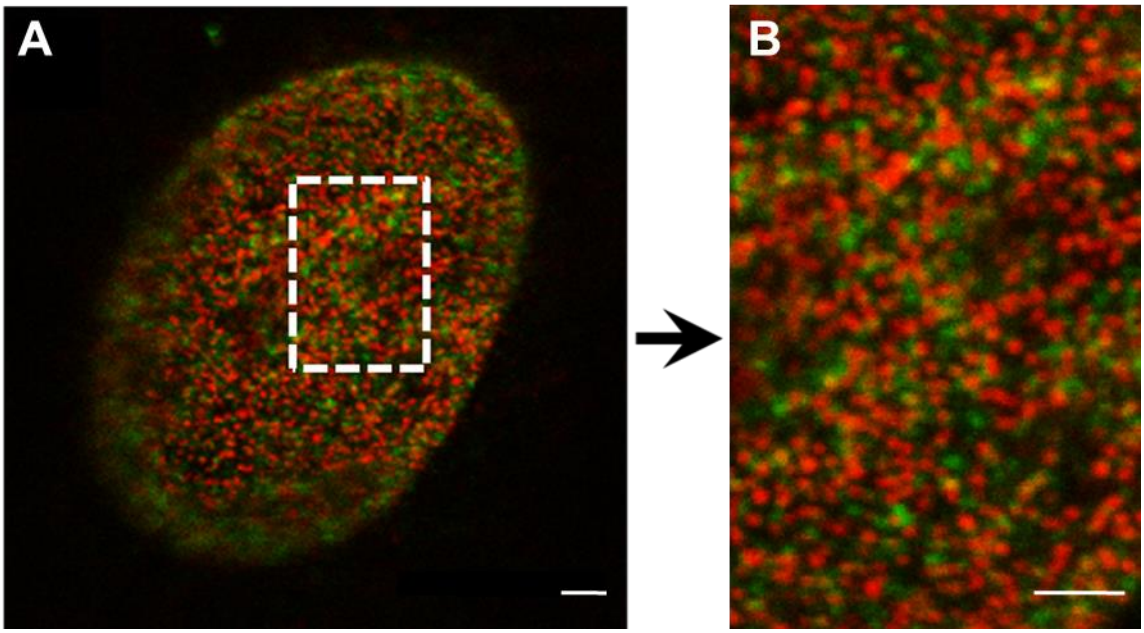

Figure 6.4: *Immunofluorescence staining against nesprin-2 C-terminal domain (green) and Nup88 (red) within HaCaT cells across the NE surface. Scale bars = 1.25 µm.*

As seen in *Figure 6.4*, the attached fluorophores between Nup88 and nesprin-2 can be clearly distinguished across the NE's surface. Using this optimised staining, following investigations aimed to quantify cellular co-localisation between the two proteins. To do this, images were taken across the NE's surface for counterstaining between Nup88, Nesprin-2's C-terminal region, NPC markers and Nup214 (a known Nup88 binding partner as a positive control) respectively. The fluorophore intensity was then assessed using the LEICA LAS AF image analysis software to establish whether the peaks of fluorophore intensity co-localised between each protein, with resulting images alongside example analysis techniques seen displayed in *Figure 6.5*.

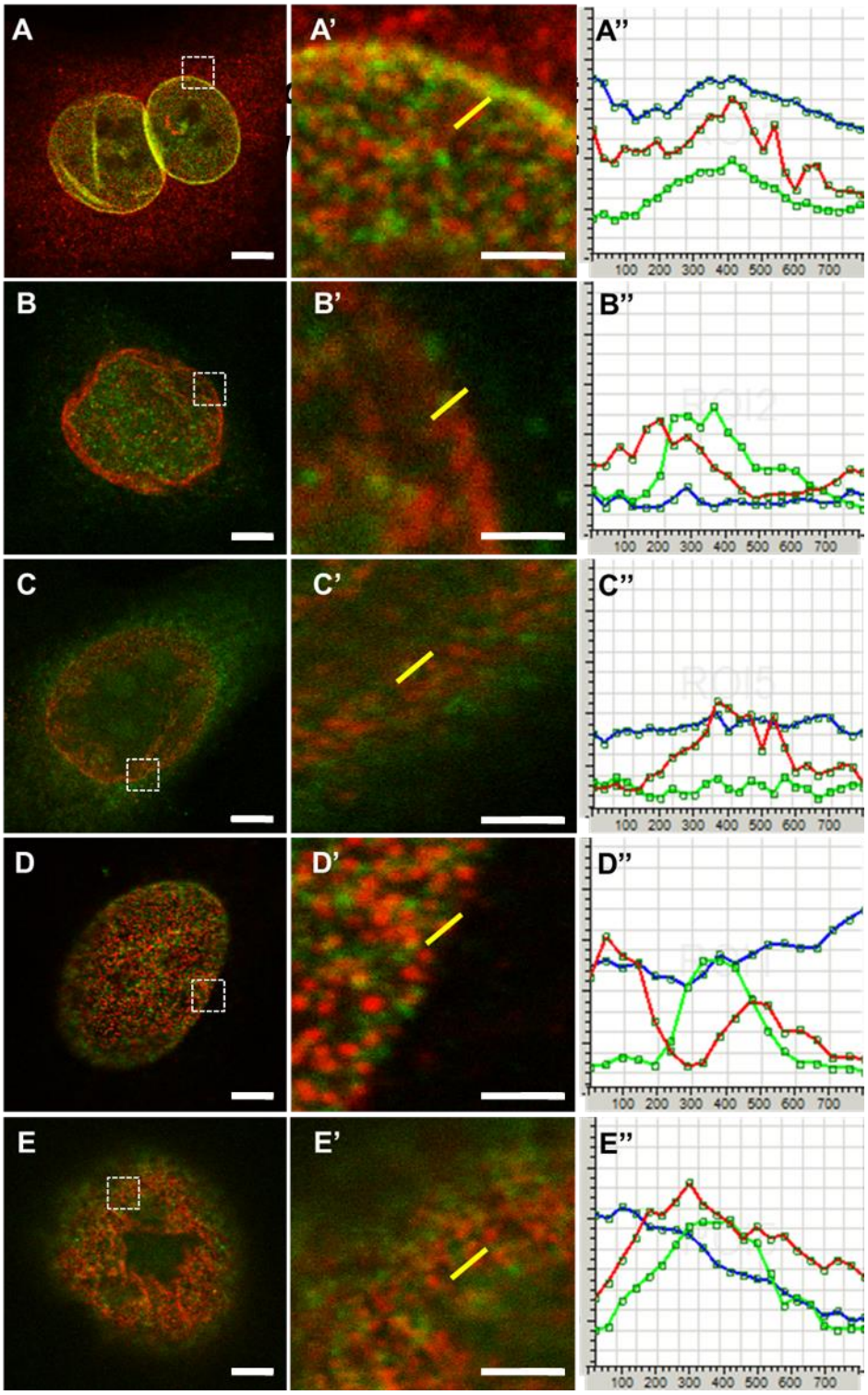

Figure 6.5: *Immunofluorescence and peak intensity analysis between Nesprin-2 CT (Green) and Nup88 (Red) (A), nesprin-2 NT (Red) and Nup214 (Green) (B), Nesprin-2 NT (Red) and Nup88 (Green) (C), nesprin-2 CT (Green) and Mab414 (Red) (D), and Nup214 (Green) and Nup88 (Red) (E) in HaCaT cells. Corresponding peak intensity between co-stains can be seen within A'', B'', C'', D'' and E'' respectively. Blue lines in the graphs display the background DAPI staining, not seen in the images. Yellow lines on the images represent regions of analysis, across which fluorophore intensity was assessed. Scale bars = 2.5 µm for A, B, C, D and E, and 1 µm in A', B', C', D', E'.*

Figure 6.5 suggests that Nup88 and Nesprin-2 C-terminal regions do indeed appear to co-localise across the NE surface. However, to increase objectivity in each set of peak analysis measurements, each fluorophore was analysed individually through switching off the counterstained channel during image analysis. Lines were then drawn across individual fluorophore dots to avoid selecting for dots which appear to display a high degree of co-localisation. Using this objective method of analysis, it is suggested that intensity peaks for Nup88 and Nesprin-2 C-terminal stained cells, alongside Nup88 and Nup214 stained cells display a high degree of signal overlap between the two fluorophores (*Figure 6.5 A and E*).

In contrast, intensity peaks for nesprin 2 N-terminal regions and Nup88/Nup214 respectively displays no-co-localisation (*Figure 6.5 B and C*), suggesting that the fluorophores are not in close proximity across the NE. Interestingly, the data also suggests a relationship between NPC's and Nesprin-2 C-terminal regions (D), in which C-terminal nesprin-2 peaks appear to situate in close proximity to Mab414 peaks of high intensity. Further quantification of this co-localisation analysis can be seen displayed within *Figure 6.6*, displaying collated co-localisation for each co-stain across the NE of HaCaT cells.

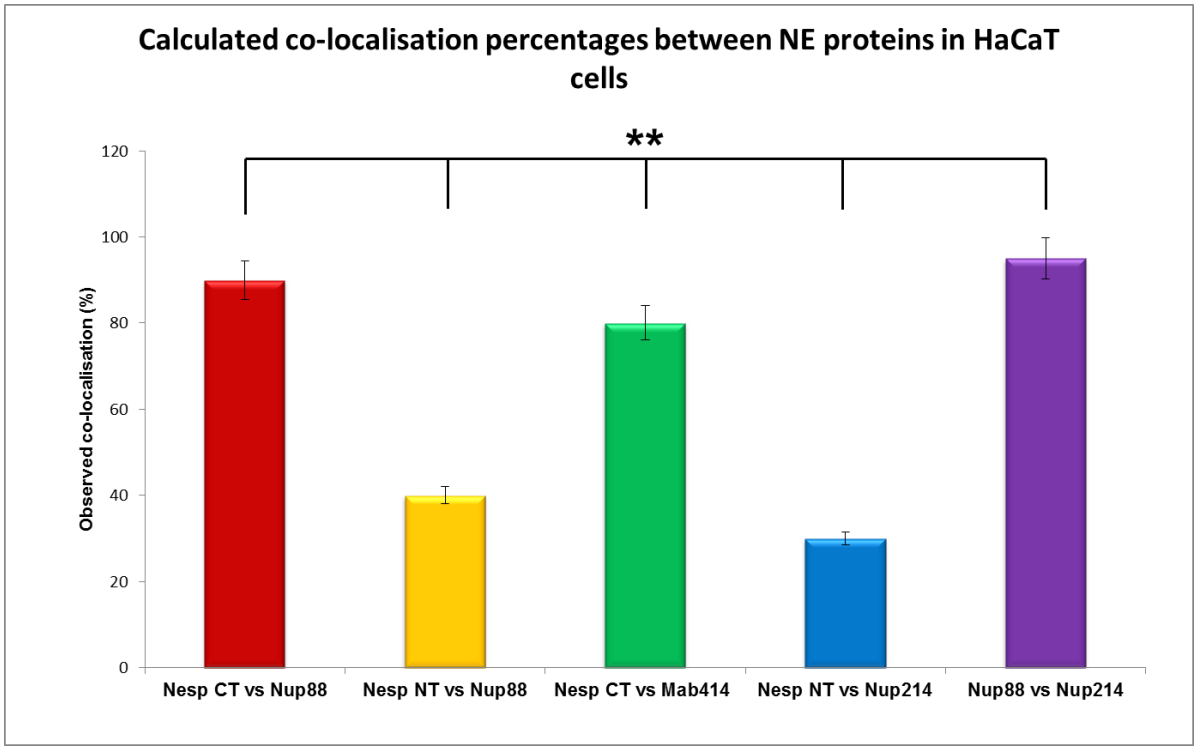

Figure 6.6: *Percentage co-localisation data for each co-stain conducted. Data collected from across 50 cells in each staining condition.*

The data presented in *Figure 6.6* suggests that significant differences are observed between the co-localisation of analysed proteins across the NE of HaCaT cells (*ANOVA, $F_{5.3525} = 3.51$, $P = 0.010$)*. Highest degrees of co-localisation are observed between the Nup88 + Nup214 co-staining and Nup88 + nesprin-2 CT co-staining. This finding suggests that the C-terminal region of nesprin-2 displays a high degree of close association with Nup88, as the comparative Nup214 + Nup88 co-stain represents co-localisation between known binding partners. High co-staining is also observed between the nesprin-2 CT and Mab414, suggesting that nesprin-2 CT regions are in close association with NPCs across the NE. Assessment of nesprin-2 NT regions displayed low levels of co-localisation with Nup88 or Nup214 across the NE, suggesting that if close associations do exist between these two proteins, it occurs at low frequency or is regulated by an intermediate protein.

To further validate our observations suggesting that in HaCaT cells, Nup88 and nesprin-2 C-terminal regions display co-localisation across the NE, FRET FLIM analysis alongside transfection techniques were employed.

The application of FRET FLIM analysis initially involved the assessment of fluorescence lifetimes for Nup88 tagged fluorophores both with and without the presence of nesprin-2 C-terminal staining in HaCaT cells. Nup88 was tagged with an Alexa Fluor 488 secondary antibody (acting as the donor), and nesprin-2 C-terminal regions with Alexa Fluor 568 (acting as the acceptor). As these two fluorophores expressing overlapping emission and excitation spectrums, this technique will allow us to assess whether a decrease in donor fluorescence lifetime occurs when co-localised with the acceptor fluorophore. If this decrease is observed, then close proximity between donor and acceptor fluorophores is suggested. Cells were fixed, stained and imaged as described in the methods section. Initial image analysis was conducted using the symPhoTime software on Nup88 only stained HaCaT cells to obtain a baseline fluorescence lifetime. An example output from this image analysis technique, alongside collated experimental data is displayed in *Figure 6.7*.

A

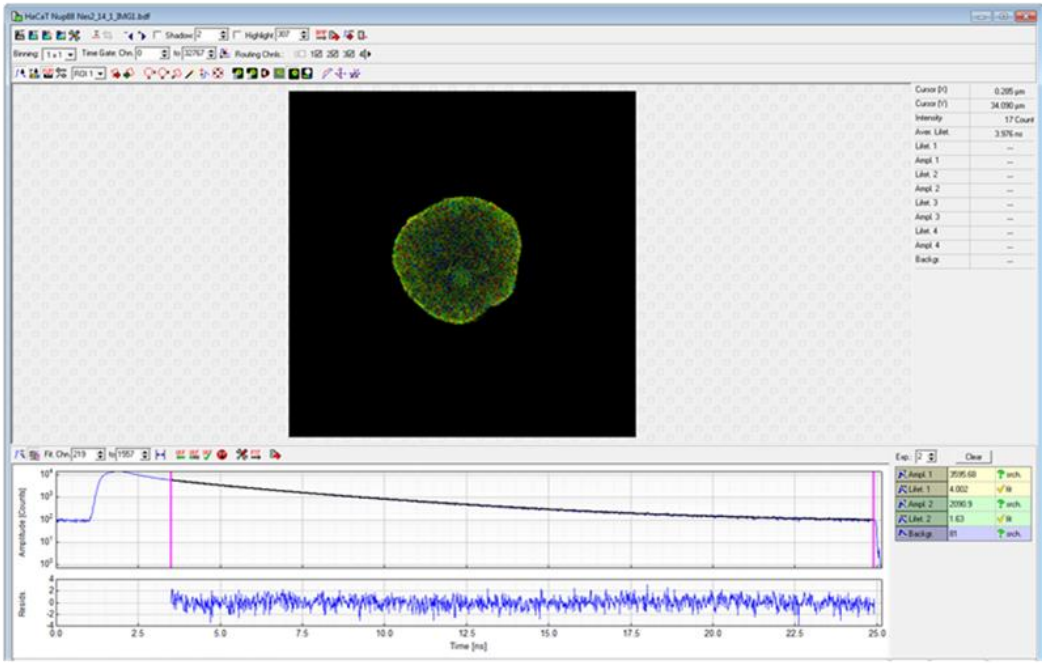

B

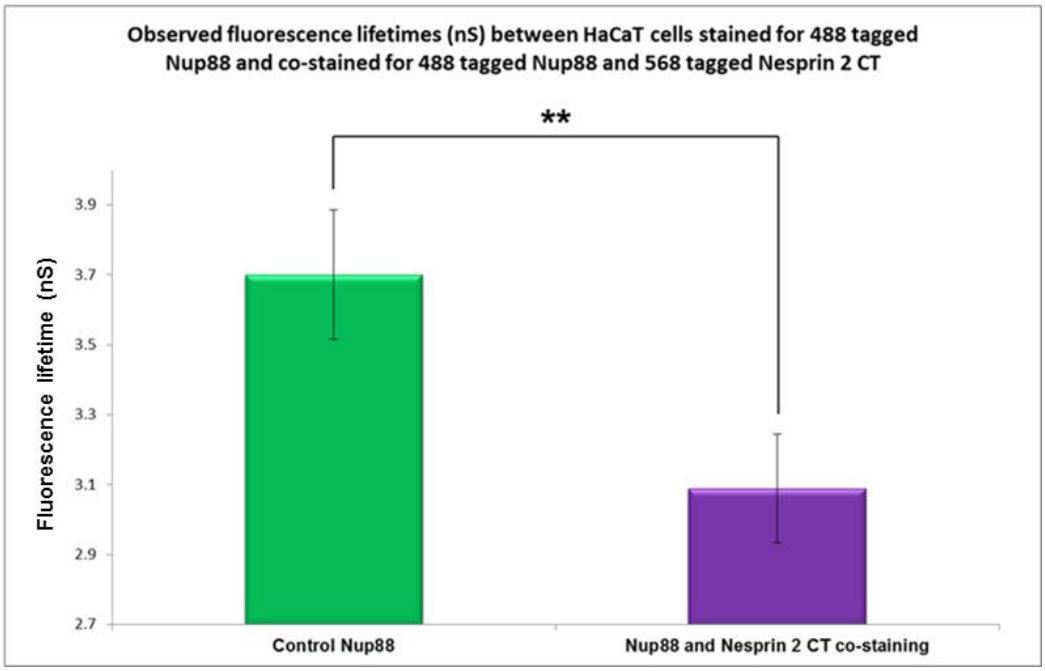

Figure 6.7: *(A) Screenshot displaying analysis output of HaCaT nuclei stained for Nup88 and nesprin-2 C-terminal regions. (B) Displays collated life time data from across 50 cells within each condition.*

Data presented in *Figure 6.7 suggests* a significant difference exists in fluorescence lifetimes between Nup88 tagged fluorophores across single and co-staining conditions using a student's t-test where $p \leq 0.005$. Data presented in (B) suggests a fluorescence lifetime difference of 0.6 nS between single Nup88 staining and co-staining between Nup88 and nesprin-2 CT regions. This suggests the Nup88 tagged donor fluorophore can

be found in close proximity to the nesprin-2 CT bound acceptor fluorophore, leading to a transfer of energy between the two. This helps to provide further suggestions as to potential co-localisation of Nup88 and nesprin-2 C-terminal regions across the NE.

To increase understanding of associations between Nup88 and nesprin-2 C-terminal regions, transfections using myc-N2-SR (a construct containing the last 4 C-terminal spectrin repeats of nesprin-2 (*Figure 6.2*) were conducted in HaCaT cells. This SR construct was that used in the initial yeast two-hybrid screen suggesting a Nup88 interaction. Overexpression of this construct in HaCaT cells would therefore lead to an increased level of observed co-localisation between Nup88 and the myc-tagged SR. Transfected cells were fixed and stained against Nup88 and the myc-tag to assess co-localisation between inserted SR fragments and Nup88. Resulting images can be seen displayed within *Figure 6.8*.

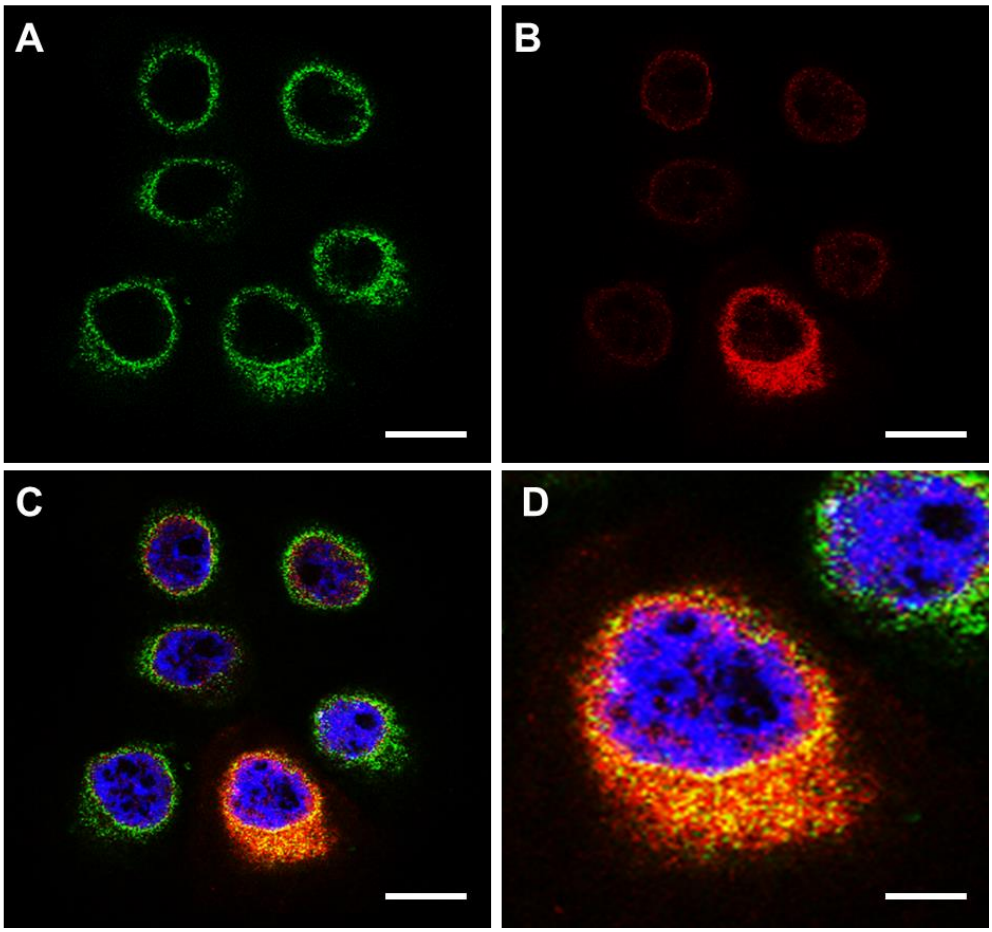

Figure 6.8: *Immunofluorescence staining against Nup88 (A), myc-SR (B) and merge (C). (D) Presents higher mag of the observed co-localisation in HaCaT cells. Scale bars = 10 µm in (A-C) and 4 µm in (D).*

Data presented in *Figure 6.8* suggests further co-localisation exists between the myc-tagged SR and Nup88. The incorporated SR appears to localise to the NE and ER regions

of the cell, in which the highest degree of co-localisation can be observed with Nup88. This therefore presents further supporting evidence that Nup88 and nesprin 2 C-terminal regions do appear to display close association *in vitro*.

6.3.2.2 Nesprin-2 N- and C-terminal regions display distinct staining across the nuclear envelope.

Observations thus far, suggest evidence for co-localisation between Nup88 and the nesprin-2 C-terminus, but not N-terminal regions across the NE. This suggests that both the N and C-terminal regions of nesprin-2 could potentially occupy distinct regions across the NE. To investigate this further, the use of super resolution microscopy was applied to discern whether distinct staining between both N- and C-terminal regions of nesprin-2 could be observed. HaCaT cells were fixed, stained and imaged as described within the methods section, with images displayed in *Figure 6.9*.

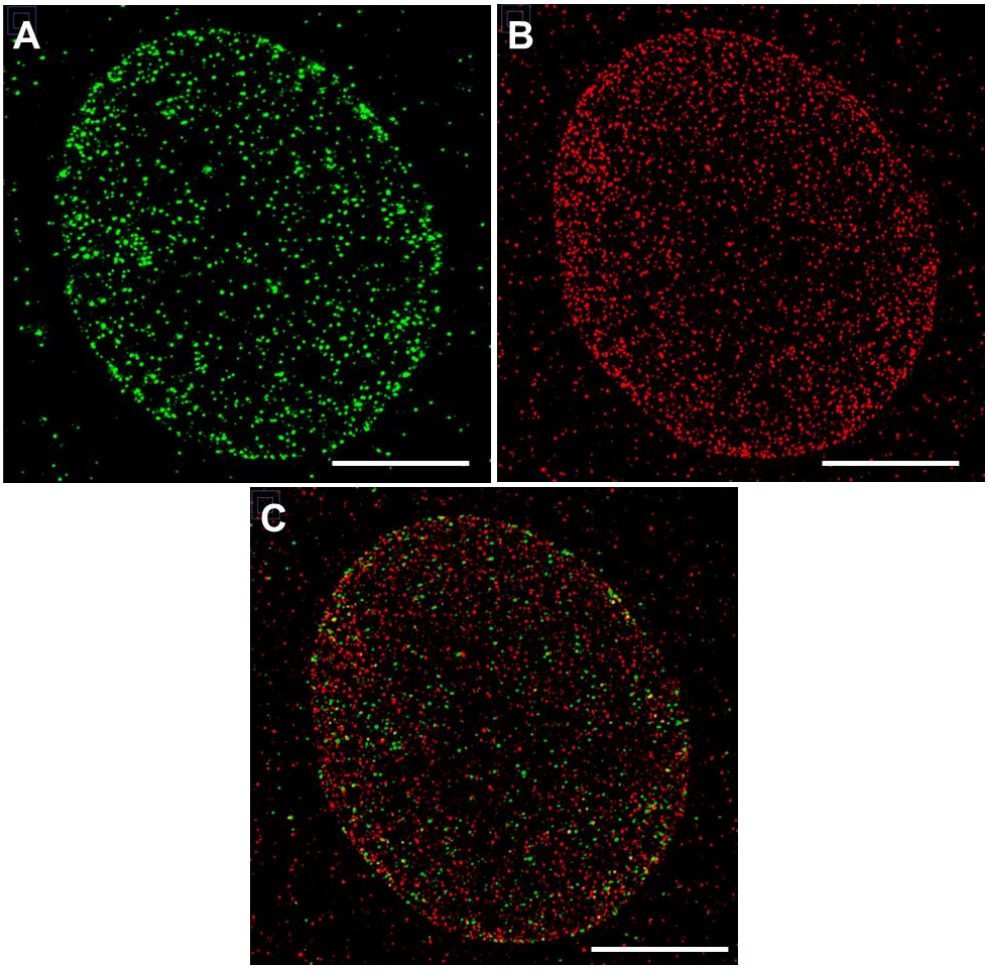

Figure 6.9: *(A+B) Immunofluorescence staining of Nesprin-2 C-terminus (Green) and Nesprin-2 N-terminus (Red) in HaCaT cells. (C) Displays merged images. Scale bars = 5 µm.*

Data presented in *Figure 6.9* suggest a nesprin-2-N- and C-terminal regions occupy distinct regions across the NE, due to clear distinctions able to be made between red and green fluorophores. It can be seen that infrequent co-localisation is observed, more frequently seen across peripheral nuclear regions. This data therefore provides further support to *Figures 6.5* and 6.*7*, suggesting that the N- and C-terminal domains of nesprin-2 occupy distinct NE regions.

Due to these observations using indirect immunofluorescence techniques, the validity as to protein localisation cannot be 100% conclusive. This is due to the fact that the binding distance between fluorophore and targeted protein is separated by a further primary antibody, which results in an indirect protein label at both low and high magnifications. To overcome this, further investigations using biochemical techniques such as GST-pulldowns and immuno-precipitations may be performed to assess protein interacting potential.

6.3.3 The N2-SR fragment displays binding to Nup88 in GST-pulldown assays.

Following investigations aimed to assess whether Nup88 and nesprin-2 C-terminal observed co-localisation correlated with physical binding potential. To assess this, GST-pulldown techniques were used. Constructs containing the last four C-terminal spectrin repeats of nesprin-2 C-terminal (termed N2-SR) were attached to GST beads, then incubated with COS7 cell lysates ectopically overexpressing pEGFP-Nup88 as described within the methods section. The resulting western blot staining against Nup88, GFP and GST can be seen displayed within *Figure 6.10*.

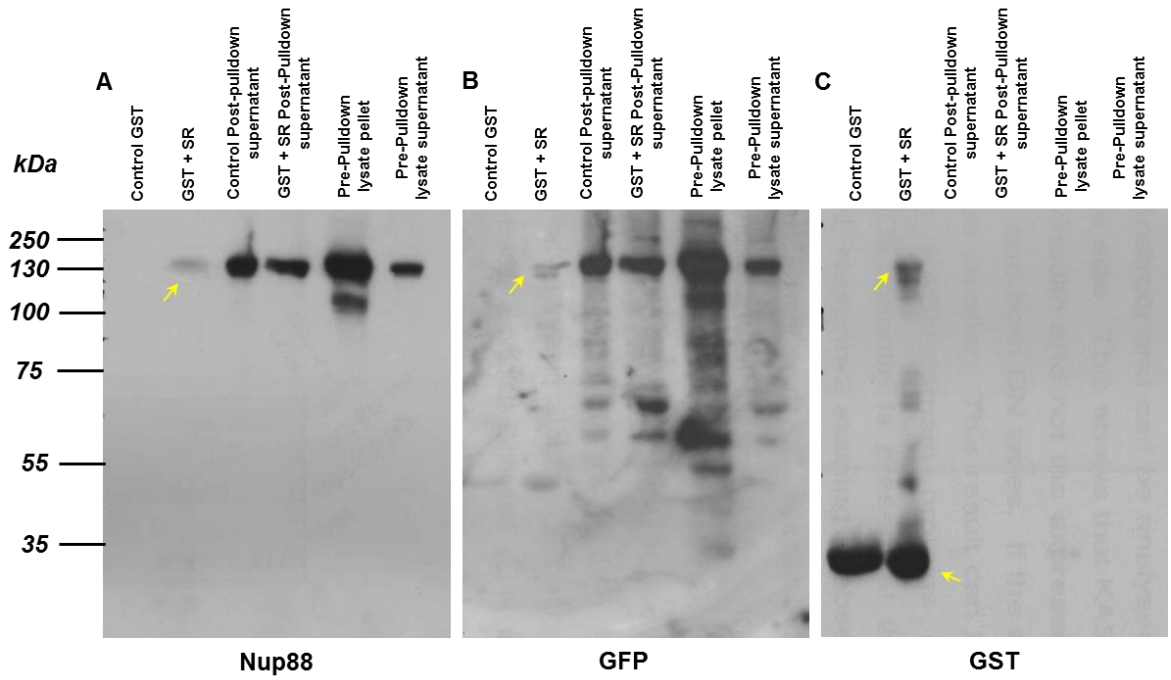

Figure 6.10: *Western blot staining against Nup88 (A), GFP (B) and GST (C) for the GST Pulldown. Arrows represent the expected ~135 kDa GST-SR bound Nup88 band in (A-B). In (C) arrows represent both GST-SR bound Nup88 and the GST bead. In this image, degradation can also be seen of the GST-SR fusion.*

Data presented in *Figure 6.10* helps suggest that a physical connection may exist between the N2-SR fragments and pEGFP-Nup88. The pre-pulldown pellet and supernatant lanes were extracted upon cell lysate production to ensure that the cells were expressing the transfected pEGFP-Nup88, whereas the following control and GST-SR post-pulldown lanes represent the cellular supernatant after incubation with GST and GST-SR beads, respectively. The final two lanes represent the isolated control GST beads and GST tagged SR beads post incubation with the COS7 + pEGFP lysate. Nup88 western blot stain suggests a pEGFP-Nup88 band can be detected at ~ 130 kDa, which correlates to the size of the Nup88 protein with pEGFP attached. Due to the absence of pEGFP-Nup88 in the control GST lane, it is suggested that the GST pulldown has specifically pulled down pEGFP-Nup88. Of further interest is the lack of endogenous Nup88 expression detected in COS7 cells. This could potentially arise from COS7 cells expressing low levels of the protein, alongside further potential of the Nup88 antibody applied not detecting non-human Nup88. To validate this, further staining against GFP and GST were conducted. Further staining can be seen for both GFP and GST correlating to the observed band displayed through Nup88 staining. Interestingly however, the GST stain displays fragmented staining within the GST-SR lane, suggesting that the construct may have begun to degrade.

This data, therefore suggests that the N2-SR fragment used in initial yeast two-hybrid screening displays potential binding potential with Nup88. However, the results from this experiment will require further validation, as these data do not control for potential intermediary proteins situated between the Nup88 and GST-SR or whether binding is mediated by the attached pEGFP, although the yeast two-hybrids suggests a direct binding. Further to this, follow on investigation will be needed to validate whether the fragments displayed upon GST staining are indeed degradation products or further binding interactions between the N2-SR fragment and alternate cellular components. A further follow on experiment could be to further narrow down the binding regions, therefore gaining further insight into which of the final 4 C-terminal SRs are responsible for this interacting potential, alongside repeating the pulldowns with fragmented Nup88 regions.

6.3.4 A potential functional relationship exists between Nup88 and nesprin-2 in vitro.

6.3.4.1 Incorporation of pEGFP-Nup88 into HaCaT cells stimulates nuclear abnormalities.

Investigations thus far have suggested Nup88 and nesprin-2 display co-localisation across the NE and potential physical interactions. However, further investigations aim to assess whether functional relationships existed between these two proteins. It is suggested that Nup88 levels are found up-regulated across a variety of metastatic cancers, alongside a high frequency of mutations in nesprins. To replicate these conditions, a series of transient transfections were performed in HaCaT cells, to establish whether increased/decreased levels of either Nup88 or nesprin-2 stimulated alterations in protein organisation or expression levels of the other. Transfections in HaCaT cells were performed as described in the methods for control pEGFP, pEGFP-Nup88, Nup88 siRNA, nesprin-2 RNAi and myc-tagged nesprin-2 SR, with resulting images of each transfection displayed in *Figure 6.11*.

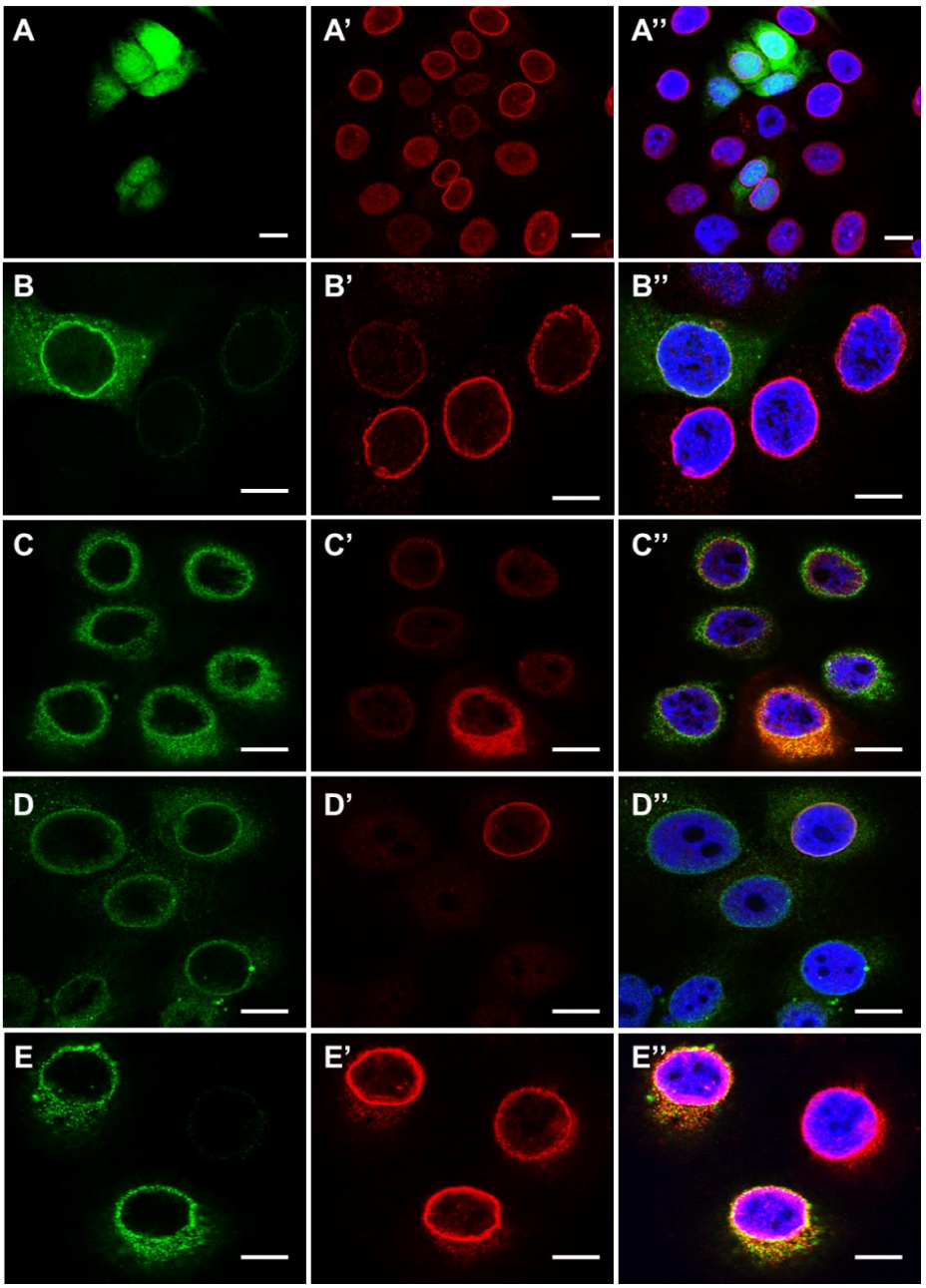

Figure 6.11: *Immunofluorescence staining displaying for control pEGFP (A), pEGFP Nup88 (B), myc-SR (C), nesprin-2 RNAi (D) and Nup88 siRNA (E). For each transfection, green staining (other than in panels A and B where green displays GFP) represents Nup88 and red staining represents nesprin 2. Scale bars = 10 µm.*

Data in *Figure 6.11* suggests the transfections performed were successful for each plasmid assessed. Incorporation of each plasmid appeared to stimulate no abnormal cell phenotypes other than within the overexpression of pEGFP-Nup88. It was found that the insertion of this plasmid into HaCaT cells stimulated the development of nuclear defects, including nuclear blebbing, enlarged nuclei and the formation of multi-nucleated cells. To

quantify these observations, 400 cells were closely observed for these abnormalities, with collated data displayed in *Figure 6.12*.

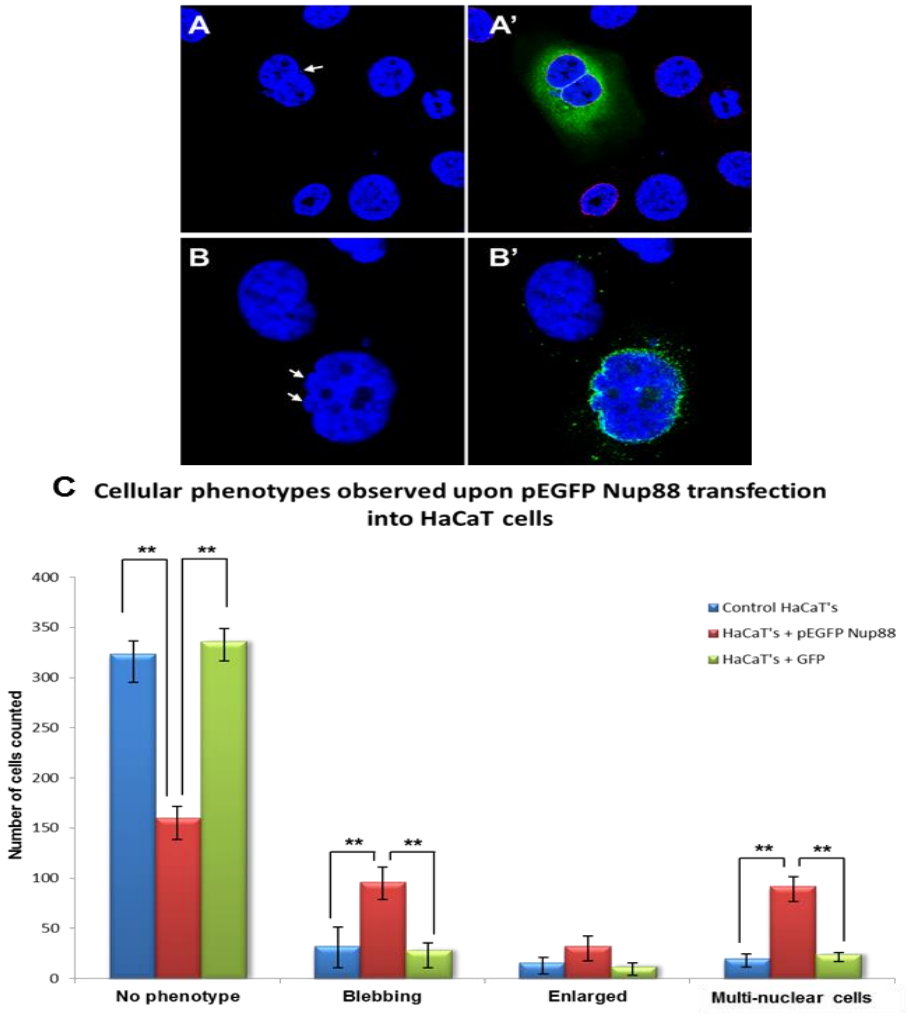

Figure 6.12: *(A) and (B) highlight example nuclear deformities observed upon pEGFP Nup88 insertion, including nuclear blebbing and multi-nucleation. (C) Displays collated data of phenotypes observed in HaCaT cells 3 days post transfection with pEGFP Nup88.*

The data presented in *Figure 6.12* suggests the introduction of pEGFP-Nup88 stimulates an increase in nuclear abnormalities detected. It is shown that observed levels of nuclear blebbing and multi-nucleated cells is significantly increased upon pEGFP-Nup88 transfection calculated using a student's t-test where $p \leq 0.005$. These observations therefore suggest that the introduction of pEGFP-Nup88 may disturb normal cellular architecture.

Following successful transfections of each construct into HaCaT cells, protein analysis was conducted through the application of western blotting techniques to assess whether the introduction of each construct stimulates a change in expression levels for Nup88 or

Nesprin-2 respectively. Lysate production and subsequent western blot analysis was conducted as described in the methods. Each sample was then stained against proteins of interest as displayed in *Figure 6.13*.

Data presented in *Figure 6.13* displays the effects of altering expression levels of either Nup88 or nesprin-2 on expression levels of specified proteins of interest. Initially, it is shown that insertion of control pEGFP displays no significant alterations in Nup88 or nesprin-2 expression. Interestingly however, it is further shown that incorporation of pEGFP-Nup88 appears to stimulate a decrease in nesprin-2G isoform expression levels. To verify this observation was a result of pEGFP-Nup88 insertion, we further stained the blot for Nup88, highlighting two distinct bands. The lower band correlates to endogenous Nup88, whereas the higher band found at ~130 kDa correlates to the expected size of pEGFP tagged Nup88, therefore suggesting the observed decrease in nesprin-2G expression may be a result of the over expressed Nup88 levels.

Alongside this, closer analysis of both Nup88 and nesprin-2 knockdown lysates suggests that no significant differences can be observed across the range of proteins analysed, other that in Nup88 and nesprin-2 respectively. However, it is seen that upon nesprin-2 RNAi introduction, lower nesprin isoforms are retained. In contrast the GIANT isoform of nesprin 2 (~800) can be seen to display reduced expression levels, suggesting that the knockdown produced was only for the GIANT isoform.

The introduction of myc-SR into the HaCaT cells appears to again stimulate no significant changes in Nup88 or nesprin-2 expression patterns across the cells. However, the success of transfection can be validated through the analysis of lower CT nesprin isoforms, in which the SR fragment can be clearly identified through the pAbK1 antibody which targets the last two SRs across the C-terminal of nesprin-2, preceding the KASH domain.

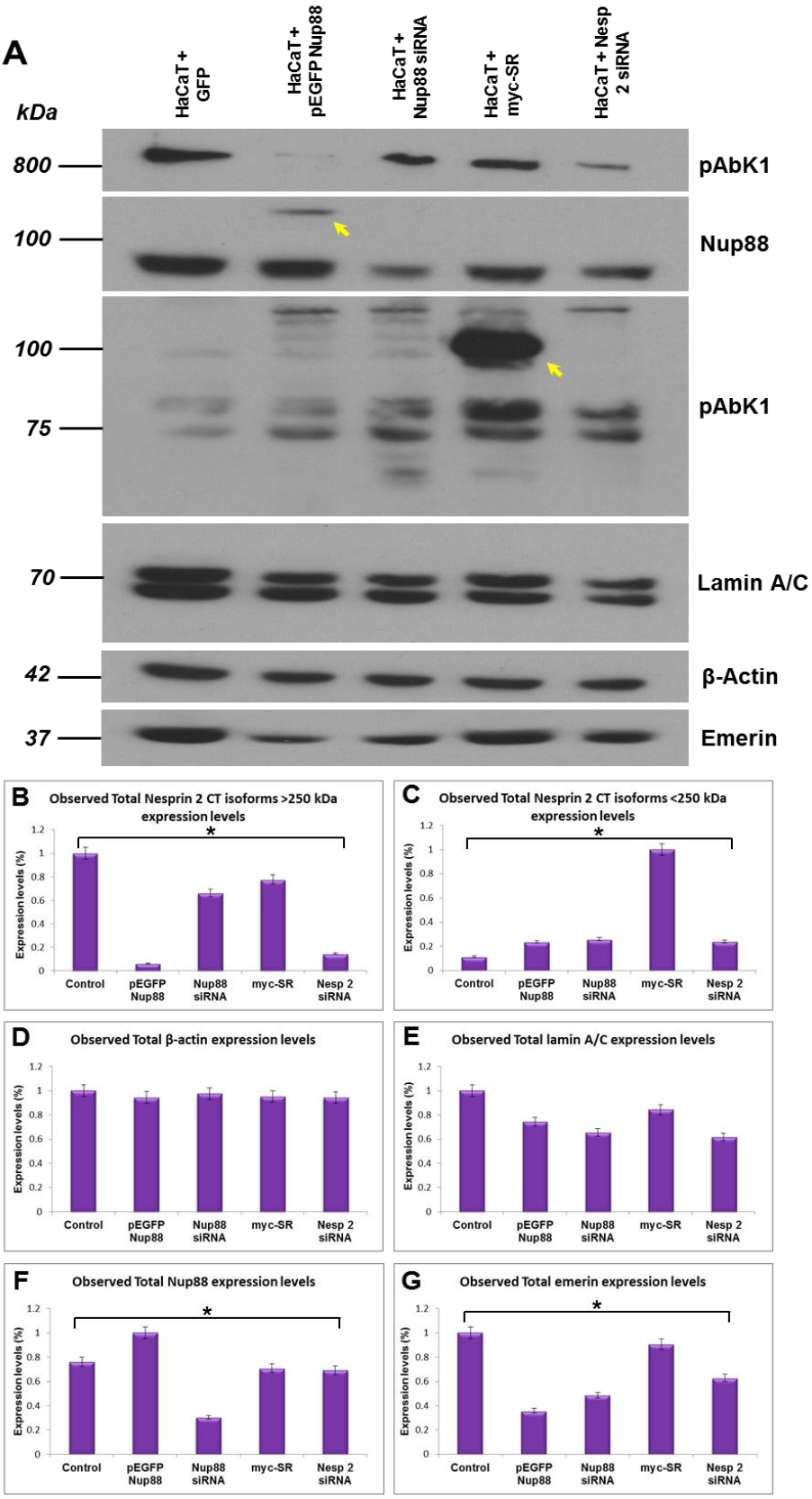

Figure 6.13: *Western blot analysis of HaCaT transfections. (A) Displays western blot staining observed. (B), (C), (D), (E), (F) an (G) display collated densitometry analysis across three repeats for each protein. Arrows represent pEGFP-Nup88 (Nup88 stain) and myc-SR (in pAbK1 stain).*

The data generated through this investigation suggests that of all transfections performed, the introduction of pEGFP Nup88 was the only condition to produce both nuclear architecture and protein expression defects in the HaCaT cells. However, due to the over expressed Nup88 construct containing a pEGFP tag, we cannot fully rule out the possibility that the attached GFP tag is stimulating these observations. This is especially crucial for Nup88 which displays both nuclear and cytoplasmic localisation, suggesting that an increase in size could restrict inserted Nup88 function in the cell, or in turn, disrupt the normal functioning of endogenous Nup88. Therefore to further validate these findings, we would aim to employ the use of smaller tags to Nup88 like myc or HA. With these smaller tags, we would be able to assess whether the resulting phenotypes observed were indeed a result of plasmid expression, or of disruptions arising from the size of the pEGFP tag.

6.3.5 Nup88 displays unique characteristics for nuclear pore proteins.

6.3.5.1 Nup88 displays co-localising potential with KLC1 in the cytoplasm.

Thus far it has been shown that Nup88 and nesprin-2 display co-localisation across the NE, alongside potential functional relationship in which nup88 levels may determine expression levels of nesprin-2G. However, through these investigations, it was also observed that Nup88 displays a high degree of cytoplasmic staining across all cell lines assessed. As Nup88 is classified as a NPC protein, its localisation is often associated across the NE, however, further experiments aimed to investigate whether Nup88 specifically co-localises with select cytoplasmic proteins, in order to gain a greater understanding of its potential roles within the cell.

Immunofluorescence techniques were used to assess whether Nup88 displayed cytoplasmic co-localisation with components of the ER, KLC1, actin or tubulin protein networks. Cells were grown, fixed and stained as described in the methods for each component, as displayed in *Figure 6.14*.

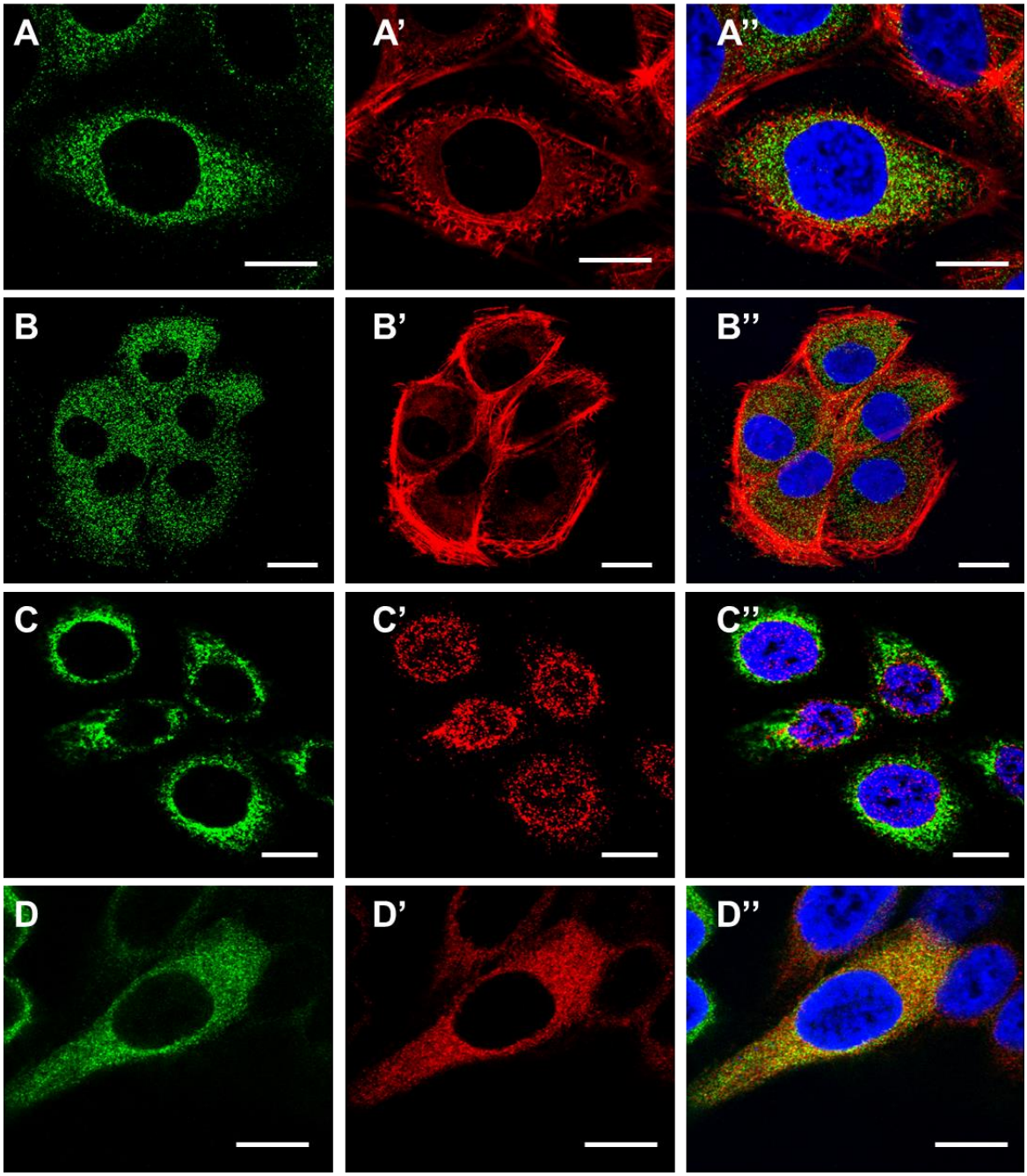

Figure 6.14: *Immunofluorescence staining of Nup88 (A, B, C' and D'), β-tubulin (A'), β-actin (B'), ER (C) and KLC1 (D) in HaCaT cells. Scale bars = 10 µm.*

As shown in *Figure 6.14,* Nup88 displays co-localisation with KLC1 in cytoplasmic regions of the HaCaT cells, whereas no further co-staining could be seen for other co-staining conditions. Cytoskeletal staining presented in (A) and (B) displays Nup88 cytoplasmic accumulation is situated within central and nuclear regions. The actin stain displays regions of the cell periphery, helping to show that Nup88 in these regions are expressed at low levels. It is further shown that no co-localisation is observed between

Nup88 and the ER other than directly across the NE (C). The use of immunofluorescence staining alone however, only provides an indication as to potential co-localisation; further investigations would be required to validate this finding, using biochemical analysis such as immuno-precipitation and more advance fluorescence analysis such as FRET-FLIM.

6.4 Summary of Experimental Findings.

Work in this chapter has sought to investigate whether co-localisation and physical interactions exist between nesprin-2 and Nup88 as suggested through unpublished yeast two-hybrid data presented by Schneider *et al.* [77]. Further aims include establishing whether *in vitro* manipulation of both Nup88 and nesprin-2 invokes a functional alteration in either protein, to investigate potential implications in the development of cancerous phenotypes.

6.4.1 C-terminal regions of nesprin-2 display close association to Nup88 in HaCaT cells through indirect immunofluorescence.

Initial investigations helped to characterise both Nup88 and nesprin-2 C-terminal distributions across a range of cell lines. It was shown that in the SW480 and SW620 colorectal cancer cell lines (low- and high-grade adenocarcinomas, respectively), no variation was observed through immunofluorescence staining for Nup88. In contrast, nesprin-2 C-terminal staining displayed specific localisation across the NE in both cell lines assessed, with the high-grade SW620 cells displaying more punctate staining, showing regions of no staining across the NE. These results appear to both support and contradict current literature views. Contradiction comes from evidence suggesting Nup88 levels are observed to increase during the progression of many cancer forms [200]. Our data does not support this view due to SW620 cells displaying similar localisation and expression for Nup88 to the low-grade SW480 cells. This finding could suggest that continuous culture in 2D environments may have altered levels of Nup88 expression in comparison to their original tissue source (As much literature data comes from primary biopsy analysis). Support for nesprin-2 staining, however, comes from evidence in the literature suggesting that nesprin-2 genes (alongside further nesprin genes) display mutations which correlate to cancer severity [316, 472].

Further characterisation of both Nup88 and nesprin-2 levels were performed in HaCaT cells, displaying that both Nup88 localised to both NE and cytoplasmic cell regions alongside nesprin-2 C-terminal staining localising specifically to the NE. From these observations, the HaCaT cell line was selected as a model for our further work to test the co-localisation potential between Nup88 and nesprin-2 *in vitro* as these cells appear to be used as a model in numerous *LINC* associated research areas [233, 473, 41].

The LEICA LAS AF image analysis software was employed to observe fluorophore intensity peaks, with aims to investigate whether these peaks correlated between nesprin C-terminal regions and Nup88 (*Figure 6.5* and *6.6*). It was observed that direct overlap of emission peaks could be seen between nesprin-2 C-terminal vs Nup88 and Nup88 vs Nup214 co-staining conditions, whereas no direct co-localisation could be observed between N-terminal nesprin-2 regions and Nup88. Further quantification displayed that across 50 cells analysed in each co-stain, the highest percentage of co-localisation occurred between nesprin-2 C-terminal regions and Nup88, Nesprin-2 C-terminal regions and NPCs, as well as Nup88 and Nup214. This suggests that nesprin-2 C-terminal regions appear to co-localise with Nup88, validated through the Nup88 vs Nup214 positive control also displaying a high degree of co-localisation. Nup88 and Nup214 are well characterised binding partners in mammalian cells [462, 474], suggesting the analysis method used is able to detect these close associations effectively.

To further strengthen observations suggesting C-terminal regions of nesprin 2 display close *in vitro* associations with Nup88, two further techniques were used, FRET FLIM analysis and overexpression of the suspected binding region N2-SR (*Figures 6.7 and 6.8*). Through FRET FLIM assessment, it was shown that when co-stained against Nup88 and nesprin-2, with Nup88 containing the donor fluorophore, a significant fluorescence life time reduction of this donor fluorophore was observed, suggesting that these two proteins are found in close association within the HaCaT cells. Alongside this, transfection of myc-tagged N2-SR into the HaCaTs displayed further co-localisation between Nup88 and the proposed binding region. These follow on investigations provide further supporting evidence that both Nup88 and nesprin-2 display potential interactions under *in vitro* conditions due to their close cellular associations, similar to that suggested in the initial yeast two-hybrid screen [77].

As nesprin-2 C-terminal but not N-terminal regions displayed co-localised staining across the NE with Nup88, further super resolution microscopy techniques were employed to support this (*Figure 6.9*). It is shown that staining for N- and C-terminal regions of nesprin-2 is distinct across the NE surface, with limited co-localisation observed across peripheral nuclear regions. This suggests both N- and C-terminal nesprin-2 regions may occupy distinct regions of the NE, forming a cage like meshwork surrounding the NE, similar to that suggested by Lu *et al.* [101], through which nesprin-1G and nesprin-2G were suggested to associate across the ONM through mediated interactions with nesprin-3.

6.4.2 Interacting potential is displayed between Nup88 and the last 4 SRs preceding nesprin-2s C-terminal KASH domain.

One drawback with the experimental approaches conducted thus far is the use of indirect immuno-fluorescence. The attachment of primary followed by secondary antibodies in our experimental systems leads to fluorophore emission observed away from the initial protein source. To overcome these limitations, observations of fluorescent tagged Nup88 and C-terminal nesprin-2 regions transfected into HaCaT cells could be conducted, as to remove the need of antibody analysis. Further to this, live cell imaging techniques could be used to gain further understanding of whether these co-localisations are consistent throughout all stages of the cell cycle. However, the use of biochemical techniques was selected to establish whether a protein-protein binding potential existed between the C-terminal region of nesprin-2 and Nup88 in the form of a GST-Pulldown (*Figure 6.10*).

Using the N2-SR construct described by Schneider *et al.* [77], N2-SR was attached to GST beads, followed by incubation in COS7 + pEGFP Nup88 lysates. Resulting western blot analysis displayed that these GST-SR beads displayed potential Nup88 binding through both Nup88 and GFP staining, displaying a ~130 kDa band correlating to pEGFP Nup88. A further GST stain displayed the same band, alongside potential degradation of the SR fragment presented as smears in the lane. These observed high molecular weight bands were not observed with GST alone, suggesting that these observations were a result of SR attachment. Although the detection of Nup88 in the GST-SR fragment suggests that a physical interaction may exist between Nup88 and nesprin-2 C-terminal, one further control would be needed to conclusively show this. The incorporation of pEGFP bound GST beads would help to validate whether the observed pulldown of pEGFP Nup88 is a result of SR binding to Nup88, rather than the possible binding of SR to the pEGFP tag attached to the Nup88 protein.

6.4.3 Overexpression of pEGFP-Nup88 stimulates a reduction in nesprin-2 expression.

Following establishment of potential interactions between Nup88 and the C-terminal region of nesprin-2 through GST-pulldown analysis, further investigations aimed to decipher whether functional relationships existed between the two proteins in model

HaCaT systems. Transfections producing overexpression and knockdowns of Nup88 and nesprin-2 components were performed and subsequently assessed through immunofluorescence and western blotting techniques. Post-transfection observations displayed limited cell and nuclear abnormalities across all transfections conducted, apart from the insertion of pEGFP-Nup88, in which increased levels of nuclear blebbing and multinucleated cells were observed (*Figure 6.12*).

Protein expression analysis through western blotting techniques displayed in *Figure 6.13* suggests functional variation in nesprin-2 levels upon pEGFP-Nup88 overexpression. Upon pEGFP-Nup88 overexpression, nesprin-2G expression appears to reduce, to similar levels observed within nesprin-2 siRNA lysates. No further significant variation could be identified across the range of transfections conducted, other than within emerin expression levels, displaying a reduction in protein expression upon both pEGFP-Nup88 and Nup88 siRNA insertion. Interestingly, little evidence is found in the literature highlighting potential implications as to these emerin decreases in cells overexpressing Nup88. However, as it has been suggested that Nup88 is able to bind directly to lamin A/C across the INM [478], it can be suggested that Nup88 may bind to the same site of lamin A/C as emerin [479], and therefore outcompete endogenous emerin for its lamin binding, resulting in a subsequent loss of emerin expression.

When correlated with work presented in Chapter 3, suggesting that loss of *LINC* connections across the NE mediated by nesprin, decreases nuclear stiffness. Work identified in this investigation suggests that this *LINC* disruption could stem from a loss of nesprin-2G isoforms expressing C-terminal regions as a result of Nup88 overexpression (as further supported in primary tissue work in chapter 4). Further evidence as to potential regulatory roles of Nup88 on the expression of nesprin-2 comes from data suggesting Nup88-Nup214 mediated CRM1 regulation controls nuclear export [462]. It was shown that overexpression of Nup88-Nup214 complexes were able to trap CRM1 and Rel to the cytoplasmic face of the NPC, resulting in immune response activation and the inhibition of protein export from the nucleus. As Nup88 overexpression is prevalent in many high grade cancer forms, it is possible that export of nesprin components under these conditions is unable to occur due to the loss of nuclear export, resulting in incorrect protein expression patterns. However, substantial investigation would be required to validate this due to the complexity of proteins and gene regulation abnormalities present in cancer cell development.

A further limitation to this experimental approach is the GFP tag attached to the overexpressed Nup88. This tag could potentially reduce the normal functioning of Nup88

through impairing protein migration through the NPC due to its increased size. As stated previously, high powered electron microscopy techniques could be used validate whether pEGFP-Nup88 displays abnormalities in cellular location in comparison to endogenously expressed Nup88 through immuno-gold double labelling.

Through these investigations, it has been observed that Nup88 displays both NE and cytoplasmic distributions. To further investigate this, immunofluorescence analysis was conducted to assess whether this observed cytoplasmic localisation was seen to correlate to selected cytoskeletal components (*Figure 6.14*). The data suggests that of the stains conducted; only KLC1 displayed potential co-localisation. This finding appears to support evidence in the literature, suggesting that an interacting potential exists between KLC1 and Nup214 (a Nup88 binding partner) [203], suggesting that these observed co-localisations may arise through Nup214 mediated binding. Further investigations however, would need to be conducted to validate this potential co-localisation through biochemical analysis methods including GST-pulldowns using KLC1 fragments published previously [77] alongside immunoprecipitation assays. This would therefore provide a clear indication as to whether a physical binding potential existed between Nup88 and KLC1.

Through the data presented in this chapter, it has been shown that cellular co-localisation alongside a potential binding interaction exists between Nup88 and nesprin-2, more specifically across the final 4 spectrin repeats of the C-terminal region (N2-SR). Further evidence also suggests functional relationships may exist between Nup88 and nesprin-2 *in vitro*; in which increased Nup88 levels stimulate a down regulation of nesprin-2 isoforms, similar to that found in many cases of highly metastatic cancers.

7. Summary and General Discussion

7.1 Thesis Background.

The nucleus and its contents (*e.g.* chromosomes and proteins) are continuously subject to mechanical forces from extracellular cues, often resulting in dynamic nuclear deformation and structural rearrangements. For example, during muscle contraction and relaxation in *Drosophila*, nuclei are often subject to variable cytoplasmic strain, but are able to maintain a stable nuclear morphology. It was proposed by Wang *et al*. that this nuclear stability was maintained through the elastic properties of MSP3000 (nesprin homolog) across the ONM [480]. Through interactions with MTs, MSP3000 is able to form a flexible perinuclear shield across the ONM, stabilised by Shot (spectraplakin) and EB1. This protective cage therefore enables the nuclei to withstand the continual mechanical forces subjected on the nucleus.

Alongside extracellular stimuli acting on the nucleus, further mechanical forces act from intracellular sources of both nucleoplasmic and cytoplasmic origins, arising from transcriptional events and DNA synthesis, alongside the dynamics of the cytoskeleton respectively. This knowledge spurred research to investigate the mechanical properties of the NE itself, aiming to understand how this double membrane system and its associated protein networks could not only resist mechanical forces, but also transmit these physical forces to the nuclear interior, eliciting a cellular response.

It was shown using a variety of experimental techniques; including micropipette aspiration, atomic force microscopy (AFM) and cellular strain assays, that the interphase nucleus is 2 ~ 10 times stiffer than the surrounding cytoplasm for endothelial cells and articular chondrocytes [286, 287, 481, ,482]. Further research aiming to understand which cellular features may be contributing to this observed nuclear stiffness, lead to implications of *LINC* complex regulation. In recent work, it has been documented that numerous *LINC* complex components including lamins [114, 483] and the *SUN-KASH* interactions [484, 59] are responsible for the maintenance of nuclear architecture and resulting nuclear stiffness. Compelling evidence was further highlighted by Lu *et al*., in which saturation of the KASH binding domains by a DN SUN1 construct (leading to a displacement of endogenous KASH-proteins (including nesprin-1/-2) from the NE and subsequent *LINC* complex disruption) lead to an enlargement of nuclear areas in HaCaT cells [101]. Through this, it was demonstrated that maintaining *LINC* connexions across

the PNS were required to preserve nuclear architecture. The further function of *LINC* components in regulating nuclear-cytoskeletal interactions has also been suggested to play significant roles in nuclear stiffness and mechanotransduction across many cellular systems [153, 485]. It is suggested that the complex interplay of KASH protein expression (nesprin-1/-2/-3 and -4) aside associated connections with MTs, IFs and actin cytoskeletal components, contribute to cellular resistance against mechanical stress induced by the environment.

Due to this evidence suggesting complex roles played by the *LINC* complex in regulating nuclear stiffness, further research began investigating the roles of nuclear stiffness in cellular migration in 3D environments. It is suggested that an increase in nuclear malleability may increase cell migration potential across 3D systems, for example, it is believed that neutrophil functionality is maintained through its ability to squeeze through space-restrictive gaps between tissue systems. On close inspection, Rowat *et al*. [202] were able to highlight that this highly mobile cells was influenced heavily by its high nuclear malleability. It was shown that in genetically modified HL-60 cells, a defined increase in lamin A composition resulted in an incremented increase in nuclear stiffness, correlating to a decrease in the cells ability to migrate through micron-scale restrictions. With research now suggesting that HL-60 cells express low levels of further *LINC* complex components including nesprin-2G, nesprin-1G, SUN1, plectin and vimentin [486], aside similar phenotypes highlighted across cell lines displaying increased migration potential through restrictive environments [272, 267], it is now suggested that nuclear deformability may constitute as a rate limiting step during cell migration in 3D environments.

Due to observations thus far suggesting strong evidence for roles of the *LINC* complex in maintaining nuclear stiffness, alongside further evidence suggesting nuclear malleability as a rate limiting step in 3D migration, current investigations are beginning to link these two research areas in an effort to increase our understanding of cancer metastasis. Of high significance in this field is current evidence presented by Matsumoto *et al*. [203], suggesting that breast cancer tissues express a significant reduction in expression levels of *LINC* complex proteins, including SUN1/2, lamin A/C and nesprin-2. This evidence, coupled with that's described thus far provides strong support for the potential roles that *LINC* complex components could play in the development of metastatic behaviours across a range of cancers.

7.2 Summary of Experimental Findings.

7.2.1 LINC complex disruptions elicit phenotypic changes in cell/nuclear shape alongside 2D and 3D migration potential.

7.2.1.1 Severing the SUN-KASH perinuclear interaction elicits increased nuclear height, decreased cell-substratum attachment and decreased 2D migration potential.

In Chapter 3, the effects of *LINC* complex disruptions through DN SUN1 interference in HaCaT cells were characterised in both 2D and 3D culture systems, leading to numerous significant findings. Firstly, the incorporation of DN SUN1 and subsequent *LINC* disruptions elicited an increase in cell-packing density (*Figure 3.5*) alongside an increase in nuclear height (*Figure 3.9*). From this data, it was shown that the DN HaCaT cells displayed a two-fold increase in both cell numbers per 100 μm^2 and observed nuclear height. These findings, though novel due to the DN system applied, appear to support findings by Anno *et al*. [139], suggesting that upon nesprin-1 silencing in HUVEC cells, nuclear heights were shown to increase. When linked more closely with further investigations displaying roles of nesprin-2 localised TAN lines across nuclear surface in maintaining mechanotransduction across the NE [93], our findings suggest that loss of *LINC* connections across this nuclear surface may result in dysfunctional cytoskeletal interactions arising from nesprin-mediated binding. This disruption to the normal *LINC* connections may therefore result in a reduction in mechanical force exerted across the nuclear surface by cytoskeletal components, leading to intranuclear forces increasing nuclear height as a result of this decreased resistance.

Further alterations in cell – substratum attachment speeds and actin organisation were also observed within early time points post trypsinisation (*Figures 3.12, 3.13*), however, the actin organisation between DN and WT HaCaT cells was found to display no discernible difference post after 48 hours post trypsinisation. Observations from this investigation could therefore have arisen due to DN HaCaT cells requiring more time to re-organise cellular networks due to a potential loss of mechano-transduction across the NE, as vinculin function is known to correlate with actin organisation [280]. Further support for our findings also comes from evidence suggesting mutations in C-terminal KASH domains of both nesprin-1 and nesprin-2, present in Emery-Dreifuss muscular dystrophy (EDMD), have been shown to lead to reduced cell-substratum attachment rates [176].

This therefore suggests potential roles for this maintained *SUN-KASH* interaction in cell-substratum attachment, meaning that our DN mutant cells display some similarities to phenotypes presented in EDMD.

It was also shown that in conventional 2D scratch wound assays, the WT HaCaT cells were able to close the wound significantly faster than that's of the DN HaCaT cells (*Figure 3.16 and 3.17)* Data obtained from this investigation supports views in the current literature, suggesting mutations or knockdowns in nesprin proteins displays a reduced 2D migration speed to close a defined wound [140, 176]. Therefore, to further interpret our results, the application of live cell imaging and single cell tracking techniques could be incorporated. This will help to validate whether the DN HaCaT cells indeed migrate at a slower rate to the WT HaCaT cells, or whether their *LINC* disruptions impair their ability to migrate into the wound, leading to migration along the length or away from the site of wounding.

7.2.1.2 DN HaCaT cells display increased nuclear malleability which may infer a migration advantage in space restrictive Strata® Scaffolds.

Through the incorporation of DN HaCaT cells into two 3D scaffold systems displaying space-restrictive and non-restrictive environments, it was further observed that the DN HaCaT cells displayed a migration advantage over WT cells in the space-restrictive scaffolds (*Figure 3.24 and 3.25*). In contrast to this, DN HaCaT cells displayed a reduced migration potential compared to WT cells in the non-restrictive scaffolds (*Figure 3.21 and 3.22*). When coupled with evidence in the literature suggesting that nuclear deformability constitutes a rate limiting step in migration through 3D environments [272], it can be suggested that the *LINC* disruptions present in DN HaCaT cells may further decrease the integrity of the NE. This suggestion is further supported by current hypothesis that *LINC* components may form an 'outer nuclear cage' through close associations between nesprin-1G, nesprin-2G and nesprin-3, similar to that of the nuclear lamina [101]. It is therefore possible that severing the *SUN-KASH* link may perturb this ONM structure, resulting in a decrease in nuclear 'stiffness'. This would therefore provide an increased ability of DN HaCaT cells to squeeze through environments in which nuclear deformability would be required.

To increase our understanding as to why DN HaCaT cells displayed a migration advantage through space-restrictive 3D environments, AFM analysis was applied to assess the nuclear stiffness of WT and DN HaCaT cells. It was shown that DN HaCaT cells were significantly softer in comparison the WT cells, displaying nuclear young's

moduli of 2.86 kPa and 4.97 kPa respectively (*Figure 3.52*). As there is no direct evidence suggesting *SUN-KASH* interactions infer NE stiffness, our data can be supported through evidence suggesting that *LINC* components are regulators of nuclear architecture [101, 111]. We theorise that this loss of correct *LINC* function across the NE may lead to an increased malleability of the nucleus. Support for these propositions comes from investigations into cancer development, suggesting that in many high grade cancers, nuclear deformities including blebs and enlarged nuclei are prevalent. These abnormalities in nuclear structure suggest the *LINC* complex may be compromised. Further support for this theory comes from the assessment of cancerous breast tissue, suggested a significant down regulation of SUN1, SUN2, lamin A/C and nesprin-2 expressions [203]. This hints at the possibility that one potential mechanism through which cancer cells may develop metastatic tendencies, could be through the loss of *LINC* components, subsequently increasing nuclear deformability. In addition to this, it was also found that the nuclei within both WT and DN HaCaT cells displayed a lower Young's modulus value than the surrounding cytoplasm. This appears to contradict current views suggesting that the nucleus is the stiffest organelle [284, 285, 286, 287, 288]. However, the discrepancy observed could be due to the model cell line used in this investigation. The human keratinocyte HaCaT cell line has a large amount of keratin in its cytoplasm [289], which in turn could be a contributing factor to the increase cytoplasmic stiffness observed. This observation could further arise from the outer cytoplasmic regions assessed being much thinner than that of the central nuclear region. This could mean that the coverslip beneath the cell may have had more of an impact on the force measurements across these thinner cell regions due to there being less distance between the surface and basal regions of the cell.

7.2.1.3 DN HaCaT cells display decreased stress signalling during growth in space restrictive growth environments aside increased cell stacking potential across the scaffolds surface.

Further investigations into known stress signalling marker expression levels were also conducted, in which increased phosphorylation levels of both P38 and JNK were found within the WT HaCaT cells grown within space-restrictive 3D scaffolds, but not found within the non-restrictive scaffolds or DN HaCaT cells (*Figure 3.64*). Limited literature is available to suggest that the *LINC* complex disruptions present within DN HaCaT cells could induce stress resistance properties, however, there is supporting evidence that

SUN-KASH disruption could result in a loss of mechano-transduction, and therefore, appropriate cellular responses to environmental cues [10, 281]. This therefore leads to suggestions that the *LINC* disruptions present in DN HaCaT cells may be the contributing factor for this observed colonisation of central scaffold regions, due to a loss of mechanotransduction, which in turn, impairs detection of the surrounding stress.

It was also evident that upon incorporation into the space-restrictive scaffolds, the DN HaCaT cells displayed an increased occurrence of cell stacking events across the surface of the scaffolds (*Figure 3.28, 3.29 and 3.30*). The role of nesprins in skin development and keratinocyte differentiation is not well understood, however, in muscle development, it has been shown that nesprins switch isoforms, replacing the larger nesprin isoforms with shorter isoforms across the nuclear envelope at specific stages [282]. The DN HaCaT cells display a disruption in endogenous *SUN-KASH* interactions. However, due to nesprin proteins displaying numerous isoforms, some of which do not express the KASH domain, this dominant negative interference approach may not disrupt the normal functioning of these isoforms, and may, in fact, increase their activity through redundancy mechanisms. As the functional roles of many KASH-less isoforms is not currently known, this theorised increase in activity may contribute the stimulation of early keratinocyte differentiation within the DN HaCaT cell lines.

Alternatively, this observed increase in cell stacking across the surface of the scaffold may also result from the increased levels of E-cadherin and increased cell density characterised in 2D. When coupled with potential mechanotransduction loss (suggested upon *LINC* complex disruptions [102]) and increased cell-cell adhesion, the DN HaCaT cells may display an impaired contact inhibition, leading to the proliferation of daughter cells into the only cell-free space available, yielding to an upwards trajectory. This however would need further validation through the assessment of contact inhibition signalling events, to investigate whether DN HaCaT cells do indeed display abnormal cell signalling when in close proximity to other cells.

Final findings indicated that significant protein expression differences could be seen between WT and DN HaCaT cells in lower N-terminal retaining isoforms of nesprin-1 (specifically across the 90 kDa band) (*Figure 3.61*). This loss of the 90 kDa N-terminal isoform expression in DN HaCaT cells remained consistent across both 2D and space-restrictive 3D environments. As it is well documented that multiple KASH and ABD retaining nesprin isoforms exist, able to infer tissue specific expression patterns and potential unique roles to cells [487, 80, 488], it could be suggested that the loss of lower N-terminal containing nesprin-2 isoforms may disrupt the organisation of the larger

nesprin-2G isoform across the ONM. This may result from a role of these lower isoforms functioning to retain the structural integrity of the *LINC* complex across the NE through aiding nesprin to nesprin interactions as suggested for an alternate role of nesprin-3 in the formation of an ONM nesprin cage [101].

7.2.2 The incorporation of LINC disruptions into human keratinocyte cell lines increased penetration and differentiation potential when co-cultured in fibroblast-seeded scaffolds.

7.2.2.1 DN HaCaT cells retain their increased penetration rates through space restrictive scaffold environments upon the introduction of co-cultured HDF cells.

In Chapter 4, the biological relevance of the migration models used thus far in chapters 3 and 4 was increased by the inclusion of a pre-seeded fibroblast layer before keratinocyte seeding; with aims to greater reflect the *in vivo* skin environment. The data presented suggests that 1) the DN HaCaT cells retained their increased penetration potential over WT cells in both space-restrictive and non-restrictive co-cultures (*Figures 4.4, 4.5, 4.7 and 4.8*), and 2) fibroblast incorporation into the scaffolds leads to an increase in cell stacking and differentiation across the surface of space-restrictive co-culture systems (*Figure 4.12 – 4.17*). Aside this, it is also observed that the DN HaCaT cells retain their uniform penetration phenotypes through both space – restrictive and non – restrictive scaffolds as previously observed in Chapter 3. Through both Vimentin and K14 staining across the co-culture conditions, it can be seen that the fibroblast cells appear to collect across the leading edge of keratinocytes within the scaffolds (*Figure 4.6*). These observations suggest that the keratinocytes may be pushing the fibroblast cells through the scaffold due to the limited space available to migrate within the system.

These observations do not directly correlate to current *in vitro* skin equivalent models as many of these systems apply fibroblasts, followed by a surface keratinocyte layer, displaying little to no migration through the basal fibroblast layer. However, this observation is supported within the cancer literature, through investigations aiming to increase understanding of the collective migration, by which cancer cells migrate as a collective sheet of cells. This collection of cells is able to develop uniform polarity, and defined front to rear asymmetry [432]. Evidence has suggested that during migration, this

mass of cells is able to stimulate an extracellular 'pushing' force on surrounding cells, forging a path for the trailing cancerous mass of cells to follow [433, 434]. Further to this, more recent investigations have highlighted that these pushing forces enabling ECM and cell remodelling comes from the formation of tube like structures in their surrounding by plastically deforming their surroundings through the use of both pushing and pulling forces [435]. This evidence could suggest that both WT and DN HaCaT cells exhibit potential phenotypes associated with cancer invasion, however, to fully verify this, live cell imaging techniques incorporating the use of light sheet technology could be employed, allowing the visualisation of both HaCaT and fibroblast cells in these 3D systems in real time. This technique would therefore provide more accurate information as to the interactions between both cell lines in this 3D co-culture environment.

The observed difference in penetration potential between WT and DN HaCaT cells upon incorporation into more *in vivo* like environments provides further support for current suggestions that nuclear stiffness may present a rate limiting step to cell migration through 3D environments [272]. As previous data in Chapter 3 suggests DN HaCaT cells exhibit increased nuclear malleability, alongside current views in the literature suggesting *LINC* components are key to the maintenance of nuclear integrity [436], it is proposed that the decreased nuclear stiffness presented by *LINC* disrupted DN mutants enables increased cell penetration through this more *in vivo* like environment.

Aside this, it can also be suggested that the reduced migration potential displayed by the WT HaCaT cells may be a result of intercellular communication between the pre-seeded fibroblast cells and the HaCaT cells. It is suggested that both paracrine and autocrine cross talk exists between keratinocytes and fibroblasts in epidermal regions of the skin [388], which in turn is able to influence keratinocyte behaviours, such as differentiation patterns and expression of interleukins [398]. This could further suggest that cross talk between the fibroblasts and keratinocytes may affect cell behaviour in these co-culture environments, leading to reduced migration potential when compared to their single culture conditions. The DN HaCaT cells may further be unable to respond to these environmental cues due to a suggested loss of mechanotransduction upon *LINC* severance [15]. This theory supports our findings as little difference in final penetration potential after the full 14 days in culture is observed between DN HaCaT cells in single and co-culture conditions.

7.2.2.2 Under Co-culture conditions, the DN HaCaT cells display increased differentiation potential compared to that of the WT HaCaT cells and single culture conditions within space restrictive Scaffolds.

Interestingly however, the increased cell stacking and differentiation observed displays similarities to further findings in the literature, suggesting that specific loss of nesprin-2 in mouse epithelium resulted in decreased proliferation and differentiation events including Ca^{2+} induced protein kinase C (PKC) activation and MAPK signalling during wound closure [251, 278]. This evidence suggests that the loss of nesprin-2 mediated *LINC* connections may negatively affect mechanotransduction events, leading to an inability of cells to respond to extracellular cues dictating cellular behaviour. The resulting loss of *LINC* connections in DN mutants may therefore stimulate a loss mechanotransduction between nuclear and peripheral cell regions through cytoskeletal linkage to the NE mediated by nesprins. When coupled to data presented in Chapter 3, suggesting increased colony cohesion for DN HaCaT cells, this could suggest that *LINC* disrupted cells no longer express contact inhibition phenotypes. In support of this theory, mounting evidence is demonstrating that in skin, the development of malignant transformations in fibroblast and keratinocyte cells is characterised by a loss of contact inhibition function [489, 490]. This therefore provides mounting speculation that *LINC* complex destabilisation is a key process in the development of highly metastatic cancers.

Upon further analysis, it can also be seen that both cell lines applied to the space – restrictive and non – restrictive scaffolds appear to display increased differentiation potential upon the incorporation of fibroblast cells to the system (*Figures 4.12. and 4.13*). It is suggested in the literature that no correlations have yet been made between the restrictive nature of 3D culturing models and differentiation potential of keratinocyte cells. However, it has been suggested that the stiffness of culturing environment is able to influence the cell-cell interactions and colony behaviour of keratinocytes [442]. It was shown that human neonatal epidermal keratinocytes (HEKn) grown on softer matrices, presented an increase in cell-cell adherence junction formation, alongside increased levels of β4 integrin expression when compared to cells grown on stiffer matrix environments. When applied to our observations, it is possible that fibroblast introduction to the restrictive scaffold may decrease the stiffness of surrounding matrix environments (as upon fibroblast inclusion, HaCaT cells are in direct contact with fibroblast cells and the ECM rather than the plastic scaffold). This decreased matrix stiffness could induce alterations in expression profiles for differentiation markers like K10 within the WT HaCaT cells. However, to fully verify this, further assessments as to protein expression would be

required using western blotting to assess whether there is indeed a change in K10 expression, similar to that observed in alternate 3D skin equivalent models [403].

7.2.2.3 Increased E-cadherin expression is observed across surface scaffold regions in DN HaCaT co-culture conditions, in comparison to the WT and non-restrictive culture conditions.

Final investigations in this chapter aimed to assess whether differences in E-Cadherin and YAP (Yes Associated Protein) expression exists across co-culture systems for both WT and DN HaCaT cells. It was observed that WT HaCaT cells appeared to display low levels of E-cadherin staining across all scaffold regions, correlated with uniform YAP staining. In contrast however, the DN HaCaT cells appeared to display an increased E-cadherin expression, alongside a further increase in YAP expression (*Figure 4.16*). This increased E-cadherin expression for DN HaCaT cells could potentially infer the observed increased migration potential displayed in *Figures 4.7* and *4.8.* These increased E-cadherin levels alongside increased migration penetration appears to correlate with phenotypes of cancer cells during metastatic invasion of surrounding tissues. Aside EMT, some cancer cells migrate as a collective body of cells, with increased E-cadherin levels observed [445]. When further combined with literature suggesting that increases in YAP expression can be associated with cancer progression [446, 447], aside a loss of contact inhibition [448], it can be suggested that the combination of both E-cadherin and YAP expression differences between WT and DN HaCaT, alongside increased nuclear malleability in DN mutant cells, may be a contributing factor allowing DN HaCaT cells to migrate through these co-culture environments.

Interestingly it is further shown that when both WT and DN HaCaT cells are placed into the more restrictive scaffold environments, E-cadherin expression appears to be localised across surface scaffold regions correlating to regions of cell stacking, with WT cells expressing a weaker signal than that of the DN HaCaT cells (*Figure 4.17*). It is further shown that YAP staining appears to remain consistent with observations in non-restrictive co-culture conditions, with DN HaCaT cells displaying increased levels to that of WT HaCaT cells. These observations appear to support current views within the literature, suggesting that increased expression of E-cadherin levels at the cell periphery is a determining factor in keratinocyte differentiation across *in vitro* systems [449]. One potential explanation for the increased peripheral E-cadherin expression in DN HaCaT cells could be due to the *LINC* roles in connecting the NE to cell periphery through

associated cytoskeletal interactions [450, 451]. *LINC* disrupted mutants may sever the direct signal transduction link between cell-cell adhesion junctions and the NE, resulting in altered regulation of adherens junction proteins like E-cadherin. However, to validate this further, complex protein analysis would be required through the application of western blotting techniques in order to assess the extent of these observed protein variations.

7.2.3 The loss of lower C-terminal retaining nesprin-1 and -2 isoforms is shown to correlate with breast cancer development.

7.2.3.1 Variations between LINC and cytoskeletal proteins are observed across the range of cancer lines, with correlations between increased cancer grade and nesprin loss evident.

In Chapter 5, the protein expression profiles and cellular localisation of *LINC* complex components was assessed across a range of breast cancer cell lines and primary tissues, highlighting two major findings. Firstly, through cell line analysis, it was observed that protein localisation of many *LINC* components was retained including lamin A/C, SUN2 and lamin B (*Figure 5.11 - 5.15*), however significant miss-localisation of C-terminal nesprin-2 staining was highlighted (*Figure 5.21 and 5.22*). As no direct evidence has yet been reported for the exact localisation of *LINC* components upon cancer progression, it can be suggested that due to known roles of nesprin-2 in the regulation of nuclear architecture through maintaining *SUN-KASH* interactions [171, 41], a disruption to expression profiles of alternate *LINC* components (such as nesprin-1/-3 or -4) may dislodge or outcompete nesprin-2 C-terminal KASH domains for SUN interactions (Similar to that displayed in our DN HaCaT mutant). This may then stimulate a displacement of C-terminal isoforms of nesprin-2 from the NE to the ER, or alternatively, a complete severance of these proteins from the NE into the cytoplasm.

Further to this it was shown that cytoskeletal organisation, specifically the actin protein network, but not protein expression levels appear to vary between the cancer grades (*Figure 5.6 and 5.7*). These observations support current views that reorganisation of the actin cytoskeleton is critical for invasive cancer behaviour [345, 346]. With more current literature suggesting the importance of ARF6 mediated Rac1 accumulation at the cell periphery, stimulating actin cytoskeletal re-organisation in the development high-grade metastatic phenotypes [347]. It can be suggested that the observed accumulation of actin

at peripheral areas of MDA-MB-231 cells could be a result of increased Rac1 activity, as Rac1 promotes actin polymerisation during lamellipodia extension, through activating the Arp2/3 activator WAVE, alongside increasing actin monomer availability through regulating cofilin (an F-actin modulator) [348]. This provides more F-actin available to aid in cell mobility.

Aside the actin cytoskeletal network, further observations suggested variability also exists in both protein expression and cellular organisation (*Figures 5.9 and 5.10*). Interestingly, observations in vimentin specifically appear to contradict views of the current literature. It is suggested that vimentin is a key marker for EMT transition, in which epithelial cells reduce expression levels of keratin IFs and increase expression levels of vimentin IFs [349]. With further evidence suggesting vimentin expression is associated with the development of mesenchymal shape development and increased motility [350], it is suggested that MDA-MB-231 cells should be high expressers of this protein. It is possible however, that due to their time in a non-restrictive 2D culture environment, and the MDA-MB-231 cells may be in a process of reverting their EMT switch in IF expression, slowly increasing expression of keratins whilst decreasing vimentin expression.

These observed organisational defects in cytokeratin components do however link closely with current literature views, suggesting that within multiple disease models, cytoskeletal organisation is reorganised, allowing alterations in cellular migration potential and function, such as within the EMT, proposed to be one hallmark displayed during metastatic cancer development [351]. Further evidence suggests that the intermediate filament and actin networks play crucial roles in maintaining cellular architecture, in which loss of functionality can stimulate cellular deformities and loss of cellular stiffness [352], a further potential hallmark of metastatic cancers.

7.2.3.2 Expression of the oncogenic marker p53 appears to increase upon cancer progression aside variable expression patterns of E-cadherin, a protein often associated with the progression of EMT.

Aside protein networks associated with the cytoskeleton, further analysis was conducted to investigate expression levels of known oncogenic markers often associated with EMT and poor patient prognosis. It was found that an increased expression of p53 was observed upon cancer progression, whereas E-cadherin displayed variable expression patterns across the cell lines assessed (*Figure 5.26*). This increased

accumulation of p53 across the increasing grades of breast cancer cell lines correlates with known literature, suggesting that the increased accumulation of p53 is linked to the loss of BRAC1 and 2 protein expression [360], which is a known marker for high metastatic breast cancers. Alongside this, lap2α upregulation has been further linked to the development of high-grade breast cancer formation [361], which again, is supported by our findings.

E-cadherin on the other hand was shown to displays a more complex picture. Loss of E-cadherin is a known marker of EMT, which is speculated as a hallmark of highly metastatic cancers, allowing penetration through surrounding tissues and to distant bodily regions. However, further evidence now suggests that loss of E-cadherin is mostly associated with the development of high-grade triple negative breast cancers [332], with further cancer phenotypes expressing equal or even more E-cadherin levels within metastatic tumour sites. Our data correlates closely with this, highlighting reduced E-cadherin expression within the triple negative breast cancer cell line, and variable expression patterns through other samples suggesting that between across low- and medium grade breast cancer lines (MCF7, T47D, HCC-38) E-cadherin expression is retained, suggesting the maintenance of normal epithelial cell-cell adherence junctions.

7.2.3.3 Known heat shock proteins displays variable expression levels across a range of cancer cell lines.

Within this chapter, we further aimed to assess whether correlations in expression patterns across known heat shock proteins and chaperones could be identified as cancer grade increases. Initially it was found that levels of CRYAB displayed increased expression levels within the two control cell lines. These obtained results appear to contradict current literature views which suggest an increased expression level of CRYAB upon metastatic cancer development [362]. However, recent evidence is beginning to suggest that even though levels of CYRAB are found within highly aggressive breast cancer forms, no direct prognosis correlation can be found between these and the metastatic potential of the cancer [363, ,364]. Alongside this, further evidence links the expression of CRYAB and VEGF regulation, in which the disruption of interactions between CRYAB and VEGF signalling through the insertion of NCL-41356 stimulated reduced tumour vascularisation [365]. This could therefore suggest that CRYAB regulation may not be a causative factor in the development of cancerous phenotypes, but rather a resulting factor, deriving from alternate changes in gene/protein expression events.

Interestingly we also found further variations in HSP27 expression levels; in which high-grade breast cancer cell lines expressed reduced expression levels, whereas low-grade breast cancers display an upregulation in comparison to their control counterparts using the monoclonal ACD5-HSP27 antibody. This again appears to contradict current views within the literature, suggesting that the up regulation of HSP27 may stimulate an increase in resistance against apoptosis [366], which is a major target for many anti-cancer drugs. This therefore suggests that observed increases in HSP27 levels upon cancer development has also been further attributed to tumour vascularisation [367].

Finally, the expression levels of GFAP across breast cancer cell lines was also assessed, displaying increased expression profiles across each cancer cell line apart from MDA-MB-231 line, which expressed a significant decreased in protein expression. Interestingly it has been demonstrated that GFAP expression may be cell specific, through which immuno-histochemical analysis has identified localised expression to a small subpopulation of myoepithelial cells in normal and cancerous breast tissue [368]. It was suggested that these GFAP levels increase within this subpopulation upon an increase in cancer severity, suggesting its potential roles as a prognostic marker of cancer aggressiveness, however, due to its localised expression, biopsies from varying tissue regions in the breast may yield conflicting results, similar to that potentially experienced in our results across the range of breast cancer cell lines.

Most strikingly however, our follow on research into further *LINC* associated protein organisation directly correlated to evidence in the literature, in which we demonstrated that C-terminal isoform expression of nesprin-2 appears to decrease in high-grade breast cancer tissue in comparison to low-grade and control tissues (*Figure 5.43 – 5.47*). This same result was observed by Matsumoto *et al.* [203], in which decrease levels of nesprin-2 was observed across high-grade breast cancer tissues. It is therefore potential that the loss of these *LINC* components may be required for cancer development. However, whether nesprin is a causative or resulting factor in this process is yet to be seen. It is our current belief that the loss of the *LINC* connections results in disruptions to the nesprin cage situated across the ONM (proposed by Lu *et al*. [101]), which in turn decreases nuclear stiffness. It is suggested that this increased nuclear malleability enhances a cells ability to migrate through tumour environments and surrounding tissue (which present space-restrictive environments), allowing cancer cells to migrate to other bodily areas. Due to this, we propose that these *LINC* disruptions aid in the development of metastatic behaviours in the cancer cells, however, they may not be the causative factor of cancer development itself.

Further western blotting analysis supported immunofluorescence observations in which variability between *LINC* complex protein expression patterns and cancer stage was observed (*Figure 5.16 – 5.25*). However, for the majority of proteins such as SUN1, lamin A/C and nesprin-3, no discernible correlation could be seen between the expression profile and breast cancer severity, similar to that observed through the literature [203]. For nesprin-2 C-terminal staining however, a clear decrease in expression was identified for lower isoforms upon cancer development (*Figure 5.19*). This, coupled with western blot analysis displayed in *Figures 5.18* and 5*.23* suggests an important role played by the lower C- and N-terminal retaining nesprin-1/-2 isoforms in cancer development, and more specifically in the potential regulation of larger nesprin-1/-2 isoforms. Loss of these protein regions may de-stabilise the NE through disrupting the distribution and level of nesprin-1/-2G across the ONM, resulting in an imbalance of force-transduction between intra and extra-nuclear regions. It is further possible that as nesprin-1 has been implicated in regulating DNA damage repair, the loss of lower isoform expression upon cancer development may impair DNA damage repair through loss of associated interactions with proteins involved in the DNA damage response pathway, including MSH2 and MSH6 [162].

7.2.4 Nup88 is an upstream regulator and binding partner of nesprin-2.

7.2.4.1 Nup88 displays close cellular associations to nesprin-2 C-terminal regions, supporting suggestions from previous yeast-two hybrid data that these two proteins physically interact.

The results presented in Chapter 6 help combine the findings from across Chapters 3,4 and 5 through investigating whether nesprin-2 C-terminal regions display interacting potential with Nup88, as dysregulation of both proteins has been suggested in the development of high grade cancer progression. A combination of immuno-fluorescence and biochemical analysis techniques showed that nesprin-2 C-terminal regions presented close cellular localisation and binding potential with Nup88 (across the last 4 SRs of nesprin-2 C-terminal) (*Figures 6.5 – 6.10*). This verifies suggestions presented by Schneider *et al*. [77], in which yeast two-hybrid screening suggested the existence of this interacting potential between nesprin-2 C-terminal regions and Nup88. Although the yeast two-hybrid data suggests that the observed interaction is direct, and that the Nup88

interactome displays common binding partners to that of nesprin-2 (e.g. lamin A/C and KLC1) [230, 491], it remains unclear whether the interaction observed is direct between the two proteins, or mediated through an intermediary protein.

Alongside this, it was further shown that close associations also exist between the C-terminal region of nesprin-2 and the NPC marker Mab414. This potential localisation is not well characterised in the literature, however associations between the nesprin binding partner SUN1 and NPCs have been suggested [475], in which SUN1 RNAi knockdowns were shown to stimulate NPC clustering. Due to nesprin to SUN binding being mediated through *SUN-KASH* domain interactions, this high degree of co-localisation could be expected due to the C-terminal nesprin-2 antibody (pAbk1) targeting regions in close proximity to the KASH binding site. Further support for this observation is also suggested due to associations between the NPC protein Nup88 and lamin across the INM [230]. This association could mean that further NPC components stained in the Mab414 display close associations to nesprin C-terminal domains found bound indirectly to the lamin network through SUN associations. However, to further validate this observation, electron microscopy techniques could be used alongside immuno-gold labelling in order to visualise the NPC in more detail, therefore providing a more accurate representation of this close association.

7.2.4.2 Nup88 may act as an upstream regulator of lower nesprin isoforms, as increased expression of Nup88 is associated with decreased nesprin-2 expression.

It was further shown that through *in vitro* up-regulation of pEGFP-Nup88 fusions, that nesprin-2G was down regulated (*Figure 6.13*). These findings appear to strongly correlates with evidence presented by Hashizume *et al.* suggesting that the *in vitro* overexpression of full length Nup88 expressing a GFP tag into HeLa cells stimulated a significant increase in multinucleated cell development [476]. This finding is similar to the *in vivo* situations observed in high-grade breast cancer development, in which increased Nup88 levels are shown to closely correlate to increased cancer aggression and metastatic potential [467, 468, 470, 477, 492]. When collated with known whole genome and exome analysis suggesting *SYNE* genes are highly mutated in multiple cancers [195, 198, 197, 196], and breast tissue assessment displaying reduced nesprin-2 expressions [203], it is suggested that Nup88 may play regulatory roles on the expression of nesprin-2.

It can be suggested that Nup88 upregulation may down regulate nesprin-2 through two potential regulatory mechanisms. Firstly, direct Nup88 interactions with nesprin-2 may potentially lead to its degradation, however, to this date; no links between Nup88 and SUMO signalling have been established, however, the Nup88 binding partner Nup358 has been shown to act as a SUMO (small ubiquitin-related modifier) [493]. This suggests potential roles of the Nup88/Nup358 complex in targeting nesprin-2 for degradation. However, no direct evidence for this action has yet been shown. Alternatively, Nup88 attachment to nesprin-2 could further alter its conformation across the NE, leading to alterations in nesprin topology across the ONM. The second mechanism by which Nup88 may regulate nesprin-2 is through the direct regulation of nesprin-2 gene transcription. Support for this comes from suggestive roles of Nup88 in the regulation of gene expression across multiple higher eukaryotes [458], suggesting that increased levels of Nup88 may directly reduce nesprin-2 transcription levels, and subsequently nesprin-2 protein levels in the cell.

One final observation from this experimental section further displays potential co-localisation between the microtubule associated motor protein KLC1 and Nup88 across the cytoplasm of the cells. This finding appears to support evidence in the literature, suggesting that an interacting potential exists between KLC1 and Nup214 (a Nup88 binding partner) [203], suggesting that these observed co-localisations may arise through Nup214 mediated binding. Further investigations however, would need to be conducted to validate this potential co-localisation through biochemical analysis methods including GST-pulldowns using KLC1 fragments published previously [77] alongside immunoprecipitation assays. This would therefore provide a clear indication as to whether a physical binding potential existed between Nup88 and KLC1.

For further detailed discussion of the experimental findings generated in this thesis, please refer to each of the primary results chapters.

7.3 Theorised model - loss of correct nesprin localisation across the ONM leads to decreased nuclear stiffness and subsequent increased metastatic potential during cancer development.

The data presented in this thesis suggests that the maintenance of *LINC* complex connections across the NE is a crucial factor in maintaining normal cellular function. It was shown that disruption to this complex protein network leads to the development of a decrease in nuclear stiffness, abnormal cell-cell/cell-substratum attachments, increased migration potentials and increased cell-stacking and differentiation under air-liquid interface conditions. Due to the known complexity of *LINC* complex function in the cell, it is difficult to discern direct mechanisms as to how this network of proteins can affect the development of cancer.

However, through further investigations suggesting Nup88 may be an upstream regulator of nesprin-2, alongside smaller isoforms displaying the largest decrease in expression profiles upon cancer progression, we propose the following model.

As previously suggested by Lu *et al*. [101], nesprin-1G, -2G and nesprin-3 form a potential ONM cage across the NE, able to regulate nuclear size and shape. We suggested that the smaller KASH containing nesprin-1/-2 isoforms function to anchor the giant isoforms across the NE, through interactions with SR regions. Upon Nup88 upregulation (often a characteristic of high grade cancers), a down-regulation of nesprin-2G is induced. Nesprin-2 down-regulation may come from Nup88 directly affecting the transcriptional regulation of lower nesprin-1/-2 isoforms, which in turn leads to a displacement of giant nesprin isoforms across the NE due to a loss of NE anchors. Alternatively, Nup88 may affect the regulation of giant nesprin isoforms through Nup358 mediated SUMO degradation, leading to nesprin loss. Both models consistently suggest a disruption to the proposed ONM nesprin cage, which in turn reduces the NE integrity. This reduced integrity may allow intranuclear forces pushing against the INM to increase nuclear size and further disrupt nuclear architecture (characteristics of cancerous nuclei). These sequences of events may in turn decreases nuclear stiffness, and subsequently increase migration potential through space-restrictive environments (*Figure 7.1*).

Further to this, these *LINC* disruptions may present a more complicated picture, as it was further suggested that these disruptions to the *LINC* complex impaired the cells ability to interpret environmental cues and constraints. It was suggested that the DN mutants were unable to detect the potential damaging effects of migrating through restrictive scaffold environments, evident through stress signalling alterations. It can therefore be proposed that as a cancer cell initially loses nuclear stiffness and begins to migrate through surrounding tissue environments, it may be unable to detect further damage to the cell, which in turn could perpetuate further DNA damage, leading to the increased development of cancerous phenotypes.

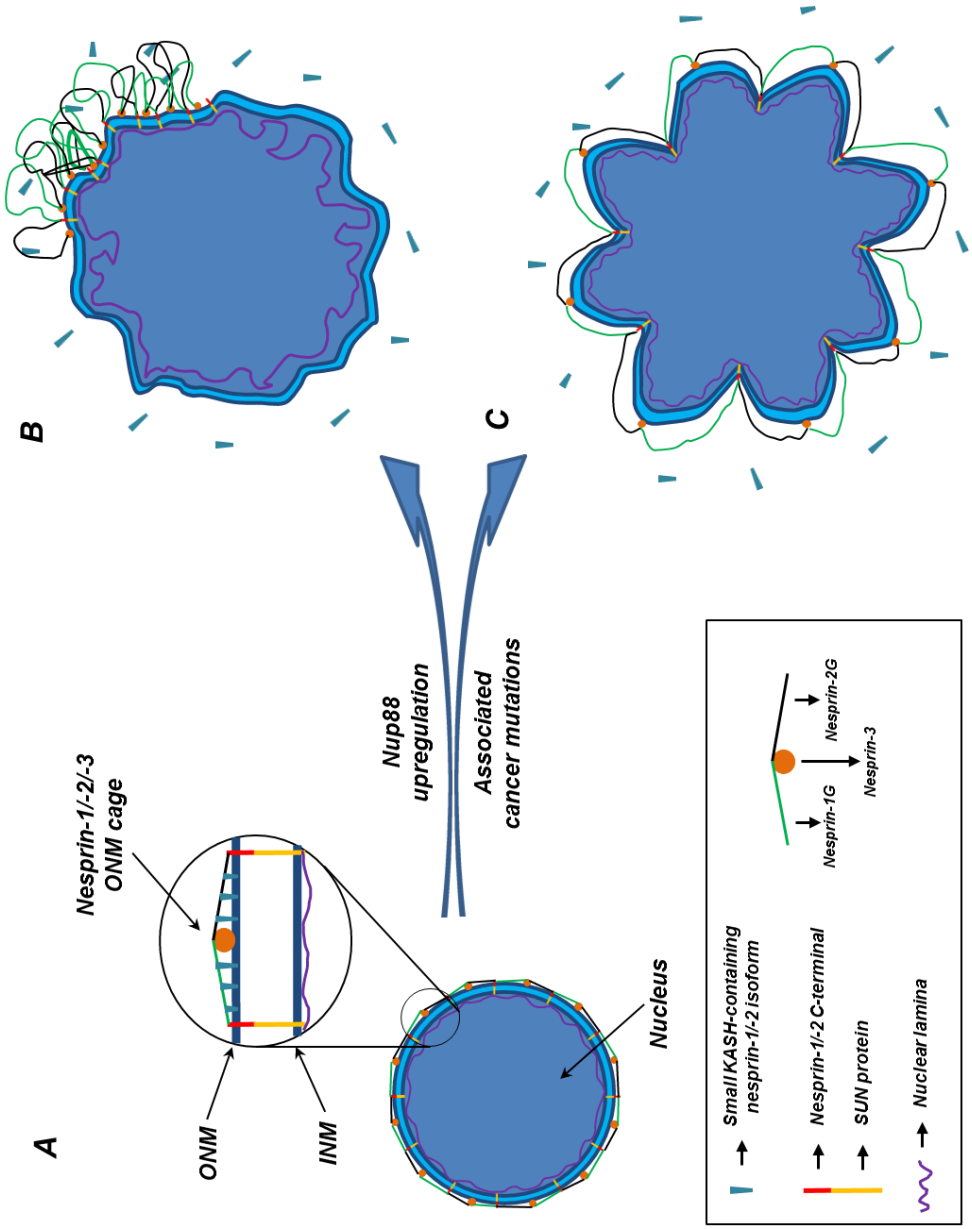

Figure 7.1: *Theorised model for the roles of lower KASH containing nesprin-1/-2 isoforms situated across the ONM in the maintenance of nuclear architecture. It is suggested that in normal nuclei, nesprin-1/-2/-3 interactions across the ONM form a cage like lattice similar to that of the INM localised lamina. The giant isoforms of both nesprin-1 and -2 are anchored across their length to the NE through SR interactions with lower KASH-retaining nesprin-1/-2 isoforms (A). Upon Nup88 upregulation or genetic abnormalities associated with cancer development, these lower nesprin-1/-2 KASH-retaining isoforms are down-regulated and displaced from the NE into the surrounding cytoplasm, resulting in a loss of anchoring for the giant nesprin isoforms. This stimulates either a loss of LINC complex order across the NE, resulting in miss-localised positioning of SUN-KASH complexes (B). It is also possible that loss of these lower isoforms may result in loss of ONM integrity. As the nucleus is under constant force, it is possible intranuclear forces may increase nuclear size in regions where no connections between INM and ONM exist (areas without NPC's or SUN-SKASH interactions) (C) due to the nesprin cage no longer being able to counteract this force. This could therefore result in nuclear enlargement in specific nuclear regions, stimulating the formation of nuclear blebbing. Both instances in (B) and (C) would disrupt LINC complex function in maintaining nuclear architecture, alongside reducing nuclear stiffness.*

7.4 Conclusions.

In conclusion, the work presented in this thesis has demonstrated that the maintenance of *LINC* complex connections across the NE is critical in maintaining normal cellular architecture in 2D culture environments. The further application of synthetic 3D culture technologies demonstrated that these *LINC* complex disruptions present in DN mutants may also be a determining factor in cellular migration potential through potentially damaging space-restrictive environments, due to an increased nuclear malleability.

This increased nuclear malleability, and resulting increase in migration potential links closely to migration properties of high-grade, metastatic cancers, through which penetration into surrounding tissue is enhanced. Investigating both immunofluorescence localisation and expression levels of *LINC* complex proteins (notably nesprin-1/-2), suggests that upon cancer development, the expression patterns of lower C-terminal retaining nesprin-1/-2 isoforms is decreased. It can therefore be concluded that the retention of lower C-terminal nesprin-1/-2 isoforms may be required for the correct assembly of *LINC* complex interactions surrounding the ONM. Loss of these lower isoforms may therefore provide a hallmark of metastasis development across a range of high-grade breast cancers, leading to a decrease in nuclear stiffness due to the loss of correct *LINC* complex assemblies.

7.5 Future Work.

The results presented in this thesis highlight several key areas of further work which would help expanding our knowledge of *LINC* complex roles in nuclear stiffness, keratinocyte differentiation potential and breast cancer metastasis.

7.5.1 Further experiments arising from Chapter 3.

As it was identified that DN HaCaT cells presented increased migration potentials in the more space-restrictive scaffolds, it was suggested that their increased nuclear malleability lead to these observed advantages. However, current data has only

highlighted this in snapshots through time point analysis. Therefore to expand on this work, further investigations should aim to investigate the mechanisms as to how cells migrate through 3D culture environments, as the exact mechanisms to how nuclei deform during restrictive-pore migration are not well understood.

As the scaffold materials employed in our investigations display opaque properties, it is difficult to assess live cell motility through both phase contrast and fluorescence techniques during cell migration. It is therefore suggested that the use of light sheet technology is applied. This microscopy technique is designed to investigate fluorescent signals within thick tissue samples [494, 495], and is therefore well suited to our culture systems. Live cell imaging of NE markers, MT, IF and actin networks could be applied to both WT and DN HaCaT cells in order to visualise nuclear behaviour during migration through space-restrictive interconnects. This would therefore provide further insight into how cells manipulate their nuclei in 3D migratory environments, alongside alluding to roles of the *LINC* complex in this process, which could prove invaluable for designing future therapeutic targets able to inhibit metastatic behaviours displayed by many cancer cells [496, 283].

From this Chapter, it was also suggested that upon culture in space-restrictive scaffold environments, WT HaCaT cells, but not DN HaCaT cells displayed increased expression levels of stress associated signalling proteins (p38 and JNK). This suggested that 1) these environments pose a potential damaging environment, and 2) the DN HaCaT cells may have been unable to sense the damaging effects of the surrounding environment, and therefore were unable to respond accordingly. From this evidence, it is suggested that further experimentation is needed in order to detect whether further DNA damage can be detected in cells migrating through these scaffolds. We propose that if migration through space-restrictive environments could induce DNA damage, then this could lead to increased levels of DNA damage in cancer cells during early stages of metastasis, which in turn may increase the cancerous phenotype through perpetual DNA damage. To verify this, DN and WT HaCaT cells should be stained for three well characterised DNA damage markers; a biotinylated oligonucleotide hairpin probe (HPP), an antibody against single stranded DNA (ssDNA) and detection of double stranded DNA (dsDNA) breaks through terminal deoxynucleotidyl transferase dUTP nick end labelling (TUNEL) staining [497]. This would therefore verify whether DNA damage is also occurring during migration through these environments, leading to further increases in migration potential.

7.5.2 Further experiments arising from Chapter 4.

One key finding within this investigation was that the production of a simplified co-culture model pre-seeded with human dermal fibroblasts lead to limited changes in the penetration potential displayed by the DN HaCaT cells in comparison to bare scaffolds tested in Chapter 3. However, this model presented limited similarities to the in vivo situation found in normal epidermis, so to increase the biological relevance of our findings, the use of more advanced 3D skin models could be applied to further investigations, similar to that developed by Carlson *et al*. [498]. This model builds the skin equivalent across a surface of collagen, which more accurately represents the basement membrane of the epidermis. Following this, fibroblast and keratinocyte cells are seeded and maintained in culture at the air-liquid interface. The use of this system would allow us to investigate whether the DN HaCaT cells express similar behavioural phenotypes when not faced with synthetic polystyrene environments. Further to this, it is also possible to investigate the differences in cell behaviour between WT and DN HaCaT cells in the same model. For example, following fibroblast seeding, a heterogeneous population of DN and WT HaCaT cells could be seeded onto the fibroblast layer and lifted to the air-liquid interface. Due to the DN HaCaT cells expressing GFP-SUN1, it would be easy to identify these cells within the heterogeneous culture, meaning that through the use of live cell imaging techniques such as light sheet microscopy, direct comparisons could be made between WT and DN HaCaT cells within the system. This would therefore allow cell-cell interactions, migration behaviour and differentiation potential to be directly compared between the two cells. In addition, it may also provide further use as a disease model, allowing the investigation as to whether these *LINC* disrupted DN HaCaT cells express similar migration behaviours to that of squamous-cell carcinomas, therefore leading to further suggestions as to roles for *LINC* components in the development of cancerous phenotypes.

It was further shown in this chapter that the DN HaCaT cells appeared to display and increased cell-stacking and differentiation potential to their WT counterparts, when grown at the air-liquid interface in space-restrictive scaffolds. We suggest that this increased cell stacking phenotype in DN HaCaT cells is a result of increased E-cadherin with potential loss of contact inhibition, leading to daughter cells proliferating into the only available space, up. However, previous data has shown that both WT and DN HaCaT cells display equal levels of E-cadherin when maintained in 3D culture environments, at the point of initial seeding, DN HaCaT cells will express higher levels of E-cadherin due to our data

suggesting that in 2D culture, DN HaCaT express increased E-cadherin levels. To validate that contact inhibition is perturbed in these DN HaCaT cells however, protein expression levels of both WT and DN HaCaT cells would need to be assessed, through specifically investigating whether $p27^{Kip1}$ expression changes.

The growth arrest in contact inhibition is stimulated by $p27^{Kip1}$ cyclin dependant cyclase, which binds cyclin CDK complexes, inferring G1 arrest in the cell cycle [499, 500, 501]. Therefore, we would expect a decrease expression of $p27^{Kip1}$ in DN HaCaT cells if contact inhibition is disrupted, similar to that expressed by multiple cancer cells [502]. This investigation would therefore help decipher whether the observed cell stacking and subsequent differentiation events displayed by the *LINC* disrupted DN HaCaT cells are indeed a result in perturbations in contact inhibition signalling pathways.

Further findings in this chapter demonstrated that YAP (a key component of the hippo signalling pathway) expression also appeared to differ between the two cell lines, however, it was unclear whether this expression change correlated to a switch in localisation from cytoplasmic to nuclear. To verify whether YAP signalling is indeed perturbed in the DN HaCaT cells, fractionated western blotting to select nuclear and cytoplasmic proteins could be assessed between the two cell lines grown in space-restrictive scaffolds [503]. This would allow the identification as to whether 1) the expression profiles of YAP do indeed change between the WT and DN HaCaT cells, and 2) whether YAP localisation is altered between the two cell lines. This would help increase our understanding as to roles of the *LINC* complex in maintaining Hippo signalling, a pathway known to regulate cell proliferation in response to extracellular cues [504].

7.5.3 Further experiments arising from Chapter 5.

In Chapter 5, one of the key findings was the reduction in nesprin-2 C-terminal isoforms expression profiles across high grade breast cancer tissues using immunofluorescence analysis; however immunofluorescence analysis only provides an indication as the expression levels of proteins, and due to this, further analysis is needed. To verify that the loss in immunofluorescence stains in triple negative tissues correlates to a reduction in protein expression levels, and not for example alterations in protein confirmation or aa sequence, resulting in impaired antibody binding, further western blot analysis should be conducted. Western blot assessment for C-terminal nesprin-2 isoform expression patterns across primary breast tissue lysates will help to increase our

understanding of changes in isoform expression patterns during cancer development, and assess whether there is a sequential loss of total C-terminal retaining nesprin-2 isoforms, or only select isoforms. Further to this, it is also suggested to conduct RT-PCR across these tissue samples, in order to gain an understanding as to whether the observed loss of nesprin-2 expression via immunofluorescence analysis is a result of reduced mRNA expression within cells.

A further key observation within this chapter was the identification of a loss of lower nesprin-1/-2 isoform expression profiles in cancerous cell lines. Very little is currently known about the functional roles played by the lower nesprin-1/-2 isoforms, and therefore their identification and subsequent sequence characterisation would be a key aspect in future work. To gain an indication as to their potential roles in the cell, and whether they do indeed play a role in maintaining nuclear stiffness, their domain compositions and cellular localisation would need to be assessed. This would require the production of antibodies specific to unique regions of these isoforms and subsequent imaging through super resolution microscopy to identify whether they are situated across the INM or ONM. Following their identified localisation in the cell, further experimental analysis would need to be conducted to gain an insight into their potential binding partners, therefore gaining an insight into their potential functions in the cell. This could be conducted through the use of GST-Pull down and immunoprecipitation assays, allowing the identification of possible interacting partners and cell/tissue localisation of these interactions.

Aside this, further rescue experiments would need to be conducted to assess whether the expression of these shorter nesprin-1/-2 isoforms could increase the nuclear stiffness, and subsequently reduce migration potential of high grade cancer cell lines such as MDA-MB-231 within space-restrictive scaffolds. For example, if a hypothetical lower nesprin-1 isoform contained the sequence SR1, SR2, SR3, SR4 followed by a C-terminal KASH domain, constructs could be made expressing each SR alone, alongside combinations (*i.e.* SR1, or SR2+SR3). These constructs could then be inserted into MDA-MB-231 cells and their effects on nuclear stiffness and migration tested, to see if their insertion displayed a significant effect. If a positive correlation is identified between specific regions and reduced migration potential/increased nuclear stiffness, following investigations would aim to assess the functional roles played by these SR regions, through yeast two-hybrid screening. This would then allow the full characterisation of the roles played by these lower-isoforms, and provide an indication as to their potential roles in the development of cancer phenotypes, either verifying or contradicting views within this thesis and the literature [496], suggesting that nuclear stiffness may constitute a rate limiting step in 3D cell migration, and that these properties are regulated through *LINC* complex connections.

7.5.4 Further experiments arising from Chapter 6.

In Chapter 6, it was shown that Nup88 displays physical interacting potential with the C-terminal region of nesprin-2, alongside further suggestions that Nup88 may acts as an upstream regulator of nesprin-2. However, the mechanism by which Nup88 regulates nesprin-2 is still unclear. One suggested hypothesis is that the physical interaction of Nup88 may stimulate the degradation of nesprin-2 through decreasing the proximity of Nup88s binding partner Nup358 and nesprin-2. It was suggested that due to Nup358s role as a small ubiquitin-like modifier (SUMO), it may be responsible for the degradation of nesprin-2 upon Nup88 upregulation. Follow on investigations would test this through transfections of Nup358 into cellular systems such as HaCaT cells, followed by subsequent western blot protein analysis. If a marked decrease in nesprin-2 levels is observed, then it provides supporting evidence for this hypothesis that Nup88 overexpression may induce increased Nup358 degradation activity on nesprin-2 within the cells.

8. References

[1] J. M. Berg, J. L. Tymoczko, and L. Stryer, “Eukaryotic Transcription and Translation Are Separated in Space and Time.” W H Freeman, 2002.

[2] S. G. Brohawn, J. R. Partridge, J. R. R. Whittle, and T. U. Schwartz, “The nuclear pore complex has entered the atomic age.,” *Structure*, vol. 17, no. 9, pp. 1156–68, Sep. 2009.

[3] D. Görlich and U. Kutay, “Transport between the cell nucleus and the cytoplasm.,” *Annu. Rev. Cell Dev. Biol.*, vol. 15, pp. 607–60, Jan. 1999.

[4] S. D. Speese, J. Ashley, V. Jokhi, J. Nunnari, R. Barria, Y. Li, B. Ataman, A. Koon, Y.-T. Chang, Q. Li, M. J. Moore, and V. Budnik, “Nuclear envelope budding enables large ribonucleoprotein particle export during synaptic Wnt signaling.,” *Cell*, vol. 149, no. 4, pp. 832–46, May 2012.

[5] A. Rose and C. Schlieker, “Alternative nuclear transport for cellular protein quality control.,” *Trends Cell Biol.*, vol. 22, no. 10, pp. 509–14, Oct. 2012.

[6] D. E. Ingber, “Tensegrity: the architectural basis of cellular mechanotransduction.,” *Annu. Rev. Physiol.*, vol. 59, pp. 575–99, Jan. 1997.

[7] S. Antoku, R. Zhu, S. Kutscheidt, O. T. Fackler, and G. G. Gundersen, “Reinforcing the LINC complex connection to actin filaments: the role of FHOD1 in TAN line formation and nuclear movement.,” *Cell Cycle*, pp. 1–6, Jun. 2015.

[8] S. Alam, D. B. Lovett, R. B. Dickinson, K. J. Roux, and T. P. Lele, “Nuclear forces and cell mechanosensing.,” *Prog. Mol. Biol. Transl. Sci.*, vol. 126, pp. 205–15, Jan. 2014.

[9] S. Neumann, M. Schneider, R. L. Daugherty, C. J. Gottardi, S. A. Eming, A. Beijer, A. A. Noegel, and I. Karakesisoglou, “Nesprin-2 interacts with {alpha}-catenin and regulates Wnt signaling at the nuclear envelope.,” *J. Biol. Chem.*, vol. 285, no. 45, pp. 34932–8, Nov. 2010.

[10] E. C. Tapley and D. A. Starr, “Connecting the nucleus to the cytoskeleton by SUN-KASH bridges across the nuclear envelope.,” *Curr. Opin. Cell Biol.*, vol. 25, no. 1, pp. 57–62, Feb. 2013.

[11] M. L. Lombardi and J. Lammerding, “Keeping the LINC: the importance of nucleocytoskeletal coupling in intracellular force transmission and cellular function.,” *Biochem. Soc. Trans.*, vol. 39, no. 6, pp. 1729–34, Dec. 2011.

[12] H. J. Worman and G. Bonne, “‘Laminopathies’: a wide spectrum of human diseases.,” *Exp. Cell Res.*, vol. 313, no. 10, pp. 2121–33, Jun. 2007.

[13] I. Méndez-López and H. J. Worman, “Inner nuclear membrane proteins: impact on human disease.,” *Chromosoma*, vol. 121, no. 2, pp. 153–67, Apr. 2012.

[14] D. A. Starr and H. N. Fridolfsson, “Interactions between nuclei and the cytoskeleton are mediated by SUN-KASH nuclear-envelope bridges.,” *Annu. Rev. Cell Dev. Biol.*, vol. 26, pp. 421–44, Jan. 2010.

[15] W. Chang, H. J. Worman, and G. G. Gundersen, “Accessorizing and anchoring the LINC complex for multifunctionality.,” *J. Cell Biol.*, vol. 208, no. 1, pp. 11–22, Jan. 2015.

[16] S. J. King, K. Nowak, N. Suryavanshi, I. Holt, C. M. Shanahan, and A. J. Ridley, “Nesprin-1 and nesprin-2 regulate endothelial cell shape and migration.,” *Cytoskeleton (Hoboken).*, vol. 71, no. 7, pp. 423–34, Jul. 2014.

[17] J. T. Patel, A. Bottrill, S. L. Prosser, S. Jayaraman, K. Straatman, A. M. Fry, and S. Shackleton, “Mitotic phosphorylation of SUN1 loosens its connection with the nuclear lamina while the LINC complex remains intact.,” *Nucleus*, vol. 5, no. 5, pp. 462–73, Jan. .

[18] R. de la Fuente, M. Manterola, A. Viera, M. T. Parra, M. Alsheimer, J. S. Rufas, and J. Page, “Chromatin organization and remodeling of interstitial telomeric sites during meiosis in the Mongolian gerbil (Meriones unguiculatus).,” *Genetics*, vol. 197, no. 4, pp. 1137–51, Aug. 2014.

[19] N. Stuurman, S. Heins, and U. Aebi, “Nuclear lamins: their structure, assembly, and interactions.,” *J. Struct. Biol.*, vol. 122, no. 1–2, pp. 42–66, Jan. 1998.

[20] Q. S. Padiath, K. Saigoh, R. Schiffmann, H. Asahara, T. Yamada, A. Koeppen, K. Hogan, L. J. Ptácek, and Y.-H. Fu, “Lamin B1 duplications cause autosomal dominant leukodystrophy.,” *Nat. Genet.*, vol. 38, no. 10, pp. 1114–23, Oct. 2006.

[21] A. Robinson, D. Partridge, A. Malhas, S. C. P. De Castro, P. Gustavsson, D. N. Thompson, D. J. Vaux, A. J. Copp, P. Stanier, A. G. Bassuk, and N. D. E. Greene, “Is LMNB1 a susceptibility gene for neural tube defects in humans?,” *Birth Defects Res. A. Clin. Mol. Teratol.*, vol. 97, no. 6, pp. 398–402, Jun. 2013.

[22] S. Sun, M. Z. Xu, R. T. Poon, P. J. Day, and J. M. Luk, “Circulating Lamin B1 (LMNB1) biomarker detects early stages of liver cancer in patients.,” *J. Proteome Res.*, vol. 9, no. 1, pp. 70–8, Jan. 2010.

[23] L. Liu, J. Wang, L. Shi, W. Zhang, X. Du, Z. Wang, and Y. Zhang, “β-Asarone induces senescence in colorectal cancer cells by inducing lamin B1 expression.,” *Phytomedicine*, vol. 20, no. 6, pp. 512–20, Apr. 2013.

[24] U. Wazir, M. H. Ahmed, J. M. Bridger, A. Harvey, W. G. Jiang, A. K. Sharma, and K. Mokbel, “The clinicopathological significance of lamin A/C, lamin B1 and lamin B receptor mRNA expression in human breast cancer.,” *Cell. Mol. Biol. Lett.*, vol. 18, no. 4, pp. 595–611, Dec. 2013.

[25] L. Li, Y. Du, X. Kong, Z. Li, Z. Jia, J. Cui, J. Gao, G. Wang, and K. Xie, “Lamin B1 is a novel therapeutic target of betulinic acid in pancreatic cancer.,” *Clin. Cancer Res.*, vol. 19, no. 17, pp. 4651–61, Sep. 2013.

[26] J. L. Broers, B. M. Machiels, H. J. Kuijpers, F. Smedts, R. van den Kieboom, Y. Raymond, and F. C. Ramaekers, “A- and B-type lamins are differentially expressed

in normal human tissues.," *Histochem. Cell Biol.*, vol. 107, no. 6, pp. 505–17, Jun. 1997.

[27] V. K. Parnaik and K. Manju, "Laminopathies: multiple disorders arising from defects in nuclear architecture.," *J. Biosci.*, vol. 31, no. 3, pp. 405–21, Sep. 2006.

[28] H. J. Worman, "Nuclear lamins and laminopathies.," *J. Pathol.*, vol. 226, no. 2, pp. 316–25, Jan. 2012.

[29] F. Haque, D. J. Lloyd, D. T. Smallwood, C. L. Dent, C. M. Shanahan, A. M. Fry, R. C. Trembath, and S. Shackleton, "SUN1 interacts with nuclear lamin A and cytoplasmic nesprins to provide a physical connection between the nuclear lamina and the cytoskeleton.," *Mol. Cell. Biol.*, vol. 26, no. 10, pp. 3738–51, May 2006.

[30] C. Ostlund, E. S. Folker, J. C. Choi, E. R. Gomes, G. G. Gundersen, and H. J. Worman, "Dynamics and molecular interactions of linker of nucleoskeleton and cytoskeleton (LINC) complex proteins.," *J. Cell Sci.*, vol. 122, no. Pt 22, pp. 4099–108, Nov. 2009.

[31] G. W. G. Luxton, E. R. Gomes, E. S. Folker, H. J. Worman, and G. G. Gundersen, "TAN lines: a novel nuclear envelope structure involved in nuclear positioning.," *Nucleus*, vol. 2, no. 3, pp. 173–81, Jan. 2011.

[32] V. C. Padmakumar, T. Libotte, W. Lu, H. Zaim, S. Abraham, A. A. Noegel, J. Gotzmann, R. Foisner, and I. Karakesisoglou, "The inner nuclear membrane protein Sun1 mediates the anchorage of Nesprin-2 to the nuclear envelope.," *J. Cell Sci.*, vol. 118, no. Pt 15, pp. 3419–30, Aug. 2005.

[33] M. Crisp, Q. Liu, K. Roux, J. B. Rattner, C. Shanahan, B. Burke, P. D. Stahl, and D. Hodzic, "Coupling of the nucleus and cytoplasm: role of the LINC complex.," *J. Cell Biol.*, vol. 172, no. 1, pp. 41–53, Jan. 2006.

[34] T. Sullivan, D. Escalante-Alcalde, H. Bhatt, M. Anver, N. Bhat, K. Nagashima, C. L. Stewart, and B. Burke, "Loss of A-type lamin expression compromises nuclear envelope integrity leading to muscular dystrophy.," *J. Cell Biol.*, vol. 147, no. 5, pp. 913–20, Nov. 1999.

[35] C. Coffinier, S. Y. Chang, C. Nobumori, Y. Tu, E. A. Farber, J. I. Toth, L. G. Fong, and S. G. Young, "Abnormal development of the cerebral cortex and cerebellum in the setting of lamin B2 deficiency.," *Proc. Natl. Acad. Sci. U. S. A.*, vol. 107, no. 11, pp. 5076–81, Mar. 2010.

[36] C. Coffinier, H.-J. Jung, C. Nobumori, S. Chang, Y. Tu, R. H. Barnes, Y. Yoshinaga, P. J. de Jong, L. Vergnes, K. Reue, L. G. Fong, and S. G. Young, "Deficiencies in lamin B1 and lamin B2 cause neurodevelopmental defects and distinct nuclear shape abnormalities in neurons.," *Mol. Biol. Cell*, vol. 22, no. 23, pp. 4683–93, Dec. 2011.

[37] Q. Zhang, C. Bethmann, N. F. Worth, J. D. Davies, C. Wasner, A. Feuer, C. D. Ragnauth, Q. Yi, J. A. Mellad, D. T. Warren, M. A. Wheeler, J. A. Ellis, J. N. Skepper, M. Vorgerd, B. Schlotter-Weigel, P. L. Weissberg, R. G. Roberts, M. Wehnert, and C. M. Shanahan, "Nesprin-1 and -2 are involved in the pathogenesis

of Emery Dreifuss muscular dystrophy and are critical for nuclear envelope integrity.," *Hum. Mol. Genet.*, vol. 16, no. 23, pp. 2816–33, Dec. 2007.

[38] S. Osmanagic-Myers, T. Dechat, and R. Foisner, "Lamins at the crossroads of mechanosignaling.," *Genes Dev.*, vol. 29, no. 3, pp. 225–37, Feb. 2015.

[39] J. M. . Mislow, J. M. Holaska, M. S. Kim, K. K. Lee, M. Segura-Totten, K. L. Wilson, and E. M. McNally, "Nesprin-1α self-associates and binds directly to emerin and lamin A in vitro," *FEBS Lett.*, vol. 525, no. 1–3, pp. 135–140, Aug. 2002.

[40] Q. Zhang, C. D. Ragnauth, J. N. Skepper, N. F. Worth, D. T. Warren, R. G. Roberts, P. L. Weissberg, J. A. Ellis, and C. M. Shanahan, "Nesprin-2 is a multi-isomeric protein that binds lamin and emerin at the nuclear envelope and forms a subcellular network in skeletal muscle.," *J. Cell Sci.*, vol. 118, no. Pt 4, pp. 673–87, Feb. 2005.

[41] S. Kandert, Y. Lüke, T. Kleinhenz, S. Neumann, W. Lu, V. M. Jaeger, M. Munck, M. Wehnert, C. R. Müller, Z. Zhou, A. A. Noegel, M.-C. Dabauvalle, and I. Karakesisoglou, "Nesprin-2 giant safeguards nuclear envelope architecture in LMNA S143F progeria cells.," *Hum. Mol. Genet.*, vol. 16, no. 23, pp. 2944–59, Dec. 2007.

[42] M. A. Wheeler, J. D. Davies, Q. Zhang, L. J. Emerson, J. Hunt, C. M. Shanahan, and J. A. Ellis, "Distinct functional domains in nesprin-1alpha and nesprin-2beta bind directly to emerin and both interactions are disrupted in X-linked Emery-Dreifuss muscular dystrophy.," *Exp. Cell Res.*, vol. 313, no. 13, pp. 2845–57, Aug. 2007.

[43] S. Gudise, R. A. Figueroa, R. Lindberg, V. Larsson, and E. Hallberg, "Samp1 is functionally associated with the LINC complex and A-type lamina networks.," *J. Cell Sci.*, vol. 124, no. Pt 12, pp. 2077–85, Jun. 2011.

[44] J. Borrego-Pinto, T. Jegou, D. S. Osorio, F. Auradé, M. Gorjánácz, B. Koch, I. W. Mattaj, and E. R. Gomes, "Samp1 is a component of TAN lines and is required for nuclear movement.," *J. Cell Sci.*, vol. 125, no. Pt 5, pp. 1099–105, Mar. 2012.

[45] C. Ostlund, T. Sullivan, C. L. Stewart, and H. J. Worman, "Dependence of diffusional mobility of integral inner nuclear membrane proteins on A-type lamins.," *Biochemistry*, vol. 45, no. 5, pp. 1374–82, Feb. 2006.

[46] D. Tunnah, C. A. Sewry, D. Vaux, E. C. Schirmer, and G. E. Morris, "The apparent absence of lamin B1 and emerin in many tissue nuclei is due to epitope masking.," *J. Mol. Histol.*, vol. 36, no. 5, pp. 337–44, Jun. 2005.

[47] A. J. Koch and J. M. Holaska, "Loss of emerin alters myogenic signaling and miRNA expression in mouse myogenic progenitors.," *PLoS One*, vol. 7, no. 5, p. e37262, Jan. 2012.

[48] J. M. Holaska and K. L. Wilson, "Multiple roles for emerin: implications for Emery-Dreifuss muscular dystrophy.," *Anat. Rec. A. Discov. Mol. Cell. Evol. Biol.*, vol. 288, no. 7, pp. 676–80, Jul. 2006.

[49] K. L. Wilson, J. M. Holaska, R. Montes de Oca, K. Tifft, M. Zastrow, M. Segura-Totten, M. Mansharamani, and L. Bengtsson, “Nuclear membrane protein emerin: roles in gene regulation, actin dynamics and human disease.,” *Novartis Found. Symp.*, vol. 264, pp. 51–58; discussion 58–62, 227–30, Jan. 2005.

[50] W. Chang, E. S. Folker, H. J. Worman, and G. G. Gundersen, “Emerin organizes actin flow for nuclear movement and centrosome orientation in migrating fibroblasts.,” *Mol. Biol. Cell*, vol. 24, no. 24, pp. 3869–80, Dec. 2013.

[51] I. Hagan and M. Yanagida, “The product of the spindle formation gene sad1+ associates with the fission yeast spindle pole body and is essential for viability.,” *J. Cell Biol.*, vol. 129, no. 4, pp. 1033–47, May 1995.

[52] C. J. Malone, W. D. Fixsen, H. R. Horvitz, and M. Han, “UNC-84 localizes to the nuclear envelope and is required for nuclear migration and anchoring during C. elegans development.,” *Development*, vol. 126, no. 14, pp. 3171–81, Jun. 1999.

[53] M. J. Puckelwartz, E. Kessler, Y. Zhang, D. Hodzic, K. N. Randles, G. Morris, J. U. Earley, M. Hadhazy, J. M. Holaska, S. K. Mewborn, P. Pytel, and E. M. McNally, “Disruption of nesprin-1 produces an Emery Dreifuss muscular dystrophy-like phenotype in mice.,” *Hum. Mol. Genet.*, vol. 18, no. 4, pp. 607–20, Feb. 2009.

[54] E. Göb, J. Schmitt, R. Benavente, and M. Alsheimer, “Mammalian sperm head formation involves different polarization of two novel LINC complexes.,” *PLoS One*, vol. 5, no. 8, p. e12072, Jan. 2010.

[55] C.-H. Yeh, P.-L. Kuo, Y.-Y. Wang, Y.-Y. Wu, M.-F. Chen, D.-Y. Lin, T.-H. Lai, H.-S. Chiang, and Y.-H. Lin, “SEPT12/SPAG4/LAMINB1 complexes are required for maintaining the integrity of the nuclear envelope in postmeiotic male germ cells.,” *PLoS One*, vol. 10, no. 3, p. e0120722, Jan. 2015.

[56] E. C. Tapley, N. Ly, and D. A. Starr, “Multiple mechanisms actively target the SUN protein UNC-84 to the inner nuclear membrane.,” *Mol. Biol. Cell*, vol. 22, no. 10, pp. 1739–52, May 2011.

[57] A. Rothballer, T. U. Schwartz, and U. Kutay, “LINCing complex functions at the nuclear envelope: what the molecular architecture of the LINC complex can reveal about its function.,” *Nucleus*, vol. 4, no. 1, pp. 29–36, Jan. .

[58] B. A. Sosa, A. Rothballer, U. Kutay, and T. U. Schwartz, “LINC complexes form by binding of three KASH peptides to domain interfaces of trimeric SUN proteins.,” *Cell*, vol. 149, no. 5, pp. 1035–47, May 2012.

[59] W. Wang, Z. Shi, S. Jiao, C. Chen, H. Wang, G. Liu, Q. Wang, Y. Zhao, M. I. Greene, and Z. Zhou, “Structural insights into SUN-KASH complexes across the nuclear envelope.,” *Cell Res.*, vol. 22, no. 10, pp. 1440–52, Oct. 2012.

[60] E. Göb, E. Meyer-Natus, R. Benavente, and M. Alsheimer, “Expression of individual mammalian Sun1 isoforms depends on the cell type.,” *Commun. Integr. Biol.*, vol. 4, no. 4, pp. 440–2, Jul. 2011.

[61] D. M. Hodzic, D. B. Yeater, L. Bengtsson, H. Otto, and P. D. Stahl, “Sun2 is a novel mammalian inner nuclear membrane protein.,” *J. Biol. Chem.*, vol. 279, no. 24, pp. 25805–12, Jun. 2004.

[62] K. K. Lee, D. Starr, M. Cohen, J. Liu, M. Han, K. L. Wilson, and Y. Gruenbaum, “Lamin-dependent localization of UNC-84, a protein required for nuclear migration in Caenorhabditis elegans.,” *Mol. Biol. Cell*, vol. 13, no. 3, pp. 892–901, Mar. 2002.

[63] S. Hasan, S. Güttinger, P. Mühlhäusser, F. Anderegg, S. Bürgler, and U. Kutay, “Nuclear envelope localization of human UNC84A does not require nuclear lamins.,” *FEBS Lett.*, vol. 580, no. 5, pp. 1263–8, Feb. 2006.

[64] D. Jahn, S. Schramm, M. Schnölzer, C. J. Heilmann, C. G. de Koster, W. Schütz, R. Benavente, and M. Alsheimer, “A truncated lamin A in the Lmna -/- mouse line: implications for the understanding of laminopathies.,” *Nucleus*, vol. 3, no. 5, pp. 463–74, Jan. .

[65] Y. Turgay, R. Ungricht, A. Rothballer, A. Kiss, G. Csucs, P. Horvath, and U. Kutay, “A classical NLS and the SUN domain contribute to the targeting of SUN2 to the inner nuclear membrane.,” *EMBO J.*, vol. 29, no. 14, pp. 2262–75, Jul. 2010.

[66] F. Haque, D. Mazzeo, J. T. Patel, D. T. Smallwood, J. A. Ellis, C. M. Shanahan, and S. Shackleton, “Mammalian SUN protein interaction networks at the inner nuclear membrane and their role in laminopathy disease processes.,” *J. Biol. Chem.*, vol. 285, no. 5, pp. 3487–98, Jan. 2010.

[67] Z. Zhou, X. Du, Z. Cai, X. Song, H. Zhang, T. Mizuno, E. Suzuki, M. R. Yee, A. Berezov, R. Murali, S.-L. Wu, B. L. Karger, M. I. Greene, and Q. Wang, “Structure of Sad1-UNC84 homology (SUN) domain defines features of molecular bridge in nuclear envelope.,” *J. Biol. Chem.*, vol. 287, no. 8, pp. 5317–26, Feb. 2012.

[68] B. A. Sosa, A. Rothballer, U. Kutay, and T. U. Schwartz, “LINC complexes form by binding of three KASH peptides to domain interfaces of trimeric SUN proteins.,” *Cell*, vol. 149, no. 5, pp. 1035–47, May 2012.

[69] Z. Jahed, H. Shams, and M. R. K. Mofrad, “A Disulfide Bond Is Required for the Transmission of Forces through SUN-KASH Complexes.,” *Biophys. J.*, vol. 109, no. 3, pp. 501–9, Aug. 2015.

[70] M. Schneider, A. A. Noegel, and I. Karakesisoglou, “KASH-domain proteins and the cytoskeletal landscapes of the nuclear envelope.,” *Biochem. Soc. Trans.*, vol. 36, no. Pt 6, pp. 1368–72, Dec. 2008.

[71] H. Xiong, F. Rivero, U. Euteneuer, S. Mondal, S. Mana-Capelli, D. Larochelle, A. Vogel, B. Gassen, and A. A. Noegel, “Dictyostelium Sun-1 connects the centrosome to chromatin and ensures genome stability.,” *Traffic*, vol. 9, no. 5, pp. 708–24, May 2008.

[72] I. Schulz, O. Baumann, M. Samereier, C. Zoglmeier, and R. Gräf, “Dictyostelium Sun1 is a dynamic membrane protein of both nuclear membranes and required for centrosomal association with clustered centromeres.,” *Eur. J. Cell Biol.*, vol. 88, no. 11, pp. 621–38, Nov. 2009.

[73] K. Graumann and D. E. Evans, “Plant SUN domain proteins: components of putative plant LINC complexes?,” *Plant Signal. Behav.*, vol. 5, no. 2, pp. 154–6, Feb. 2010.

[74] K. Zhou and W. Hanna-Rose, “Movers and shakers or anchored: Caenorhabditis elegans nuclei achieve it with KASH/SUN.,” *Dev. Dyn.*, vol. 239, no. 5, pp. 1352–64, May 2010.

[75] W. Lu, J. Gotzmann, L. Sironi, V.-M. Jaeger, M. Schneider, Y. Lüke, M. Uhlén, C. A.-K. Szigyarto, A. Brachner, J. Ellenberg, R. Foisner, A. A. Noegel, and I. Karakesisoglou, “Sun1 forms immobile macromolecular assemblies at the nuclear envelope.,” *Biochim. Biophys. Acta*, vol. 1783, no. 12, pp. 2415–26, Dec. 2008.

[76] D. A. Starr and J. A. Fischer, “KASH ’n Karry: the KASH domain family of cargo-specific cytoskeletal adaptor proteins.,” *Bioessays*, vol. 27, no. 11, pp. 1136–46, Nov. 2005.

[77] M. Schneider, W. Lu, S. Neumann, A. Brachner, J. Gotzmann, A. A. Noegel, and I. Karakesisoglou, “Molecular mechanisms of centrosome and cytoskeleton anchorage at the nuclear envelope.,” *Cell. Mol. Life Sci.*, vol. 68, no. 9, pp. 1593–610, May 2011.

[78] K. J. Roux, M. L. Crisp, Q. Liu, D. Kim, S. Kozlov, C. L. Stewart, and B. Burke, “Nesprin 4 is an outer nuclear membrane protein that can induce kinesin-mediated cell polarization.,” *Proc. Natl. Acad. Sci. U. S. A.*, vol. 106, no. 7, pp. 2194–9, Feb. 2009.

[79] E. D. Apel, R. M. Lewis, R. M. Grady, and J. R. Sanes, “Syne-1, a dystrophin- and Klarsicht-related protein associated with synaptic nuclei at the neuromuscular junction.,” *J. Biol. Chem.*, vol. 275, no. 41, pp. 31986–95, Oct. 2000.

[80] N. T. Duong, G. E. Morris, L. T. Lam, Q. Zhang, C. A. Sewry, C. M. Shanahan, and I. Holt, “Nesprins: tissue-specific expression of epsilon and other short isoforms.,” *PLoS One*, vol. 9, no. 4, p. e94380, Jan. 2014.

[81] J. A. Mellad, D. T. Warren, and C. M. Shanahan, “Nesprins LINC the nucleus and cytoskeleton.,” *Curr. Opin. Cell Biol.*, vol. 23, no. 1, pp. 47–54, Feb. 2011.

[82] J. M. K. Mislow, J. M. Holaska, M. S. Kim, K. K. Lee, M. Segura-Totten, K. L. Wilson, and E. M. McNally, “Nesprin-1alpha self-associates and binds directly to emerin and lamin A in vitro.,” *FEBS Lett.*, vol. 525, no. 1–3, pp. 135–40, Aug. 2002.

[83] M. H. Wilson and E. L. F. Holzbaur, “Nesprins anchor kinesin-1 motors to the nucleus to drive nuclear distribution in muscle cells.,” *Development*, vol. 142, no. 1, pp. 218–28, Jan. 2015.

[84] M. H. Wilson and E. L. F. Holzbaur, “Nesprins anchor kinesin-1 motors to the nucleus to drive nuclear distribution in muscle cells.,” *Development*, vol. 142, no. 1, pp. 218–28, Jan. 2015.

[85] A. Morimoto, H. Shibuya, X. Zhu, J. Kim, K. Ishiguro, M. Han, and Y. Watanabe, “A conserved KASH domain protein associates with telomeres, SUN1, and dynactin during mammalian meiosis.,” *J. Cell Biol.*, vol. 198, no. 2, pp. 165–72, Jul. 2012.

[86] K. Wilhelmsen, S. H. M. Litjens, I. Kuikman, N. Tshimbalanga, H. Janssen, I. van den Bout, K. Raymond, and A. Sonnenberg, “Nesprin-3, a novel outer nuclear membrane protein, associates with the cytoskeletal linker protein plectin.,” *J. Cell Biol.*, vol. 171, no. 5, pp. 799–810, Dec. 2005.

[87] R. Gräf, P. Batsios, and I. Meyer, “Evolution of centrosomes and the nuclear lamina: Amoebozoan assets.,” *Eur. J. Cell Biol.*, vol. 94, no. 6, pp. 249–56, Apr. 2015.

[88] A. Méjat and T. Misteli, “LINC complexes in health and disease.,” *Nucleus*, vol. 1, no. 1, pp. 40–52, Jan. 2010.

[89] H. Lodish, A. Berk, S. L. Zipursky, P. Matsudaira, D. Baltimore, and J. Darnell, “Molecular Cell Biology.” W. H. Freeman, 2000.

[90] A. O. Sperry, “The dynamic cytoskeleton of the developing male germ cell.,” *Biol. Cell*, vol. 104, no. 5, pp. 297–305, May 2012.

[91] S. V Strelkov, H. Herrmann, and U. Aebi, “Molecular architecture of intermediate filaments.,” *Bioessays*, vol. 25, no. 3, pp. 243–51, Mar. 2003.

[92] D. A. Starr and M. Han, “Role of ANC-1 in tethering nuclei to the actin cytoskeleton.,” *Science*, vol. 298, no. 5592, pp. 406–9, Oct. 2002.

[93] G. W. G. Luxton, E. R. Gomes, E. S. Folker, E. Vintinner, and G. G. Gundersen, “Linear arrays of nuclear envelope proteins harness retrograde actin flow for nuclear movement.,” *Science*, vol. 329, no. 5994, pp. 956–9, Aug. 2010.

[94] S. Kutscheidt, R. Zhu, S. Antoku, G. W. G. Luxton, I. Stagljar, O. T. Fackler, and G. G. Gundersen, “FHOD1 interaction with nesprin-2G mediates TAN line formation and nuclear movement.,” *Nat. Cell Biol.*, vol. 16, no. 7, pp. 708–15, Jul. 2014.

[95] E. R. Gomes, S. Jani, and G. G. Gundersen, “Nuclear movement regulated by Cdc42, MRCK, myosin, and actin flow establishes MTOC polarization in migrating cells.,” *Cell*, vol. 121, no. 3, pp. 451–63, May 2005.

[96] G. W. G. Luxton, E. R. Gomes, E. S. Folker, H. Worman, and G. G. Gundersen, “TAN lines,” *Nucleus*, vol. 2, no. 3, pp. 173–181, Oct. 2014.

[97] G. G. Gundersen and H. J. Worman, “Nuclear positioning.,” *Cell*, vol. 152, no. 6, pp. 1376–89, Mar. 2013.

[98] D. Rajgor, J. A. Mellad, D. Soong, J. B. Rattner, M. J. Fritzler, and C. M. Shanahan, “Mammalian microtubule P-body dynamics are mediated by nesprin-1.,” *J. Cell Biol.*, vol. 205, no. 4, pp. 457–75, May 2014.

[99] H. F. Horn, D. I. Kim, G. D. Wright, E. S. M. Wong, C. L. Stewart, B. Burke, and K. J. Roux, “A mammalian KASH domain protein coupling meiotic chromosomes to the cytoskeleton.,” *J. Cell Biol.*, vol. 202, no. 7, pp. 1023–39, Sep. 2013.

[100] X. Zhang, K. Lei, X. Yuan, X. Wu, Y. Zhuang, T. Xu, R. Xu, and M. Han, “SUN1/2 and Syne/Nesprin-1/2 complexes connect centrosome to the nucleus during

neurogenesis and neuronal migration in mice.," *Neuron*, vol. 64, no. 2, pp. 173–87, Oct. 2009.

[101] W. Lu, M. Schneider, S. Neumann, V.-M. Jaeger, S. Taranum, M. Munck, S. Cartwright, C. Richardson, J. Carthew, K. Noh, M. Goldberg, A. A. Noegel, and I. Karakesisoglou, "Nesprin interchain associations control nuclear size.," *Cell. Mol. Life Sci.*, vol. 69, no. 20, pp. 3493–509, Oct. 2012.

[102] M. L. Lombardi, D. E. Jaalouk, C. M. Shanahan, B. Burke, K. J. Roux, and J. Lammerding, "The interaction between nesprins and sun proteins at the nuclear envelope is critical for force transmission between the nucleus and cytoskeleton.," *J. Biol. Chem.*, vol. 286, no. 30, pp. 26743–53, Jul. 2011.

[103] J. T. Morgan, E. R. Pfeiffer, T. L. Thirkill, P. Kumar, G. Peng, H. N. Fridolfsson, G. C. Douglas, D. A. Starr, and A. I. Barakat, "Nesprin-3 regulates endothelial cell morphology, perinuclear cytoskeletal architecture, and flow-induced polarization.," *Mol. Biol. Cell*, vol. 22, no. 22, pp. 4324–34, Nov. 2011.

[104] R. B. Dickinson, S. Neelam, and T. P. Lele, "Dynamic, mechanical integration between nucleus and cell- where physics meets biology.," *Nucleus*, Sep. 2015.

[105] A. L. Olins, M. Zwerger, H. Herrmann, H. Zentgraf, A. J. Simon, M. Monestier, and D. E. Olins, "The human granulocyte nucleus: Unusual nuclear envelope and heterochromatin composition.," *Eur. J. Cell Biol.*, vol. 87, no. 5, pp. 279–90, May 2008.

[106] J. Lammerding, J. Hsiao, P. C. Schulze, S. Kozlov, C. L. Stewart, and R. T. Lee, "Abnormal nuclear shape and impaired mechanotransduction in emerin-deficient cells.," *J. Cell Biol.*, vol. 170, no. 5, pp. 781–91, Aug. 2005.

[107] J. Liu, T. Rolef Ben-Shahar, D. Riemer, M. Treinin, P. Spann, K. Weber, A. Fire, and Y. Gruenbaum, "Essential roles for Caenorhabditis elegans lamin gene in nuclear organization, cell cycle progression, and spatial organization of nuclear pore complexes.," *Mol. Biol. Cell*, vol. 11, no. 11, pp. 3937–47, Nov. 2000.

[108] M. Eriksson, W. T. Brown, L. B. Gordon, M. W. Glynn, J. Singer, L. Scott, M. R. Erdos, C. M. Robbins, T. Y. Moses, P. Berglund, A. Dutra, E. Pak, S. Durkin, A. B. Csoka, M. Boehnke, T. W. Glover, and F. S. Collins, "Recurrent de novo point mutations in lamin A cause Hutchinson-Gilford progeria syndrome.," *Nature*, vol. 423, no. 6937, pp. 293–8, May 2003.

[109] A. E. Rusiñol and M. S. Sinensky, "Farnesylated lamins, progeroid syndromes and farnesyl transferase inhibitors.," *J. Cell Sci.*, vol. 119, no. Pt 16, pp. 3265–72, Aug. 2006.

[110] M. P. Mallampalli, G. Huyer, P. Bendale, M. H. Gelb, and S. Michaelis, "Inhibiting farnesylation reverses the nuclear morphology defect in a HeLa cell model for Hutchinson-Gilford progeria syndrome.," *Proc. Natl. Acad. Sci. U. S. A.*, vol. 102, no. 40, pp. 14416–21, Oct. 2005.

[111] B. C. Capell, M. R. Erdos, J. P. Madigan, J. J. Fiordalisi, R. Varga, K. N. Conneely, L. B. Gordon, C. J. Der, A. D. Cox, and F. S. Collins, "Inhibiting farnesylation of progerin prevents the characteristic nuclear blebbing of Hutchinson-Gilford progeria

syndrome.," *Proc. Natl. Acad. Sci. U. S. A.*, vol. 102, no. 36, pp. 12879–84, Sep. 2005.

[112] A. Kaufmann, F. Heinemann, M. Radmacher, and R. Stick, "Amphibian oocyte nuclei expressing lamin A with the progeria mutation E145K exhibit an increased elastic modulus.," *Nucleus*, vol. 2, no. 4, pp. 310–9, Jan. 2011.

[113] J. Lammerding, L. G. Fong, J. Y. Ji, K. Reue, C. L. Stewart, S. G. Young, and R. T. Lee, "Lamins A and C but not lamin B1 regulate nuclear mechanics.," *J. Biol. Chem.*, vol. 281, no. 35, pp. 25768–80, Sep. 2006.

[114] D. Ferrera, C. Canale, R. Marotta, N. Mazzaro, M. Gritti, M. Mazzanti, S. Capellari, P. Cortelli, and L. Gasparini, "Lamin B1 overexpression increases nuclear rigidity in autosomal dominant leukodystrophy fibroblasts.," *FASEB J.*, vol. 28, no. 9, pp. 3906–18, Sep. 2014.

[115] Y. Lüke, H. Zaim, I. Karakesisoglou, V. M. Jaeger, L. Sellin, W. Lu, M. Schneider, S. Neumann, A. Beijer, M. Munck, V. C. Padmakumar, J. Gloy, G. Walz, and A. A. Noegel, "Nesprin-2 Giant (NUANCE) maintains nuclear envelope architecture and composition in skin.," *J. Cell Sci.*, vol. 121, no. Pt 11, pp. 1887–98, Jun. 2008.

[116] S. Kandert, Y. Lüke, T. Kleinhenz, S. Neumann, W. Lu, V. M. Jaeger, M. Munck, M. Wehnert, C. R. Müller, Z. Zhou, A. A. Noegel, M.-C. Dabauvalle, and I. Karakesisoglou, "Nesprin-2 giant safeguards nuclear envelope architecture in LMNA S143F progeria cells.," *Hum. Mol. Genet.*, vol. 16, no. 23, pp. 2944–59, Dec. 2007.

[117] N. E. Cain, E. C. Tapley, K. L. McDonald, B. M. Cain, and D. A. Starr, "The SUN protein UNC-84 is required only in force-bearing cells to maintain nuclear envelope architecture.," *J. Cell Biol.*, vol. 206, no. 2, pp. 163–72, Jul. 2014.

[118] N. E. Cain and D. A. Starr, "SUN proteins and nuclear envelope spacing.," *Nucleus*, vol. 6, no. 1, pp. 2–7, Jan. 2015.

[119] N. R. Morris, "Nuclear Migration: From Fungi to the Mammalian Brain," *J. Cell Biol.*, vol. 148, no. 6, pp. 1097–1102, Mar. 2000.

[120] A. Yamamoto and Y. Hiraoka, "Cytoplasmic dynein in fungi: insights from nuclear migration.," *J. Cell Sci.*, vol. 116, no. Pt 22, pp. 4501–12, Nov. 2003.

[121] R. B. Vallee and J.-W. Tsai, "The cellular roles of the lissencephaly gene LIS1, and what they tell us about brain development.," *Genes Dev.*, vol. 20, no. 11, pp. 1384–93, Jun. 2006.

[122] S. Reinsch and P. Gönczy, "Mechanisms of nuclear positioning.," *J. Cell Sci.*, vol. 111 (Pt 1, pp. 2283–95, Aug. 1998.

[123] K. L. Weber, A. M. Sokac, J. S. Berg, R. E. Cheney, and W. M. Bement, "A microtubule-binding myosin required for nuclear anchoring and spindle assembly.," *Nature*, vol. 431, no. 7006, pp. 325–9, Sep. 2004.

[124] R. M. Grady, D. A. Starr, G. L. Ackerman, J. R. Sanes, and M. Han, “Syne proteins anchor muscle nuclei at the neuromuscular junction.,” *Proc. Natl. Acad. Sci. U. S. A.*, vol. 102, no. 12, pp. 4359–64, Mar. 2005.

[125] X. Zhang, R. Xu, B. Zhu, X. Yang, X. Ding, S. Duan, T. Xu, Y. Zhuang, and M. Han, “Syne-1 and Syne-2 play crucial roles in myonuclear anchorage and motor neuron innervation.,” *Development*, vol. 134, no. 5, pp. 901–8, Mar. 2007.

[126] M. Maninová, Z. Klímová, J. T. Parsons, M. J. Weber, M. P. Iwanicki, and T. Vomastek, “The reorientation of cell nucleus promotes the establishment of front-rear polarity in migrating fibroblasts.,” *J. Mol. Biol.*, vol. 425, no. 11, pp. 2039–55, Jun. 2013.

[127] W. Chang, S. Antoku, C. Östlund, H. J. Worman, and G. G. Gundersen, “Linker of nucleoskeleton and cytoskeleton (LINC) complex-mediated actin-dependent nuclear positioning orients centrosomes in migrating myoblasts.,” *Nucleus*, vol. 6, no. 1, pp. 77–88, Jan. 2015.

[128] J. R. Sims, S. Karp, and D. E. Ingber, “Altering the cellular mechanical force balance results in integrated changes in cell, cytoskeletal and nuclear shape.,” *J. Cell Sci.*, vol. 103 (Pt 4, pp. 1215–22, Dec. 1992.

[129] A. J. Maniotis, C. S. Chen, and D. E. Ingber, “Demonstration of mechanical connections between integrins, cytoskeletal filaments, and nucleoplasm that stabilize nuclear structure.,” *Proc. Natl. Acad. Sci. U. S. A.*, vol. 94, no. 3, pp. 849–54, Feb. 1997.

[130] N. Wang, K. Naruse, D. Stamenović, J. J. Fredberg, S. M. Mijailovich, I. M. Tolić-Nørrelykke, T. Polte, R. Mannix, and D. E. Ingber, “Mechanical behavior in living cells consistent with the tensegrity model.,” *Proc. Natl. Acad. Sci. U. S. A.*, vol. 98, no. 14, pp. 7765–70, Jul. 2001.

[131] D. Stamenović, S. M. Mijailovich, I. M. Tolić-Nørrelykke, J. Chen, and N. Wang, “Cell prestress. II. Contribution of microtubules.,” *Am. J. Physiol. Cell Physiol.*, vol. 282, no. 3, pp. C617–24, Mar. 2002.

[132] N. Wang, I. M. Tolić-Nørrelykke, J. Chen, S. M. Mijailovich, J. P. Butler, J. J. Fredberg, and D. Stamenović, “Cell prestress. I. Stiffness and prestress are closely associated in adherent contractile cells.,” *Am. J. Physiol. Cell Physiol.*, vol. 282, no. 3, pp. C606–16, Mar. 2002.

[133] Y.-C. Poh, S. P. Shevtsov, F. Chowdhury, D. C. Wu, S. Na, M. Dundr, and N. Wang, “Dynamic force-induced direct dissociation of protein complexes in a nuclear body in living cells.,” *Nat. Commun.*, vol. 3, p. 866, Jan. 2012.

[134] K. Burridge, K. Fath, T. Kelly, G. Nuckolls, and C. Turner, “Focal adhesions: transmembrane junctions between the extracellular matrix and the cytoskeleton.,” *Annu. Rev. Cell Biol.*, vol. 4, pp. 487–525, Jan. 1988.

[135] N. Wang, J. P. Butler, and D. E. Ingber, “Mechanotransduction across the cell surface and through the cytoskeleton.,” *Science*, vol. 260, no. 5111, pp. 1124–7, May 1993.

[136] D. N. Simon and K. L. Wilson, “The nucleoskeleton as a genome-associated dynamic ‘network of networks,’” *Nat. Rev. Mol. Cell Biol.*, vol. 12, no. 11, pp. 695–708, Oct. 2011.

[137] W. F. Liu, “Mechanical regulation of cellular phenotype: implications for vascular tissue regeneration.,” *Cardiovasc. Res.*, vol. 95, no. 2, pp. 215–22, Jul. 2012.

[138] R. M. Stewart, A. E. Zubek, K. A. Rosowski, S. M. Schreiner, V. Horsley, and M. C. King, “Nuclear-cytoskeletal linkages facilitate cross talk between the nucleus and intercellular adhesions.,” *J. Cell Biol.*, vol. 209, no. 3, pp. 403–18, May 2015.

[139] T. Anno, N. Sakamoto, and M. Sato, “Role of nesprin-1 in nuclear deformation in endothelial cells under static and uniaxial stretching conditions.,” *Biochem. Biophys. Res. Commun.*, vol. 424, no. 1, pp. 94–9, Jul. 2012.

[140] T. J. Chancellor, J. Lee, C. K. Thodeti, and T. Lele, “Actomyosin tension exerted on the nucleus through nesprin-1 connections influences endothelial cell adhesion, migration, and cyclic strain-induced reorientation.,” *Biophys. J.*, vol. 99, no. 1, pp. 115–23, Jul. 2010.

[141] S. B. Khatau, C. M. Hale, P. J. Stewart-Hutchinson, M. S. Patel, C. L. Stewart, P. C. Searson, D. Hodzic, and D. Wirtz, “A perinuclear actin cap regulates nuclear shape.,” *Proc. Natl. Acad. Sci. U. S. A.*, vol. 106, no. 45, pp. 19017–22, Nov. 2009.

[142] D.-H. Kim, S. B. Khatau, Y. Feng, S. Walcott, S. X. Sun, G. D. Longmore, and D. Wirtz, “Actin cap associated focal adhesions and their distinct role in cellular mechanosensing.,” *Sci. Rep.*, vol. 2, p. 555, Jan. 2012.

[143] S. B. Khatau, R. J. Bloom, S. Bajpai, D. Razafsky, S. Zang, A. Giri, P.-H. Wu, J. Marchand, A. Celedon, C. M. Hale, S. X. Sun, D. Hodzic, and D. Wirtz, “The distinct roles of the nucleus and nucleus-cytoskeleton connections in three-dimensional cell migration.,” *Sci. Rep.*, vol. 2, p. 488, Jan. 2012.

[144] S. B. Khatau, S. Kusuma, D. Hanjaya-Putra, P. Mali, L. Cheng, J. S. H. Lee, S. Gerecht, and D. Wirtz, “The differential formation of the LINC-mediated perinuclear actin cap in pluripotent and somatic cells.,” *PLoS One*, vol. 7, no. 5, p. e36689, Jan. 2012.

[145] D. Splinter, M. E. Tanenbaum, A. Lindqvist, D. Jaarsma, A. Flotho, K. Lou Yu, I. Grigoriev, D. Engelsma, E. D. Haasdijk, N. Keijzer, J. Demmers, M. Fornerod, F. Melchior, C. C. Hoogenraad, R. H. Medema, and A. Akhmanova, “Bicaudal D2, dynein, and kinesin-1 associate with nuclear pore complexes and regulate centrosome and nuclear positioning during mitotic entry.,” *PLoS Biol.*, vol. 8, no. 4, p. e1000350, Jan. 2010.

[146] J. Wu, K. C. Lee, R. B. Dickinson, and T. P. Lele, “How dynein and microtubules rotate the nucleus.,” *J. Cell. Physiol.*, vol. 226, no. 10, pp. 2666–74, Oct. 2011.

[147] J. Lammerding, P. C. Schulze, T. Takahashi, S. Kozlov, T. Sullivan, R. D. Kamm, C. L. Stewart, and R. T. Lee, “Lamin A/C deficiency causes defective nuclear mechanics and mechanotransduction.,” *J. Clin. Invest.*, vol. 113, no. 3, pp. 370–8, Feb. 2004.

[148] C. Y. Ho, D. E. Jaalouk, M. K. Vartiainen, and J. Lammerding, “Lamin A/C and emerin regulate MKL1-SRF activity by modulating actin dynamics.,” *Nature*, vol. 497, no. 7450, pp. 507–11, May 2013.

[149] E. Markiewicz, K. Tilgner, N. Barker, M. van de Wetering, H. Clevers, M. Dorobek, I. Hausmanowa-Petrusewicz, F. C. S. Ramaekers, J. L. V Broers, W. M. Blankesteijn, G. Salpingidou, R. G. Wilson, J. A. Ellis, and C. J. Hutchison, “The inner nuclear membrane protein emerin regulates beta-catenin activity by restricting its accumulation in the nucleus.,” *EMBO J.*, vol. 25, no. 14, pp. 3275–85, Jul. 2006.

[150] E. D. Tulgren, S. M. Turgeon, K. J. Opperman, and B. Grill, “The Nesprin family member ANC-1 regulates synapse formation and axon termination by functioning in a pathway with RPM-1 and β-Catenin.,” *PLoS Genet.*, vol. 10, no. 7, p. e1004481, Jul. 2014.

[151] P. Isermann and J. Lammerding, “Nuclear mechanics and mechanotransduction in health and disease.,” *Curr. Biol.*, vol. 23, no. 24, pp. R1113–21, Dec. 2013.

[152] G. Uzer, W. R. Thompson, B. Sen, Z. Xie, S. S. Yen, S. Miller, G. Bas, M. Styner, C. T. Rubin, S. Judex, K. Burridge, and J. Rubin, “Cell Mechanosensitivity to Extremely Low-Magnitude Signals Is Enabled by a LINCed Nucleus.,” *Stem Cells*, vol. 33, no. 6, pp. 2063–76, Jun. 2015.

[153] C. Guilluy, L. D. Osborne, L. Van Landeghem, L. Sharek, R. Superfine, R. Garcia-Mata, and K. Burridge, “Isolated nuclei adapt to force and reveal a mechanotransduction pathway in the nucleus.,” *Nat. Cell Biol.*, vol. 16, no. 4, pp. 376–81, Apr. 2014.

[154] J. Schmitt, R. Benavente, D. Hodzic, C. Höög, C. L. Stewart, and M. Alsheimer, “Transmembrane protein Sun2 is involved in tethering mammalian meiotic telomeres to the nuclear envelope.,” *Proc. Natl. Acad. Sci. U. S. A.*, vol. 104, no. 18, pp. 7426–31, May 2007.

[155] A. M. Penkner, A. Fridkin, J. Gloggnitzer, A. Baudrimont, T. Machacek, A. Woglar, E. Csaszar, P. Pasierbek, G. Ammerer, Y. Gruenbaum, and V. Jantsch, “Meiotic chromosome homology search involves modifications of the nuclear envelope protein Matefin/SUN-1.,” *Cell*, vol. 139, no. 5, pp. 920–33, Nov. 2009.

[156] D. J. Wynne, O. Rog, P. M. Carlton, and A. F. Dernburg, “Dynein-dependent processive chromosome motions promote homologous pairing in C. elegans meiosis.,” *J. Cell Biol.*, vol. 196, no. 1, pp. 47–64, Jan. 2012.

[157] D. Jahn, S. Schramm, R. Benavente, and M. Alsheimer, “Dynamic properties of meiosis-specific lamin C2 and its impact on nuclear envelope integrity.,” *Nucleus*, vol. 1, no. 3, pp. 273–83, Jan. 2010.

[158] J. Link, D. Jahn, J. Schmitt, E. Göb, J. Baar, S. Ortega, R. Benavente, and M. Alsheimer, “The meiotic nuclear lamina regulates chromosome dynamics and promotes efficient homologous recombination in the mouse.,” *PLoS Genet.*, vol. 9, no. 1, p. e1003261, Jan. 2013.

[159] P. Oza, S. L. Jaspersen, A. Miele, J. Dekker, and C. L. Peterson, “Mechanisms that regulate localization of a DNA double-strand break to the nuclear periphery.,” *Genes Dev.*, vol. 23, no. 8, pp. 912–27, Apr. 2009.

[160] R. K. Swartz, E. C. Rodriguez, and M. C. King, “A role for nuclear envelope-bridging complexes in homology-directed repair.,” *Mol. Biol. Cell*, vol. 25, no. 16, pp. 2461–71, Aug. 2014.

[161] K. Lei, X. Zhu, R. Xu, C. Shao, T. Xu, Y. Zhuang, and M. Han, “Inner nuclear envelope proteins SUN1 and SUN2 play a prominent role in the DNA damage response.,” *Curr. Biol.*, vol. 22, no. 17, pp. 1609–15, Sep. 2012.

[162] I. Sur, S. Neumann, and A. A. Noegel, “Nesprin-1 role in DNA damage response.,” *Nucleus*, vol. 5, no. 2, pp. 173–91, Jan. 2014.

[163] N. Cabanelas and V. P. Martins, “Laminopathies: a Pandora’s box of heart failure, bradyarrhythmias and sudden death.,” *Rev. Port. Cardiol.*, vol. 34, no. 2, pp. 139.e1–5, Feb. 2015.

[164] D. Camozzi, C. Capanni, V. Cenni, E. Mattioli, M. Columbaro, S. Squarzoni, and G. Lattanzi, “Diverse lamin-dependent mechanisms interact to control chromatin dynamics. Focus on laminopathies.,” *Nucleus*, vol. 5, no. 5, pp. 427–40, Jan. 2014.

[165] Y. Gruenbaum and O. Medalia, “Lamins: the structure and protein complexes.,” *Curr. Opin. Cell Biol.*, vol. 32, pp. 7–12, Feb. 2015.

[166] F. Gros-Louis, N. Dupré, P. Dion, M. A. Fox, S. Laurent, S. Verreault, J. R. Sanes, J.-P. Bouchard, and G. A. Rouleau, “Mutations in SYNE1 lead to a newly discovered form of autosomal recessive cerebellar ataxia.,” *Nat. Genet.*, vol. 39, no. 1, pp. 80–5, Jan. 2007.

[167] Y. Izumi, R. Miyamoto, H. Morino, A. Yoshizawa, K. Nishinaka, F. Udaka, M. Kameyama, H. Maruyama, and H. Kawakami, “Cerebellar ataxia with SYNE1 mutation accompanying motor neuron disease.,” *Neurology*, vol. 80, no. 6, pp. 600–1, Feb. 2013.

[168] N. Dupré, F. Gros-Louis, J.-P. Bouchard, A. Noreau, and G. A. Rouleau, “SYNE1-Related Autosomal Recessive Cerebellar Ataxia.” University of Washington, Seattle, 13-Oct-2011.

[169] A. Noreau, C. V. Bourassa, A. Szuto, A. Levert, S. Dobrzeniecka, J. Gauthier, S. Forlani, A. Durr, M. Anheim, G. Stevanin, A. Brice, J.-P. Bouchard, P. A. Dion, N. Dupré, and G. A. Rouleau, “SYNE1 Mutations in Autosomal Recessive Cerebellar Ataxia,” *JAMA Neurol.*, vol. 70, no. 10, pp. 1296–31, Aug. 2013.

[170] D. Razafsky and D. Hodzic, “A variant of Nesprin1 giant devoid of KASH domain underlies the molecular etiology of autosomal recessive cerebellar ataxia type I.,” *Neurobiol. Dis.*, vol. 78, pp. 57–67, Jun. 2015.

[171] Y. Lüke, H. Zaim, I. Karakesisoglou, V. M. Jaeger, L. Sellin, W. Lu, M. Schneider, S. Neumann, A. Beijer, M. Munck, V. C. Padmakumar, J. Gloy, G. Walz, and A. A. Noegel, “Nesprin-2 Giant (NUANCE) maintains nuclear envelope architecture and composition in skin.,” *J. Cell Sci.*, vol. 121, no. Pt 11, pp. 1887–98, Jun. 2008.

[172] J.-Y. Wang, I.-S. Yu, C.-C. Huang, C.-Y. Chen, W.-P. Wang, S.-W. Lin, K.-T. Jeang, and Y.-H. Chi, “Sun1 deficiency leads to cerebellar ataxia in mice.,” *Dis. Model. Mech.*, vol. 8, no. 8, pp. 957–67, Aug. 2015.

[173] B. J. O’Roak, L. Vives, S. Girirajan, E. Karakoc, N. Krumm, B. P. Coe, R. Levy, A. Ko, C. Lee, J. D. Smith, E. H. Turner, I. B. Stanaway, B. Vernot, M. Malig, C. Baker, B. Reilly, J. M. Akey, E. Borenstein, M. J. Rieder, D. A. Nickerson, R. Bernier, J. Shendure, and E. E. Eichler, “Sporadic autism exomes reveal a highly interconnected protein network of de novo mutations,” *Nature*, vol. 485, no. 7397, pp. 246–250, Apr. 2012.

[174] T. W. Yu, M. H. Chahrour, M. E. Coulter, S. Jiralerspong, K. Okamura-Ikeda, B. Ataman, K. Schmitz-Abe, D. A. Harmin, M. Adli, A. N. Malik, A. M. D’Gama, E. T. Lim, S. J. Sanders, G. H. Mochida, J. N. Partlow, C. M. Sunu, J. M. Felie, J. Rodriguez, R. H. Nasir, J. Ware, R. M. Joseph, R. S. Hill, B. Y. Kwan, M. Al-Saffar, N. M. Mukaddes, A. Hashmi, S. Balkhy, G. G. Gascon, F. M. Hisama, E. LeClair, A. Poduri, O. Oner, S. Al-Saad, S. A. Al-Awadi, L. Bastaki, T. Ben-Omran, A. S. Teebi, L. Al-Gazali, V. Eapen, C. R. Stevens, L. Rappaport, S. B. Gabriel, K. Markianos, M. W. State, M. E. Greenberg, H. Taniguchi, N. E. Braverman, E. M. Morrow, and C. A. Walsh, “Using whole-exome sequencing to identify inherited causes of autism.,” *Neuron*, vol. 77, no. 2, pp. 259–73, Jan. 2013.

[175] E. K. Green, D. Grozeva, L. Forty, K. Gordon-Smith, E. Russell, A. Farmer, M. Hamshere, I. R. Jones, L. Jones, P. McGuffin, J. L. Moran, S. Purcell, P. Sklar, M. J. Owen, M. C. O’Donovan, and N. Craddock, “Association at SYNE1 in both bipolar disorder and recurrent major depression.,” *Mol. Psychiatry*, vol. 18, no. 5, pp. 614–7, May 2013.

[176] S. Taranum, E. Vaylann, P. Meinke, S. Abraham, L. Yang, S. Neumann, I. Karakesisoglou, M. Wehnert, and A. A. Noegel, “LINC complex alterations in DMD and EDMD/CMT fibroblasts.,” *Eur. J. Cell Biol.*, vol. 91, no. 8, pp. 614–28, Aug. 2012.

[177] D. Rajgor and C. M. Shanahan, “Nesprins: from the nuclear envelope and beyond.,” *Expert Rev. Mol. Med.*, vol. 15, p. e5, Jan. 2013.

[178] R. Attali, N. Warwar, A. Israel, I. Gurt, E. McNally, M. Puckelwartz, B. Glick, Y. Nevo, Z. Ben-Neriah, and J. Melki, “Mutation of SYNE-1, encoding an essential component of the nuclear lamina, is responsible for autosomal recessive arthrogryposis.,” *Hum. Mol. Genet.*, vol. 18, no. 18, pp. 3462–9, Sep. 2009.

[179] J. L. V Broers, F. C. S. Ramaekers, G. Bonne, R. Ben Yaou, and C. J. Hutchison, “Nuclear lamins: laminopathies and their role in premature ageing.,” *Physiol. Rev.*, vol. 86, no. 3, pp. 967–1008, Jul. 2006.

[180] C.-Y. Chen, Y.-H. Chi, R. A. Mutalif, M. F. Starost, T. G. Myers, S. A. Anderson, C. L. Stewart, and K.-T. Jeang, “Accumulation of the inner nuclear envelope protein Sun1 is pathogenic in progeric and dystrophic laminopathies.,” *Cell*, vol. 149, no. 3, pp. 565–77, Apr. 2012.

[181] Z.-J. Chen, W.-P. Wang, Y.-C. Chen, J.-Y. Wang, W.-H. Lin, L.-A. Tai, G.-G. Liou, C.-S. Yang, and Y.-H. Chi, “Dysregulated interactions between lamin A and SUN1 induce abnormalities in the nuclear envelope and endoplasmic reticulum in progeric laminopathies.,” *J. Cell Sci.*, vol. 127, no. Pt 8, pp. 1792–804, Apr. 2014.

[182] M. Ketema, K. Wilhelmsen, I. Kuikman, H. Janssen, D. Hodzic, and A. Sonnenberg, “Requirements for the localization of nesprin-3 at the nuclear envelope and its interaction with plectin.,” *J. Cell Sci.*, vol. 120, no. Pt 19, pp. 3384–94, Oct. 2007.

[183] M. Ketema, M. Kreft, P. Secades, H. Janssen, and A. Sonnenberg, “Nesprin-3 connects plectin and vimentin to the nuclear envelope of Sertoli cells but is not required for Sertoli cell function in spermatogenesis.,” *Mol. Biol. Cell*, vol. 24, no. 15, pp. 2454–66, Aug. 2013.

[184] H. F. Horn, Z. Brownstein, D. R. Lenz, S. Shivatzki, A. A. Dror, O. Dagan-Rosenfeld, L. M. Friedman, K. J. Roux, S. Kozlov, K.-T. Jeang, M. Frydman, B. Burke, C. L. Stewart, and K. B. Avraham, “The LINC complex is essential for hearing.,” *J. Clin. Invest.*, vol. 123, no. 2, pp. 740–50, Feb. 2013.

[185] M. Schwander, B. Kachar, and U. Müller, “Review series: The cell biology of hearing.,” *J. Cell Biol.*, vol. 190, no. 1, pp. 9–20, Jul. 2010.

[186] H. J. Worman and N. Segil, “Nucleocytoplasmic connections and deafness.,” *J. Clin. Invest.*, vol. 123, no. 2, pp. 553–5, Feb. 2013.

[187] G. P. Richardson, J. B. de Monvel, and C. Petit, “How the genetics of deafness illuminates auditory physiology.,” *Annu. Rev. Physiol.*, vol. 73, pp. 311–34, Jan. 2011.

[188] P. Dallos, “Cochlear amplification, outer hair cells and prestin.,” *Curr. Opin. Neurobiol.*, vol. 18, no. 4, pp. 370–6, Aug. 2008.

[189] I. Sziklai, M. Szõnyi, and P. Dallos, “Phosphorylation mediates the influence of acetylcholine upon outer hair cell electromotility.,” *Acta Otolaryngol.*, vol. 121, no. 2, pp. 153–6, Jan. 2001.

[190] P. Dallos, X. Wu, M. A. Cheatham, J. Gao, J. Zheng, C. T. Anderson, S. Jia, X. Wang, W. H. Y. Cheng, S. Sengupta, D. Z. Z. He, and J. Zuo, “Prestin-based outer hair cell motility is necessary for mammalian cochlear amplification.,” *Neuron*, vol. 58, no. 3, pp. 333–9, May 2008.

[191] G. I. Frolenkov, F. Mammano, and B. Kachar, “Regulation of outer hair cell cytoskeletal stiffness by intracellular Ca2+: underlying mechanism and implications for cochlear mechanics.,” *Cell Calcium*, vol. 33, no. 3, pp. 185–95, Mar. 2003.

[192] C. L. Stewart and B. Burke, “The missing LINC: a mammalian KASH-domain protein coupling meiotic chromosomes to the cytoskeleton.,” *Nucleus*, vol. 5, no. 1, pp. 3–10, Jan. 2013.

[193] M. Plessner and R. Grosse, “Extracellular signaling cues for nuclear actin polymerization,” *Eur. J. Cell Biol.*, Jun. 2015.

[194] A. Rothballer and U. Kutay, “The diverse functional LINCs of the nuclear envelope to the cytoskeleton and chromatin.,” *Chromosoma*, vol. 122, no. 5, pp. 415–29, Oct. 2013.

[195] S. Yachida, S. Jones, I. Bozic, T. Antal, R. Leary, B. Fu, M. Kamiyama, R. H. Hruban, J. R. Eshleman, M. A. Nowak, V. E. Velculescu, K. W. Kinzler, B.

Vogelstein, and C. A. Iacobuzio-Donahue, “Distant metastasis occurs late during the genetic evolution of pancreatic cancer.,” *Nature*, vol. 467, no. 7319, pp. 1114–7, Oct. 2010.

[196] A. Marmé, H.-P. Zimmermann, G. Moldenhauer, M. Schorpp-Kistner, C. Müller, O. Keberlein, A. Giersch, J. Kretschmer, B. Seib, E. Spiess, A. Hunziker, F. Merchán, P. Möller, U. Hahn, R. Kurek, F. Marmé, G. Bastert, D. Wallwiener, and H. Ponstingl, “Loss of Drop1 expression already at early tumor stages in a wide range of human carcinomas.,” *Int. J. Cancer*, vol. 123, no. 9, pp. 2048–56, Nov. 2008.

[197] C. Turnbull, S. Ahmed, J. Morrison, D. Pernet, A. Renwick, M. Maranian, S. Seal, M. Ghoussaini, S. Hines, C. S. Healey, D. Hughes, M. Warren-Perry, W. Tapper, D. Eccles, D. G. Evans, M. Hooning, M. Schutte, A. van den Ouweland, R. Houlston, G. Ross, C. Langford, P. D. P. Pharoah, M. R. Stratton, A. M. Dunning, N. Rahman, and D. F. Easton, “Genome-wide association study identifies five new breast cancer susceptibility loci.,” *Nat. Genet.*, vol. 42, no. 6, pp. 504–7, Jun. 2010.

[198] S. P. Shah, A. Roth, R. Goya, A. Oloumi, G. Ha, Y. Zhao, G. Turashvili, J. Ding, K. Tse, G. Haffari, A. Bashashati, L. M. Prentice, J. Khattra, A. Burleigh, D. Yap, V. Bernard, A. McPherson, K. Shumansky, A. Crisan, R. Giuliany, A. Heravi-Moussavi, J. Rosner, D. Lai, I. Birol, R. Varhol, A. Tam, N. Dhalla, T. Zeng, K. Ma, S. K. Chan, M. Griffith, A. Moradian, S.-W. G. Cheng, G. B. Morin, P. Watson, K. Gelmon, S. Chia, S.-F. Chin, C. Curtis, O. M. Rueda, P. D. Pharoah, S. Damaraju, J. Mackey, K. Hoon, T. Harkins, V. Tadigotla, M. Sigaroudinia, P. Gascard, T. Tlsty, J. F. Costello, I. M. Meyer, C. J. Eaves, W. W. Wasserman, S. Jones, D. Huntsman, M. Hirst, C. Caldas, M. A. Marra, and S. Aparicio, “The clonal and mutational evolution spectrum of primary triple-negative breast cancers.,” *Nature*, vol. 486, no. 7403, pp. 395–9, Jun. 2012.

[199] M. Tessema, R. Willink, K. Do, Y. Y. Yu, W. Yu, E. O. Machida, M. Brock, L. Van Neste, C. A. Stidley, S. B. Baylin, and S. A. Belinsky, “Promoter methylation of genes in and around the candidate lung cancer susceptibility locus 6q23-25.,” *Cancer Res.*, vol. 68, no. 6, pp. 1707–14, Mar. 2008.

[200] T. Sjöblom, S. Jones, L. D. Wood, D. W. Parsons, J. Lin, T. D. Barber, D. Mandelker, R. J. Leary, J. Ptak, N. Silliman, S. Szabo, P. Buckhaults, C. Farrell, P. Meeh, S. D. Markowitz, J. Willis, D. Dawson, J. K. V Willson, A. F. Gazdar, J. Hartigan, L. Wu, C. Liu, G. Parmigiani, B. H. Park, K. E. Bachman, N. Papadopoulos, B. Vogelstein, K. W. Kinzler, and V. E. Velculescu, “The consensus coding sequences of human breast and colorectal cancers.,” *Science*, vol. 314, no. 5797, pp. 268–74, Oct. 2006.

[201] M. Zwerger, C. Y. Ho, and J. Lammerding, “Nuclear mechanics in disease.,” *Annu. Rev. Biomed. Eng.*, vol. 13, pp. 397–428, Aug. 2011.

[202] A. C. Rowat, D. E. Jaalouk, M. Zwerger, W. L. Ung, I. A. Eydelnant, D. E. Olins, A. L. Olins, H. Herrmann, D. A. Weitz, and J. Lammerding, “Nuclear envelope composition determines the ability of neutrophil-type cells to passage through micron-scale constrictions.,” *J. Biol. Chem.*, vol. 288, no. 12, pp. 8610–8, Mar. 2013.

[203] A. Matsumoto, M. Hieda, Y. Yokoyama, Y. Nishioka, K. Yoshidome, M. Tsujimoto, and N. Matsuura, “Global loss of a nuclear lamina component, lamin A/C, and LINC

complex components SUN1, SUN2, and nesprin-2 in breast cancer.," *Cancer Med.*, Jul. 2015.

[204] A. Wang, X. Ma, M. A. Conti, C. Liu, S. Kawamoto, and R. S. Adelstein, "Nonmuscle myosin II isoform and domain specificity during early mouse development," *Proc. Natl. Acad. Sci.*, vol. 107, no. 33, pp. 14645–14650, Aug. 2010.

[205] R. S. Fischer, M. Gardel, X. Ma, R. S. Adelstein, and C. M. Waterman, "Local cortical tension by myosin II guides 3D endothelial cell branching.," *Curr. Biol.*, vol. 19, no. 3, pp. 260–5, Mar. 2009.

[206] M. Vicente-Manzanares, K. Newell-Litwa, A. I. Bachir, L. A. Whitmore, and A. R. Horwitz, "Myosin IIA/IIB restrict adhesive and protrusive signaling to generate front-back polarity in migrating cells.," *J. Cell Biol.*, vol. 193, no. 2, pp. 381–96, Apr. 2011.

[207] A. M. Pasapera, I. C. Schneider, E. Rericha, D. D. Schlaepfer, and C. M. Waterman, "Myosin II activity regulates vinculin recruitment to focal adhesions through FAK-mediated paxillin phosphorylation," *J. Cell Biol.*, vol. 188, no. 6, pp. 877–890, Mar. 2010.

[208] J. R. Beach, L. Shao, K. Remmert, D. Li, E. Betzig, and J. A. Hammer, "Nonmuscle Myosin II Isoforms Coassemble in Living Cells," *Curr. Biol.*, vol. 24, no. 10, pp. 1160–1166, May 2014.

[209] J. R. Beach, G. S. Hussey, T. E. Miller, A. Chaudhury, P. Patel, J. Monslow, Q. Zheng, R. A. Keri, O. Reizes, A. R. Bresnick, P. H. Howe, and T. T. Egelhoff, "Myosin II isoform switching mediates invasiveness after TGF-β-induced epithelial-mesenchymal transition.," *Proc. Natl. Acad. Sci. U. S. A.*, vol. 108, no. 44, pp. 17991–6, Nov. 2011.

[210] D. G. Thomas, A. Yenepalli, C. M. Denais, A. Rape, J. R. Beach, Y.-L. Wang, W. P. Schiemann, H. Baskaran, J. Lammerding, and T. T. Egelhoff, "Non-muscle myosin IIB is critical for nuclear translocation during 3D invasion.," *J. Cell Biol.*, vol. 210, no. 4, pp. 583–94, Aug. 2015.

[211] O.-Y. Revach, A. Weiner, K. Rechav, I. Sabanay, A. Livne, and B. Geiger, "Mechanical interplay between invadopodia and the nucleus in cultured cancer cells.," *Sci. Rep.*, vol. 5, p. 9466, Jan. 2015.

[212] L. G. Griffith and M. A. Swartz, "Capturing complex 3D tissue physiology in vitro.," *Nat. Rev. Mol. Cell Biol.*, vol. 7, no. 3, pp. 211–24, Mar. 2006.

[213] W. Mueller-Klieser, "Three-dimensional cell cultures: from molecular mechanisms to clinical applications.," *Am. J. Physiol.*, vol. 273, no. 4 Pt 1, pp. C1109–23, Oct. 1997.

[214] J. Bin Kim, "Three-dimensional tissue culture models in cancer biology.," *Semin. Cancer Biol.*, vol. 15, no. 5, pp. 365–77, Oct. 2005.

[215] A. Birgersdotter, R. Sandberg, and I. Ernberg, “Gene expression perturbation in vitro--a growing case for three-dimensional (3D) culture systems.,” *Semin. Cancer Biol.*, vol. 15, no. 5, pp. 405–12, Oct. 2005.

[216] P. A. Kenny, G. Y. Lee, C. A. Myers, R. M. Neve, J. R. Semeiks, P. T. Spellman, K. Lorenz, E. H. Lee, M. H. Barcellos-Hoff, O. W. Petersen, J. W. Gray, and M. J. Bissell, “The morphologies of breast cancer cell lines in three-dimensional assays correlate with their profiles of gene expression.,” *Mol. Oncol.*, vol. 1, no. 1, pp. 84–96, Jun. 2007.

[217] Y.-M. Wu, J. Tang, P. Zhao, Z.-N. Chen, and J.-L. Jiang, “Morphological changes and molecular expressions of hepatocellular carcinoma cells in three-dimensional culture model.,” *Exp. Mol. Pathol.*, vol. 87, no. 2, pp. 133–40, Oct. 2009.

[218] H. R. Kalhor, F. Shahin V, M. H. Fouani, and H. Hosseinkhani, “Self-assembly of tissue transglutaminase into amyloid-like fibrils using physiological concentration of Ca2+.,” *Langmuir*, vol. 27, no. 17, pp. 10776–84, Sep. 2011.

[219] S. Mohajeri, H. Hosseinkhani, N. G. Ebrahimi, L. Nikfarjam, M. Soleimani, and A.-M. Kajbafzadeh, “Proliferation and differentiation of mesenchymal stem cell on collagen sponge reinforced with polypropylene/polyethylene terephthalate blend fibers.,” *Tissue Eng. Part A*, vol. 16, no. 12, pp. 3821–30, Dec. 2010.

[220] W. Li, D. Machule, C. Gao, and P. K. DenBesten, “Growth of ameloblast-lineage cells in a three-dimensional Matrigel environment.,” *Eur. J. Oral Sci.*, vol. 114 Suppl , pp. 159–63; discussion 164–5, 380–1, May 2006.

[221] R. B. Trinca, G. A. Abraham, and M. I. Felisberti, “Electrospun nanofibrous scaffolds of segmented polyurethanes based on PEG, PLLA and PTMC blocks: Physico-chemical properties and morphology,” *Mater. Sci. Eng. C*, vol. 56, pp. 511–517, Nov. 2015.

[222] J. Lee, M. J. Cuddihy, and N. A. Kotov, “Three-dimensional cell culture matrices: state of the art.,” *Tissue Eng. Part B. Rev.*, vol. 14, no. 1, pp. 61–86, Mar. 2008.

[223] C. R. Langford, D. W. Johnson, and N. R. Cameron, “Preparation of hybrid thiol-acrylate emulsion-templated porous polymers by interfacial copolymerization of high internal phase emulsions.,” *Macromol. Rapid Commun.*, vol. 36, no. 9, pp. 834–9, May 2015.

[224] H.-J. Stark, K. Boehnke, N. Mirancea, M. J. Willhauck, A. Pavesio, N. E. Fusenig, and P. Boukamp, “Epidermal homeostasis in long-term scaffold-enforced skin equivalents.,” *J. Investig. Dermatol. Symp. Proc.*, vol. 11, no. 1, pp. 93–105, Sep. 2006.

[225] B. Inanç, A. E. Elçin, and Y. M. Elçin, “Human embryonic stem cell differentiation on tissue engineering scaffolds: effects of NGF and retinoic acid induction.,” *Tissue Eng. Part A*, vol. 14, no. 6, pp. 955–64, Jun. 2008.

[226] H.-T. Liao, Y.-Y. Chen, Y.-T. Lai, M.-F. Hsieh, and C.-P. Jiang, “The osteogenesis of bone marrow stem cells on mPEG-PCL-mPEG/hydroxyapatite composite scaffold via solid freeform fabrication.,” *Biomed Res. Int.*, vol. 2014, p. 321549, Jan. 2014.

[227] K.-C. Hung, C.-S. Tseng, and S.-H. Hsu, “Synthesis and 3D printing of biodegradable polyurethane elastomer by a water-based process for cartilage tissue engineering applications.,” *Adv. Healthc. Mater.*, vol. 3, no. 10, pp. 1578–87, Oct. 2014.

[228] Y. Ouyang, C. Huang, Y. Zhu, C. Fan, and Q. Ke, “Fabrication of seamless electrospun collagen/PLGA conduits whose walls comprise highly longitudinal aligned nanofibers for nerve regeneration.,” *J. Biomed. Nanotechnol.*, vol. 9, no. 6, pp. 931–43, Jul. 2013.

[229] M. Eichhorn, C. Stannard, K. Anselme, and J. Rühe, “Nucleus deformation of SaOs-2 cells on rhombic µ-pillars.,” *J. Mater. Sci. Mater. Med.*, vol. 26, no. 2, p. 108, Feb. 2015.

[230] Y. C. Lussi, I. Hügi, E. Laurell, U. Kutay, and B. Fahrenkrog, “The nucleoporin Nup88 is interacting with nuclear lamin A.,” *Mol. Biol. Cell*, vol. 22, no. 7, pp. 1080–90, Apr. 2011.

[231] E. Knight, B. Murray, R. Carnachan, and S. Przyborski, “Alvetex®: polystyrene scaffold technology for routine three dimensional cell culture.,” *Methods Mol. Biol.*, vol. 695, pp. 323–340, 2011.

[232] V. C. Padmakumar, S. Abraham, S. Braune, A. A. Noegel, B. Tunggal, I. Karakesisoglou, and E. Korenbaum, “Enaptin, a giant actin-binding protein, is an element of the nuclear membrane and the actin cytoskeleton.,” *Exp. Cell Res.*, vol. 295, no. 2, pp. 330–9, May 2004.

[233] T. Libotte, H. Zaim, S. Abraham, V. C. Padmakumar, M. Schneider, W. Lu, M. Munck, C. Hutchison, M. Wehnert, B. Fahrenkrog, U. Sauder, U. Aebi, A. A. Noegel, and I. Karakesisoglou, “Lamin A/C-dependent localization of Nesprin-2, a giant scaffolder at the nuclear envelope.,” *Mol. Biol. Cell*, vol. 16, no. 7, pp. 3411–24, Jul. 2005.

[234] Y.-Y. Zhen, T. Libotte, M. Munck, A. A. Noegel, and E. Korenbaum, “NUANCE, a giant protein connecting the nucleus and actin cytoskeleton.,” *J. Cell Sci.*, vol. 115, no. Pt 15, pp. 3207–22, Aug. 2002.

[235] A. Sandilands, X. Wang, A. M. Hutcheson, J. James, A. R. Prescott, A. Wegener, M. Pekny, X. Gong, and R. A. Quinlan, “Bfsp2 mutation found in mouse 129 strains causes the loss of CP49 and induces vimentin-dependent changes in the lens fibre cell cytoskeleton,” *Exp. Eye Res.*, vol. 78, no. 1, pp. 109–123, Jan. 2004.

[236] M. Tanno, “Tumor necrosis factor-induced protection of the murine heart is independent of p38-MAPK activation,” *J. Mol. Cell. Cardiol.*, vol. 35, no. 12, pp. 1523–1527, Dec. 2003.

[237] J. L. Elliott, M. Der Perng, A. R. Prescott, K. A. Jansen, G. H. Koenderink, and R. A. Quinlan, “The specificity of the interaction between αB-crystallin and desmin filaments and its impact on filament aggregation and cell viability.,” *Philos. Trans. R. Soc. Lond. B. Biol. Sci.*, vol. 368, no. 1617, p. 20120375, May 2013.

[238] X. Wu, B. Currall, T. Yamashita, L. L. Parker, R. Hallworth, and J. Zuo, “Prestin-prestin and prestin-GLUT5 interactions in HEK293T cells.,” *Dev. Neurobiol.*, vol. 67, no. 4, pp. 483–97, Mar. 2007.

[239] B. Thaa, A. Herrmann, and M. Veit, “Intrinsic cytoskeleton-dependent clustering of influenza virus M2 protein with hemagglutinin assessed by FLIM-FRET.,” *J. Virol.*, vol. 84, no. 23, pp. 12445–9, Dec. 2010.

[240] C. R. Bone, E. C. Tapley, M. Gorjánácz, and D. A. Starr, “The Caenorhabditis elegans SUN protein UNC-84 interacts with lamin to transfer forces from the cytoplasm to the nucleoskeleton during nuclear migration.,” *Mol. Biol. Cell*, vol. 25, no. 18, pp. 2853–65, Sep. 2014.

[241] B. Burke and K. J. Roux, “Nuclei take a position: managing nuclear location.,” *Dev. Cell*, vol. 17, no. 5, pp. 587–97, Nov. 2009.

[242] J. L. V. Broers, “Decreased mechanical stiffness in LMNA-/- cells is caused by defective nucleo-cytoskeletal integrity: implications for the development of laminopathies,” *Hum. Mol. Genet.*, vol. 13, no. 21, pp. 2567–2580, Sep. 2004.

[243] J. W. Foster, R. R. Jones, C. A. Bippes, R. M. Gouveia, and C. J. Connon, “Differential nuclear expression of Yap in basal epithelial cells across the cornea and substrates of differing stiffness.,” *Exp. Eye Res.*, vol. 127, pp. 37–41, Oct. 2014.

[244] S. C. Wei, L. Fattet, J. H. Tsai, Y. Guo, V. H. Pai, H. E. Majeski, A. C. Chen, R. L. Sah, S. S. Taylor, A. J. Engler, and J. Yang, “Matrix stiffness drives epithelial-mesenchymal transition and tumour metastasis through a TWIST1-G3BP2 mechanotransduction pathway.,” *Nat. Cell Biol.*, vol. 17, no. 5, pp. 678–688, Apr. 2015.

[245] S. Prauzner-Bechcicki, J. Raczkowska, E. Madej, J. Pabijan, J. Lukes, J. Sepitka, J. Rysz, K. Awsiuk, A. Bernasik, A. Budkowski, and M. Lekka, “PDMS substrate stiffness affects the morphology and growth profiles of cancerous prostate and melanoma cells.,” *J. Mech. Behav. Biomed. Mater.*, vol. 41, pp. 13–22, Jan. 2015.

[246] J. Ahringer, “Control of cell polarity and mitotic spindle positioning in animal cells,” *Curr. Opin. Cell Biol.*, vol. 15, no. 1, pp. 73–81, Feb. 2003.

[247] I. Dupin and S. Etienne-Manneville, “Nuclear positioning: mechanisms and functions.,” *Int. J. Biochem. Cell Biol.*, vol. 43, no. 12, pp. 1698–707, Dec. 2011.

[248] M. A. Chapman, J. Zhang, I. Banerjee, L. T. Guo, Z. Zhang, G. D. Shelton, K. Ouyang, R. L. Lieber, and J. Chen, “Disruption of both nesprin 1 and desmin results in nuclear anchorage defects and fibrosis in skeletal muscle.,” *Hum. Mol. Genet.*, vol. 23, no. 22, pp. 5879–92, Nov. 2014.

[249] J. Zhang, A. Felder, Y. Liu, L. T. Guo, S. Lange, N. D. Dalton, Y. Gu, K. L. Peterson, A. P. Mizisin, G. D. Shelton, R. L. Lieber, and J. Chen, “Nesprin 1 is critical for nuclear positioning and anchorage.,” *Hum. Mol. Genet.*, vol. 19, no. 2, pp. 329–41, Jan. 2010.

[250] K. Lei, X. Zhang, X. Ding, X. Guo, M. Chen, B. Zhu, T. Xu, Y. Zhuang, R. Xu, and M. Han, “SUN1 and SUN2 play critical but partially redundant roles in anchoring nuclei in skeletal muscle cells in mice.,” *Proc. Natl. Acad. Sci. U. S. A.*, vol. 106, no. 25, pp. 10207–12, Jun. 2009.

[251] R. N. Rashmi, B. Eckes, G. Glöckner, M. Groth, S. Neumann, J. Gloy, L. Sellin, G. Walz, M. Schneider, I. Karakesisoglou, L. Eichinger, and A. A. Noegel, “The nuclear envelope protein Nesprin-2 has roles in cell proliferation and differentiation during wound healing.,” *Nucleus*, vol. 3, no. 2, pp. 172–86, Mar. 2012.

[252] D. T. Warren, T. Tajsic, J. A. Mellad, R. Searles, Q. Zhang, and C. M. Shanahan, “Novel nuclear nesprin-2 variants tether active extracellular signal-regulated MAPK1 and MAPK2 at promyelocytic leukemia protein nuclear bodies and act to regulate smooth muscle cell proliferation.,” *J. Biol. Chem.*, vol. 285, no. 2, pp. 1311–20, Jan. 2010.

[253] G. Mazzoleni, D. Di Lorenzo, and N. Steimberg, “Modelling tissues in 3D: the next future of pharmaco-toxicology and food research?,” *Genes Nutr.*, vol. 4, no. 1, pp. 13–22, Dec. 2008.

[254] D. Bazou, “Biochemical properties of encapsulated high-density 3-D HepG2 aggregates formed in an ultrasound trap for application in hepatotoxicity studies : Biochemical responses of encapsulated 3-D HepG2 aggregates.,” *Cell Biol. Toxicol.*, vol. 26, no. 2, pp. 127–41, Apr. 2010.

[255] G. Y. Lee, P. A. Kenny, E. H. Lee, and M. J. Bissell, “Three-dimensional culture models of normal and malignant breast epithelial cells.,” *Nat. Methods*, vol. 4, no. 4, pp. 359–65, Apr. 2007.

[256] A. S. Salimath and A. J. García, “Biofunctional hydrogels for skeletal muscle constructs.,” *J. Tissue Eng. Regen. Med.*, Mar. 2014.

[257] H. Taketa, G. A. Sathi, M. Farahat, K. A. Rahman, T. Sakai, Y. Hirano, T. Kuboki, Y. Torii, and T. Matsumoto, “Peptide-modified Substrate for Modulating Gland Tissue Growth and Morphology In Vitro.,” *Sci. Rep.*, vol. 5, p. 11468, Jan. 2015.

[258] M. Sušec, S. C. Ligon, J. Stampfl, R. Liska, and P. Krajnc, “Hierarchically porous materials from layer-by-layer photopolymerization of high internal phase emulsions.,” *Macromol. Rapid Commun.*, vol. 34, no. 11, pp. 938–43, Jul. 2013.

[259] C. Decaestecker, O. Debeir, P. Van Ham, and R. Kiss, “Can anti-migratory drugs be screened in vitro? A review of 2D and 3D assays for the quantitative analysis of cell migration.,” *Med. Res. Rev.*, vol. 27, no. 2, pp. 149–76, Mar. 2007.

[260] N. Kramer, A. Walzl, C. Unger, M. Rosner, G. Krupitza, M. Hengstschläger, and H. Dolznig, “In vitro cell migration and invasion assays.,” *Mutat. Res.*, vol. 752, no. 1, pp. 10–24, Jan. 2013.

[261] J. Marshall, “Transwell(®) invasion assays.,” *Methods Mol. Biol.*, vol. 769, pp. 97–110, Jan. 2011.

[262] A. L. Olins, T. V Hoang, M. Zwerger, H. Herrmann, H. Zentgraf, A. A. Noegel, I. Karakesisoglou, D. Hodzic, and D. E. Olins, “The LINC-less granulocyte nucleus.,” *Eur. J. Cell Biol.*, vol. 88, no. 4, pp. 203–14, Apr. 2009.

[263] X. M. Xu, “A Molecular Basis Accounted for the Malignant Features of Breast Cancer Cells,” Apr. 2012.

[264] K. N. Dahl, A. J. S. Ribeiro, and J. Lammerding, “Nuclear shape, mechanics, and mechanotransduction.,” *Circ. Res.*, vol. 102, no. 11, pp. 1307–18, Jun. 2008.

[265] M. Nagayama, H. Haga, and K. Kawabata, “Drastic change of local stiffness distribution correlating to cell migration in living fibroblasts.,” *Cell Motil. Cytoskeleton*, vol. 50, no. 4, pp. 173–9, Dec. 2001.

[266] P. M. Davidson, C. Denais, M. C. Bakshi, and J. Lammerding, “Nuclear deformability constitutes a rate-limiting step during cell migration in 3-D environments.,” *Cell. Mol. Bioeng.*, vol. 7, no. 3, pp. 293–306, Sep. 2014.

[267] T. Harada, J. Swift, J. Irianto, J.-W. Shin, K. R. Spinler, A. Athirasala, R. Diegmiller, P. C. D. P. Dingal, I. L. Ivanovska, and D. E. Discher, “Nuclear lamin stiffness is a barrier to 3D migration, but softness can limit survival.,” *J. Cell Biol.*, vol. 204, no. 5, pp. 669–82, Mar. 2014.

[268] G. Giannone, “Super-resolution links vinculin localization to function in focal adhesions,” *Nat. Cell Biol.*, vol. 17, no. 7, pp. 845–847, Jun. 2015.

[269] M.-F. Carlier, S. Wiesner, C. Le Clainche, and D. Pantaloni, “Actin-based motility as a self-organized system: mechanism and reconstitution in vitro.,” *C. R. Biol.*, vol. 326, no. 2, pp. 161–70, Feb. 2003.

[270] J. Qiu, L. Zhong, M. Zhou, D. Chen, X. Huang, J. Chen, M. Chen, H. Ni, and Z. Cai, “Establishment and characterization of a reconstructed Chinese human epidermis model.,” *Int. J. Cosmet. Sci.*, Jun. 2015.

[271] R. L. Eckert, “Structure, function, and differentiation of the keratinocyte.,” *Physiol. Rev.*, vol. 69, no. 4, pp. 1316–46, Oct. 1989.

[272] P. M. Davidson, C. Denais, M. C. Bakshi, and J. Lammerding, “Nuclear deformability constitutes a rate-limiting step during cell migration in 3-D environments.,” *Cell. Mol. Bioeng.*, vol. 7, no. 3, pp. 293–306, Sep. 2014.

[273] R. Chiotaki, H. Polioudaki, and P. A. Theodoropoulos, “Differential nuclear shape dynamics of invasive andnon-invasive breast cancer cells are associated with actin cytoskeleton organization and stability,” *Biochem. Cell Biol.*, vol. 92, no. 4, pp. 287–295, Aug. 2014.

[274] K. Richter, M. Nessling, and P. Lichter, “Experimental evidence for the influence of molecular crowding on nuclear architecture.,” *J. Cell Sci.*, vol. 120, no. Pt 9, pp. 1673–80, May 2007.

[275] E. Louvet, A. Yoshida, M. Kumeta, and K. Takeyasu, “Probing the stiffness of isolated nucleoli by atomic force microscopy.,” *Histochem. Cell Biol.*, vol. 141, no. 4, pp. 365–81, Apr. 2014.

[276] X. Sui, N. Kong, L. Ye, W. Han, J. Zhou, Q. Zhang, C. He, and H. Pan, “p38 and JNK MAPK pathways control the balance of apoptosis and autophagy in response to chemotherapeutic agents.,” *Cancer Lett.*, vol. 344, no. 2, pp. 174–9, Mar. 2014.

[277] F. van Roy and G. Berx, “The cell-cell adhesion molecule E-cadherin.,” *Cell. Mol. Life Sci.*, vol. 65, no. 23, pp. 3756–88, Nov. 2008.

[278] F. M. Watt, “Terminal differentiation of epidermal keratinocytes.,” *Curr. Opin. Cell Biol.*, vol. 1, no. 6, pp. 1107–15, Dec. 1989.

[279] Y. Li, D. Lovett, Q. Zhang, S. Neelam, R. A. Kuchibhotla, R. Zhu, G. G. Gundersen, T. P. Lele, and R. B. Dickinson, “Moving Cell Boundaries Drive Nuclear Shaping during Cell Spreading.,” *Biophys. J.*, vol. 109, no. 4, pp. 670–86, Aug. 2015.

[280] W. H. Ziegler, R. C. Liddington, and D. R. Critchley, “The structure and regulation of vinculin.,” *Trends Cell Biol.*, vol. 16, no. 9, pp. 453–60, Sep. 2006.

[281] M. Brosig, J. Ferralli, L. Gelman, M. Chiquet, and R. Chiquet-Ehrismann, “Interfering with the connection between the nucleus and the cytoskeleton affects nuclear rotation, mechanotransduction and myogenesis.,” *Int. J. Biochem. Cell Biol.*, vol. 42, no. 10, pp. 1717–28, Oct. 2010.

[282] K. N. Randles, L. T. Lam, C. A. Sewry, M. Puckelwartz, D. Furling, M. Wehnert, E. M. McNally, and G. E. Morris, “Nesprins, but not sun proteins, switch isoforms at the nuclear envelope during muscle development.,” *Dev. Dyn.*, vol. 239, no. 3, pp. 998–1009, Mar. 2010.

[283] E. Faurobert, A.-P. Bouin, and C. Albiges-Rizo, “Microenvironment, tumor cell plasticity, and cancer.,” *Curr. Opin. Oncol.*, vol. 27, no. 1, pp. 64–70, Jan. 2015.

[284] M. Krause, J. Te Riet, and K. Wolf, “Probing the compressibility of tumor cell nuclei by combined atomic force-confocal microscopy.,” *Phys. Biol.*, vol. 10, no. 6, p. 065002, Dec. 2013.

[285] B. Hampoelz and T. Lecuit, “Nuclear mechanics in differentiation and development.,” *Curr. Opin. Cell Biol.*, vol. 23, no. 6, pp. 668–75, Dec. 2011.

[286] N. Caille, O. Thoumine, Y. Tardy, and J.-J. Meister, “Contribution of the nucleus to the mechanical properties of endothelial cells.,” *J. Biomech.*, vol. 35, no. 2, pp. 177–87, Feb. 2002.

[287] F. Guilak, J. R. Tedrow, and R. Burgkart, “Viscoelastic properties of the cell nucleus.,” *Biochem. Biophys. Res. Commun.*, vol. 269, no. 3, pp. 781–6, Mar. 2000.

[288] A. C. Rowat, L. J. Foster, M. M. Nielsen, M. Weiss, and J. H. Ipsen, “Characterization of the elastic properties of the nuclear envelope.,” *J. R. Soc. Interface*, vol. 2, no. 2, pp. 63–9, Mar. 2005.

[289] E. Tinois, M. Faure, P. Chatelain, P. Vallier, and D. Schmitt, “Growth and differentiation of human keratinocytes on extracellular matrix.,” *Arch. Dermatol. Res.*, vol. 279, no. 4, pp. 241–6, Jan. 1987.

[290] N. Haddad and M. Paulin-Levasseur, “Effects of heat shock on the distribution and expression levels of nuclear proteins in HeLa S3 cells.,” *J. Cell. Biochem.*, vol. 105, no. 6, pp. 1485–500, Dec. 2008.

[291] C. Capanni, R. Del Coco, S. Squarzoni, M. Columbaro, E. Mattioli, D. Camozzi, A. Rocchi, K. Scotlandi, N. Maraldi, R. Foisner, and G. Lattanzi, “Prelamin A is involved in early steps of muscle differentiation.,” *Exp. Cell Res.*, vol. 314, no. 20, pp. 3628–37, Dec. 2008.

[292] E. Mattioli, M. Columbaro, C. Capanni, N. M. Maraldi, V. Cenni, K. Scotlandi, M. T. Marino, L. Merlini, S. Squarzoni, and G. Lattanzi, “Prelamin A-mediated recruitment of SUN1 to the nuclear envelope directs nuclear positioning in human muscle.,” *Cell Death Differ.*, vol. 18, no. 8, pp. 1305–15, Aug. 2011.

[293] A. E. Boggs, M. I. Vitolo, R. A. Whipple, M. S. Charpentier, O. G. Goloubeva, O. B. Ioffe, K. C. Tuttle, J. Slovic, Y. Lu, G. B. Mills, and S. S. Martin, “α-Tubulin acetylation elevated in metastatic and basal-like breast cancer cells promotes microtentacle formation, adhesion, and invasive migration.,” *Cancer Res.*, vol. 75, no. 1, pp. 203–15, Jan. 2015.

[294] A. B. Chambliss, S. B. Khatau, N. Erdenberger, D. K. Robinson, D. Hodzic, G. D. Longmore, and D. Wirtz, “The LINC-anchored actin cap connects the extracellular milieu to the nucleus for ultrafast mechanotransduction.,” *Sci. Rep.*, vol. 3, p. 1087, Jan. 2013.

[295] M. Brosig, J. Ferralli, L. Gelman, M. Chiquet, and R. Chiquet-Ehrismann, “Interfering with the connection between the nucleus and the cytoskeleton affects nuclear rotation, mechanotransduction and myogenesis.,” *Int. J. Biochem. Cell Biol.*, vol. 42, no. 10, pp. 1717–28, Oct. 2010.

[296] Y.-H. Chi, K. Haller, J.-M. Peloponese, and K.-T. Jeang, “Histone acetyltransferase hALP and nuclear membrane protein hsSUN1 function in de-condensation of mitotic chromosomes.,” *J. Biol. Chem.*, vol. 282, no. 37, pp. 27447–58, Sep. 2007.

[297] Y. Gruenbaum, A. Margalit, R. D. Goldman, D. K. Shumaker, and K. L. Wilson, “The nuclear lamina comes of age.,” *Nat. Rev. Mol. Cell Biol.*, vol. 6, no. 1, pp. 21–31, Jan. 2005.

[298] B. Mitmaker, L. R. Begin, and P. H. Gordon, “Nuclear shape as a prognostic discriminant in colorectal carcinoma,” *Dis. Colon Rectum*, vol. 34, no. 3, pp. 249–259, Mar. 1991.

[299] K. L. Wydner, J. A. McNeil, F. Lin, H. J. Worman, and J. B. Lawrence, “Chromosomal Assignment of Human Nuclear Envelope Protein Genes LMNA, LMNB1, and LBR by Fluorescencein SituHybridization,” *Genomics*, vol. 32, no. 3, pp. 474–478, Mar. 1996.

[300] M. Giacca, L. Zentilin, P. Norio, S. Diviacco, D. Dimitrova, G. Contreas, G. Biamonti, G. Perini, F. Weighardt, and S. Riva, “Fine mapping of a replication origin of human DNA.,” *Proc. Natl. Acad. Sci. U. S. A.*, vol. 91, no. 15, pp. 7119–23, Jul. 1994.

[301] L. Vergnes, M. Péterfy, M. O. Bergo, S. G. Young, and K. Reue, “Lamin B1 is required for mouse development and nuclear integrity.,” *Proc. Natl. Acad. Sci. U. S. A.*, vol. 101, no. 28, pp. 10428–33, Jul. 2004.

[302] V. Butin-Israeli, S. A. Adam, N. Jain, G. L. Otte, D. Neems, L. Wiesmüller, S. L. Berger, and R. D. Goldman, “Role of lamin b1 in chromatin instability.,” *Mol. Cell. Biol.*, vol. 35, no. 5, pp. 884–98, Mar. 2015.

[303] G. Bonne, M. R. Di Barletta, S. Varnous, H. M. Bécane, E. H. Hammouda, L. Merlini, F. Muntoni, C. R. Greenberg, F. Gary, J. A. Urtizberea, D. Duboc, M. Fardeau, D. Toniolo, and K. Schwartz, “Mutations in the gene encoding lamin A/C cause autosomal dominant Emery-Dreifuss muscular dystrophy.,” *Nat. Genet.*, vol. 21, no. 3, pp. 285–8, Mar. 1999.

[304] S. Quijano-Roy, B. Mbieleu, C. G. Bönnemann, P.-Y. Jeannet, J. Colomer, N. F. Clarke, J.-M. Cuisset, H. Roper, L. De Meirleir, A. D’Amico, R. Ben Yaou, A. Nascimento, A. Barois, L. Demay, E. Bertini, A. Ferreiro, C. A. Sewry, N. B. Romero, M. Ryan, F. Muntoni, P. Guicheney, P. Richard, G. Bonne, and B. Estournet, “De novo LMNA mutations cause a new form of congenital muscular dystrophy.,” *Ann. Neurol.*, vol. 64, no. 2, pp. 177–86, Aug. 2008.

[305] Z. Wu, L. Wu, D. Weng, D. Xu, J. Geng, and F. Zhao, “Reduced expression of lamin A/C correlates with poor histological differentiation and prognosis in primary gastric carcinoma.,” *J. Exp. Clin. Cancer Res.*, vol. 28, p. 8, Jan. 2009.

[306] J. L. Broers, Y. Raymond, M. K. Rot, H. Kuijpers, S. S. Wagenaar, and F. C. Ramaekers, “Nuclear A-type lamins are differentially expressed in human lung cancer subtypes.,” *Am. J. Pathol.*, vol. 143, no. 1, pp. 211–20, Jul. 1993.

[307] B. Stadelmann, E. Khandjian, A. Hirt, A. Lüthy, R. Weil, and H. P. Wagner, “Repression of nuclear lamin A and C gene expression in human acute lymphoblastic leukemia and non-Hodgkin’s lymphoma cells.,” *Leuk. Res.*, vol. 14, no. 9, pp. 815–21, Jan. 1990.

[308] C. D. Capo-chichi, K. Q. Cai, F. Simpkins, P. Ganjei-Azar, A. K. Godwin, and X.-X. Xu, “Nuclear envelope structural defects cause chromosomal numerical instability and aneuploidy in ovarian cancer.,” *BMC Med.*, vol. 9, p. 28, Jan. 2011.

[309] C. D. Capo-chichi, K. Q. Cai, J. Smedberg, P. Ganjei-Azar, A. K. Godwin, and X.-X. Xu, “Loss of A-type lamin expression compromises nuclear envelope integrity in breast cancer.,” *Chin. J. Cancer*, vol. 30, no. 6, pp. 415–25, Jun. 2011.

[310] M. E. Hudson, I. Pozdnyakova, K. Haines, G. Mor, and M. Snyder, “Identification of differentially expressed proteins in ovarian cancer using high-density protein microarrays.,” *Proc. Natl. Acad. Sci. U. S. A.*, vol. 104, no. 44, pp. 17494–9, Oct. 2007.

[311] N. D. Willis, T. R. Cox, S. F. Rahman-Casañs, K. Smits, S. A. Przyborski, P. van den Brandt, M. van Engeland, M. Weijenberg, R. G. Wilson, A. de Bruïne, and C. J. Hutchison, “Lamin A/C is a risk biomarker in colorectal cancer.,” *PLoS One*, vol. 3, no. 8, p. e2988, Jan. 2008.

[312] L. Kong, G. Schäfer, H. Bu, Y. Zhang, Y. Zhang, and H. Klocker, “Lamin A/C protein is overexpressed in tissue-invading prostate cancer and promotes prostate cancer cell growth, migration and invasion through the PI3K/AKT/PTEN pathway.,” *Carcinogenesis*, vol. 33, no. 4, pp. 751–9, Apr. 2012.

[313] C. M. L. J. Tilli, F. C. S. Ramaekers, J. L. V Broers, C. J. Hutchison, and H. A. M. Neumann, “Lamin expression in normal human skin, actinic keratosis, squamous cell carcinoma and basal cell carcinoma.,” *Br. J. Dermatol.*, vol. 148, no. 1, pp. 102–9, Jan. 2003.

[314] L. Crabbe, A. J. Cesare, J. M. Kasuboski, J. A. J. Fitzpatrick, and J. Karlseder, “Human telomeres are tethered to the nuclear envelope during postmitotic nuclear assembly.,” *Cell Rep.*, vol. 2, no. 6, pp. 1521–9, Dec. 2012.

[315] V. Nikolova-Krstevski, C. Leimena, X.-H. Xiao, S. Kesteven, J. C. Tan, L. S. Yeo, Z.-Y. Yu, Q. Zhang, A. Carlton, S. Head, C. Shanahan, M. P. Feneley, and D. Fatkin, “Nesprin-1 and actin contribute to nuclear and cytoskeletal defects in lamin A/C-deficient cardiomyopathy.,” *J. Mol. Cell. Cardiol.*, vol. 50, no. 3, pp. 479–86, Mar. 2011.

[316] T. W. Chittenden, E. A. Howe, A. C. Culhane, R. Sultana, J. M. Taylor, C. Holmes, and J. Quackenbush, “Functional classification analysis of somatically mutated genes in human breast and colorectal cancers.,” *Genomics*, vol. 91, no. 6, pp. 508–11, Jun. 2008.

[317] J. A. Doherty, M. A. Rossing, K. L. Cushing-Haugen, C. Chen, D. J. Van Den Berg, A. H. Wu, M. C. Pike, R. B. Ness, K. Moysich, G. Chenevix-Trench, J. Beesley, P. M. Webb, J. Chang-Claude, S. Wang-Gohrke, M. T. Goodman, G. Lurie, P. J. Thompson, M. E. Carney, E. Hogdall, S. K. Kjaer, C. Hogdall, E. L. Goode, J. M. Cunningham, B. L. Fridley, R. A. Vierkant, A. Berchuck, P. G. Moorman, J. M. Schildkraut, R. T. Palmieri, D. W. Cramer, K. L. Terry, H. P. Yang, M. Garcia-Closas, S. Chanock, J. Lissowska, H. Song, P. D. P. Pharoah, M. Shah, B. Perkins, V. McGuire, A. S. Whittemore, R. A. Di Cioccio, A. Gentry-Maharaj, U. Menon, S. A. Gayther, S. J. Ramus, A. Ziogas, W. Brewster, H. Anton-Culver, and C. L. Pearce, “ESR1/SYNE1 polymorphism and invasive epithelial ovarian cancer risk: an Ovarian Cancer Association Consortium study.,” *Cancer Epidemiol. Biomarkers Prev.*, vol. 19, no. 1, pp. 245–50, Jan. 2010.

[318] S. Cartwright and I. Karakesisoglou, “Nesprins in health and disease.,” *Semin. Cell Dev. Biol.*, vol. 29, pp. 169–79, May 2014.

[319] “WHO breast cancer statistics.” [Online]. Available: http://www.iarc.fr/en/media-centre/pr/2013/pdfs/pr223_E.pdf. [Accessed: 13-Sep-2015].

[320] S. Oved and Y. Yarden, “Signal transduction: molecular ticket to enter cells.,” *Nature*, vol. 416, no. 6877, pp. 133–6, Mar. 2002.

[321] A. D. Thor, I. I. Moore DH, S. M. Edgerton, E. S. Kawasaki, E. Reihsaus, H. T. Lynch, J. N. Marcus, L. Schwartz, L. C. Chen, and B. H. Mayall, “Accumulation of p53 tumor suppressor gene protein: an independent marker of prognosis in breast cancers.,” *J. Natl. Cancer Inst.*, vol. 84, no. 11, pp. 845–55, Jun. 1992.

[322] A. Ioakim-Liossi, P. Karakitsos, C. Markopoulos, K. Aroni, P. Athanassiadou, K. Delivelioti, P. Athanassiades, and G. Vaiopoulos, “p53 protein expression and

oestrogen and progesterone receptor status in invasive ductal breast carcinomas.," *Cytopathology*, vol. 12, no. 3, pp. 197–202, Jun. 2001.

[323] K. Vermeulen, D. R. Van Bockstaele, and Z. N. Berneman, "The cell cycle: a review of regulation, deregulation and therapeutic targets in cancer.," *Cell Prolif.*, vol. 36, no. 3, pp. 131–49, Jun. 2003.

[324] P. S. Steeg and Q. Zhou, "Cyclins and breast cancer.," *Breast Cancer Res. Treat.*, vol. 52, no. 1–3, pp. 17–28, Jan. 1998.

[325] M. Lodén, M. Stighall, N. H. Nielsen, G. Roos, S. O. Emdin, H. Ostlund, and G. Landberg, "The cyclin D1 high and cyclin E high subgroups of breast cancer: separate pathways in tumorogenesis based on pattern of genetic aberrations and inactivation of the pRb node.," *Oncogene*, vol. 21, no. 30, pp. 4680–90, Jul. 2002.

[326] S. Zhao, M. Yi, Y. Yuan, W. Zhuang, D. Zhang, X. Yu, X. Chen, B. Teng, Z. Guan, and Y. Zhang, "Expression of AKAP95, Cx43, CyclinE1 and CyclinD1 in esophageal cancer and their association with the clinical and pathological parameters.," *Int. J. Clin. Exp. Med.*, vol. 8, no. 5, pp. 7324–32, Jan. 2015.

[327] R. Siegel, D. Naishadham, and A. Jemal, "Cancer statistics, 2013.," *CA. Cancer J. Clin.*, vol. 63, no. 1, pp. 11–30, Jan. 2013.

[328] J. H. Tsai and J. Yang, "Epithelial-mesenchymal plasticity in carcinoma metastasis.," *Genes Dev.*, vol. 27, no. 20, pp. 2192–206, Oct. 2013.

[329] B. T. Hennessy, A.-M. Gonzalez-Angulo, K. Stemke-Hale, M. Z. Gilcrease, S. Krishnamurthy, J.-S. Lee, J. Fridlyand, A. Sahin, R. Agarwal, C. Joy, W. Liu, D. Stivers, K. Baggerly, M. Carey, A. Lluch, C. Monteagudo, X. He, V. Weigman, C. Fan, J. Palazzo, G. N. Hortobagyi, L. K. Nolden, N. J. Wang, V. Valero, J. W. Gray, C. M. Perou, and G. B. Mills, "Characterization of a naturally occurring breast cancer subset enriched in epithelial-to-mesenchymal transition and stem cell characteristics.," *Cancer Res.*, vol. 69, no. 10, pp. 4116–24, May 2009.

[330] A. Prat and C. M. Perou, "Deconstructing the molecular portraits of breast cancer.," *Mol. Oncol.*, vol. 5, no. 1, pp. 5–23, Feb. 2011.

[331] N. R. Bertos and M. Park, "Breast cancer - one term, many entities?," *J. Clin. Invest.*, vol. 121, no. 10, pp. 3789–96, Oct. 2011.

[332] B. E. Gould Rothberg and M. B. Bracken, "E-cadherin immunohistochemical expression as a prognostic factor in infiltrating ductal carcinoma of the breast: a systematic review and meta-analysis.," *Breast Cancer Res. Treat.*, vol. 100, no. 2, pp. 139–48, Nov. 2006.

[333] P. J. Kowalski, M. A. Rubin, and C. G. Kleer, "E-cadherin expression in primary carcinomas of the breast and its distant metastases.," *Breast Cancer Res.*, vol. 5, no. 6, pp. R217–22, Jan. 2003.

[334] C. Gaggioli, S. Hooper, C. Hidalgo-Carcedo, R. Grosse, J. F. Marshall, K. Harrington, and E. Sahai, "Fibroblast-led collective invasion of carcinoma cells with differing roles for RhoGTPases in leading and following cells.," *Nat. Cell Biol.*, vol. 9, no. 12, pp. 1392–400, Dec. 2007.

[335] K. J. Cheung, E. Gabrielson, Z. Werb, and A. J. Ewald, “Collective invasion in breast cancer requires a conserved basal epithelial program.,” *Cell*, vol. 155, no. 7, pp. 1639–51, Dec. 2013.

[336] S. P. Carey, A. Starchenko, A. L. McGregor, and C. A. Reinhart-King, “Leading malignant cells initiate collective epithelial cell invasion in a three-dimensional heterotypic tumor spheroid model.,” *Clin. Exp. Metastasis*, vol. 30, no. 5, pp. 615–30, Jun. 2013.

[337] J. Condeelis and J. W. Pollard, “Macrophages: obligate partners for tumor cell migration, invasion, and metastasis.,” *Cell*, vol. 124, no. 2, pp. 263–6, Jan. 2006.

[338] R. Guiet, E. Van Goethem, C. Cougoule, S. Balor, A. Valette, T. Al Saati, C. A. Lowell, V. Le Cabec, and I. Maridonneau-Parini, “The process of macrophage migration promotes matrix metalloproteinase-independent invasion by tumor cells.,” *J. Immunol.*, vol. 187, no. 7, pp. 3806–14, Oct. 2011.

[339] M. Roh-Johnson, J. J. Bravo-Cordero, A. Patsialou, V. P. Sharma, P. Guo, H. Liu, L. Hodgson, and J. Condeelis, “Macrophage contact induces RhoA GTPase signaling to trigger tumor cell intravasation.,” *Oncogene*, vol. 33, no. 33, pp. 4203–12, Aug. 2014.

[340] V. Masola, A. Carraro, G. Zaza, G. Bellin, U. Montin, P. Violi, A. Lupo, and U. Tedeschi, “Epithelial to mesenchymal transition in the liver field: the double face of Everolimus in vitro.,” *BMC Gastroenterol.*, vol. 15, no. 1, p. 118, Jan. 2015.

[341] M. M. Vantangoli, S. J. Madnick, S. M. Huse, P. Weston, and K. Boekelheide, “MCF-7 Human Breast Cancer Cells Form Differentiated Microtissues in Scaffold-Free Hydrogels.,” *PLoS One*, vol. 10, no. 8, p. e0135426, Jan. 2015.

[342] W. Kamphuis, C. Mamber, M. Moeton, L. Kooijman, J. A. Sluijs, A. H. P. Jansen, M. Verveer, L. R. de Groot, V. D. Smith, S. Rangarajan, J. J. Rodríguez, M. Orre, and E. M. Hol, “GFAP isoforms in adult mouse brain with a focus on neurogenic astrocytes and reactive astrogliosis in mouse models of Alzheimer disease.,” *PLoS One*, vol. 7, no. 8, p. e42823, Jan. 2012.

[343] A. Batistatou, D. Stefanou, E. Arkoumani, and N. J. Agnantis, “The usefulness of p63 as a marker of breast myoepithelial cells.,” *In Vivo*, vol. 17, no. 6, pp. 573–6, Jan. 2003.

[344] A. A. McDonough, L. C. Veiras, J. N. Minas, and D. L. Ralph, “Considerations when quantitating protein abundance by immunoblot.,” *Am. J. Physiol. Cell Physiol.*, vol. 308, no. 6, pp. C426–33, Mar. 2015.

[345] C. Albiges-Rizo, O. Destaing, B. Fourcade, E. Planus, and M. R. Block, “Actin machinery and mechanosensitivity in invadopodia, podosomes and focal adhesions.,” *J. Cell Sci.*, vol. 122, no. Pt 17, pp. 3037–49, Sep. 2009.

[346] R. Poincloux, F. Lizárraga, and P. Chavrier, “Matrix invasion by tumour cells: a focus on MT1-MMP trafficking to invadopodia.,” *J. Cell Sci.*, vol. 122, no. Pt 17, pp. 3015–24, Sep. 2009.

[347] V. Marchesin, G. Montagnac, and P. Chavrier, “ARF6 Promotes the Formation of Rac1 and WAVE-Dependent Ventral F-Actin Rosettes in Breast Cancer Cells in Response to Epidermal Growth Factor,” *PLoS One*, vol. 10, no. 3, p. e0121747, Mar. 2015.

[348] S. J. Heasman and A. J. Ridley, “Mammalian Rho GTPases: new insights into their functions from in vivo studies.,” *Nat. Rev. Mol. Cell Biol.*, vol. 9, no. 9, pp. 690–701, Sep. 2008.

[349] E. D. Hay, “The mesenchymal cell, its role in the embryo, and the remarkable signaling mechanisms that create it.,” *Dev. Dyn.*, vol. 233, no. 3, pp. 706–20, Jul. 2005.

[350] M. G. Mendez, S.-I. Kojima, and R. D. Goldman, “Vimentin induces changes in cell shape, motility, and adhesion during the epithelial to mesenchymal transition.,” *FASEB J.*, vol. 24, no. 6, pp. 1838–51, Jun. 2010.

[351] Y.-S. Chou and M.-H. Yang, “Epithelial-mesenchymal transition-related factors in solid tumor and hematological malignancy.,” *J. Chin. Med. Assoc.*, vol. 78, no. 8, pp. 438–45, Aug. 2015.

[352] E. Gladilin, P. Gonzalez, and R. Eils, “Dissecting the contribution of actin and vimentin intermediate filaments to mechanical phenotype of suspended cells using high-throughput deformability measurements and computational modeling.,” *J. Biomech.*, vol. 47, no. 11, pp. 2598–605, Aug. 2014.

[353] G. Gong, P. Chen, L. Li, H. Tan, J. Zhou, Y. Zhou, X. Yang, and X. Wu, “Loss of lamin A but not lamin C expression in epithelial ovarian cancer cells is associated with metastasis and poor prognosis.,” *Pathol. Res. Pract.*, vol. 211, no. 2, pp. 175–82, Feb. 2015.

[354] T.-H. Hsieh, C.-L. Chien, Y.-H. Lee, C.-I. Lin, J.-Y. Hsieh, M.-E. Chao, D.-J. Liu, S.-S. Chu, W. Chen, S.-C. Lin, D. M.-T. Ho, R.-S. Liu, C.-H. Lin, T.-T. Wong, and H.-W. Wang, “Downregulation of SUN2, a novel tumor suppressor, mediates miR-221/222-induced malignancy in central nervous system embryonal tumors.,” *Carcinogenesis*, vol. 35, no. 10, pp. 2164–74, Oct. 2014.

[355] G. A. Pihan, A. Purohit, J. Wallace, R. Malhotra, L. Liotta, and S. J. Doxsey, “Centrosome defects can account for cellular and genetic changes that characterize prostate cancer progression.,” *Cancer Res.*, vol. 61, no. 5, pp. 2212–9, Mar. 2001.

[356] G. Pihan and S. J. Doxsey, “Mutations and aneuploidy: co-conspirators in cancer?,” *Cancer Cell*, vol. 4, no. 2, pp. 89–94, Aug. 2003.

[357] B. Delaval and S. J. Doxsey, “Pericentrin in cellular function and disease.,” *J. Cell Biol.*, vol. 188, no. 2, pp. 181–90, Jan. 2010.

[358] N. Martínez, A. Alonso, M. D. Moragues, J. Pontón, and J. Schneider, “The nuclear pore complex protein Nup88 is overexpressed in tumor cells.,” *Cancer Res.*, vol. 59, no. 21, pp. 5408–11, Nov. 1999.

[359] L. Martignetti, B. Tesson, A. Almeida, A. Zinovyev, G. C. Tucker, T. Dubois, and E. Barillot, “Detection of miRNA regulatory effect on triple negative breast cancer transcriptome.,” *BMC Genomics*, vol. 16, p. S4, Jan. 2015.

[360] A. A. Thike, T. Puay Hoon, M. Ikeda, and J. Iqbal, “Increased ID4 expression, accompanied by mutant p53 accumulation and loss of BRCA1/2 proteins in triple negative breast cancer adversely affects survival.,” *Histopathology*, Aug. 2015.

[361] K. Milde-Langosch, T. Löning, and A.-M. Bamberger, “Expression of the CCAAT/enhancer-binding proteins C/EBPalpha, C/EBPbeta and C/EBPdelta in breast cancer: correlations with clinicopathologic parameters and cell-cycle regulatory proteins.,” *Breast Cancer Res. Treat.*, vol. 79, no. 2, pp. 175–85, May 2003.

[362] J. V Moyano, J. R. Evans, F. Chen, M. Lu, M. E. Werner, F. Yehiely, L. K. Diaz, D. Turbin, G. Karaca, E. Wiley, T. O. Nielsen, C. M. Perou, and V. L. Cryns, “AlphaB-crystallin is a novel oncoprotein that predicts poor clinical outcome in breast cancer.,” *J. Clin. Invest.*, vol. 116, no. 1, pp. 261–70, Jan. 2006.

[363] A. J. M. Campbell-Lloyd, J. Mundy, R. Deva, G. Lampe, C. Hawley, G. Boyle, R. Griffin, C. Thompson, and P. Shah, “Is alpha-B crystallin an independent marker for prognosis in lung cancer?,” *Heart. Lung Circ.*, vol. 22, no. 9, pp. 759–66, Sep. 2013.

[364] M. Kabbage, M. Trimeche, H. Ben Nasr, P. Hammann, L. Kuhn, B. Hamrita, A. Chaieb, L. Chouchane, and K. Chahed, “Expression of the molecular chaperone αB-crystallin in infiltrating ductal breast carcinomas and the significance thereof: an immunohistochemical and proteomics-based strategy.,” *Tumour Biol.*, vol. 33, no. 6, pp. 2279–88, Dec. 2012.

[365] Z. Chen, Q. Ruan, S. Han, L. Xi, W. Jiang, H. Jiang, D. A. Ostrov, and J. Cai, “Discovery of structure-based small molecular inhibitor of αB-crystallin against basal-like/triple-negative breast cancer development in vitro and in vivo.,” *Breast Cancer Res. Treat.*, vol. 145, no. 1, pp. 45–59, May 2014.

[366] W. Ma, Y. Teng, H. Hua, J. Hou, T. Luo, and Y. Jiang, “Upregulation of heat shock protein 27 confers resistance to actinomycin D-induced apoptosis in cancer cells.,” *FEBS J.*, vol. 280, no. 18, pp. 4612–24, Sep. 2013.

[367] C.-H. Lee, Y.-T. Wu, H.-C. Hsieh, Y. Yu, A. L. Yu, and W.-W. Chang, “Epidermal growth factor/heat shock protein 27 pathway regulates vasculogenic mimicry activity of breast cancer stem/progenitor cells.,” *Biochimie*, vol. 104, pp. 117–26, Sep. 2014.

[368] G. Viale, M. Gambacorta, G. Coggi, P. Dell’Orto, M. Milani, and C. Doglioni, “Glial fibrillary acidic protein immunoreactivity in normal and diseased human breast.,” *Virchows Arch. A. Pathol. Anat. Histopathol.*, vol. 418, no. 4, pp. 339–48, Jan. 1991.

[369] S. S. Banerjee and M. Harris, “Morphological and immunophenotypic variations in malignant melanoma.,” *Histopathology*, vol. 36, no. 5, pp. 387–402, May 2000.

[370] R. D. Abbott and D. L. Kaplan, “Strategies for improving the physiological relevance of human engineered tissues.,” *Trends Biotechnol.*, vol. 33, no. 7, pp. 401–7, Apr. 2015.

[371] “Epidermal Structure and Function,” *J. Invest. Dermatol.*, vol. 132, no. S2, pp. S75–S88, Sep. 2012.

[372] H. J. Wearing and J. A. Sherratt, “Keratinocyte growth factor signalling: a mathematical model of dermal–epidermal interaction in epidermal wound healing,” *Math. Biosci.*, vol. 165, no. 1, pp. 41–62, May 2000.

[373] R. Moll, W. W. Franke, D. L. Schiller, B. Geiger, and R. Krepler, “The catalog of human cytokeratins: Patterns of expression in normal epithelia, tumors and cultured cells,” *Cell*, vol. 31, no. 1, pp. 11–24, Nov. 1982.

[374] E. Fuchs and H. Green, “Changes in keratin gene expression during terminal differentiation of the keratinocyte,” *Cell*, vol. 19, no. 4, pp. 1033–1042, Apr. 1980.

[375] L. Ma, S. Yamada, D. Wirtz, and P. A. Coulombe, “A ‘hot-spot’ mutation alters the mechanical properties of keratin filament networks.,” *Nat. Cell Biol.*, vol. 3, no. 5, pp. 503–6, May 2001.

[376] P. A. Coulombe, M. L. Kerns, and E. Fuchs, “Epidermolysis bullosa simplex: a paradigm for disorders of tissue fragility.,” *J. Clin. Invest.*, vol. 119, no. 7, pp. 1784–93, Jul. 2009.

[377] V. Vasca, E. Vasca, P. Freiman, D. Marian, A. Luce, M. Mesolella, M. Caraglia, F. Ricciardiello, and T. Duminica, “Keratin 5 expression in squamocellular carcinoma of the head and neck.,” *Oncol. Lett.*, vol. 8, no. 6, pp. 2501–2504, Dec. 2014.

[378] F. Otterbach, A. Bankfalvi, S. Bergner, T. Decker, R. Krech, and W. Boecker, “Cytokeratin 5/6 immunohistochemistry assists the differential diagnosis of atypical proliferations of the breast,” *Histopathology*, vol. 37, no. 3, pp. 232–240, Sep. 2000.

[379] a. Stoler, R. Kopan, M. Duvic, and E. Fuchs, “Use of monospecific antisera and cRNA probes to localize the major changes in keratin expression during normal and abnormal epidermal differentiation,” *Journal of Cell Biology*, vol. 107, no. 2. The Rockefeller University Press, pp. 427–446, 01-Aug-1988.

[380] R. A. Weiss, R. Eichner, and T. T. Sun, “Monoclonal antibody analysis of keratin expression in epidermal diseases: a 48- and 56-kdalton keratin as molecular markers for hyperproliferative keratinocytes.,” *J. Cell Biol.*, vol. 98, no. 4, pp. 1397–406, Apr. 1984.

[381] P. J. Koch and D. R. Roop, “The role of keratins in epidermal development and homeostasis--going beyond the obvious.,” *J. Invest. Dermatol.*, vol. 123, no. 5, pp. x–xi, Nov. 2004.

[382] J. Reichelt, G. Furstenberger, and T. M. Magin, “Loss of keratin 10 leads to mitogen-activated protein kinase (MAPK) activation, increased keratinocyte turnover, and decreased tumor formation in mice.,” *J. Invest. Dermatol.*, vol. 123, no. 5, pp. 973–81, Nov. 2004.

[383] E. Proksch, J. M. Brandner, and J.-M. Jensen, “The skin: an indispensable barrier.,” *Exp. Dermatol.*, vol. 17, no. 12, pp. 1063–72, Dec. 2008.

[384] D. Keswell, S. H. Kidson, and L. M. Davids, “Melanocyte migration is influenced by E-cadherin-dependent adhesion of keratinocytes in both two- and three-dimensional in vitro wound models.,” *Cell Biol. Int.*, vol. 39, no. 2, pp. 169–76, Feb. 2015.

[385] A. Kobielak and E. Fuchs, “Alpha-catenin: at the junction of intercellular adhesion and actin dynamics.,” *Nat. Rev. Mol. Cell Biol.*, vol. 5, no. 8, pp. 614–25, Aug. 2004.

[386] S. Kuphal and A. K. Bosserhoff, “E-cadherin cell-cell communication in melanogenesis and during development of malignant melanoma.,” *Arch. Biochem. Biophys.*, vol. 524, no. 1, pp. 43–7, Aug. 2012.

[387] T. Sun, S. Jackson, J. W. Haycock, and S. MacNeil, “Culture of skin cells in 3D rather than 2D improves their ability to survive exposure to cytotoxic agents.,” *J. Biotechnol.*, vol. 122, no. 3, pp. 372–81, Apr. 2006.

[388] M. Li, A. Moeen Rezakhanlou, C. Chavez-Munoz, A. Lai, and A. Ghahary, “Keratinocyte-releasable factors increased the expression of MMP1 and MMP3 in co-cultured fibroblasts under both 2D and 3D culture conditions.,” *Mol. Cell. Biochem.*, vol. 332, no. 1–2, pp. 1–8, Dec. 2009.

[389] S. Frank, G. H bner, G. Breier, M. T. Longaker, D. G. Greenhalgh, and S. Werner, “Regulation of Vascular Endothelial Growth Factor Expression in Cultured Keratinocytes,” *J. Biol. Chem.*, vol. 270, no. 21, pp. 12607–12613, May 1995.

[390] A. Elkhal, L. Tunggal, and M. Aumailley, “Fibroblasts contribute to the deposition of laminin 5 in the extracellular matrix.,” *Exp. Cell Res.*, vol. 296, no. 2, pp. 223–30, Jun. 2004.

[391] D. T. Woodley, J. R. Stanley, M. J. Reese, and E. J. O’keefe, “Human Dermal Fibroblasts Synthesize Laminin.,” *J. Invest. Dermatol.*, vol. 90, no. 5, pp. 679–683, May 1988.

[392] M. Kawamoto, D. J. Romberger, Y. Nakamura, Y. Adachi, L. Tate, R. F. Ertl, J. R. Spurzem, and S. I. Rennard, “Modulation of fibroblast type I collagen and fibronectin production by bovine bronchial epithelial cells.,” *Am. J. Respir. Cell Mol. Biol.*, vol. 12, no. 4, pp. 425–33, Apr. 1995.

[393] A. Saalbach, T. Janik, M. Busch, D. Herbert, U. Anderegg, and J. C. Simon, “Fibroblasts support migration of monocyte-derived dendritic cells by secretion of PGE2 and MMP-1.,” *Exp. Dermatol.*, vol. 24, no. 8, pp. 598–604, Aug. 2015.

[394] E. A. O’Toole, “Extracellular matrix and keratinocyte migration.,” *Clin. Exp. Dermatol.*, vol. 26, no. 6, pp. 525–30, Sep. 2001.

[395] S. Guo and L. A. Dipietro, “Factors affecting wound healing.,” *J. Dent. Res.*, vol. 89, no. 3, pp. 219–29, Mar. 2010.

[396] A. el-Ghalbzouri, S. Gibbs, E. Lamme, C. A. Van Blitterswijk, and M. Ponec, “Effect of fibroblasts on epidermal regeneration.,” *Br. J. Dermatol.*, vol. 147, no. 2, pp. 230–43, Aug. 2002.

[397] S. Aoki, S. Toda, T. Ando, and H. Sugihara, “Bone marrow stromal cells, preadipocytes, and dermal fibroblasts promote epidermal regeneration in their distinctive fashions.,” *Mol. Biol. Cell*, vol. 15, no. 10, pp. 4647–57, Oct. 2004.

[398] I. Boxman, C. Löwik, L. Aarden, and M. Ponec, “Modulation of IL-6 production and IL-1 activity by keratinocyte-fibroblast interaction.,” *J. Invest. Dermatol.*, vol. 101, no. 3, pp. 316–24, Sep. 1993.

[399] C. Marchese, A. Felici, V. Visco, G. Lucania, M. Igarashi, M. Picardo, L. Frati, and M. R. Torrisi, “Fibroblast growth factor 10 induces proliferation and differentiation of human primary cultured keratinocytes.,” *J. Invest. Dermatol.*, vol. 116, no. 4, pp. 623–8, Apr. 2001.

[400] S. Werner and H. Smola, “Paracrine regulation of keratinocyte proliferation and differentiation.,” *Trends Cell Biol.*, vol. 11, no. 4, pp. 143–6, Apr. 2001.

[401] E. A. Blomme, Y. Sugimoto, Y. C. Lin, C. C. Capen, and T. J. Rosol, “Parathyroid hormone-related protein is a positive regulator of keratinocyte growth factor expression by normal dermal fibroblasts.,” *Mol. Cell. Endocrinol.*, vol. 152, no. 1–2, pp. 189–97, Jun. 1999.

[402] N. Maas-Szabowski, A. Shimotoyodome, and N. E. Fusenig, “Keratinocyte growth regulation in fibroblast cocultures via a double paracrine mechanism.,” *J. Cell Sci.*, vol. 112 (Pt 1, pp. 1843–53, Jun. 1999.

[403] G. Imokawa, “Mechanism of UVB-induced wrinkling of the skin: paracrine cytokine linkage between keratinocytes and fibroblasts leading to the stimulation of elastase.,” *J. Investig. Dermatol. Symp. Proc.*, vol. 14, no. 1, pp. 36–43, Aug. 2009.

[404] N. Nath, S. K. Saraswat, S. Jain, and S. Koteshwar, “Inhibition of proliferation and migration of stricture fibroblasts by epithelial cell-conditioned media.,” *Indian J. Urol.*, vol. 31, no. 2, pp. 111–5, Jan. 2015.

[405] P. Huang, J. Bi, G. R. Owen, W. Chen, A. Rokka, L. Koivisto, J. Heino, L. Häkkinen, and H. Larjava, “Keratinocyte Microvesicles Regulate the Expression of Multiple Genes in Dermal Fibroblasts.,” *J. Invest. Dermatol.*, Aug. 2015.

[406] R. J. Pelham and Y. l Wang, “Cell locomotion and focal adhesions are regulated by substrate flexibility.,” *Proc. Natl. Acad. Sci. U. S. A.*, vol. 94, no. 25, pp. 13661–5, Dec. 1997.

[407] M. Chiquet, A. S. Renedo, F. Huber, and M. Flück, “How do fibroblasts translate mechanical signals into changes in extracellular matrix production?,” *Matrix Biol.*, vol. 22, no. 1, pp. 73–80, Mar. 2003.

[408] K. R. Levental, H. Yu, L. Kass, J. N. Lakins, M. Egeblad, J. T. Erler, S. F. T. Fong, K. Csiszar, A. Giaccia, W. Weninger, M. Yamauchi, D. L. Gasser, and V. M. Weaver, “Matrix crosslinking forces tumor progression by enhancing integrin signaling.,” *Cell*, vol. 139, no. 5, pp. 891–906, Nov. 2009.

[409] J. Rautela, N. Baschuk, C. Y. Slaney, K. M. Jayatilleke, K. Xiao, B. N. Bidwell, E. C. Lucas, E. D. Hawkins, P. Lock, C. S. Wong, W. Chen, R. L. Anderson, P. J. Hertzog, D. M. Andrews, A. Möller, and B. S. Parker, “Loss of Host Type-I IFN Signaling Accelerates Metastasis and Impairs NK-Cell Antitumor Function in Multiple Models of Breast Cancer.,” *Cancer Immunol. Res.*, Jul. 2015.

[410] G. Venugopalan, D. B. Camarillo, K. D. Webster, C. D. Reber, J. A. Sethian, V. M. Weaver, D. A. Fletcher, H. El-Samad, and C. H. Rycroft, “Multicellular Architecture of Malignant Breast Epithelia Influences Mechanics,” *PLoS One*, vol. 9, no. 8, p. e101955, Aug. 2014.

[411] R. W. Tilghman, C. R. Cowan, J. D. Mih, Y. Koryakina, D. Gioeli, J. K. Slack-Davis, B. R. Blackman, D. J. Tschumperlin, and J. T. Parsons, “Matrix rigidity regulates cancer cell growth and cellular phenotype.,” *PLoS One*, vol. 5, no. 9, p. e12905, Jan. 2010.

[412] S. L. Schor, A. M. Schor, and G. W. Bazill, “The effects of fibronectin on the adhesion and migration of chinese hamster ovary cells on collagen substrata.,” *J. Cell Sci.*, vol. 49, pp. 299–310, Jun. 1981.

[413] T. A. Ulrich, A. Jain, K. Tanner, J. L. MacKay, and S. Kumar, “Probing cellular mechanobiology in three-dimensional culture with collagen–agarose matrices,” *Biomaterials*, vol. 31, no. 7, pp. 1875–1884, Mar. 2010.

[414] J. N. Beck, A. Singh, A. R. Rothenberg, J. H. Elisseeff, and A. J. Ewald, “The independent roles of mechanical, structural and adhesion characteristics of 3D hydrogels on the regulation of cancer invasion and dissemination.,” *Biomaterials*, vol. 34, no. 37, pp. 9486–95, Dec. 2013.

[415] M. P. Schwartz, B. D. Fairbanks, R. E. Rogers, R. Rangarajan, M. H. Zaman, and K. S. Anseth, “A synthetic strategy for mimicking the extracellular matrix provides new insight about tumor cell migration.,” *Integr. Biol. (Camb).*, vol. 2, no. 1, pp. 32–40, Jan. 2010.

[416] R. C. Siegel, “Biosynthesis of collagen crosslinks: increased activity of purified lysyl oxidase with reconstituted collagen fibrils.,” *Proc. Natl. Acad. Sci. U. S. A.*, vol. 71, no. 12, pp. 4826–30, Dec. 1974.

[417] W. M. Elbjeirami, E. O. Yonter, B. C. Starcher, and J. L. West, “Enhancing mechanical properties of tissue-engineered constructs via lysyl oxidase crosslinking activity.,” *J. Biomed. Mater. Res. A*, vol. 66, no. 3, pp. 513–21, Sep. 2003.

[418] K. Wolf, I. Mazo, H. Leung, K. Engelke, U. H. von Andrian, E. I. Deryugina, A. Y. Strongin, E.-B. Bröcker, and P. Friedl, “Compensation mechanism in tumor cell migration: mesenchymal-amoeboid transition after blocking of pericellular proteolysis.,” *J. Cell Biol.*, vol. 160, no. 2, pp. 267–77, Jan. 2003.

[419] D. Kedrin, B. Gligorijevic, J. Wyckoff, V. V Verkhusha, J. Condeelis, J. E. Segall, and J. van Rheenen, “Intravital imaging of metastatic behavior through a mammary imaging window.,” *Nat. Methods*, vol. 5, no. 12, pp. 1019–21, Dec. 2008.

[420] L. Gibot, T. Galbraith, J. Huot, and F. A. Auger, “A preexisting microvascular network benefits in vivo revascularization of a microvascularized tissue-engineered skin substitute.,” *Tissue Eng. Part A*, vol. 16, no. 10, pp. 3199–206, Oct. 2010.

[421] L. Gibot, T. Galbraith, J. Huot, and F. A. Auger, “Development of a tridimensional microvascularized human skin substitute to study melanoma biology.,” *Clin. Exp. Metastasis*, vol. 30, no. 1, pp. 83–90, Jan. 2013.

[422] V. M. Schoop, N. Mirancea, and N. E. Fusenig, “Epidermal organization and differentiation of HaCaT keratinocytes in organotypic coculture with human dermal fibroblasts.,” *J. Invest. Dermatol.*, vol. 112, no. 3, pp. 343–53, Mar. 1999.

[423] G. Sriram, P. L. Bigliardi, and M. Bigliardi-Qi, “Fibroblast heterogeneity and its implications for engineering organotypic skin models in vitro.,” *Eur. J. Cell Biol.*, Aug. 2015.

[424] E. Tamariz and F. Grinnell, “Modulation of fibroblast morphology and adhesion during collagen matrix remodeling.,” *Mol. Biol. Cell*, vol. 13, no. 11, pp. 3915–29, Nov. 2002.

[425] C. Ballestrem, B. Hinz, B. A. Imhof, and B. Wehrle-Haller, “Marching at the front and dragging behind: differential alphaVbeta3-integrin turnover regulates focal adhesion behavior.,” *J. Cell Biol.*, vol. 155, no. 7, pp. 1319–32, Dec. 2001.

[426] J. J. Christiansen and A. K. Rajasekaran, “Reassessing epithelial to mesenchymal transition as a prerequisite for carcinoma invasion and metastasis.,” *Cancer Res.*, vol. 66, no. 17, pp. 8319–26, Sep. 2006.

[427] Z.-H. Zheng, X.-J. Sun, H.-T. Zhou, C. Shang, H. Ji, and K.-L. Sun, “Analysis of metastasis suppressing function of E-cadherin in gastric cancer cells by RNAi.,” *World J. Gastroenterol.*, vol. 11, no. 13, pp. 2000–3, Apr. 2005.

[428] S. H. Lang, C. Hyde, I. N. Reid, I. S. Hitchcock, C. A. Hart, A. A. G. Bryden, J.-M. Villette, M. J. Stower, and N. J. Maitland, “Enhanced expression of vimentin in motile prostate cell lines and in poorly differentiated and metastatic prostate carcinoma.,” *Prostate*, vol. 52, no. 4, pp. 253–63, Sep. 2002.

[429] K. Boehnke, N. Mirancea, A. Pavesio, N. E. Fusenig, P. Boukamp, and H.-J. Stark, “Effects of fibroblasts and microenvironment on epidermal regeneration and tissue function in long-term skin equivalents.,” *Eur. J. Cell Biol.*, vol. 86, no. 11–12, pp. 731–46, Dec. 2007.

[430] R. D. Lillie, R. E. Tracy, P. Pizzolato, P. T. Donaldson, and C. Reynolds, “Differential staining of collagen types in paraffin sections: A color change in degraded forms,” *Virchows Arch. A Pathol. Anat. Histol.*, vol. 386, no. 2, pp. 153–159, Apr. 1980.

[431] P. N. Marshall, “Papanicolaou staining--a review.,” *Microsc. Acta*, vol. 87, no. 3, pp. 233–43, May 1983.

[432] P. Friedl and K. Wolf, “Plasticity of cell migration: a multiscale tuning model.,” *J. Cell Biol.*, vol. 188, no. 1, pp. 11–9, Jan. 2010.

[433] A. A. Khalil and P. Friedl, “Determinants of leader cells in collective cell migration,” *Integr. Biol.*, vol. 2, no. 11–12, p. 568, Nov. 2010.

[434] A. J. Ewald, A. Brenot, M. Duong, B. S. Chan, and Z. Werb, “Collective epithelial migration and cell rearrangements drive mammary branching morphogenesis.,” *Dev. Cell*, vol. 14, no. 4, pp. 570–81, Apr. 2008.

[435] J. Notbohm, A. Lesman, D. A. Tirrell, and G. Ravichandran, “Quantifying cell-induced matrix deformation in three dimensions based on imaging matrix fibers.,” *Integr. Biol. (Camb).*, May 2015.

[436] R. P. Martins, J. D. Finan, F. Guilak, and D. A. Lee, “Mechanical regulation of nuclear structure and function.,” *Annu. Rev. Biomed. Eng.*, vol. 14, pp. 431–55, Jan. 2012.

[437] T. Sun, D. Norton, A. J. Ryan, S. MacNeil, and J. W. Haycock, “Investigation of fibroblast and keratinocyte cell-scaffold interactions using a novel 3D cell culture system,” *J. Mater. Sci. Mater. Med.*, vol. 18, no. 2, pp. 321–328, Feb. 2007.

[438] L. N. Castor, “Contact regulation of cell division in an epithelial-like cell line.,” *J. Cell. Physiol.*, vol. 72, no. 3, pp. 161–72, Dec. 1968.

[439] A. Puliafito, L. Hufnagel, P. Neveu, S. Streichan, A. Sigal, D. K. Fygenson, and B. I. Shraiman, “Collective and single cell behavior in epithelial contact inhibition.,” *Proc. Natl. Acad. Sci. U. S. A.*, vol. 109, no. 3, pp. 739–44, Jan. 2012.

[440] C. A. Heckman, “Contact inhibition revisited.,” *J. Cell. Physiol.*, vol. 220, no. 3, pp. 574–5, Sep. 2009.

[441] S.-I. Iwasaki and H. Aoyagi, “Expression of keratin 14 in the basal cells of the lingual epithelium of mice during the morphogenesis of filiform papillae: visualization by fluorescent immunostaining and confocal laser-scanning microscopy in the transmission mode.,” *Odontology*, vol. 95, no. 1, pp. 61–5, Jul. 2007.

[442] H. Zarkoob, S. Bodduluri, S. V Ponnaluri, J. C. Selby, and E. A. Sander, “Substrate Stiffness Affects Human Keratinocyte Colony Formation.,” *Cell. Mol. Bioeng.*, vol. 8, no. 1, pp. 32–50, Mar. 2015.

[443] K. Wang, C. Degerny, M. Xu, and X.-J. Yang, “YAP, TAZ, and Yorkie: a conserved family of signal-responsive transcriptional coregulators in animal development and human disease.,” *Biochem. Cell Biol.*, vol. 87, no. 1, pp. 77–91, Feb. 2009.

[444] M. Liu, S. Zhao, Q. Lin, and X.-P. Wang, “YAP regulates the expression of Hoxa1 and Hoxc13 in mouse and human oral and skin epithelial tissues.,” *Mol. Cell. Biol.*, vol. 35, no. 8, pp. 1449–61, Apr. 2015.

[445] A. G. Clark and D. M. Vignjevic, “Modes of cancer cell invasion and the role of the microenvironment,” *Curr. Opin. Cell Biol.*, vol. 36, pp. 13–22, Oct. 2015.

[446] F. Nallet-Staub, V. Marsaud, L. Li, C. Gilbert, S. Dodier, V. Bataille, M. Sudol, M. Herlyn, and A. Mauviel, “Pro-invasive activity of the Hippo pathway effectors YAP

and TAZ in cutaneous melanoma.," *J. Invest. Dermatol.*, vol. 134, no. 1, pp. 123–32, Jan. 2014.

[447] J. E. Kim, G. J. Finlay, and B. C. Baguley, "The role of the hippo pathway in melanocytes and melanoma.," *Front. Oncol.*, vol. 3, p. 123, Jan. 2013.

[448] Q. Zeng and W. Hong, "The emerging role of the hippo pathway in cell contact inhibition, organ size control, and cancer development in mammals.," *Cancer Cell*, vol. 13, no. 3, pp. 188–92, Mar. 2008.

[449] J. Arnemann, K. H. Sullivan, A. I. Magee, I. A. King, and R. S. Buxton, "Stratification-related expression of isoforms of the desmosomal cadherins in human epidermis.," *J. Cell Sci.*, vol. 104 (Pt 3, pp. 741–50, Mar. 1993.

[450] M. Plessner, M. Melak, P. Chinchilla, C. Baarlink, and R. Grosse, "Nuclear F-actin formation and reorganization upon cell spreading.," *J. Biol. Chem.*, vol. 290, no. 18, pp. 11209–16, May 2015.

[451] Z. Jahed, H. Shams, M. Mehrbod, and M. R. K. Mofrad, "Mechanotransduction pathways linking the extracellular matrix to the nucleus.," *Int. Rev. Cell Mol. Biol.*, vol. 310, pp. 171–220, Jan. 2014.

[452] Q. Zhang, J. N. Skepper, F. Yang, J. D. Davies, L. Hegyi, R. G. Roberts, P. L. Weissberg, J. A. Ellis, and C. M. Shanahan, "Nesprins: a novel family of spectrin-repeat-containing proteins that localize to the nuclear membrane in multiple tissues.," *J. Cell Sci.*, vol. 114, no. Pt 24, pp. 4485–98, Dec. 2001.

[453] A. Schönichen, H. G. Mannherz, E. Behrmann, A. J. Mazur, S. Kühn, U. Silván, C.-A. Schoenenberger, O. T. Fackler, S. Raunser, L. Dehmelt, and M. Geyer, "FHOD1 is a combined actin filament capping and bundling factor that selectively associates with actin arcs and stress fibers.," *J. Cell Sci.*, vol. 126, no. Pt 8, pp. 1891–901, Apr. 2013.

[454] D. Stoffler, B. Feja, B. Fahrenkrog, J. Walz, D. Typke, and U. Aebi, "Cryo-electron tomography provides novel insights into nuclear pore architecture: implications for nucleocytoplasmic transport.," *J. Mol. Biol.*, vol. 328, no. 1, pp. 119–30, Apr. 2003.

[455] M. Beck, F. Förster, M. Ecke, J. M. Plitzko, F. Melchior, G. Gerisch, W. Baumeister, and O. Medalia, "Nuclear pore complex structure and dynamics revealed by cryoelectron tomography.," *Science*, vol. 306, no. 5700, pp. 1387–90, Nov. 2004.

[456] R. Bernad, H. van der Velde, M. Fornerod, and H. Pickersgill, "Nup358/RanBP2 attaches to the nuclear pore complex via association with Nup88 and Nup214/CAN and plays a supporting role in CRM1-mediated nuclear protein export.," *Mol. Cell. Biol.*, vol. 24, no. 6, pp. 2373–84, Mar. 2004.

[457] R. Bernad, D. Engelsma, H. Sanderson, H. Pickersgill, and M. Fornerod, "Nup214-Nup88 nucleoporin subcomplex is required for CRM1-mediated 60 S preribosomal nuclear export.," *J. Biol. Chem.*, vol. 281, no. 28, pp. 19378–86, Jul. 2006.

[458] M. Capelson, Y. Liang, R. Schulte, W. Mair, U. Wagner, and M. W. Hetzer, "Chromatin-bound nuclear pore components regulate gene expression in higher eukaryotes.," *Cell*, vol. 140, no. 3, pp. 372–83, Feb. 2010.

[459] T. U. Schwartz, “Modularity within the architecture of the nuclear pore complex.,” *Curr. Opin. Struct. Biol.*, vol. 15, no. 2, pp. 221–6, Apr. 2005.

[460] M. Fornerod, J. van Deursen, S. van Baal, A. Reynolds, D. Davis, K. G. Murti, J. Fransen, and G. Grosveld, “The human homologue of yeast CRM1 is in a dynamic subcomplex with CAN/Nup214 and a novel nuclear pore component Nup88.,” *EMBO J.*, vol. 16, no. 4, pp. 807–16, Feb. 1997.

[461] E. R. Griffis, S. Xu, and M. A. Powers, “Nup98 localizes to both nuclear and cytoplasmic sides of the nuclear pore and binds to two distinct nucleoporin subcomplexes.,” *Mol. Biol. Cell*, vol. 14, no. 2, pp. 600–10, Feb. 2003.

[462] P. Roth, N. Xylourgidis, N. Sabri, A. Uv, M. Fornerod, and C. Samakovlis, “The Drosophila nucleoporin DNup88 localizes DNup214 and CRM1 on the nuclear envelope and attenuates NES-mediated nuclear export.,” *J. Cell Biol.*, vol. 163, no. 4, pp. 701–6, Nov. 2003.

[463] N. Xylourgidis, P. Roth, N. Sabri, V. Tsarouhas, and C. Samakovlis, “The nucleoporin Nup214 sequesters CRM1 at the nuclear rim and modulates NFkappaB activation in Drosophila.,” *J. Cell Sci.*, vol. 119, no. Pt 21, pp. 4409–19, Nov. 2006.

[464] N. Takahashi, J. W. J. van Kilsdonk, B. Ostendorf, R. Smeets, S. W. M. Bruggeman, A. Alonso, F. van de Loo, M. Schneider, W. B. van den Berg, and G. W. M. Swart, “Tumor marker nucleoporin 88 kDa regulates nucleocytoplasmic transport of NF-kappaB.,” *Biochem. Biophys. Res. Commun.*, vol. 374, no. 3, pp. 424–30, Sep. 2008.

[465] V. B. Andela, A. H. Gordon, G. Zotalis, R. N. Rosier, J. J. Goater, G. D. Lewis, E. M. Schwarz, J. E. Puzas, and R. J. O’Keefe, “NFkappaB: a pivotal transcription factor in prostate cancer metastasis to bone.,” *Clin. Orthop. Relat. Res.*, no. 415 Suppl, pp. S75–85, Oct. 2003.

[466] H. Zhang, J. Schneider, and I. Rosdahl, “Expression of p16, p27, p53, p73 and Nup88 proteins in matched primary and metastatic melanoma cells.,” *Int. J. Oncol.*, vol. 21, no. 1, pp. 43–8, Jul. 2002.

[467] J. Schneider, F. Martínez-Arribas, and R. Torrejón, “Nup88 expression is associated with myometrial invasion in endometrial carcinoma.,” *Int. J. Gynecol. Cancer*, vol. 20, no. 5, pp. 804–8, Jul. 2010.

[468] D. Agudo, F. Gómez-Esquer, F. Martínez-Arribas, M. J. Núñez-Villar, M. Pollán, and J. Schneider, “Nup88 mRNA overexpression is associated with high aggressiveness of breast cancer.,” *Int. J. Cancer*, vol. 109, no. 5, pp. 717–20, May 2004.

[469] Z.-Y. Zhang, Z.-R. Zhao, L. Jiang, J.-C. Li, Y.-M. Gao, D.-S. Cui, C.-J. Wang, J. Schneider, M.-W. Wang, and X.-F. Sun, “Nup88 expression in normal mucosa, adenoma, primary adenocarcinoma and lymph node metastasis in the colorectum.,” *Tumour Biol.*, vol. 28, no. 2, pp. 93–9, Jan. 2007.

[470] Z.-R. Zhao, L.-J. Zhang, Y.-Y. Wang, F. Li, M.-W. Wang, and X.-F. Sun, “Increased serum level of Nup88 protein is associated with the development of colorectal cancer.,” *Med. Oncol.*, vol. 29, no. 3, pp. 1789–95, Sep. 2012.

[471] R. E. Hewitt, A. McMarlin, D. Kleiner, R. Wersto, P. Martin, M. Tsokos, G. W. Stamp, W. G. Stetler-Stevenson, and M. Tsoskas, “Validation of a model of colon cancer progression.,” *J. Pathol.*, vol. 192, no. 4, pp. 446–54, Dec. 2000.

[472] S. Xu and M. A. Powers, “Nuclear pore proteins and cancer.,” *Semin. Cell Dev. Biol.*, vol. 20, no. 5, pp. 620–30, Jul. 2009.

[473] Y. Lüke, H. Zaim, I. Karakesisoglou, V. M. Jaeger, L. Sellin, W. Lu, M. Schneider, S. Neumann, A. Beijer, M. Munck, V. C. Padmakumar, J. Gloy, G. Walz, and A. A. Noegel, “Nesprin-2 Giant (NUANCE) maintains nuclear envelope architecture and composition in skin.,” *J. Cell Sci.*, vol. 121, no. Pt 11, pp. 1887–98, Jun. 2008.

[474] W. Shu, Y. Chen, Q. Wu, R. Li, and G. Cui, “Deguelin represses both the expression of nucleophosmin and some nucleoporins: Nup88 and Nup214 in Jurkat cells.,” *Biol. Pharm. Bull.*, vol. 31, no. 1, pp. 27–32, Jan. 2008.

[475] Q. Liu, N. Pante, T. Misteli, M. Elsagga, M. Crisp, D. Hodzic, B. Burke, and K. J. Roux, “Functional association of Sun1 with nuclear pore complexes.,” *J. Cell Biol.*, vol. 178, no. 5, pp. 785–98, Aug. 2007.

[476] C. Hashizume, H. Nakano, K. Yoshida, and R. W. Wong, “Characterization of the role of the tumor marker Nup88 in mitosis.,” *Mol. Cancer*, vol. 9, p. 119, Jan. 2010.

[477] H. Brustmann and M. Hager, “Nucleoporin 88 expression in normal and neoplastic squamous epithelia of the uterine cervix.,” *Ann. Diagn. Pathol.*, vol. 13, no. 5, pp. 303–7, Oct. 2009.

[478] Y. C. Lussi, I. Hügi, E. Laurell, U. Kutay, and B. Fahrenkrog, “The nucleoporin Nup88 is interacting with nuclear lamin A.,” *Mol. Biol. Cell*, vol. 22, no. 7, pp. 1080–90, Apr. 2011.

[479] M. Sakaki, H. Koike, N. Takahashi, N. Sasagawa, S. Tomioka, K. Arahata, and S. Ishiura, “Interaction between emerin and nuclear lamins.,” *J. Biochem.*, vol. 129, no. 2, pp. 321–7, Feb. 2001.

[480] S. Wang, A. Reuveny, and T. Volk, “Nesprin provides elastic properties to muscle nuclei by cooperating with spectraplakin and EB1,” *J. Cell Biol.*, vol. 209, no. 4, pp. 529–538, May 2015.

[481] H. N. Kha, B. K. Chen, G. M. Clark, and R. Jones, “Stiffness properties for Nucleus standard straight and contour electrode arrays,” *Med. Eng. Phys.*, vol. 26, no. 8, pp. 677–685, Oct. 2004.

[482] A. Vaziri and M. R. K. Mofrad, “Mechanics and deformation of the nucleus in micropipette aspiration experiment.,” *J. Biomech.*, vol. 40, no. 9, pp. 2053–62, Jan. 2007.

[483] J. Swift, I. L. Ivanovska, A. Buxboim, T. Harada, P. C. D. P. Dingal, J. Pinter, J. D. Pajerowski, K. R. Spinler, J.-W. Shin, M. Tewari, F. Rehfeldt, D. W. Speicher, and

D. E. Discher, “Nuclear lamin-A scales with tissue stiffness and enhances matrix-directed differentiation.,” *Science*, vol. 341, no. 6149, p. 1240104, Aug. 2013.

[484] B. A. Sosa, U. Kutay, and T. U. Schwartz, “Structural insights into LINC complexes.,” *Curr. Opin. Struct. Biol.*, vol. 23, no. 2, pp. 285–91, Apr. 2013.

[485] T. P. Driscoll, B. D. Cosgrove, S.-J. Heo, Z. E. Shurden, and R. L. Mauck, “Cytoskeletal to Nuclear Strain Transfer Regulates YAP Signaling in Mesenchymal Stem Cells,” *Biophys. J.*, vol. 108, no. 12, pp. 2783–2793, Jun. 2015.

[486] A. L. Olins, T. V Hoang, M. Zwerger, H. Herrmann, H. Zentgraf, A. A. Noegel, I. Karakesisoglou, D. Hodzic, and D. E. Olins, “The LINC-less granulocyte nucleus.,” *Eur. J. Cell Biol.*, vol. 88, no. 4, pp. 203–14, Apr. 2009.

[487] D. Rajgor, J. A. Mellad, F. Autore, Q. Zhang, and C. M. Shanahan, “Multiple novel nesprin-1 and nesprin-2 variants act as versatile tissue-specific intracellular scaffolds.,” *PLoS One*, vol. 7, no. 7, p. e40098, Jan. 2012.

[488] J. G. Simpson and R. G. Roberts, “Patterns of evolutionary conservation in the nesprin genes highlight probable functionally important protein domains and isoforms.,” *Biochem. Soc. Trans.*, vol. 36, no. Pt 6, pp. 1359–67, Dec. 2008.

[489] E. J. Vlug, R. A. H. van de Ven, J. F. Vermeulen, P. Bult, P. J. van Diest, and P. W. B. Derksen, “Nuclear localization of the transcriptional coactivator YAP is associated with invasive lobular breast cancer.,” *Cell. Oncol. (Dordr).*, vol. 36, no. 5, pp. 375–84, Oct. 2013.

[490] M. Demetriou, I. R. Nabi, M. Coppolino, S. Dedhar, and J. W. Dennis, “Reduced contact-inhibition and substratum adhesion in epithelial cells expressing GlcNAc-transferase V.,” *J. Cell Biol.*, vol. 130, no. 2, pp. 383–92, Jul. 1995.

[491] S. Strunze, M. F. Engelke, I.-H. Wang, D. Puntener, K. Boucke, S. Schleich, M. Way, P. Schoenenberger, C. J. Burckhardt, and U. F. Greber, “Kinesin-1-Mediated Capsid Disassembly and Disruption of the Nuclear Pore Complex Promote Virus Infection,” *Cell Host Microbe*, vol. 10, no. 3, pp. 210–223, Sep. 2011.

[492] Z.-R. Zhao, Z.-Y. Zhang, X.-Q. He, Y.-M. Hu, Y.-F. Tian, L.-J. Zhang, and X.-F. Sun, “Nup88 mRNA overexpression in colorectal cancers and relationship with p53.,” *Cancer Biomark.*, vol. 8, no. 2, pp. 73–80, Jan. 2010.

[493] S. Wälde, K. Thakar, S. Hutten, C. Spillner, A. Nath, U. Rothbauer, S. Wiemann, and R. H. Kehlenbach, “The nucleoporin Nup358/RanBP2 promotes nuclear import in a cargo- and transport receptor-specific manner.,” *Traffic*, vol. 13, no. 2, pp. 218–33, Feb. 2012.

[494] W. Jahr, B. Schmid, C. Schmied, F. O. Fahrbach, and J. Huisken, “Hyperspectral light sheet microscopy.,” *Nat. Commun.*, vol. 6, p. 7990, Jan. 2015.

[495] F. Pampaloni, B.-J. Chang, and E. H. K. Stelzer, “Erratum to: Light sheet-based fluorescence microscopy (LSFM) for the quantitative imaging of cells and tissues.,” *Cell Tissue Res.*, vol. 362, no. 1, p. 265, Oct. 2015.

[496] L. A. Lautscham, C. Kämmerer, J. R. Lange, T. Kolb, C. Mark, A. Schilling, P. L. Strissel, R. Strick, C. Gluth, A. C. Rowat, C. Metzner, and B. Fabry, “Migration in Confined 3D Environments Is Determined by a Combination of Adhesiveness, Nuclear Volume, Contractility, and Cell Stiffness,” *Biophys. J.*, vol. 109, no. 5, pp. 900–913, Sep. 2015.

[497] C. Zhu, X. Wang, H. Hagberg, and K. Blomgren, “Correlation Between Caspase-3 Activation and Three Different Markers of DNA Damage in Neonatal Cerebral Hypoxia-Ischemia,” *J. Neurochem.*, vol. 75, no. 2, pp. 819–829, Jan. 2002.

[498] M. W. Carlson, A. Alt-Holland, C. Egles, and J. A. Garlick, “Three-dimensional tissue models of normal and diseased skin.,” *Curr. Protoc. Cell Biol.*, vol. Chapter 19, p. Unit 19.9, Dec. 2008.

[499] S. Levenberg, A. Yarden, Z. Kam, and B. Geiger, “p27 is involved in N-cadherin-mediated contact inhibition of cell growth and S-phase entry,” *Oncogene*, vol. 18, no. 4, pp. 869–876, Feb. 1999.

[500] K. Polyak, J. Y. Kato, M. J. Solomon, C. J. Sherr, J. Massague, J. M. Roberts, and A. Koff, “p27Kip1, a cyclin-Cdk inhibitor, links transforming growth factor-beta and contact inhibition to cell cycle arrest.,” *Genes Dev.*, vol. 8, no. 1, pp. 9–22, Jan. 1994.

[501] C. Dietrich, K. Wallenfang, F. Oesch, and R. Wieser, “Differences in the mechanisms of growth control in contact-inhibited and serum-deprived human fibroblasts.,” *Oncogene*, vol. 15, no. 22, pp. 2743–7, Nov. 1997.

[502] T. Fuse, M. Tanikawa, M. Nakanishi, K. Ikeda, T. Tada, H. Inagaki, K. Asai, T. Kato, and K. Yamada, “p27Kip1 expression by contact inhibition as a prognostic index of human glioma.,” *J. Neurochem.*, vol. 74, no. 4, pp. 1393–9, Apr. 2000.

[503] H. R. Gatla, B. Singha, V. Persaud, and I. Vancurova, “Evaluating cytoplasmic and nuclear levels of inflammatory cytokines in cancer cells by western blotting.,” *Methods Mol. Biol.*, vol. 1172, pp. 271–83, Jan. 2014.

[504] S. Piccolo, S. Dupont, and M. Cordenonsi, “The biology of YAP/TAZ: hippo signaling and beyond.,” *Physiol. Rev.*, vol. 94, no. 4, pp. 1287–312, Oct. 2014.

[505] B. A. Sosa, A. Rothballer, U. Kutay, and T. U. Schwartz, “LINC complexes form by binding of three KASH peptides to domain interfaces of trimeric SUN proteins.,” *Cell*, vol. 149, no. 5, pp. 1035–47, May 2012.

[506] “The Cytoplasm and Cellular Organelles · Anatomy & Physiology.” [Online]. Available: http://philschatz.com/anatomy-book/contents/m46023.html. [Accessed: 15-Sep-2015].

[507] J. A. Segre, “Epidermal barrier formation and recovery in skin disorders.,” *J. Clin. Invest.*, vol. 116, no. 5, pp. 1150–8, May 2006.

[508] S. Cartwright and I. Karakesisoglou, “Nesprins in health and disease.,” *Semin. Cell Dev. Biol.*, vol. 29, pp. 169–79, May 2014.

[509] J. Pascual, M. Pfuhl, D. Walther, M. Saraste, and M. Nilges, “Solution structure of the spectrin repeat: a left-handed antiparallel triple-helical coiled-coil.,” *J. Mol. Biol.*, vol. 273, no. 3, pp. 740–51, Oct. 1997.